39th Cement and Concrete Science Conference 2019

9th – 10th September 2019

Editors:

Richard J Ball, Barrie Dams, Veronica Ferrandiz-Mas, Xinyuan Ke, Kevin Paine, Mark Tyrer, Peter Walker

UNIVERSITY OF BATH bre cicm IOM3 The Institute of Materials, Minerals and Mining

39th Cement and Concrete Science Conference

9th – 10th September 2019. Held at University of Bath, UK

BRE Centre for Innovative Construction Materials,

Department of Architecture & Civil Engineering.

Published by University of Bath in association with Cementitious Materials Group,

Institute of Materials Minerals and Mining, London, UK

https://www.iom3.org/cementitious-materials-group

Membership enquiries: membership@iom3.org or call +44 (0)1782 221717

ISBN 978-0-86197-201-2

Remembering

Mohammed Imbabi

We mark the loss of a friend and colleague, Dr Mohammed Imbabi, who sadly passed away at his home in Aberdeen on August 10, 2019. Mohammed was born in Khartoum, Sudan on February 28, 1955. He studied civil engineering at the University of Khartoum and attained his Bachelors degree in 1978. He was the convenor of our 2015 CCS conference in Aberdeen and an accomplished researcher in the field of cement science. An active committee member and Fellow of the Institute, Mohammed led work of carbon capture from the cement industry and will be greatly missed.

39th Cement and concrete Science Conference

9th-10th September 2019

Welcome to the University of Bath

On behalf of the conference organising committee, I warmly welcome the delegates and speakers to the 39th annual Cement and Concrete Science Conference. The conference is hosted by the BRE Centre for Innovative Structural Materials, Department of Architecture and Civil Engineering at the University of Bath and organised by the *Cementitious Materials* special interest group of the Institute of Materials, Minerals and Mining.

The Cement and Concrete Science Conference series is an annual event that aims to bring together academic and industrial partners with an interest in the development of cement and concrete research. In recent years the conference has been held at Imperial College, London (2011), Queen's University Belfast (2012), University of Portsmouth (2013), University of Sheffield (2014), University of Aberdeen (2015), The Royal College of Music and Drama, Cardiff (2016), University College London (2017) and Coventry University (2018). It provides an important opportunity for researcher groups to share their findings, form partnerships and identify future research directions.

This year the programme includes 2 keynote lectures, 48 oral presentations and 11 poster presentations.

The conference series is to encourage and promote participation of student researchers, providing an opportunity to present their work and network with other researchers and industrialists. This year we are delighted to welcome a truly international cohort of researchers and to congratulate all for the high quality of the submissions.

Finally we would like to thank all who have contributed to the conference and in particular the companies and organisations who have generously provided sponsorship.

We hope you enjoy your time in Bath.

Richard Ball, Convenor 39CCS, on behalf of the conference committee.

We hope to see everyone at the University of Sheffield in 2020.

Organising and Scientific Committee

Conference Chair

Dr Richard Ball, University of Bath

Local organising committee

Barrie Dams, University of Bath

Dr Veronica Ferrandiz-Mas, University of Bath

Dr Xinyuan Ke, University of Bath

Dr Kevin Paine, University of Bath

Professor Peter Walker, University of Bath

Scientific committee

Prof. Yun Bai, University College London

Dr Stephanie Barnett, University of Portsmouth

Prof. Leon Black, University of Leeds

Dr Steve Brooks, Ardex

Robert Cather, Industrial Consultant

Prof. Chris Cheeseman, Imperial College London

Dr Andrew Dunster, BRE

Dr Chris Goodier, Loughborough University

Dr Riccardo Maddalena, Cardiff University

Dr Andrew McIntosh, Banah UK

Dr Gary Perkins, University of South Wales

Dr Giovanni Pesce, Northumbria University

Prof. John Provis, University of Sheffield

Prof. Ian G Richardson, University of Leeds

Dr Mark Russell, Queens University Belfast

Prof. Julia Stegemann, University College London

Prof. Mark Tyrer, Coventry University

Dr Renhe Yang, Fosroc

Sponsors and Exhibitors

The Institute of Concrete Technology

NETZSCH

Table of Contents

39th Cement and Concrete Science Conference
9-10th September 2019
University of Bath
Paper Number 001

Fabrication of new geopolymer binder from demolition waste and ignimbrite slits for application in the construction industry

D.L. Mayta-Ponce, P. Soto-Cruz and F.A. Huamán-Mamani
Grupo de Investigación en Ciencia y Tecnología de Materiales-CITEM, Universidad Católica San Pablo, Arequipa, Perú.

ABSTRACT

Geopolymeric mortars with volumetric fractions of 0.6:1:0.3 for a binder powder, fine sand and sodium hydroxide solution (12M), respectively; have been fabricated by mixing the solid materials and the subsequent addition of sodium hydroxide solution 12M to form a workable paste, to later be cured for 28 days at room temperature. The microstructures of the fabricated materials reveal the existence of two phases with notable difference, one continuous to the geopolymer binder phase and another discontinuous of fine sand particles agglutinated by the binder phase. Mechanical compression tests are performed at a constant compression rate of 0.05 mm/min and at temperatures ranged from room temperature to 500°C. The mechanical results are ranged from 19 and 69 MPa for all the materials studied. On the other hand, there was an increase in mechanical resistance up to test temperatures of 200°C and the progressive reduction of resistance at temperatures above 200°C, with a fragile-ductile transition zone between 400 and 500°C and completely ductile behavior from test temperatures of 500°C.

1. INTRODUCTION

In recent years, construction in Peru has had significant growth, which has generated a greater demand for construction materials. Traditional building materials such as Portland cement (PC) and clay bricks need a large amount of raw material to be fabricated. The PC, for example, plays a leading role in construction, because it is the main ingredient of mortars and concrete, however, the production of PC requires large amounts of raw material and generates a significant amount of CO2. It has been reported that 1.5 T of raw material is required to produce 1 T of PC and 0.9 T of CO2 is released into the atmosphere [1,2]. The knowledge of the harmful effects of global warming on our planet and a greater environmental awareness has allowed us to promote the search for alternative environmentally friendly construction materials [3], and geopolymeric materials are a very promising Eco-friendly alternative [4].

Repairs and/or infrastructure improvements generate a huge amount of concrete waste, mortar and clay bricks (construction and demolition waste - C&D), in addition to the difficulty of finding a suitable place for the disposal of C&D. There are several works based on the recycling of C&D, but most of them focus on its use as an aggregate of new mortars and concrete for non-structural applications [5-7]. The difference between using recycled C&D aggregate and natural aggregate is that the first one has greater water absorption, abrasion loss and crushing capacity, but lower bulk density, the use of C&D recycled aggregate in the fabrication of new concrete and mortars generally leads to materials with lower resistance and durability, therefore, the use of recycled aggregate is quite limited. Other researchers have tried to re-clinker the cement coming from the C&Ds to obtain a new cement, this process includes stages of separation of the cement and the aggregates, and re-clinkering that consumes a large amount of energy and, therefore, generated large amounts greenhouse gases [8,9]

On the other hand, the city of Arequipa is knowing as the white city, because its heritage buildings were made using a rock known as “SILLAR” (ignimbrite). The ignimbrite is an igneous rock produced by the sudden cooling of magma, composed mainly of rhyolite, andesite and dacite, currently it is used as a construction material because it can be easily extracted from quarries [10]. However, the uncontrolled exploitation of this material has generated the accumulation of large amounts of dust and slits in the quarries, limiting the consolidation of important tourism projects.

2. EXPERIMENTAL PROCEDURE

Geopolymeric mortars were prepared from four types of raw materials: ignimbrite, demolition mortar, calcined clay and commercial fine sand. The ignimbrite was collected from the area called “Quebrada de Añashuayco” (Arequipa-Peru), while the demolition mortar and calcined clay were obtained from a demolition zone near the city of Arequipa. The four types of raw materials were ground and sieved by ASTM No. 140 mesh (mesh

size of 106 microns). In parallel, a solution of sodium hydroxide with 12 molar concentration was prepared.

The actual density, particle size distribution, crystalline phases and microstructures of the raw materials were determined by helium pycnometry, laser diffraction granulometry, X-ray diffraction and scanning electron microscopy, respectively, performed at the Centro de Investigación, Tecnología e Innovación of the Universidad de Sevilla - CITIUS (Spain).

For the preparation of geopolymeric mortars, volumetric fractions in 0.6:1:0.3 ratio of raw material (ignimbrite, demolition mortar or calcined clay), fine sand and 12M sodium hydroxide solution were measured separately. The powder materials (binder powder and fine sand) were dry mixed for 10 minutes and then the sodium hydroxide solution was added and mixed for an additional 10 minutes. Workable pastes were obtained which were pressed uniaxially for 5 minutes in a cylindrical mold of 20 mm diameter and then were dried, first, hermetically for 48 hours and then at room temperature for 28 days.

Prismatic samples of 5x5x10 mm were cut from dry geopolymeric cylinders for mechanical testing. Uniaxial compression tests were carried out at different temperatures, from room temperature to 500°C in air and at a constant compression rate of 0.05 mm/min, corresponding to an initial deformation rate of 8 x 10^{-5}. The data obtained of strength and position were analyzed in stress vs. strain curves.

3. RESULTS AND DISCUSSION

Table 1 shows the real density data obtained for the four types of raw materials, which were used to calculate the mass fractions of the mixtures prepared in this research.

Table 1. Determination of the real density of the starting materials.

Raw material	Mass (g.)	Volume (cm^3)	Average real density ($g./cm^3$)
Ignimbrite	5.0702	2.0466	2.4774
Calcined clay	6.2478	2.3502	2.6584
Demolition mortar	6.3599	2.4802	2.5643
Fine sand	7.1178	2.6394	2.6967

Figure 1 shows the distribution of particle sizes for the four types of starting materials, where the average particle size values for the ignimbrite, calcined clay, demolition mortar and fine sand are: 61, 68, 64 and 83 microns, respectively.

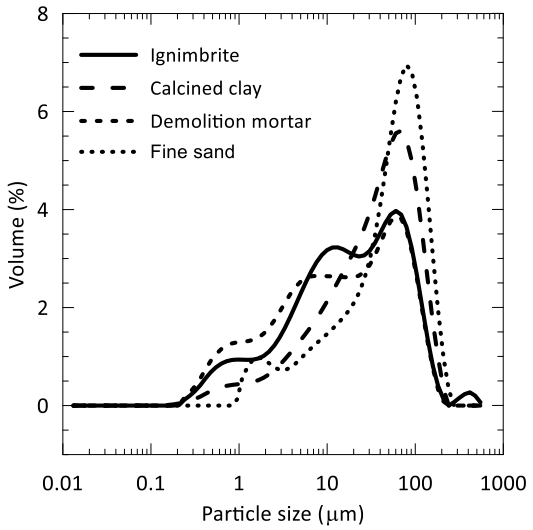

Figure1. Particle size distribution for raw material powders.

On the other hand, Figure 2 shows the typical microstructure of fabricated geopolymeric mortars, which consists of a continuous phase of geopolymeric binder in dark contrast and a discontinuous phase of fine sand particles in gray contrast.

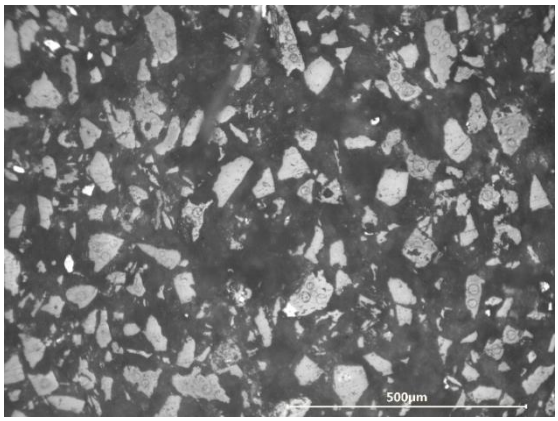

Figure 2. Typical micrograph of a geopolymeric mortar sample obtained from ignimbrite powder.

From the X-ray diffraction spectra, the presence of various crystalline powder phases of the raw materials could be identified

- **Ignimbrite:** *Albite* ($NaAlSi_3O_8$), *Muscovite* ($KAl_3Si_3O_{10}(OH)_2$), *Cristobalite* (SiO_2) and *Microcline* ($KAlSi_3O_8$)
- **Demolition mortar:** *Quartz* (SiO_2), *Albite* ($NaAlSi_3O_8$), *Muscovite* ($KAl_3Si_3O_{10}(OH)_2$), *Cristobalite* (SiO_2), *Actinolite* ($Ca_2(Mg,Fe^{2+})_5Si_8O_{22}(OH)_2$), *Anorthite* ($CaAl_2Si_2O_8$), *Portlandite* ($Ca(OH)_2$), *Calcite* ($Ca(CO)_3$) y *Chlorite* ($(Mg,Al)_6(Si,Al)_4O_{10}(OH)_8$).
- **Calcined clay:** *Quartz* (SiO_2), *Albite* ($NaAlSi_3O_8$), *Muscovite* ($KAl_3Si_3O_{10}(OH)_2$), *Cristobalite* (SiO_2), *Actinolite* ($Ca_2(Mg,Fe^{2+})_5Si_8O_{22}(OH)_2$) y *Anatase* ($TiO_2$) para el polvo de arcilla calcinada.

- **Fine sand:** *Albite* ($NaAlSi_3O_8$), *Muscovite* ($KAl_3Si_3O_{10}(OH)_2$), *Cristobalite* (SiO_2), *Actinolite* ($Ca_2(Mg,Fe^{2+})_5Si_8O_{22}(OH)_2$) y *Anorthite* ($CaAl_2Si_2O_8$)

Figures 3 to 5 show stress vs. strain curves at room temperature for the three types of geopolymeric mortars studied. The maximum and minimum stress values are in the range of 19 to 69 MPa.

These preliminary results show the potential for industrial application of these new construction materials, at least according of Peruvian regulations.

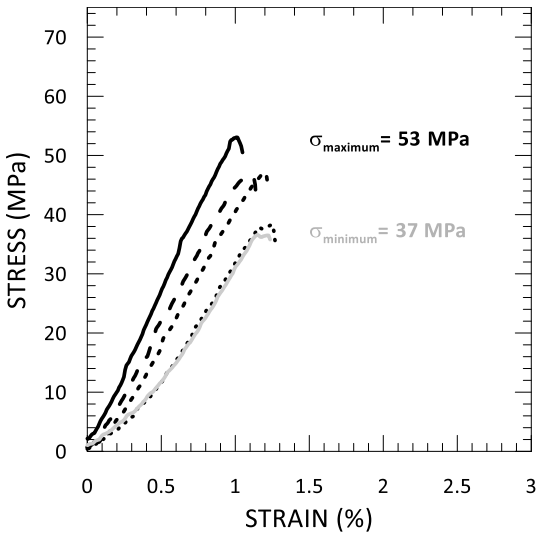

Figure 3. Stress vs strain curves for geopolymeric mortar derived from ignimbrite powder and deformed in air at room temperature.

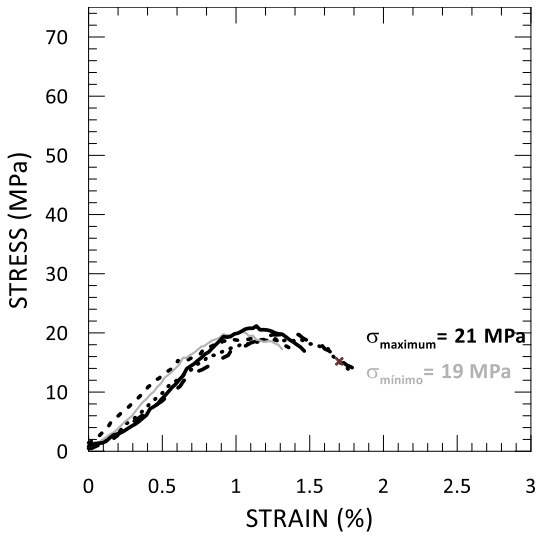

Figure 4. Stress vs strain curves for geopolymeric mortar derived from demolition mortar and deformed in air at room temperature.

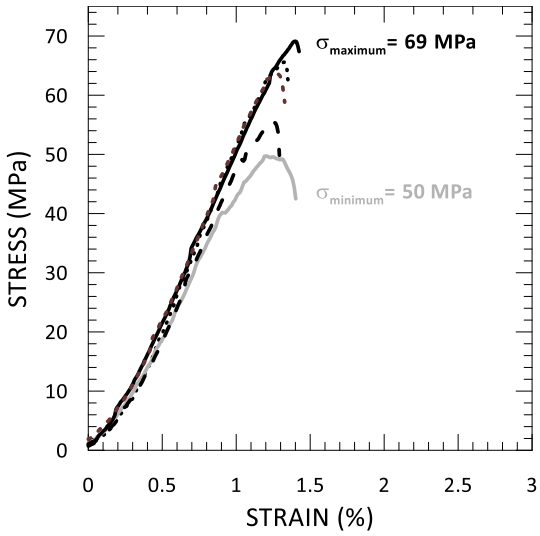

Figure 5. Stress vs strain curves for geopolymeric mortar derived from calcined clay and deformed in air at room temperature.

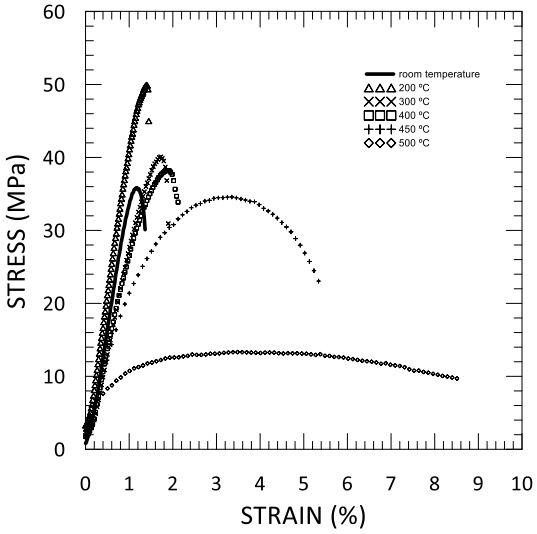

Figura 6. Stress vs strain curves for geopolymeric mortar derived from ignimbrite powder and deformed in air at room temperature, 200 ºC. 300 ºC, 400 ºC, 450 ºC and 500 ºC

Figure 6 shows stress vs. strain curves obtained at test temperatures from room temperature to 500°C in air for samples of geopolymeric mortar derived from ignimbrite powder. The results reveal an increase in maximum resistance with a test temperature up to 200°C. From test temperatures of 200°C onwards a progressive reduction of the maximum resistance values occurs, accompanied by a transition from totally fragile to semi-ductile behavior.

At a test temperature of 450°C a semi-ductile behavior is noticed, with deformation of the sample of up to 5% without catastrophic failure, unlike the sample tested at 300°C, where the fault is clearly fragile with deformation of 1.8% before catastrophic failure.

At a test temperature of 500°C, the sample shows a semi-ductile behavior with a deformation of up to 9% without fracture.

From the curves of Figure 6 and considering the typical microstructure of the materials studied in this research, it is suggested that the fragile-semi-ductile transition is due to the softening of the geopolymeric aligant phase, which allows the movement of individual particles of fine sand in the continuous softened phase. This possible deformation mechanism is sensitive (accelerates) to the increase in temperature, as shown in Figure 6.

4. CONCLUSIONS

- Geopolymeric mortars derived from demolition waste have been successfully fabricated by mixing solid materials, adding 12 molar sodium hydroxide solution, and hardening at room temperature.
- The typical microstructure of the geopolymeric mortars studied consists of a discontinuous phase of fine sand embedded in a continuous one of geopolymeric binder.
- The increase in temperature from room temperature to 200°C produces an increase in the maximum resistance values.
- Test temperatures greater than 200°C produce a progressive decrease in mechanical resistance, which is accompanied by a fragile-semi-ductile transition.
- The mechanism of deformation suggested to explain the fragile-semi-ductile transition noticed in the materials studied is the softening of the geopolymeric binder phase with the increase in temperatures.

REFERENCES

[1] Ahmari S, Ren X, Toufigh V, Zhang L. Production of geopolymer binder from blended waste concrete powder and fly ash. Constr Build Master 2012; 35: 718-729.

[2] Choi H, Lim M, Choi H, Kitagaki R, Noguchi T. Using microwave heating to completely recycle concrete. J Environ Prot 2014; 5: 583-596.

[3] McKelvey D, Sivakumar V, Bell A, McLaverty G. Shear strength of recycled construction materials intended for use in vibro ground improvement. Ground Improve 2002; 6(2): 59–68.

[4] Duxson P, Fernandez-Jimenez A, Provis JL, Lukey GC, Palomo A, van Deventer JSJ.
Geopolymer technology: the current state of the art. Journal of Materials Science 2007;42(9):2917-2933.

[5] Hack DR, Bryan DP. Aggregates. Industrial Minerals and Rocks, Kogel EK, Trivedi NC, Barker JM, Krukowski ST (eds), 7th Edition, Littleton, Colorado, Society for Mining, Metallurgy and Exploration; 2006. p. 1105-1119.

[6] Khatib JM. Sustainability of construction materials. Cambridge (UK): Woodhead Publishing Limited; 2009.

[7] Arulrajah A, Piratheepan J, Disfani MM, Bo MW. Geotechnical and geoenvironmental properties of recycled construction and demolition materials in pavement subbase applications. J Mater Civ Eng 2013; 25(8): 1077–1088.

[8] Tomosawa F, Noguchi T. Towards completely recyclable concrete. In: Sakai K, editor.
Integrated design and environmental issues in concrete technology. E & FN Spon, London,
UK; 1996. p. 263–372.

[9] Costes JR, Majcherczyk C, Binkhorst IP. Total Recycling of Concrete 2007; http://omogine.blogspot.com/.

[10] Aygun Z and Aygun M. (2016) Spectroscopic analysis of Ahlat stone (ignimbrite) and pumice formed by
volcanic activity. Spectrochimica Acta Part A: Molecular and Biomolecular spectrocopy. ELSEVIER. Vol, 166:
73 – 78.

ACKNOWLEDGEMENTS

This work was supported by the project no. 106-2017–FONDECYT.
Consejo Nacional de Ciencia, Tecnología e Innovación Tecnológica and Servicio Nacional de Capacitación para la Industria de la Construcción, Peru.

39th Cement and Concrete Science Conference **Paper Number 002**
9-10th September 2019
University of Bath

Waste-based alkali activated materials for wastewater treatment

R.M. Novais, J. Carvalheiras, G. Ascensão, D.M. Tobaldi, M.P. Seabra and J.A. Labrincha
Department of Materials and Ceramic Engineering / CICECO-Aveiro Institute of Materials, University of Aveiro, Portugal

G. Ascensão
Italcementi S.p.A, HeidelbergCement group, via Stezzano, 87, 24126, Bergamo, Italy

ABSTRACT

Alkali-activated materials, also known as geopolymers, are a class of binders that have emerged as an excellent alternative to the use of Portland cement. However, the geopolymers full potential has yet to be fully exploited. A key driver to foster the use of geopolymers is by extending their application range beyond those where Portland cement can be applied. Wastewater treatment is vital to mitigate the distressing worldwide water scarcity. The Organization for Economic Co-operation and Development (OECD) predicts that in the next 30 years ~40% of the world's population will live in areas with extreme water scarcity. In this context, new, low cost and highly efficient materials must be developed. One stimulating approach is the use of bulk-type geopolymeric adsorbents. These novel materials can be easily handled and installed in packed beds without the need for expensive support materials. In this work, highly porous geopolymeric monoliths and spheres were used to extract methylene blue (a common dye in industrial effluents) from synthetic wastewaters. Very high methylene blue uptake by the monoliths and the spheres was observed, surpassing several literature studies using powdered geopolymeric adsorbents, which demonstrates the huge potential of using bulk-type (not powders) adsorbents for wastewater treatment.

1. INTRODUCTION

Alkali-activated materials are binders, which have been emerging as a promising alternative to the use of Portland cement due to their much lower embodied CO_2, provided that appropriate mixture design is employed (Assi et al., 2018). Nevertheless, these materials present other remarkable properties that might endow their use in less investigated, but high added-value, applications such as thermal insulators (Feng et al, 2015; Novais et al., 2018a), pH regulators (Novais et al, 2018b; Novais et al, 2019), adsorbents (Al-Zboon et al, 2011; Novais et al., 2016d), and catalysts (Alzeer and MacKenzie, 2018).

Water scarcity is probably the major concern of this millennium and according to recent estimations by the OECD will reach unprecedented levels in the next 30 years. By 2050, over 40% of the world population is expected to live in areas with extreme water paucity. In this context, the development of effective and low cost technologies for wastewater depollution is paramount.

Adsorption is widely considered as the most effective and simple technology for wastewater treatment, being activated carbon the benchmark adsorbent material. However, despite the remarkable adsorption potential of this material, it's very high production cost has led to extensive research for lower cost alternatives.

One promising possibility could be the use of alkali activated materials as low cost and environmental friendly adsorbents. In fact, these materials can be synthesized using mainly/solely waste materials as solid precursors, and they can set at room temperature, thus preventing the use of high cost and energy demanding thermal steps, such as those needed to produce activated carbons.

The possibility of using alkali-activated materials as adsorbents has only recently been investigated. However, most of the studies were focused on the use of powders whose recovery after use is challenging, and adds cost to wastewater treatment systems. In this study, an innovative and safer alternative is described, the use of bulk-type (not powders) adsorbents. These innovative materials might be directly used in wastewater treatment systems without the need for expensive support materials, thus simplifying the wastewater treatment process.

2. EXPERIMENTAL CONDITIONS

2.1 Materials

Metakaolin (Argical M1200S; Univar) and biomass fly ash waste were used as precursors, while a mixture of sodium hydroxide and sodium silicate was used as activating solution.

Two different foaming agents were employed: hydrogen peroxide (to produce the monoliths) and sodium dodecyl sulfate (to produce the spheres).

2.2 Geopolymer synthesis

The geopolymer monoliths were prepared following previous investigations by the authors (Novais et al., 2016a). Briefly, 66 wt.% of fly ash and 33% of metakaolin were mixed with the activating solution for 10 min. Then, two different amounts of foaming agent (0.11 and 0.57 wt.%) were added to the slurry and mixed for 2 min.

The geopolymer spheres were prepared through suspension solidification procedure, described elsewhere (Novais et al., 2017). In this work, equal amounts of fly ash and metakaolin were added to the activating solution, and mechanically mixed to produce the slurry. Then sodium dodecyl sulfate was added as foaming agent.

After synthesis the monoliths and the spheres were cured at 40 ºC for 24 h, and then demoulded and cured at room temperature until the adsorption tests (28 day).

2.3 Methylene blue adsorption tests

The dye extraction from the synthetic wastewater was evaluated by using different adsorbent bodies, namely cylindrical monoliths (d = 22 mm and l = 3 mm) and spheres (d = 2.6 mm). The bodies were immersed in 200 mL of a specified methylene blue concentration, and then magnetically stirred during a predetermined period of time at room temperature.

The amount of dye adsorbed by the porous geopolymers was calculated by using the following equation:

$$q_e = \frac{(C_0 - C_e)}{m} \times V$$

where q_e is the dye uptake by the adsorbent (mg/g), C_0 is the dye initial concentration (mg/g), C_e the dye concentration after the adsorption (mg/g), V is the solution volume (L), and m is the adsorbent mass (g).

The dye removal efficiency (E) was determined using the following equation:

$$\mathrm{E}\ (\%) = \frac{\mathrm{C_0} - \mathrm{C_e}}{\mathrm{C_0}} \times 100$$

2.4 Materials characterization

The geopolymers microstructure was studied by using scanning electron microscopy (SEM – Hitachi S4100).

The methylene blue adsorption by the porous geopolymers (monoliths and spheres) was evaluated by determining the absorbance of the liquid solution after the adsorption tests in a spectrometer (Shimadzu UV-3100, JP) at a λ = 664 nm.

3. RESULTS AND DISCUSSION

3.1. Geopolymer monoliths

Fig. 1 shows the microstructure of the porous geopolymeric monoliths. The bodies' porosity can be easily tuned by modifying the foaming agent amount, higher amounts significantly increasing the specimens' porosity. The apparent density of the lower porosity samples is 1.19 g/cm^3, while their higher porosity counterparts show much lower density (0.39 g/cm^3). The samples' total porosity, as well as the nature of the pores (open or closed), are expected to strongly affect the specimens' adsorption behavior.

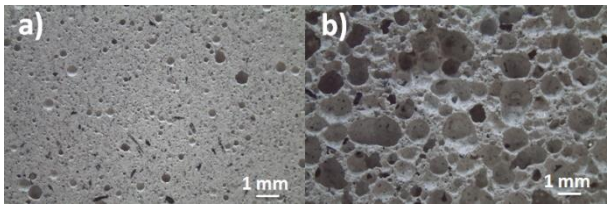

Figure 1. Digital photographs of the porous monoliths exhibiting different total porosities: a) 41% and b) 81%.

To evaluate the influence of sorption time on monoliths removal efficiency, the bodies were immersed in synthetic wastewaters containing different concentration of methylene blue. This way, the influence of the dye initial concentration is also clarified. Fig. 2 shows very high initial sorption occurring in the first ten hours, while afterwards a slower pace is observed, until a plateau is reached at ~30 h, this being the equilibrium time. Fig. 2 also shows that the removal efficiency decreases as the dye C_0 rises. This behavior is attributed to the decrease in the number of available active sites when the methylene concentration increases.

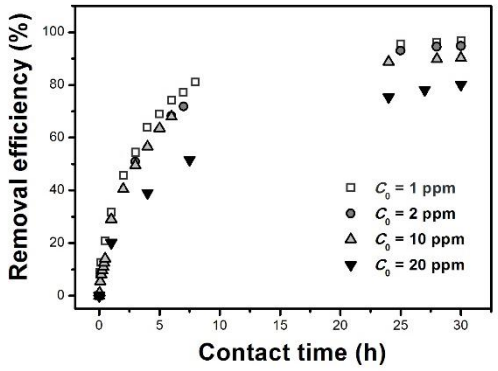

Figure 2. Influence of contact time on the methylene blue removal efficiency by the lower porosity (41%) geopolymer monoliths.

Fig. 3 presents the dyes uptake and removal efficiency by the monolithic bodies. When the dye initial concentration increases the uptake of the pollutant by the monoliths strongly increases for both monoliths. The specimens' porosity crucially affected the dyes uptake, the maximum uptake being 15.35 mg/g (C_0 =50 ppm) for the higher porosity bodies and 5.40 mg/g for the lower porosity specimens.

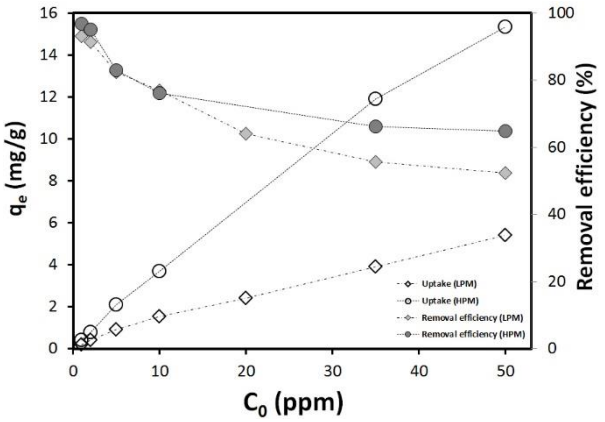

Figure 3. Methylene blue uptake and removal efficiency by the lower (LPM) and higher (HPM) porosity geopolymer monoliths.

3.2. Geopolymer spheres

Fig. 4 presents a representative optical and SEM micrograph of the geopolymers spheres. The spheres have a diameter of around 2.6 mm, which may allow their direct use in packed beds without the need of support materials, such as those required for powdered materials. The spheres surface is smooth and contains pores that may allow the dye diffusion into the specimens.

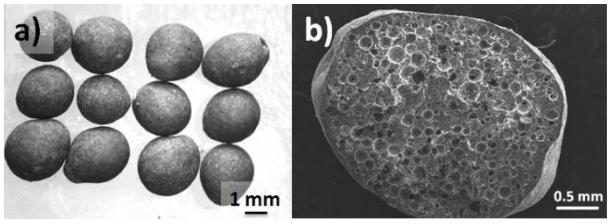

Figure 4. Optical (a) and SEM (b) characterization of the geopolymer spheres.

Fig. 5 shows the influence of contact time on the pollutants removal efficiency by the porous mm size spheres. Once again, fast methylene blue sorption is observed, however, the sorption by the spheres is faster that that observed when using the

monoliths. In fact, in the first five hours 83% removal efficiency was observed when using the spheres (C_0 =50 ppm), while much lower values where seen with the monoliths (65% removal efficiency) despite the higher contact time (24 h). This feature is attributed to the expected higher specific surface area of the spheres.

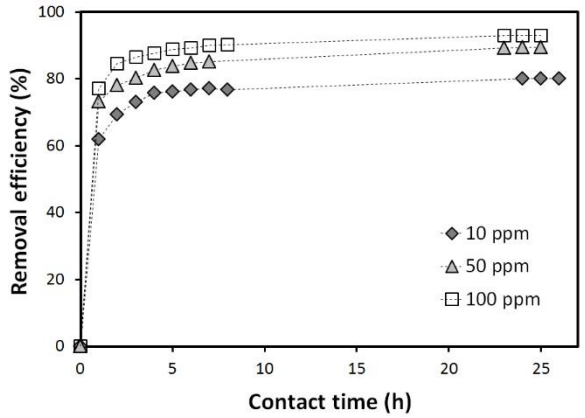

Figure 5. Influence of contact time on the methylene blue removal efficiency by the geopolymer spheres (adsorbent dose: 1.5 g).

Fig. 6 illustrates the influence of the dyes initial concentration on the uptake and removal efficiency by the porous spheres. It should be highlighted that the dyes initial concentrations where much higher than those used for the monoliths, and this is explained by their superior adsorption capacity. As shown, a major increase in the dyes uptake from 1.1 to 30.1 mg/g when the C_0 jumped from 10 to 250 ppm was observed. Interestingly, the removal efficiency increased from 82.3 to 94.3% when the C_0 varied from 10 to 125 ppm, and then slightly decreased to 90.3% for dyes concentrations higher than 200 ppm.

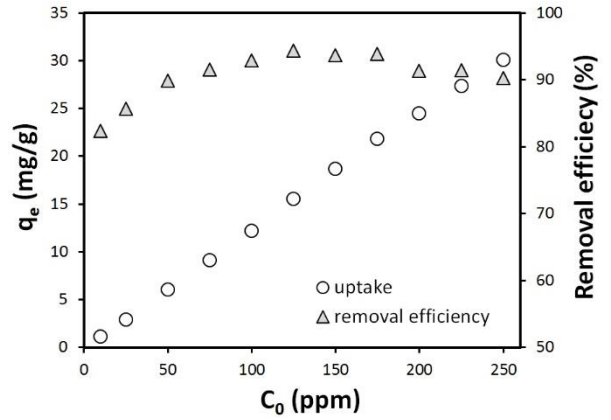

Figure 6. Influence of methylene blue initial concentration on the pollutant uptake and removal efficiency by the geopolymer spheres (adsorbent dose: 1.5 g; contact time: 24 h).

3.3. Performance comparison between the monolithic and the spherical adsorbents with other values reported in literature for powdered geopolymer adsorbents

A comparison between the maximum methylene blue uptake shown by the monoliths and the spheres with other reported values for powdered adsorbents is shown in Fig. 7. The spheres show a twofold increase in the dyes uptake in comparison with the monoliths (30.1 mg/g rather than 15.4). Interestingly, the spheres surpass several other studies in which powdered geopolymers were used which demonstrate their huge potential as dye adsorbent material.

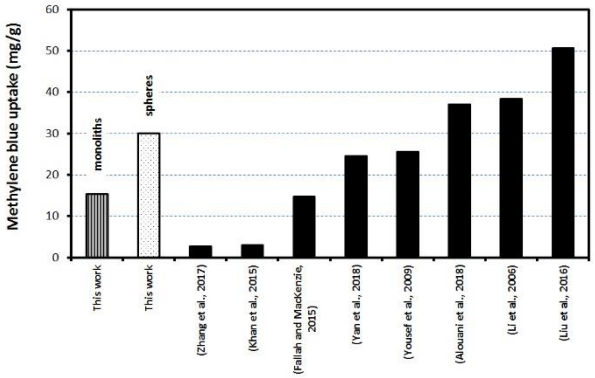

Figure 7. Methylene blue uptake for various geopolymer adsorbents reported in literature. Black bars correspond to powdered geopolymer adsorbents.

4. CONCLUSIONS

In this study the possibility of using bulk-type adsorbents for extracting methylene blue from synthetic wastewaters was evaluated. The cylindrical monoliths showed a maximum dye uptake of 15.4 mg/g, while the porous mm-size spheres showed roughly a twofold increase (30.4 mg/g). These are very interesting results suggesting that the use on bulk-type adsorbents (not powders) for wastewaters treatment is feasible.

ACKNOWLEDGEMENTS

R.M. Novais wishes to thank FCT (Portuguese Foundation for Science and Technology) for supporting his work (researcher grant Ref. CEECIND/00335/2017). This work was developed within the scope of the project CICECO-Aveiro Institute of Materials, FCT Ref. UID/CTM/50011/2019, financed by national funds through the FCT/MCTES. G. Ascensão collaboration with this work was performed before his integration in the NEW-MINE project.

REFERENCES

Alouani, M. EL, Alehyen, S., Achouri, M. EL, Taibi, M., 2018. Removal of Cationic Dye – Methylene Blue- from Aqueous Solution by Adsorption on Fly Ash-based Geopolymer. J. Mater. Environ. Sci. 9:32–46.

Al-Zboon, K., Al-Harahsheh, M.S., Hani, F.B., 2011. Fly ash-based geopolymer for Pb removal from aqueous solution. Journal of Hazardous Materials, 188:414–421.

Alzeer, M.I.M., MacKenzie, K.J.D., 2018. Synthesis and Catalytic Properties of New Sustainable Aluminosilicate Heterogeneous Catalysts Derived from Fly Ash. ACS Sustain. Chem. Eng., 6:5273–5282.

Assi, L., Carter, K., Deaver, E., Anay, R., Ziehl, P., 2018. Sustainable concrete: building a greener future. Journal of Cleaner Production 198:1641-1651.

Falah, M., MacKenzie, K.J.D., 2015. Synthesis and properties of novel photoactive composites of P25 titanium dioxide and copper (I) oxide with inorganic polymers. Ceram. Int., 41:13702–13708

Feng, J., Zhang, R., Gong, L., Li, Y., Cao, W., Cheng, X., 2015. Development of porous fly ash-based geopolymer with low thermal conductivity. Materials and Design, 65:529–533.

Khan, M.I., Min, T.K., Azizli, K., Sufian, S., Ullah, H., Man, Z., 2015. Effective removal of methylene blue from water using phosphoric acid based geopolymers: Synthesis, characterizations and adsorption studies. RSC Adv., 5: 61410–61420.

Li, L., Wang, S., Zhu, Z., 2006. Geopolymeric adsorbents from fly ash for dye removal from aqueous solution. J. Colloid Interface Sci., 300:52–59.

Liu, Y., Yan, C., Zhang, Z., Gong, Y., Wang, H., Qiu, X., 2016. A facile method for preparation of floatable and permeable fly ash-based geopolymer block. Mater. Lett., 185:370–373.

Novais, R.M., Ascensão, G., Ferreira, N., Seabra, M.P., Labrincha, J.A., 2018a. Influence of water and aluminium powder content on the properties of waste-containing geopolymer foams. Ceramics International, 44:6242–6249.

Novais, R.M., Buruberri, L.H., Seabra, M.P., Bajare, D., Labrincha, J.A., 2016a. Novel porous fly ash-containing geopolymers for pH buffering applications. Journal of Cleaner Production, 124:345-404.

Novais, R.M., Buruberri, L.H., Seabra, M.P., Labrincha, J.A., 2016b. Novel porous fly-ash containing geopolymer monoliths for lead adsorption from wastewaters. Journal of Hazardous Materials, 318: 631–640.

Novais, R.M., Carvalheiras, J., Seabra, M.P., Pullar, R.C., Labrincha, J.A., 2018b. Innovative application for bauxite residue: Red mud-based inorganic polymer spheres as pH regulators. Journal of Hazardous Materials, 358:69–81.

Novais, R.M., Carvalheiras, J., Seabra, M.P., Pullar, R.C., Labrincha, J.A., 2019. Red mud-based inorganic polymer spheres bulk-type adsorbents and pH regulators. Materials Today, 23:105-106.

Novais, R.M., Seabra, M.P., Labrincha, J.A., 2017. Geopolymer spheres as novel pH buffering materials. Journal of Cleaner Production, 143:1114-1122.

Yan, S., He, P., Jia, D., Wang, Q., Liu, J., Yang, J., Huang, Y., 2018. Synthesis of novel low-cost porous gangue microsphere/geopolymer composites and their adsorption properties for dyes. Int. J. Appl. Ceram. Technol., 15:1602–1614.

Yousef, R.I., El-Eswed, B., Alshaaer, M., Khalili, F., Khoury, H., 2009. The influence of using Jordanian natural zeolite on the adsorption, physical, and mechanical properties of geopolymers products. J. Hazard. Mater., 165:379–387.

Zhang, Y.J., He, P.Y., Yang, M.Y., Kang, L., 2017. A new graphene bottom ash geopolymeric composite for photocatalytic H_2 production and degradation of dyeing wastewater. Int. J. Hydrogen Energy 42: 20589–20598.

39th Cement and Concrete Science Conference **Paper Number 003**
9-10th September 2019
University of Bath

Moisture uptake and its associated kinetics in cement using the DVS

Majid Naderi[1], Nachal Subramanian[1], Naima Ali[1], Manaswini Acharya[1] and Daryl Williams[1]

1: Surface Measurement Systems Ltd., 5 Wharfside, Rosemont Road, Alperton London HA4 0PE, UK.

Abstract

Water vapour (moisture) interaction with solid materials has an impact over a wide range of industries and materials including pharmaceuticals [1], foods [2,3], fuel cell membranes [4], and polymers. In addition, there is also a large impact on building materials [5]. Moisture sorption has significant implications for cements [5-6], woods [1], insulation materials [7], and fibres where it plays a significant role limiting a building's lifespan. Moreover, moisture infusion through a building's outer structure can have a significant effect on indoor air quality and air-conditioning loads. The use of automated gravimetric vapour sorption instruments has become standard practice in many industries for investigating the vapour sorption properties of solid materials. This work outlines how Dynamic Vapour Sorption (DVS) instruments can be used to investigate several different types of materials used in the building industry. In particular, this study examines the use of DVS in cement.

An important factor in the long-term storage stability of cements is the rate at which moisture is taken up by the cements under specific storage conditions. Traditionally this is done by storing large containers of cement under controlled conditions and periodically weighing over many months or even years. The moisture sorption kinetics of two different cements using a rapid Dynamic Vapour Sorption (DVS) methodology has been shown in this work.

[1] Khankari, R.K. and Zografi, G., Sorption of water by solids. In: Brittain H.G., editor. Physical Characterization of Pharmaceutical Solids. New York: Marcel Dekker, Inc., pp 387-418.

[2] Fennema, O.R. Food Chemistry, Marcel Dekker: New York, 1985.

[3] Chirafe, J. and Beura, M.D., 1996. Critical Reviews in Food Science and Nutrition, 36, 465-513.

[4] Zawodzinski, T.A., Neeman, M., Sillerud, L.O., and Shimshon, G., 1991. J. Phys. Chem., 95, 6040-4044.

[5] Lieff, M. and Trechsel, HR, editors, Moisture Migration in Buildings, ASTM: PA, 1982.

[6] Maekawa, K., Ishida, T., and Kishi, T., 2003. J. of Advanced Concrete Technology, 1, 91-126

[7] Marchand, R.G. and Kumaran, M.K., Journal of Thermal Insulation and Building Envelopes, 1994. 17, 362-367.

39th Cement and Concrete Science Conference
9-10th September 2019
University of Bath

Paper Number 005

Effect of Partial Replacement of Coarse Aggregates with E-Waste on Strength Properties of High Volume Fly ash Concrete

Shreelaxmi Prashant, Vikram Jolly and Deepankar Sharma
Department of Civil Engineering, Manipal Institute of Technology, Constituent of MAHE, Manipal

ABSTRACT

Cement concrete is a well-known building material due to its mould-ability in the plastic state and when it solidifies, becomes a hard material capable to withstand very high compressive strengths. However considering the environmental impact of large scale use of cement in concrete making, researchers have shifted their focus on alternative binder materials that can partially or completely replace Portland cement. High Volume Fly ash concrete is one such attempt where 50% or more of the binder is fly ash. About 70% of the concrete volume comprises of aggregates, which not only gives bulk to the concrete mix but also takes considerable amount of load. Properties of aggregates play a major role in defining the properties of concrete produced from it. This paper reports an experimental work carried out to study the effectiveness of e-waste which can be used as a partial replacement to Coarse aggregates in HVFAC. E-waste consists of discarded electrical or electronic devices. M30 mix has been designed and the replacement levels which were tested are 10%, 15% and 20%. For every replacement level slump test and compressive strength test was carried out and reported in this paper. Use of electronic waste in concrete along with HVFA is one of the effective ways of disposing E-waste, which otherwise would be lying in landfills creating further environmental issues.

1. INTRODUCTION

Concrete is the primary construction material used because of its mouldability, durability and high compressive strength properties. The properties of concrete can be engineered to suit the infrastructure requirements. However recent concerns about the degrading environment has attracted the concrete technologists towards the use of industrial wastes in concrete making.

Industrial wastes that possess pozzolanic properties have the potential to be used as a binder replacement thereby reducing the use of cement and preventing the augmentation of waste generation. One such industrial waste is fly ash. The production of cement releases a lot of CO_2 in the atmosphere which further leads to

Global Warming and increment of Greenhouse Gases.

The construction industry constitutes about roughly a quarter of the global CO_2 emissions. The basic function of cement in the concrete system is to bind all other ingredients and keep them intact as stated earlier. If the cement is replaced with Fly Ash, a byproduct of thermal power plants, it could make the concrete manufacturing more sustainable and resource efficient.

Aggregates are yet another natural resource that are being used in large scale by the concrete industry. Since the natural resources have to be conserved, researchers have tried using alternative waste that can act as inert fillers in concrete. E-waste or electronic waste is the remnant of gadgets and electronic items after its life cycle. It usually contains 80% plastic. This paper reports experimental study conducted on High volume fly ash containing e-waste as partial replacement of coarse aggregates.

2. LITERATURE REVIEW

Research on possible use of e-waste as partial replacement of coarse aggregates has been carried out in the past. It has been found that the percentage most suitable for replacing aggregate with E-waste lies between 15-20% (S. Manoj Kumar (2015)), (R Lakshmi (2011))) (Suchithra S, Manoj Kumar and Indu V.S (2015)).

This is the optimum range at which the properties of concrete such as compression and flexural strength are optimum or are at the same levels when compared to the ones without replacement,

showcasing that at 15-20% replacement maximum compression and flexural strength can be achieved. Alongside improvement of compressive and flexural strength we noticed that the workability of the studied concrete samples were also affected.

Hence, when fly ash had been added to concrete with E-waste (Bharat Dawande, Devansh Jain and Dr. Gyanendra Singh (2016)) it was found to be beneficial in enhancing the workability characteristics of concrete. Experimental study from which the present study is inspired has suggested the use of 30% fly ash of the total binder content. (N Panneer Selvam (2016)).

Another observation was that as we kept on augmenting the percentage value for replacing cement, the compressive and flexural strength (Panneer Selvam and Gopala Krishna GVT (2016)) as well as overall weight (P Krishna Prasanna (2014)), (P.Krishna Prasanna and M.Kanta Rao (2014)) of the concrete displayed tendency to diminish.

MATERIALS AND METHODS

For studying the properties of High Volume fly ash Concrete cubic specimens were prepared with OPC. M30 mix was designed using the guidelines stipulated in IS: 10262-2009. Table 1 gives the details of the mix proportion. Mix proportion used for the work is 1: 1.6: 2.931. For HVFAC 50% of cement was replaced by Fly ash by weight. Coarse aggregates were replaced by e-waste at the levels of 0%, 10%, 15% and 20% by weight of course aggregates.

Table 1: Proportions of materials in various concrete mixes

MIX ID	PROPORTION OF MATERIALS USED				
	BINDER		COARSE AGGREGATES		SAND
	CEMENT	FLY ASH	C.A	E-WASTE	
MIX0/0	100 %	0 %	100 %	0 %	100 %
MIX50/0	50 %	50 %	100 %	0 %	100 %
MIX0/10	100 %	0 %	90 %	10 %	100 %
MIX50/10	50 %	50 %	90 %	10 %	100 %
MIX0/15	100 %	0 %	85 %	15 %	100 %
MIX50/15	50 %	50 %	85 %	15 %	100 %
MIX0/20	100 %	0 %	80 %	20 %	100 %
MIX50/20	50 %	50 %	80 %	20 %	100 %

Workability was assessed by measuring slump and the compressive strength was tested on 10mm cubed cast for each of the mentioned mixes.

Sieve Analysis of e-waste and aggregate ingredients was done to establish the particle size grading wherein the particle size affects the strength and workability of a concrete mix.

Specific Gravity is the ratio of the weight of a given volume of aggregate to the weight of an equal volume of water. This also is a measure of strength or quality of the specific material. Specific Gravity test was done for the same ingredients as stated for the previous test.
Water absorption test was done for E-Waste to identify its overall strength and porosity of the materials used.

The cement used in all mixtures was commercially available Ordinary Portland Cement (OPC) of 43 grade manufactured by RAMCO company confirming to IS: 12269. The specific gravity of the cement was 3.15. Slump test was performed corresponding to IS: 1199-1959 to get the optimum water- cement ratio and determine the workability of the mix. Cubes of size 100mm x 100mm x 100mm were cast to test for the compressive strength of various mixes after 7 and 28 days of curing.

RESULTS AND DISCUSSION

The cubes were tested for their compressive strength on 7^{th} and 28^{th} day of casting. The results of slump, weight and strength are presented in this section.

The E-waste (mostly plastic) was used as a course aggregate replacement which had a lower specific gravity of 1.4 compared to 2.67 and 2.69 of fine and coarse aggregates. This has resulted in lower weight of sample with E waste. Table 2 shows the reduction in weight with inclusion of E-waste in the concrete samples.

Table 2: Reduction in weight of concrete by addition of E- waste in different mix types

Concrete Mix Type	**Weight of Sample**	**Percentage Reduction**
Mix 0/0	2.05 kg	---
Mix 0/10	1.93 kg	6%
Mix 0/15	1.89 kg	7.80%
Mix 0/20	1.86 kg	9.40%

Table 3 shows the slump and compressive strength of the various concrete mixes studied. It can be observed that workability is reduced by using E-waste as an aggregate. However, using fly ash in the concrete significantly improves the slump of concrete.

Table 3: Slump and compressive strength of various mixes

MIX ID	Slump (mm)	Compressive Strength (MPa)	
		7 days	28days
Mix 0/0	110	24.26	34.92
Mix 50/0	123	16.19	25.61
Mix 0/10	98	24.97	29.58
Mix 50/10	110	12.89	23.68
Mix 0/15	85	20.8	26.22
Mix 50/15	97	12.63	22.06
Mix 0/20	74	17.58	23.76
Mix 50/20	85	11.09	20.67

From Table 3 it can be seen that the control mix of M30 has an average compressive strength of 24.263 MPa. However, the mix containing 10% E-waste has the highest strength which is 2.93% more than the control mix. Strength decreased with addition of E- waste beyond 10% and also with the addition of fly ash. Strength also decreased by 26.6% on replacement of 50% cement with fly ash as compared to control mix. Lastly strength showed depreciation by 15.29% when 10% E- waste was added. Any addition of E- waste or fly ash lead to reduction in strength.

CONCLUSION

1. High volume Fly ash is a suitable alternative to conventional cement as a binder. However the problem of slow setting results in an overall reduction of 7 day strength.

2. Even though HVFA gains strength at a later stage, the strength obtained at the 28th day is still lower than conventional OPC based concrete.

3. Since E-waste has a very low specific gravity compared to normal aggregates, it results in a lower weight and strength.

4. E-waste with high volume fly ash can be used for normal strength concretes upto M40. For higher strength grades better packing densities are required.

REFERENCES

1. S Manoj Kumar: Study on Replacement of coarse Aggregate by E-Waste in concrete (International Journal of Technical Research and Applications, Vol 3, Issue 4, July-August 2015, Pg. 266-270)
2. N Panneer Selvam: Recycle of E-waste in concrete (International Journal of Science and Research, Vol 5, Issue 4, April 2016, Pg. 1590-1593)
3. P Krishna Prasanna: Strength variations in concrete by Using E-Waste as coarse aggregate (International Journal of Education and Applied Research, Vol 4, Issue Spl-2, June 2014, Pg. 82-84)
4. R Lakshmi: Investigations on Durability Characteristics of e- plastic waste Incorporated Concrete (Asian Journal of Civil Engineering – Building and Housing, Vol 12, No. 6, 2011, Pg. 773-787)
5. Bharat Dawande, Devansh Jain and Dr. Gyanendra Singh: Utilization of E- Waste as a partial replacement of coarse aggregate in concrete (IJSRD - International Journal for Scientific Research & Development| Vol. 3, Issue 11, 2016 | ISSN (online): 2321-0613)
6. Suchithra S, Manoj Kumar and Indu V.S: Study on replacement of coarse aggregate by E- Waste in concrete (International Journal of Technical Research and Applications e- ISSN: 2320-8163, www.ijtra.com Volume 3, Issue4 (July-August 2015), PP. 266-270)
41

7. Panneer Selvam and Gopala Krishna GVT: Recycle of E- Waste in concrete (International Journal of Science and Research (IJSR) ISSN (Online): 2319-7064 Index Copernicus Value (2013): 6.14 | Impact Factor (2015): 6.391 Volume 5 Issue 4, April 2016 www.ijsr.net)
8. P.Krishna Prasanna and M.Kanta Rao: Strength variations in concrete by using E- Waste as coarse aggregate (International Journal of Education and Applied Research (IJEAR) | Vol. 4, Issue Spl-2, Jan-June 2014| ISSN 2348-0033 (Online)
9. IS: 10262-2009: Concrete mix proportioning guidelines

10. IS: 383-1970: Specification for coarse and fine aggregates from natural sources for Concrete
11. IS: 2386(Part I and III) 1963-: Methods for test for aggregates for concrete

12. IS: 516-1959: Method of Tests for Strength of Concrete

13. IS: 1727-1967: Physical and chemical requirements for fly ash

39th Cement and Concrete Science Conference
9-10th September 2019
University of Bath
Paper Number 006

Cement-fibre composites for additive building manufacturing

B. Dams, N. Amornrattanasereegul, P. Shepherd and R. J. Ball
Department of Architecture and Civil Engineering, University of Bath, UK

ABSTRACT

The fused deposition principal of additive manufacturing (AM) involves the deposition of a material one layer at a time allowing the creation of an object from a 3D digital design. The associated reduction in the amount of waste material produced offers benefits and over the last decade, investigations have been carried out using cementitious materials for AM within the construction industry. Central to the profile of the technology increasing in the industry is the development of a suitable cementitious material which may be deposited without formwork. Research currently consists of ground based gantry or robotic arm methods reliant upon suitable terrain and environmental conditions. This paper presents development of fibrous cementitious mortars and pastes suitable for a miniaturised deposition system designed for use in a multiple-agent AM approach. Synthetic PVA, aramid and kevlar fibres along with natural fibres from the banana plant were investigated to evaluate contributions to the workability, buildability, mechanical strength and failure mechanisms of the cementitious composite material. The addition of fibres to a cementitious matrix augmented by synthetic hydrocolloids results in compressive and flexural strength increases and transforms the method of failure from brittle to ductile. Results suggest PVA and kevlar fibres are suitable for a composite cementitious material with optimised rheology specifically designed for a multiple-agent, miniaturised deposition approach for AM.

1. INTRODUCTION

Research into the use of cementitious materials in additive manufacturing (AM, often referred to as '3D printing') has developed considerably over the past decade, with an estimated thirty projects worldwide investigating 3D printing with material of a cementitious nature for building and civil use in the construction industry (Buswell et al. 2018). The majority of projects are based upon the AM principal of fused deposition modelling (FDM), which involves the extrusion of a suitably viscous-like material through a nozzle to create an object one discreet layer at a time (Kalsoom et al. 2016) without the use of supporting formwork. This additive approach, which only uses material specifically required, is in stark contrast to the traditional subtractive methods (Buswell et al. 2007) employed in the conservative and risk-averse construction industry (Arora et al. 2014), in which AM technology is still in a relative state of infancy (Bos et al. 2016).

A cementitious material suitable for AM must possess an appropriate balance between 'pumpability' (the ability of a fresh mix to move through a deposition system), 'printability' (the level of ease at which material passes through a nozzle) and 'buildability' (the ability of freshly deposited material to retain shape following extrusion and when subjected to load from subsequent layers) (Le et al. 2012). In this study, 'pumpability' and 'printability' will be encompassed by the term 'workability'. A workable mix requires liquid-like behavior and low viscosity, whereas a buildable mix exhibits more solid-like behavior and high viscosity.

Studies concerning cementitious materials in AM have involved differing deposition approaches. Equipment could be of building envelope scale, housed on a large frame or gantry, with examples being concrete printing, developed at Loughborough University, UK (Le et al. 2012), (Lim et al. 2012) and Contour Crafting, developed at the University of Southern California, USA (Zhang and Khoshnevis 2013). A further method is the use of a large compound robotic arm with multiple degrees of freedom, which could be stationary, or mobile on a moving platform, an example being the digital construction platform project developed by the Massachusetts Institute of Technology, USA (Keating et al. 2017). Another possibility is the use of smaller, coordinated multiple mobile agents.

Concrete is weak in tension and prone to brittle failure (Soltan and Li 2018), with design traditionally focusing upon compressive strength and the use of structural steel reinforcement to carry tensile forces and facilitate ductile failure (Bos et al. 2017). When considering the use of multiple smaller robots in AM construction, and the inherent relative miniaturisation of the deposition process required, traditional steel rebar is not naturally compatible. Indeed, rebar may be detrimental to an AM construction procedure (Asprone et al. 2018). Alternative options to integrate reinforcement must be investigated to increase tensile capacity and resist drying shrinkage and crack propagation. Options include fibrous reinforcement as part of the cementitious mix, automated placement of passive reinforcement during deposition or digital fabrication post-deposition (Asprone et al. 2018).

This study investigated multiple types of chopped fibres, adding them in differing quantities to a cementitious paste mix suitable for a miniaturised AM extrusion process. The study used natural, untreated fibres from the banana plant along with synthetic aramid, kevlar and polyvinyl alcohol (PVA) fibres. Workability, buildability, morphology, mechanical properties and failure modes of the fibrous cement pastes were evaluated for suitability with a miniaturised AM process.

2. Materials and Methodology

High fibre volume fraction (2%+) materials present challenges regarding workability (Noushini et al. 2014). Fibres were added in this study to a cementitious paste of density ≈1400 kg/m^3 at volume fractions <1%, levels usually associated with reducing drying shrinkage and resisting crack propagation, in order to facilitate enough workability for the material to pass through the miniature deposition system. PVA fibres, (supplied by Flints Theatrical Chandlers, London) were uniformly cut to a length of 12mm as part of the manufacturing process, whereas the aramid, kevlar (both supplied by Easy Composites, Staffordshire) and banana fibres (supplied by Moomin, UK) were hand-cut to a length of 12mm ±5mm from bulk quantities. Kevlar is a type, or brand name, of the synthetic fibre class aramid, which is based around a chemical reaction between an amine group and a carboxylic acid halide group. In this study, the woven fibre strands Kevlar tex 40, supplied in sewing reel form, are termed 'kevlar' and the dtex 1600 yarn, manufactured as strands of unwoven fibres, are termed 'aramid'. Fibre properties are presented in Table 1. Kevlar fibres were the most expensive option, with banana and PVA the least.

Table 1. Properties of the fibres. Please refer to Figure 5 for macro-images.

FIBRE	LENGTH (mm)	DIAMETER (microns)	DENSITY (g/cm^3)
PVA	12	280-350	1.29
ARAMID	12 ±5	12-14	1.40
KEVLAR	12 ±5	210 (thread)	1.40
BANANA	12 ±5	35-50	1.35

Nine mixes were formulated for the experiments – a control mix without fibres and the four fibres each added at 0.35% and 0.75% by mix volume. The cementitious matrix was based upon Dragon Alfa CEM I 42.5 R Portland cement blended with Cemex EN-450 pulverised fuel ash (PFA) in a respective ratio of 65:35. Cellulose gum and a lignin-based plasticiser were added to aid both workability and buildability. Coarse aggregate is inherently incompatible with the miniaturised system. Fine aggregate is possible, but this study focused upon fibre concentrations and fine aggregate was not used. A water/binder ratio of 0.46 and superplasticiser content of 1% by mass of binder were kept consistent throughout all mixes. Prisms for mechanical tests were cast in 160 mm x 40 mm x 40 mm moulds, cured and tested in accordance with BS EN 1015-11:1999, at both 7 days and 28 days, to attain compressive and flexural strengths with the use of a 50kN loading capacity Instron Universal 2630-120/305632 device.

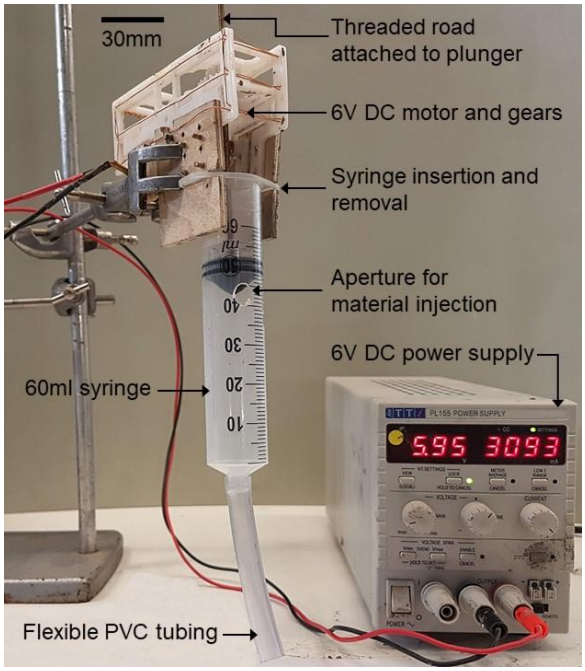

Figure 1. Adapted automated deposition device facilitating swift removal and insertion of syringes.

Workability and buildability of freshly mixed pastes were evaluated using an adapted miniature syringe-based deposition device (Figure 1). The device consisted of one 60 ml, 28mm internal diameter concentric luer-loc syringe, with plunger movement in the vertical direction actuated by a 6V DC brushed motor (Dams et al. 2017). Each mix was injected into the 60ml syringe through a circular aperture thereby allowing subsequent extrusion through an 8mm circular nozzle and an 80mm length of 8mm internal diameter flexible PVC tubing. This allowed extrusion of a smooth bead of material in four circular layers. Workability was assessed by the level of ease at which the deposition device could extrude the fresh mix, as quantified by the electrical current required. Buildability was evaluated through the ability of the extruded fresh mix to retain its shape and resist excessive deformation when subjected to loading from subsequent layers.

Fibre morphology and fracture surfaces of the tested flexural specimens (at 7-day strength) were investigated using a JEOL SEM6480LV Scanning Electron Microscope (SEM). Magnifications of 1000x and 43x were used for the fibres and the flexural prism fractured surfaces respectively. A gold coating of thickness 10 nm was applied to the SEM samples immediately prior to insertion into the microscope chamber in order to prevent charging and increase signal-to-noise ratio.

3. Results and Discussion

Figure 2 shows 7-day and 28-day compressive and flexural strengths. Aramid, kevlar and banana fibres all increased flexural strength at 0.75% fibre volume. Standard deviations, though largely <1 MPa, demonstrated variable concentrations of fibres within cementitious matrices. While compressive strength categorically increased between 7 and 28 days, flexural strength did not, suggesting the molecular bonding between fibre and cementitious matrix was established at 7 days. All fibres improved compressive strength at 28 days in comparison to the non-fibrous control mix. Figure 3 shows modes of failure following flexural tests. The non-fibrous control mix exhibited brittle failure, while all 0.35% fibrous specimens failed in a ductile manner and resisted crack propagation, improving further with 0.75% volume (0.75% banana fibre specimen is shown in Figure 3).

The current required for the deposition device to extrude the fresh mixes is shown in Table 2, with mixes too stiff to be processed identified as 'Could Not Process' (CNP). The presence of cellulose gum allowed extruded mixes to retain structure to varying extents in the buildability tests (shown in Figure 4). PVA and Kevlar fibres performed well. Banana fibres at 0.35% volume, showed greater layer deformation. Mixes with aramid fibres performed well in mechanical tests but the stiff mixes possessed poor workability. This is also true to a lesser extent with 0.75% volume banana fibres, as aramid and Banana fibre mixes couldn't be processed at 0.75% volume.

Table 2. Current required for deposition device extrusion. CNP = could not process.

Fibres contained in the mix	Fibre volume	Current required
	(%)	(mA)
Control (none)	-	160-181
PVA	0.35	162-184
PVA	0.75	172-220
ARAMID	0.35	169-209
ARAMID	0.75	CNP
KEVLAR	0.35	156-192
KEVLAR	0.75	174-210
BANANA	0.35	171-212
BANANA	0.75	CNP

Figure 5 shows macro (left) and SEM (centre, right) images of fibres and fracture surfaces. The larger PVA fibres were relatively uniform in being broadly aligned parallel to the specimen length axis compared to the random orientation of banana and aramid fibre strands. Kevlar can be observed as both uniform (while intact in woven reel form) and randomly aligned (the result of a reel de-woven into component fibre-strands due to manual and mechanical mixing processes). Aramid has the smoothest surface and it is reasoned that the multiple orientation of low-diameter fibre strands forms an effective mat of reinforcement, resisting crack propagation and improving flexural strength, rather than relying on an uneven surface providing anchorage as is the case for PVA and Kevlar fibres. Banana fibres provide both, with a natural uneven surface and multiple orientation of fibre strands providing a mat of reinforcement located more consistently throughout the cementitious matrices.

Rupture was observed with aramid and banana fibres, a combination of the mat effect and brittle nature of the fibres. A major drawback of the mat effect is the detrimental effect on workability, which threatens suitability for a miniaturised AM process. PVA fibres were observed to fail by pull-out, as confirmed by Figure 5 (top, centre) which shows a smooth, unbroken fibre-end. It is suggested this is due to high tensile capacity rather than inadequacy in molecular bonding or mechanical anchorage.

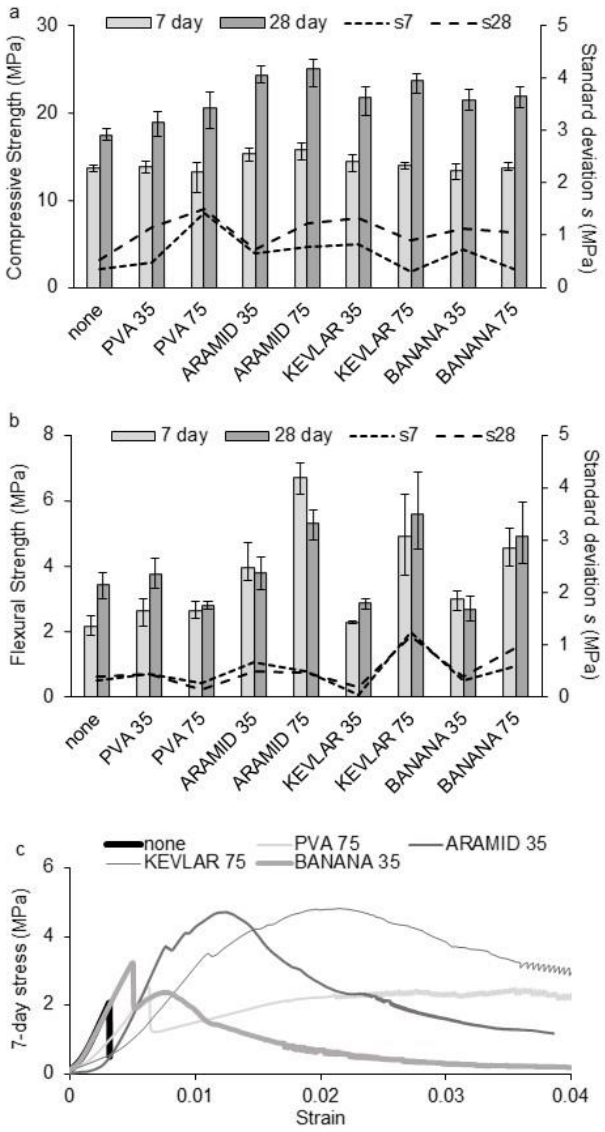

Figure 2. 7-day and 28-day compressive (a) and flexural (b) strengths. 35 and 75 refer to 0.35% and 0.75% fibre volume. *s*7 and *s*28 denote standard deviation (secondary vertical axis). Error bars represent highest and lowest recorded values. Stress/strain profiles of 7-day specimens (c) show mixes successfully processed autonomously by the deposition device.

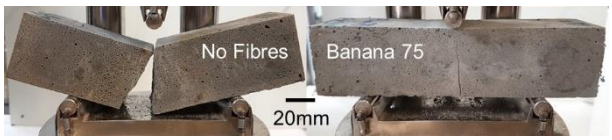

Figure 3. Flexural failure at 2mm displacement, with brittle failure of a non-fibrous prism (left) and a more ductile 0.75% banana fibre prism resisting crack propagation (right).

Figure 4. Buildability tests with four fresh circular layers extruded by the powered deposition device for each mix shown.

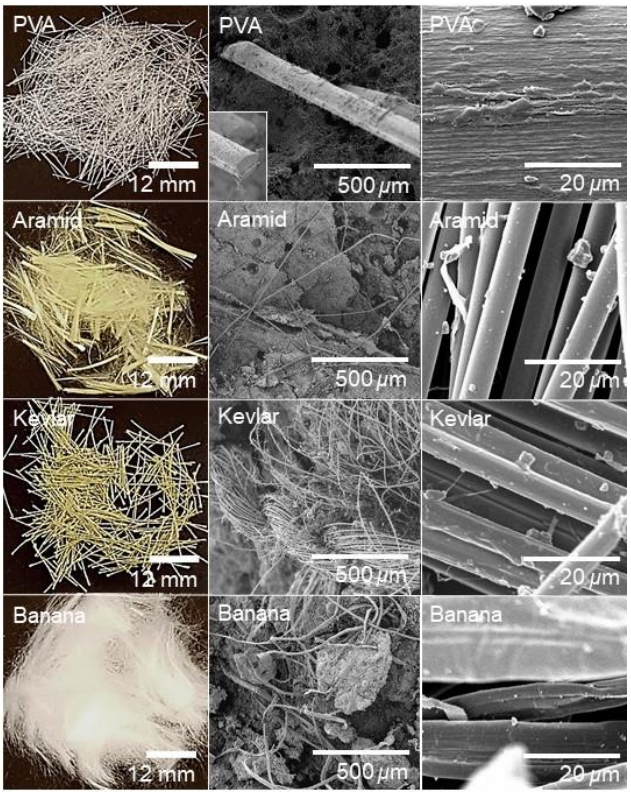

Figure 5. Macro (left) and SEM (centre, right) micro images, top to bottom: PVA, Aramid, Kevlar and Banana. Fibre images are 43x magnification (within matrices, centre) and 1000x (right).

4. Conclusions and further work

All fibres used in this study contributed to the buildability and ductility of cementitious pastes but impacted upon workability. Though Aramid and banana fibres provided the highest flexural strengths and most ductile failure, they are challenging for the deposition device to process and in higher volumes are concluded to be unsuitable for miniaturised AM. Pastes containing 0.75% volume PVA and Kevlar fibres possessed a suitable balance between workability and buildability, being competitive in mechanical tests and possessing sufficient workability for the deposition device. Uneven surfaces of fibres facilitated good anchorage in cementitious paste matrices, transforming method of failure but not necessarily flexural strength. It is concluded that for higher fibre volumes, PVA and Kevlar (aramid in woven reel form) are the most suitable, as fibres are discreet from each other and do not entangle (though a drawback of Kevlar is the high cost). Further work would encompass development of a more powerful deposition system and mix modification to further increase the fibre volume, which may require foam or further rheological modifying agents to decrease density and strength and attain viable workability. A suitable parallel approach would focus miniaturised AM design on compression-loaded structures.

References

Arora, S.K., Foley, R.W., Youtie, J., Shapira, P., and Wiek, A., 2014. Drivers of technology adoption - the case of nanomaterials in building construction. *Technological Forecasting and Social Change*, 87, pp.232–244.

Asprone, D., Menna, C., Bos, F.P., Salet, T.A.M., Mata-Falcón, J., and Kaufmann, W., 2018. Rethinking reinforcement for digital fabrication with concrete. *Cement and Concrete Research*, 112(May), pp.111–121.

Bos, F., Wolfs, R., Ahmed, Z., and Salet, T., 2016. Additive manufacturing of concrete in construction: potentials and challenges of 3D concrete printing. *Virtual and Physical Prototyping*, 2759(October).

Bos, F.P., Ahmed, Z.Y., Jutinov, E.R., and Salet, T.A.M., 2017. Experimental exploration of metal cable as reinforcement in 3D printed concrete. *Materials*, 10(11).

Buswell, R.A., Leal de Silva, W.R., Jones, S.Z., and Dirrenberger, J., 2018. 3D printing using concrete extrusion: A roadmap for research. *Cement and Concrete Research*, 112(June), pp.37–49.

Buswell, R.A., Soar, R.C., Gibb, A.G.F., and Thorpe, A., 2007. Freeform Construction : Mega-scale Rapid Manufacturing for construction. , 16, pp.224–231.

Dams, B., Wu, Y., Shepherd, P., and Ball, R.J., 2017. Aerial Additive Building Manufacturing of 3D printed Cementitious Structures. In: *37th Cement and Concrete Science Conference UCL*.

Kalsoom, U., Nesterenko, P.N., and Paull, B., 2016. Recent developments in 3D printable composite materials. *RSC Advances*, 6.

Keating, S.J., Leland, J.C., Cai, L., and Oxman, N., 2017. Toward site-specific and self-sufficient robotic fabrication on architectural scales. *Science Robotics*.

Le, T.T., Austin, S.A., Lim, S., Buswell, R.A., Gibb, A.G.F., and Thorpe, T., 2012. Mix design and fresh properties for high-performance printing concrete.

, pp.1221–1232.
Lim, S., Buswell, R.A., Le, T.T., Austin, S.A., Gibb, A.G.F., and Thorpe, T., 2012. Developments in construction-scale additive manufacturing processes. *Automation in Construction*, 21, pp.262–268.
Noushini, A., Vessalas, K., and Samali, B., 2014. Static mechanical properties of polyvinyl alcohol fibre reinforced concrete (PVA-FRC). *Magazine of Concrete Research*, 66(9), pp.465–483.
Soltan, D.G. and Li, V.C., 2018. A self-reinforced cementitious composite for building-scale 3D printing. *Cement and Concrete Composites*.
Zhang, J. and Khoshnevis, B., 2013. Optimal machine operation planning for construction by Contour Crafting. *Automation in Construction*, 29, pp.50–67.

39th Cement and Concrete Science Conference **Paper Number 010**
9-10th September 2019
University of Bath

Definitive guide for synthetic calcium-silicate-hydrate growth

M. Harris, P. Bowen, and K. Scrivener
Laboratory of Construction Materials, EPFL

ABSTRACT

As concrete-based infrastructure becomes more commonplace in the world, cement's contribution to CO_2 emissions will increase. Consequently, it is imperative that more sustainable cementitious materials with the same costs, same strengths, and lower emissions are put into use. To effectively supplement the materials on the market, strength mechanisms of cement must be understood and controlled.
Calcium-silicate-hydrate or C-S-H is the glue of Portland Cement. C-S-H is the main product of the hydration phase and the chief contributor to early-age strength. As a result, a sound understanding of C-S-H nucleation and growth will allow cement scientists to copy and control these mechanisms in supplemental materials, increasing cement sustainability.
This study focuses on constructing the definitive protocol to synthesize and store pure, single-phase C-S-H with Ca:Si ratios between 1.0 and 2.0 by using a modified version of the dropwise precipitation method as designed by Kumar et al. in addition to other considerations to optimize and consistently control fine particle nucleation.

1. INTRODUCTION

Calcium-silicate-hydrate, or C-S-H is the main hydration product of cement and is chiefly responsible for early-age strength. However, in a cementitious system, C-S-H precipitation often occurs with the formation of other phases including ettringite, $Ca(OH)_2$, and $CaCO_3$ (Scrivener and Nonat, 2011). Additionally, C-S-H has a variable stoichiometry; the Ca:Si ratio depends on the pH of the local environment. As a result, experimental characterization of C-S-H is difficult, and can be best studied in an isolated system.

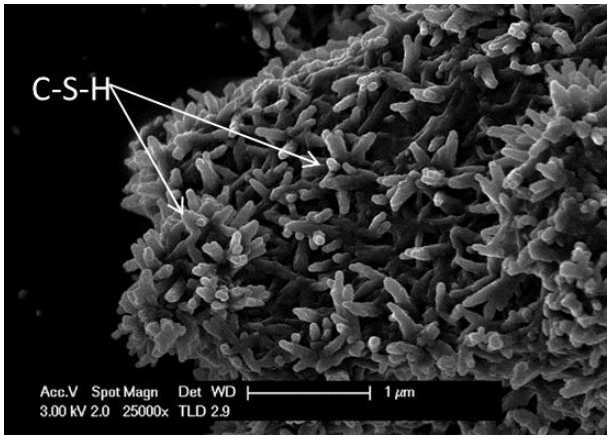

Figure 1. SEM – Ca_3SiO_5 hydration stopped at 6 hours

The dropwise precipitation method was developed to synthesize pure, single-phase C-S-H, isolated from other materials found in cement. The method gives insight on the required materials to precipitate batches of C-S-H with Ca:Si ratios from 1.0 to 2.0. Temperatures and pHs required in order to receive the target Ca:Si ratio is given based on thermodynamic predictions (Lothenbach and Winnefeld, 2006). However, the exact protocol and details for handling of materials before, during, and after synthesis are less clear.

To study the sensitivities of this system in more detail, C-S-H was synthesized at different Ca:Si ratios from 1.0 to 2.0. Methods to best control the precipitation collection process, drying, storage, substrate handling, and cleaning were modified to best control the system. Afterwards, the precipitates were analyzed with XRD, TGA, and ICP.

2. MATERIALS AND METHODS

Ten different samples of C-S-H were synthesized following a modified version of the dropwise precipitation method (Kumar, et al., 2017). The Ca:Si ratio was varied between 1.0 and 2.0 by modifying the pH of the solution in the reactor.

2.1 Materials

Materials for the synthesis of synthetic C-S-H include a 12 cm diameter poly(methyl methacrylate) (PMMA) reactor. The reactor lid is comprised of six slots for in-situ measurements, PMMA bars to increase turbulence and mixing inside reactor, and glass inlet and outlet tubes for a gas purge. Additionally, the lid includes a 3-input y-shaped micromixer system with a spiral static mixer.

Free calcium concentration and pH are monitored *in-situ*. Temperature is regulated by a thermostat.

2.2 Preparation and maintenance

In advance to synthesis, all materials are washed with deionized water and dried in a laminar flow hood.

Piston pump tubes are purged with a solution of 50% ethanol, 50% pure water, and rinsed with a 50 mL solution of pure water before and after use. Ion electrodes and pH meters are stored in the respective storing solutions, calibrated twice before usage, and washed with deionized water.

Solutions of calcium nitrate tetrahydrate, sodium metasilicate, and sodium hydroxide are prepared with decarbonated water. After preparation, the solutions are covered with a lid to avoid any contamination by dust. The solutions are only stored for a maximum of two weeks before usage.

2.3 Precipitation

100 mL of silicate solution is placed in the reactor with the designated amount of 10M NaOH. The system is purged under a flow of nitrogen at 10 mL/min, and is mixed at 700 RPM for 30 minutes. The pH and required amount of NaOH is described in Table 1.

Table 1. GEMS predicted pH and required amount of NaOH to receive target Ca:Si ratio, 200mL reactor volume (Kulik, 2011)

Ca:Si ratio	pH (GEMS)	10 M NaOH (GEMS)
1	10.9	25 µL
1.25	11.5	2.6 mL
1.5	12.1	5.3 mL
1.75	12.6	8.3 mL
2	12.8	10 mL

The mixing speed is then increased to 1100 RPM, and a calcium solution is pumped into the reactor at a rate of 2 mL/min.

2.4 Collection & Drying

After 3 hours of reaction, the precipitate and the supernatant are separated over a 20 nm organic filter via a vacuum-filtration system. The supernatant from the first filtration is collected when 100 mL of supernatant still remains unfiltered. The precipitate is then washed with a 1:1 pure water and ethanol solution, filtered again, and separated into wet and dry product.

To dry, the C-S-H precipitate is placed in a -80 ℃ freezer for 24 hours and in a freeze dryer for an additional 24 hours.

3. RESULTS & DISCUSSION

Figure 2 shows XRD diffractograms of three different samples of C-S-H all synthesized with a target Ca:Si ratio of 1.87.

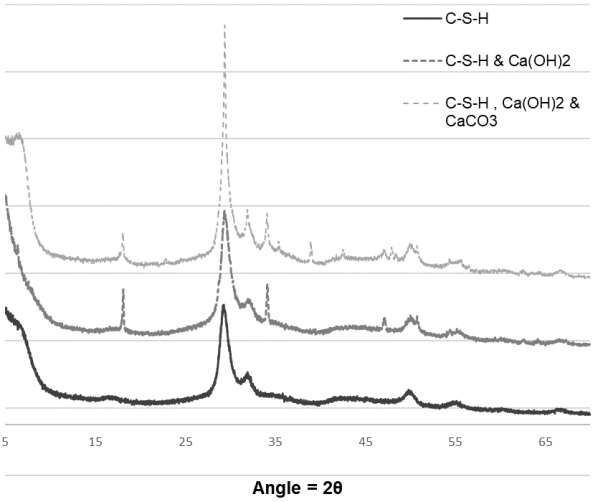

Figure 2 Diffractogram comparison of pure C-S-H and impure C-S-H with presence of $Ca(OH)_2$ and $CaCO_3$, Ca:Si = 1.87

All three diffractograms in Figure 2 display the presence of C-S-H, indicated by the characteristic peaks at at 29.4, 32.1, and 50.1 ± 0.1° (Snellings, 2016). However the top diffractograms indicate the presence of $CaCO_3$ and $Ca(OH)_2$.

Although all three samples were synthesized with the same recipe, temperature, and pH, improper protocol after synthesis caused impurities to form.

In the diffractogram that shows presence of C-S-H and $Ca(OH)_2$, impurity is believed to have formed during vacuum filtration and drying. The precipitate was allowed to filter for too long, taking the C-S-H out of equilibrium with the mother liquor causing the precipitate to be more suceptible to change.

In the top diffractogram of Figure 2, $CaCO_3$ is also seen in addition to $Ca(OH)_2$, having formed due to poor handling and exposure to CO_2.

4. CONCLUSIONS

In fine particle nucleation, careful handling of solutions and materials before, during, and after synthesis is imperative to ensure that results are consistent and reproducible. Even if the correct recipes, temperatures, pHs, and mixing speeds are in practice, it is still possible to form impurities in the C-S-H precipitation system.

The diffractograms in Figure 2 confirm the synthesis of pure C-S-H at a target Ca:Si ratio of 1.87. However, they also reveal that improper protocol after synthesis can lead to the presence of impurities in the sample.

As a result, the purpose of this study is to find the optimal conditions and parameters for the entire process of making and storing pure, single-phase C-S-H.

REFERENCES

Kulik, D. (2011). Improving the structural consistency of C-S-H solid solution thermodynamic models. *Cement Concrete Research*, 477-495.

Kumar, A., Walder, B. J., Mohamed, A. K., Hofstetter, A., Srinivasan, B., Rossini, A. J., . . . Bowen, P. (2017). The Atomic-Level Structure of Cementitious Calcium Silicate Hydrate. *The Journal of Physical Chemistry C*, 17188-17196.

Lothenbach, B., & Winnefeld, F. (2006). Thermodynamic Modelling of the Hydration of Portland Cement. *Cement Concrete Research*, 209-226.

Scrivener, K., & Nonat, A. (2011). Hydration of Cementitious Materials, Present and Future. *Cement Concrete REsearch*, 651-665.

Snellings, R. (2016). X-ray powder diffraction applied to cement. In R. S. Karen Scrivener, *A Practical Guide to Microstructural Analysis of Cementitious Materials* (pp. 107-176). Boca Raton: Taylor & Francis Group.

39th Cement and Concrete Science Conference **Paper Number 011**
9-10th September 2019
University of Bath

Advances in understanding tricalcium aluminate hydration

R.J. Myers

School of Engineering, University of Edinburgh, Edinburgh, EH9 3FB, UK

G. Geng

Laboratory for Waste Management, Paul Scherrer Institute, 5232 Villigen PSI, Switzerland

ABSTRACT

This contribution presents a summary of recent advances in understanding the hydration of tricalcium aluminate (C_3A), which is key to controlling a number of important properties of fresh PC concrete, such as workability and setting time. We focus on the two main hypotheses used to explain the retarding effect of gypsum on the dissolution of the cubic form of C_3A (cub-C_3A), (1) the 'barrier' and (2) 'adsorption' hypotheses. Our results show that ettringite is the only product in the cub-C_3A-gypsum-H_2O system during the initial stages of hydration, which is when the retarding effect is active. We also find that the surface of cubC_3A is only partially covered, on the length scale of tens of nanometers, during this period. These results provide direct evidence to disprove a physical barrier to cub-C_3A dissolution, and thus also the 'barrier hypothesis'. Additional results from chemical analysis of the solid and solution phases in this cub-C_3Agypsum-H_2O system indicate that neither Ca or S specifically adsorb to the surface of partially hydrated cubC_3A, and thus that neither Ca cations or SO_4^{2-} alone inhibit cub-C_3A dissolution in fresh PC systems.

Therefore, we present a more complex yet plausible explanation for the retarding effect of gypsum on cubC_3A hydration, which is through weak adsorption of aquo Ca-S ion-pair complexes onto partially dissolved cub-C_3A. Our proposed mechanism is discussed in light of its implications on fresh PC concrete performance.

39th Cement and Concrete Science Conference **Paper Number 012**
9-10th September 2019
University of Bath

Modelling the addition of limestone in cement using HYDCEM

N. Holmes[1], D. Kelliher[2] and M. Tyrer[3]
[1]School of Civil & Structural Engineering, Technological University Dublin, Ireland
[2]School of Civil, Structural & Environmental Engineering, University College Cork, Ireland; [3]Centre for Research in the Built and Natural Environment, Coventry University, UK

ABSTRACT
Hydration models can aid in the prediction, understanding and description of hydration behaviour over time as the move towards more sustainable cements continues.
HYDCEM is a new model to predict the phase assemblage, degree of hydration and heat release over time for cements undergoing hydration for any w/c ratio and curing temperatures up to 45^0C. HYDCEM, written in MATLAB, complements more sophisticated thermodynamic models by predicting these properties over time using user-friendly inputs within one code. A number of functions and methods based on up to date cement hydration behaviour from the literature are hard-wired into the code along with user-changeable inputs including w/c ratio, curing temperature, chemical compositions, densities and enthalpies. Predictions of hydration product volumes from the silicate, aluminate and ferrite phases can be determined, including C-SH, calcium hydroxide, hydrogarnet (if applicable) ettringite and monosulfate. A number of comparisons have been made with published phase assemblages using thermodynamic models and HYDCEM predictions to assess its accuracy and usefulness.
This paper presents simulations of cement hydration and microstructure development with and without the additional of ground limestone using the HYDCEM model, both in terms of monocarbonate growth at the expense of monosulfate and ettringite. Comparisons with published phase assemblages show good agreement in terms of volumetric growth and behaviour.

1. INTRODUCTION

The use of cements with added limestone has been increasing in Europe and across the world over the past decade. Within the European cement standard, EN-197, limestone-cements are classed as CEM II/A-L and CEM II/B-L where up to 20 and 35% limestone is allowed respectively (BS EN 1971, 2000). The addition of limestone is also permitted in the United States (ASTM C150, 2018) and many other countries throughout the world. Indeed, Bonavetti *et al* (2003) states that the addition of limestone filler in low w/c concrete is a rational option to reduce energy consumption, emissions and costs.
While the use of Supplementary Cementitious Materials (SCM's) in concrete is increasing, their local and worldwide availability compared to limestone is much less. The literature (Lothenbach *et al*, 2008; Matschei *et al*, 2007; Matschei and Glasser, 2006; Antoni *et al*, 2012; Zajac *et al*, 2014; Ingram and Daugherty, 1991) suggests that limestone or calcite additions up to 5% can enhance performance while reducing ettringite dissolution when gypsum/sulfate is depleted. AFm phases like monocarbonate and hemicarbonate are formed in place of monosulfate with reduced consumption of ettringite. Without limestone additions, ettringite becomes unstable and monosulfate is formed over time. With limestone, monocarbonate is formed which stabilises ettringite. As a result, there is an increased volume of hydrates, decreased porosity and improved strength.
The effects of limestone addition were shown to increase the effective w/c of the cementitious material and accelerate hydration, while only mildly reactive. This is due to the fine filler effect where the ground limestone provides additional surfaces to develop nucleation sites for the precipitation of C-SH (Stark, 2004; Pera *et al*, 1999).

2. MODELLING LIMESTONE ADDITIONS DURING CEMENT HYDRATION

A review of the literature around cement hydration modelling including limestone additions suggests that, outside of thermodynamic analysis, only CEMHYD3D (Bentz , 2000) has been used. The *μic* microstructure platform (Bishnoi & Scrivener, 2009) allows for the inclusion of limestone with the filler C-S-H can be modelled on the surface of the particle.
The influence of limestone, both for chemical reactivity and 'fine filler effects' was included in the CEMHYD3D V. 2.0 model (Bentz, 2006) by modifying the CEMHYD3D code and including the reaction in Equation 1, based on experimental observations in the literature (Hawkins *et al*, 2003; Klemm & Adams, 1990; Kuzel & Pollmann, 1991; Bonavetti *et al*, 2001; Kakali *et al*, 2000). Monocarbonate is formed in preference to monsulfate and only becomes active in

CEMHYD3D when the initial calcium sulfate (gypsum) is depleted and the previously formed ettringite converts to the Afm phase by reaction with more of the cement clinker aluminate phases.
$3(CaO)_3(Al_2O_3) \cdot CaSO_4 \cdot 12H + 2CaCO_3 + 18H \rightarrow 2(CaO)_3(Al_2O_3) \cdot CaCO_3 \cdot 11H + (CaO)_3(Al_2O_3) \cdot 3CaSO_4 \cdot 32H$ Eqn. 1

In terms of the 'filler effect', the early time dissolution probabilities in CEMHYD3D were altered so to be proportional to the ratio of the initial total (cement clinker and limestone) surface area divided by the initial cement clinker surface area raised to the second power (Bentz, 2000). This methodology implies that hydration during the induction period is 'accelerated' where a thinner C–S–H[1] layer is formed over a larger surface area. It was concluded that the revised model provided good agreement with experimental results.

The effect of limestone on the hydration of cementitious systems has also been undertaken using thermodynamic modelling using the Gibbs free energy minimization (GEMS) programme. GEMS (Kulik, 2007) is a broad-purpose geochemical modelling code that has been used to compute phase assemblage from the systems total bulk elemental composition (Lothenbach et al, 2008). Chemical solid interactions, solid solutions and aqueous electrolyte are considered simultaneously along with the speciation of the dissolved species including the kind and amount of solids precipitated.

Thermodynamic modelling was undertaken using a w/c ratio of 0.4 at a curing temperature of 20^0C with the cementitious systems in (Lothenbach et al, 2008). Figure 1 shows the thermodynamically modelled phase assemblages for the cements with limestone. As may be seen, monocarbonate forms in place of monosulfate in the limestone cement. Also shown is the stability of ettringite through the hydration in the limestone cements which is unstable in the Portland cements as it is converted to monosulfate over time. Furthermore, monosulfate begins to form at approximately 3 days where monocarbonate is formed after approximately 1 day. Finally, the total volume of the limestone cement is slightly higher than the Portland cement, which confirms the higher compressive strengths seen in the literature.

Figure 2 presents comparisons between modelled and experimentally measured (using XRD & TGA) amounts of ettringite, monosulfate and monocarbonate over time (Lothenbach et al, 2008). The authors noted that the differences between measured and modelled is due to the underestimation of AFm phases deduced by XRD was due to its low crystallinity and variations in composition. It was also concluded that thermodynamic modelling is capable to reasonably accurately predicting the formulation of C-S-H, portlandite, ettringite, monosulfate and traces of hydrotalcite and hemicarbonate, as shown in Figure 2. However, the XRD measurements show more ettringite than predicted by the model.

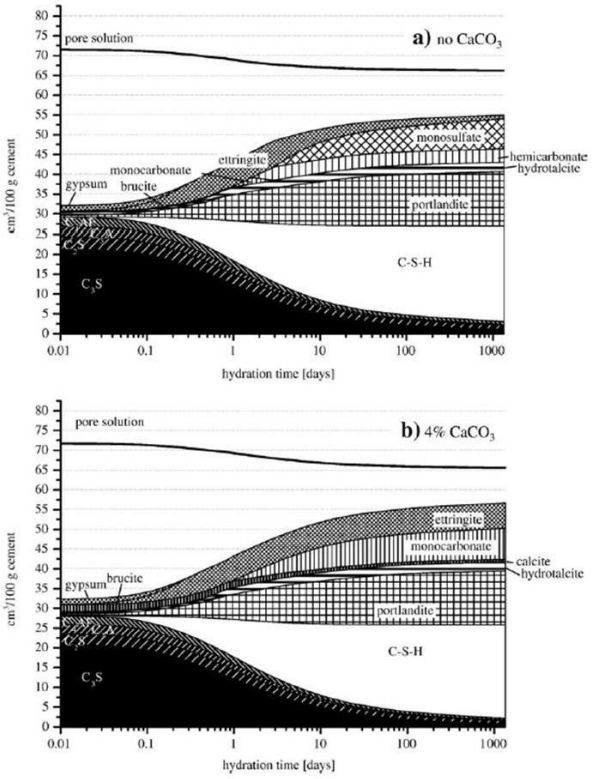

Figure 1: Results from Thermodynamic modelled changes during the hydration of a Portland cement (a) without and (b) with
4 wt.% limestone (Lothenbach et al, 2008)

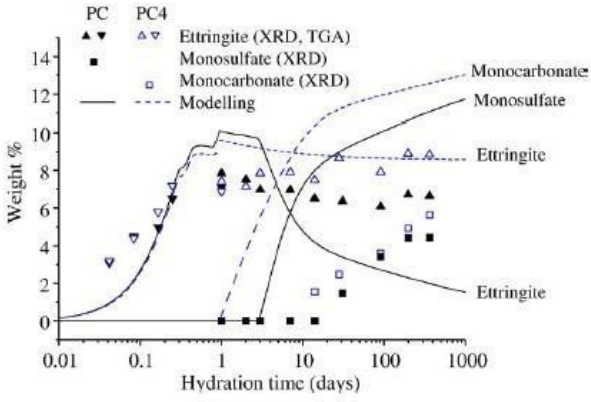

Figure 2: Measured and predicted (thermodynamic modelling) hydrated crystalline products as a function of hydration time (Lothenbach et al, 2008).

The above review suggests that any hydration model simulating the effect of limestone inclusion must be capable of predicting the development of monocarbonate in place of monosulfate after the

[1] Conventional cement chemistry notation: C=CaO, S=SiO_2, A=Al_2O_3, F=Fe_2O_3, and H=H_2O.

depletion of sulfates/gypsum while maintaining the stability of ettringite using appropriate chemical relationships. The following presents how the HYDCEM cement and hydration microstructure model (Holmes *et al*, 2019) can simulate the hydration of limestone cements.

3. HYDCEM HYDRATION MODEL

HYDCEM was developed with the user in mind by providing clearly laid out and easy to change input flat (*.txt) files. The analysis/calculation flow for HYDCEM is shown in
Figure 3. As may be seen, when the input data files are read into the model, the analysis follows a wellstructured methodology by using multiple functions within the main HYDCEM script along with preallocation of single precision outputs for quicker analysis without a loss of accuracy. The data is stored within predefined single column vectors with the number of rows equal to the number of hourly time steps.
Using the four input text (*.txt) files, the cement phase and gypsum proportions are determined using modified Bogue equations (ASTM C150, 2018). The volume stoichiometries are calculated based on the molar mass reaction of the cement phase, the molar mass of the phase (C_3S, etc.) or hydration product (C-S-H, etc.) and the density, all of which are customisable by the user.
The dissolution of the four cement phases are calculated using the approach presented by Parrot and Killoh (1984) that uses a set of empirical expressions to estimate the degree of hydration of each phase as a function of time. Previous work has shown that the approach gave good comparisons with experimental results for any temperature shown in Figure 3 (Lothenbach et al, 2007).
The change in volume of hydration products, water and gypsum are calculated using the volume stoichiometries calculated from the molar ratios in reactions within using a series of programming operations. HYDCEM has implemented accepted cement hydration behaviour found in the literature.

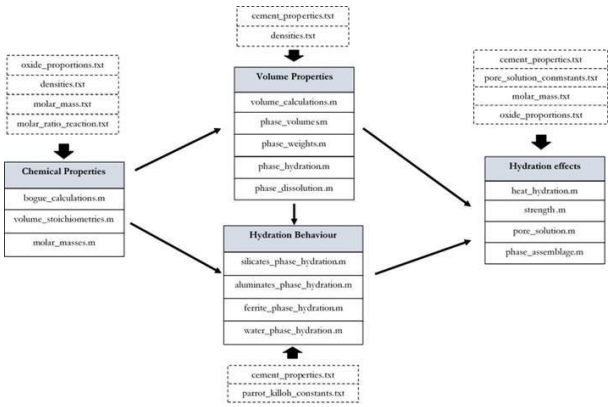

Figure 3: Diagram of HYDCEM's Matlab functions (*.m) and customisable input text files (*.txt)
3. HYDCEM SIMULATIONS

To assess the accuracy of HYDCEM simulations, comparison were made against the published experimentally determined and modelled behaviour in Figure 1 and Figure 2 above. Table 1 shows the cement properties used as input for the HYDCEM model based on work by Lothenbach *et al* (2008). Table 2 shows the Parrot and Killoh (1984) parameters used to calculate the hydration of the four cement phases.

The volume stoichiometry used in HYDCEM for the growth of monocarbonate (AFmc) due to the addition of calcite/limestone (CaCO3) is shown in Equation 2 (Mohamed *et al,* 2015) where H represents water.

$$1.0V_{AFm} + 0.12V_{CaCO3} + 0.347V_H = 0.6281V_{AFmc} \quad \text{Eqn. 2}$$

Table 1: Details of the PC and limestone cements (Lothenbach et al, 2008)

Composition	PC	Limestone
CaO	63.9	55.0
SiO_2	20.2	0.8
Al_2O_3	4.9	0.3
Fe_2O_3	3.2	0.3
CaO (free)	0.93	< 0.01
MgO	1.8	1.8
K_2O	0.78	<0.01
Na_2O	0.42	<0.01
CO_2	0.26	42.5
SO_3	2.29	0.05
Blaine (m^2/kg)	413	429

Table 2: Parott & Killoh (1984) parameters to calculate the hydration of the individual clinker phases

Parameter	C_3S	C_2S	C_3A	C_4AF
K_1	1.5	0.5	1.0	0.37
N_1	0.7	1.0	0.85	0.7
K_2	0.05	0.02	0.04	0.015
K_3	1.1	0.7	1.0	0.4
N_3	3.3	5.0	3.2	3.7
H	1.8	1.35	1.6	1.45

Figure 4 and Figure 5 shows the HYDCEM predicted phase assemblages over a 1,000 day period (24,000 hrs) for the cements with and without limestone using the inputs above. The growth of monocarbonate and monosulfate is programmed to begin 1) after the depletion of gypsum and 2) at one and three days respectively. Comparing the HYDCEM simulations with the thermodynamic predictions, there is good agreement both in terms of volumetric calculations and behaviour. Furthermore, the model accurately

simulates the behaviour of the ettringite, monocarbonate and monosulfate with and without limestone.

4. CONCLUSIONS

HYDCEM has been shown to provide reasonably accurate predictions of the phase assemblage with and without limestone for all four cement phases. The phase assemblages produced shown close agreement with published thermodynamic model predictions for silicate, aluminates and ferrite hydrates. HYDCEM therefore provides a very useful tool for the study of cementitious materials currently and into the future as the cement industry continues to seek more environmentally friendly materials to include in its products. HYDCEM is particularly suited to these developments owing to its ease of use both in terms of model structure and customisable input and analysis features.

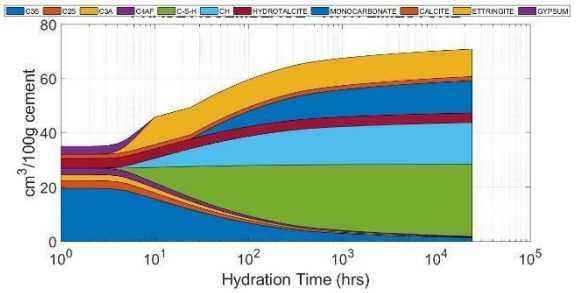

Figure 4: HYDCEM phase assemblage with limestone

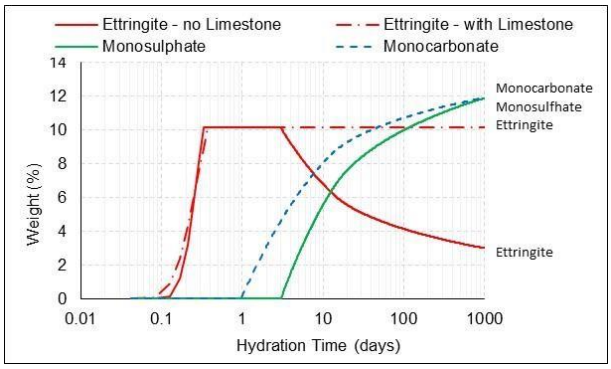

Figure 5: HYDCEM predicted ettringite, monocarbonate and monosulfate growth with and without limestone respectively over a 1,000 day hydration time.

REFERENCES

BS EN 197-1, Cement: Composition, Specifications and Conformity Criteria for Common Cements, British Standards Institution, London, 2000.

ASTM C150 / C150M-18, Standard Specification for Portland Cement, ASTM International, West Conshohocken, PA, 2018

Bonavetti V., Donza H., Menéndez G., Cabrera O. and Irassar E.F. (2003) Limestone filler cement in low w/c concrete: A rational use of energy, Cement and Concrete Research, Vol. 33, pp.865-871

Lothenbach, B., Le Saout, G., Gallucci, E and Scrivener, K (2008), Influence of limestone on the hydration of Portland cements, Cement and Concrete Research 38 (6), pp. 848–860.

Matschei, T., Lothenbach, B. & Glasser, F.P (2007) The role of calcium carbonate in cement hydration, Cement and Concrete Research 37 (4), pp. 551–558.

Matschei, T. & Glasser, F.P (2006) The influence of limestone on cement hydration. Zum Einfluss von Kalkstein auf die Zementhydratation, 59(12): p. 78–86

Antoni, M., Rossen, J., Martirena, F & Scrivener, K (2012) Cement substitution by a combination of metakaolin and limestone, Cement and Concrete Research 42, pp. 1579–1589

Zajac, M., Rossberg, A., Le Saout, G & Lothenbach, B (2014), Influence of limestone and anhydrite on the hydration of Portland cements, Cement and Concrete Research.46, pp. 99–108.

Ingram, K.D., & Daugherty, K.E (1991), A review of limestone additions to Portland cement and concrete, Cement and Concrete Composites 13, pp. 165–170.

Stark, J (2004), Optimierte Bindemittelsysteme für die Betonindustrie, Beton 54 (10), pp. 486–490.

Pera, J., Husson, S & Guilhot, B (1999), Influence of finely ground limestone on cement hydration, Cement and Concrete Composites 21 (2), pp. 99–105.

Bentz D.P. CEMHYD3D: A three-dimensional cement hydration and microstructure development modelling package. Version 2.0. NISTIR 6485, US Department of Commerce,
April 2000.

Bishnoi, S and Scrivener, K.L (2009) µic: A new platform for modelling the hydration of cements,
Cement and Concrete Research 39, pp. 266–
274

Bentz, D.P (2006) Modelling the influence of limestone filler on cement hydration using CEMHYD3D, Cement & Concrete Composites 28, pp. 124–129

Hawkins P, Tennis P, Detwiler R (2003). The use of limestone in Portland cement: a state-of-the-art review. EB227. Skokie IL: Portland Cement Association; 44pp.

Klemm W.A, Adams L.D. An investigation of the formation of carboaluminates. In: Klieger P, Hooton RD, editors. Carbonate additions to cement. ASTM STP, 1064. Philadelphia: American Society for Testing and Materials; 1990. p. 60–72.

Kuzel H-J & Pollmann H (1991). Hydration of C3A in the presence of Ca(OH)2, CaSO42H2O and CaCO3. Cement and Concrete Research, 21:885–95.

Bonavetti V.L, Rahhal V.F & Irassar E.F (2001). Studies on the carboaluminate formation in limestone filler-blended cements. C Cement and Concrete Research 31:853–9.

Kakali G, Tsivilis S, Aggeli E, Bati M (2000). Hydration products of C3A, C3S and Portland

cement in the presence of CaCO3. Cement and Concrete Research 30:1073–7.
Kulik, D (2007) GEMS-PSI 2.1, available at http://gems.web.psi.ch/, PSI-Villigen, Switzerland
Holmes, N., Kelliher, D and Tyrer, M (2019) HYDCEM: A new cement hydration model, ICSBM 2019, 2nd International Conference of Sustainable Building Materials, 12-15 August, Eindhoven The Netherlands
Parrot, L.J & Killoh, D.C (1984) Prediction of cement hydration, Br. Ceram. Proc. 35 41–53.
Lothenbach, B., Winnefeld, F., Alder, C., Wieland, E., and Lunk, P. (2007) Effect of temperature on the pore solution, microstructure and hydration products of Portland cement pastes, Cement and Concrete Research 37 (4) pp. 483–491.
Mohamed, A.R., Elsalamawy, M and Ragab, M (2015) Modelling the influence of limestone addition on cement hydration, Alexandria Engineering Journal 54, pp. 1–5

39th Cement and Concrete Science Conference **Paper Number 013**
9-10th September 2019
University of Bath

The effect of high gamma irradiation on sodium and potassium based metakaolin geopolymers

T.A. Mubasher and L.Leay
The University of Manchester, Dalton Cumbrian Facility

M.Hayes and E.Butcher
National Nuclear Laboratory (NNL)

ABSTRACT

Ongoing work within the nuclear industry is to understand the radiation stability of new materials for waste encapsulation and determine any advantages over the currently used cementitious grout. In this preliminary study, the use of essentially calcium-free geopolymers derived from pure metakaolin is investigated. These materials are produced by a chemical reaction between an alkali solution and the aluminosilicate precursor (metakaolin). Four different Si:Al ratios (1.70, 1.90, 2.25 and 2.50) have been investigated along with two different activating alkali ions (Na and K). An experimental investigation involving Na and K based metakaolin geopolymer formulations, irradiated with a dose rate of around 300 – 390 Gy min-1 and a total dose of around 4.70 MGy was conducted. To determine radiation-induced changes to the material, gas adsorption/desorption, FT-IR and pXRD techniques were used. The results have revealed significant changes to the structure and morphology of the material. In particular, we note a reduction in total porosity and a change in the pore size distribution which could affect gas transport properties relevant to radiolysis products from the pore water. We observe changes in compressive strength indicative of structural changes within the matrix; an important consideration for materials used to immobilize nuclear waste.

1. INTRODUCTION

Currently, in the UK the preferred method of immobilising most intermediate-level wastes is through the use of Portland cement (PC) (blended with a Secondary Cementitious Material (SCM's) such as blast furnace slag (BFS) or pulverised fuel ash – fly ash (FA)) to produce a passively safe waste package. It is expected that cementitious encapsulation will be continued as part of a suite of technologies for waste treatment as the UK transitions from reprocessing to broad front decommissioning. For the most complex sites decommissioning is scheduled to take until 2120, and therefore requires long-term security of supply of materials to provide an encapsulation matrix with the desired properties.

There are challenges associated with current SCM's, due to the changes in the UK steel industry and the significant reduction in coal-fired power stations, with the result that the long-term guaranteed consistent supply of BFS or FA to the required nuclear specification is a significant issue. Therefore, alternative materials such as geopolymers may offer advantages over conventional cementitious systems both in terms of a long-term supply and for certain waste streams that will require treatment during the decommissioning operations. These include:

The high volume of certain reactive metals
Oils, sludge, greases and ion exchange resins
Effluents liquids - cheating reagents
Lower volume wastes which may significantly retard Portland cement (PC) systems (e.g. Zn)
Particulate solids

Any alternative method of immobilisation that is developed is required to be stable, cost-effective and to be able to incorporate larger volumes of the above wastes than may be attainable in PC systems. Geopolymers could offer an attractive alternative option in the immobilisation of such wastes, as the exact formulation can be tailored to suit a particular application.

Geopolymers are 3-D aluminosilicate materials produced from a condensation reaction between an aluminosilicate precursor and an alkali activating solution, commonly Na or K. They possess low levels of crystallinity and can be considered as amorphous zeolites, due to the aluminates and silicates being tetrahedrally interlinked. The condensation reaction leads to an amorphous structure. Even though the reaction is fast, nanocrystallites have been observed. The geopolymerisation process can be separated into three stages, dissolution, polymerisation and stabilisation (Sagoe et al. 2007) (Provis & Deventer, 2007).

2. EXPERIMENTAL

Samples were prepared using Metakaolin (Metamax- Lawrence industries), potassium silicate (k120 - Tennants distribution Ltd), potassium hydroxide pellet (Fisher Scientific), sodium silicate (extra pure - VWR international), sodium hydroxide pellets (Alfa Aesar), and deionised water.
Hydroxide pellets, silicate solutions and water were mixed under low shear (~61 rpm) in a Hobart mixer for 15 minutes, then allowed to cool for 24 hours, ensuring that room temperature was reached. Metakaolin was added and mixed under the same low shear conditions, for 20 minutes (Table 1).

Table 2: Molar ratios used for the geopolymers formulations (X = Na or K)

Si:Al	$H_2O:X_2O$	X:Al
1.70	11.00	1.50
1.90	11.00	1.50
2.25	11.15	1.50
2.50	11.45	1.50

The rheology of the geopolymer grout was measured after mixing, using a Rheometer, and then cast into cylindrical silicone moulds of 30 mm diameter and 115 mm height. These were cured at a temperature of 20 °C +/ 1 °C and an RH of 95% +/- 5% for 7 days. The FT-IR spectra were obtained using a Bruker Vertex 70 with a resolution of 2 cm^{-1} between 5000 – 400 cm^{-1}. The pore structure was studied with a Micromeritics Tristar II 3020 surface area and porosity analyser. Results were collected three times for each sample and averaged.
Gamma irradiation was carried out in a self-contained ^{60}Co irradiator at the Dalton Cumbrian Facility. The irradiation regime involved two periods of irradiation due to the availability of equipment. The first irradiation period was for 111 hours giving a total dose of 2.3 MGy. The second irradiation period was for 115 hours, with a total dose of around 2.39 MGy. Overall, every sample received around 4.69 MGy, at a dose rate of 300 - 390 Gy min^{-1} using a turntable. The temperature in the irradiator chamber reaches 50°C and the effect of heating alone will be determined in future work.

3. RESULTS AND DISCUSSION

All four K-geopolymer formulations exhibited low viscosity and highly fluid behaviour (Table 2). This is important as the material may need to flow around the waste including tortuous pathways to effect encapsulation with minimal voidage. For BFS/OPC grouts this is typically around 500 mPa.s (106.0 s^{-1}) at time zero. Formulations with Si:Al molar ratio of 1.70 and 1.90 are below this value, whereas 2.25 and 2.50 are slightly above. For molar ratio of Si:Al 1.70, 1.90 and 2.25 setting time was within 24 hours, whereas for 2.50, the set took longer: between 24 and 48 hours (Table 2).

Table 3: K-Geopolymer setting time and Viscosity

Si:Al	Setting time (hr)	Viscosity (mPa.s) (106.0s^{-1})
1.70	24	359.7
1.90	24	409.2
2.25	24	614.8
2.50	24 - 48	614.8

The Na-geopolymer was a more viscous material when compared with K-geopolymer. The workability of the material was also difficult. Setting time was also different, the formulations with Si:Al molar ratio of 1.70 and 1.90 set within 24 hours, whereas 2.25 took 48 hours. However, Si:Al 2.50 did not set at ambient temperature (Table 3). One of the reasons for not setting at ambient temperature could be due to the addition of extra silicate solution, and insufficient alkali to carry out the dissolution of Metakaolin as readily as other formulations.

Table 4: Na-Geopolymer setting time and viscosity

Si:Al	Setting time (hr)	Viscosity (mPa.s) (106.0s^{-1})
1.70	24	1198.0
1.90	24	2434.0
2.25	48	853.1
2.50	Fail	495.2

The formulation with Si:Al ratio of 2.50 for Na geopolymer did not set within 24 - 48 hours at ambient temperature, therefore this formulation will not be carried forward for further analysis and irradiation trials. This is because one of the criteria for ILW immobilisation is that the cementitious encapsulating material should set within 24 - 48 hours at ambient temperatures.

3.1 GAMMA IRRADIATION RESULTS

The XRD analysis (not shown) revealed that all the samples have an amorphous structure that did not change significantly as a result of irradiation.

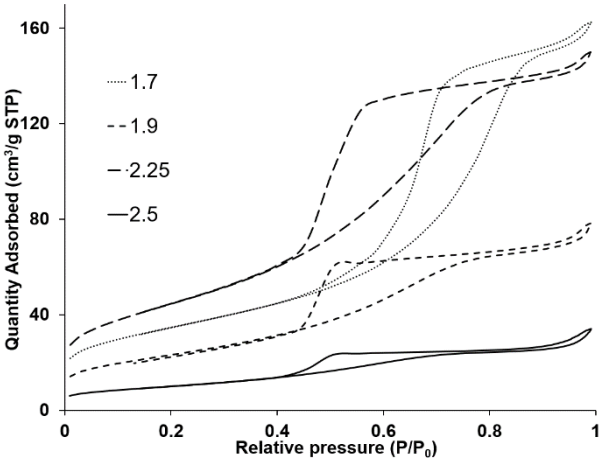

Figure 3: Isotherms for non-irradiated K-Geopolymers

The porosity of the material forms a key part in understanding the suitability of the material for ILW

immobilisation. The K-geopolymer non-irradiated samples (Figure 1) all exhibit a type IV isotherm with a hysteresis loop which is similar to H2 (a) or H2 (b), which indicates that the pore network is complex. Gas adsorbed for Si:Al 1.70 is higher compared to the other ratios (Figure 1). This can indicate that Si:Al 1.70 material may contain larger amount of interconnected pores (Thommes et al. 2015).

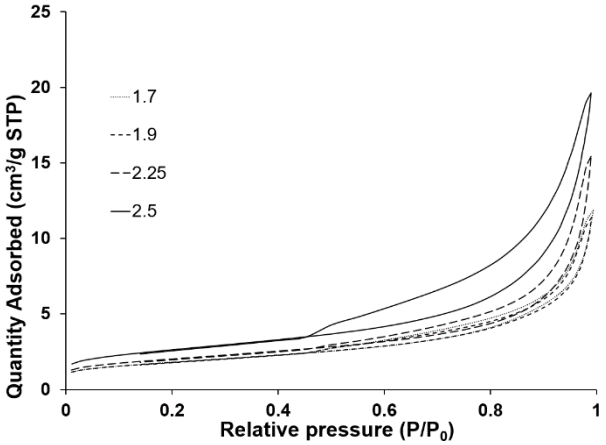

Figure 2: Isotherms for irradiated K-Geopolymers.

All the irradiated K-geopolymer samples have similar isotherms (Type III) (Figure 2). Also, the isotherms shapes have changed significantly and the gas adsorbed is considerably less, when compared with the non-irradiated samples (Thommes et al. 2015).

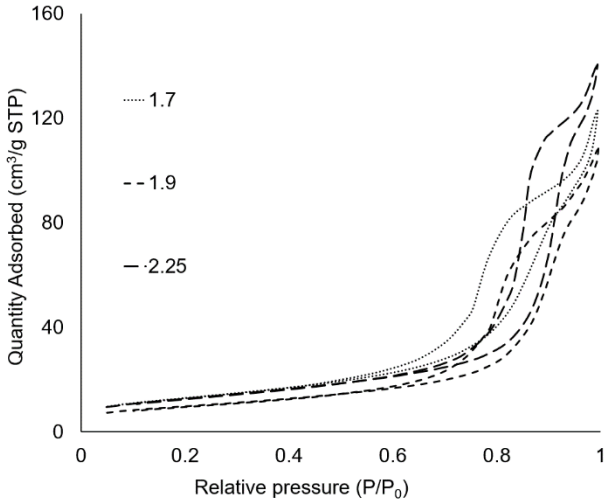

Figure 3: Isotherm for non-irradiated Na-Geopolymers

The non-irradiated Na-geopolymer samples (Figure 3) have also shown isotherms similar to a type IV, with a hysteresis loop which is comparable to an H2 (a) or H2 (b). The gas adsorbed for the non-irradiated samples (Figure 3) is higher when compared with the irradiated samples (Figure 4). The change in isotherms also shows that gamma radiation has led to significant changes in the pore structure.

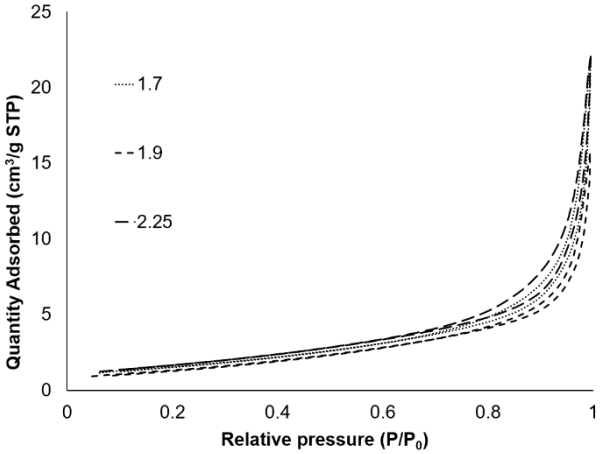

Figure 4: Isotherm for Na-geopolymer irradiated

3.1.1 ISOTHERM ANALYSIS

The gas adsorption/desorption isotherm analysis for the K-geopolymers shows that the non-irradiated samples are mesoporous, meaning the pore diameter is predominantly between 2 - 50 nm (Calculated by BJH method). The pore width distribution for irradiated samples exceeded 100 nm, making them macroporous, while also containing pores between 2 - 50 nm (mesopores) (Thommes et al. 2015). Gamma irradiation caused the pore width distribution and average pore size to increase; however, the total pore volume decreased (Table 4).

Table 5: Average pore size and pore volume before and after irradiation for K-geopolymer.

	Non-Irradiated		**Irradiated**	
Si:Al	Average pore size (nm)	Total Pore Volume (cm^3g^{-1})	Average pore size (nm)	Total Pore Volume (cm^3g^{-1})
1.70	7.32	0.27	12.12	0.015
1.90	5.12	0.12	11.95	0.015
2.25	5.07	0.23	14.38	0.021
2.50	5.22	0.05	13.67	0.028

Gas adsorption/desorption analysis for non-irradiated Na-geopolymers also showed that the material is mesoporous with pore diameters between 2 – 50 nm. In contrast to the K-geopolymers, the pore distribution in the irradiated samples did not exceed 100 nm (Thommes et al. 2015). In fact, irradiation led the opposite effect: the average pore size decreased. However, the total pore volume still decreased, albeit by a small amount (Table 5).

Table 6: Average pore size and pore volume before and after irradiation for Na-geopolymer.

	Non-Irradiated		Irradiated	
Si:Al	Average pore size (nm)	Total Pore Volume (cm^3g^{-1})	Average pore size (nm)	Total Pore Volume (cm^3g^{-1})
1.70	4.07	0.14	2.80	0.010
1.90	4.70	0.12	2.50	0.010
2.25	5.80	0.17	2.90	0.011

3.1.2 FT-IR ANALYSIS

The FT-IR spectra show broad bands between 3400 - 3480 cm^{-1} for both irradiated and non-irradiated samples (Na and K-geopolymer), correlating to stretching (O-H) and bending (O-H). Figure 5 shows an example of one of the formulations Si:Al 1.90 for Na and K-geopolymer. This can indicate that there is more water in the non-irradiated samples as compared to the irradiated samples. This trend was noticed across all formulations.

The pronounced peak at 950 - 1000 cm^{-1} is recognized as Si-O-Si or Si-O-Al asymmetric stretching vibration. The change in this peak noticed for K-geopolymer suggests that irradiation leads to a higher degree of polymerisation and is consistent across all formulations, irrespective of the change in Si:Al molar ratios. Figure 6 shows an example of one of the spectra for formulation (Na and K-geopolymer) Si:Al 1.90.

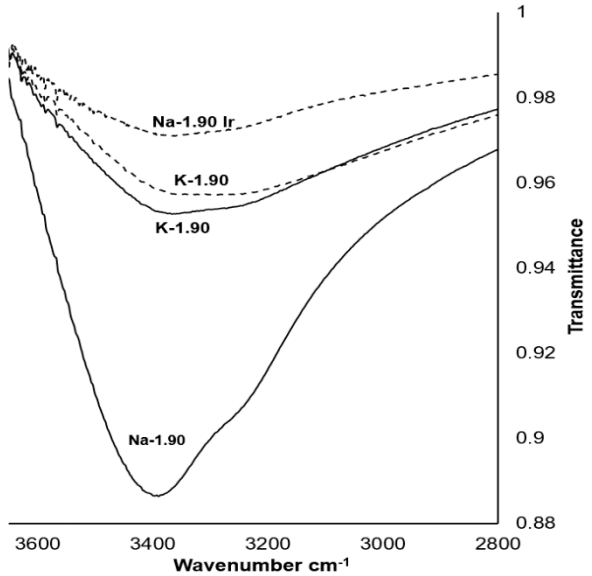

Figure 5: FT-IR spectra for K and Na geopolymer (Si:Al 1.90) Wavenumber 3400 – 3480 cm^{-1}

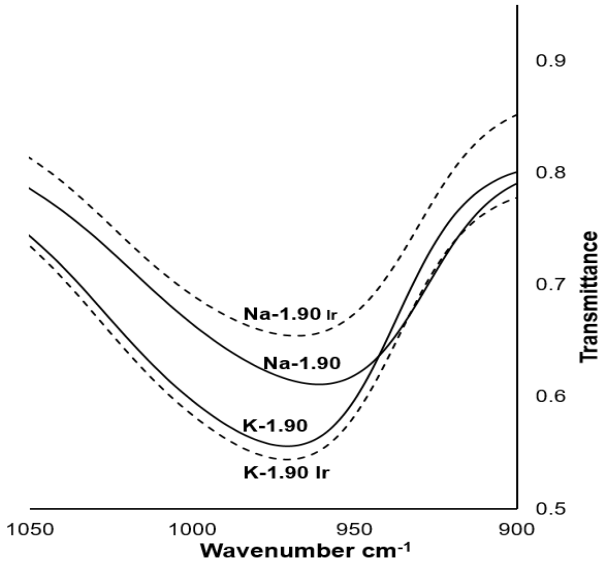

Figure 6: FT-IR spectra for K and Na-geopolymer (Si:Al 1.90) Wavenumber 950 – 1000 cm^{-1}

For Na-geopolymer the trend was noticed to be opposite, irradiation led to a decrease in polymerisation and bonding of Si-O-Si or Si-O-Al.

4. CONCLUSION

The analysis shows that the K-geopolymer formulation produced a highly fluid system when compared with Na-geopolymer.

FT-IR analysis showed that gamma irradiation led to an increase in polymerisation in the K-geopolymer, irrespective of the change in molar ratios, at wavenumber 950 – 1000 cm^{-1}. Conversely, the Na-geopolymer showed a decrease in polymerization.

Gas adsorption/desorption revealed that geopolymers (non-irradiated) are mesoporous (2 – 50 nm) with a small volume of macroporosity (>50 nm) for K and Na-geopolymers. Gamma irradiation led to a significant change in the porosity of K and Na-geopolymers. Increase in average pore size and a decrease in total pore volume was noticed for K-geopolymer, whereas a decrease in average pore size and total pore volume was noticed for Na-geopolymer.

ACKNOWLEDGEMENT

This PhD project is supported by the University of Manchester and National Nuclear Laboratory. This research was conducted at the University of Manchester's Dalton Cumbrian Facility and National Nuclear Laboratory Workington, Cumbria

REFERENCES

Sagoe-Crentsil, K., and L Weng, 2007. Dissolution processes, hydrolysis and condensation reactions during geopolymer synthesis: Part II. High Si/Al ratio systems. Journal of Material science, 3007-3014.

Provis, John L., and Jannie S.J. van Deventer., 2007. Geopolymerisation kinetics In situ energy-dispersive X-ray diffractometry. Chemical engineering science, 2309-2317.
Thommes, M., Kaneko, K., Neimark, A., Olivier, J., Rodriguez-Reinoso, F., Rouquerol, J. and Sing, K., 2015. Physisorption of gases, with special reference to the evaluation of surface area and pore size distribution (IUPAC Technical Report). Pure Applied Chemistry.

39th Cement and Concrete Science Conference **Paper Number 014**
9-10th September 2019
University of Bath

Manufacture of lightweight aggregate granules Containing phase change materials

Ahmad Wadee, Pete Walker, Nick McCullen, Veronica Ferrandiz-Mas
Department of Architecture and Civil Engineering
University of Bath, UK

ABSTRACT

Buildings are responsible for more than 40% of total energy consumption and 25% of anthropomorphic derived carbon emissions. Hence, the development of energy efficient materials, which help to minimise these issues, is important. Phase change materials (PCMs) are known as latent heat storage units, as they can store latent heat energy within a specific temperature range. Energy is absorbed when the material changes from a solid to liquid state, and released when the material changes back from a liquid to solid state. PCMs can reduce the energy requirements of a building by reducing peak demand for either summer cooling or winter heating. PCMs also have the potential of reducing the amount of energy lost and increasing thermal comfort in buildings, by buffering temperature fluctuations throughout the day. This research explores more efficient ways to host PCMs and further develop new methods of encapsulating PCMs and incorporating them into the built environment. This paper presents experimental findings from an on-going study investigating how to incorporate the PCMs into cement mortars by impregnating PCMs into lightweight aggregates (LWA), to obtain high heat-storage capacity granules. Commercial PCMs with melting points at 18°C, 22°C and 25°C were used. Methods and conditions for optimal absorption of these PCMs into two types of LWA, aerated concrete and perlite have been evaluated. The results show the influence of the microstructure of the LWA, PCM/LWA ratio, impregnation temperature and time in the heat storage capacity of the granules. The LWA containing PCMs have potential to be incorporated into a variety of building materials, including mortars, plasters, blocks, and concrete panels. The compatibility between PCM aggregates and the surrounding matrix, as well as thermal performance and structural properties, will be investigated in future work

1. INTRODUCTION

Phase change materials capture and release thermal energy when changing from one phase to another allowing them to control temperature fluctuations in buildings and increase thermal mass (Akeiber *et al.*, 2016). They can store heat gains as latent heat within a specific temperature range. The use of PCMs allows the building to reduce the amount of energy lost and increase thermal comfort, by adjusting temperature fluctuations throughout the day (Akeiber *et al.*, 2016). They are therefore considered latent heat storage units.

Paraffin wax is an organic PCM commonly used as a latent heat storage unit, due to its wide range of applications (Kalnæs and Jelle, 2015). The advantages of using paraffin wax PCM are that it is nontoxic, chemically stable and has a high latent heat capacity (Rubitherm, 2019).

Several methods have previously been studied to incorporate PCMs into construction materials (Kalnæs and Jelle, 2015) (Akeiber *et al.*, 2016; Baetens *et al.*, 2010). These include directly mixing the PCM with the construction material known as direct incorporation and microencapsulation, where the phase change material is enclosed as a micron size particle in an inert organic or synthetic polymer (Hawlader *et al.*, 2003). These methods have the risk of the PCM leaking whilst in its liquid form (Özonur *et al.*, 2005).

The work reported in this paper aims to find a suitable method to incorporate the PCM into construction materials such as mortar and gypsum plaster. The method that has been selected for this research soaks commercial lightweight aggregates (LWA) in the Phase change material (PCM). Vacuum impregnation and immersion are the two methods compared. Aerated concrete and perlite were selected as potential host granules for the phase change material. Once the method of impregnating the PCM into the LWA has been established the work has aimed to establish the optimal conditions for incorporating the phase change materials into the LWA, such as: impregnation temperature; LWA:PCM ratio and absorption time. The granules were then coated with a mixture of CEMI cement powder, which constitutes 95-100% clinker with the remaining 05% minor additional constituents (British Standard Publication, 2011) and sodium silicate.

2. MATERIALS AND METHODS

Rubitherm RT was selected as the phase change material with the desired characteristics, with specific melting points of 18°C, 22°C and 25°C (Rubitherm, 2019). The LWA of sizes between

0.5mm - 4mm granules were kept in a 50°C oven for a minimum of 24 hours to remove any moisture, with the aggregates measured for every preceding hour until two identical results were obtained. A 50g sample of the aerated concrete was placed in a mesh container to prevent anything from being lost. The phase change material was measured to get specific LWA:PCM ratios (Table 1)

Table 1. LWA:PCM mass ratio

LWA :PCM Mass Ratio	LWA (g)	PCM (g)
0.3	50	15
0.5	50	25
0.7	50	35
1.0	50	50
1.3	50	65
1.5	50	75

The Immersion test was performed by placing 50g of the LWA within mesh and subsequently immersed in the phase change material, Rubitherm RT18/22/25HC phase change material for 1 hour. The phase change material was held in a desiccator and kept in a water bath at a temperature of 40°C, so it can remain in a liquid phase throughout the immersion period. The impregnated lightweight aggregate was then removed and surface dried with absorbent paper for 5 minutes to remove any phase change material attached to the surface. The weight of the impregnated LWA was then taken so that the absorption by percentage weight can be calculated.

The procedure for the vacuum impregnation test was similar to the immersion test, however, there was an additional use of a vacuum to remove air from the pores of the aerated concrete so that the phase change material can be absorbed by force into the pores of the aerated concrete. The phase change material was poured in to the desiccator and placed in the fridge for a minimum of 24 hours to solidify. The aerated concrete was then placed in the desiccator on top of the solid PCM. The air was removed from the pores using a vacuum pressure of -82kPa for 1 hour. The temperature at this point was kept below the melting temperature of the specific phase change material with the use of a water bath. After the initial hour the vacuum was switched off and the temperature of the water bath was increased to 40°C causing the phase change material to melt. The lightweight aggregate was submerged into liquid phase change material, which filled up the pores for 1 hour. The impregnated lightweight aggregate was then removed and surface dried with absorbent paper for 5 minutes to remove any phase change material attached. The weight of the impregnated lightweight aggregate was then taken so that the absorption by percentage weight can be calculated. The Vacuum Impregnation test was then repeated for the perlite with the same parameters.

The viscosities of the PCMs were then measured using a TA Discovery HR-2 hybrid rheometer to see how temperature affected the viscosity of each of the PCMs. It was predicted that as the viscosity of the PCM decreases it could be easier to force it into less accessible pores of the LWA using the vacuum. The vacuum test as previously described was conducted at a constant viscosity (Table 3). The same test was again conducted at a constant temperature of 80°C. Another variable to be considered is how time would affect absorption. The tests were repeated with the granules being allowed to absorb the PCM for 2 and 4 hours.

The PCM impregnated LWA granules were then coated using 4 different combinations of CEMI cement powder and sodium silicate, to ensure the granules were completely coated and Polyvinyl Acetate (Table 2). The PCM impregnated granules were kept at a temperature of 4°C for the PCM within the pores to remain solid. A 550W Bosh MUM46A1GB Mixer was used at speed 2 to mix the PCM impregnated granules with the coating material forming a layer on the surface of the granules. The mixing time was set to 15 minutes, as this time was deemed sufficient to coat the granules evenly. The coated granules were then left to dry for a period of 48 hours. Once the coated granules were dry they were placed in a 50°C oven to measure the amount of PCM which had leaked, although in reality the material would never be subjected to a temperature this high. This method was conducted following the PCM retention test conducted by Kastiukas *et al.*, 2016.

Table 2. Coating Materials

Coating Material	Ratio
Sodium Silicate / CEMI cement powder	1 : 0.3 : 0.6
Sodium Silicate / CEMI cement powder	1 : 1 : 1.3
Sodium Silicate / CEMI cement powder	1 : 1 : 1
Sodium Silicate / CEMI cement powder	1 : 1.4 : 1.4
Polyvinyl Acetate	1 : 1

3. RESULTS AND DISCUSSION

The current results indicate that vacuum impregnation is more efficient in impregnating the lightweight aggregate, particularly for the phase change materials with a higher melting temperature. It is seen when handling the phase change materials that the phase change materials with a higher melting temperature also have a higher viscosity, at the specific temperature chosen 40°C. This is the reason that the vacuum method has a greater impact on the percentage weight absorption of Rubitherm RT25HC when compared to Rubitherm RT18HC. The vacuum method is more effective than simple immersion when the viscosity of the phase change material is higher.

The data shown in Figures 1 – 3 and 5 – 8 are an average of results obtained from three tests with the standard deviation shown in the form of error bars. Some error bars cannot be seen due to a very low standard deviation.

(a)

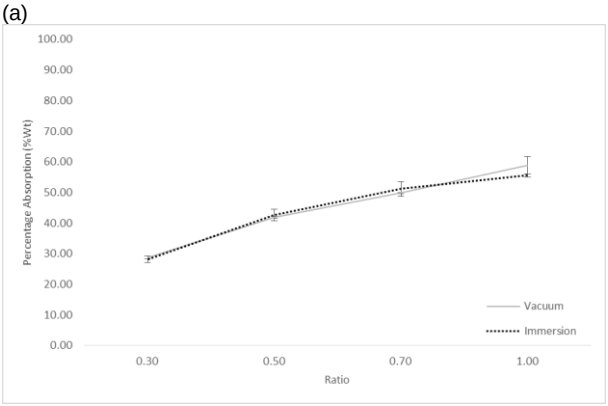

(b)

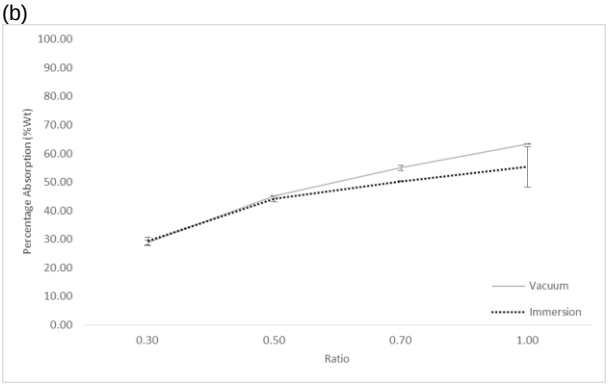

(c)

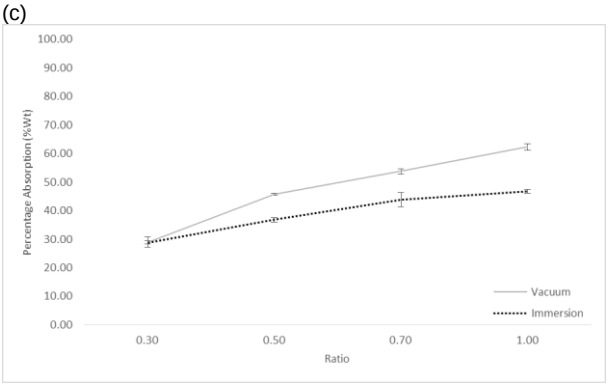

Figure 1: (a)Rubitherm RT18HC (b)Rubitherm RT22HC (c)Rubitherm RT25HC. Comparison of Vacuum Impregnation and Immersion.

The results also show that the higher the ratio the greater the percentage by weight absorption, with the graphs for all the tests showing the highest absorption for a ratio of 1.0. Figures 1 (a), (b) and (c) indicate that increasing the amount of phase change material will not necessarily mean a comparable increase in the rate of absorption, as the graphs are not linear.

With vacuum impregnation found to be the more suitable method of incorporating the PCM within the pores of the LWA further tests were conducted to find the optimum PCM:LWA ratio. Figure 2 identifies a ratio of 1.3 from which the percentage absorption wt. does not increase. Therefore, a ratio of 1.3 has been used as the optimum impregnation ratio for the absorption of Rubitherm RT into aerated concrete using vacuum impregnation.

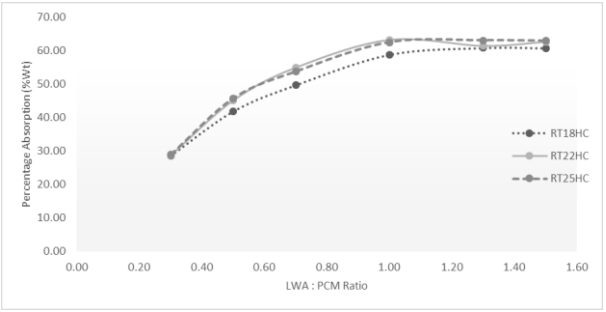

Figure 2: Optimum impregnation Ratio for the 3 PCMs, The optimum point is found to be 1.3.

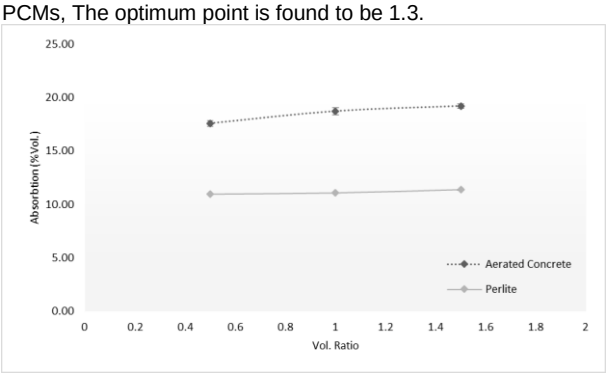

Figure 3: Comparison between the percentage volume absorption of aerated concrete and perlite at different volume ratios.

When a comparison is made between Aerated Concrete and Perlite using percentage weight initial observations show perlite to significantly outperform the aerated concrete. However, perlite is a much lighter material than the aerated concrete and therefore occupies a much larger volume of space than aerated concrete for the same mass. This is of importance when the granules are mixed into mortar as the PCM granules will replace the standard sand within the mortar by percentage volume. A comparison has been done to analyse how much PCM has been absorbed in the same volume of the LWA. Figure 3 shows the aerated concrete to have absorbed a larger amount of PCM at each of the volume ratios tested. At a ratio of 1 the percentage volume absorption of perlite is 8.6%Vol. compared to 17.3%Vol. of aerated concrete. At a ratio of 1.5 the percentage volume absorption of perlite is 9.8%Vol. compared to 17.6%Vol. of aerated concrete. The optimum LWA:PCM mass ratio has previously been identified as of 1.3. When this mass ratio is converted into a volume ratio a value of 0.5 is obtained. Figure 3 shows the volume absorption from this point to a volume ratio of 1.5. This was carried out to explore potential increase in the volume absorption of perlite. Following these results it was assumed that the optimum impregnation ratio (vol.) was below 0.5, making it a less effective carrier for the PCM than aerated concrete. Therefore, the material was no longer used.

The rheometer viscosity test was conducted to explore how temperature affects the viscosity. It was hypothesised that as the viscosity of the PCM decreases it would be easier to force it into less accessible pores of the LWA using the vacuum. Figure 4 displays how an increase in temperature decreases the viscosity of the PCM.

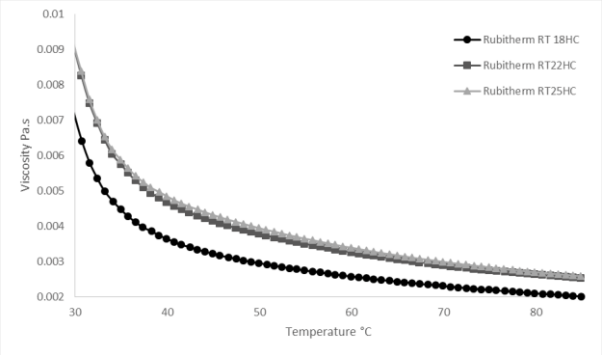

Figure 4: Viscosity test using a rheometer. Analysing how increasing the temperature would affect the viscosity of the three PCMs.

Previous works have used a temperature of 40°C to produce the PCM in a liquid form. This could have been done with the idea that once the PCM is liquid, absorption would be possible as the temperature is significantly higher than the melting temperature of the PCM. Figure 4 shows that the viscosity of all three PCMs decreases as the temperature increases. It also shows that at a specific temperature (i.e. 40°C) the viscosities of all three PCMs are different. This indicates that viscosity could be a variable affecting both the absorption of the PCM into the granules and the difference in %Wt. absorption for the three PCMs, when the LWA:PCM ratio and impregnation temperature are kept constant. Table 3 displays the specific difference in viscosities at 40°C and the increase in temperature required to get a constant viscosity of 0.0036Pa.s.

Table 3. Viscosity and Temperature of the PCMs at 40°C and 0.0036Pa.s

PCM	Temperature °C	Viscosity Pa.S
Rubitherm RT18HC	40	0.0036
Rubitherm RT22HC	40	0.0046
Rubitherm RT22HC	53	0.0036
Rubitherm RT25HC	40	0.0047
Rubitherm RT25HC	56	0.0036

In order to form a comparison between temperature and viscosity control for the absorption, the absorption tests were conducted at a viscosity of 0.0036Pa.s.

The data in Figure 5 shows a very slight increase in the absorption of the PCM for Rubitherm RT22HC, 2.57% and Rubitherm RT25HC, 3.87% with a constant viscosity. The value for Rubitherm RT18HC remains the same when the standard deviation is considered as the temperature for both tests was 40°C. Increases in absorption could be considered negligible as temperature is easier to control than viscosity.

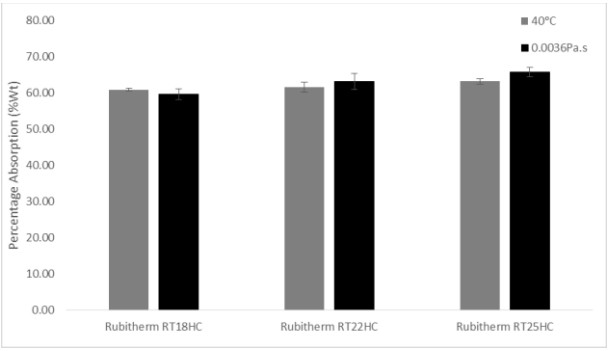

Figure 5: Comparison of absorption at constant viscosity and constant temperature.

An alternative approach was to significantly increase the impregnation temperature. This test has initially only been done for Rubitherm RT25HC as it showed the highest increase in absorption when the temperature was increased. The temperature was increased to 80°C as at this point in Figure 4 each of the PCMs reach its most viscous point.

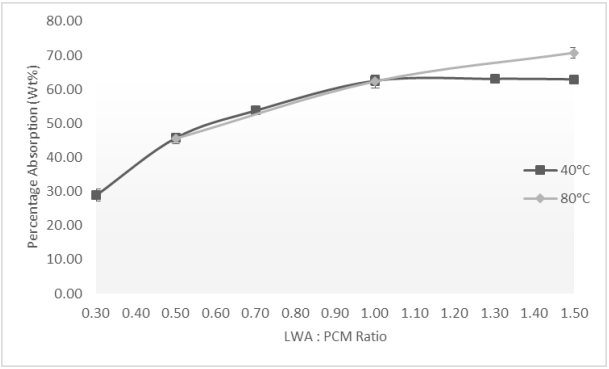

Figure 6: Comparison of absorption of Rubitherm R25HC at 40°C and 80°C.

When comparing the effect of temperature on the PCM absorption, Figure 6 shows that at a lower PCM:LWA ratio the %Wt absorption is similar at a temperature of 80°C and 40°C. However, there is more absorption at 80°C than 40°C when there is more PCM available to be absorbed. An explanation for this could be when there is more PCM available to be absorbed at a higher LWA:PCM ratio the vacuum forces the PCM into the less accessible pores of the LWA more easily when the viscosity is lower. Further work is needed to determine whether increasing the optimum impregnation temperature to 80°C would have as significant impact on the absorption of Rubitherm RT18HC and Rubitherm RT22HC.

To analyse whether the variable of time would affect the amount of PCM absorbed the time allowed for absorption was increased to 2 and 4 hours once the vacuum had been switched off. The PCM material used for this test was Rubitherm RT22HC.

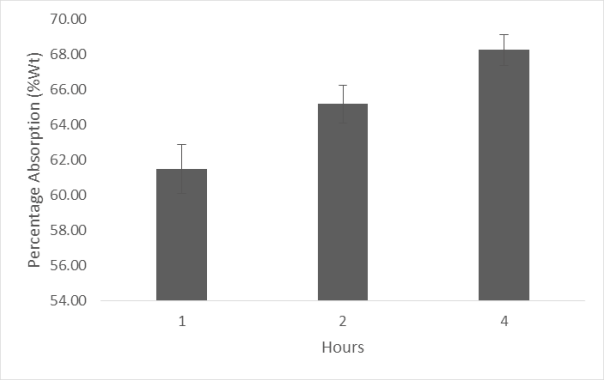

Figure 7: Effect of time on the amount of Rubitherm RT22HC into aerated concrete using vacuum impregnation.

Figure 7 shows that increasing the absorption time has an effect on the amount of PCM absorption. However, difference in absorption between 1 hour and 2 hours is 3.7%, whilst the difference between 1 hour and 4 hours is 6.8%.These results indicate that aerated concrete reaches close to its full absorption potential within the first hour, when the PCM:LWA ratio is 1.3 and the vacuum impregnation temperature is 40°C. When the additional amount of PCM absorbed over this time is compared to the time required for this to take place, the additional absorption is not considered a productive use of time.

The selection of the coating material was dependant on the material which allowed the least amount of PCM to leak out. Based on the results in Figure 8, and a visual analysis of the coated granules, a combination of sodium silicate and CEMI cement powder showed the most promising results. The visual analysis showed the granules were completely coated without any gaps and the data for the leak test shows the lowest amount of PCM leaked in a single cycle.

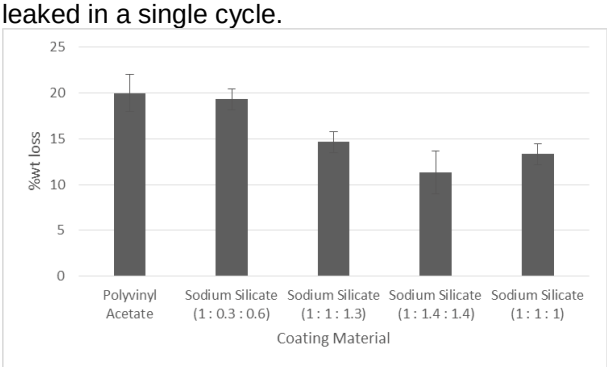

Figure 8: Amount of PCM leaking from a material during a single cycle using different coating materials.

Further work Including Scanning Electron Microscopy (SEM) will need to be conducted on the coating material and testing the leaking of the PCM over several feeze-thaw cycles. Further to this point, future work will include manufacturing of mortars with a percentage of standard sand replaced according to BS EN 196-1.
Once the mortars have been manufactured the, thermal, physical and mechanical properties of the material will be analysed.

4. CONCLUSION

The following conclusions can be drawn from the results obtained thus far:
Vacuum impregnation is a more effective method of absorbing the PCM into the LWA than immersion.
The optimum impregnation ratio using a aerated concrete LWA and a temperature of 40°C is 1.3.
The viscosity of the PCM does have an influence on the amount of PCM absorbed although at lower temperature this is less significant.
The time allowed for absorption does have an effect on the amount of PCM absorbed, however this amount of absorption isn't considered substantial enough when compared to the additional time required.
A combination of sodium silicate and cement powder does produce an effective coating to prevent the PCM from leaking from the LWA although this requires further testing.

ACKNOWLEDGMENTS

The authors would like to thank the BRE and EPSRC for funding the project.

REFERENCES

Akeiber, H., Nejat, P., Abd Majid, M.Z., Wahid, M.A., Jomehzadeh, F., Famileh, I.Z., Calautit, J.K., Hughes, B. & Zaki, S.A., 2016. A review on phase change material (PCM) for sustainable passive cooling in building envelopes. *Renew Sust Energ Rev,* 60, pp. 1470-1497.
Baetens, R., Jelle, B.P. & Gustavsen, A., 2010. Phase change materials for building applications: A state-of-the-art review. *Energy and Buildings,* 42(9), pp. 1361-1368.
Hawlader, M.N.A., Uddin, M.S. & Khin, M.M., 2003. Microencapsulated PCM thermal-energy storage system. *Applied Energy,* 74(1-2), pp. 195-202.
Kalnæs, S.E. & Jelle, B.P., 2015. Phase change materials and products for building applications: A state-of-the-art review and future research opportunities. *Energy and Buildings,* 94, pp. 150176.
Kastiukas, G., Zhou, X.M. & Castro-Gomes, J., 2016. Development and optimisation of phase change material-impregnated lightweight aggregates for geopolymer composites made from aluminosilicate rich mud and milled glass powder. *Construction and Building Materials,* 110, pp. 201210.
Özonur, Y., Mazman, M., Paksoy, H.Ö. & Evliya, H., 2005. Microencapsulation of coco fatty acid mixture for thermal energy storage with phase change material. *International Journal of Energy Research,* 30(10), pp. 741-749.

Publication, B.B.S., 2011. *Cement BS EN 1971:2011.*
Rubitherm. (2019, 05 05). Rubitherm GmbH. Retrieved from https://www.rubitherm.eu/en/index.php/productcategory/organische-pcm-rt

39th Cement and Concrete Science Conference **Number 015**
9-10th September 2019
University of Bath

High Resolution Solid State NMR Structural Study of a Fast-Setting Ternary Binder during its Early Stage Hydration

R. Sassi, F. Fayon, E. Veron, V. Montouillout
CEMHTI, CNRS-UPR3079, Univ. Orléans, F-45071 Orléans, France
M. Chaouche
ENS Paris-Saclay, 94230 Cachan, France

ABSTRACT

The chemical phenomena that characterize cement hydration are quite complex and interdependent, and even after almost two centuries of studies, they are still subject to debate.
This difficulty becomes even more challenging with complex mixtures combining different hydraulic binders. XRD have been widely used for analyses of crystalline phases in both anhydrous and hydrated cements, but only advanced NMR can provide quantitative description of non-crystalline phases.
In this work, the structural modifications occurring during hydration of a fast-setting ternary binder based on white Portland cement, white calcium aluminate cement and calcium sulfate were investigated. We particularly focused on the early stage of the hydration up to 28 days, working with samples whose hydration was controlled and stopped.
^{27}Al MQ-MAS NMR experiments as well as editing techniques as {^{1}H}-^{27}Al and {^{1}H}-^{29}Si Cross Polarization MAS NMR were combined to distinguish all the aluminum and silicon species formed during the hydration. The consumption of initial products as well as the precipitation of hydraulic phases (Ettringite, monosulfate, Stratlingite, CSH and CASH) were unambiguously quantified.
Finally, the drawing of the consumption and formation of phases was correlated with mechanical strength measurements

1. INTRODUCTION

Ternary binders based on ordinary Portland cement OPC, calcium aluminate cements CAC and calcium sulfates C$, are used as rapid setting cements with high early age strength.
In order to understand the strength development of these binders, it is important to understand their hydration mechanisms and the kinetic of formation of the hydration products. In the early stage of hydration, i.e. the 24 first hours, aluminates phases are predominant but their evidence by the commonly used XRD techniques is difficult.
In this work, a panel of high resolution solid state Nuclear Magnetic Resonance techniques were applied to study the ternary binder hydration. ^{27}Al and ^{29}Si MAS NMR experiments allow the highlighting and unambiguous quantification of silicates and aluminates species even at early stage of hydration.
The consumption and formation of phases was followed ex-situ on samples hydrated between two hours and 28 days.

2. MATERIALS AND METHODS

2.1. MATERIALS

Our system is composed of Portland cement (CEM II 52.5 N white Le Tail) and calcium aluminate cement CAC (Ternal White) obtained from Lafarge-Holcim cement Co. and IMERYS cement Co. respectively. The main source of calcium sulphate was anhydrite originated from SMA Faulquemont. CAC was mainly composed of calcium aluminate (CA) and calcium di-aluminate (CA2) while White OPC was composed of alite (C3S), Belite (C2S) and tri-calcium aluminate (C3A). Their mineralogical compositions have been initially determined by Rietveld XRPD analysis. The proportions of the raw materials in the anhydrous cements are reported in Table 1.

Table 1. Mineralogical composition of the white Portland cement and the calcium aluminates cement

	White OPC	CAC	Anhydrite
	Wt.%	Wt.%	Wt.%
C2S	19.1		
C3S	71.2		
C3A	3.89		
C4AF	0.74		
Anhydrite	2.08		100
Calcite	1.5		
Lime	1.02		
Other	0.48	0.7	
CA2		41.76	
CA		55.78	
Corundum		0.44	
Gehlenite C2A$		1.27	

The homogeneous mixtures were hydrated in endogenous conditions to avoid their carbonation, then stopped by solvent exchange method [1], using acetone. The pastes were mashed then dipped in acetone for 15 minutes before being filtered on a Büchner filter. In a last step, the powders were dried in a vacuum (10^{-3} bars) for 15 minutes. The obtained samples were then characterized shortly after the hydration stoppage to prevent any possible evolution or contamination with atmospheric CO_2.

2.2. METHODS

All the samples have been characterized by high resolution solid state ^{29}Si and ^{27}Al NMR. In addition to the quantitative 1D MAS NMR spectra, ^{27}Al shifted echo MQ-MAS [2] providing very high resolution 2D spectra and ^{1}H-^{29}Si and ^{1}H-^{27}Al CP-MAS [3] experiments allowing the selective observation of nuclei in the hydrated phases were conducted.

All the ^{29}Si MAS NMR experiments were acquired on a Bruker AVANCE 400MHz spectrometer at a spinning rate of ν_{rot}=10kHz, while ^{27}Al MAS NMR experiments were acquired on a Bruker AVANCE 850MHz spectrometer and ν_{rot}=30kHz. 5ms and 500µs were used as contact time for ^{1}H-^{29}Si and ^{1}H-^{27}Al CP-MAS respectively. All the spectra obtained were simulated using the DMFit software [4].

3. RESULTS AND DISCUSSION

The figure 1 shows an example of ^{27}Al MAS quantitative spectra with its deconvolution obtained for a three days hydrated sample.

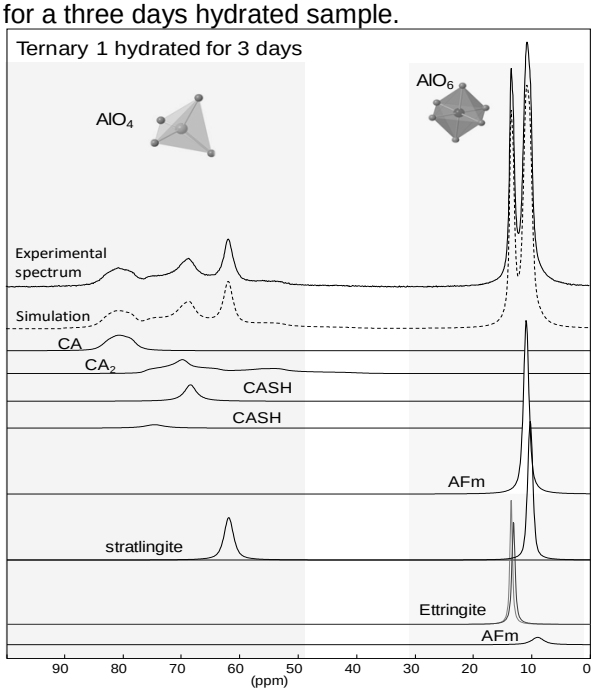

Figure 1. Experimental and simulated ^{27}Al MAS spectra of ternary mixture hydrated for three days with the complete deconvolution and assignment

The signals extend on two different ranges of chemical shifts. The first one going from 0 to 20 ppm corresponds to aluminum six-fold coordinated to oxygen (AlO_6) mostly present in hydrated phases. The second domain going from 50 to 90 ppm corresponds to aluminum four-fold coordinated to oxygen (AlO_4) encountered in both anhydrous and hydrated aluminate phases. The assignment of the different components was based on spectra of pure phases when possible or on literature.

Hence, the tetrahedral environments were assigned to the two most abundant anhydrous phases, the calcium aluminate and calcium di-aluminate. Two peaks of calcium aluminate silicate hydrates [5] CASH were also detected at 68.5 and 74.5 ppm as well as the tetrahedral peak of the Stratlingite at 62.0 ppm [6].

In the octahedral part of spectra, two peaks at 13.5 and 13.1 ppm correspond of aluminum in Ettringite [7], two others at 10.9 and 9.0 ppm were attributed to AFm phases and finally a signal at 10.2 ppm corresponds to the hexacoordinated aluminum of the Stratlingite [6].

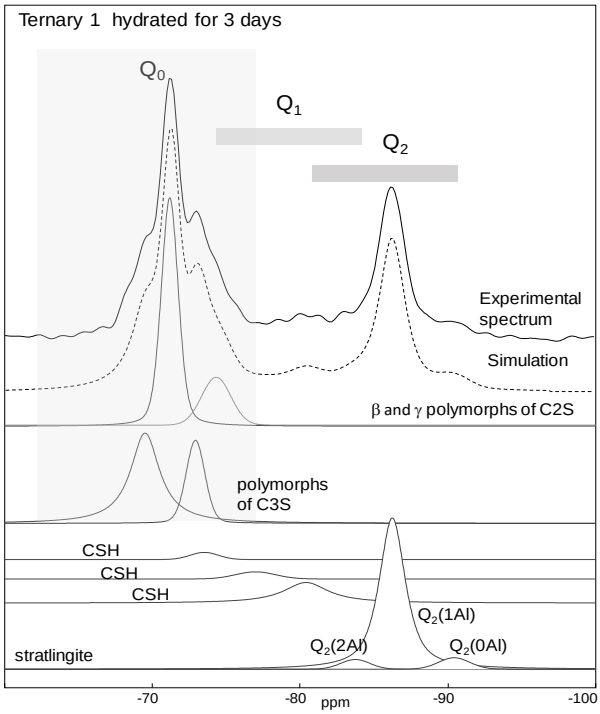

Figure 2. Experimental and simulated ^{29}Si MAS spectra of ternary mixture hydrated for three days with the complete deconvolution and assignment

The figure 4 shows the example of experimental ^{29}Si spectrum of a three days hydrated then stopped sample with its simulation and the complete assignment of the different components. The signal extends on chemical shifts range from -60 to -95 ppm corresponding to Q_0, Q_1 and Q_2 species, i.e. silicon surrounded by 4, 3 and 2 non-bridging oxygen respectively. Its simulation evidences 4 peaks located between -64 and -76 ppm that can be assigned to Q0 species of the different polymorphs of C3S and C2S [8]. Three small bands located at -73.5, -77.0 and -80.4 ppm are coherent with calcium silicate hydrates environments [8]. Finally, the three signals centered at -84.5, -86.5 and -91.5 ppm, have been attributed to the different Q_2 environments of Stratlingite according to Santacruz et al [6].

Based on these assignments all the ^{27}Al and ^{29}Si MAS spectra acquired for samples hydrated from 2 hours to 28 days were simulated allowing to trace the kinetic of disappearance of aluminum and silicon in the initial phases and formation of aluminum and silicon species in hydrated phases as a function of time. These results are shown on Figures 2 to 4.

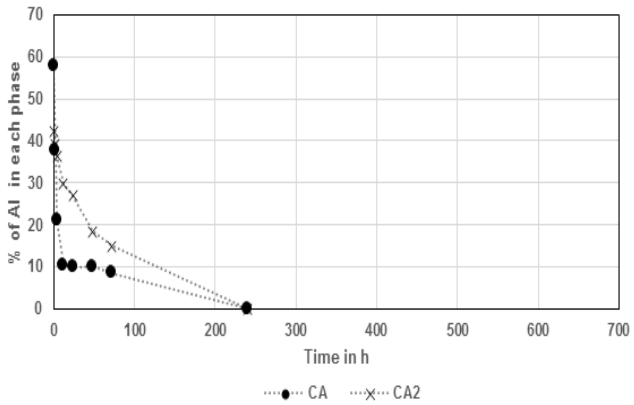

Figure 2. Kinetic of aluminium in anhydrous aluminate phases consumption from 0 to 28 days

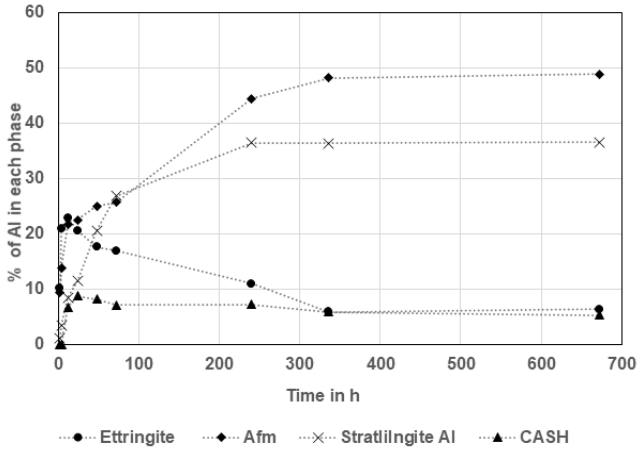

Figure 3. Kinetic of aluminate hydrates precipitation between 2 hours and 28 days

In view of the curves, the hydration process of our system seems to be divided into four reaction stages.

During the first stage i. e. the 12 first hours of hydration, CA's dissolution is very quick (almost all the phase has disappeared after 12h) while the CA2's dissolution is slower. The released calcium and aluminum combined instantly with sulfate species to form Ettringite and the AFm phases. These two phases keep growing rapidly above the time and the Ettringite reaches a maximum at 12 hours.

In the same time, C3S silica proportion starts decreasing while C2S remains untacked, it follows a slow precipitation of silicate hydrates Stratlingite and CASH.

From 12 hours to 3 days, the CA dissolution marks a sharp slowdown while the consumption of CA2 increases. The Ettringite alumina proportion starts decreasing probably in favor of AFm phases that keep to increase but more slowly. In the same time C3S and C2S start to react significantly releasing silicon in the system. It results an important precipitation of Stratlingite while CASH, observed both by ^{27}Al and ^{29}Si NMR increase slowly and reach a plateau at about 3 days.

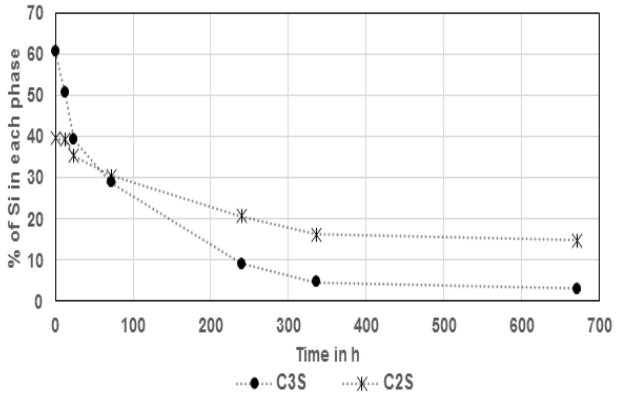

Figure 5. Kinetic of anhydrous silicate phases consumption from 0 to 28 days

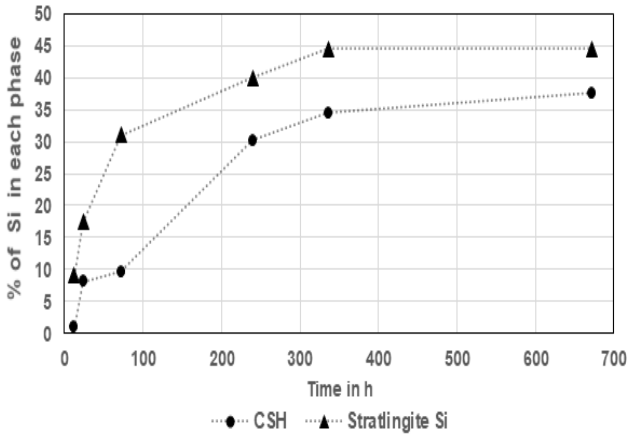

Figure 6. Kinetic oh silicate hydrates precipitation from 0 to 28 days

Between 3 and 14 days CA and CA2 end up dissolving; they have completely disappeared at 10 days. In parallel Ettringite keeps to decompose and AFm precipitation increases. In the same time, C3S and C2S dissolution continues with the same rate. Stratlingite shows a very similar kinetic profile seen by both ^{29}Si and ^{27}Al MAS NMR, and keeps to increase to reach its maxima at 14 days. On the contrary, while ^{27}Al signal attributed to CASH reached a plateau, ^{29}Si signal increases rapidly indicating the formation rather of CSH than of CASH. This could be explained by the lack of alumina in the system comparing to the first 24 hours of hydration, contrary to the silicon which is now more available. Within 14 days, the anhydrous CA and CA2 having completely disappeared, there is no newer aluminum intake. The disappearance of Ettringite stops at the same time that the formation of AFm has reached a plateau. The precipitation of Stratlingite also stagnates both from the point of view of ^{27}Al and ^{29}Si. Only C3S and C2S continue to dissolve slowly bringing silicon into the medium that precipitate in CSH. The kinetic is slowed down and almost stabilized.

CONCLUSION

In this work, the hydration of a white OPC-CAC-calcium sulfate ternary binder was investigated using high resolution ^{27}Al and ^{29}Si MAS NMR from the very early stages to 28 days. The simultaneous or consecutive precipitation of hydrated phases such as Ettringite AFm, Stratlingite and CASH phases were highlighted in parallel with the dissolution of the anhydrous components Four different steps seems to emerge that could be related to mechanical strength properties.

REFERENCES

[1] Snellings R., Chwast J., Cizer Ö., De Belie N., Dhandapani Y., Durdzinski P., Elsen J., Haufe J., Hooton D., Patapy C., Santhanam M., Scrivener K., Snoeck D., Steger L., Tongbo S., Vollpracht A., Winnefeld F., Lothenbach B., 2018. Report of TC 238-SCM: hydration stoppage methods for phase assemblage studies of blended cements – results of a round robin test, Mat Struc, 51:111.

[2] Massiot D., 1996. Sensitivity and lineshape improvements of MQ-MAS by rotor synchronized data acquisition, J. Magn. Reson. Ser. A, 122 240-244.

[3] Hartmann S.R., Hahn E.L., 1962. Nuclear Double Resonance in the Rotating Frame. Phys. Rev. 128 (5): 2042–2053.

[4] Massiot D., Fayon F., Capron M., King I., Le Calvé S., Alonso B., Durand J. O., Bujoli B., Gan Z., Hoatson G., 2002. Modelling one- and two-dimensional solid-state NMR spectra, Mag Res Chem, 40 (1): 70-76.

[5] Skibsted J., Jakobsen H.J., 1998. Characterization of the calcium silicate and aluminate phases in anhydrous and hydrated Portland cements, Nuclear Magnetic Resonance Spectroscopy of Cement-Based Materials, Berlin, pp. 3–45.

[6] Santacruz I., De la Torre Á.G., Álvarez-Pinazo G., Cabeza A., Cuesta A., Sanz J.,et al., 2016. Structure of strätlingite and effect of hydration methodology on microstructure, Adv. Cem. Res. 28: 13–22.

[7] Andersen M.D., Jakobsen H.J., Skibsted J., 2006. A new aluminium-hydratespecies in hydrated Portland cements characterized by 27Al and 29Si MAS NMR spectroscopy, Cem. Concr. Res. 36: 3–17.

[8] Rawal A., Smith B. J., Athens G. L., Edwards C. L., Roberts L., Gupta V., Chmelka B. F., 2010. Molecular Silicate and Aluminate Species in Anhydrous and Hydrated Cements, J. Am. Chem. Soc. 132, 7321–7337.

39th Cement and Concrete Science Conference
9-10th September 2019
University of Bath
Paper Number 016

Enhanced self-healing using conventional supplementary cementitious materials

R. Maddalena, D. Gardner
School of Engineering, Cardiff University, UK

H. M. Taha
Department of Architecture & Civil Engineering, University of Bath, UK

ABSTRACT
Crack formation is one of the main causes of deterioration in cement and concrete. Cracks in the cover zone lead to fluid ingress and subsequent modification of the pH of the cement matrix. This, in turn may result in disruption to the passive film that protects steel reinforcement, the onset of rust formation and the overall safety of a concrete element being compromised.
In this work, we present a comparison between cement mortar mixes using ordinary Portland cement (CEM I) with different replacements of supplementary cementitious materials typically used in the construction industry: silica fume, ground granulated blast-furnace slag (GGBS) and pulverised fuel ash (PFA). Samples were subjected to mechanical damage to open micro-cracks and then placed in a healing bath to trigger autogenous self-healing. The latter occurs via the additional formation of calcium (aluminium) silicate hydrates (C-(A)-S-H) due to further hydration of the starting reactants. Micro-structure characterisation analysis, powder X-Ray diffraction (XRD) and thermogravimetric analysis (TGA/DSC) were used to identify and quantify the hydration products pre- and post-healing. Pore structure and physical property measurements (i.e. open porosity, density, water absorption and sorptivity) were used to determine the effectiveness of the self-healing process in reducing crack-widths and recovering the water-tightness of the mortar matrix post-healing.

1. INTRODUCTION

Crack formation in cementitious building materials is a common phenomenon, which can occur either on the surface or inside structural elements. Cracks are often related to a structure's deterioration as they facilitate water ingress, hence triggering reinforcement depassivation leading eventually to reinforcement corrosion (Liu and Shi, 2011). The exposure of pores containing water and salts to a temperature gradient may result in crystallisation of the salts, the expansive nature of which is sufficient to induce microcracking in the cement matrix (Espinosa-Marzal *et al.*, 2011).

A number of technologies have been studied and developed to prevent cracks formation or to provide cracks closure. So-called self-healing concrete provides a solutions to repair cracks at different scales. Micro-cracks could be sealed by adding microcapsules that contain a healing agent into the fresh paste (Ferrara *et al.*, 2018). Recently, bacteria have also been used as a crack healing technique via the inclusion of bacteria spores and nutrients in the fresh paste. The formation of cracks allows water to penetrate into the cementitious matrix, therefore stimulating the bacteria to precipitate calcium carbonate using the calcium hydration products which are already present in hydrated concrete (i.e. portlandite($Ca(OH)_2$)). The precipitation of calcium carbonate from this process contributes to crack blockage (Wang *et al.*, 2014). Other researchers examined external intervention methods for healing damage. (Gardner *et al.*, 2017) investigated the self-healing capability of flowing healing-liquid agents (i.e. cyanoacrylate) into hollow channels within cement and concrete specimens. Cracks can be mechanically closed as well by using shape memory polymers tendons, placed in concrete elements during casting. At the onset of a crack, the tendons are heated to trigger the shape memory effect and close the crack by exerting a compressive force across the crack plane (Teall *et al.*, 2017).
Self-healing properties of fibre reinforced cement using plastic fibres (e.g. polyvinyl alcohol, polypropylene, etc) have been investigated (Nishiwaki *et al.*, 2014). The fibres act as crack-bridges and their high specific surface area offer additional nucleation and growth sites for the formation and precipitation of further hydration products.

Supplementary cementitious materials (SCM) are industrial by-products (e.g. manufacturing industry, excavation and mining sites etc.). Their amorphousness and elevated specific surface area provide a nucleation site for the formation of calcium silicate hydrate (C-S-H) from unreacted reactants. The usage of SCM as cement replacement is regulated by international standards, and their usage is widely encouraged as a viable environmental friendly solution.
In this study we investigated the self-healing capability of mortar cement partially replaced by silica fume, pulverised fuel ash and grounded

granulated blast-furnace slag. Further hydration and additional formation of hydrated minerals is evaluated by water transport properties and thermal and mineralogical analysis.

2. MATERIALS AND METHODS

Cement mortar was prepared using ordinary Portland cement CEM I (strength class 52.5 MPa), silica sand, at sand to binder ratio (s/b) of 3, and deionized water at water to binder ratio (w/b) of 0.45. Portland cement was partially replaced by supplementary cementitious materials (SCM) at different percentages. Commercially available SCMs were used; amorphous silica fume (SF), ground granulated blast-furnace slag (GGBS) and pulverized fuel ash (PFA). Samples and replacement proportions are reported in Table 1. The percentage of replacement was chosen in agreement to the highest content allowed by BS EN197.

Table 1. Sample ID name and mixing proportions of cement replacement using silica fume (SF), pulverised fuel ash (PFA) or ground granulated blast-furnace slag (GGBS).

Sample name	OPC (%)	SF (%)	PFA (%)	GGBS (%)
OPC	100	-	-	-
S	90	10	-	-
P	70	-	30	-
B	50	-	-	50

Mortar paste was mixed according to the BS EN 196-1 and cast into steel moulds of 25 x 25 x 25 mm. After 24 hours specimens were demoulded and cured for 28 days in a sealed environment at 95% relative humidity and 20 °C to prevent carbonation (Cerveny *et al.*, 2011).

After curing, the samples were gently oven-dried at 55 °C until no further change in weight was recorded (Zhang and Scherer, 2011). Specimens were then subjected to mechanical damage, using a uniaxial loading cell with a load up to 90% of the maximum peak before failure, to cause micro-cracks and internal damage. The cubes were then placed in a static healing bath of deionised water to promote further hydration and crack-healing.

Physical characteristics and water transport properties (sorptivity) were measured in (u) undamaged conditions (after curing), (d) damaged conditions (after mechanical loading and micro-cracking), and (h) healed conditions (after 60 days in deionised water).

Mineral composition by means of X-ray diffraction measurements and thermogravimetric analysis were conducted on samples at damaged (d) and healed (h) conditions.

The sorptivity test measures the water uptake through the capillary rise effect in the pore structure with time. The test was used to determine the healing capability of the different mixes. For each mix, three samples were used. The samples were placed in a container with 1 mm of their bottom surface in contact with deionised water. The water uptake was measured indirectly through the sample weight increase with time, over a period of 100 minutes at defined intervals. The methodology was adapted from the HAMSTAD Round Robin test method (Ioannou, Hamilton and Hall, 2008). The same test method was followed to perform open porosity measurements, bulk density and matrix density on three specimens for each mix, at each stage ((u), (d) and (h)).

Powder X-ray diffraction patterns were collected from 5° to 60° 2θ at a rate of 1°/min and a step size of 0.02 °2θ.

Thermal analysis were used to quantify mineral phases due to the healing process and further hydration. TGA/DSC curves were collected from 25 °C to 1000 °C at a heating rate of 10 °C/min under constant nitrogen flow. The mass loss was calculated using the tangent method (Matschei, Lothenbach and Glasser, 2007) at three different temperature ranges; 90-150 °C, temperature range of pore-water evaporation, and the decomposition of both C-S-H and ettringite; 440-440 °C, dehydroxilation of portlandite and 660-700 °C, decomposition of carbonated products (Maddalena, Hall and Hamilton, 2019). TGA mass loss at the specific temperature range was used to estimate the mineral phase relative content on damaged samples, condition (d), and healed samples, condition (h).

3. RESULTS AND DISCUSSION

The physical characteristics of the different mixes are reported in Table 2. The porosity and the density values are typical of mortar and concrete matrices. The pore volume, measured as open porosity (ϕ) and the material density values (bulk and matrix density) are constant throughout the three stages (undamaged, damaged and healed). The water uptake after 100 minutes decreased by ca. 24% in sample OPC, and by ca. 50% in sample S, P and B, with 10%, 30% and 50% replacement of SF, PFA and GGBS respectively. The measurement of open porosity provides an estimate of the accessible pore volume but does not take into account pores with an average diameter at the micro-scale.

Table 2. Average values of open porosity (ϕ), bulk density (ρ), matrix density (ρ_{mat}), and water uptake at 100 minutes (W_{100}) in undamaged (u), damaged (d) and healed (h) conditions.

Sample name		ϕ (%)	ρ (g/cm^3)	ρ_{mat} (g/cm^3)	W_{100} (g/mm^{2}10^{-3})
OPC	(u)	0.18	2.05	2.49	4.2
	(d)	0.18	2.03	2.47	4.1
	(h)	0.19	2.03	2.51	3.3
S	(u)	0.17	2.02	2.44	4
	(d)	0.18	2.01	2.43	3.7
	(h)	0.19	2.00	2.46	2
P	(u)	0.19	2.01	2.46	4.1
	(d)	0.19	2.02	2.49	4
	(h)	0.20	2.02	2.51	2.9
B	(u)	0.18	2.01	2.46	4.5
	(d)	0.18	2.00	2.46	4.3
	(h)	0.19	2.01	2.48	2.9

Conversely, the reduction in water uptake (W_{100}) suggested that self-healing due to further hydration took place most probably in the micro-pores. The

sorptivity curves for OPC and sample P are reported in Figure 3.

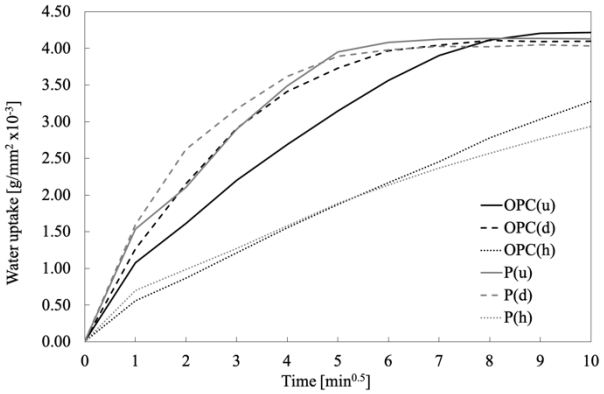

Figure 3. Water uptake recorded during sorptivity measurements for sample OPC and sample P (30% replacement of PFA) as a function of time, in undamaged (d), damaged (d) and healed (h) conditions.

While the water uptake values at 100 min are similar for undamaged (u) and damaged (d) conditions due to the size of the sample, their slope is different in the two cases. The decreased rate of water absorption in samples OPC(h) and P(h) shows the effect of further hydration, reducing the pore volume and crack spacing by formation of C-S-H or calcium carbonate.

The formation of C-S-H is balanced by a reduction in portlandite, naturally present in hydrated cement paste, since silica reacts with $Ca(OH)_2$ and water to form C-S-H.

XRD patterns of sample OPC damaged (d) and healed (h), and sample P (30% PFA) damaged (d) and healed (d) are shown in Figure 4. The peaks at ca. 18°, 34° and 47° 2θ are the reflection of Portlandite crystals. A reduction in intensity is observed, suggesting that portlandite was consumed to form additional C-S-H. The patterns showed also an increase in intensity of the peaks associated to C-S-H, at ca. 29°, 32°, 50° and 55° 2θ.

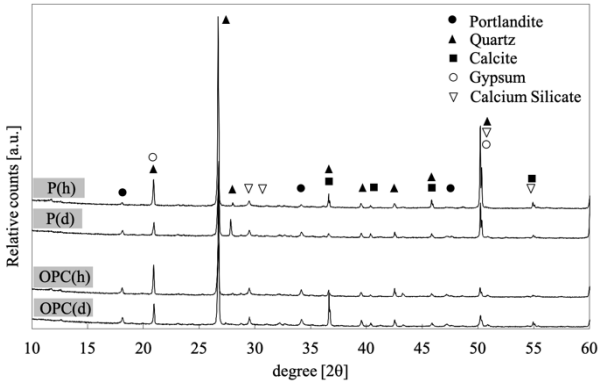

Figure 4. X-Ray diffractogram of sample OPC and sample P after mechanical damaging (d) and after 60 days in healing bath (h). [Only the major mineral phases are indicate].

Further evidence of C-S-H formation, followed by a reduction in portlandite is shown in Figure 5. Thermogravimetric (TG) curves and differential scanning calorimetry (DSC) response are reported for sample P (30% PFA) damaged (d) and healed (h). In this graph, downward DSC peaks indicate exothermic reactions, while upwards peaks indicate an endothermic reaction. In case of OPC replacement by PFA, we found that an increase weight loss in the temperature range 90-150 °C, associated to evaporation of pore water and dehydration of C-S-H, indicated a higher amount of C-S-H present in the sample P(h) in agreement with (Garbev *et al.*, 2008). The formation of C-S-H is possible because of the consumption of portlandite, as shown in the thermal step 410-440 °C (Maddalena and Hamilton, 2017). The relative mass loss change, between damaged (d) and healed (h) conditions, calculated for all the mixes (OPC, S, P and GGBS) at each thermal step is reported Figure 6.

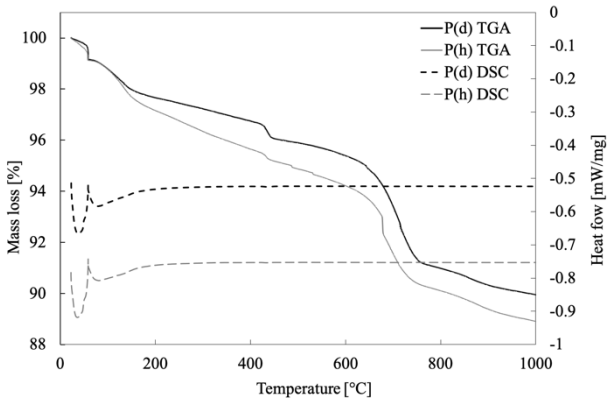

Figure 5. Thermogravimetric analysis (TGA) and differential scanning calorimetry measurements for sample P (30% replacement of PFA) in damaged (d) and healed (h) conditions. [TGA: continuous line. DSC: dashed line].

The additional formation of C-S-H is more significant in sample mixed with PFA and GGBS. This is due to their chemical composition and their high pozzolanic reactivity. Samples prepared with GGBS showed an increase in C-S-H by ca. 44% and a reduction in calcium carbonate by 22%.

Silica fume samples did not show a significant increase in C-S-H (5%) but rather an increase in carbonated products, balanced by a reduction in portlandite (-17%).

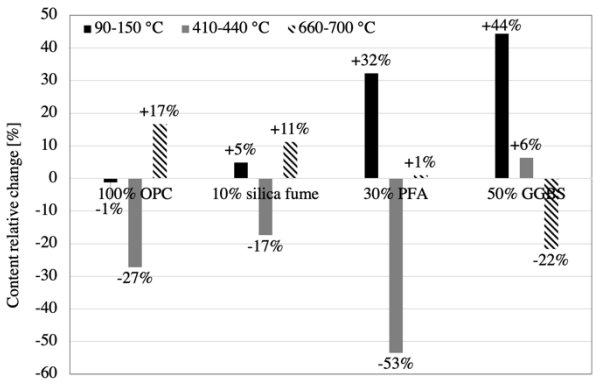

Figure 6. Phase content relative change (at damaged and healed conditions) calculated from TGA loss mass measurements at three different temperature ranges, 90-150 °C, 410-440 °C and 660-700 °C respectively.

The water absorption rate for the silica fume however, showed a similar behaviour to the other mixes (PFA and GGBS), suggesting that silica fume improved the self-healing through its physical filling effect (Quercia *et al.*, 2012). Finally, the mix with PFA resulted in a higher reduction of portlandite (-53%) and an increase of C-S-H of ca. 32%.

4. CONCLUSIONS

This work investigated the self-healing capability of OPC mortar mixes partially replaced by 10% of silica fume, 30% PFA, and 50% GGBS. it has been found that the reactivity of SCM mixes promoted the formation of additional calcium silicate hydrate (C-S-H) which decreases their water absorption rate by ca. 50%.

The results showed that each SCM promoted the self-healing through different mechanisms (specific surface area, chemical composition, pozzolanic reactivity), indicating that ternary replacement combining different percentages of SF, PFA and GGBS could further enhance the self-healing capability of cementitious materials.

Further work will investigate the pore size distribution at the micro-scale using mercury intrusion porosimetry (MIP) measurements. Scanning electron microscopy will be also used to characterise the healing products in cracks and pores.

ACKNOWLEDGEMENT

The authors acknowledge the EPSRC funding, Resilient Materials 4 Life, grant EP/P02081X/1 for the support that has made this work possible.

REFERENCES

Cerveny, S. *et al.* (2011) 'Effect of hydration on the dielectric properties of C-S-H gel', *The Journal of Chemical Physics*. AIP Publishing, 134(3), p. 034509. doi: 10.1063/1.3521481.

Espinosa-Marzal, R. M. *et al.* (2011) 'The chemomechanics of crystallization during rewetting of limestone impregnated with sodium sulfate', *Journal of Materials Research*, 26(12), pp. 1472–1481. doi: 10.1557/jmr.2011.137.

Ferrara, L. *et al.* (2018) 'Experimental characterization of the self-healing capacity of cement based materials and its effects on the material performance: A state of the art report by COST Action SARCOS WG2', *Construction and Building Materials*. Elsevier Ltd, 167, pp. 115–142. doi: 10.1016/j.conbuildmat.2018.01.143.

Garbev, K. *et al.* (2008) 'Cell dimensions and composition of nanocrystalline calcium silicate hydrate solid solutions. Part 1: Synchotron-based X-Ray Diffraction', *Journal of the American Ceramic Society*, 91(9), pp. 3005–3014. doi: 10.1111/j.1551-2916.2008.02601.x.

Gardner, D. *et al.* (2017) 'Capillary Flow Characteristics of an Autogenic and Autonomic Healing Agent for Self-Healing Concrete', *Journal of Materials in Civil Engineering*, 29(11), p. 04017228. doi: 10.1061/(ASCE)MT.1943-5533.0002092.

Ioannou, I., Hamilton, A. and Hall, C. (2008) 'Capillary absorption of water and n-decane by autoclaved aerated concrete', *Cement and Concrete Research*, 38(6), pp. 766–771. doi: 10.1016/j.cemconres.2008.01.013.

Liu, Y. and Shi, X. (2011) 'Ionic transport in cementitious materials under an externally applied electric field: Finite element modeling', *Construction and Building Materials*, 27(1), pp. 450–460. doi: 10.1016/j.conbuildmat.2011.07.019.

Maddalena, R., Hall, C. and Hamilton, A. (2019) 'Effect of silica particle size on the formation of calcium silicate hydrate (C-S-H) using thermal analysis', *Thermochimica Acta*. Elsevier, 672(August 2018), pp. 142–149. doi: 10.1016/j.tca.2018.09.003.

Maddalena, R. and Hamilton, A. (2017) 'Low-pressure silica injection for porosity reduction in cementitious materials', *Construction and Building Materials*, 134. doi: 10.1016/j.conbuildmat.2016.11.016.

Matschei, T., Lothenbach, B. and Glasser, F. P. (2007) 'Thermodynamic properties of Portland cement hydrates in the system CaO–Al2O3–SiO2–CaSO4–CaCO3–H2O', *Cement and Concrete Research*, 37(10), pp. 1379–1410. doi: 10.1016/j.cemconres.2007.06.002.

Nishiwaki, T. *et al.* (2014) 'Self-Healing Capability of Fiber-Reinforced Cementitious Composites for Recovery of Watertightness and Mechanical Properties', *Materials*, 7, pp. 2141–2154. doi: 10.3390/ma7032141.

Quercia, G. *et al.* (2012) 'Effects of amorphous nano-silica addition on mechanical and durability performance of SCC mixtures', in *International Congree on Durability of Concrete*.

Teall, O. *et al.* (2017) 'Development of high shrinkage polyethylene terephthalate (PET) shape memory polymer tendons for concrete crack closure', *Smart Materials and Structures*. IOP Publishing, 26(4), p. 045006. doi: 10.1088/1361-665X/aa5d66.

Wang, J. Y. *et al.* (2014) 'Self-healing concrete by use of microencapsulated bacterial spores', *Cement and Concrete Research*. Elsevier Ltd, 56, pp. 139–152. doi: 10.1016/j.cemconres.2013.11.009.

Zhang, J. and Scherer, G. W. (2011) 'Comparison of methods for arresting hydration of cement', *Cement and Concrete Research*, 41(10), pp. 1024–1036. doi: 10.1016/j.cemconres.2011.06.003.

.

39th Cement and Concrete Science Conference
9-10th September 2019
University of Bath
Paper Number 017

Crack detection on heterogeneous High Performance Computing architectures

Erika Pellegrino
Electrical and Electronic Engineering , Imperial College London

Dr. Tania Stathaki
Electrical and Electronic Engineering , Imperial College London

ABSTRACT

With the objective of quality assessment, cracks on concrete buildings have to be identified and monitored continuously. Due to the availability of cheap devices, techniques based on image processing have been gaining in popularity, but they require a rigorous analysis of large amounts of data. Moreover, the detection of fractures in images is still a challenging task, being these structures sensitive to noise and to changes in environmental conditions. This paper proposes a variational method to detect cracks in images along with a parallel implementation on heterogeneous High Performance Architectures aiming both at automatizing the whole process and at reducing its execution time.

1. INTRODUCTION

The concrete infrastructure requires a constant monitoring due to the deterioration caused by several factors. In current practice the detection of defects is absolved manually by inspectors, but this modality is time consuming and error prone (Protopapadakis et al., 2019; Dams et al., 2017). This task is critical also for assessing the concrete quality (Lee et al., 2016). Due to availability of cheaper devices, image-based techniques have been gaining in popularity, but they require large volumes of data to be processed as quickly as possible.
The detection of fractures is still challenging in image processing. The main reasons are that they have a complex topology, a thickness similar to the image resolution and are easily corrupted by noise.
One of the scopes of this paper is to propose a variational model to detect cracks in images. It is well known that classical edge detection techniques based on gradient information are not successful with these structures. The intuitive idea is that, assuming that a fracture can be modeled by an indicator function supported by a smooth curve, it can be approximated by a sequence of functions whose Hessian blow up in its perpendicular direction, while their gradient is null. Motivated by these observations, showing that a suitable model should involve higher order derivatives, we propose a crack recovery method that falls within second order variational models. It is based on the Blake-Zisserman (Blake and Zisserman, 1987) functional or, to be more precise, on its approximation by elliptic functionals defined on Sobolev spaces (Ambrosio, Faina and March, 2001). In this paper we propose an implementation on High Performance Computing (HPC) architectures that are designed to execute massive parallel tasks.
The paper is organized as follow: in Section 2 we describe the mathematical model and the parallel implementation, in Section 3 we discuss performance results and in Section 4 we draw some conclusions.

2. MATHEMATICAL MODEL AND PARALLEL IMPLEMENTATION

Variational methods have addressed successfully problems such as image segmentation and edge detection. They propose as solution a minimizer of a global energy. A first example is described by Mumford and Shah (MS) in their famous paper (Mumford and Shah, 1989) where they proposed a first order functional, whose minimization determines an approximation of the image by means of a piecewise smooth function and detects edges as singularities in the image intensity. However, this model is not suitable for cracks because they do not represent singularities in the intensity function, but in its gradient instead. For this reason, we

propose a second order variational model based on the Blake-Zissermann (BZ) functional (Blake and Zisserman, 1987). This was introduced with the the aim of overcoming some limitations of the MS approach, such as the over segmentation and the lack in detecting gradient discontinuities. Being the original formulation not suitable for numerical treatment, we had to work on a different approach that is based on the approximation proposed by Ambrosio and Tortorelli (AT) for the MS functional (Ambrosio and Tortorelli, 1990, 1992). In their model, they replaced the unknown discontinuity set by an auxiliary function which smoothly approximates its indicator function. In our case two auxiliary functions are introduced as indicators of both intensity discontinuity and gradient discontinuity sets. As numerical minimization algorithm we chose an "inexact" block-coordinate descent scheme (BCD) in order to address the heterogeneous environment. Although the model is global, several numerical experiments have highlighted that the solutions weakly depend on boundary conditions and are energetically close to the initial data. This motivate the adoption of a tiling scheme to address very large images: the minimizer is assembled by merging together local solutions restricted to portion of images.

3. NUMERICAL RESULTS

We tried our methods on images of cracks taken in tunnels in Greece and back-scattered electron images of concrete samples. In the former case the challenge was to reconstruct the whole structure avoinding the effect of the noise and the environmental conditions (i.e. lights). In the latter the aim was to "insulate" the structure from the complex texture in the background.

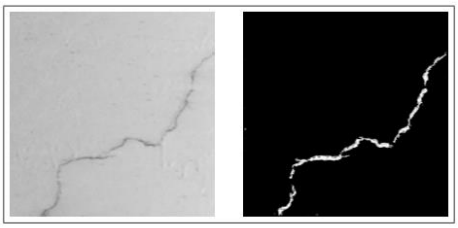

Fig. 1. Crack on a concrete wall

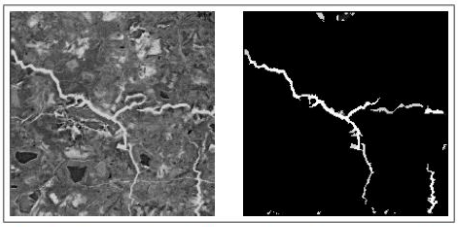

Fig. 2. Microcracks on a BSE microscopy of concrete materials

Table 1. Run time comparisons for a single image

	run time (s)
sequential	13.184868
parallel 24 cores	1.056701
parallel 48 cores	0.5915374

In both cases the structures have been detected correctly (Fig.1,2). As future work, It would be interesting to compare the quality of the reconstruction with labelled dataset provided by the engineers involved in the assessment process.

In order to reduce the execution time and to provide a automatic procedure we tested a sequential implementation with a parallel one based on the OpenMP framework that implements two strategies for collaboratively executing a program on an environment composed by devices of different types (aka heterogeneous architectures). The experiments were performed both on a commodity PC and on a High Performance Computing cluster at Imperial College. A sequential version was executed on a workstation equipped with a processor Intel (R) Xeon CPU E6-79 at 3.40 GHz with 32GB of RAM and total number of cores 12, running an Ubuntu 18.04 operating system. The parallel version based was executed on a heterogeneous cluster equipped with x86-64 processors, running a CentOS 7.6 operating system. Overall, the results show a significant reduction in the execution time with respect to the sequential algorithm.

4. CONCLUSIONS

In this paper we proposed a variational method to detect cracks in images and a parallel implementation targeting modern High Performance Computing architectures with the aim of automatizing the detection process and of reducing its execution time. We got promising results for both the quality of the reconstruction and the reduction of its duration. As future plan, we would like to test our procedure on real world scenarios in order to understand if it could be used as useful tool for assessing the building infrastructure and the concrete quality. We plan also to reduce further the execution time by designing a domain specific hardware accelerator tailored specifically to detect cracks in real time. Moreover, it would be interesting to understand how the algorithm work with isotropic structures such as bubbles.

5. ACKOWLEDGEMENT

We would like to thank the National Technical University of Athens for having provided images of cracks in the tunnels of Egnatia Motorway in Metsovo and the Concrete Durability Laboratory at Imperial College London for the back-scattered electron images.

REFERENCES

Protopapadakis, E., Voulodimos, A., Doulamis, A., Doulamis, N. and Stathaki, T., 2019. Automatic crack detection for tunnel inspection using deep learning and heuristic image post-processing. Applied Intelligence, pp.1-14.

Lee, H.X.D., Wong, H.S. and Buenfeld, N.R., 2016. Self-sealing of cracks in concrete using superabsorbent polymers. Cement and Concrete Research, 79, pp.194-208.

Dams, B., Sareh, S., Zhang, K., Shepherd, P., Kovac, M. and Ball, R., 2017. Aerial additive building manufacturing: three-dimensional printing of polymer structures using drones. Proceeding of the Institution of Civil Engineers: Construction Materials., pp.1-12.

Blake, A. and Zisserman, A., 1987. Visual reconstruction. MIT press.

Ambrosio, L., Faina, L. and March, R., 2001. Variational approximation of a second order free discontinuity problem in computer vision. SIAM Journal on Mathematical Analysis, 32(6), pp.1171-1197.

Ambrosio, L. and Tortorelli, V.M., 1990. Approximation of functional depending on jumps by elliptic functional via t- convergence. Communications on Pure and Applied Mathematics, 43(8), pp.999-1036.

Ambrosio, L. and Tortorelli, V.I.N.C.E.N.Z.O., 1992. On the approximation of free discontinuity problems.

Mumford, D. and Shah, J., 1989. Optimal approximations by piecewise smooth functions and associated variational problems. Communications on pure and applied mathematics, 42(5), pp.577-685.

39th Cement and Concrete Science Conference **Paper Number 018**
9-10th September 2019
University of Bath

A Comprehensive Review of Recycled Concrete Aggregate in Cementitious Materials

Rekha Rampit, Jovanca Smith
Department of Civil and Environmental Engineering,
The University of the West Indies, St. Augustine Campus, Trinidad and Tobago.

ABSTRACT

In recent years, there has been an expansion in the world's urbanization which has given rise to an increase in the consumption of natural resources, consequently leading to a substantial quantity of construction and demolition waste. It is beneficial that researchers continue to investigate alternative materials that can be generated from construction and demolition waste. One such material retrieved from this waste is recycled concrete aggregate, which is currently being considered by researchers as an alternative to natural aggregates as a substitution in the concrete mix. Recycled concrete aggregates present several main benefits as it reduces the wastes deposited on landfills and the consumption of energy and natural aggregates from quarrying. Studies on the behavior of recycled concrete aggregates has been on the rise since the 1970's after world war II. This study reviews and summarizes the literature on the properties of recycled concrete produced from coarse recycled aggregates. This literature review examined the issues related to recycled concrete by analyzing over 200 published papers to provide a comprehensive synthesis of the material properties which includes: mechanical properties, treatment methods, structural performance, measurement techniques. and performance in the coastal environment. This review has benefits to both academic researchers and industry practitioners across the world.

Keywords: recycled concrete aggregate, recycled coarse aggregate, recycled aggregate concrete, mechanical properties, durability properties, coastal environment.

1. INTRODUCTION

The increase in the world's population has resulted in an expansion in construction developments across the globe (Agyekum 2018). Many sky-scrapers, bridges and roads are being constructed yearly with the use of natural resources, consequently leading to a magnification of construction and demolition waste (CDW) (Alengaram, Salam et al. 2011, Silva, De Brito et al. 2015, Agyekum 2018). Quarrying not only uses a vast amount of energy to retain natural aggregates (NAs), but destroys plant and animal ecosystems.

In conjunction with this environmental issue, there is a scarcity of land, particularly in the Caribbean countries making it difficult to accommodate waste (Lowndes and Jeffrey 2009). CDW comprises mainly of concrete from laboratory samples, wastage from site, natural aggregates, bricks and to a lesser extent wood and other materials (Kou, Poon et al. 2012). Additionally, concrete waste can stem from natural disasters. It is approximated that RCA makes up 40% of the CDW (Oikonomou 2005).

Corresponding authors.
E-mail addresses:
rekharampit@hotmail.com (R. Rampit)
jovancals@gmail.com (J. Smith)

Recent studies have highlighted major benefits of recycling concrete waste as potential alternatives to natural aggregates. These include: reduction of the use of natural aggregates hence protecting the ecological balance of nature and reducing energy consumption, reduction in the volume of concrete waste disposed on landfills, reduction of cost of waste treatment (Agyekum 2018). Recycled concrete aggregates (RCAs) are classified into three main groups: aggregates composed of masonry rubble (group 1), aggregates from concrete rubble (group 2) and a combination of NAs and rubbles from groups 1 and 2 (group 3) (RILEM 1994, Katz 2003).

2. PROPERTIES AND STRUCTURE OF RCA

The properties of RCAs are inferior to that of NAs. The residual mortar is the reason for this, affecting the properties of porosity, density and water absorption of the RCA (McNeil and Kang 2013). The adhered mortar consists of hydrated and unhydrated cement particles together with fine aggregates (Behera, Bhattacharyya et al. 2014). The porosity of the attached mortar depends on the water to cement ratio (w/c) of the original concrete (Etxeberria, Vázquez et al. 2007). A high w/c ratio results in a very porous RCA as minute pores and cracks are more susceptible to develop as a consequence of crushing (Olorunsogo and Padayachee 2002, Kou, Poon et al. 2012).The volume of the attached mortar can vary from 25% to

60% (Hansen and Narud 1983). The density of the RCA is generally lower than the NA due to the attached mortar which varies with different sources of RCA. A study showed that the relative density of RCA in the saturated surface dry (SSD) state was 7-9% lower than that of NA (Limbachiya, Leelawat et al. 2000).

Another investigation stated that there was a 17% difference between the density of RCA and NA (Sagoe-Crentsil, Brown et al. 2001). The presence of the pores and cracks on the attached mortar of the RCA allows a greater amount of water to be absorbed into the pores as compared to NA. The water absorption ranges from 3-12% for RCA and 1-5% as compared to NA (Gómez-Soberón 2002, Katz 2003). In addition to variations caused by the old mortar, the RCA differs from NA mainly because of the interfacial transition zone (ITZ). The ITZ is the weakest region in concrete due to the higher porosity. The old ITZ is between the original aggregate and the old attached mortar, whereas the new ITZ is between the old attached mortar and the new mortar matrix which forms another weak link due to poor bonding (Medina, Zhu et al. 2015).

3. MECHANICAL PROPERTIES OF RCA

In the case of RCA, the workability required is difficult to acquire due to the high water absorptivity. A study concluded that recycled aggregate concrete (RAC) required 10% more water, to achieve a slump equivalent to natural aggregate concrete (NAC) (Tabsh and Abdelfatah 2009). The aggregate type, quantity, angularity and amount of attached mortar of the RCA influences the water demand and energy for compaction due to the inter-particle friction (Fathifazl 2008). Studies have shown that up to 30% replacement of coarse recycled aggregates the reduction in compressive strength ($f'c$) is not very prominent (Behera, Bhattacharyya et al. 2014). However, with 100% of RCA there was a reduction in $f'c$ by 20-25% as compared to NA, due to its poor quality (Etxeberria, Vázquez et al. 2007).

The w/c ratio influences the $f'c$ of concrete. It was suggested that using RCA in the SSD state compensates for the workability loss in the mix (Hansen 2014). However this exhibited a lower $f'c$ than oven dried (OD) RCA, due to the bleeding of excess water with the SSD samples during mixing (Poon, Shui et al. 2004). Many researchers stated, that the desired $f'c$ can be achieved by lowering the w/c by 4-10% (Etxeberria, Vázquez et al. 2007). As the parent concrete strength increases so does the RAC $f'c$. This influence was related to the w/c ratio. In concretes with a low w/c ratio (<0.2) the new mortar strength and the ITZ strength between the new and old mortar is higher than the mortar in the RCA, hence cracks propagates from the mortar in the RCA. On the other hand, in concretes with high w/c ratio (>0.7), failure starts in the new mortar region or the ITZ between the new and old mortar because of the effects of the lower $f'c$ (Xie, Gholampour et al. 2018).

A recent study observed that with 100% replacement of RCA there was a reduction in tensile strength between 23-31% (Seara-Paz, Corinaldesi et al. 2016). Other studies revealed that with an increase in RCA replacement there is a decrease in tensile strength (González-Taboada, González-Fonteboa et al. 2016). Kang et al. (2012) showed that a 15% addition of RCA results in a 9% decrease in strength, and doubling the replacement doubled the strength reduction. The lower stiffness of the attached mortar on the surface of the RCA contributes to a reduced modulus of elasticity (E_c).

It was found that RCA behaves in a brittle manner, experiencing more deformations as compared to NA. A reduction of 45% in the E_c was observed with 100% replacement of RCA at a fixed w/c ratio (Rahal 2007). However, other authors reported that the reduction in E_c can be as high as 80% at 100% replacement of RCA (Günçan 1995). Flexural strength of RAC decreased with an increase in percentage replacement of RCA due to the lower modulus of elasticity. Studies shown that the flexural strength of RAC varied by 16-23% with different replacement levels (Tavakoli and Soroushian 1996).

4. TREATMENT METHODS FOR RCA

Several treatment methods have been developed to enhance the properties of RCAs to be used as a potential alternative to NAs. Two main approaches used were: presoaking to remove the attached mortar on the aggregate surface or by using reactive or non-reactive fine minerals to modify the surface and interior of the RCA. A recent study pre-soaked the RCA in hydrochloric acid (HCL) for 24 hours which resulted in a 3% loss in mortar, reduced the water absorption and resulted in an improvement in $f'c$ by 10% as compared to the untreated RCA (Ismail and Ramli 2014).

Pre-soaking of RCA in nitric acid (HNO_3) improved the $f'c$ by 6-12% as compared to the untreated aggregates due to the deterioration of the old mortar and hence improved ITZ (Murali, Vardhan et al. 2012). Ismail and Ramli (2014) further treated the aggregates with calcium metasilicate (CM) solution which increased the particle density and reduced the water absorption capacity. A coating was formed over the RCA, which filled the pores thereby improving the bond strength and the ITZs in the matrix. A similar study used microorganisms to induce calcium carbonation precipitation on the RCA surface, hence plugging the pores and cracks which reduced the water absorption by 15% (Qiu, Tng et al. 2014).

5. STRUCTURAL PERFORMANCE OF RCA

RCA has not only been used as backfill material for foundations and road fill material but has been used for structural purposes. Many countries developed technical guides to facilitate the use of RCA including but not limited to: Hong Kong, Germany and Brazil. In Hong Kong, 10 local projects consumed a maximum RCA of 22,700m^3 which were incorporated in reinforced concrete piles and walls (Rao, Jha et al. 2007). The Vilbeler Weg and Waldspirale buildings incorporated the use of RCA which satisfied the $f'c$ at 28 days (Marinković, Ignjatović et al. 2012). A study showed that the mid-span deflections and crack width were greater for the RAC beam compared to the NAC beam, but were within the acceptable standard specified in the ACI 318-11 building code, which does not hinder the use of RCA for structural concrete members (Maruyama, Masaru et al. 2004, Fathifazl, Razaqpur et al. 2009).

Uncertainty exists among researchers regarding the durability of RAC, against chloride ion ingress. One author utilized three sources of RCA in structural concretes to determine the response to chloride ion penetration. The results showed detrimental effects on the chloride ion ingress when RCA was used. It was concluded that using ground granulated blast furnace slag (GGBS) to produce structural CEM III concretes increased the resistance to chloride ion ingress. CEM III concrete with 100% RCA outperformed CEM I concrete with 100% NA. However, the replacement of GGBS and RCA should be limited to 50% and 60% respectively to conform to previous findings (Dodds, Christodoulou et al. 2017).

6. PERFORMANCE OF RCA IN THE COASTAL ENVIRONMENT

A study investigated the effects of wetting and drying cycles with various percentage replacements of RCA including 30% and 60%. Three samples per group were cast using 4" cubes which were cured for 28 days, after which the samples were submerged in sea water for 8 hours and removed for 16 hours to simulate the tidal zone in the marine environment. This circulation lasted for 4, 8, 12 and 16 months. A microcomputer-controlled electrohydraulic servo tester was used to collect compression strengths and deformations results. There was a decrease in $f'c$ with an increase in RCA replacement and corrosion time, as compared to the NAC. This could have been attributed to the lower elastic modulus of the RAC and the internal bonding being destroyed by chloride ion ingress (Wang, Huang et al. 2013).
The optimum percentage replacement of RCA to be used in the marine environment was investigated by manipulating three variables: percentage of RCA (30%, 40%, 50%), curing period (28, 60, 90 days) and saline water concentration (1N, 3N, 5N). It was concluded that 30% replacement of RCA was optimum to be used in construction in the marine environments as it achieved more than 95% of $f'c$ at 28 days (Mukhlis, R Hoque et al. 2014). Both authors were silent on the use of treated RCA.

7. CONCLUSIONS

RCA has inferior properties as compared to NA due to the residual mortar and ITZs.
There is a reduction in concrete strength with an increase in percentage replacement of RCA, however with treatment the strengths are improved. RCA have been used for structural purposes, however more investigations are required to clarify the durability performance using RCA.

8. REFERENCES

Agyekum, K. (2018). "STATE-OF-THE-ART REVIEW OF CURRENT LITERATURE AND DEVELOPMENT STUDIES ON RECYCLED AGGREGATE CONCRETE." Acta Technica Corviniensis-Bulletin of Engineering 11(3): 121-134.

Alengaram, U. J., A. Salam, M. Z. Jumaat, F. F. Jaafar and H. B. Saad (2011). "Properties of high-workability concrete with recycled concrete aggregate." Materials Research 14(2): 248-255.

Behera, M., S. K. Bhattacharyya, A. K. Minocha, R. Deoliya and S. Maiti (2014). "Recycled aggregate from C&D waste & its use in concrete–A breakthrough towards sustainability in construction sector: A review." Construction and Building Materials 68: 501-516.

Dodds, W., C. Christodoulou, C. Goodier, S. Austin and D. Dunne (2017). "Durability performance of sustainable structural concrete: Effect of coarse crushed concrete aggregate on rapid chloride migration and accelerated corrosion." Construction and Building Materials 155: 511-521.

Etxeberria, M., E. Vázquez, A. Marí and M. Barra (2007). "Influence of amount of recycled coarse aggregates and production process on properties of recycled aggregate concrete." Cement and concrete research 37(5): 735-742.

Fathifazl, G. (2008). Structural performance of steel reinforced recycled concrete members, Carleton University.

Fathifazl, G., A. G. Razaqpur, O. B. Isgor, A. Abbas, B. Fournier and S. Foo (2009). "Flexural Performance of Steel-Reinforced Recycled Concrete Beams." ACI Structural Journal 106(6).

Gómez-Soberón, J. M. (2002). "Porosity of recycled concrete with substitution of recycled concrete aggregate: an experimental study." Cement and concrete research 32(8): 1301-1311.

González-Taboada, I., B. González-Fonteboa, F. Martínez-Abella and D. Carro-López (2016). "Study of recycled concrete aggregate quality and its relationship with recycled concrete compressive strength using database analysis." Materiales de Construcción 66(323): 089.

Günçan, N. F. (1995). "Using waste concrete as aggregate." Cement and concrete research 25(7): 1385-1390.

Hansen, T. C. (2014). Recycling of demolished concrete and masonry, CRC Press.

Hansen, T. C. and H. Narud (1983). "Strength of recycled concrete made from crushed concrete coarse aggregate." Concrete International 5(1): 79-83.
Ismail, S. and M. Ramli (2014). "Mechanical strength and drying shrinkage properties of concrete containing treated coarse recycled concrete aggregates." Construction and Building Materials 68: 726-739.
Katz, A. (2003). "Properties of concrete made with recycled aggregate from partially hydrated old concrete." Cement and concrete research 33(5): 703-711.
Kou, S.-C., C.-S. Poon and H.-W. Wan (2012). "Properties of concrete prepared with low-grade recycled aggregates." Construction and Building Materials 36: 881-889.
Limbachiya, M., T. Leelawat and R. Dhir (2000). "Use of recycled concrete aggregate in high-strength concrete." Materials and structures 33(9): 574.
Lowndes, I. and K. Jeffrey (2009). "Optimising the efficiency of primary aggregate production." Mineral Industry Research Organisation: 74.
Marinković, S. B., I. S. Ignjatović, V. S. Radonjanin and M. M. Malešev (2012). Recycled aggregate concrete for structural use–an overview of technologies, properties and applications. Innovative Materials and Techniques in Concrete Construction, Springer: 115-130.
Maruyama, I., S. Masaru, S. Takahisa, S. Ryoichi and K. Kenji (2004). "Flexural properties of reinforced recycled concrete beams." In Proceedings of the international RILEM conference on the use of recycled materials in buildings and structures, Barcelona, Spain: 8-11.
McNeil, K. and T. H.-K. Kang (2013). "Recycled concrete aggregates: A review." International Journal of Concrete Structures and Materials 7(1): 61-69.
Medina, C., W. Zhu, T. Howind, M. I. S. De Rojas and M. Frías (2015). "Influence of interfacial transition zone on engineering properties of the concrete manufactured with recycled ceramic aggregate." Journal of Civil Engineering and Management 21(1): 83-93.
Mukhlis, M., M. R Hoque and M. T Alam (2014). AN EXPERIMENTAL STUDY ON INFLUENCE OF RECYCLED AGGREGATES ON CONCRETE COMPRESSIVE STRENGTH IN MARINE ENVIRONMENT.
Murali, G., C. V. Vardhan, G. Rajan, G. Janani, N. S. Jajan and R. Ramyasri (2012). "Experimental study on recycled aggregate concrete." International Journal of Engineering Research and Applications (IJERA) 2(2): 407-410.
Oikonomou, N. D. (2005). "Recycled concrete aggregates." Cement and concrete composites 27(2): 315-318.
Olorunsogo, F. and N. Padayachee (2002). "Performance of recycled aggregate concrete monitored by durability indexes." Cement and concrete research 32(2): 179-185.
Poon, C., Z. Shui, L. Lam, H. Fok and S. Kou (2004). "Influence of moisture states of natural and recycled aggregates on the slump and compressive strength of concrete." Cement and concrete research 34(1): 31-36.
Qiu, J., D. Q. S. Tng and E.-H. Yang (2014). "Surface treatment of recycled concrete aggregates through microbial carbonate precipitation." Construction and Building Materials 57: 144-150.
Rahal, K. (2007). "Mechanical properties of concrete with recycled coarse aggregate." Building and environment 42(1): 407-415.
Rao, A., K. N. Jha and S. Misra (2007). "Use of aggregates from recycled construction and demolition waste in concrete." Resources, conservation and Recycling 50(1): 71-81.
RILEM, T.-D. (1994). "Specifications for Concrete with Recycled Aggregates." Materials and Structures 27: 557-559.
Sagoe-Crentsil, K. K., T. Brown and A. H. Taylor (2001). "Performance of concrete made with commercially produced coarse recycled concrete aggregate." Cement and concrete research 31(5): 707-712.
Seara-Paz, S., V. Corinaldesi, B. González-Fonteboa and F. Martínez-Abella (2016). "Influence of recycled coarse aggregates characteristics on mechanical properties of structural concrete." European Journal of Environmental and Civil Engineering 20(sup1): s123-s139.
Silva, R., J. De Brito and R. Dhir (2015). "Tensile strength behaviour of recycled aggregate concrete." Construction and Building Materials 83: 108-118.
Tabsh, S. W. and A. S. Abdelfatah (2009). "Influence of recycled concrete aggregates on strength properties of concrete." Construction and Building Materials 23(2): 1163-1167.
Tavakoli, M. and P. Soroushian (1996). "Drying shrinkage behavior of recycled aggregate concrete." Concrete International 18(11): 58-61.
Wang, J., T. Huang, X. Liu, P. Wu and Z. Guo (2013). Mechanical Properties of Recycled Concrete in Marine Environment.
Xie, T., A. Gholampour and T. Ozbakkaloglu (2018). "Toward the development of sustainable concretes with recycled concrete aggregates: comprehensive review of studies on mechanical properties." Journal of Materials in Civil Engineering 30(9): 04018211.

39th Cement and Concrete Science Conference
9-10th September 2019
University of Bath
Paper Number 019

The influence of superabsorbent polymers on drying shrinkage of fibre reinforced mortars

Rohollah Rostami, and Agnieszka J. Klemm
School of Computing, Engineering and Built Environment, Glasgow Caledonian University

Abstract

The paper forms part of a wider research study directed to explore the effect of Superabsorbent polymers (SAP) on the performance of fibre reinforced cementitious materials containing different binders.
Despite their worldwide popularity and versatility, cementitious materials may suffer from a number of deteriorative processes, including drying shrinkage and a consequent cracking. In order to reduce the effect of drying shrinkage Polymeric fibres (PF) are often added to cementitious matrices. However, this technique is not always sufficient to protect concrete and some form of internal curing is essential, for example by Super Absorbent Polymers (SAPs). The effectiveness of SAPs in different blended cements depends on a number of parameters, including their chemical composition, particle grading and ionic concentration in surrounding pore solution.

This paper presents the results of experimental study of the effect of SAPs on drying shrinkage of fibre reinforced mortars (FRM). Three commercially available cements: CEM I (PC), CEM II (PC-FA 70-30)) and CEM III (PC-GGBS 50-50) and three types of SAP were analysed.
The experimental results showed that SAPs could reduce slightly drying shrinkage in fibre reinforced mortars as governed by their absorption/desorption kinetics. Overall, the type of binder has much more important role in DS and the effect of fly ash on DS reduction is very prominent
.

INTRODUCTION

Supplementary cementitious materials (SCMs), such as fly ash (FA) and ground granulated blast-furnace slag (GGBS), are often used as a partial replacement of cements to improve sustainability of Portland cement-based materials and reduce their environmental impact. However, SCMs are known to be more sensitive to different curing regimes and hence more susceptible to early cracking. This is primarily caused by slow pozzolanic reactions in FA (De Belie et al., 2018) and limited degree of later reactions in GGBS due to a lack of space already filled by early products of PC hydration (Almeida and Klemm, 2018). Moreover, drying-shrinkage resulting from the loss of water to surrounding atmosphere (Mechtcherine et al., 2012) may significantly compromise concrete durability and serviceability. Although the Polymeric fibres (PF) are often recommended (Gong et al., 2018; Yousefie et al., 2017) as a technique to cope with this phenomenon, it is often insufficient and some form of internal curing is still required to decrease self-desiccation and promote cement hydration (Wyrzykowski and Lura, 2016). Superabsorbent polymers (SAPs) have been proved to be a promising internal curing agent for cementitious materials, which can facilitate hydration process and control water supply in both fresh and hardened state (Mechtcherine et al., 2012). The most remarkable successes of SAPs have been in mitigation of autogenous shrinkage, plastic shrinkage (Mechtcherine et al., 2016), enhancing freezing and thawing resistance (Sikora and Klemm, 2013), self-sealing (Snoeck et al., 2012) and self-healing (Snoeck et al., 2016) in various types of mortar and concrete. However, SAP effectiveness in cementitious matrices depends not only on its intrinsic characteristics (shape, size, crosslinking density, chemical structure) but also on the ionic concentration in surrounding pore solution. Therefore, the main objective of this study is to assess the effect of different SAPs on drying shrinkage of Fibre Reinforced Mortars (FRMs).

METHODOLOGY

Materials

Three types of cement have been used in this study: CEM I 52.5N (Portland cement - PC), CEM II/B-V 42.5N (PC-FA 70-30), and CEM III/A 42.5N (PC-GGBS 50-50). CEM I, II and III have been supplied by Hanson Cements (UK), Lafarge (UK) and Ecocem (Ireland) respectively. Their Chemical and physical characteristics, as provided by manufacturers, are presented in Table 1.

Table 1 Chemical and physical analysis of CEM I, II and III

Compound (%)	CEM I (PC)	CEM II (FA)	CEM III (GGBS)
CaO	64.3	43.48	57.13
SiO2	20.76	32.69	24.50
Al2O3	4.99	13.13	8.99
MgO	2.19	1.33	5.33
Fe2O3	2.57	3.29	1.76
K2O	0.27	1.26	-
Cl	0.06	-	0.04
MnO	-	0.07	5.33
TiO2	-	0.56	0.58
ZnO	-	0.02	-
Mn3O4	-	-	0.16
Loss on ignition	2.39	-	1.19

The micro polypropylene fibres (Fig. 1) used in this study were provided by ADFIL Construction Fibers (UK). Fibres have length of 6-mm, diameter 18µm and density 0.91 kg/m^3.

SAP characterization

Three types of SAPs provided by BASF Construction Chemicals GmbH, were investigated. These were SAP A (copolymer of acrylamide and acrylic acid), SAP C and SAP E (both modified polyacrylamide). Shapes and size of SAPs have been characterized by SEM image analysis (Fig. 1).

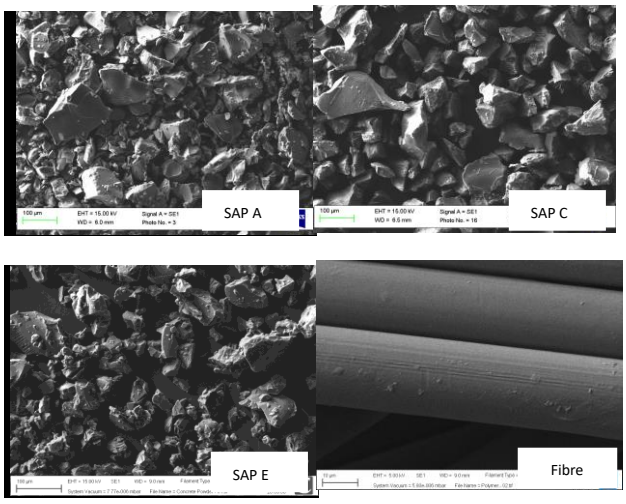

Figure 1 The SEM micrographs of SAP A, C, E and Fibre

SAP's particle sizes were measured by the laser diffraction. The results are shown in Figure 2(a). Figure 2(b) shows Raman spectra which confirm the base polymer being polyacrylamide and the same chemical composition of SAPs C and E. However, their differences in sorption characteristics could be attributed to their respective particular monomers (Zohuriaan-Mehr and Kabiri, 2008). The water absorption capacity (WAC) of SAPs in cement paste solutions have been determined by the tea-bag method (Almeida et al., 2018; Mechtcherine et al., 2018) and shown in Figs. 2(c).

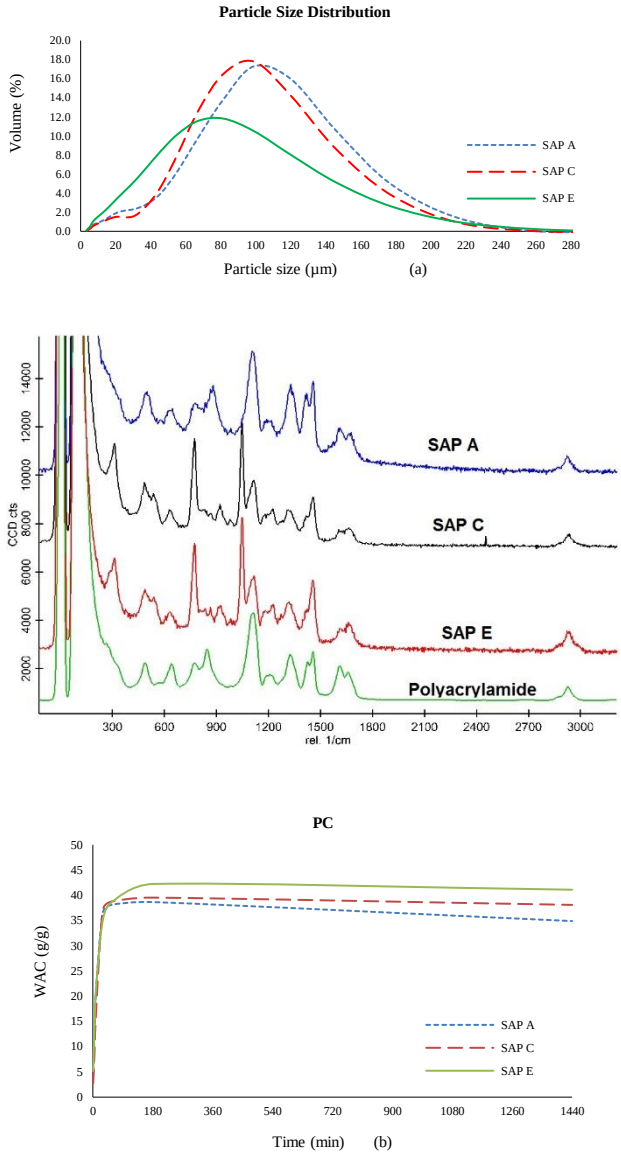

Figure 2 (a) Particle size distribution of SAPs (b) Comparison of molecular structure of the studied SAPs and polyacrylamide by Raman spectroscopy (c) Sorption behaviour of SAPs in cement paste solution.

Mix compositions

In order to assess the effect of SAPs on drying shrinkage of FRMs different SAPs with different particle size, WAC and chemical composition were analysed.
Table 2 shows fifteen different compositions of FRMs were designed to carry out this study with different water/binder ratios. All studied mortars were prepared with the proportion of binder to fine sand of 1:2 (by weight). The water-to-binder ratio

(w/b) was increased, in SAP modified mortars in order to compensate for water absorbed by polymer (Snoeck et al., 2018). Three types of SAPs were added to mixtures in the proportion of 0.25% by mass of binder.

Table 2 Mix proportion of mortars and water/binder ratios

Cement	Sample Name	SAP type	SAP Content	Fibre Content	W/B ratio
	I	-	-	-	0.48
	I1	-	-	0.50%	0.52
CEM I (PC)	I1A	A	0.25%	0.50%	0.58
	I1C	C	0.25%	0.50%	0.58
	I1E	E	0.25%	0.50%	0.58
	II	-	-	-	0.45
	II1	-	-	0.50%	0.50
CEM II (FA)	II1A	A	0.25%	0.50%	0.56
	II1C	C	0.25%	0.50%	0.56
	II1E	E	0.25%	0.50%	0.57
	III	-	420	-	0.48
	III1	-	-	0.50%	0.52
CEM III (GGBS)	III1A	A	0.25%	0.50%	0.58
	III1C	C	0.25%	0.50%	0.58
	III1E	E	0.25%	0.50%	0.58

The amount of fiber used was 0.50% by mass of binder. Fine sand had 90% of particles smaller than 0.425mm.

Drying shrinkage (DS) and mass loss

The drying shrinkage in mortars was measured on prismatic specimens (75 × 75 × 280 mm³) according to BS ISO 1920-8 (2009). Samples were demoulded after 24h and the unsealed specimens were left drying in laboratory environment (T = 21±2ºC and RH = 40±5%) for 180 days. The length and weight of specimens were measured daily in the first 28 days.

Figure 3 Drying shrinkage tests

Between 28-180 days, measurements were taken weekly to evaluate the effect of SAPs on drying shrinkage and mass loss of the specimens.

RESULTS AND DISCUSSIONS

Figure 4 shows drying shrinkage (DS) development during 180 days. The similar trends have been observed for the reference samples (PC, FA and GGBS). Mortars with CEM II (PC-FA) had the lowest values of shrinkage while, mortars with CEM III (PC-GGBS) displayed the highest values in comparison with the PC samples. These differences can be explained by the fact that DS is greatly affected by the water-binder ratio (w/b) (Juenger et al., 2002) and differences in hydration rate (Scrivener et al., 2015). As previously reported (Gong et al., 2018; Yousefie et al., 2017), addition of fiber can lessen DS and this reduction is more pronounced in matrices with CEM II cement.

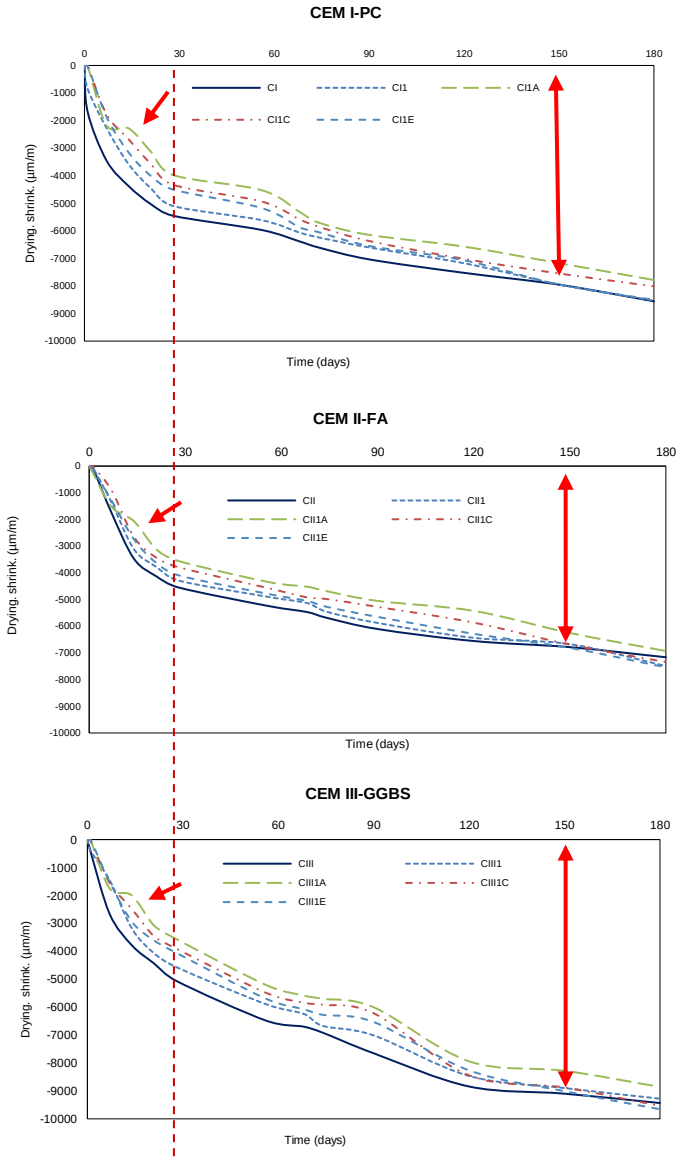

Figure 4 Drying shrinkage development of FRM with SAPs

Addition of SAPs can reduce DS in all mortars when compared to the corresponding reference samples. However, the extent of reduction depends very much on the type of SAP used. As seen on Fig 4,

SAP A seemed to be more effective in reduction of shrinkage owing to its lowest WAC (Fig. 2b) and as a result of swelling in the second week (Snoeck et al., 2015; Lee et al., 2018). As shown on Fig. 4 addition of both SAPs C and E resulted in a similar or slightly reduced DS, when compared to the reference samples. This reduction was higher for SAP C due to its slower water absorption capacity.

Figure 5 shows the results of mass loss rates recorded during 180 days. For the clarity purposes, only results for the references samples, and two samples of cements were presented. However, other samples had similar general pattern to the results displayed. Overall, samples with SAPs had the highest mass loss rates. The reference samples (without SAPs and PF) had the lowest mass loss rate compared to the SAPs mortars.

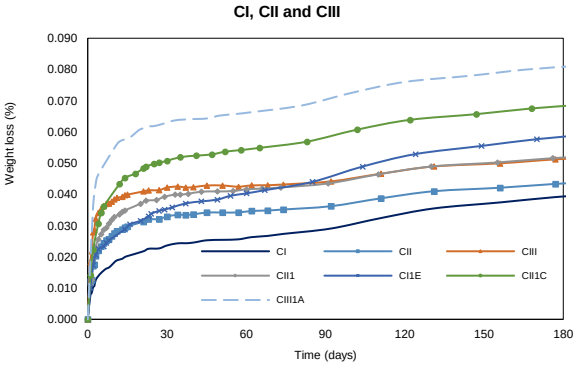

Figure 5 Weight loss rates during drying shrinkage tests

Furthermore, SAP A in mortars with CEM III had the highest mass loss rate due to lower WAC. The mass loss is higher in mortars with higher W/B ratio, while the respective shrinkage is the highest.

CONCLUSIONS

Drying shrinkage in FRMs can be reduced slightly by addition of SAPs. The effect of PF is minimal; the type of cement has much more important role in drying shrinkage. This is more pronounced for mortars with CEM III (PC-GGBS), but the effect of fly ash on DS reduction is very prominent. SAP effectiveness depends on the water absorption capacity. The highest reduction of drying shrinkage was observed for mortars with SAP A with the lowest WAC. It can be concluded that SAPs with lower WAC lead to increased mass loss rate, reducing drying shrinkage.

REFERENCES

Almeida, F. C. R., and Klemm, A. J. (2018). Cement and Concrete Composites, 88, 41–51.

Almeida, F.C.R., Rostami. R., Klemm, A.J. (2018). MATEC Web of Conferences, 2018, 199, 02023.

BS EN 1920-8. (2009). “Part 8: Determination of drying shrinkage of concrete for samples prepared in the field or in the laboratory.” British Standard, 50.

De Belie, N. Soutsos, M. Gruyaert, E., 2018. RILEM. 238-SCM.

Gong, J., Zeng, W., and Zhang, W. (2018). Construction and Building Materials 159 (2018) 155–163 Contents.

Juenger, M. C. G. and H. M. Jennings (2002). Cement and Concrete Research 32(2): 289-296.

Lee, H. X. D. Wong, H. S. and Buenfeld, N. R., 2018. Cement and Concrete Composites 88 (2018) 150e164.

Mechtcherine V, Reinhardt HW (eds) (2012). The RILEM TC 225–SAP. Springer, Hei- delberg, 165 p. ISBN 978-94-007-2732-8

Mechtcherine V (2016) Use of superabsorbent polymers (SAP) as concrete additive. RILEM Tech Lett 1:81–87.

Mechtcherine, V., et al. Testing superabsorbent polymer (SAP) sorption properties prior to implementation in concrete: results of a RILEM Round-Robin Test. Materials and Structures, 2018, 51:28.

Mechtcherine V. and H.-W. Reinhardt (eds.)(2012). Application of Superabsorbent Polymers (SAP) in Concrete Construction, RILEM State of the Art Reports 2, DOI 10.1007/978-94-007-2733-5_7, © RILEM 2012.

Snoeck, D., Schaubroeck, D., Dubruel, P. and De Belie, N. (2014). Construction and Building Materials, 2014, 72, pp.148–157.

Scrivener, K. L., Lothenbach, B., De Belie, N., Gruyaert, E., Skibsted, J., Snellings, R., & Vollpracht, A. (2015). TC 238-SCM: hydration and microstructure of concrete with SCMs. Materials and Structures, 48(4), 835–862.

Snoeck, D., Jensen, O.M. & De Belie, N. (2015). Cement and Concrete Research, 2015, 74, pp.59–67.

Snoeck D, Steuperaert S, Van Tittelboom K, Dubruel P, De Belie N (2012). Cem Concr Res 42(8):1113–1121.

Sikora KS, Klemm AJ (2013). Int J Comput Methods Exp Measur 2(3):255–268.

Snoeck D, Dewanckele J, Cnudde V, De Belie N (2016). Cem Concr Compos 65:83–93.

Wyrzykowski, M. Lura, P., (2016). Effect of relative humidity decrease due to self-desiccation on the hydration kinetics of cement. Cem Concr Res (2016) 85: 75-81.

Yousefie, N., Joshaghani A., Hajibandeh, E., and Shekarchi, M. (2017). “Influence of fibers on drying shrinkage in restrained concrete.” Construction and Building Materials 148 (2017) 833–845 Contents.

Zohuriaan-Mehr, M.J., and Kabiri K., (2008). “Superabsorbent Polymer Materials: A Review” Iranian Polymer Journal 17 (6), 2008, 451-477.

39th Cement and Concrete Science Conference
9-10th September 2019
University of Bath
Paper Number 020

Effects of Steam Slaking on the Characteristics of Portlandite Crystals

C. Pesce and G. Pesce
Department of Architecture and Built Environment, Northumbria University Newcastle

ABSTRACT

This contribution describes the effect of various slaking methods on the microstructural and mineralogical characteristics of Portlandite crystals ($Ca(OH)_2$). Aim of this research is to develop lime-based construction materials for the modern construction industry. Microstructural changes of $Ca(OH)_2$ crystals obtained by slaking calcium oxide in different conditions were investigated using Scanning Electron Microscopy (SEM) and X-ray Diffraction Analysis (XRD). Results suggest that the slaking conditions affect the crystal size and shape resulting in an increase of surface area and, in turn, a potential improvement of mortars performances.

1. INTRODUCTION

Lime (CaO) is a material that has been used by humankind for millennia and that has had (and still has) an important impact on everyday people's lives. It is used in a number of industrial processes such as in food and pharmaceutical processing and in steel production, as well as in other industries such as agriculture and construction industry where it is mainly used as a binder in mixtures such as mortars and plasters.

Despite this importance and the long history, during the 20th century, the use of lime in the constructions gradually phased out in favour of the new hydraulic binders with improved performances that had been developed since the 17th century such as Portland cement. Nowadays most of the empirical knowledge on the production and use of lime that built up over the centuries is lost but there is an increasing pressure to re-discover this material by developing some new scientific (rather than empirical, as it was in the past centuries) knowledge.

As a binder for the construction industry, lime has several advantages over other cementitious materials. These include a low Young's module (Grant et al., 2016; Hendry, 2001; Lanas and Alvarez, 2003; Rosson et al., 1998), a high gas permeability, self-healing properties, higher resistance to soluble salts (Ball et al., 2016; Cizer et al., 2018, 2012; Cultrone et al., 2005), as well as mild antiseptic properties (Auvinen and Wirtanen, 2008; Grant et al., 2016; Martínez-Ramírez et al., 1998; Maskell et al., 2017; Shirakawa et al., 2003), lower CO_2 emissions, and reduced costs of production (Ball et al., 2016; Grant et al., 2016; Vance et al., 2015).

However, despite these properties, some limitations prevent lime from becoming once again an attractive material for the modern industry. A major drawback is the slow rate of the carbonation reaction, as the setting time is a crucial factor in terms of costs for the modern construction industry. Overcoming such limitations could make once again lime an appealing product for construction companies, aiming at minimising time and costs of operations as well as their environmental impact. Only recently, with the so-called 'lime revival', the interest of the industry and academy in lime-based materials increased again. However, a sound scientific understanding of the characteristics of lime is still needed, in order to create the platform necessary to develop new lime-based products that can be successfully used in construction.

In this paper, the initial results of a set of experiments on the vapour hydration of CaO – a process commonly used in environmental sciences to produce CO_2 sorbents – are reported. The vapour hydration reaction mechanism, firstly investigated by Ramachandran et al. (1964) and later by Beruto et al. (1981), is based on a solid-state topotactic reaction which results in the formation of smaller, poorly crystalline $Ca(OH)_2$ able to rapidly react with the CO_2. Such characteristic could be advantageous when lime is used as a binder in mortars and plasters.

Our investigation is based on the comparison of the properties of Portlandite crystals formed upon different slaking methods. Investigating the hydration reaction of CaO and how the slaking conditions can affect the properties of the newly-formed Portlandite crystals has been the focus of some recent studies (Blamey, 2016; Serris, 2011; Mascolo et al., 2010; Paiva et al., 2010; Rodriguez-Navarro et al., 2017) and it has already pointed out that the outcome of this research has the potential to be exploited for the development of high-performance lime-based building materials.

2. Materials and Methods

Commercial CaO *Calbux Granular 15* (*Tarmac, Buxton Lime*) with particles size <22.4 mm was

used in these tests. Granules of >5 mm size and of the whitest colour were selected for the experiments and placed inside a glove box filled with nitrogen gas (N_2) to prevent any reaction with the CO_2 contained in the air. The granules were crushed with an agate mortar and pestle and the powder produced was sieved to obtain particles with diameter <500μm. During crushing and sieving, the CO_2 concentration was constantly monitored using a CO_2 sensor and kept <200 ppm by washing the glovebox with N_2 when needed. Using the coning and quartering method, 9 CaO samples were obtained from the entire batch. The samples were, then, slaked using the following methods (all tests were repeated 3 times):

Slaking with liquid water at 90˚C

Steam slaking:

Below the water boiling point (90˚C)

Above the water boiling point (200˚C)

During slaking with liquid water, CaO samples contained in PTFE jars were put in an oven at 90˚C together with a sealed beaker containing de-gassed distilled water. After about 1 hour, when the water and the CaO powder reached an equilibrium, 10 mL of degassed distilled water were added to the CaO and mixed thoroughly to promote slaking. The slaked lime was left in the oven for 4 hours at 90˚C. At the end of the test, the temperature inside the oven was gradually reduced to room temperature and the samples were dried in a desiccator for 24 hours before analysis.

During slaking with steam, the CaO samples contained in PTFE jars were placed in a bigger glass container partially filled with de-gassed distilled water so that no contact was possible between the CaO and the liquid water. The glass container was, then, covered with aluminium foil to prevent the rapid evaporation of water and kept in the oven for 8 hours to allow the steam generated by the heat to slake the CaO. The same procedure was repeated for temperatures of the oven at 90˚C and at 200˚C. At the end of the test, the temperature of the oven was reduced to room temperature and the samples were dried in a desiccator for 24 hours before analysis.

The CaO powder was characterised using a Scanning Electron Microscope (SEM), X-ray Diffraction Analysis (XRD) and X-ray fluorescence (XRF), whereas the Portlandite crystals produced were characterised using SEM and XRD. In particular, the micro-morphological characterisation was carried out using a Tescan Mira 3 Scanning Electron Microscope in high vacuum mode. Prior to analysis, the samples were coated with a 5 nm thick Platinum layer. Mineralogical characteristics of the samples before and after slaking were investigated using a Siemens D5000 diffractometer with Cu-Kα radiation, in the 2-θ range 10-90° with an increment of 0.02/step and scan speed of 1 sec/step, at 30 KV and 30 mA. Samples after slaking were mixed with 10% w/w of Zincite as an internal standard to investigate existence of a possible amorphous phase. Quantification was performed using the Rietveld refinement method using the Profex software. Quantitative XRF analysis of CaO powder was performed using a Spectro Xepos benchtop XRF analyser. The 'Geochemistry traces' method was used as internal calibration. Resolution was 131.5eV at 5.89KeV. Pressed pellets with a mixture of CaO and an inert wax binder (Fluxana Cereox wax, $C_{38}H_{76}O_2N_2$) were produced for analysis to improve consistency of the results.

3. Results and Discussion

The XRD pattern of the CaO powder is shown in Fig. 1 where only the characteristic peaks of the CaO are visible suggesting that the procedure to avoid hydration or carbonation of the sample was applied correctly. No peaks related to any form of calcium carbonate or portlandite were detected. The same sample was observed at the SEM at low and high magnification. The microstructure of CaO particles (Fig. 2a) showed a porous fabric similar to that observed by Witoon et al. (2011) in calcined waste eggshells.

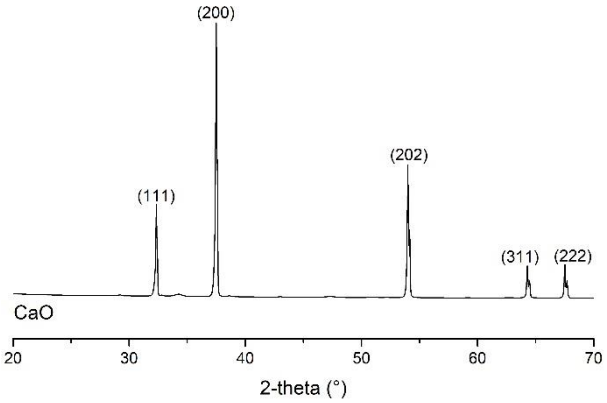

Figure 1. Diffractogram of the Calcium oxide.

Table 1 shows the results of the XRF analysis of CaO. Percentages of the elements added up to 90.5% because the sample was embedded in an organic wax (undetectable by XRF). It is reasonable to assume that the undetected material was only due to the presence of the wax, and not to other materials.

Table 1. Chemical analysis of Calcium oxide

Chemical composition	Weight %
CaO	89.4
MgO	0.480
SiO_2	0.327
Al_2O_3	0.0750
Fe_2O_3	0.0683
SO_3	0.0451
Cl	0.0137
P_2O_5	0.00804
Na_2O	<0.0055
K_2O	$<10^{-5}$

Results confirmed that the product is a high purity CaO and that during handling and analysis of the samples, carbonation or hydration reactions did not occur.

SEM images of the products of the slaking with liquid water at 90˚C, and with steam at 90˚C and at 200˚C are reported in Figure 2b-d, respectively. The analysis shows that the samples slaked with liquid water were characterized by several hexagonal prisms up to 3 µm diameter with thickness ranging from 0.5 to 1 µm. These crystals were embedded in a matrix of nanometer-sized $Ca(OH)_2$ particles (Figure 2b). Such microstructure is commonly observed in lime putties where crystals of Portlandite grow in aqueous solution via a dissolution/re-precipitation process (Rodriguez-Navarro et al., 2017; Navrátilová, 2017).

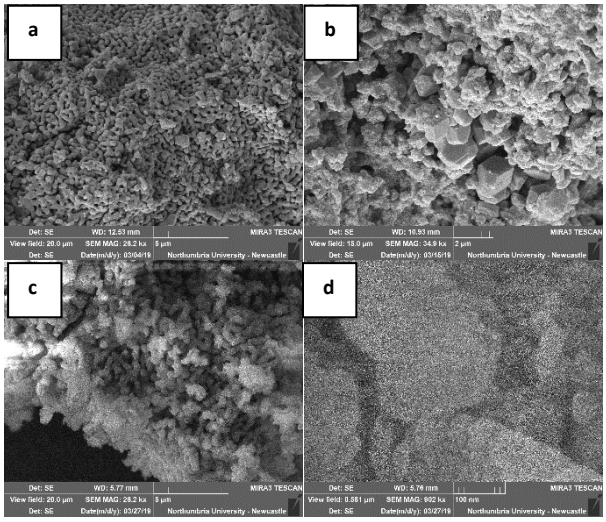

Figure 2. SEM micrographs of (a) CaO powder; portlandite crystals formed upon slaking with (a) water and (b) steam at 200 ˚C; (d) nanometric, plate-like portlandite crystals formed upon slaking with steam at 200 ˚C.

The microstructure observed in the samples slaked with steam was very different from the one observed in the samples slaked with liquid water. In fact, whereas after slaking with liquid water big well-formed prismatic crystals were observed, after steam slaking (both at 90˚C and 200˚C) smaller plate-like hexagonal crystals up to 1 µm diameter with thickness between 50 and 100 nm were observed (Fig. 2d) and the crystal fabric resembled that of the parent material (i.e. CaO; Fig. 2a-c).
The XRD analyses allowed verifying that all samples were fully converted to $Ca(OH)_2$ after the slaking with both, liquid water and steam (Fig. 3). No peaks related to CaO or any form of $CaCO_3$ were found, confirming that the hydration process proceeded to completion and that no relevant carbonation occurred during the experiments or the handling of the sample prior to analysis.

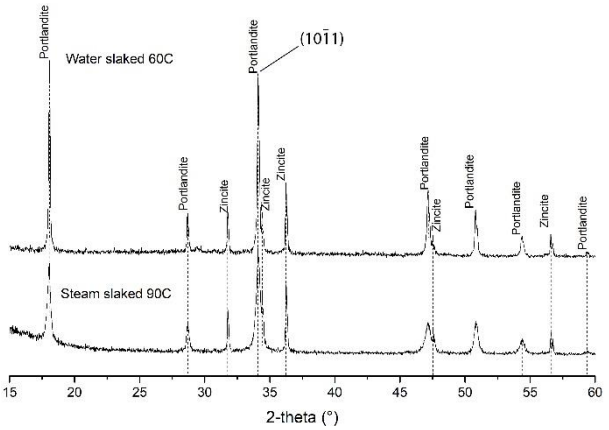

Figure 3. Diffractograms of lime slaked with water and steam.

Additionally, XRD patterns of the samples slaked with steam showed broader peaks compared to the sample slaked with liquid water. A similar result was obtained by Beruto et al. (1981) who suggested that the broad peaks were a consequence of finer crystallites of the $Ca(OH)_2$ obtained with water vapour with respect to liquid water. This is shown by a broadening of the (10 $\overline{1}$ 1) diffraction peak (Fig. 3), due to the presence of crystals with size <1000 Å (Rodriguez-Navarro et al., 1998). Crystal size was calculated from XRD data by using Scherrer's equation:

$$B(2\theta) = \frac{K\lambda}{L\cos\theta}$$

Where *L* is the mean crystallite size, *K* is the grain shape dependent constant 0.92, *λ* is the wavelength of the incident beam (1.5408 Å for Cu*Kα*), *θ* is the Bragg reflection angle, and *B* is the line broadening at half-height of the diffraction peak (in radians). Crystals with average size ~430 Å appear in the water-slaked lime, while a broadening of the diffraction line was produced by crystals with the average size of ~170 Å in the steam-slaked lime.

4. Conclusions

Overall, these results suggest that full a conversion of CaO in $Ca(OH)_2$ was obtained with both, water and steam slaking at various temperature. However, the former slaking method produced a slurry whereas the latter resulted in a product that can be described as a hydrated lime powder. Differences in the shape and size of the newly-formed Portlandite crystals were found between the products obtained with different slaking methods. After slaking with liquid water, micrometre-sized hexagonal prisms of Portlandite were embedded in a matrix of finer nanometer-sized $Ca(OH)_2$ particles. After slaking with steam, smaller hexagonal plate-like Portlandite crystals up to 1 µm diameter were embedded in a fabric similar to that of the parent material. Results of SEM analysis were supported by the results of the XRD analyses and the results of the literature

review (i.e. Beruto et al., 1981; Rodriguez-Navarro et al., 2017).

Overall, steam slaking seems to produce finer $Ca(OH)_2$ crystals with, consequently, higher specific surface area. According to several studies (Rodriguez-Navarro et al., 2017; Mascolo et al., 2010; Van Balen et al., 2005; Cazalla et al., 2000) a higher surface area enhances both, workability and reactivity of lime as well as the carbonation reaction, which could be advantageous when lime is used as a binder in mortars for the modern construction.

REFERENCES

Auvinen, J., Wirtanen, L., 2008. The influence of photocatalytic interior paints on indoor air quality. Atmospheric Environment 42:4101–4112.

Ball, R.J., Molinari, M., Grant, J., Parker, S.C., 2016. Atomistic Modelling for the Study of Dissolution and Carbonation of Lime, in: 36th Cement and Concrete Science Conference. Cardiff, UK.

Beruto, D., Barco, L., Belleri, G., Searcy, A.W., 1981. Vapor-Phase Hydration of Submicrometer CaO Particles. Journal of the American Ceramic Society 64:74–80.

Blamey, J., Zhao, M., Manovic, V., Anthony, E.J., Dugwell, D.R., Fennell, P.S., 2016. A shrinking core model for steam hydration of CaO-based sorbents cycled for CO2 capture. Chemical Engineering Journal 291:298–305.

Cazalla, O., Rodriguez-Navarro, C., Sebastian, E., Cultrone, G., 2000. Effects on Traditional Lime Mortar Carbonation. Journal of the American Ceramic Society 83:1070–1076.

Cizer, Ö., Rodriguez-Navarro, C., Ruiz-Agudo, E., Elsen, J., Van Gemert, D., Van Balen, K., 2012. Phase and morphology evolution of calcium carbonate precipitated by carbonation of hydrated lime. Journal of Materials Science 47:6151–6165.

Cizer, Ö., Ruiz-Agudo, E., Rodriguez-Navarro, C., 2018. Kinetic effect of carbonic anhydrase enzyme on the carbonation reaction of lime mortar. International Journal of Architectural Heritage 12:779–789.

Cultrone, G., Sebastián, E., Huertas, M.O., 2005. Forced and natural carbonation of lime-based mortars with and without additives: Mineralogical and textural changes. Cement and Concrete Research 35:2278–2289.

Grant, J., Pesce, G.L., Ball, R.J., Molinari, M., Parker, S.C., 2016. An experimental and computational study to resolve the composition of dolomitic lime. RSC Adv. 6, 16066–16072.

Hendry, E.A.W., 2001. Masonry walls: Materials and construction. Construction and Building Materials 15:323–330.

Lanas, J., Alvarez, J.I., 2003. Masonry repair lime-based mortars: Factors affecting the mechanical behavior. Cement and Concrete Research 33: 1867–1876.

Martínez-Ramírez, S., Puertas, F., Blanco-Varela, M.T., Thompson, G.E., Almendros, P., 1998. Behaviour of repair lime mortars by wet deposition process. Cement and Concrete Research 28:221–229.

Mascolo, G., Mascolo, M.C., Vitale, A., Marino, O., 2010. Microstructure evolution of lime putty upon aging, Journal of Crystal Growth 312:2363–2368.

Maskell, D., Ferreira Pinto Da Silva, C., Mower, K., Cheta, R., Dengel, A., Ball, R., Ansell, M., Thomson, A., Peter, U., Walker, P., 2017. Bio-Based Plaster for Improved Indoor Air Quality, in: International Conference on Bio-Based Building Materials. Clermont-Ferrand.

Navrátilová E., Tihlaříková, E., Neděla, V., Rovnaníková P., Pavlík, J., 2017. Effect of the preparation of lime putties on their properties. Scientific Reports 7:17260.

Ramachandran, V.S., Sereda, P.J., Feldman, R.F., 1964. Mechanism of Hydration of Calcium Oxide. Nature 201:288–289.

Rodriguez-Navarro, C., Hansen, E., Ginell, W.S., 1998. Calcium Hydroxide Crystal Evolution upon Aging of Lime Putty. Journal of the American Ceramic Society, 81(11):3032-34.

Rodriguez-Navarro, C., Ruiz-Agudo, E., Burgos-Cara, A., Elert, K., Hansen, E.F., 2017. Crystallization and Colloidal Stabilization of Ca(OH)2 in the Presence of Nopal Juice (Opuntia ficus indica): Implications in Architectural Heritage Conservation. Langmuir 33:10936–10950.

Rosson, B.T., Søyland, K., Boothby, T.E., 1998. Inelastic behavior of sand-lime mortar joint masonry arches. Engineering Structures 20:14–24.

Serris, E., Favergeon, L., Pijolat, M., Soustelle, M., Nortier, P., Gärtner, R.S., Chopin, T., Habib, Z., 2011. Study of the hydration of CaO powder by gas-solid reaction. Cement and Concrete Research 41:1078–1084.

Shirakawa, M.A., Beech, I.B., Tapper, R., Cincotto, M.A., Gambale, W., 2003. The development of a method to evaluate bioreceptivity of indoor mortar plastering to fungal growth. International Biodeterioration and Biodegradation 51:83–92.

Van Balen, K., 2005. Carbonation reaction of lime, kinetics at ambient temperature. Cement and Concrete Research 35:647–657.

Vance, K., Falzone, G., Pignatelli, I., Bauchy, M., Balonis, M., Sant, G., 2015. Direct Carbonation of Ca(OH)2 Using Liquid and Supercritical CO2: Implications for Carbon-Neutral Cementation. Industrial & Engineering Chemistry Research 54:8908–8918.

Witoon, T., 2011. Characterization of calcium oxide derived from waste eggshell and its application as CO2 sorbent. Ceramics International 37:3291–3298.

39th Cement and Concrete Science Conference **Paper Number 021**
9-10th September 2019
University of Bath

Insights into the Atomic Structure of Calcium Aluminate Silicate Hydrates

Aslam Kunhi Mohamed [1)], Sandra Galmarini [2)], Steve Parker [3)]., Karen Scrivener [1)], Paul Bowen[1)]

[1)]EPFL Switzerland,[2)]EMPA Dubendorf Switzerland,[3)] University of Bath, UK

aslam.kunhimohamed@epfl.ch

ABSTRACT

Calcium aluminate silicate hydrates (C-A-S-H) is the main hydration product of blended cements. Although this nanomaterial has been the subject of intense research, the atomic level structural features are not fully understood. The atomic structure of C-S-H is similar to that of 14Å tobermorite, a layered mineral. We have a good knowledge of the calcium silicate sheet structure which forms the repetitive layers in C-S-H and are separated by an interlayer space. However, the exact nature of the interlayer space and the aluminium location in C-A-S-H is still inconclusive. Here, we use a brick model, an atom level building block description of C-S-H structures, to study the interlayer structural features and the nature of the different aluminium species in C-A-S-H as observed experimentally by ^{27}Al NMR. Brick model simplifies the generation of C-S-H structure. Small chemical entities, derived from the breaking down of a 14 Å tobermorite unit cell, are arranged in three-dimensional space to create a variety of defective tobermorite structural units which form the building blocks of C-S-H. In this work, we show some of the intricate calcium-water relationship in the interlayer space and the extension of the brick model to incorporate aluminium in C-S-H resulting in C-A-S-H structures
.

1. INTRODUCTION

Blended cements are widely used in the construction industry for over three decades[1]. These cements are generally rich in aluminium and leads to the incorporation of aluminium in the main hydration product, calcium silicate hydrates (C-S-H), to form calcium aluminate silicate hydrates (C-A-S-H) [1]. C-S-H or C-A-S-H is a disordered nano material with some degree of crystallinity with its atomic-level structure [2] similar to that of 14 Å tobermorite, a natural mineral. C-S-H is thus considered as a defective tobermorite structure and is generally created by depolymerizing silicon chains and/or by the addition of calcium in the interlayer space to match the Ca/Si ratio. In short, C-S-H has a layered structure with a main calcium oxide layer flanked on both sides by linear silicate chains and this calcium silicate layers are separated by an interlayer space containing water molecules, hydroxyl ions and calcium ions.

To systematically study the different structural features of C-S-H at the atomic level, Kunhi Mohamed et al.[3] proposed a brick model, an atom level building block description of C-S-H structures. In this model, a 14 Å tobermorite unit cell is broken down into small chemical molecular or atomic entities. These entities when arranged in three-dimensional space can create a variety of defective tobermorite structural units which then form the building blocks of C-S-H. The advantage of this method over the existing random generation of defects to create C-S-H structure[4–6] is that we can have a precise knowledge over the type of defects in each structural unit. A methodological study on the stabilities of these structural units were carried out through a combination of density functional theory calculations and classical molecular dynamics simulations. Thus allowing precise control over the type of chemical units that can be considered to make C-S-H structures.

Kumar et al.[2] constructed a variety of structural units using the brick model and calculated the NMR chemical shifts of the relaxed units using first principles. It was observed that only those structural units with a calcium bridging the silicate tetrahedra units induced a strong hydrogen bonding close to a terminal silicate tetrahedra, thus explaining the origin of the observed strong hydrogen bonding close to the terminal silicate species in synthetic C-S-H from Dynamic Nuclear Polarization (DNP) NMR. The authors concluded that this calcium at the bridging site is a characteristic feature of high Ca/Si ratio C-S-H. Thus, the brick model in combination with experimental results was proved to be a good tool to unravel the complex atomic structure of C-S-H.

From the work of Kumar et al. [2] and other ^{29}Si NMR studies[7–10], the structure of the main layer of C-S-H is mostly understood. However, due to the disordered nature of the interlayer space, the exact nature and location of the interlayer species is

largely unknown. In this work, using the brick model approach we try to look at the structure of the interlayer species.

We also show the extension of the brick model to incorporate aluminium in C-S-H at the atomic scale. Aluminium exists in four, five and six-fold coordination geometries in C-A-S-H [9,11–13] as observed by ^{27}Al NMR experiments. The tetra coordinated aluminium is shown to be located at the bridging site of the silicate chain [14]. The penta-coordinated aluminium is speculated to be in the interlayer space. The six-fold coordinated aluminium is however thought to exist as a different phase, 'third aluminate hydrate' (TAH) phase, in close proximity to C-A-S-H [15]. We use a combination of density functional theory calculation and classical molecular dynamics simulations in this work.

2. RESULTS

A variety of structural units with different interlayer species were studied using classical molecular dynamics simulations and key insights into the intricate relationship between the interlayer calcium atoms and water molecules were studied. We were able to identify different types of water molecules in the interlayer space. I will be discussing more detailed results in the conference.

In figure 1, a C-A-S-H structural unit with aluminium in four-fold coordination generated with the brick model[16] is shown. The positions of the atoms are optimized with a variable cell calculation in Quantum Espresso[17]. We calculated an NMR chemical shift of 70 ppm for the aluminium in Figure 1 using the GIPAW [19] method and is in agreement with the ^{27}Al NMR chemical shifts for four coordinated aluminum species in C-A-S-H [20].

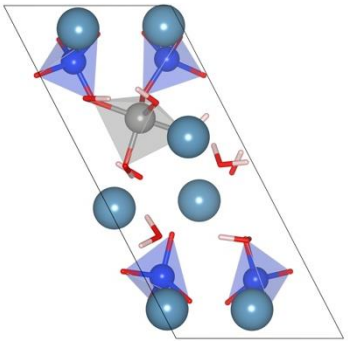

Figure 1. C-A-S-H structural unit with aluminium in four-fold coordination geometry and with a stoichiometric formula of $(\boldsymbol{CaO})_{\mathbf{1.75}}(\boldsymbol{Al_2O_3})_{\mathbf{0.25}}(\boldsymbol{SiO_2})(\boldsymbol{H_2O})_{\mathbf{1.63}}$. Atomic color codes are Al:grey, Ca:turquoise, H:white, O:red, Si:blue

A bulk structure with a stoichiometric formula of $(CaO)_{1.7}(Al_2O_3)_{0.05}SiO_2(H_2O)_{1.9}$ generated with the brick model is shown in figure 2. This structure is relaxed with classical molecular dynamics simulation using CementFFv2 force field [21]. The stoichiometry and the silicate speciation are similar to that observed by Dai et al. [22] for C-A-S-H in a 28 days hydrated white Portland cement.

We have also been able to calculate the relative energies of the structural units with new insights into the location of aluminium in C-A-S-H which will be the subject of future publications.

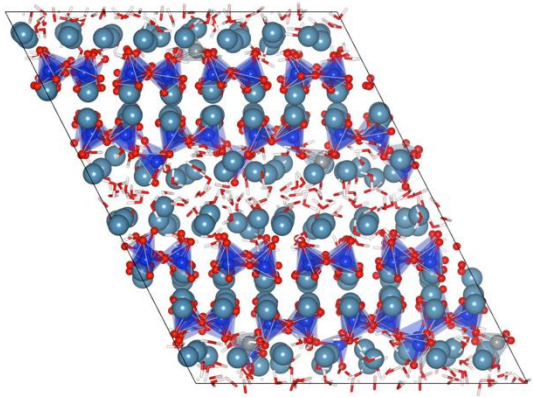

Figure 2. Bulk C-A-S-H structure. Atomic color codes are Al:grey, Ca:turquoise, H:white, O:red, Si:blue

REFERENCES

(1) Lothenbach, B.; Scrivener, K.; Hooton, R. D. Supplementary Cementitious Materials. *Cem. Concr. Res.* **2011**, *41* (12), 1244–1256.

(2) Kumar, A.; Walder, B. J.; Kunhi Mohamed, A.; Hofstetter, A.; Srinivasan, B.; Rossini, A. J.; Scrivener, K.; Emsley, L.; Bowen, P. The Atomic-Level Structure of Cementitious Calcium Silicate Hydrate. *J. Phys. Chem. C* **2017**, *121* (32), 17188–17196.

(3) Kunhi Mohamed, A.; Parker, S. C.; Bowen, P.; Galmarini, S. An Atomistic Building Block Description of C-S-H - Towards a Realistic C-S-H Model. *Cem. Concr. Res.* **2018**, *107*, 221–235.

(4) Pellenq, R. J.-M. M.; Kushima, A.; Shahsavari, R.; Van Vliet, K. J.; Buehler, M. J.; Yip, S.; Ulm, F.-J. J. A Realistic Molecular Model of Cement Hydrates. *Proc. Natl. Acad. Sci.* **2009**, *106* (38), 16102–16107.

(5) Abdolhosseini Qomi, M. J.; Krakowiak, K. J.; Bauchy, M.; Stewart, K. L.; Shahsavari, R.; Jagannathan, D.; Brommer, D. B.; Baronnet, a; Buehler, M. J.; Yip, S.; et al. Combinatorial Molecular Optimization of Cement Hydrates. *Nat. Commun.* **2014**, *5*, 4960.

(6) Kovačević, G.; Persson, B.; Nicoleau, L.; Nonat, A.; Veryazov, V. Atomistic Modeling of Crystal Structure of Ca1.67SiHx. *Cem. Concr. Res.* **2015**, *67*, 197–203.

(7) Brunet, F.; Bertani, P.; Charpentier, T.; Nonat, A.; Virlet, J. Application of 29Si Homonuclear and 1H−29Si Heteronuclear NMR Correlation to Structural Studies of Calcium Silicate Hydrates. *J. Phys. Chem. B* **2004**, *108* (40), 15494–15502.

(8) Cong, X.; Kirkpatrick, R. J. 29Si MAS NMR Study of the Structure of Calcium Silicate Hydrate. *Adv. Cem. Based Mater.* **1996**, *3* (3–4), 144–156.
(9) Renaudin, G.; Russias, J.; Leroux, F.; Caudit-Coumes, C.; Frizon, F. Structural Characterization of C-S-H and C-A-S-H Samples-Part II: Local Environment Investigated by Spectroscopic Analyses. *J. Solid State Chem.* **2009**, *182* (12), 3320–3329.
(10) Pustovgar, E.; Sangodkar, R. P.; Andreev, A. S.; Palacios, M.; Chmelka, B. F.; Flatt, R. J.; d'Espinose de Lacaillerie, J.-B. Understanding Silicate Hydration from Quantitative Analyses of Hydrating Tricalcium Silicates. *Nat. Commun.* **2016**, *7*, 10952.
(11) Andersen, M. D.; Jakobsen, H. J.; Skibsted, J. Incorporation of Aluminum in the Calcium Silicate Hydrate (C−S−H) of Hydrated Portland Cements: A High-Field 27 Al and 29 Si MAS NMR Investigation. *Inorg. Chem.* **2003**, *42* (7), 2280–2287.
(12) Sun, G. K.; Young, J. F.; Kirkpatrick, R. J. The Role of Al in C-S-H: NMR, XRD, and Compositional Results for Precipitated Samples. *Cem. Concr. Res.* **2006**, *36* (1), 18–29.
(13) L'Hôpital, E.; Lothenbach, B.; Le Saout, G.; Kulik, D.; Scrivener, K. Incorporation of Aluminium in Calcium-Silicate-Hydrates. *Cem. Concr. Res.* **2015**, *75*, 91–103.
(14) Pegado, L.; Labbez, C.; Churakov, S. V. Mechanism of Aluminium Incorporation into C–S–H from Ab Initio Calculations. *J. Mater. Chem. A* **2014**, *2* (10), 3477.
(15) Andersen, M. D.; Jakobsen, H. J.; Skibsted, J. A New Aluminium-Hydrate Species in Hydrated Portland Cements Characterized By27Al And29Si MAS NMR Spectroscopy. *Cem. Concr. Res.* **2006**, *36* (1), 3–17.
(16) Kunhi Mohamed, A.; Parker, S. C.; Bowen, P.; Galmarini, S. An Atomistic Building Block Description of C-S-H - Towards a Realistic C-S-H Model. *Cem. Concr. Res.* **2018**, *107* (March 2017), 221–235.
(17) Giannozzi, P.; Baroni, S.; Bonini, N.; Calandra, M.; Car, R.; Cavazzoni, C.; Ceresoli, D.; Chiarotti, G. L.; Cococcioni, M.; Dabo, I.; et al. QUANTUM ESPRESSO: A Modular and Open-Source Software Project for Quantum Simulations of Materials. *J. Phys. Condens. Matter* **2009**, *21* (39).
(18) Grimme, S. Semiempirical {GGA}-Type Density Functional Constructed with a Long-Range Dispersion Correction. *J. Comput. Chem.* **2006**, *27* (15), 1787–1799.
(19) Yates, J. R.; Pickard, C. J.; Mauri, F. Calculation of NMR Chemical Shifts for Extended Systems Using Ultrasoft Pseudopotentials. *Phys. Rev. B* **2007**, *76* (2), 024401.
(20) Faucon, P.; Delagrave, A.; Richet, C.; Marchand, J. M.; Zanni, H. Aluminum Incorporation in Calcium Silicate Hydrates (C−S−H) Depending on Their Ca/Si Ratio. *J. Phys. Chem. B* **1999**, *103* (37), 7796–7802.
(21) Kunhi Mohamed, A. Atomistic Simulations of The Structure of Calcium Silicate Hydrates: Interlayer Positions, Water Content And A General Structural Brick Model. **2018**.
(22) Dai, Z.; Tran, T. T.; Skibsted, J. Aluminum Incorporation in the C-S-H Phase of White Portland Cement-Metakaolin Blends Studied by 27 Al and 29 Si MAS NMR Spectroscopy. *J. Am. Ceram. Soc.* **2014**, *97* (8), 2662–2671.

39th Cement and Concrete Science Conference
9-10th September 2019
University of Bath

Paper Number 022

Cellulose-cement carbonation

Gonzalo Mármol*, Holmer Savastano Jr
Research Nucleus on Materials for Biosystems, Department of Biosystems Engineering
University of Sao Paulo, Pirassununga, SP Brazil
*Corresponding author – gonzalo.marmol@usp.br

ABSTRACT

This work is an overview regarding the addition of lignocellulose material in aqueous suspensions on cement-based products to be subjected to accelerated carbonation curing conditions. Cellulose in the form of pulp may be added properly dispersed in water to improve tensile properties of cementitious products. In addition to the better tensile behavior, the addition of cellulose yields products with higher porosity due to the hygroscopic nature of cellulose as well as durability issues related to chemical degradation and dimensional instability. The cement carbonation, in which $Ca(OH)_2$ turns into $CaCO_3$, leads to a reduced permeability of this type of materials along with an improvement of the durability of the product. Thus, accelerated carbonation curing conditions facilitate the encapsulation of CO_2 -$CaCO_3$ content is increased in approximately 30% by mass-, while enables the addition of cellulose elements in cementitious materials with no deleterious effects over time. Moreover, cementitious materials with up to 10% by mass of cellulose exhibit better flexural performance – flexural strength and fracture toughness are increased by 50% and 700% respectively- compared to plain cement pastes. At the same time, cellulose favors the cement carbonation, assuring the optimal porosity and humidity conditions, as well as it becomes carbon sink since cellulose is photosynthesized by plants from atmospheric CO_2. In spite of the current limitation of cellulose-cement products, this technology presents a great potential to face the environmental challenges by the production of reduced carbon footprint materials with attractive mechanical and physical characteristics.

Cellulose-cement carbonation

Cellulose fibers are highly accessible worldwide from wood or annual plants, while offer numerous remarkable technical features, such as bio-degradability, economic processing and wide range of morphologies and aspect ratios [1,2]. All these attributes together with its low density, make of lignocellulosic fibers an excellent draft for reinforcing elements. Therefore, this material is commonly used in polymer composites [1], although in the recent decades it is also possible to find alternative applications, as fiber–cement products [3,4].

In cement composites, cellulose-based fibers have not attracted much interest due to some chemical incompatibilities between fiber and matrix. However, the urgent challenge of obtaining more energy-efficient materials makes interesting the incorporation of cellulose in building materials to reduce the carbon-footprint. On one side, cellulose itself is synthetized by plants from atmospheric CO_2, so the partial replacement of Portland cement by cellulose tissues introduces a more favorable CO_2 balance in the material. On the other side, part of the CO_2 emissions consequence of Portland cement production can be reincorporated into the cementitious materials because of carbonation reactions. Simultaneously, this carbonation reaction enables a better environment for cellulosic fibers, so chemical incompatibility between high-alkaline Portland cement matrices and cellulose-based fibers is solved (Figure 1).

This article addresses the addition of cellulose in cement elements and the evolution of the different techniques used to make this type of material viable. Initially, the advantages of using cellulose as a reinforcement material in cement composites are shown. The different disadvantages involved in the use of cellulose in cement matrices are also addressed. Finally, it deals with different solutions to solve the problems of incompatibility between cellulose and cement, focusing on the curing of cellulose- cement systems when they are exposed to environments with high CO_2 concentrations.

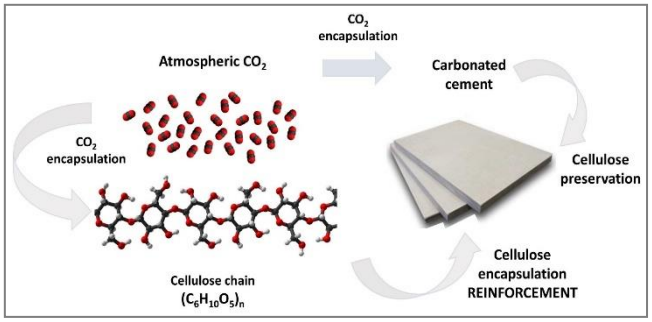

Figure 1- Schematic representation of the CO_2 capture in cement products by the addition of cellulose and carbonation reactions.

Cellulose features in cementitious materials

In order to be properly dispersed in water and, thus, contribute to obtain a composite material with better tensile properties, cellulose fibers require an optimal geometry and volume fraction [5,6]. After dispersion in water and mixing with cement, cellulose introduces additional water content during cement setting due to its hygroscopic nature [7,8]. Thus, cellulose fibers release the initial uptaken water because of the hydration heat of the cement paste in which fibers are embedded, which leads to binders that are more porous after cement hydration. In spite of having a greater porosity, this less dense material presents both further increased specific tensile strength and toughness [5]. In other words, when cellulose is properly added to cement paste, the result is a lighter, stronger and tougher material after hydration (Figure 2).

Cellulose drawback in alkali environments

The addition of cellulose to cement pastes is long ago related to several inconveniences that traditionally have denied its use [6,9]. The main disadvantage of adding cellulose to cement has been the high alkalinity of pore water in cementitious matrices (pH>12.5) [10,11]. In pore water suspensions, this desired alkalinity to avoid steel corrosion in reinforced concrete structures is attributed to the dissolved Ca(OH)2, which is widely agreed to be responsible for cellulose-based elements degradation [12,13]. Every amorphous lignocellulose fraction is susceptible to be hydrolyzed under very alkaline environments. Consequently, cellulose degree of polymerization is decreased over time, as well as the benefits of its use as addition in cementitious materials. Moreover, fiber embrittlement also takes place because of the presence of Ca(OH)2, which reduces the fiber reinforcing capacity.

Cellulose hygroscopy and dimensional variation

Another critical point for preventing the cellulose use in hydraulic binders is the hygroscopic nature of cellulose fibers itself [7]. This capacity of absorbing water in humid environments and releasing it back under dry conditions is responsible for excessive shrinking-expansion episodes. Besides the shortcoming of overall dimensional instability, the cellulose-cement interface (Figure 2) is also negatively affected by the cellulose hygroscopic character [14].

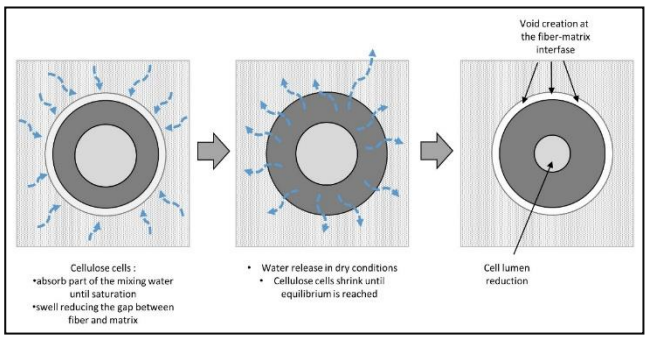

Figure 2- Schematic water movement inside a cement matrix induced by the hygroscopic behavior of cellulose fibers.

Cellulose hygroscopy and interface

The capacity of cement materials to resist tensile loads is very low, so catastrophic cracking events take place easily. At this point, cellulose elements act as bridging agent to avoid cracking spread and final material collapse along with a contribution to increase of tensile strength. This reinforcing mechanism is attributed to a combination of physical-chemical phenomena that happen in the cellulose-cement interface [15]. Cellulosic fiber shrinkage breaks the hydrogen bonding between the cellulose hydroxyl groups and alkaline anions from cement and diminishes the physical adherence between fiber and cement. In addition, the modification of the cellulose-cement interface is boosted due to the extra porosity induced by the initial extra water introduced to the system [11,16]. The greater porosity promotes the great water release to the environment and, therefore, the reinforcing capacity of cellulose fibers is further reduced [16].

In view of these circumstances, carbonation becomes a tailored technical solution to take advantage of cellulose addition in cementitious materials in order to achieve more valuable and, at the same time, sustainable materials.

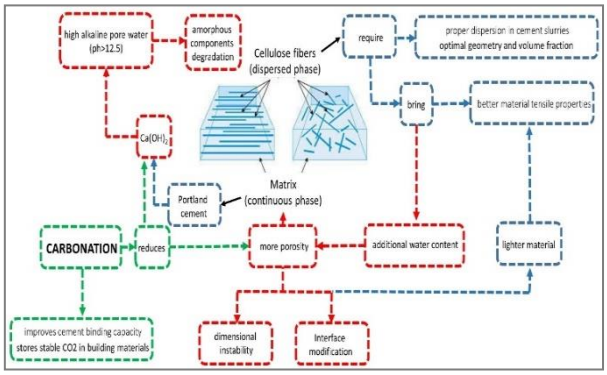

Figure 3- Flowchart of the different features in carbonated cellulose-cement systems. In blue, the features of the fiber-cement components; in red, the inconveniences of this type of material; in green, the effect of carbonation on the system.

The origin of cellulose in precast building materials

The addition of cellulose to hydraulic binders is far from being an innovative concept. An example of a well established building material that uses cellulose in its composition is drywall [17,18]. This composite material made of a calcium sulfate dihydrate (gypsum) binder and cellulose additives, which is used as a building material with reduced exposure to humid environments. This building material takes advantage of the good compressive strength of gypsum with the good bending moment resistance given by cellulose. However, drywall is extremely vulnerable in high humidity conditions due to the intrinsic properties of the materials used for its manufacture: gypsum and cellulose that are

very soluble in aqueous suspensions and prone to absorb water respectively [19]. Accordingly, drywall is not applied for structural purposes since leaching and mold processes are likely to occur and lead to the material collapse.

Fiber-cement industry, another use of cellulose

A singular example of the use of cellulose in cementitious materials is fiber-cement products. Replacing gypsum by cement as binder matrix, the problems found in drywall were solved. In this case, cellulose pulp was used as an additive to improve the rheology of water-cement suspensions [9]. The most employed technique for fiber-cement production is the Hatschek process, which consists in a dewatering-pressing technique for molding thin cementitious elements. The Hatschek process involves a much-diluted slurry, with a water to cement ratio up to 5, that is later removed by filtration in rotatory sieves, Figure 4 [6]. The fiber-cement slurry is transferred to rotatory wire sieves in which solid particles are retained and excess of water is removed until a water to binder ratio of 0.3 is reached [16]. From the sieves, the material is conveyed on a felt where several layers of filtered materials are stacked until the desired thickness and, immediately after, compaction through a forming roller takes place (Figure 4).

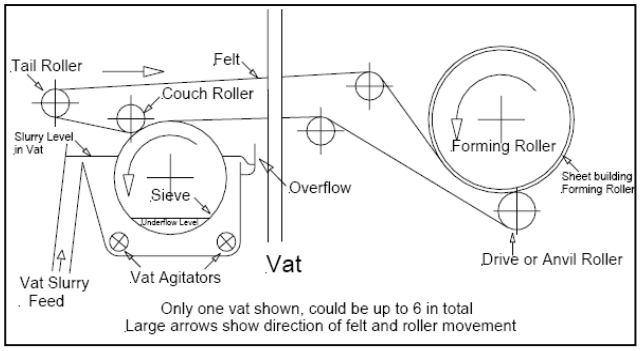

Figure 4- Schematic representation of the most common fiber-cement production process: Hatschek technique. Source: http://www.freepatentsonline.com

Traditionally, fiber-cement industry used asbestos fibers in its formulations, but nowadays synthetic polymer fibers are used, which have little interaction with free ions in cement aqueous suspensions [20–22]. Since synthetic polymer fibers are expensive, they are only dosed to improve the mechanical performance of fiber-cement products and cellulose is added (up to 3% w.t.) to aid with the flocculation process of the cement slurries and improve the water drainage [23]. Cellulose, in combination of polyacrylamide flocculants, forms large fiber-cement flocs that help to reduce flowability and retain fine particles during the product dewatering. The addition of refined cellulose pulp made possible the transition from asbestos-cement products to fiber-cement asbestos-free elements.

Papermaking production resembling

The Hatschek technology for fiber-cement production is an adaptation of the papermaking process. During the production process, fiber-cement and paper are initially diluted in water and later dewatered to obtain very thin sheets [6]. The main difference between these two materials is that fiber-cement is mainly made of cement that confers a rigid behavior to the material, while paper is a net of interconnected cellulose fibers that make the product highly flexible. So far, fiber-cement has been mainly used in non-structural elements, such as siding and roofing products. Because of the thin shape of the material and the non-structural application, most of the resisted loads come from bending loads.

Improved flexural properties of cementitious products

In case of higher flexural strength demand, it is possible to increase the amount of cellulose content to increase the reinforcing contribution of cellulose fibers. This technical solution began to attract research attention in the 80's, when sheet products with Portland cement matrices were only reinforced with cellulose pulp [6,9,24].

In fiber-cement products made of plain Portland cement with no mineral additions, it is possible to increase flexural strength by around 200% by adding around 8-12% w.t. of cellulose-based fibers [25]. The increased flexural strength favored by the addition of cellulose fibers also leads to an increase of porosity. For greater cellulose contents, the porosity in the structure of the material exceeds the reinforcing capacity of cellulose and material becomes less resistant.

In spite of the increased flexural strength when cellulose is added to cement, the greatest advantage of using this type of reinforcement is the outstanding flexural fracture toughness that can be increased by 700% when compared to unreinforced cement matrices [25]. Ultimately, cellulose makes thin cementitious sheets more resistant for applications where bending loads are applied. Nevertheless, several drawbacks have to be considered to make this technical solution feasible.

Table 1- Flexural and physical properties of fiber-cement products with different types of cellulose resources - P. radiata (PR) and Sisal (S))- and contents by mass – 4, 8 and 12% [25].

Fiber-content (%w/w)	Flexural strength (MPa) 28 days	42 days	Fracture ($kJ \cdot m^{-2}$) 28 days
0	11.8 ± 3.7	12.9 ± 2.5	0.04 ± 0.01
PR-4	19.2 ± 1.9	19.9 ± 1.7	0.64 ± 0.09
PR-8	23.5 ± 0.8	24.3 ± 1.4	1.32 ± 0.11
PR-12	25.0 ± 2.1	26.0 ± 1.5	1.93 ± 0.42
S-4	16.5 ± 0.6	16.5 ± 1.3	0.39 ± 0.06
S-8	21.5 ± 1.6	20.7 ± 1.6	0.92 ± 0.13
S-12	20.3 ± 1.4	19.4 ± 2.0	1.41 ± 0.20

Fiber-content (%w/w)	Water absorption (%w/w)	Density ($g \cdot cm^{-3}$)	Permeable void volume (%v/v)
0	10.7 ± 0.5	2.18 ± 0.03	23.4 ± 0.8
PR-4	18.5 ± 0.5	1.69 ± 0.02	31.1 ± 0.5
PR-8	22.3 ± 0.5	1.69 ± 0.03	34.3 ± 0.5
PR-12	24.4 ± 0.6	1.69 ± 0.04	35.6 ± 0.3
S-4	17.9 ± 0.3	1.69 ± 0.05	30.5 ± 0.5
S-8	19.9 ± 0.7	1.69 ± 0.06	30.7 ± 0.8
S-12	19.9 ± 0.8	1.69 ± 0.07	33.2 ± 1.2

Limitations, fiber degradation and dimensional instability

Around the time that cellulose became a possible addition to cementitious materials, it was found that these materials underwent significant degradation processes that limited their long-term performance, dimensional instability of the products due to cellulose hygroscopy and reduction of mechanical performance associated to fiber degradation [6]. Vegetal fibers with high content in cellulose may reach up to 80% w.t. in cellulose [12,16]. The rest of the mass fraction is mainly hemicellulose and lignin, which are amorphous and, therefore, very susceptible to alkaline attack. This alkaline attack reduces the reinforcing efficiency of these fibers.

A vegetal fiber microstructure is composed of a bundle of fibrils (60-100) which walls are mainly made of cellulose (Figure 5). These fibrils are bonded by other polymeric compounds (lignin and hemicellulose mainly) that present a reduced crystallinity and undergo alkaline hydrolysis that causes fibril detachment (zone pointed with yellow arrows in Figure 5b). Figure 5d clearly displays how hemicellulose filaments are torn apart and cellulose microfibrils are isolated. The result of a long exposure of cellulose-based fibers to cementitious environments (Figure 5c) leads to a fiber defragmentation that drastically reduces the mechanical capacity of these fibers. In addition Figure 5c shows a clear mineralization of the fibers that present deposition of hydration products at the fiber lumen and interface.

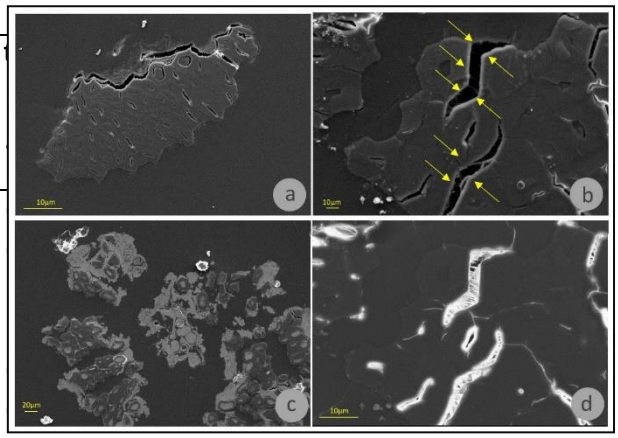

Figure 5- Backscattered secondary electrons SEM micrographs of a single sisal fiber (a), sisal fiber embedded in Portland cement for 5 months (b), sisal fiber embedded in Portland cement after 400 cycles of soaking-drying cycles (c) and SEM images of sisal fiber embedded in Portland cement for 5 months (d) [26].

It is possible to obtain cellulose fibrils through a pulping process after which cellulose pulp fibers present a reduced geometry, with a length of 0.5-2.5 mm and a width of around 10-40 μm, and a higher content in cellulose, around 90-93% of the total mass in the case of bleached pulp [5,27,28]. In the case of cellulose pulp, amorphous components of the vegetal fibers are removed. Therefore, cellulose pulp is more resistant to alkali attack and can be effectively used in cement products. However, it has been widely reported that the long exposure of cellulose pulp to the alkaline environment of hydrated Portland cement leads to a loss of the fiber reinforcing capacity and, consequently, to a loss of the fiber-cement mechanical properties [10–13]. A possible way to mitigate this degradation process is fiber treatment to avoid the fiber contact with alkaline water, though it is expensive and sometimes is far from effective [29–31].

Tailored solutions to improve cellulose-cement compatibility

Solutions to decrease pH

The most used technique to sort the degradation problem out has been the reduction of $Ca(OH)_2$ content present in the cement matrix [28,32–36]. Thus, the use of pozzolans as supplementary cementitious materials succeeded in this purpose, albeit this reaction it is not immediate and fibers are in contact with alkaline water in the meantime. Likewise, expansive reactions in hardened cements can take advantage of the excessive porosity introduced by cellulose when it is mixed with water. Thus, it was possible to replace up to 50% by mass of cement by gypsum and 35% by fly ash to produce fiber-cement products with reduced alkalinity with no deleterious effects over time [33,37]. Fiber

degradation was avoided by reducing pH of pore aqueous solutions from 12.8 to values under 11. Using this type of binders was proved that, reducing $Ca(OH)_2$ by the reaction with fly ash and gypsum to form calcium silicate hydrates (C-S-H) and calcium sulfate aluminates (AFt and AFm), cellulose degradation was avoided with no adverse side effects related to expensive reactions of later formation of ettringite [37].

Total replacement of Portland cement by clinker-free cements

A successful case to preserve cellulose from alkali degradation is the use of magnesium-based cements. The reduced alkalinity of this type of cement compared to Portland cement avoids fiber degradation and improves the long-term performance of fiber-cement products. Since Magnesium Oxychloride and Magnesium Oxysulfate cements present leaching problems under wet conditions [38], as happens for drywall elements, $MgO\text{-}SiO_2$ systems were reinforced with cellulose pulp (Figure 6). The result after using this cement was the preservation of all the fracture toughness after ageing and this toughness conservation was accompanied by an increase of flexural strength [39,40].

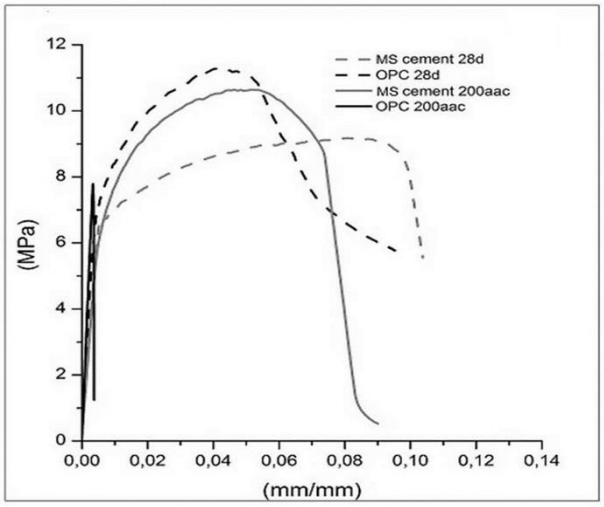

Figure 6- Flexural strength/specific deflection curves for fiber-cement products reinforced with bleached eucalyptus fibers for 4 point bending tests. In black samples with Portland cement matrices and in grey samples with $MgO\text{-}SiO_2$ matrices. Straight lines display curves at 28 days of age and dashed lines display curves after 200 cycles of soaking-drying cycles [40].

Thus, stronger and tougher materials were achieved using $MgO\text{-}SiO_2$ cement after ageing compared to Portland fiber-cement. At this stage it is noteworthy that, since $MgO\text{-}SiO_2$ cement has a higher water demand, this binder system is greatly benefitted by the extra water available provided due to the presence of cellulose. Although these cellulose-cement products are very porous at the early hydration stages, hydration takes place over time, which leads to a less porous and more rigid materials.

Carbonation as a solution to degradation and dimensional instability problems

Carbonation of cellulose-cement materials has also been reported from the beginning of cellulose reinforced cementitious materials development, where CO_2 rich environments were considered beforehand as an ageing treatment [6]. Despite the lack of understanding of this phenomenon in those initial experiments, it was noted that cellulose-cement products cured under rich CO_2 conditions presented an improved performance. The beneficial effects of carbonation arise from the transformation of $Ca(OH)_2$ into $CaCO_3$. This mechanism begins with the diffusion of CO_2 from the environment through unsaturated pores of cementitious materials (Figure 7). Inside the pores, CO_2 dissolves in water to form carbonic acid (H_2CO_3), which is dissociated ion HCO_3^- and CO_3^{2-}. Concurrently, CH is dissolved in Ca^{2+} and OH^- that react with carbonates ions to precipitate the final $CaCO_3$ polymorphs [41].

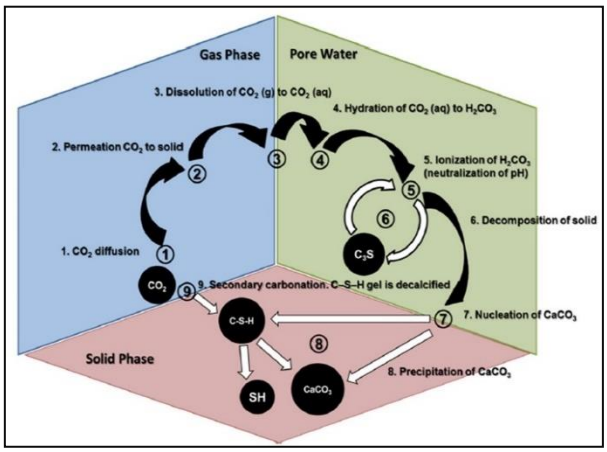

Figure 7- Diagram with principal mechanisms for accelerated carbonation in Portland cement [41].

Steps to improvement of fiber-cement products through carbonation

Fiber-cement products with 77 % of Portland cement and 10% of cellulose pulp by dry mass, when subjected for 2 days to CO_2 saturated environment at 60oC and 90% RH, exhibited better mechanical properties compared to specimens cured at atmospheric CO_2 concentration [42]. The most important outcome of this experiment was the difference observed between the samples after ageing. Non-carbonated samples after ageing displayed a flexural modulus of rupture of 4 MPa, while carbonated samples remain with values of 19 MPa. In addition, samples submitted to carbonation displayed a decrease in average pore diameter in between 26 and 51% for the different ageing conditions studied.

Similar effects were found when cellulose fiber reinforced cement was submitted to supercritical carbonation, this is to conditions where pressure and temperature allow CO_2 to behave like a dense gas solving agent with no surface tension, which permits its diffusion through very fine pores [41]. This type of carbonation procedure was applied to extruded cellulose-cement materials to assure enough CO_2 diffusion, since these materials present a lower pore size distribution. In both cases, carbonation was effective to reduce the CH content present in the binder matrix. In accordance to that, $CaCO_3$ was precipitated, which results into a fiber protection against alkaline degradation along with a refinement of the microstructure of the binder matrix. Thereby, water absorption was reduced as a very beneficial side effect.

Table 2- Variation (by %) of the mechanical properties, $Ca(OH)_2$ content and physical properties of fiber-cement products after carbonation based on different literature results.

	Mechanical properties				Ca(OH)2 reduction		Physical properties			
	MOR		Toughness				Bulk density		Water absorption	
Ref.	Non-aged	Aged	Non-aged	Aged	Non-aged	Aged	Non-aged	Aged	Non-aged	Aged
[41]	16,1	11,2	-9,4	55,9	16,7	32,6	4,9	9,5	-5,7	-6,5
[42]	116,9	353,7	22,2	625,0	71,8	71,8	12,5	13,5	-10,4	-8,4
[21]	**	**	**		100	100	12,6	**	-12,7	**

This fact was confirmed in a later research conducted on fiber-cement from industrial production [43]. Samples submitted to carbonation for 10h in a CO_2 concentration of 15% presented a significant improved dimensional stability. Tests performed to evaluate the drying shrinkage of these fiber-cement products revealed that carbonated samples present 4 times lower dimensional variation values. With these experiences, in essence, cellulose-cement carbonation was proved to be effective against fiber degradation and dimensional variability. Nevertheless, one more aspect remained unveiled to properly understand and govern this technology: fracture mechanism.

Carbonation effect on the interface between cellulose elements and hydrated cement

Cellulose plays a key role during the hydration and carbonation processes of cellulose fiber reinforced cement. A region with higher water content is generated at the interface after cellulose releases water to the cement matrix. For non-carbonated fiber-cement, this region is richer in $Ca(OH)_2$ since this water adsorption of fiber surface promotes the constant dissolution of Ca^{2+} and OH^- and later precipitation of Portlandite [13]. $Ca(OH)_2$ crystals are considered as one of the weakest compounds derived from Portland cement hydration [44], so the fiber-matrix interface can be considered as a weak region in these materials. In Figure 8, non-carbonated fiber-cement regions of low density (1) around the cellulose present a very cracked structure compared to carbonated samples, where the interface shows a denser structure (2).

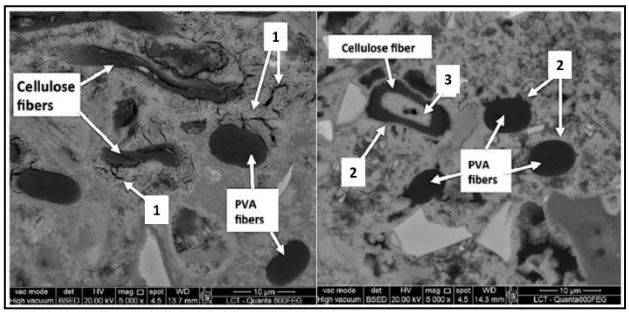

Figure 8- SEM micrographs of polished fiber-cement surfaces (left) non-carbonated and (right) carbonated [21]. 1 indicates regions of the matrix with low density around cellulose fibers, 2 points to higher density regions of the matrix after carbonation and 3 points to crystals inside the cellulose fiber lumen.

However, lower density regions cannot be considered as a completely undesired situation since weaker hydration products around cellulose promote a fracture mechanism in which pullout is favored instead of reinforcement breakage. Pullout fracture is fundamental to experience larger deformations before material collapses and, therefore, it has to be ensured. In addition, when the excess water is evaporated, the surroundings of the fiber become a region with a greater porosity that drives the CO_2 diffusion through the material (Figure 9b). The combined effect of greater porosity to allow the CO_2 inlet and the higher concentration of $Ca(OH)_2$ makes the fiber-matrix interface an optimal region for $CaCO_3$ precipitation [43] (Figure 9c). The immediate consequence of this $CaCO_3$ precipitation is the refinement of the voids with bigger and denser particles (Figure 9d).

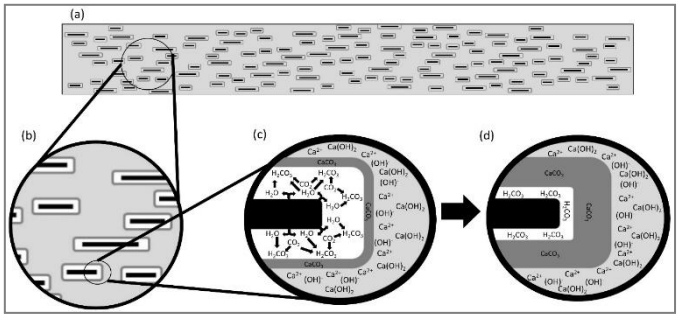

Figure 9- Schematic representation of carbonation process at the fiber-matrix interface.

Thus, the cementitious matrix is stronger and presents a greater binding capacity. However, the carbonation of fiber-cement products modifies the fracture mechanism, reducing the capacity of absorbing energy of the product. Santos et al. reported this episode after submitting fiber-cement extruded samples to wetting-drying cycles, since the fracture toughness values for both carbonated and non-carbonated samples decreased around 28% and 56% respectively [41]. The conversion of the

fracture mode from fiber pull-out to fiber failure may also be associated with large stresses prior to matrix cracking due to the stronger binding capacity of carbonated compounds that leads to fiber failure before the matrix collapses [41,42].
In order to mitigate this drastic collapse, a simple fiber treatment was applied before molding cellulose-cement products: hornification [45,46]. Fiber hornification is an economic and easy way to reduce water absorption of cellulose up to 33% by soaking-drying cycles. Thus, fiber swelling is reduced in high humidity conditions, by successive wetting-drying cycles. When hornificated cellulose fiber is added in cement sheets, the fracture mechanism modification is reduced since no statistical difference in toughness was found. Although carbonation reaction is expected to convert $Ca(OH)_2$ into $CaCO_3$ in any of its polymorphs, it has to be noted that carbonation also affects other hydrated phases, such as C-S-H gels [41].
One of the consequences of C-S-H gels carbonation at high CO_2 concentration (> 10%) is the precipitation of silica gel. Once the carbonation reaction is over, silica gel remains available to react and form any other hydrated phases. In order to simulate accelerated ageing conditions, soaking-drying cycles are conventionally used, during which this secondary hydration reactions may take place. Re-hydration of cement after carbonation is deduced from the statistical difference in apparent porosity before and after soaking-drying cycles, with values of 32.0 % and 28.9 % respectively. Thus, fiber-cement suffers another refinement process related to a modification of the fiber-matrix interface along with this secondary hydration.

Cellulose nanofibers and carbonation

Nanoparticles are attracting the interest of many scientific scenarios and fiber-cement composites are a possible application for this type of materials. The use of cellulose nanofibers is particularly interesting, since this material combines the properties of cellulose fibers and nanoparticles. Besides the advantages of using cellulose fibers mentioned beforehand, these nanoparticles bid new prospects for better mechanical performance of cementitious composites. This improvement is due to the great specific surface area of nanofibers (50-70 m2/g) [47] that reduces inter-fiber spacing and promotes more interactions between cellulose and the cement system [48]. As a result, cellulose nanoparticles are a forthcoming technique to control micro-cracking and increase the strength of the composites.
However, the addition of cellulose nanofibers has also been related to a higher water retention due to the elevated specific area [49]. In regards to nanoparticles, correct dispersion in a cementitious paste and extra water demand for fresh cement workability are another concern as well [48]. All these factors related to the water absorption of cellulose nanofibers generate more porosity that decreases the binding capacity of the cement. Again, carbonation becomes an optimal solution to sort out the undesired side effects associated to an excess of porosity.

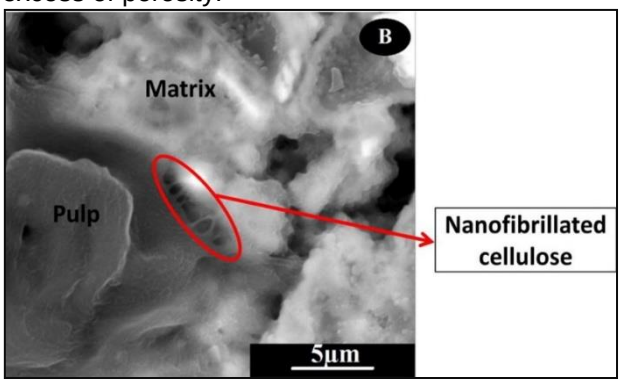

Figure 10- SEM micrograph where nanofibrillated cellulose is bridging a cellulose microfiber and a hydrated cement particle [50].

When cement-cellulose composites with different reinforcement scale, 1% by mass of cellulose nanofibers and 8% of cellulose microfibers, are submitted to high environmental CO_2 curing conditions, a bridging effect on the nano-scale is observed. This composite toughening, combined with the micro-cracking bridging of cellulose pulp, furthers the flexural modulus of the composite [50]. On the same work, an improvement of the nanofibers packing with the particles of the matrix was reported due to the high specific surface area of the nanofibrillated cellulose. Consequently, the production of hybrid composites with both nano and microfibers is arising as a promissory solution for cement-cellulose composites where carbonation is essential to improve the binder and interface properties.

Conclusions

The use of high CO_2 concentrations for curing cellulose-cement systems is a promising technique that may contribute to both mitigate dimensional instability and avoid the degradation of cellulose-based fibers in cement matrices. As happens for conventional Portland cement products, the carbonation reaction leads to stronger materials because of the cement pore refinement. The advantage of this type of materials is the extra water introduced by cellulose fibers due to their hygroscopic nature. After cement hydration is complete and under low humidity environment, cellulose fibers release the additional water, which takes place with cellulose shrinkage. As a consequence, the fiber-matrix interface becomes more porous, which favors the diffusion of CO_2 inside the matrix to later react with $Ca(OH)_2$ and later form $CaCO_3$.
It is possible to conclude that flexural strength of fiber-cement products is preserved, even increased, over time for carbonated materials in comparison with non-carbonated ones. Since an effect of the carbonation reaction is the consumption of $Ca(OH)_2$,

it is concluded that this technique avoids high-alkalinity of water in the cement pores, so lignocellulosic fibers are not deteriorated after ageing. Likewise, the reduction of $Ca(OH)_2$ content and its conversion to $CaCO_3$ are mainly produced in the surroundings of the fibers, which modifies the density of the fiber-matrix interface. Thus, the denser interface leads to lower water absorption of the materials, in addition to a better dimensional stability. One more aspect that is interesting is the addition of nanofibrillated cellulose materials. Although nanocellulose may introduce an excessive amount of water as a result of the high specific surface area, when properly dosed and dispersed, these materials play an excellent role as bridging agent at the nanoscale that makes fiber-cellulose products more rigid and with higher flexural strength. In spite of all the advantages that have been presented in this work, there is still missing a decisive characteristic that needs improvement: the modification of the fracture mechanism after carbonation. The densification of the cement matrix reduces the material toughness as original pullout fracture in non-carbonated materials is replaced by a fiber failure fracture mechanism. In this regard, fibers functionalization or the use of longer lignocellulosic fibers may contribute to sort this difficulty out.

Increasing the cellulose reinforcing volume in the system would be an additional prospect to increment the porosity of the matrix and, thus, counterbalance the densification of the interface. This solution would suppose an optimization of the different cellulose contents utilized up today since most of the fiber-cement formulations have been adjusted for non-carbonated products. Besides, an increase in the cellulose content would introduce a better thermal and acoustic performance of new fiber-cement products due to the insulating capacity of cellulose-based products. Therefore, a solution for cellulose chemical and physical stability in cement matrix may contribute for more energy-efficient cement-based materials. Taken together, the carbonation of cellulose-cement systems becomes an optimal solution to achievement of smarter materials with a reduced CO_2 footprint.

We also assume that the principles presented here for Portland cement products are valid for other types of hydraulic binders that are susceptible of being carbonated. In this sense, any clinker-free cement is also a promissory material to be reinforced and functionalized with cellulose particles.

Acknowledgments

The authors would like to thank FAPESP for funding this work under the Thematic Project #2012/51467-3 - Agroindustrial wastes and its potential use as appropriate materials for housing and infrastructures (Agrowaste), and Thematic Project FAPESP #2014/50948-3, CNPq #465593/2014-3 - Eco-efficient and advanced technologies in cement based products (aeCEM). The first author would like to thank FAPESP to the Post-doctorate grant #2018/20913-4 and the second author is grateful to CNPq grant #307723/2017-8. The participation in the 39 CCSC event is possible due to the financial support by FAPESP thru the SPRINT Program, #2018/22512-7.

References

[1] T. Huber, J. Müssig, O. Curnow, S. Pang, S. Bickerton, M.P. Staiger, A critical review of all-cellulose composites, J. Mater. Sci. 47 (2012) 1171–1186. doi:10.1007/s10853-011-5774-3.

[2] D. Klemm, B. Heublein, H.-P. Fink, A. Bohn, Cellulose: Fascinating Biopolymer and Sustainable Raw Material, Angew. Chem. Int. Ed. 44 (2005) 3358–3393. doi:10.1002/anie.200460587.

[3] H. Savastano, P.G. Warden, Special theme issue, Cem. Concr. Compos. 27 (2005) 517. doi:10.1016/j.cemconcomp.2004.09.014.

[4] V. Agopyan, H. Savastano, V.M. John, M.A. Cincotto, Developments on vegetable fibre–cement based materials in São Paulo, Brazil: an overview, Cem. Concr. Compos. 27 (2005) 527–536. doi:10.1016/j.cemconcomp.2004.09.004.

[5] G.H.D. Tonoli, H. Savastano, E. Fuente, C. Negro, A. Blanco, F.A. Rocco Lahr, Eucalyptus pulp fibres as alternative reinforcement to engineered cement-based composites, Ind. Crops Prod. 31 (2010) 225–232. doi:10.1016/j.indcrop.2009.10.009.

[6] S.A.S. Akers, J.B. Studinka, Ageing behaviour of cellulose fibre cement composites in natural weathering and accelerated tests, Int. J. Cem. Compos. Lightweight Concr. 11 (1989) 93–97. doi:10.1016/0262-5075(89)90119-X.

[7] H. O'Neill, S.V. Pingali, L. Petridis, J. He, E. Mamontov, L. Hong, V. Urban, B. Evans, P. Langan, J.C. Smith, B.H. Davison, Dynamics of water bound to crystalline cellulose, Sci. Rep. 7 (2017). doi:10.1038/s41598-017-12035-w.

[8] A. Célino, S. Fréour, F. Jacquemin, P. Casari, The hygroscopic behavior of plant fibers: a review, Front. Chem. 1 (2014). doi:10.3389/fchem.2013.00043.

[9] W.R. Sharman, Durability of fiber-concrete sheet claddings, N. Z. Concr. Constr. (1983) 3–7.

[10] B.J. Mohr, H. Nanko, K.E. Kurtis, Durability of kraft pulp fiber–cement composites to wet/dry cycling, Cem. Concr. Compos. 27 (2005) 435–448. doi:10.1016/j.cemconcomp.2004.07.006.

[11] B.J. Mohr, J.J. Biernacki, K.E. Kurtis, Microstructural and chemical effects of wet/dry cycling on pulp fiber–cement composites, Cem. Concr. Res. 36 (2006) 1240–1251. doi:10.1016/j.cemconres.2006.03.020.

[12] J. de A. Melo Filho, F. de A. Silva, R.D. Toledo Filho, Degradation kinetics and aging mechanisms on sisal fiber cement composite systems, Cem. Concr. Compos. 40 (2013) 30–39. doi:10.1016/j.cemconcomp.2013.04.003.

[13] R.D. Toledo Filho, K. Scrivener, G.L. England, K. Ghavami, Durability of alkali-sensitive sisal and coconut fibres in cement mortar composites, Cem. Concr. Compos. 22 (2000) 127–143. doi:10.1016/S0958-9465(99)00039-6.

[14] G.H.D. Tonoli, M.N. Belgacem, G. Siqueira, J. Bras, H. Savastano Jr., F.A. Rocco Lahr, Processing and dimensional changes of cement based composites reinforced with surface-treated cellulose fibres, Cem. Concr. Compos. 37 (2013) 68–75. doi:10.1016/j.cemconcomp.2012.12.004.
[15] S.F. Santos, R.S. Teixeira, H. Savastano Junior, Interfacial transition zone between lignocellulosic fiber and matrix in cement-based composites, in: Sustain. Nonconv. Constr. Mater. Using Inorg. Bond. Fiber Compos., Elsevier, 2017: pp. 27–68. http://linkinghub.elsevier.com/retrieve/pii/B9780081020012000036 (accessed August 17, 2018).
[16] H. Savastano Jr., V. Agopyan, Transition zone studies of vegetable fibre-cement paste composites, Cem. Concr. Compos. 21 (1999) 49–57. doi:10.1016/S0958-9465(98)00038-9.
[17] L. Fiorino, B. Bucciero, R. Landolfo, Evaluation of seismic dynamic behaviour of drywall partitions, façades and ceilings through shake table testing, Eng. Struct. 180 (2019) 103–123. doi:10.1016/j.engstruct.2018.11.028.
[18] T. Matsumoto, M. Uchida, H. Sugaya, H. Tachibana, Development of multiple drywall with high sound insulation performance, Appl. Acoust. 67 (2006) 595–608. doi:10.1016/j.apacoust.2005.09.005.
[19] R.I. Adams, W. Chen, K. Kumagai, J.M. Macher, M.J. Mendell, Relating measured moisture of gypsum board to estimated water activity using moisture meters, Build. Environ. 147 (2019) 284–298. doi:10.1016/j.buildenv.2018.10.030.
[20] E.M. Bezerra, A.P. Joaquim, H. Savastano, V.M. John, V. Agopyan, The effect of different mineral additions and synthetic fiber contents on properties of cement based composites, Cem. Concr. Compos. 28 (2006) 555–563. doi:10.1016/j.cemconcomp.2006.02.001.
[21] V.D. Pizzol, L.M. Mendes, L. Frezzatti, H. Savastano Jr., G.H.D. Tonoli, Effect of accelerated carbonation on the microstructure and physical properties of hybrid fiber-cement composites, Accel. Carbonation Environ. Mater. Eng. 59 (2014) 101–106. doi:10.1016/j.mineng.2013.11.007.
[22] C.M.R. Dias, H. Savastano Jr., V.M. John, Exploring the potential of functionally graded materials concept for the development of fiber cement, Inorg.-Bond. Fiber Compos. 24 (2010) 140–146. doi:10.1016/j.conbuildmat.2008.01.017.
[23] G.H.D. Tonoli, E. Fuente, C. Monte, H. Savastano, F.A.R. Lahr, A. Blanco, Effect of fibre morphology on flocculation of fibre–cement suspensions, Cem. Concr. Res. 39 (2009) 1017–1022. doi:10.1016/j.cemconres.2009.07.010.
[24] A. Bentur, S.A.S. Akers, The microstructure and ageing of cellulose fibre reinforced cement composites cured in a normal environment, Int. J. Cem. Compos. Lightweight Concr. 11 (1989) 99–109. doi:10.1016/0262-5075(89)90120-6.
[25] H. Savastano, P.. Warden, R.S.. Coutts, Brazilian waste fibres as reinforcement for cement-based composites, Cem. Concr. Compos. 22 (2000) 379–384. doi:10.1016/S0958-9465(00)00034-2.
[26] G. Mármol, A. Ribes, V. Amigó, H. Savastano, Assessment of Sisal Fiber Integrity as a Reinforcing Element in MgO-Based Cement Matrices, Waste Biomass Valorization. (2019). doi:10.1007/s12649-019-00605-0.
[27] L.Y. Mwaikambo, M.P. Ansell, Chemical modification of hemp, sisal, jute, and kapok fibers by alkalization, J. Appl. Polym. Sci. 84 (2002) 2222–2234. doi:10.1002/app.10460.
[28] L. Yan, B. Kasal, L. Huang, A review of recent research on the use of cellulosic fibres, their fibre fabric reinforced cementitious, geo-polymer and polymer composites in civil engineering, Compos. Part B Eng. 92 (2016) 94–132. doi:10.1016/j.compositesb.2016.02.002.
[29] B.N. Barra, S.F. Santos, P.V.A. Bergo, C. Alves, K. Ghavami, H. Savastano, Residual sisal fibers treated by methane cold plasma discharge for potential application in cement based material, Ind. Crops Prod. 77 (2015) 691–702. doi:10.1016/j.indcrop.2015.07.052.
[30] J. Wei, C. Meyer, Improving degradation resistance of sisal fiber in concrete through fiber surface treatment, Appl. Surf. Sci. 289 (2014) 511–523. doi:10.1016/j.apsusc.2013.11.024.
[31] F. Zhou, G. Cheng, B. Jiang, Effect of silane treatment on microstructure of sisal fibers, Appl. Surf. Sci. 292 (2014) 806–812. doi:10.1016/j.apsusc.2013.12.054.
[32] G. Mármol, H. Savastano Jr, J. Monzó, M.. Borrachero, L. Soriano, M. Bonilla, J. Payá, Low-alkaline ternary binder systems containing Portland cement, gypsum and fly ash for lignocellulosic fibers reinforced composites, Cem. Concr. Compos. (2015).
[33] G. Mármol, S.F. Santos, H. Savastano, M.V. Borrachero, J. Monzó, J. Payá, Mechanical and physical performance of low alkalinity cementitious composites reinforced with recycled cellulosic fibres pulp from cement kraft bags, Ind. Crops Prod. 49 (2013) 422–427. doi:10.1016/j.indcrop.2013.04.051.
[34] A. Hakamy, F.U.A. Shaikh, I.M. Low, Effect of calcined nanoclay on microstructural and mechanical properties of chemically treated hemp fabric-reinforced cement nanocomposites, Constr. Build. Mater. 95 (2015) 882–891. doi:10.1016/j.conbuildmat.2015.07.145.
[35] R.D. Tolêdo Filho, K. Ghavami, G.L. England, K. Scrivener, Development of vegetable fibre–mortar composites of improved durability, Cem. Concr. Compos. 25 (2003) 185–196. doi:10.1016/S0958-9465(02)00018-5.
[36] H. Savastano, P.. Warden, R.S.. Coutts, Potential of alternative fibre cements as building materials for developing areas, Cem. Concr. Compos. 25 (2003) 585–592. doi:10.1016/S0958-9465(02)00071-9.
[37] G. Mármol, H. Savastano, J.M. Monzó, M.V. Borrachero, L. Soriano, J. Payá, Portland cement, gypsum and fly ash binder systems characterization for lignocellulosic fiber-cement, Constr. Build. Mater.

124 (2016) 208–218. doi:10.1016/j.conbuildmat.2016.07.083.
[38] C.E.M. Gomes, G. Camarini, Magnesium Oxysulfate Fibercement, Key Eng. Mater. 600 (2014) 308–318. doi:10.4028/www.scientific.net/KEM.600.308.
[39] G. Mármol, H. Savastano, M.M. Tashima, J.L. Provis, Optimization of the MgOSiO2 binding system for fiber-cement production with cellulosic reinforcing elements, Mater. Des. 105 (2016) 251–261. doi:10.1016/j.matdes.2016.05.064.
[40] G. Mármol, H. Savastano, Study of the degradation of non-conventional MgO-SiO 2 cement reinforced with lignocellulosic fibers, Cem. Concr. Compos. 80 (2017) 258–267. doi:10.1016/j.cemconcomp.2017.03.015.
[41] S.F. Santos, R. Schmidt, A.E.F.S. Almeida, G.H.D. Tonoli, H. Savastano, Supercritical carbonation treatment on extruded fibre–cement reinforced with vegetable fibres, Cem. Concr. Compos. 56 (2015) 84–94. doi:10.1016/j.cemconcomp.2014.11.007.
[42] A.E.F.S. Almeida, G.H.D. Tonoli, S.F. Santos, H. Savastano Jr., Improved durability of vegetable fiber reinforced cement composite subject to accelerated carbonation at early age, Cem. Concr. Compos. 42 (2013) 49–58. doi:10.1016/j.cemconcomp.2013.05.001.
[43] G.H.D. Tonoli, V.D. Pizzol, G. Urrea, S.F. Santos, L.M. Mendes, V. Santos, V.M. John, M. Frías, H. Savastano, Rationalizing the impact of aging on fiber–matrix interface and stability of cement-based composites submitted to carbonation at early ages, J. Mater. Sci. 51 (2016) 7929–7943. doi:10.1007/s10853-016-0060-z.
[44] F.M. Lea, P.C. Hewlett, Lea's chemistry of cement and concrete, (2004).
[45] J.E.M. Ballesteros, S.F. Santos, G. Mármol, H. Savastano, J. Fiorelli, Evaluation of cellulosic pulps treated by hornification as reinforcement of cementitious composites, Constr. Build. Mater. 100 (2015) 83–90. doi:10.1016/j.conbuildmat.2015.09.044.
[46] J.E.M. Ballesteros, V. dos Santos, G. Mármol, M. Frías, J. Fiorelli, Potential of the hornification treatment on eucalyptus and pine fibers for fiber-cement applications, Cellulose. (2017). doi:10.1007/s10570-017-1253-6.
[47] K. Missoum, M. Belgacem, J. Bras, Nanofibrillated Cellulose Surface Modification: A Review, Materials. 6 (2013) 1745–1766. doi:10.3390/ma6051745.
[48] Y. Cao, P. Zavaterri, J. Youngblood, R. Moon, J. Weiss, The influence of cellulose nanocrystal additions on the performance of cement paste, Cem. Concr. Compos. 56 (2015) 73–83. doi:10.1016/j.cemconcomp.2014.11.008.
[49] V.C. Correia, S.F. Santos, H. Savastano Jr, V.M. John, Utilization of vegetable fibers for production of reinforced cementitious materials, RILEM Tech. Lett. 2 (2018) 145. doi:10.21809/rilemtechlett.2017.48.
[50] V. da Costa Correia, S.F. Santos, R. Soares Teixeira, H. Savastano Junior, Nanofibrillated cellulose and cellulosic pulp for reinforcement of the extruded cement based materials, Constr. Build. Mater. 160 (2018) 376–384. doi:10.1016/j.conbuildmat.2017.11.066.

39th Cement and Concrete Science Conference
9-10th September 2019
University of Bath
Paper Number 023

Sorptivity of mortars with sol-gel treatment

Fiona Gleed[a], Dr. Juliana Holley[a], Dr. Julie Bregulla[b], Prof. Pete Walker[a]
[a]BRE Centre for Innovative Construction Materials,
Department of Architecture and Civil Engineering, University of Bath
[b]BRE (Building Research Establishment), Watford UK

ABSTRACT

This study presents the results of a trial of silica-based sol-gel modifications for mortar, as a component of brickwork in cavity-walls. Preventing transfer of moisture in to the building is an important function of cavity-walls, with mortar specified based on exposure to wind driven rain. As exposure from meteorological events is of finite duration, reductions in the rate of absorption make a significant difference to the volume of water taken up and the depth of penetration. Silica-based sol-gel has been successfully used to enhance clay and bio-based construction materials. In this work a silica-based sol-gel derived solution was used as a bulk additive at 3% of cement content for samples of mortar. Specimens were tested for water absorption and sorptivity using established techniques and monitored during drying under controlled conditions. Microstructural characterisation included nitrogen adsorption and imaging with scanning electron microscopy. Silica-based sol-gel treatment was found to modify the pore structure of mortar, reducing the water absorption by 50% without compromising subsequent drying times.

1. INTRODUCTION

The likelihood of flooding is increasing as climate changes, with higher intensity rainfall leading to more frequent localized, surface-water flooding and downstream, fluvial flooding (Sayers et al, 2015). The number of properties at risk of flooding is also increasing because of planned development within current flood risk zones and extension of the zones due to changes to coastlines or catchments. Mitigation measures such as flood warning systems have reduced the risk to life but buildings remain as receptors when occupants evacuate. Property level flood resilience (PLFR) aims to reduce the consequences of flooding and make buildings quicker and cheaper to repair, with interventions including changes of use of rooms most likely to flood, deploying temporary barriers and retrofitting fixtures and fittings to be water resistant (Lamond et al, 2017). However, the fabric of the building is fundamental to resilience. External walls are exposed to water even where flooding is kept out of the building and the resulting moisture load not only delays refurbishment but also reduces the thermal efficiency. Materials that have lower absorption rates therefore have an important role in PLFR.

The mortars in this study were produced as part of an investigation in to improving drying times of buildings after flood inundation. Current advice on selection of materials for flood resilience is based on Escarameia et al (2007) study of domestic walls, which tested masonry panels for leakage rates, with monitoring of subsequent drying. All panels were constructed using the same mortar mix so there is no guidance on specification, beyond noting that leakage occurred at mortar joints and thin joints performed better. Testing mortar samples with varying compositions, will therefore provide novel evidence to inform specification of mortars for resilient construction.

Mortars have complex pore structures, which draw water from the surface by capillary action (Hall and Hoff, 2011). Pore structure also affects drying behaviour (Prime et al, 2015) so a modification that reduces water absorption could have a minimal or negative effect overall if it increases moisture retention. Silica-based sol-gel has been used to reduce water absorption of adobe (Calabria et al, 2010) and bio-based materials (Hussain et al, 2017) by increasing hydrophobicity of the porous structure. In this work, silica-based sol-gel as a bulk additive in cementitious materials (mortars) to explore changes in water transport properties and relate them to the modified pore structure.

2. MATERIALS

Mortar samples were prepared in the ACE laboratories at University of Bath using proportions (Table 1) based on PD 6678 (BSI, 2005, p. 8). Batches were sized at 6kg to allow testing of the fresh mortar, produce three prism specimens for strength testing at each of 7, 28 and 56 days and construct a triplet component of three bricks (Figure 1).

Table 1. Mortar proportions as mass per cubic metre of mortar after PD 6678 (BSI, 2005, p. 8)

Strength class (designation)	Masonry Cement kg	Lime kg	Sand kg	Target 28 day strength MPa
M4 (iii)	110		755	4
M4L (iii)	105	35	725	4
M6 (ii)	155		710	6

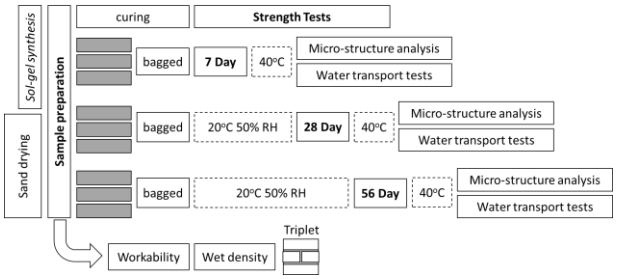

Figure 1. Preparation and testing of mortar samples.

For comparability between mixes, quantities were specified by mass using sand that had been dried and sieved prior to batching. Mortar samples included an M4 cement:lime:sand mortar (M4 L), with CL90 non-hydraulic lime. An M6 L cement:lime:sand mortar was considered but not developed as, in practice, lime is used in weaker, more flexible mixes. Each mix was prepared as a conventional sample (X) and a modified sample (B), with a silica-based sol-gel additive (Table 2).

Table 2. Mix proportions of mortars with and without additive SGB (silica-based sol-gel).

Mix	CEM II (g)	CL90 (g)	sand (g)	water (g)	SGB (g)	liquid : binder ratio
M4X	660	-	4530	1250	-	1.89
M4L	630	210	435	1140	-	1.81
M6X	930	-	426	1163	-	1.25
M4B	660	-	453	912	20	1.41
M4L	630	210	435	770	20	1.25
M6B	930	-	426	926	28	1.03

For better compatibility with cement, the sol-gel synthesis followed an alkaline protocol (SGB) using a (3-glycidyloxypropyl) trimethoxysilane precursor catalysed by a sodium hydroxide solution at room temperature. The silica-based sol-gel dose was calculated as 3% of the cement content for M4 and M6, with the sol-gel synthesis timed to allow 48 hours of curing prior to mixing.

A workable mix was used to allow comparison with mixes used in field trials. This required a liquid:binder ratio greater than the 0.5 used in standard mixes. A flow table (BSI, 1999) was used to test workability at the time of mixing as silica-based sol-gel and lime modify the behaviour of the fresh mortar.

Specimens were prepared and stored in line with the draft prEN 1015-11:2017 (BSI, 2017) allowing the modified mortars, which had a low early strength to be retained in moulds for up to three days. After demoulding, specimens were transferred to an environmentally controlled room (ECR) at 20ºC/50%RH, curing in polythene bags for the balance of 7 days (Figure 1). Specimens for testing at 28 and 56 days were then stored on wire racks in the ECR until required.

3. PHYSICAL TESTS

A set of three prisms from each sample were broken in three-point bending at 7, 28 and 56 days. The resulting half-prisms were then sprayed with phenolphthalein to indicate carbonation (1 specimen), used to determine the compressive strength (3 specimens), or preserved for water transport testing (2 specimens). Results for tests on the 28 day specimens are given in Table 3.

Table 3. Properties of mortar determined at 28 days.

Mix	28 day strength MPa	Dry Density kg/m³	Water Absorption kg m^{-2} min$^{-1/2}$	Volume fraction porosity
M4X	3.6	1630	1.56	27%
M4L	4.7	1640	1.38	26%
M6X	11.3	1720	0.89	26%
M4B	5.2	1650	0.75	20%
M4L	9.8	1730	0.46	18%
M6B	13.5	1550	0.44	16%

A modified test based on BS EN 1015-18 (BSI, 2002) was used to investigate water absorption of the mortars. Specimens were tested in groups, arranged on a wire rack to give a consistent depth of immersion, unsealed and with the formed face downwards to reflect flood exposure. Each specimen was weighed at 10, 40, 90 160 and 250 minutes (Figure 1) providing 5 data points to determine sorptivity (Hall and Hoff, 2011, p. 135) as well as water absorption,

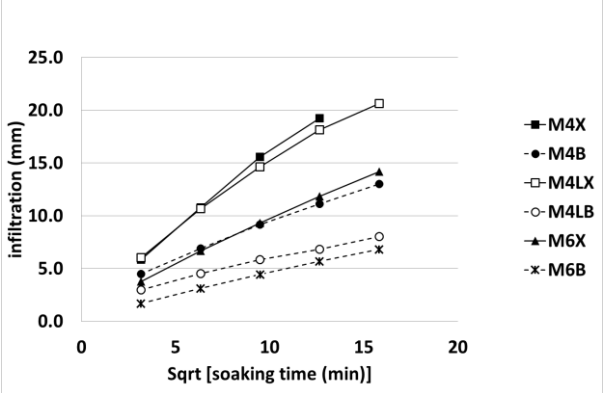

Figure 2. Sorptivity of standard (X) and silica-based sol-gel modified (B) mortars for 28 day specimens

Volume fraction porosity (Table 3) was calculated from the saturated mass at the end of the absorption test, with further immersion where infiltration continued at 24 hours. Saturated specimens were prepared for drying by capping the broken face with aluminium foil tape. The capping was positioned to leave a consistent exposed height of 70mm, with additional foil used to achieve a level base for stability during drying. Specimens were dried on wire racks in a controlled environment (20°C/50% RH) until a stable mass was recorded. Moisture content reduced rapidly on the first day (Table 4) and stabilised within 10 days but did not return to the original dry mass. Normalised moisture contents at 1 day have therefore been calculated based on the final dry mass.

Table 4. Moisture content by mass of 56 day mortar specimens during drying relative to dry mass prior to soak-dry cycle.

Mix	Saturated moisture content	Moisture content at 1 day	Residual Moisture content	Normalised mc at 1 day
M4X	16.9%	4.2%	1.0%	0.20
M4L	15.8%	4.2%	1.5%	0.19
M6X	14.4%	4.8%	1.8%	0.24
M4B	12.5%	3.2%	1.2%	0.17
M4L	11.3%	3.5%	1.7%	0.18
M6B	9.6%	3.4%	1.8%	0.20

4. MICROSTRUCTURE ANALYSIS

Specimens for microstructure analysis were obtained from prisms after compressive strength testing. The pore distributions of core (Figure 3) and face (Figure 4) specimens for each mix were analysed using nitrogen absorption porosimetry. Drying and in-situ degassing temperatures were kept at or below 60°C to minimise changes of the silica-based sol-gel compounds. X-ray diffraction analysis showed the expected phases for ettringite, quartz, calcite and portlandite. Specimens with silica-based sol-gel had reduced calcium hydroxide content compared to conventional specimens.

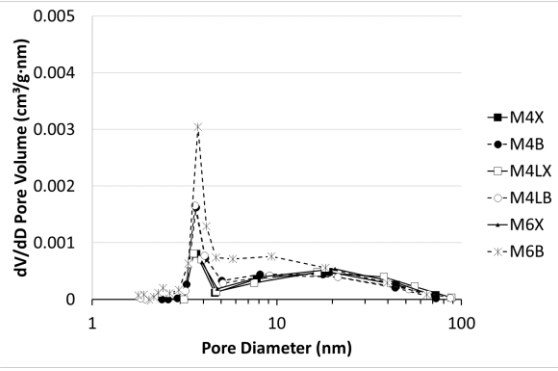

Figure 3 Pore volume distribution of specimens from core of 56 day prisms.

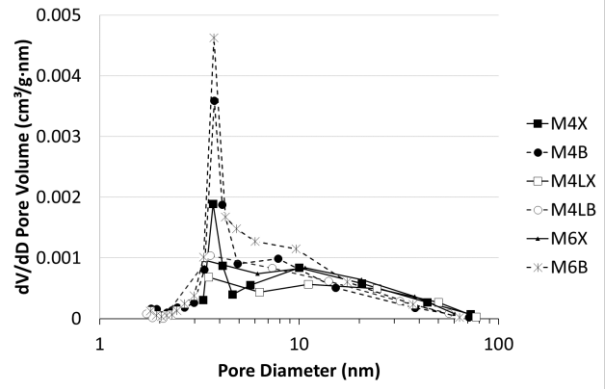

Figure 4 Pore volume distribution of specimens from face of 56 day prisms.

Following each analysis, specimens were selected and mounted for imaging of fracture surfaces with a scanning electron microscope (Figure 5). Portlandite plates were observed in all specimens but supported a finer network of interlaced crystals in the silica-based sol-gel mixes.

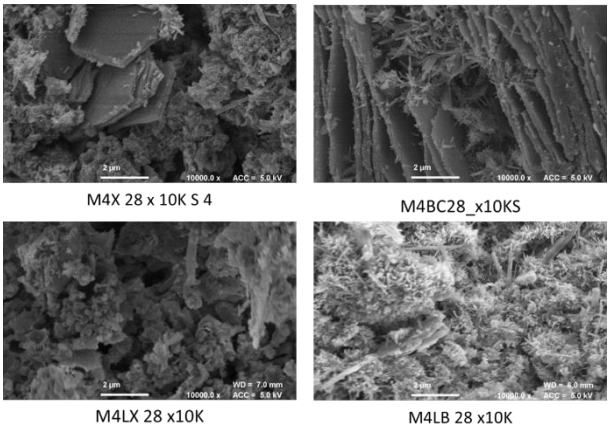

Figure 5 SEM imaging of 28 day specimens.

4. DISCUSSION

The addition of silica-based sol-gel reduced the liquid:binder ratio required for the mortars, but the mixes without CL90 were difficult to compact for prism specimens and had poor adhesion to brick when used to construct triplet specimens.All the mortars were stronger and less absorbent with the addition of silica-based sol-gel, particularly the mix with CL90 where strength increased by a factor of two and absorption decreased by a factor of three. This may in part be due to the greater density achieved.

Volume fraction porosity was calculated from the total mass of water absorbed during the sorptivity test, with subsequent immersion where necessary to saturate the sample. Factoring the infiltration by volume fraction porosity gives an indication of the rise of water during the test (Figure 6). The silica-

based sol-gel modified specimens have a reduced rise as well as reduced infiltration so the reduction in absorption cannot be explained by reduced porosity alone.

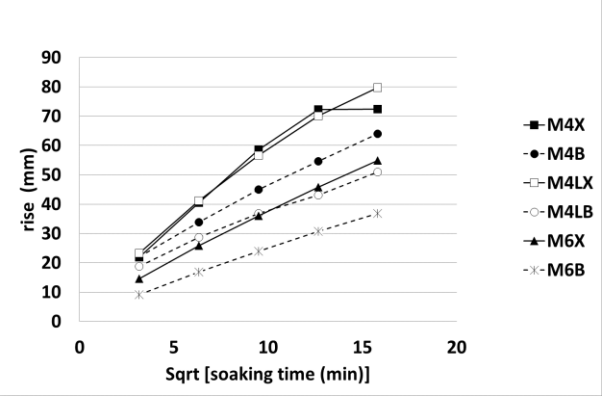

Figure 6. Rise of water in standard (X) and solgel modified (B) mortars for 28 day specimens.

The combined effect of silica-based sol-gel and CL90 is also evident in Figure 6. The M4X and M4LX mortars show similar absorption rates. However the rise for M4LB is less than 80% of M4B. All the curves can be approximated by a straight line ($r^2 \geq 0.99$) but it is evident that the rate of rise reduces. This may in part be due to evaporation from an increasing wetted area, but the curve is more pronounced for samples with CL90 indicating that pore structure does contribute to the reduction.

Drying of the specimens was consistent with an initial constant drying rate period and subsequent falling drying rate period (Hall and Hoff, 2011, p.203). None of the specimens returned to their original mass, suggesting that some water was retained through adsorption or further reaction.

The pore distribution showed a peak at about 3nm in all core specimens. This was greater with the addition of silica-based sol-gel, which also extended the distribution below 2nm. Face specimens had a more distinct peak, with the exception of the CL90 mixes. This is consistent with a finer porosity developing during carbonation of the non-hydraulic lime, as seen in the SEM images (Figure 5).

5. CONCLUSIONS

The use of silica-based sol-gel as an additive affected the workability, physical properties and microstructure of mortar mixes. The modified mortars had a higher compressive strength and lower water absorption than conventional mortars, particularly for the mix including CL90. Further work would be useful to compare drying rates for fully congruent specimens, with a single exposed face. Subsequent analysis of pore distribution and chemical composition should also be completed to investigate the extent of renewed reaction on wetting.

REFERENCES

BSI, 1999. BS EN 1015-3:1999 Methods of test for mortar for masonry. Determination of consistence of fresh mortar (by flow table). BSI

BSI, 2002. BS EN 1015-18:2002 Methods of test for mortar for masonry. Determination of water absorption coefficient due to capillary action of hardened mortar. BSI

BSI, 2005. PD 6678:2005 Guide to the specification of masonry mortar. BSI

BSI, 2017. 17/30351887 DC BS EN 1015-11. Methods of test for mortar for masonry. Part 11. Determination of flexural and compressive strength of hardened mortar. BSI.

Calabria, J., Vasconcelos, W. L., Doni, D. J., Chater, R., McPhail, D. and Boccaccini, A. R., 2010. Synthesis of sol-gel titania bactericide coatings on adobe brick. Construction and Building Materials, 24 (3), pp. 384-389.

Escarameia, M., Karanxha, A. and Tagg, A., 2007. Quantifying the flood resilience properties of walls in typical UK dwellings. *Building Services Engineering Research and Technology*, *28*(3), pp.249-263.

Hall C, Hoff WD. Water transport in brick, stone and concrete. CRC Press; 2011 Oct 31

Hussain, A., Schorr, D., Blanchet, P., Calabria-Holley, J. and Lawrence, R., 2017. Forthcoming. Hydrophobic sol-gel coatings on bio-based materials- influence of catalyst and solvent concentration. In: 2nd International Conference in Bio-Based materials, 2017-06-21 - 2017-06-23.

Lamond, J., McEwen, L., Twigger-Ross, C., Rose, C., Joseph, R., Wragg, A., Papadopolou, L., White, O. and Proverbs, D. (2017) Supporting the uptake of low cost resilience: Final report (FD2682). Project Report. Defra, UK.

Prime, N., Housni, Z., Fraikin, L., Léonard, A., Charlier, R. and Levasseur, S., 2015. On water transfer and hydraulic connection layer during the convective drying of rigid porous material. Transport in Porous Media, 106(1), pp.47-72.

Sayers, P. B., M. S. Horritt, E. Penning-Rowsell and A. McKenzie (2015). Climate Change Risk Assessment 2017: Projections of future flood risk in the UK. London, Committee on Climate Change

39th Cement and Concrete Science Conference
9-10th September 2019
University of Bath
Paper Number 024

Ultra-High Performance Concrete with One-part Alkali-Activated Slag

Priyadharshini Perumal, Tero Luukkonen, Paivo Kinnunen, Mirja Illikainen
Fibre and Particle Engineering Research Unit
University of Oulu, Finland

ABSTRACT

One-part (just-add-water) alkali activated binders are of interest due to their ease in practical applications, particularly in on-site works. This paper focuses on a method to develop ultra-high performance one-part alkali activated concrete using particle packing technology. Modified Andreassen particle packing model is employed to optimize the binder and aggregate content that results in a denser matrix. Two different q-parameter values are used in designing the mixes to evaluate its influence in properties like flowability and compressive strength. Lower q-value leads to higher binder content i.e., it moves towards the finer gradation of particles. Mixes with higher fines content show better workability with high flow percentages measured by the spread table (>120% flow). Variation in water-to-binder ratio (0.25 - 0.35) affects the flow and compressive strength of alkali activated concrete irrespective of q value used in the design. Compressive strengths over 120 MPa is achieved after 28-day curing. The concept of ultra-high performance concrete with particle packing technology is well established by concrete technologists. However, its application in geopolymer concrete, in specific to one-part alkali activated materials is explored for the first time in this work.

1. INTRODUCTION

Mix design plays an important role in achieving the desired fresh and hardened properties of a concrete. There are many standard mix design methods adopted for Ordinary Portland cement (OPC) concrete which have been followed for special binding systems like alkali activated binders. One such methods is particle packaking method that is used to achieve the maximum packing density of particles (Fennis and Walraven, 2012, Shi et al., 2015; Zuo et al., 2018). The main advantage of alternative binding systems is to reduce CO_2 emission of OPC which is almost 7% of world's CO_2 emissions (Barcelo et al., 2014). Alkali activated binders perform outstanding in this case by using industrial by-products and waste materials as a source (Gartner and Hirao, 2015).

Conventionally, alkali activation is performed in two-parts by using aqueous solution of alkali hydroxides and silicates to activate aluminosilicate precursors such as fly ash or slag. However, this processing technique restricts the application of this material due to the problem of handling the corrosive alkali activators. This results in the development of technique called one-part or "just-add-water" alkali-activated cements that can be used similar as OPC concrete (Luukkonen et al., 2018). Though this technique has been developed as early as 1940 (Purdon, 1940), this material is not studied extensively as that of two-part geopolymers. In this paper, an attempt is made to design an ultra-high performance of ground granulated blast furnace slag (GGBFS) based geopolymer mix with particle packing technique using modified Andreassen model. The effect of choosing different distribution modulus (Q value) and water-to-binder ratio on the fresh and hardened properties of one-part alkali-activated cements were explored.

2. MATERIALS AND METHODOLOGY

Ground granulated blast furnace slag (GGBFS was used as binder material which is obtained from Finnsementti, Finland. GGBFS was co-grinded with anhydrous sodium silicate (SiO_2/Na_2O = 0.9) in the ratio of 9:1. Fine aggregate was sieved in to two size fractions as fine sand and coarse sand which was passing and retained in 500 µm size sieve, respectively.

Mixture proportion was designed using modified Andreassen model which gives the maximum packing density from the following equation,

$$P(d) = \left(\frac{d}{d_{max}}\right)^{Q}$$

Where, P(d) is the Cumulative percent finer than d (particle diameter) and d_{max} is the maximum size of particle used in the mixture. Q is the distribution modulus, takes values of 0.25 and 0.3 in this study to know its effect on concrete properties. Commercially available software (EMMA particle analyzer) was used to arrive at the mix design as shown in Table 1.

Table 1. Mix proportion based on particle packing model.

Q value	Co-grinded slag	Fine sand	Coarse sand
0.25	1	0.8	1
0.3	0.8	1	1

Mixture distribution of the ingredients to fit the modified Andreassen model for specified Q values are shown in Figure 1. It can be noted that lower Q value shows better fitting as it means more fine particles that fills the voids formed by coarser aggregates (Kumar and Santhanam, 2003).

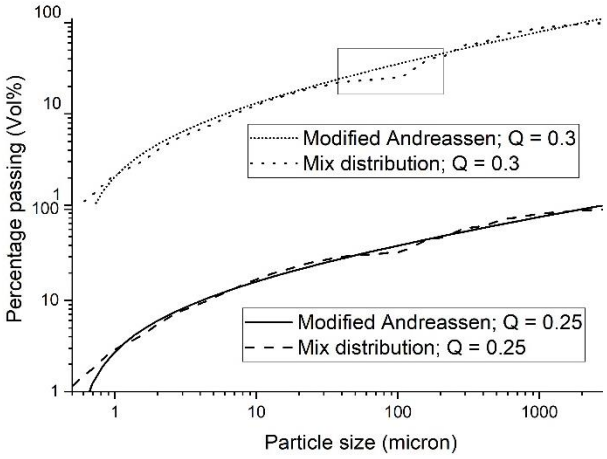

Figure 1. Mixture distribution compared with modified Andreassen model for Q values 0.3 and 0.25.

Co-grinded GGBFS, fine and coarse sand as specified in the Table 1, were mixed in Hobart mixture for 3 minutes. Calculated quantity of water (Water-binder ratio = 0.25, 0.3 and 0.35) was added to the dry mix and further mixed for 2 minutes to get a homogenous alkali activated GGBFS mortar. Flow percentage of the fresh mortar was calculated with flow table (ASTM C1437). Prismatic (40 × 40 × 160 mm) and cubic (50 mm) specimens were cast and demoulded after hardening in 24 hours. The specimens were maintained in curing chamber of 100% RH and 20°C until testing at 28th day. Eighteen prismatic beams were tested for flexural strength of different mixtures and the results are average of triplet for each mix. Three-point bending test as per ASTM C78 recommendation was followed with a deflection rate of 0.6 mm/min. The compressive strength (average of six specimens) was measured with the broken pieces of flexture testing as per ASTM C349. Cubic specimens were used to measure the porosity (average of three specimens) of the matrix as per EN 1936, with the oven drying performed at 105 ± 5˚C instead of the specified 70± 5˚C for fast drying.

3. RESULTS AND DISCUSSION

Figure 2, gives the flow percentage of geopolymer mortar with GGBFS designed with different Q values. It can be observed that mix with Q=0.25 results in higher flow percentage compared to Q=0.3, irrespective of water-binder ratio. For example, flow increased from 60% to 125% when Q value was increased from 0.3 to 0.35 at a water-binder ratio of 0.35. This can be related to the better fit to the model curve noted for lower Q value in Figure 1. Hence, optimum packing of mix ingredients plays an important role in fresh properties of mortar/concrete. Finer the ingredient, lower Q values gives good workable mix. As expected, the flow increased with increasing water content for both the Q values.

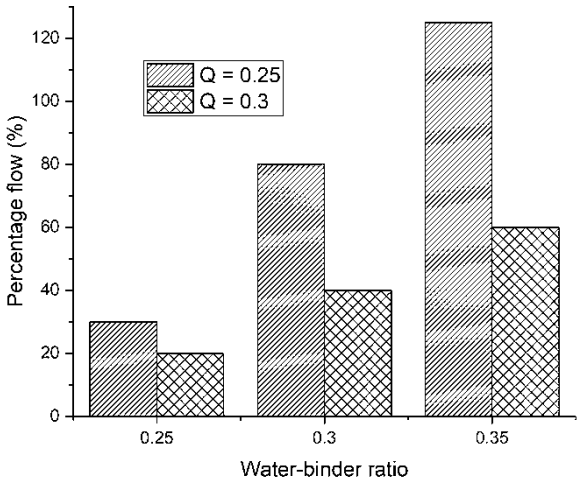

Figure 2. Effect of Q values and W/B ratio on flow percentage.

The hardened properties of the designed mixtures were analysed, and the results are shown in Figure 3 and 4. Interestingly, compressive strength increased with increasing water-binder ratio with higher Q value. As in the case of one-part geopolymer, addition of water results in four consecutive reactions as follows: (1) ion exchange, (2) hydrolysis, (3) network breakdown, and (4) release of Si and Al ions (Matalkah et al., 2017). Hence, water plays an important role in reaction initiation though further kinetics are similar to the two-part geopolymers.

Together with the packing method of mix proportion and availability of water content must have affected the release rate of Si and Al, resulting in strength increase with water-binder ratio. However, this is not the case when Q value is 0.25. Compressive strength was increasing with increasing water content and reached maximum for a water-binder (w/b) ratio of 0.3 and, reducing for further increment in water (Fig. 3). This trend is also observed with the permeable pore percentage of the mixtures as shown in Figure 4. Permeable pores are 6.5% for a w/b ratio of 0.3 and increases to 7.5% for w/b ratio of 0.35. This can be explained by the existence of an optimum water content which could result in enhanced properties of the one-part geopolymer mixtures based on the kinetics involved. For Q-value of 0.25, the optimum water content is 0.3, whereas for Q-value of 0.30 optimum water content is 0.35 or above.

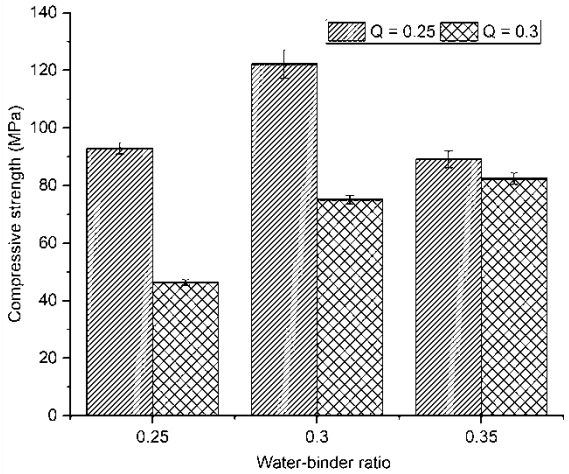

Figure 3. Effect of Q values and W/B ratio on compressive strength.

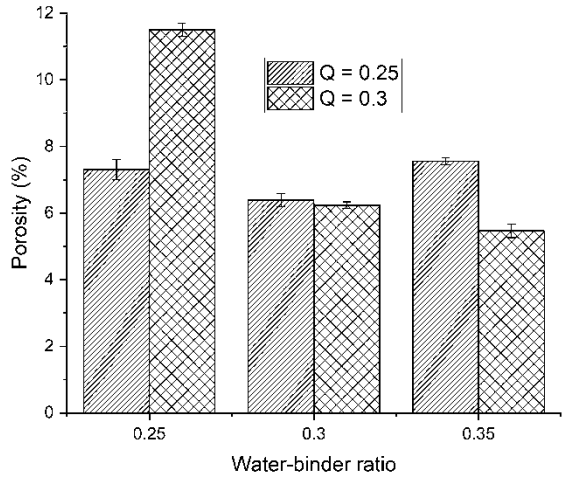

Figure 4. Effect of Q values and W/B ratio on porosity of mortar matrix.

Further analysis was made to know the reason for such a trend. Representative micrographs of one-part geopolymer made of GGBFS were captured and presented in Figure 5. In the mixtures with Q=0.25, Formation of microcracks are clearly observed in mix with w/b ratio of 0.35 whereas mix with w/b ratio of 0.3 is intact without any crack formation. It can also be noteworthy to mention that the white portions represent the unreacted GGBFSpresent in the matrix which is high in mix with w/b ratio of 0.3 (Fig. 5a) that would act as restraint in crack formation. High paste content in the other mix results in shrinkage and crack formation. Considering lower w/b ratio of 0.25, the lower compressive strength can be related to the insufficient water content for the dissolution of solid alkali sources to initiate the activation of alumino-silicate precursors.

4. CONCLUSIONS

The following conclusions are drawn based on the experiments conducted on particle packing technique of mix design in one-part alkali activated GGBFS mortar:

Workability of the mix depends on the efficient particle packing and the best fit with the model. Q value of 0.25 was superior to 0.30 in terms of fresh state flow properties.

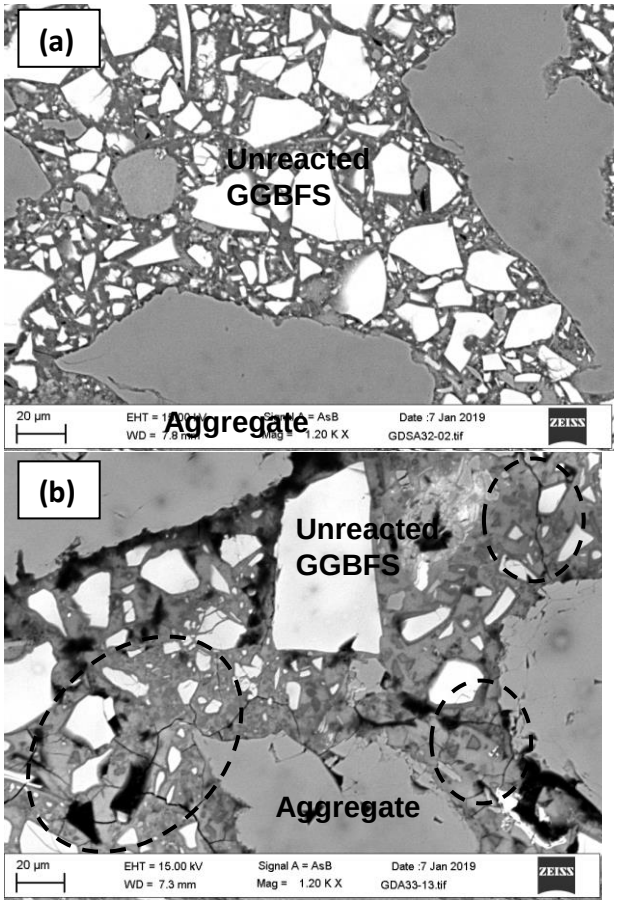

Figure 5. Representative microstructure of GGBFS-geopolymer mortar with Q value 0.25 and water-binder ratio a) 0.3 and b) 0.35.

Mechanical properties and permeable porosity depend on the water-binder ratio, which in turn depends on the mixture proportioning and Q value of the mix.

At lower w/b ratio, compressive strength is reduced. This is presumably due to insufficient water provided for the dissolution and activation of the GGBFS.

The optimum water content varies with the amount and type of mix ingredients used, and the Q value chosen. For the chosen mix design, the optimum w/b ratio was found to be 0.3 resulting in effective particle packing, lowest permeable pore percentage (6.5%) and highest compressive strength (122 MPa) for the Q value of 0.25.

REFERENCES

ASTM C1437. (2015). Standard test method for flow of hydraulic cement mortar, ASTM International, West Conshohocken, PA, USA.

ASTM C78. (2016). Standard test method for flexural strength of concrete (using simple beam

with third-point loading), ASTM International, West Conshohocken, PA, USA.
ASTM C349-14. (2014). Standard test method for compressive strength of hydraulic-cement mortars (using portions of prisms broken in flexure), ASTM International, West Conshohocken, PA, USA.
Barcelo, M., Kline, J., Walenta, G., Gartner, E. (2014). Cement and carbon emissions, International Journal of Material and Structure, 47, 1055–1065.
Brew, D.R.M., Glasser, F.P., 2005. Synthesis and characterisation of magnesium silicate hydrate gels. Cement and Concrete Research, 35(1):85-98.
EN 1936. (2006). Natural stone test methods. Determination of real density and apparent density, and of total and open porosity, BSI, London, UK.
Fennis, S.A.A.M., Walraven, J.C. (2012). Using particle packing technology for sustainable concrete mixture design. Heron 57, 73–101.
Gartner, E., Hirao, H. (2015). A review of alternative approaches to the reduction of CO2 emissions associated with the manufacture of the binder phase in concrete, International Journal of Cement and Concrete Research, 78, 126–142.
Kumar, S.V., Santhanam, M. (2003). Particle packing theories and their application in concrete mixture proportioning: A review, The Indian Concrete Journal, 77(9), 324-1331.
Luukkonen, T., Abdollahnejad, Z., Yliniemi, J., Kinnunen, P., Illikainen, M. (2018). One-part alkali-activated materials: A review, Cement and Concrete Research, 103, 21–34.
Matalkah, F., Xu, L., Wu, W., Soroushian, P. (2017). Mechanochemical synthesis of one-part alkali aluminosilicate hydraulic cement, Materials and Structures, 50:97.
Milestone, N.B. (2006). Reactions in cement encapsulated nuclear wastes: need for toolbox of different cement types, Advances in Applied Ceramics, 105(1), 13-20.
Purdon, A. (1940). The action of alkalis on blast-furnace slag, Journal of the Society of Chemical Industry, 59, 191–202.
Shi, C., Wu, Z., Xiao, J., Wang, D., Huang, Z., Fang, Z. (2015). A review on ultra-high-performance concrete: Part I. Raw materials and mixture design. Construction and Building Materials, 101, 741–751.
Zuo, W., Liu, J., Tian, Q., Xu, W., She, W., Feng, P., Miao, C. (2018). Optimum design of low-binder Self-Compacting Concrete based on particle packing theories. Construction and Building Materials, 163, 938–948.

39th Cement and Concrete Science Conference
9-10th September 2019
University of Bath
Paper Number 025

Electrochemical characterisation of Portland cement hydration

Aldo F. Sosa Gallardo
Department of Materials Science and Engineering, University of Sheffield

John L. Provis
Department of Materials Science and Engineering, University of Sheffield

ABSTRACT

Various individual analytical tools and techniques have been used to study the complexity of cement hydration and its microstructural development at early age. Nevertheless, a combination of these techniques is needed to understand the complexity of cement (i.e. chemical composition, hydration kinetics, microstructural development, admixture effects) and obtain sufficient data to enable interpretation of the underlying reaction processes. To understand the major aspects that influence the electrochemical response of cement paste during hydration, the complementary application of multiple techniques is of great importance. Alternating current impedance spectroscopy (ACIS) assesses the electrical response of a material (in the fluid or hardened state) as a function of time and frequency. However, this technique is not fully accepted by the cement research community due to certain limitations such as electrode contact, current dispersion and the influence of parasitic effects and data interpretation. In order to demonstrate the true value of ACIS as a characterisation technique for cement hydration at early ages, this paper evaluates the electrochemical behaviour of Portland cement during the first 24 hrs after mixing using ACIS and other supporting techniques. The results demonstrate that ACIS is able to differentiate changes in the chemical composition, temperature and microstructural development during cement hydration throughout the period of setting and hardening, providing a valuable tool in understanding the chemical details of this complex process.

1. INTRODUCTION

In the last decades, due to its many advantages over other materials, Portland cement has been one of the most used construction materials in the world. However, to improve its mechanical properties and applications, it has been of crucial importance to understand the mechanism of reaction, dielectric properties, and changes in its microstructure during the hydration process (McCarter, 1994; Langan, Weng and Ward, 2002; Lothenbach, Scrivener and Hooton, 2011; Cruz *et al.*, 2013; Tang *et al.*, 2017). The hydration of cement at early ages is not entirely understood yet, since it is a complex process which involves mixing a multiphase material (cement powder) with water, triggering a large number of simultaneous and successive reactions, leading to the production of chemical and physical changes, release of heat, and formation of new hydrated products (Kohlhaas, 1983; Taylor, 1997; Hewlett, 1998; Mehta and Monteiro, 2006).

Over the years many different analytical tools and techniques have been used to assess cement hydration. One of these techniques is alternating current impedance spectroscopy (ACIS), a non-destructive technique which is designed to probe the electrical response of a system as a function of frequency, and potentially in a time-resolved manner. The system-electrode response (at low frequency) and the system bulk response (at high frequency) can be obtained from the electrical response obtained from impedance assessment of the sample; this is frequently represented by a Nyquist plot which is divided into the real (Z') and the imaginary (-Z'') components of complex impedance (Z) (Macdonald and Johnson, 2005; Orazem and Tribollet, 2008; Yuan *et al.*, 2010).
Although ACIS has been applied to assess cement hydration and its microstructural development by numerous researchers, this technique is not fully recognised as a cement characterisation technique due to certain limitations such as challenging data interpretation, undesired inductance effects at high frequency (impedance values below Z' plane), electrode effects and ground coupling effects, among others (Hsieh, Mason and Pederson, 1996; Hwang *et al.*, 1997; Cormack, Macphee and Sinclair, 1998; Mason *et al.*, 1998; Spragg *et al.*, 2013).

The aim of this paper is to evaluate, using ACIS, the electrochemical response of white Portland cement (wPc) pastes in the early stages of hydration (the first 24 hours after mixing). By assessing these data in parallel with information about the thermochemical response and setting times of wPc pastes, new insight can be gained.

2. MATERIAL AND METHODS

2.1 Sample preparation

Each sample was hand mixed at room temperature by mixing white Portland cement (wPc; Lafarge Blue Circle Snowcrete) classified as CEM I 52.5R under BS EN 197-1 (European Committee for Standardization, 2011) with water at a 0.45 water to cement mass ratio.
The paste obtained was transferred into three different vessels: 300 g into a custom-built electrochemical cell designed for ACIS measurements, 20 g into a plastic ampoule for thermochemistry measurements, and 300 g into a plastic mould for setting times testing. The chemical composition and physical properties of wPc are shown in Table 1.

Table 11. Chemical composition of wPc as determined by X-ray fluorescence analysis

wPc compound (wt%)			
SiO_2	23.7	Na_2O	0.23
Al_2O_3	3.9	K_2O	0.5
CaO	66.5	SO_3	2.6
Fe_2O_3	0.2	Others	1.0
MgO	0.9	LOI	1.2
Density (kg/m^3)	2800-3200		
Particle size (μm)	5-30		

2.2 Instrumental analysis

ACIS measurements were obtained using an impedance analyser (Metrohm AutoLab, PGSTAT204) connected to a custom-built electrochemical cell with two threaded stainless steel electrodes, whose specifications are shown in Figure 1. The experimental procedure involves the use of a perturbation amplitude of 10 mV and a current range of 1 mA. Each measurement consisted of 50 data points per cycle over a frequency range of 100 Hz to 1 MHz. Measurements were obtained every 5 minutes over a period of 24 hours.
The Nyquist plot was used to represent the impedance response of wPc paste, in which Z' (real component) and -Z'' (imaginary component) were plotted from the electrical response of the pastes. Parasitic effects were recognised as the impedance values below the Z' plane.
The conductivity of wPc paste was acquired by dividing the intercept point in the Z' plane of the impedance spectra with a cell-constant (obtained by measuring different concentrations of NaOH solution of known resistivity (Prichard and Barwick, 2003; Shreiner and Pratt, 2004; Provis, Walls and van Deventer, 2008; Rosemount Analytical, 2010).

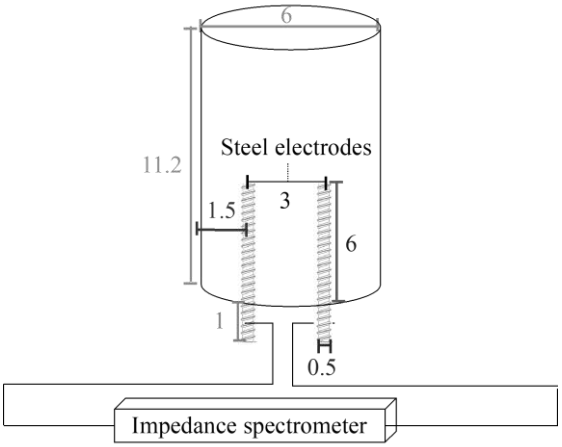

Figure 1. Custom-electrochemical cell illustration (scale in cm).

Thermochemistry analysis was conducted by using an 8-channel TAM air isothermal calorimeter (TA Instruments). Measurements were obtained during the first 24 hours after mixing following the standard procedures (ASTM Committee C09.48, 2014).
The setting time test was conducted using a Vicatronic apparatus (Matest, E044N) according to the 90 penetration standard procedure (ASTM Committee C01, 2003). The measurements were obtained during the first 15 hours after mixing.

2.3 Calibration and ACIS measurements correction

In order to decrease any parasitic effects (caused by the device, the electrochemical cell and the leads), the impedance response of the custom-built electrochemical cell in a short circuit without cement paste was measured. The measurements obtained (short circuit) at each frequency were considered as additive values to the sample impedance measurements.

3. RESULTS AND DISCUSSION

While grey Portland cement (gPc) is one of the most used materials in the construction field, wPc is commonly used for decorative and aesthetical purposes due to its higher manufacturing cost and energy consumption. Often, wPc has a higher surface area and compressive strength, higher content of C_3A, smaller particle size, and lower content of Fe_2O_3 and MnO than gPc (Taylor, 1997; Hewlett, 1998; Mehta and Monteiro, 2006).
Figures 2 and 3 show the calorimetric and setting time data (which are consistent with the broader literature for Portland cement hydration), and Figures 4 and 5 show the impedance response, and conductivity and resistivity measurements, respectively, for wPc during the first 24 hours after mixing.
The impedance results in Figure 4 show a low impedance and bulk resistance semicircle arc is present 5 minutes after mixing, which is attributed to the high conductivity, high particle surface area and

free water content of the cement paste at early age (Zhang and Napier-Munn, 1995).

Approximately 1 hour after mixing, a perturbation correlated to the beginning of the dormant period (Figure 5) is observed in the conductivity measurements. This perturbation is followed by an increasing tendency in the conductivity as a result of the increase of the concentration of ionic species in the aqueous solution within the cement paste, and a high mobility of these ions.

The appearance of inductance effects in the impedance measurements is observed approximately 4 hours after mixing. These effects are related to the beginning of the acceleration period (Figure 2) and a second perturbation in the conductivity measurements. At this time, directly after saturation of the pore solution is reached, the precipitation of new hydrated products begins, which causes a decreasing tendency in the conductivity as ionic mobility is reduced.

During the deceleration period, wPc shows an increasing tendency in the resistivity and a perturbation is observed at around 8 hours after mixing. These effects are related to the final setting time (Figure 3) (Dotelli and Mari, 2001; Ylmén, Wadsö and Panas, 2010; Pang *et al.*, 2013).

At 24 hours after mixing, the ACIS measurements show a more developed bulk semicircle arc of higher impedance which is attributed to a low free water content, a limited space for the production of new hydrated products, and a more developed microstructure (Christensen *et al.*, 1994; McCarter, 1994, 1996; Moss *et al.*, 1996; Dong *et al.*, 2014).

3. CONCLUSIONS

- The experimental results demonstrate that ACIS can be used as a characterisation tool to assess the microstructural development and electrical properties of cement during hydration.
- To obtain a better interpretation of impedance data, the use of different supporting techniques is needed.
- The impedance and electrical conductivity response obtained correspond to those reported in previous investigations.
- The emergence and behaviour of inductance effects at high frequency need further investigation.

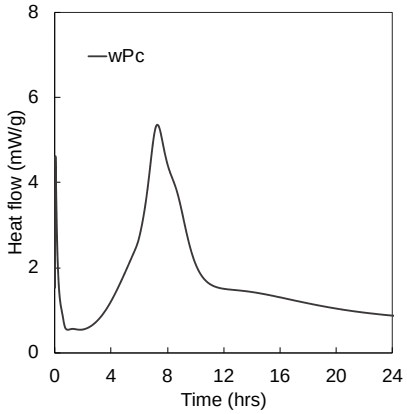

Figure 2. Calorimetric curve of wPc during the first 24 hours after mixing.

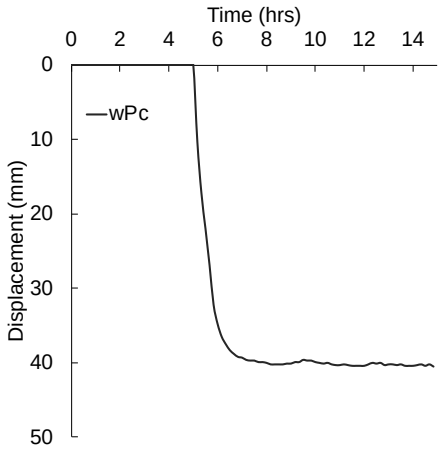

Figure 3. Penetration displacement of wPc in Vicat testing during the first 15 hours after mixing.

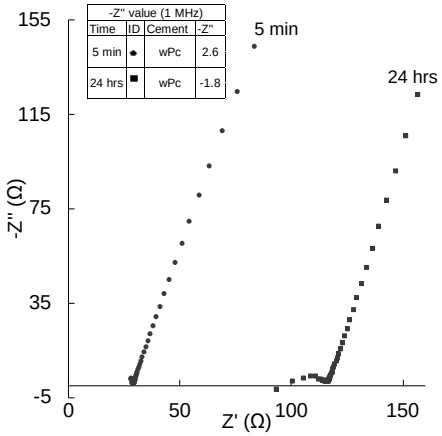

Figure 4. Impedance response of wPc at 5 minutes and 24 hours after mixing.

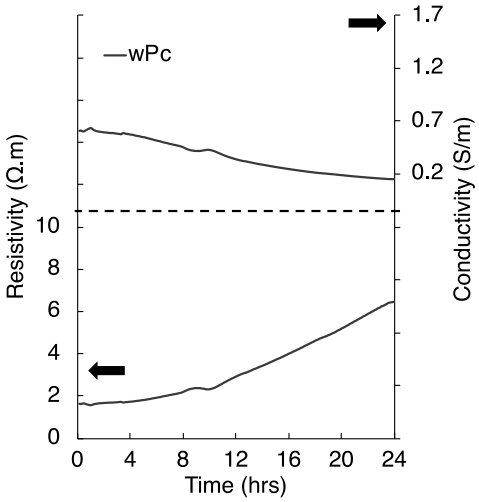

Figure 5. Resistivity and conductivity of wPc during the first 24 hours after mixing.

REFERENCES

ASTM Committee C01 (2003) 'ASTM C191–04: Time of setting of hydraulic cement mortar by modified Vicat needle', *ASTM International*, pp. 1–8.

ASTM Committee C09.48 (2014) *ASTM C1679-14: Standard practice for measuring hydration kinetics*

of hydraulic cementitious mixtures Using isothermal calorimetry, *ASTM International*.
Christensen, B. J. *et al.* (1994) 'Impedance spectroscopy of hydrating cement-based materials: measurement, interpretation, and application', *Journal of the American Ceramic Society*, 77(11), pp. 2789–2804.
Cormack, S. L., Macphee, D. E. and Sinclair, D. C. (1998) 'An AC impedance spectroscopy study of hydrated cement pastes', *Advances in Cement Research*, 10(4), pp. 151–159.
Cruz, J. M. *et al.* (2013) 'The use of electrical impedance spectroscopy for monitoring the hydration products of Portland cement mortars with high percentage of pozzolans', *Cement and Concrete Research*, 50, pp. 51–61.
Dong, B. *et al.* (2014) 'Study on the carbonation behavior of cement mortar by electrochemical impedance spectroscopy', *Materials*, 7, pp. 218–231. doi: 10.3390/ma7010218.
Dotelli, G. and Mari, C. M. (2001) 'The evolution of cement paste hydration process by impedance spectroscopy', *Materials Science and Engineering A*, 303(1–2), pp. 54–59.
European Committee for Standardization (2011) *Cement - Part 1: Composition, specifications and conformity criteria for common cements*. Brussels.
Hewlett, P. C. (1998) *Lea's Chemistry of Cement and Concrete*. 4th edn. Oxford: Elsevier.
Hsieh, G., Mason, T. O. and Pederson, L. R. (1996) 'Experimental limitations in impedance spectroscopy: Part II. Electrode artifacts three point measurements on Pt/YSZ', *Solid State Ionics*, pp. 203–212.
Hwang, J. H. *et al.* (1997) 'Experimental limitations in impedance spectroscopy: Part IV. Electrode contact effects', *Solid State Ionics*, pp. 93–104.
Kohlhaas, B. (1983) *Cement Engineers' Handbook*. 4th edn. Wiesbaden; Berlin: Bauverlag.
Langan, B. W., Weng, K. and Ward, M. A. (2002) 'Effect of silica fume and fly ash on heat of hydration of Portland cement', *Cement and Concrete Research*, 32(7), pp. 1045–1051.
Lothenbach, B., Scrivener, K. and Hooton, R. D. (2011) 'Supplementary cementitious materials', *Cement and Concrete Research*, 41(12), pp. 1244–1256.
Macdonald, J. R. and Johnson, W. B. (2005) *Impedance spectroscopy theory, experiment, and applications*. Second. Wiley.
Mason, T. O. *et al.* (1998) 'Experimental limitations in impedance spectroscopy of materials systems', *Advances in Cement Research*, pp. 143–150.
McCarter, W. J. (1994) 'A parametric study of the impedance characteristics of cement-aggregate systems during early hydration.', *Cement and Concrete Research*. Edinburgh, UK., 24(6), pp. 1097–1110.
McCarter, W. J. (1996) 'The a.c. impedance response of concrete during early hydration', *Journal of Materials Science Materials Science*, 31(23), pp. 6285–6292.
Mehta, P. K. and Monteiro, P. J. M. (2006) *Concrete: microstructure, properties, and materials*. 3rd edn. California: McGraw-Hill.
Moss, G. M. *et al.* (1996) 'Microstructural analysis of young cement pastes using impedance spectroscopy during pore solution exchange', *Advanced Cement Based Materials*, 4(2), pp. 68–75.
Orazem, M. E. and Tribollet, B. (2008) *Electrochemical impedance spectroscopy*, *Analysis*. Hoboken: Wiley.
Pang, X. *et al.* (2013) 'A comparison study of Portland cement hydration kinetics as measured by chemical shrinkage and isothermal calorimetry', *Cement and Concrete Composites*, 39, pp. 23–32.
Prichard, L. and Barwick, V. (2003) 'Preparation of calibration curves', *National Measurement System Valid Analytical Measurement*, 32, pp. 1–27.
Provis, J. L., Walls, P. A. and van Deventer, J. S. . (2008) 'Geopolymerisation kinetics. 3. Effects of Cs and Sr salts', *Chemical Engineering Science*, 63(4480–4489).
Rosemount Analytical (2010) 'Conductance data for commonly used chemicals', *Emerson*, 44, pp. 1–33.
Shreiner, R. H. and Pratt, K. W. (2004) 'Primary standards and standard reference materials for electrolytic conductivity', *NIST*, pp. 1–31.
Spragg, R. *et al.* (2013) 'Factors that influence electrical resistivity measurements in cementitious systems', *Transportation Research Record*, 2342, pp. 1–12.
Tang, S. W. *et al.* (2017) 'The review of early hydration of cement-based materials by electrical methods', *Construction and Building Materials*, 146, pp. 15–29.
Taylor, H. F. W. (1997) *Cement chemistry*. 2nd edn, *Academic Press*. 2nd edn. London: Thomas Telford.
Ylmén, R., Wadsö, L. and Panas, I. (2010) 'Insights into early hydration of Portland limestone cement from infrared spectroscopy and isothermal calorimetry', *Cement and Concrete Research*, 40(10), pp. 1541–1546.
Yuan, X.-Z. *et al.* (2010) *Electrochemical impedance spectroscopy in PEM fuel cells*. London: Springer.
Zhang, Y. M. and Napier-Munn, T. J. (1995) 'Effect of particle size distribution, surface area and chemical composion on Portland cement strength', *Powder Technology*, 83, pp. 245–252.

39th Cement and Concrete Science Conference
9-10th September 2019
University of Bath
Paper Number 026

Hydration and Strength development of ternary cement blends containing calcined alum water treatment sludge and limestone powder

Mubarak Shamaki, Mathew Lock, Sam Adu-Amankwah and Leon Black
Department of Civil Engineering, University of Leeds

ABSTRACT

Alum salts are commonly used as coagulants in the purification of surface water for potable supplies. The large volumes of waste alumina-rich sludge generated are a waste management problem. At present, these are disposed in landfills, thus pose environmental challenge. This study has sought to valorise the sludge by investigating the interaction between calcined alum water treatment sludge and limestone powder in ternary composite cement. The mechanical properties were studied in mortars and microstructural development in pastes using X-ray diffraction (XRD), thermogravimetric analysis (TGA) and Fourier Transform Infrared spectroscopy. As the aluminate phase in cement clinker is limited, the chemical effect of limestone powder in cement-based materials is restricted. Our results show that calcium carbonate reacts with the additional aluminates from the calcined sludge, forming supplementary AFm phases and thereby stabilizing ettringite, which translates to improved mechanical properties that persist over time. This synergistic effect between the alumina-rich calcined sludge and limestone powder suggests a potential waste management solution for water treatment sludges by incorporating them in composite limestone cements

INTRODUCTION

Due to rapid urbanization and population growth, there is a growing increase in industrial wastes and their disposal has become a challenge. A possible waste management solution is to use these wastes as mineral additions in cement-based materials. Economically, this will lower the cost and consumption of energy associated with the manufacture of construction materials such as Portland cement. Environmentally, the disposal challenge of these wastes is solved and reducing the clinker content of cement reduces greenhouse gas emissions.

Water treatment facilities generate large amounts of waste residue, known as water treatment sludge (WTS), during the purification of surface water for potable supplies. The purification of water is composed of a coagulation/flocculation process where chemical coagulants are added to agglomerate impurities, aiding sedimentation and filtration of the contaminants from the liquid phase. In the UK, aluminium sulfate is commonly used as a chemical coagulant which leads to the generation of an alumina-rich waste commonly known as alum water treatment sludge (AWTS). The physical and chemical characteristics of AWTS mainly depends on the source water quality and dosage of coagulants added during the water treatment process [1]. Previous studies indicate that AWTS ashes that are also rich in silica exhibit pozzolanic activity with cement without sacrificing quality of cementitious materials [2, 3].

Limestone powder is widely used in cement and it has been confirmed that limestone additions can react with aluminates in cement and improve mechanical properties [4, 5]. Calcium hemi- and monocarboaluminate are produced rather than monosulfoaluminate [5-8], thus stabilizing ettringite. Using thermodynamic modelling, it has been reported that the increase in solid volume in a ternary blend of cement-limestone-SCM when replacing limestone by an SCM is related to the reactive alumina content of the SCM [9]. In this sense, the use of calcined alum sludge is interesting because of its reactive alumina content. The aim of this study is to investigate the synergistic interaction between calcined AWTS and limestone powder in ternary composite cements. Both compressive strength and flexural strength of mortars have been measured. In addition, blended cement pastes were characterized by TGA, XRD and FTIR techniques.

1. MATERIALS AND METHODS

CEM I 52.5R, limestone powder (L) and ground alum sludge (S) which had been calcined at 825^{o}C for 2 hours, were used for the preparation of blended cement pastes. Natural sand sieved to a maximum size of 2.0 mm was used to prepare mortars. The sludge ash has a high water demand, so a polycarboxylate based superplasticizer (Sika Viscocrete 25MP) was used at constant dosages to maintain workability. Physical and chemical properties of cementitious materials are shown in Table 1.

Table 1. Physical and chemical properties of OPC and SCMs

Characteristics	Cement (C)	Calcined Sludge (S)	Limestone (L)
Oxide composition (wt. %):			
SiO_2	20.5	17..67	2.00
Al_2O_3	4.60	67.39	0.80
Fe_2O_3	2.40	4.75	0.32
CaO	63.4	4.55	53.13
MgO	2.00	0.54	0.64
SO_3	3.60	2.12	0.07
Density (g/cm^3)	3.17	3.09	2.72
Blaine fineness (m^2/kg)	349	1108	328
D_{50}(μ)	11.66	24.76	20

Mortar samples (1:3:0.55) were prepared in (40 x 40 x 160 mm) moulds. Reduced workability due to fineness of calcined sludge was mitigated by adding 1% superplasticizer by mass of total binder. Each prism was halved to determine the compressive strength at 2, 7 and 28 days. Table 2 shows the mix proportions of mortars used. The corresponding blended pastes were characterized by XRD and FTIR to identify hydration products. Thermogravimetric analysis (TGA) was used to determine the bound water, residual carbonate and Portlandite contents. Bound water (W_n) was taken as mass loss between 50 and 550°C and then normalized to the ignited weight at 550°C. Meanwhile, $Ca(OH)_2$ and $CaCO_3$ were quantified by the tangent method and normalized to the anhydrous binder content. The consumed calcium carbonate content was calculated by subtracting the residual calcium carbonate content obtained by TGA from the initial content.

Table 2. Mix proportions of cement blends

Mix description C-S--L	Cement (C)	Calcined Sludge (S)	Limestone (L)	Sand	W/B	SP
100-0-0	450			1350	0.55	1%
80-20-0	360	90		1350	0.55	1%
80-0-20	360		90	1350	0.55	1%
80-6.7-13.3	360	30	60	1350	0.55	1%
80-10-10	360	45	45	1350	0.55	1%
80-13.3-6.7	360	60	30	1350	0.55	1%

2. RESULTS AND DISCUSSION

Figure 1 shows compressive strength of the cement blends up to 28 days. At all ages, the binary mixes containing either limestone or calcined sludge produced significantly lower strengths than the ternary blends. Majority of the strength gain in the binary 80-20-0 takes place at early ages. Calcined alum is known to be pozzolanic [10]. However, whilst reactive alumina influences setting time and rheology, their strength contribution is small [11] except in combinations with porosity modifying anions [12]. On the other hand, because the aluminate phase in cement clinker is small, the chemical reactivity of limestone is limited [4]. Therefore, cement replacement with limestone reduces the amount of hydration products formed, increase effective w/c ratio and hence reduction in strength at all ages. However, ternary limestone cement blends generally showed higher strengths comparable to plain CEM I at later ages and consistent with the observations from PFA and slag ternary blended cements [6, 7]. This could be attributed to the synergistic interaction between the extra aluminates provided by the sludge ash and the carbonates in the limestone powder. Aluminates react with carbonates to form carboaluminates instead of consuming ettringite to form monosulfoaluminate [8]. This means there is higher volume of hydrates as indicated by the bound water content (Figure 3). Consequently, porosity is reduced leading to higher strength.

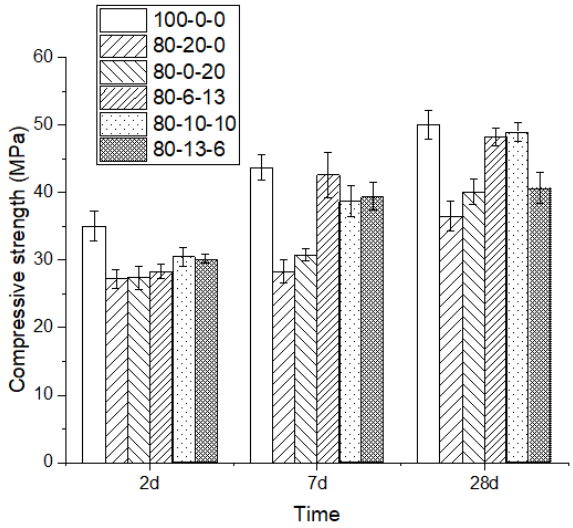

Figure 1. Strength development for sludge ash blended cements.

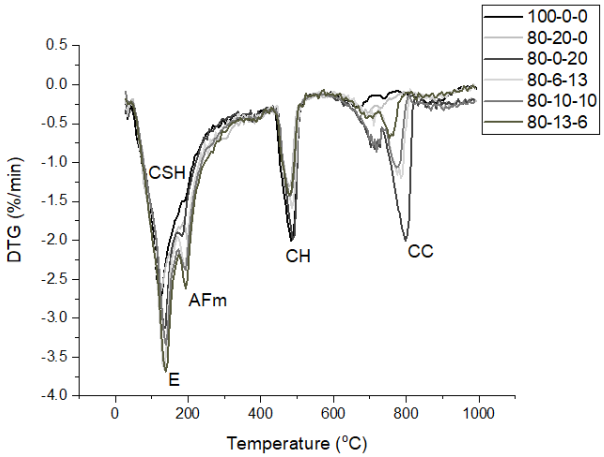

Figure 2. DTG curves for sludge ash samples at 28 days of hydration. . Cc – calcite, CH – portlandite, C–S–H – calcium silicate hydrate, E – ettringite

The DTG curves in Figure 2 show that the incorporation of calcined sludge leads to the formation of AFm phases: monosulfoaluminate and carboaluminates in the binary and ternary blends respectively. The reduction in portlandite and carbonate peaks with sludge ash addition is an indication of its reactivity in the respective blended systems. Figure 3 shows that the normalized portlandite content reduces with the addition of calcined sludge. While limestone powder participates to a limited extent in the cement hydration process, the incorporation of calcined sludge led to higher carbonate consumption, which declined at sludge ash additions higher than 6%. This could mean that the sludge ash consumes portlandite more rapidly at the expense of carbonates.

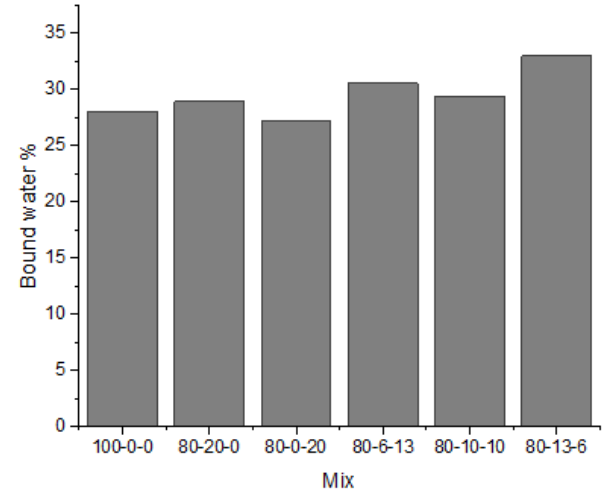

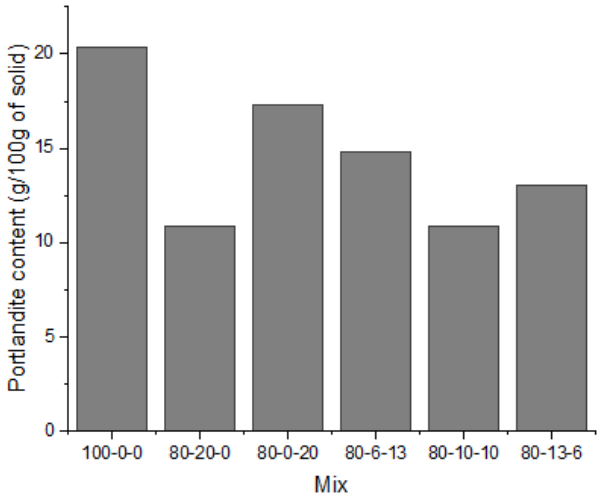

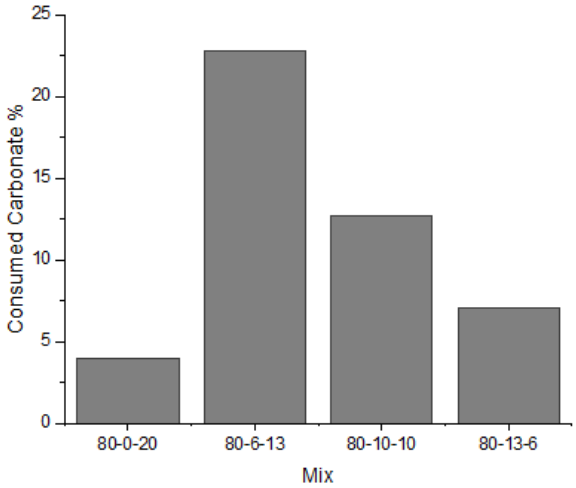

Figure 3. Bound water, Portlandite and consumed carbonate contents at 28 days of hydration.

The phases present in samples hydrated for 28 days have been identified by FTIR (Figure 4) and agree with those from TGA (**Figure 2)**. The O-H vibration at 3640cm^{-1} marks the presence of Portlandite [13]. The broad peak at 3410cm^{-1} is due to the vibration of H_2O in hydrating cement. Ettringite is stable if there are sufficient sulfate ions present in the system. In the pure CEM I paste, the characteristic peak due to the vibration υ3-SO_4^{2-} at 1120cm^{-1} indicates the presence of ettringite. This is supported by the presence of υ2-H_2O at 1675cm^{-1} assigned to the deformation of water in ettringite [14, 15]. In the binary 80-20-0 blend, additionally dissolved aluminates from the sludge converted ettringite to monosulfoaluminate as indicated by the disappearance of the ettringite and the emergence of the sharp Al-O peak at 525cm^{-1} and peak at 1120cm^{-1} respectively [13]. This is consistent with the XRD data in Figure 5.

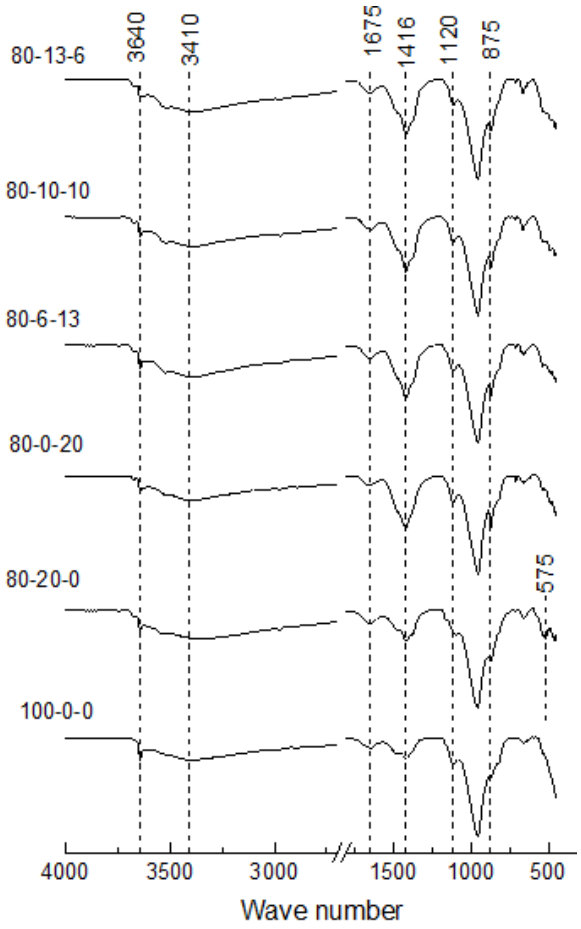

Figure 4. FTIR spectra of cement blends at 28 days of hydration.

In the pastes containing limestone powder, the monosulfoaluminate almost disappears and the ettringite peak at 1120cm^{-1} is reinforced. In the absence of gypsum, aluminates react with $CaCO_3$ to form monocarboaluminate and/or the lower carbonate content phase hemicarboaluminate. Monocarboaluminate is a more stable phase due to its insolubility at ambient temperature and this may be the reason why it is the observed in all limestone blends. The spectra of carboaluminates can be assigned on the basis of the carbonate ion being a planar tetra-atomic species with trigonal-D3h symmetry [15]. Monocarboaluminates are indicated by the υ3CO_3^{2-} (1416cm^{-1}) together with υ2-CO_3^{2-} (875cm^{-1}) and υ4-CO_3^{2-} (712cm^{-1}) [15]. Assignments of the spectra is consistent with XRD analysis (Figure 5).

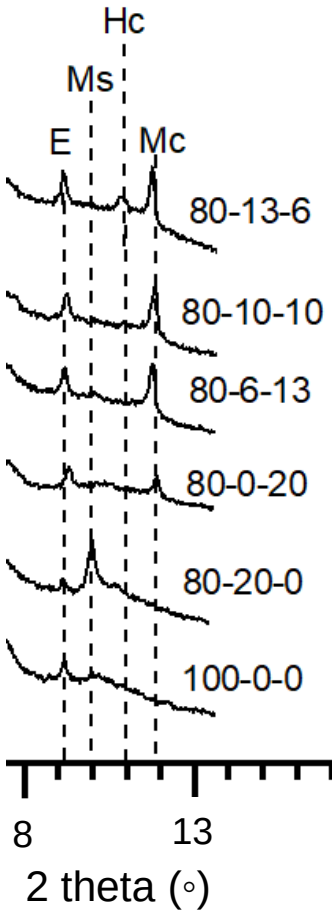

Figure 5. XRD for sludge ash samples at 28 days of hydration. Ms –monosulfoaluminate, E – ettringite, Hc – hemicarbonate, Mc – monocarbonate.

CONCLUSIONS

Calcined alum sludge was shown to be a viable substitute to conventional SCMs. At 28 days, coupled substitutions of the sludge ash and limestone produced higher performance than the individual contributions of each SCM.

XRD, FTIR and TGA showed that the presence of limestone leads to the formation of hemi- and monocarboaluminate instead of mono-sulphoaluminate hydrate and thus stabilizes ettringite. This leads to an increase in the volume of hydrates, reduction in porosity and increase in strength.

REFERENCES

[1] U.S. EPA, Drinking Water Treatment Plant Residuals. Management Technical Report. Summary of residuals generation, treatment and disposal at large community water systems, 2011, pp. 378.

[2] A.L.G. Gastaldini, M.F. Hengen, M.C.C. Gastaldini, F.D. do Amaral, M.B. Antolini, T. Coletto, The use of water treatment plant sludge ash as a mineral addition, Construction and Building Materials, 94 (2015) 513-520.

[3] H.M. Owaid, R. Hamid, M.R. Taha, Influence of thermally activated alum sludge ash on the engineering properties of multiple-blended binders concretes, Construction and Building Materials, 61 (2014) 216-229.
[4] D. Wang, C. Shi, N. Farzadnia, Z. Shi, H. Jia, Z. Ou, A review on use of limestone powder in cement-based materials: Mechanism, hydration and microstructures, Construction and Building Materials, 181 (2018) 659-672.
[5] B. Lothenbach, G. Le Saout, E. Gallucci, K. Scrivener, Influence of limestone on the hydration of Portland cements, Cement and Concrete Research, 38 (2008) 848-860.
[6] S. Adu-Amankwah, M. Zajac, C. Stabler, B. Lothenbach, L. Black, Influence of limestone on the hydration of ternary slag cements, Cement and Concrete Research, 100 (2017) 96-109.
[7] K. De Weerdt, K.O. Kjellsen, E. Sellevold, H. Justnes, Synergy between fly ash and limestone powder in ternary cements, Cement and Concrete Composites, 33 (2011) 30-38.
[8] T. Matschei, B. Lothenbach, F.P. Glasser, The role of calcium carbonate in cement hydration, Cement and Concrete Research, 37 (2007) 551-558.
[9] D. Damidot, B. Lothenbach, D. Herfort, F.P. Glasser, Thermodynamics and cement science, Cement and Concrete Research, 41 (2011) 679-695.
[10] M.A. Tantawy, Characterization and pozzolanic properties of calcined alum sludge, Materials Research Bulletin, 61 (2015) 415-421.
[11] H.F.W. Taylor, Cement Chemistry, 2nd ed., Thomas Telford1997.
[12] L. Zhang, F.P. Glasser, Hydration of calcium sulfoaluminate cement at less than 24 h, Advances in Cement Research, 14 (2002) 141-155.
[13] M. Horgnies, J.J. Chen, C. Bouillon, Overview about the use of Fourier Transform Infrared spectroscopy to study cementitious materials, in: C.A. Brebbia, A. Klemm (Eds.) Materials Characterization WIT Press2013, pp. 251–262.
[14] J. Bensted, S.P. Varma, Some applications of infrared and raman spectroscopy in cement chemistry. Part 3 - hydration of portland cement and its constituents, Cement technology 5(1974) 440-445.
[15] M.A. Trezza, A.E. Lavat, Analysis of the system 3CaO·Al2O3–CaSO4·2H2O–CaCO3–H2O by FT-IR spectroscopy, Cement and Concrete Research, 31 (2001) 869-872.

39th Cement and Concrete Science Conference
9-10th September 2019
University of Bath

Paper Number 027

Modelling chloride transport in cementitious materials at the atomistic scale

Khalil Ferjaoui, Fabien Georget and Karen Scrivener
Department of Material Science, Ecole Polytechnique Fédérale de Lausanne

ABSTRACT

Predicting the durability of concrete structures is a complex task that requires the quantification of a number of poorly understood phenomena. In the context of durability, chloride attack is the most common reason for steel rebars to corrode. Chloride ingress in cementitious materials is thought to be influenced, at the nanoscale, by the physical binding i.e. the adsorption of ions on the C-S-H surface. Nonetheless, most of the existing models fail to predict new experimental results, particularly when Supplementary Cementitious Materials are used [1]. Therefore, the proper quantification of the ionic transport in the C-S-H gel at different scales is necessary. The first step to compute the effective diffusion coefficient of chloride is to quantify the effect of the pore size on the diffusivity of all transporting ions. Monte-Carlo simulations will be used to correctly compute charge distributions nearby the surfaces. Afterwards, a Finite Element Method-based resolution of the nanoscopic Poisson-Nernst-Planck equations will be carried out for a system where interparticle forces cannot be neglected. Once the transport at the nanoscale is addressed, the influence of the microstructure at the micron-scale needs to be investigated since the connectivity and the tortuosity of the pore network add an extra barrier that affects the ionic transport. To that end, a microstructural model of the C-S-H needs to be developed in order to capture the contribution of the geometry of the pore network. In this presentation, the modelling approach is first developed for a porous calcite system.

1. INTRODUCTION

Chloride ingress in cementitious materials is the most common reason for steel to corrode especially when exposed to humid atmosphere and a source of chlorides such as seawater or deicer salts...Therefore, the proper understanding of ion diffusion mechanisms in hardened cement paste is of paramount importance for predicting the long-term durability of concrete structures. The transport of chloride ions in the pore network of cementitious material is a complex process which is affected by several underlying phenomena:(i) the chemical reactivity between the solid phases and the solution, (ii) the influence of the C-S-H surface on the ionic transport hydrates (mainly the C-S-H) at a nanoscopic scale and (iii) , at a mesoscopic scale, the morphology of the porous network (connectivity, tortuosity…).

It has been proved that chloride ions get involved in chemical reactions with monocarbo and monosulfo-aluminates in order to form Friedel's salt [2]. It is assumed that the formation of this salt is a permanent way to trap the chloride. X-ray Diffraction with Rietveld analysis for quantification shows the existence of a non-negligible amount of chloride which is, supposedly, physically bound in the C-S-H phase (Fig.1). Physical binding means that the ion is adsorbed on the surface of solid phases without actually getting trapped in covalent bonds. Therefore, a relevant question would be: Since the "physically bound" chloride ions are still part of the pore solution, how does the physical binding stop or at least delay the chloride ingress?

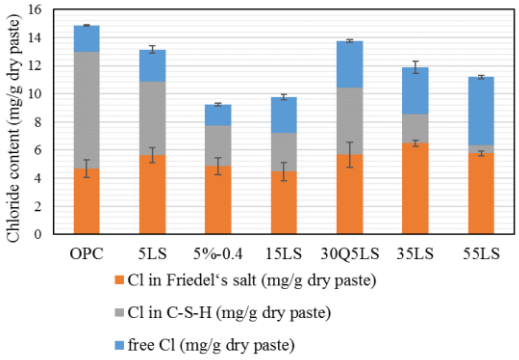

Figure 1. Total chloride proportions in various systems (LS=Limestone)

To answer this question, it seems inevitable to downscale to the atomic level where the fundamental interactions arise. In 1853, Helmholtz was the first to discover the formation of a layered structure which forms around a charged solid surface when it interacts with a fluid; the so-called Electrical Double Layer (EDL) (Fig.2). As a matter of fact, for cementitious systems, when the pore solution's pH goes beyond values of 12.5, the deprotonation of silanol groups of the C-S-H occurs. The degree of deprotonation goes up as the pH increases, thus charging negatively the surface of

the C-S-H. Counter-ions build up near the surface to neutralize the surface charge, and co-ions are depleted in this region due to Colombian repulsion.

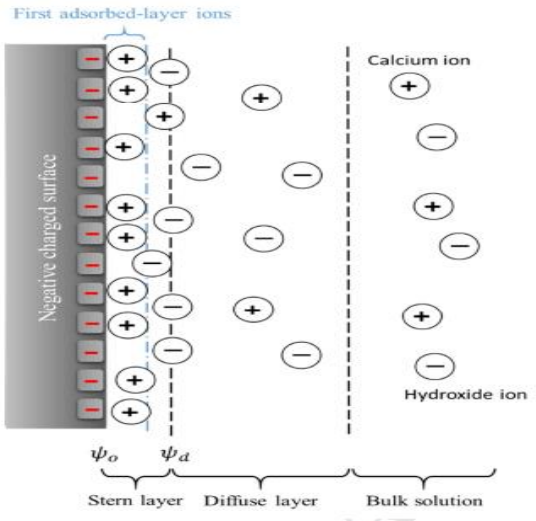

Figure 2. Schematic of the EDL [4]

In the case of C-S-H, it is the EDLs forming in gel pores (2~10nm) which are assumed to drastically attenuate the diffusivity of chloride anions and amplify that of cations in such a way that chloride gets "almost permanently" physically bound [3]. Nonetheless, a rigorous estimation of the diffusivity of different ions as a function of the pore size or the associated Zeta potential (ζ) are still an object of research.

Another critical point for the proper modelling of the nanoscale transport of chloride ions is a correct surface model for C-S-H. Even if good bulk models have been created recently [8], surface models is still an active research area. To avoid this problem, but still develop the methodology, we will focus on a porous calcite system which is better understood.

2. Modelling approach

2.1. The Classical Gouy-Chapman Theory

The Gouy-Chapman (GC) theory describes the EDL via the combination of the Poisson equation for electrical potential and the Boltzmann distribution of charge within an electric field next to a planar charged solid surface i.e. the Poisson-Boltzmann equation (eq.(1)). The usual system of equations for a multi-species system is written as follow:

$$\begin{cases} \Delta\Psi = -\frac{\rho}{\epsilon_0 \epsilon} \\ \rho = eN_A \sum_i z_i C_{b,i} \exp\left(\frac{-z_i e\Psi}{k_B T}\right) \end{cases} \quad (1)$$

where ε_o is the permittivity of free space, ε is the dielectric constant of the solution, ρ the charge distribution, e is the elementary electrostatic charge, N_A is Avogadro's number, z_i the valence of the species i, $C_{b,i}$ is the concentration in the bulk pore solution of i and k_B is the Boltzmann constant.

This approach treats ions as non-interacting point charges in the vicinity of a single-charged surface in contact with a bulk solution. Stern modified this theory by accounting for the finite size of ions, but the modified GC theory is still limited for modelling most of real systems. Torrie et al. [5] has indeed shown that in the case of systems with divalent counter-ions, the classical theory fails to predict correctly the potential profile even for low ionic strength and low surface charge. Nonetheless, many alternative theories to the GC exist, mainly molecular modelling techniques which are usually very accurate but also computationally costly.

In this work, the Monte Carlo method has been chosen in order to overcome the limitations of the GC theory.

2.2. Monte Carlo Method

For most adsorption studies, the grand-canonical ensemble is the natural statistical ensemble to use. In this ensemble, the temperature, volume and chemical potential are fixed but the number of the particles is allowed to fluctuate during the simulation.

Concerning the surface modelling of the calcite, the charge density has been estimated using the number of crystallographically defined functional groups. But the values varied substantially (from 0.5 to 10 sites/nm^2) depending on the physicochemical models chosen in the calculations and the chemical reactivity of the surface functional groups which can be substantially different from those in solution. Nonetheless, Lee et al. [6] used Resonant Anomalous X-Ray Reflectivity (RAXR) to provide an estimate of the upper limit to the effective surface charge density which is about -0.02 C/m^2.

The output of the Grand-Canonical Monte Carlo (GCMC) is the equilibrium number of ions which translates into the charge density distribution used for the computation of the mean electrostatic potential in eq.(2):

$$\Phi(z) = \frac{-e}{\varepsilon_0 \varepsilon} \sum_i q_i \int_z^\infty (t - z)\rho_i(t)\mathrm{d}t \quad (2)$$

where q_i is the charge of the ion i, ρ_i the charge distribution of the species i.

During the simulation, three types of moves were performed in order to reach the equilibrium configuration: (i) random displacement of one ion, (ii) the addition of an electroneutral pair of ions and (iii) the deletion of an electroneutral pair of ions. The decision of actually making one move or the other depends on a generated random number. It also

depends on the energy difference due to each one of the possible moves. In order to compute that shift, we consider three main energies to characterize the state of our system which are (i) the Coulombic ion-ion interaction and the interaction with the external charge distribution. The latter includes both the long-range interaction with ions outside the simulation box and with charged solid-phase walls.

Assuming that the pore solution is depicted by the primitive model, each ion is assigned a hard sphere radius r_i and a charge q_i. Therefore, the total energy at a fixed configuration writes as

$$U^{\text{conf}} = \sum_{i}^{N_o} v^{\text{ex}}(z_i) + \sum_{i<j}^{N_o} \nu_{i,j} \quad (3)$$

where N_o the number of ions, v_{ij} the ion-ion pair potential and v^{ex} is the energy produced by the external charge distribution calculated by the method of Torrie et al. [5].

3. Outlook

The implementation of the Metropolis algorithm for the Grand Canonical ensemble is ongoing. Once the charge distribution is determined with the GCMC and the mean electrostatic potential accordingly computed (eq.(2)), the numerical resolution of the Poisson-Nernst-Planck (PNP) equations (eq.(1)+eq.(4)) will be conducted with Finite Element Method (FEM). The transport of the *i*th species at the pore scale is indeed described by the following NP system:

$$\frac{\partial C_i}{\partial t} + \nabla \cdot \boldsymbol{J}_i = 0,$$

$$\boldsymbol{J}_i = -D_{i,0}\nabla C_i - D_{i,0}\frac{z_i e C_i}{kT}\nabla \psi, \quad (4)$$

where C_i is the concentration of ions i, $D_{i,o}$ the diffusion coefficient in free water, $\mathbf{J}_i$ the flux vector and z_i represents the valence.

Finally effective diffusivities (eq.(5)) at the nanoscale calcite will be calculated as depicted in [7]:

$$D_{i,e}^{\text{Micro}} = \frac{\int J_i \mathrm{d}S}{S} \cdot \frac{L}{\Delta C_i} \quad (5)$$

where L is the medium travelled length and ΔC_i the concentration difference that induces the gradient. Ultimately, it would be possible to plot the diffusivity of ions with respect to the pore size like in [4] for the case of C-S-H**.**

Nonetheless, recent results where the diffusivity of chloride [4] drops with the pore size can be criticized. In fact, Sterric and electrostatic effects are usually stronger as the pore size goes down. Indeed, the code under development is actually considering pores as finite structures where the pore solution is bounded by two walls rather than a semi-infinite spaces as suggested in eq.(2). This is an important point since electrostatic effects in gel pores take mainly place due to the overlapping of EDLs which usually doesn't occur in big pores (>= 50nm).

REFERENCES

[1] S. Sui et al., Developing a generic approach to durability: Factors affecting chloride transport in binary and ternary cementitious materials (Cement and Concrete Research, submitted 2018)

[2] U.Birnin-Yauri and F. Glasser, "Friedel's salt ca2al (oh) 6 (cl,oh) 2h2o: its solid solutions and their role in chloride binding" Cement and Concrete Research, vol. 28, no. 12, pp. 1713-1723, 1998

[3] Friedmann, H., Amiri, O., & Aït-Mokhtar, A. (2008). Physical modeling of the electrical double layer effects on multispecies ions transport in cement-based materials. *Cement and Concrete Research*, *38*(12), 1394-1400.

[4] Yang, Y., Patel, R. A., Churakov, S. V., Prasianakis, N. I., Kosakowski, G., & Wang, M. (2019). Multiscale modeling of ion diffusion in cement paste: electrical double layer effects. *Cement and Concrete Composites*, *96*, 55-65.

[5] Torrie, G. M., & Valleau, J. P. (1980). Electrical double layers. I. Monte Carlo study of a uniformly charged surface. *The Journal of Chemical Physics*, *73*(11), 5807-5816.

[6] Lee, S. S., Heberling, F., Sturchio, N. C., Eng, P. J., & Fenter, P. (2016). Surface charge of the calcite (104) terrace measured by Rb+ adsorption in aqueous solutions using resonant anomalous X-ray reflectivity. *The Journal of Physical Chemistry C*, *120*(28), 15216-15223.

[7] Yang, Y., & Wang, M. (2018). Pore-scale modeling of chloride ion diffusion in cement microstructures. *Cement and Concrete Composites*, *85*, 92-104.

[8] Kunhi Mohamed, A. (2018). *Atomistic Simulations of The Structure of Calcium Silicate Hydrates: Interlayer Positions, Water Content And A General Structural Brick Model* (No. THESIS). EPFL.

39th Cement and Concrete Science Conference **Paper Number 028**
9-10th September 2019
University of Bath

THE EFFECT OF ZINC ON ALITE AND CEMENT HYDRATION

A. E. Teixeira and K. Scrivener
Laboratory of Construction Materials, EPFL, 1015 Lausanne, Switzerland

ABSTRACT

In the next 30 years, concrete production is expected to increase. Due to its environmental impact and energy consumption, industrial wastes and by-products are increasingly used as partial substituents in Portland cement manufacture. On the other hand, replacing cement with SCMs induces low early age strength since SCMs are slow to react.

Recent work showed that introducing small amounts of zinc to C_3S causes a notable increase in reactivity, increasing the hydration of cement. As a result, this work studies this effect in an alite system composed of C_3S with minor amounts of Al_2O_3, MgO and Fe_2O_3. Different amounts of ZnO are added, and hydration is observed. The system is characterized by isothermal calorimetry, X-Ray diffraction (XRD) and scanning electron microscopy (SEM). Characterizations reveal a strong non-linearity effect of zinc on reactivity, leaving discussion on the underlying mechanisms. Results from this work will be translated into more applicable systems to see if zinc has the same effect.

An understanding of zinc's effect on cement reactivity is a key to better optimize the substitution of clinker which allows to reduce CO2 emissions.

1. INTRODUCTION

It is known that minor elements can have an effect on cement hydration and its properties. In the past few years, studies on this subject are focused on the effect of minor elements on cement reactivity, defining its threshold limits [1] [2]. However, it was not well documented what is the mechanism behind this effect.

Very different effects are observed at different concentrations. Therefore, in order to understand how do minor elements influence the hydration, alite systems were synthetized with different amount of Zinc oxide. X-Ray diffraction and PSD were used to characterize the unhydrated systems. The hydration kinetics were followed by isothermal calorimetry and SEM-EDX analysis.

2. MATERIALS AND METHODS

Four alites were synthetized following the method developed by Li et. al. [1] with different amounts of zinc, 0, 1, 3 and 5wt% (Table 1). The raw materials were mixed with distilled water in a milling jar for 24 hours and then dried in cylinder moulds. The dried mix was calcined at 1600 °C for 3 hours and the final product was grinded with the disc mill [3].

Table 1. Mix design.

Mass [g]	Alite	Alite 1wt%ZnO	Alite 3wt%ZnO	Alite 5wt%ZnO
CaO	350.18	350.14	350.14	350.16
SiO_2	133.11	133.11	133.14	133.12
Al_2O_3	3.65	3.66	3.68	3.67
MgO	5.80	5.80	5.78	5.83
Fe_2O_3	3.60	3.60	3.62	3.62
ZnO	0.00	5.01	15.34	26.11

The unhydrated alite was characterize with X-Ray diffraction (XRD) and particle size distribution (PSD).

The alite hydration was studied by isothermal calorimetry at 20 C with a w/c=0.5.

The hydrated products were characterized by scanning electron microscopy (SEM) with the BSE mode coupled with EDS at 1, 3, 7 and 28 days of age. The hydration process was stopped by immersion in isopropanol.

3. RESULTS AND DISCUSSION

3.1. Characterization of the alite powder

With the XRD analysis was possible to identify the type of polymorph of the alites (Figure 1). It is observed that all the alites are monoclinic (M) but

alite without and with 3% ZnO are M3 and with 5% ZnO is a combination of M1 and M3 structures.

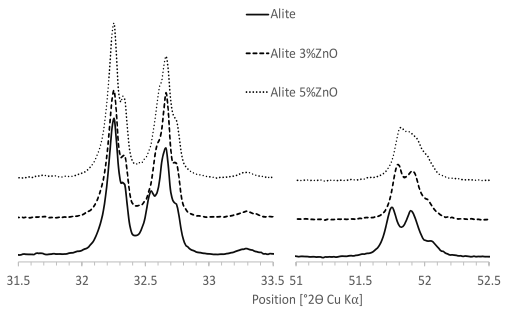

Figure 1. Identification of the polymorph by XRD.

The PSD results showed differences between the samples, even though the grinding was the same for all using the disc mill. The Dv_{50} is in Table 2, which increases with the Zn dosage.

Table 2. Particle size.

	Alite	Alite 1%ZnO	Alite 3%ZnO	Alite 5%ZnO
Dv_{50} [µm]	9.1	11.9	12.5	18.9

3.2. Characterization of the hydrates

Figure 2 shows the heat flow per gram of alite. With a dosage of 3% ZnO, the heat flow is enhaced almost by double. With 1% of zinc no big difference is noticed. This result was also observed by Bazzoni et. al. previously, who relates this with the needle length of the C-S-H. Longer needles are forming in the presence of zinc. It seems that 3% is the optimal dosage of zinc oxide in alite [4].

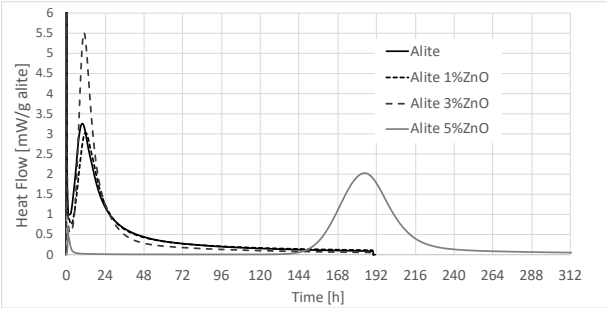

Figure 2. Heat flow for alite doped with Zinc (w/c=0.5).

With a higher ZnO dosage, the hydration of alite is seriously retarded. The main hydration peak occurs after 7 days. This is in accordance with earlier works as [5] , who explained this effect with the formation of a new phase. The consequence of this formation is that the concentration of Ca^{2+} and OH^- is kept low and the required supersaturation does not occur until the formation of $Ca(Zn(OH)_3)_2$. $2H_2O$ is completed [5].

The microstructure of alite with and without 3% of zinc at 1 day of hydration is shown in figure 3. More Hadley grains were seen in the system with zinc and also portlandite clusters. EDX analysis were done to check if the zinc is really incorporated in the alite grains. The results showed that effectively, zinc is incorporated.

a)

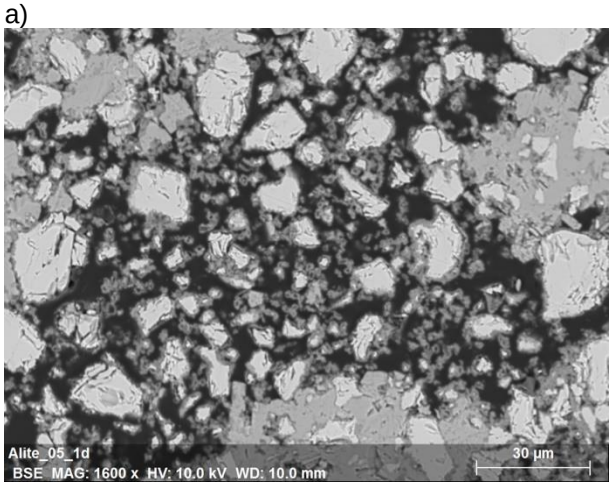

b)

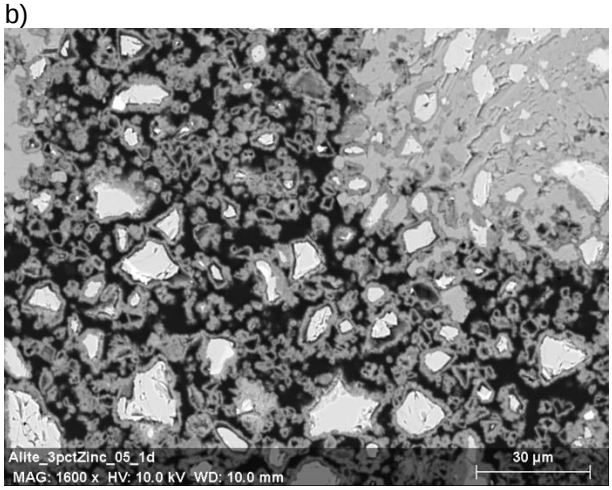

Figure 3. SEM images 1 day of hydration a) Alite b) Alite with 3% ZnO.

4. CONCLUSIONS

The effect of Zinc on alite hydration was investigated. Very different effects are obtained at different concentrations. A dosage of 1% is not enough to observe a big difference on the hydration kinetics. When 3% of zinc oxide is added, the heat release is increased almost by 50%. The opposite behaviour was seen for the system with 5%ZnO.

The EDX results confirm the presence of zinc in the alite grains. At 1 day of hydration, clusters of portlandite are forming in alite and in presence of 3% of zinc more Hadley grains are formed. The same study will be done for the 5%ZnO system to understand the retarding effect.

These dosages of zinc oxide will be studied in more applicable systems to observe if the same results are obtained.

REFERENCES

[1] Gineys, Aouad, Sorrentino, Damidot, 2011. Incorporation of trace elements in Portland cement clinker: Thresholds limits for Cu, Ni, Sn or Zn. Cement and Concrete Research, 41, 1177-1184.

[2] Soga, Merko, Hayashi, Uchida, 2017. Effect of minor elements on clinker mineral and cement hydration. Cement Science and Concrete Technology, 71 [1] 32-39.

[3]Li, Ouzia, Scrivener, 2018. Laboratory synthesis of C3S on the kilogram scale. Cement and Concrete Research, 108:201-207.

[4] Bazzoni, Ma, Wang, Shen, Cantoni, Scrivener, 2014. The effect of Magnesium and Zinc ions on the hydration kinetics of C3S. J. Am. Ceram. Soc., 97 [11] 3684-3693.

[5] Trezza, 2007. Hydration Study of Ordinary Portland Cement in the Presence of Zinc Ions. Materials Research, 10 [4] 331-334.

Atomistic simulation of cementitious phases

S.C. PARKER

Department of Chemistry, University of Bath, BA2 7AY, UK (s.c.parker@bath.ac.uk)

One of the key challenges for atom-level modelling studies of cementitious materials is in evaluating both the composition and structure as a function of external conditions, including the dependence on the amount of mineral phases present. I will present our work on how we are addressing these issues. Our approach is to combine electronic structure methods based with potential-based simulation techniques for modelling the bulk and interface phases. We begin with a potential based approach to screen different structures and the most stable are then modelled using DFT including van der Waals to allow us to explore the surface composition. I will illustrate these approaches by showing where we have applied them to a number of hydroxylated minerals, including hydrated calcium silicates. Finally, we apply potential based molecular dynamics and Monte Carlo simulations on the predicted surfaces of these materials to obtain interfacial structure and composition and their role on the material properties.

39th Cement and Concrete Science Conference
9-10th September 2019
University of Bath
Paper Number 030

A Study of PZT Sensors for Crack Detection in Reinforced Concrete

E. Tzoura, R. Vine, R.J. Ball and K. Paine
BRE Centre for Innovative Construction Materials (CICM), University of Bath

ABSTRACT

Over the past two decades structural health monitoring (SHM) of civil infrastructure using piezoceramic materials has received growing attention. The majority of studies carried out have focused on lead zirconate titanate (PZT). An important factor which influences the performance of these sensors is the distance from the defect, which is often a crack. Here we present the performance of PZT disc shaped sensors for SHM employing the electro-mechanical impedance (EMI) approach. The sensors were embedded in small scale reinforced concrete beams loaded in three-point bending and impedance measurements of the sensors were taken at various strain levels during the loading cycle. Sensor performance was assessed in relation to the distance from the cracks formed. Damage quantification was determined using the root mean square deviation (RMSD) index. The results indicate that the performance of the PZT material tested in this loading regime was significantly affected by the distance from the cracks. Differences in the range of 10mm were detected. The results demonstrate that when the distance from the crack is approximately 20mm the damage can be detected at an early stage and the damage level can be determined with very high precision. The research reported is part of a much wider programme of work aimed at developing a smart concrete system capable of self-sensing, diagnosing and healing cracks, and other forms of damage, without any need for human intervention.

1. INTRODUCTION

Over the past two decades structural health monitoring (SHM) for civil infrastructure has been a rapidly growing research field. As the vast majority of this infrastructure is constructed with reinforced concrete, numerous researchers have been focussing on damage detection of reinforced concrete elements and structures (i.e. Kim et al., 2007; Chang et al., 2003; Brownjohn, 2007; Talakokula et al., 2016). The use of lead zirconate titanate (PZT) transducers in combination with the electromechanical impedance method has been proposed by Liang et al. (1997) for structural health monitoring purposes and since then significant research has been carried out in damage detection of concrete structures employing the specific method (Park et al., 2001; Soh and Bhalla, 2005; Park et al., 2006). Even though several parameters that affect the performance of the PZT transducers have been investigated there is limited research concerning the influence of the distance of the PZTs from the damage (Tzoura et al., 2015).

In this study the influence of the distance between cracks and embedded PZT sensors for damage detection in reinforced concrete beams is investigated. The electro-mechanical impedance approach was employed for obtaining impedance measurements within a specific frequency range at various load/strain levels. Comparisons between the healthy state and the various strain levels were achieved calculating the root mean square deviation (RMSD) index as it is one of the most reliable damage indices

2. METHODOLOGY

The damage detection in this study was performed employing the electro-mechanical impedance (EMI) approach. Measurements of the impedance with respect to frequency were obtained at various strain levels during testing using an impedance analyser interface. The frequency range was between 50-400 kHz. Each PZT was utilised as both actuator and sensor.

3. TEST SPECIMENS

Four beams were cast from the same concrete batch with similar dimensions equal to 100 x 100 x 500 mm. In each beam two PZT transducers were embedded. The beams indicated as 20A and 20B were identical for repeatability reasons and the distance between the PZTs was equal to 20 mm. The beams 30A and 30B were also identical with distance between the PZTs being equal to 30mm. The arrangement of the PZTs is illustrated in Figure 1. The most significant electrical properties of the transducers are given in Table 1. The beams were reinforced with 8 mm diameter longitudinal steel and 3 mm diameter shear links (Figure 2).

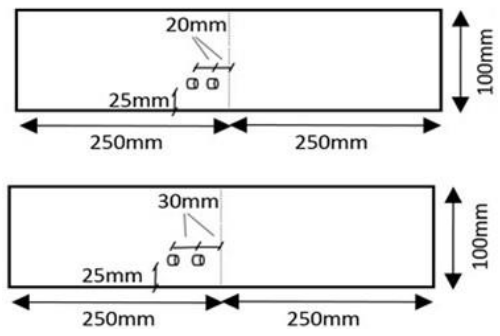

Figure 1. Schematic diagram of concrete beam showing the location of the embedded piezoelectric sensors

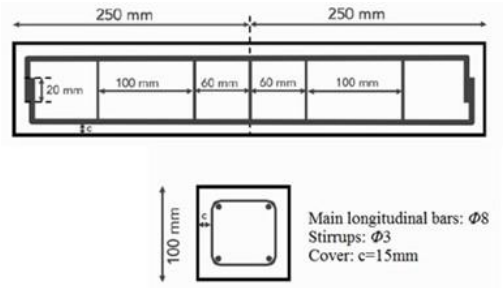

Figure 2. Schematic diagram of beam showing the location of the steel reinforcement

Table 1. Physical properties of the lead zirconate titanate (PZT) sensors

Property	Value
Density, (g/cm^3)	7.80
Electric Permittivity,	1750
Piezoelectric Strain Coefficient,(10^{-12} C/N)	-180
Elastic Compliance Coefficient, (10^{-12} m^2/N)	16.1
Elastic Compliance Coefficient, (10^{-12} m^2/N)	20.7
Dielectric Loss Factor, tanδ (10^{-3})	20

4. EXPERIMENTAL PROGRAMME

The beams were subjected to three-point bending. The external load was applied at a rate equal to 0.1mm/min. The experimental setup is illustrated in Figure 3. The final image of the beams after completion of the tests is presented in Figure 4.

Figure 3. Experimental set-up for three-point bending

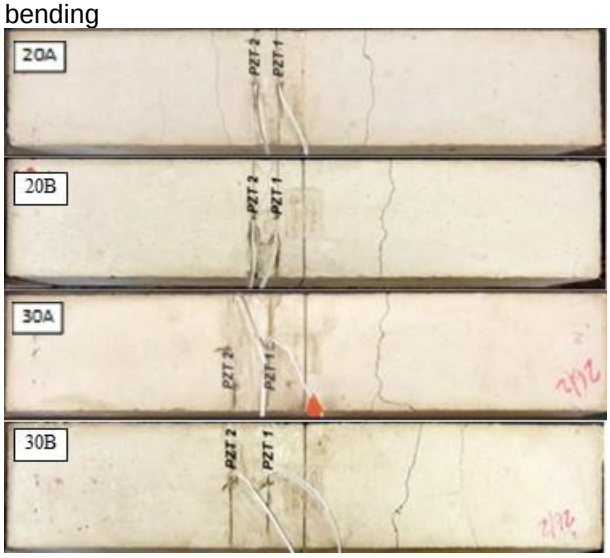

Figure 4. Image of beams at the end of the test showing the location of the PZT sensors and cracks

5. RESULTS AND DISCUSSION

The results obtained concern the load-displacement (Figure 5) and the impedance-frequency graphs for a range of frequencies between 135-260 kHz where the most significant variations were observed. An indicative impedance-frequency graph is illustrated in Figure 6. The variations of the impedance with the increase of strain level indicate the propagation of damage. The quantification of damage was achieved with the RMSD index (Figure 7) which is calculated according to equation (1).

$$RMSD = \left(\sqrt{\frac{\sum_{k=0}^{n} [V_0(\omega_k) - V_i(\omega_k)]^2}{\sum_{k=0}^{n} [V_0(\omega_k)]^2}} \right) \quad (1)$$

where n is the number of frequency points, V0(ωk) is the initial measurement of the voltage of the kth frequency point (undamaged condition) and Vi(ωk) is the measurement of the voltage at the ith displacement value of the kth frequency point. As damage propagates, the damage index should increase. Measurements of the impedance were obtained at five strain/damage levels. The results are presented initially for each specimen separately before comparisons are made.

20A: The trend of the RMSD values was similar for both PZT1 and PZT2. Furthermore, the difference between the RMSD values from both sensors was small. PZT2 exhibited a smoother increase, most probably as a result of being closer to a visible crack, specifically at a distance of 50mm away from it.

20B: Again, a similar trend was observed for the RMSD values of PZT1 and PZT2 – although there were some differences from the last measurement (at 18 kN). PZT2 may have exhibited a more accurate performance as a visible crack was formed next to its position. It is possible that the crack initiated at this point due to the presence of the sensor.

30A: Although the trend of the RMSD values was, again, similar for PZT1 and PZT2 – the actual RMSD values differed significantly. Again, for PZT2 the crack formed close to its position and may have been initiated due to its presence.

30B: For PZT1 a smoother performance than PZT2 was observed; if the first measurement (at 3 kN) is excluded. For PZT2 the RMSD index increased between the measurements from 3 kN to 7 kN then stayed almost constant for the remainder of the test.

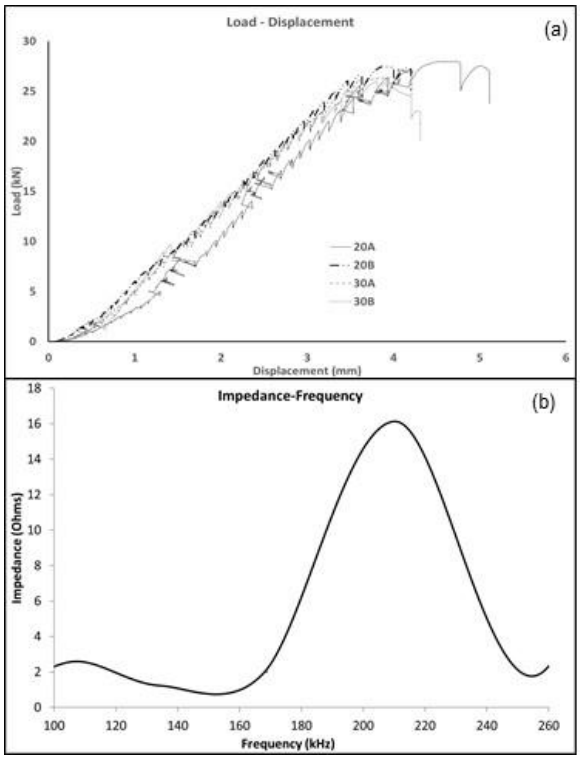

Figure 5. (a) Load – Displacement curves, (b) Indicative Impedance – Frequency graph

It is worth noting that although mid-span cracks were formed in all cases the major crack was formed at different locations as illustrated in Figure 4. In all cases the RMSD index starts from a value equal to 0.3-0.4 for loads between 1.5-11.5% of the maximum load. That indicates that the PZT material with the specific properties is sensitive enough to early stage damage detection. The high accuracy of this method is illustrated when the similarity of the RMSD index values for the PZT1 and PZT2 sensors within specimens 20A and 20B are considered. Repeatability is indicated since the PZT2 exhibited exactly the same trend in specimens 30A and 30B.

Concerning the comparison of the values between PZT1 and PZT2 for the five damage stages and for each specimen, the difference is presented in table 2 by taking into account the absolute value of the subtraction of the RMSD values of PZT1 and PZT2.

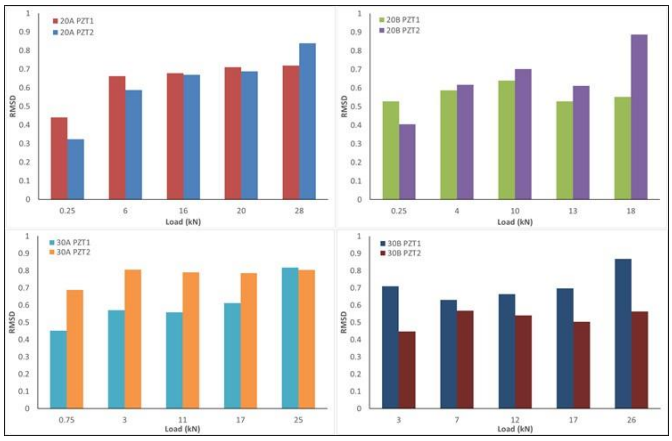

Figure 6. Root mean square deviation (RMSD) index values for PZT1 and PZT2 in specimens 20A, 20B, 30A and 30B at loads of 2, 7, 12, 17 and 26 kN

Table 2. Root mean square deviation (RMSD) variation between PZT1 and PZT2 (%)

Damage Stage	Specimen			
	20A	20B	30A	30B
1	11.7	16.6	23.6	26.2
2	7.4	12.2	23.5	6.3
3	0.7	2.8	23.2	12.3
4	2.2	6.2	17.3	19.3
5	11.9	33.4	1.4	30.5

It can be observed that for the beams 20A and 20B the difference between the RMSD values of PZT 1 and PZT2 was significantly lower than for the beams 30A and 30B. More specifically, for 20A the difference ranged between 0.8% - 11.9% while for beam 20B it was limited to below 16.6%; apart from damage stage 5 which increased to 33.4%. However, when the distance between the two transducers was equal to 30 mm the RMSD index values for 30A were all higher than 17.3%; apart from damage in stage 5.
Similarly, for 30B apart from damage level 2 the difference in RMSD values was higher than 12.3%.

6. RESULTS AND DISCUSSION

In this study the damage detection sensitivity of PZT transducers embedded in reinforced concrete

beams has been evaluated. One pair of sensors was placed 20 and 40 mm from the mid span, and a second pair of sensors was placed 30 and 60 mm from the midspan. The results indicate that distances of 10 mm from the nearest visible crack can have a significant effect on the results of the RMSD values with variations higher than 10% for most of the measurements as indicated in Table 2. However, more experimental data of the impedance variations will be required from other types of structural elements (i.e. slabs) and different experimental setups (i.e. elements subjected to fatigue load, axial compression, etc.) in order to further confirm the conclusions concerning both the accuracy of the results and the quantification of the influence of the distance on them. The values of Table 2 provide evidence that the sensitivity of the specific PZT transducers is significantly affected when placed 10 mm further from the damage area as stated in the previous section.

It is also probable that the size of the specific transducers is large enough in comparison to the beams' size as the size effect is significant enough in structural health monitoring applications. In future applications it would probably be better either to increase the size of the specimens or employ sensors of smaller sizes to avoid the initiation of damage at the position where the sensors are placed.

ACKNOWLEDGEMENTS

The authors gratefully acknowledge the support of EPSRC through the programme grant, Resilient Materials for Life (RM4L), reference: EP/P02081X/1. The authors would also like to thank the technicians William Bazeley and Martin Naidu for their invaluable help.

REFERENCES

Brownjohn, J. M., 2007. Structural health monitoring of civil infrastructure. Philosophical Transactions of the Royal Society of London A: Mathematical, Physical and Engineering Sciences, 365 (1851) 589-622.

Chang, P. C., Flatau, A. and Liu, S. C., 2003. Health monitoring of civil infrastructure. Structural health monitoring, 2 (3) 257-267.

Kim, S., Pakzad, S., Culler, D., Demmel, J., Fenves, G., Glaser, S. and Turon, M., 2007. Health monitoring of civil infrastructures using wireless sensor networks. Proceedings of the 6th international conference on Information processing in sensor networks, Cambridge, Massachusetts, USA, April, 2007 (ACM) 254-263

Liang, C., Sun, F. P. and Rogers, C. A., 1997 Coupled electro-mechanical analysis of adaptive material systems-determination of the actuator power consumption and system energy transfer. Journal of intelligent material systems and structures, 8 (4) 335-343

Park, G., Cudney, H. H. and Inman, D. J., 2001. Feasibility of using impedance-based damage assessment for pipeline structures. Earthquake engineering & structural dynamics, 30 (10) 1463-1474.

Park, S., Ahmad, S., Yun, C. B., & Roh, Y., 2006. Multiple crack detection of concrete structures using impedance-based structural health monitoring techniques. Experimental Mechanics, 46 (5) 609-618

Soh, C. K., & Bhalla, S., 2005. Calibration of piezo-impedance transducers for strength prediction and damage assessment of concrete. Smart materials and structures, 14 (4) 671.

Talakokula, V., Bhalla, S., Ball, R. J., Bowen, C. R., Pesce, G. L., Kurchania, R., Bhattacharjee, B., Gupta, A. and Paine, K., 2016. Diagnosis of carbonation induced corrosion initiation and progression in reinforced concrete structures using piezo-impedance transducers. Sensors and Actuators A-Physical, 242 79-91.

Tzoura, E. A., Triantafillou, T. C., Providakis, C., Tsantilis, A., Papanicolaou, C. G., and Karabalis, D., 2015. Damage detection of reinforced concrete columns retrofitted with FRP jackets by using PZT sensors. Structural Monitoring and Maintenance, 2 (2) 165-180.

39th Cement and Concrete Science Conference
9-10th September 2019
University of Bath
Paper Number 034

The Behaviour of Self-Compacting Concrete with Ultra-Fine Fly Ash

B. K. T. Kandie
Abdul Mullick Associates Limited, Consulting Engineers
Department of Civil and Structural Engineering, University of Sheffield

K. Pilakoutas
Department of Civil and Structural Engineering, University of Sheffield

ABSTRACT

This paper outlines laboratory study on Ultra-Fine Fly Ash (UFFA) self-compacting concrete. Self-Compacting Concrete (SCC) has grown significantly in the resent years due to tightening health and safety regulation and good concrete practice. High cement contents and volumes of admixtures required for satisfactory SCC make it uneconomical. The test results of Ultra-Fine Fly Ash application achieve the required workability and coherent for SCC with low cement contents and with 0% - 0.2% admixtures. UFFA concrete displays both high workability and stability with as low as 0.2 and that UFFA is significantly more economical than other forms of SCC.

1. INTRODUCTION

The development of Self-Compacting Concrete SCC originated in Japan in 1980s, following the chronic reduction of skilled workers in the construction industry, which lead to a reduction in the quality of construction works. The achievement of durable concrete structures without the dependency on the quality of construction work was the employment of self-compacting concrete, which can be compacted into the confined zones of reinforcement bars and every corner of complex formwork by mean of its own weight and without the need for vibrating compaction was the solution to adopt for this problem. In 1986, Okamura and Ozawa proposed this type of concrete and the methods to achieve self-compactability of fresh concrete: with limited aggregate content; low water-powder ratio and use of superplasticizer [1].

A major driving force encouraging the use of SCC is the impending European Health and Safety Directive covering hand-arm vibration [2]. However, SCC also has implications for traditional large concrete pour and post-tensioning placement where its uniform strength development may benefit the stressing procedure and reduce cracking. In addition, with SCC the associated reduction in labour and plant reduce cost and improve Quality Assurance QA procedures as the sample test cubes are more representative of in-situ concrete than vibrated normal workability cubes.

2. INTRODUCTION

The aims of this research were to optimise UFFA concrete mixes to maximise workability and cohesion and achieve self-compacting at low water cement ratios; characterize the UFFA powder, fresh, hard engineering and durability performance of UFFA concrete in comparison to concrete made with OPC, a range of UK fly ashes and Micro Silica.

The objectives that were defined are as follows:

1. To assess the effects of UFFA on water demand of concrete.
2. To optimize the aggregate grading used in combination with flowing concrete paste to create cohesive flowing UFFA concrete
3. To minimize the cement content used in very high performance self-compacting UFFA concrete mixes.
4. To compare the economic and performance of UFFA self-compacting concrete mixes with concrete made with other cementitious materials of equal proportions.

3. MATERIALS AND METHODS

3.1. Materials

The cement was Blue Circle Ordinary Portland Cement confirming to BS 12 1996, class 42.5 N/mm^2. Seven UK Class F fly ashes conforming to BS 3892, Part 1: 1997. Micro Silica was aqueous slurry (50/50 by weight) conforming to ASTM 1240: 1999, Ground Granulated Blast furnace Slag conforming to BS6699: 1992 and UFFA used a commercially available Class F fly ash confirming to BS 3892: Part 1: 1997. The chemical compositions

are shown in Table 1. The aggregates were 5 and 10 mm river aggregates and sand conforming to BS 812: 1985, the sieve analysis is shown on Table 2. A Polycarboxylate Polymer water-reducing superplasticizer conforming to BS 5075: Part 3 was used. Figure 1 shows the various Class F ashes researched on.

Table 1. Chemical Properties of the cementitious materials used

PERCENTAGE COMPOSITION											
Chemcal composition			**UK BS 3892 Part 1: PFAs**								
Oxides	**OPC***	**UFFA**	**1**	**2**	**3**	**4**	**5**	**6**	**7**	**MS***	**GGBS***
Silica diaxide (SiO_2)	20.7	53.4	55.1	53	54.3	55.6	48.6	51.2	50.6	92	35.84
Aluminium oxide (Al_2O_3)	5.7	32.3	25.1	25.1	23.1	25	24.6	26.1	26.1	1	13
Ferric Oxide (Fe_2O_3)	2.3	4.09	10.7	10.2	9.2	10.4	13	7.8	9.4	1	0.55
Calcium oxide (CaO)	64.8	5.05	1.6	3.8	4.1	1.9	2.8	6.4	3.7	0.3	39.53
Magnesium oxide (MgO)	1.1	1.29	1.5	2	2	1.6	1.7	1.9	2.2	0.6	8.28
Sodium Oxide (Na_2O)	0.19	<0.05	0.4	0.2	0.2	0.4	0.4	0.4	0.5	0.3	0.35
Potassium oxide (K_2O)	0.6	0.08	0.1	0.2	0.1	0.2	0.1	0.1	0.2	0.8	0.5
Sulphate (So_3)	3.21	0.32	1.2	0.9	1.4	1.1	1.3	1.4	1.3	0.3	0.1
Equivalent alkali	0.58	0.1	0.47	0.27	0.27	0.53	0.47	0.47	0.63	0.83	0.68
Titanium oxide (TiO_2)	-	1.97	1	1.2	1	1.1	1.1	1.6	1.2	-	-
Loss of Inginition (LIO)	0.92	0.23	3.1	4.9	5.8	2.5	6.1	3.3	4.7	-	-
*Provied by the manufactures											

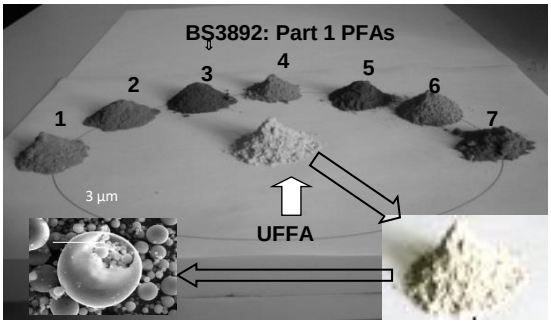

Figure 1. UFFA and various types of UK PFAs

3.2. Curing conditions

The curing conditions used are listed in Table 3.

Table 3. Curing environments

Curing Environment	Conditions
E1	Water, 23°C
E2	Air, 23°C, 65% RH

3.3. Particle distribution analysis

A laser Malvern Mastersizer E was used to measure the particle size and surface area of the various pozzolans and cementitious materials. The particle distribution analysis is shown on Table 4 of Figure 1 samples.

3.4. Determination of water demand

This test was undertaken in accordance to BS 3892: Part 1: 1993. Fine, medium and coarse sand was mixed in accordance to BS EN 196: Part 1: 1987.

Table 2. Aggregate Sieve Analysis

SIEVE SIZE (mm)	% PASSING BY MASS	
	5-10mm	Sand
28	100	100
20	100	100
14	100	100
10	99.4	100
6.3	42.6	100
5	15.2	98.6
2.36	6.2	85.5
1.18	-	76
0.6	-	62.1
0.3	-	17
0.15	-	3.7
0.075	-	0.1

3.5. Self-compacting concrete rheology

These methods were employed to test the fresh concrete rheology.

3.5.1. Slump test and Slump flow test

This test was used on stiffer mixes.

Where the concrete displayed a significant fluidity, it was tested using the slump test. A 600mm spread was selected to be the lower boundary for SCC and those mixes had excessive segregation or bleeding at this stage were rejected.

Table 4. Mineral admixture lazar particle properties.

Cementitious Materials	Sp. Surface Area Area m^2/kg	Carbon Content (%)	Fineness >45(µm)	Particle Diameter D[v.0.1]	D[v,0.5]	D[v,0.9]	Span
UFFA	2,893	0.23	0	0.4	2.32	5.28	2.1
PFA1	715	3.1	6.5	1.5	8.47	36.81	4.17
PFA2	359	4.9	11.1	3.37	15.82	46.33	2.72
PFA3	509	5.8	10.1	2.14	12.18	44.56	3.48
PFA4	681	2.5	6.3	1.58	9.2	36.5	3.8
PFA5	448	6.1	14.3	2.43	19.97	52.1	3.32
PFA6	499	3.3	9.3	2.24	12.79	42.91	3.18
PFA7	340	4.7	14.2	3.65	15.28	52.19	23.1
MS*	4,952	-	0	0.25	1.02	22.27	2.8
GGBS*	1,448	-	0.5	0.9	6.64	19.52	
* for comparison							

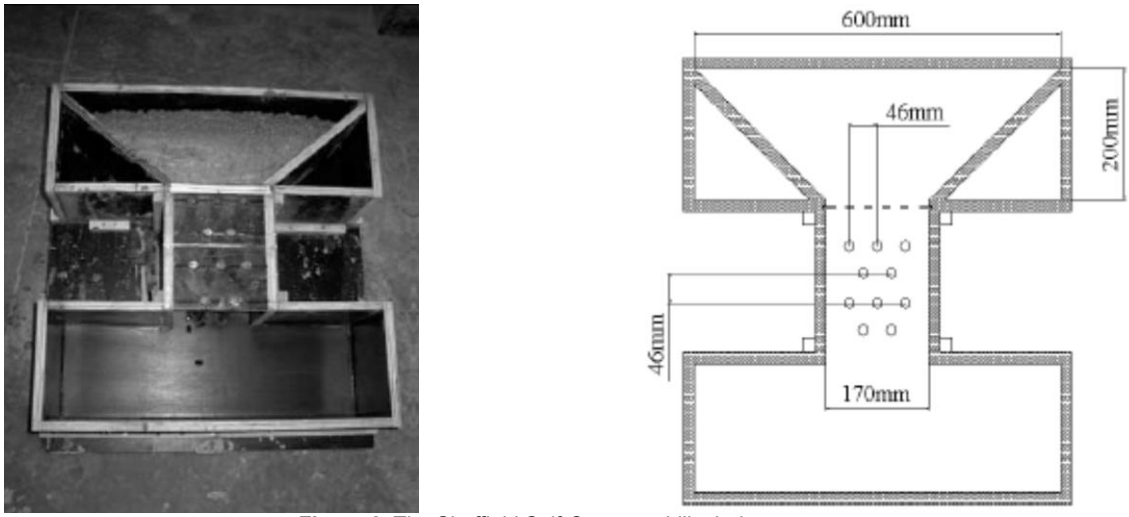

Figure 2. The Sheffield Self-Compactability Index test

3.5.2. Sheffield self-compactability index test

The Sheffield Self-Compactability Index (SSCI) test, Figure 2, was developed as part of this research. The top funnel section of the apparatus is filled with concrete then a gate removed, which allows the concrete to flow down a shallow slop through a throat which is heavily congested with rebar. A comparison of the results obtained using the slump test and the SCCI test led to the conclusion that Self-Compactability of 600mm flow correspond to the concrete flow to touch the four corners of the lower reservoir when the SSCI apparatus was inclined at 15° to the horizontal. SSCI was found to be very sensitive to lack of cohesion in SCC mixes than the slump flow. Visual observation showed aggregate "balling" in the SSCI throat in some instances and therefore a further restriction on SCC acceptance was imposed of zero segregation in the SCCI test.

Table 5. Summary of the Proportions used during the development of SCC with 30% UFFA

	MIX PROPORTIONS (KG/M^3)										
MIX					AGGREGATE			SP		Flow	SSCI
CODE	OPC	UFFA	WATER	W/B	10mm	Fines	Total	(%Cem)	Total	(mm)	TEST
Trial 1	218	93	140	0.45	1179	786	1965	0.5	2416	600	X
Trial 2	218	93	140	0.45	1100	864	1964	0.5	2415	560	X
Trial 3	187	80	120	0.45	1173	885	2058	2	2445	450	X
Trial 4	233	100	150	0.45	1055	863	1918	0.25	2401	580	X
Trial 5	249	107	160	0.45	1029	842	1871	0.3	2387	640	✔
UFFA1	249	107	160	0.45	1029	842	1871	0.3	2387	650	✔

Table 6. Summary of the mix proportion used to develop mix 30% UFFA2

	MIX PROPORTIONS (KG/M^3)										
MIX					AGGREGATE			SP		Flow	SSCI
CODE	OPC	UFFA	WATER	W/B	10mm	Fines	Total	(%Cem)	Total	(mm)	TEST
Trial 6	420	180	120	0.2	962	787	1749	2	2481	720	X
Trial 7	420	180	120	0.2	962	787	1749	1.5	2415	710	X
UFFA2	420	180	120	0.2	962	787	1749	1	2387	710	✔

4. RESULT AND DISCUSSIONS

Table 5 and 6 shows the SSCI for all the trials SCC mixes with 30% UFFA partial replacement of cement cast with 0.45 w/b ratio and 0.2 w/b ratio. These UFFA mixes were stable throughout the testing procedure and the rheology testing showed that UFFA displaying an excellent degree of cohesion as shown on Figure 3. Cutting through a cylinder of UFFA1 confirmed the cohesivity of the mix, with excellent aggregate distribution throughout the sample and no bleeding or laitance.

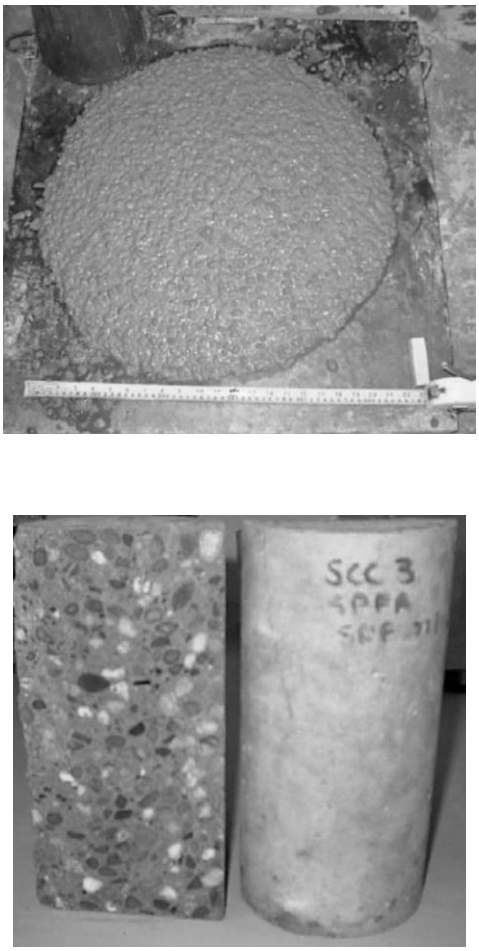

Figure 3. UFFA1 mix after a slump flow test and the aggregate distribution in hardened sample

UFFA has proven to be extremely effective in making self-compacting concrete. Indeed, when the total binder contents used in this study to make 0.45 w/b ratio SCC are compared with those from other worldwide studies, it can be seen that the use of UFFA resulted in SCC with binder content of 105-270 kg/m^3 lower than that used in comparative studies around the world.

5. CONCLUSIONS

1. UFFA has been shown to be suitable for low cementitious content, extreme cohesive, self-compacting concrete at water-binder ratios 0.2 and 0.45.
2. 30% replacement of UFFA for cement has been found to be the optimum replacement level.
3. UFFA usage in SCC remarkably lowered the cementitious content is up to 280 kg/m^3 than other SCC concretes made with conventional materials.
4. Virtually zero segregation or bleeding and extremely high cohesiveness and flow characteristic are observed in SCC made with UFFA.
5. The SSCI test has shown to be more sensitive to the tendency for SCC mixes to segregate than the slump-flow test and has been adopted as a second check on SCC developed at The University of Sheffield.
6. UFFA Self-compacting concrete mixes may be considerably more durable than similarly proportioned concrete mixes made with other alternative cement replaced materials

REFERENCES

1. Okamura H and Ouchi M, 2003, Self-compacting Concrete, Journal of Advanced Concrete Technology, Vol. 1. No. 1, page 5-15.
2. Internet source, www.britishsafetycouncil.co.uk/safetymanagement/news/vibration.htm, visited 10/07/2018.
3. British standards Institution. Pulverised –fuel ash cementitious component in cement. BS 3892: Part 1, BSI, London, 1997.
4. British standards Institution. Testing Aggregates: BS 812, BSI, London, 1085.
5. British standards Institution. Concrete admixtures, Specification for superplasticizing admixtures, BS 5075, BSI, London, 1985.
6. British standards Institution. Testing Aggregates: Part 102, Methods for determination of slump, BSI, London, 1983.
7. British standards Institution. Testing concrete: Part 111, Methods of normal curing of test specimens (20°C method), BSI, London, 1983.
8. British standards Institution. Testing concrete: Part 116, Methods of determination of compressive strength of concrete cubes, BS 1881, BSI, London, 1983.

39th Cement and Concrete Science Conference
9-10th September 2019
University of Bath
Paper Number 036

Microstructural analysis of cement-based mortars combining X-ray microtomography, XRD and FTIR

Travincas, R[1]; Flores-Colen, I[2].; Pereira, M.F.C. [3]; Maurício, A. [3]; Torres, I. [4]

[1]Research fellow IST, University of Lisbon, PhD student at University of Coimbra, rafaeltravincas@gmail.com
[2]CERIS, DECivil, IST, University of Lisbon, ines.flores.colen@tecnico.ulisboa.pt
[3]CERENA, DECivil, IST, University of Lisbon, mfcp@tecnico.ulisboa.pt
[4]ADAI/LAETA, DECivil, University of Coimbra, itorres@dec.uc.pt

ABSTRACT

The variability of the internal structure of cement-based coating mortars (conventional, industrial or innovative) makes complex the analysis and comparison of the various properties. In this sense, the use of advanced characterization and diagnostic techniques can contribute to a better analysis of the compositional and microstructural properties of these mortars, and to the establishment of the most relevant performance parameters. In this work, the application of X-ray computerized microtomography (MicroCT) to characterize the properties of cement-based mortars on specimens is discussed. Also, the combination of MicroCT with other techniques is considered, such as X-ray diffraction (XRD) and infrared spectroscopy by Fourier transform (FTIR). With the support of those techniques, we intend to access the porous structure of cement-based mortars and the mortar-substrate interface in terms of the quantity, shape, dimension and connection of the pores, and on the binder/aggregate interaction. Complementary techniques enable us to understand the compositional evolution and reactional mechanisms involved in the curing process. The proposed methodology is based on the suitability of each of the microstructural characterization techniques and their potential for the interpretation of mechanical and physical performance tests currently carry out on laboratory testing of cement-based mortars at hardened state.

1. INTRODUCTION

With the discovery of the great contribution of X-ray Computed Tomography in the medical area, several studies were started with the objective of applying the technique in the industrial field. The possibility of visualization of materials such as wood, polymer, ceramics and archaeological objects increased the study of the performance of X-ray Computed Tomography in materials with bigger attenuation such as concrete, mortars, steel, metals, among others. X-ray technology enables the development of faster, non-destructive, and three-dimensional assay methods for material analysis. (Braz et al., 1998; Mendes, 2010; Ketcham and Carlson, 2007). This non-destructive technique has been expanded to the field of cement-based materials and with this, it becomes possible the internal visualization without the need of causing damages to the pieces under study. (Mendes, 2010).

The increasing interest in new formulations of more sustainable cement-based materials, have led to a deepen knowledge need of microstructure characterization, including a more complete analysis of physical, structural, mechanical, chemical and mineralogical properties (Hanke, 2016; Cnudde and Boone, 2013; Stock, 2008; Bogas et al, 2012).

To perform a study of this nature, advanced laboratory techniques such as computerized microtomography of x-rays, XRD and FTIR are used. These techniques in combination with other observations allow obtaining detailed information about the solid and porous structure of the mortars and the results aid in the analysis of their behavior. Each one of the techniques has a certain range of applicability and some limitations, being necessary to combine different techniques to describe the microstructure in detail. (Gominho, 2016).

2. DESCRIPTION OF METHODS OF ANALYSIS

2.1. X-RAY COMPUTED MICROTOMOGRAPHY (MICROCT)

X-ray Computed Microtomography (MicroCT) is a non-destructive test technique that allows observing the internal structure of solid objects. The micro prefix indicates that the resolution is in the order of micrometers. This technique has application in the study of cement-based materials, because it allows the characterization of its internal components, its porosity and evaluation of the development of

cracks. (Teixeira, 2017; Ketcham and Carlson 2007; Cnudde and Boone, 2013; Stock, 2008; Kerckhofs et al., 2008; De Witte et al., 2008; Maurício et al., 2010; 2013).

MicroCT is based on the interaction of the X-rays with the solid matter of the sample. When the X-ray beam passes through the material, the material undergoes an attenuation, the intensity of which depends on the density and atomic number of the material. We use a mathematical algorithm to compose a three-dimensional image and make possible the analysis of the sample in question. As potentialities of the computerized x-ray microtomography technique can indicate the ability to analyze the three-dimensional spatial distribution of components, the possibility of repetition of the tests, considering that they are not destructive, analysis of the interior of the sample making possible the detection of defects, evaluation of the porosity of the materials and the evaluation of the development of cracks. The limitation of this technique is not applicable to materials opaque to the x-ray, samples with very small size, the resolution of the image is limited and has the need to use complementary techniques for analysis of chemical and mineral composition.

The 3D visualization of the samples by means of MicroCT allows to analyze the volumetric content of voids in samples of mortar or concrete, helps to obtain a better understanding of fractures and mechanisms of failure in the meso-scale, allows the quantification of the damages by the variation of the fraction of volume of cracks and voids, is able to determine the compactness, enable the distinction of the constituents through the compactness and measure the amount of the binder. (Teixeira, 2017; Ketcham and Carlson 2007; Cnudde and Boone, 2013; Stock, 2008; Kerckhofs et al., 2008; De Witte et al., 2008; Maurício et al., 2010; Bogas et al., 2012; Maurício et al., 2013).

2.2. INFRARED SPECTROSCOPY WITH FOURIER TRANSFORM (FTIR)

Fourier Transform Infrared Spectroscopy (FTIR) is a technique that seeks to identify the organic materials and most inorganic materials. This technique measures the absorption of the sample's UV radiation relative to the wavelength. When a material is irradiated with infrared radiation, the absorbed IR radiation generally excites molecules to a higher vibratory state. Soon, the wavelengths that are absorbed are characteristic of its molecular structure. The FTIR spectrometer uses an interferometer to modulate the wavelength from an infrared source. A detector measures the intensity of transmitted or reflected light as a function of its wavelength. The signal is analyzed by means of the Fourier transform and thus a single-beam infrared spectrum is obtained. FTIR spectra are usually presented as graphs of intensity in function of wave number (cm-1). The intensity can be plotted as the percentage of light transmittance or absorbance at each wave number. (Gominho, 2016; Hanke, 2016).

As potentialities of the FTIR technique, the capacity of qualitative and quantitative analysis, the possibility of determination of the mineralogical composition of the sample and the identification and structural analysis of organic substances can be perceived. FTIR complemented XRD analysis enabling the identification of low crystallinity or amorphous products generated by cement reactions. As a limitation, it is pointed out that the conditions of the medium around the equipment can cause variations in the spectrum, the technique sensitive to the presence of functional groups, complex mixtures produce overlapping of spectra that can lead to misinterpretations, difficulty analyzing aqueous solution and inability to detect monatomic entities and diatomic molecules.

2.3. X-RAY DIFFRACTOMETRY (XRD)

X-ray diffraction (XRD) is a technique commonly used to identify minerals. The interaction between the crystalline matter and the X-radiation gives rise to a dispersion, which is caused by the internal arrangement of the crystalline matter. The technique can be used in structural or non-structural constructive elements and must be performed in the laboratory and this is a non-destructive test. There are different ways of applying the XRD, depending on the type and object being studied, the most used in the identification of crystalline solid materials is the powder method. X-ray diffraction is based on the placement of the sample on a flat sample holder which is rotated about an axis. The X-ray beam, produced by an X-ray source, is collimated by a system of windows, until it strikes the sample that diffracts it in directions that comply with Bragg's law. The diffracted beam is then collimated by another set of slits until it enters a radiation counting system, which sends the information to a computer that shows the diffractogram record of the sample. (Fontes, 2011; Teixeira, 2017).

The XRD technique has the potential to identify the mineralogical composition of the crystalline phases, allows the evaluation of the degree of crystallinity of the minerals, their processing condition and the identification of efflorescence, aggregates and ligands with crystalline phases. Regarding the limitations, the need for complementary techniques is highlighted, because XRD does not allow identifying with certainty the products with very low crystallinity or detecting the presence of scarce phases (Tuna et al, 2015).

3. EXAMPLES OF THE MICROSTRUCTURAL ANALYSIS APPLIED TO MORTARS

The following is the main results of work developed by researchers at Instituto Superior Técnico in

Lisbon. The study developed by Fontes (2011) concerns carbonation in lime-based mortars (lime or lime-cement), which is important because it is compatible with the materials used in old buildings. The carbonation process is responsible for the hardening and strength gain of the aerial lime mortar.

It has been found that high relative humidity values (95 ± 5%) retard the carbonation process and may even reverse it - as seen in the carbonation depth test using a phenolphthalein indicator, on mortars subjected to wet curing, confirming this tendency in the analysis of XRD fines. The mineralogical analysis of the mortars by X-ray diffraction (XRD) showed good results, allowing the analysis of the evolution of carbonation, as well as the confirmation of the trends presented by the phenolphthalein indicator.

The experimental study, which aimed at confirming the water/binder ratio of the mortars through the mineralogical analysis of an integral sample, by X-ray diffraction, was not possible because there was no relation between the peaks of calcite intensity and the portlandite (binder) and the peaks of quartz and feldspar intensity (aggregate), which were constant over time, or between different cure conditions. This may be due to the fact that very recent mortars have been analyzed, in which the carbonation process is underdeveloped.

As regards the analysis of mortars by X-ray microtomography, it is concluded that this technique allows visualizing the interior of the sample, analyzing it and quantifying it (Fig 1).

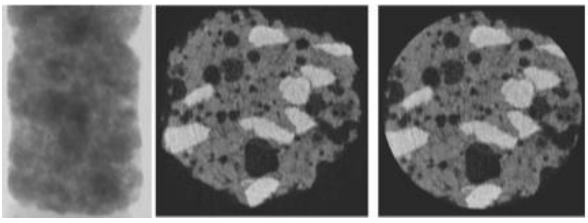

Figure 1. Radiography, reconstruction and analyzed area - MicroCT (Fontes, 2011)

Concerning porosity, it was found that only macropores would be visible and quantifiable, and the micropores are not distinguishable with the adopted resolution (Fig 2). This is due to the fact that, in order to obtain a sample that is representative of the mortar, it cannot have very small dimensions. On the other hand, this means that parameters, such as micropores, that have very small dimensions, cannot be analyzed.

In general, the analytical methods used were useful for the study of carbonation. It has been found that the phenolphthalein indicator, X-ray diffraction and tests for determination of mechanical strengths and bulk density are good indicators of the evolution of carbonation over time. As far as X-ray microtomography is concerned, the methodology shows potential, but its study must be refined.

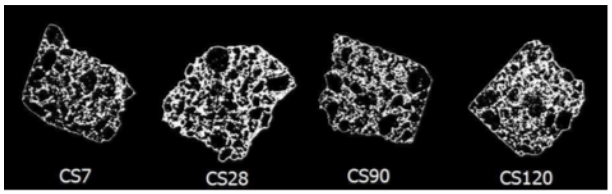

Figure 2. Micropores visualization with MicroCT (Fontes, 2011)

In the study carried out by Gominho (2016), several mortar formulations with expanded cork aggregates, sand, expanded clay and silica aerogel were characterized using x-ray computerized microtomography (MicroCT), scanning electron microscope (SEM), X-ray diffraction (XRD) and Fourier transform infrared spectroscopy (FTIR). In this way, it was intended to study the solid structure, and the porous structure. Gominho also proposes an analysis methodology that includes the following steps: aggregate analysis (pores); binder analysis (thickness and % in weight); binder / aggregate interface analysis; porous structure analysis (pores amount and dimensions); and other microstructural parameters (e.g. portlandite/calcite ratio).

As conclusion and result, we can highlight that in observation techniques the different magnification scales allow a global and particular analysis of the object of study. The MicroCT allows access to the inside of the material and is able to characterize different types of microstructures of distinguish mortars (Fig 3).

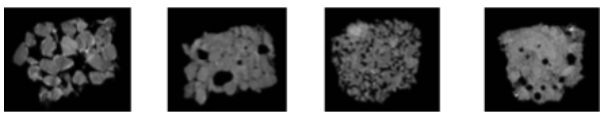

Figure 3. Tomographic sections of different types of mortars (Gominho, 2016)

The use of advanced characterization techniques such as MicroCT, XRD and FTIR combined conducted the following conclusion:

- Mortars with admixtures tend to form microstructures with bridging and open porous network;
- Its addition gives rise to an increase in porosity and changes the distribution and morphology of the pores;
- The bonding paste volume is one of the parameters where the microstructure can be manipulated to produce mortars with thermal and/or acoustic properties;
- The aggregates of the thermal mortars present in their microstructure high porosity;

- it is possible to characterize the mortars according to certain parameters of the microstructure;
- There is a correlation between the microstructures and the performance tests in the hardened state.

These results are advantageous in the research area, because they constitute a basis tool for the comparative analysis of thermal mortars.

4. CONCLUSION

In general, the microstructural characterization of mortars is useful in optimizing the performance of mortars in the hardened state and serves for the detailed study of the interactions of mortar constituents. The knowledge of the microstructure is important when one intends to act at the formulation level, to obtain the specific results, or when one intends to compare mortars at the nanoscale and millimeter scale. However, it is necessary to consider that the techniques of microstructural analysis have advantages and limitations. The combination of more than one technique optimizes the characterization and minimizes the uncertainty of the analysis.

The present study is part of an investigation within the scope of a research project, which aims to analyze the influence of the properties of the substrates on the mortar characteristics, using advanced characterization techniques including MicroCT, XRD and FTIR.

ACKNOWLEDGEMENTS

The work presented was carried out within the framework of the IF MORTAR project (POCI-01-0145-FEDER-032223), within the scope of the Portugal 2020 program, financed by FEDER through the POCI program. The funding provided is kindly acknowledged. The authors also thank CERIS and CERENA, research units from IST.

REFERENCES

Bogas, J.A., Maurício, A.; Pereira, M.F., 2012. Microstructural Analysis of Iberian Expanded Clay Aggregates, 18 (5): 1190-1208

Braz, D., Mota, L.M., Lopes, R.T., 1998. Computed tomography in the fatigue test analysis of na asphaltic mixture. Applied Radiation and Isotopes:661-671.

Cnudde, V., Boone, M.N. 2013. High-resolution X-ray computed tomography in geosciences: A review of the current technology and applications Earth-Science Reviews, 123:1–17.

De Witte, Y., Cnudde, V., Pieters, K., Masschaele, B., Dierick, M., Vlassenbroeck, J., Van Hoorebeke, L., Jacobs, P. (2008). X-ray micro-CT applied to natural building materials and art objects, X-Ray Spectrometry 37(4): 383-387

Fontes, A., 2011.The infuence of curing conditions of traditional lime-based mortars. Analysis methods. Master thesis (in portuguese). IST, University of Lisbon, Portugal.

Gominho, M., 2016. Microstructural characterization of mortars. Master Thesis (in portuguese), IST, University of Lisbon, Portugal.

Hanke, L., 2016. Handbook of Analytical Methods for Materials, Materials Evaluation and Engineering, Inc.

Kerckhofs, G., Schrooten, J., Van Cleynenbreugel, Lomov, S.V., Wevers, M., 2008. Validation of x-ray microfocus computed tomography as an imaging tool for porous structures, American Institute of Physics. doi: 10.1063/1.2838584.

Ketcham, R., Carlson, W. 2007. Acquisition, optimization an interpretation of X-ray computed tomographic imagery: application to the geosciences, University of Texas.

Mauricio, A., Figueiredo, C., Alves, C., Pereira, F.C., 2013. Non-destructive microtomography-based imaging and measuring laboratory-induced degradation of travertine, a random heterogeneous geomaterial used in urban heritage laboratory-induced degradation of travertine, a random heterogeneous geomaterial used in urban heritage, Environmental Earth Sciences, 69 (4): 1471-1480.

Mauricio, A., Figueiredo, C., Alves, C., Pereira, M.F., Aires-Barros, L., Neto, J.A.N, 2010. Microtomography-based Pore Structure Modelling of Geologic Materials used as Building and Dimension Stones,Materials Science Forum. 636-637: 1306-1312.

Mendes, R. 2010. MicroCT nondestructive method to analyse the concrete volumetry. Case Study. Master Thesis. (in portuguese).Universidade Federal do Pará, Brasil.

Stock, S.R., 2008. Recent advances in X-ray microtomography applied to materials, Materials Reviews, 53(3):129-181.

Teixeira, P.M. 2017. Catalogue of laboratorial diagnosis technicques on samples collected on in-service walls. Master Thesis (in portugues), IST, Universitty of Lisbon, Portugal.

Tuna, J.; Feiteira, J.; Flores-Colen, I.; Pereira, M.F., Brito, J.de, 2015. In situ characterization of damaging soluble salts in walls construction materials, Journal of Performance of Constructed Facilities, 29(5).

39th Cement and Concrete Science Conference
9-10th September 2019
University of Bath
Paper Number 037

Study on the thermal conductivity performance of cement-based composites incorporating natural organic fibres

M. Pedroso, I. Flores-Colen*, J. Dinis Silvestre, M. Glória Gomes
CERIS, DECivil, IST, Universidade de Lisboa, Portugal
marco.pedroso@tecnico.ulisboa.pt *ines.flores.colen@tecnico.ulisboa.pt
jose.silvestre@tecnico.ulisboa.pt maria.gloria.gomes@tecnico.ulisboa.pt

ABSTRACT

With the environmental awareness and legislation encouraging a more sustainable use of construction materials, there is a growing effort of studying the incorporation of natural organic fibres in cement-based composites. This trend aims at improving the overall performance of those composites, but also at reducing their environmental impact. At the same time, there is an increasing need for buildings to present improved energy efficiency, using highly thermal insulating materials. The present paper presents a review on the research carried out with natural organic fibres, discussing their characteristics and how they can contribute to lower the thermal conductivity of the cement-based composites. It starts with a brief review of the main characteristics of natural organic fibres and, from there, presents the state-of-the-art of their inclusion in cement-based composites and their influence on thermal conductivity. Therefore, a brief insight is given on the consequences of using natural organic fibres, and future trends for their use. The results suggest that fibre's incorporation provide improvements in the thermal conductivity, showing the current potential of using natural organic fibres on cement composites, and the implications on their performance.

1. INTRODUCTION

Cement-based products are one of the most used group of materials in the world with many applications in construction (Khatib, 2009). Nevertheless, they present high values of thermal conductivity (λ) limiting their application in buildings due to the increasingly demanding thermal insulation requisites present in the law (Abu-Jdayil *et al.*, 2019). In recent years, the use of fibres has received more attention because of their effectiveness at improving different physical and mechanical properties of cement-based composite materials, including the lowering of their thermal conductivity.

The recent efforts to further reduce the environmental footprint of several products within the construction industry are, in a considerable way, related to the reduction of the use of cement (Khatib, 2009). Moreover, the need for increasing the thermal performance of buildings to reduce either their cooling or heating needs, led to the need of developing various materials in which the cement-based composites incorporating these natural organic fibres can have an important role to play (du Plessis, 2016).

Nevertheless, most of the research has focused on the mechanical performance of the composites incorporating natural organic fibres, with less focus given to their thermal conductivity (Medina and Dzalto, 2017). The current research presents values for the thermal conductivities of composites incorporating natural organic fibres, but there is a lack of a statistical review in order to understand how the fibre volume fraction can promote this effect in the cement-based composites.

In the present paper, it was analysed a set of results associated with cement-based composites, namely cement pastes, mortars and concrete with different levels (by total volume) of natural organic fibre's incorporation.

1.1. RESEARCH SIGNIFICANCE

The literature clearly shows that much of the research has been carried out without considering the importance of understanding the influence of fibre volume on the thermal conductivity behaviour of the cement-based composites, with different works using different units of measure for the fibre quantity (such as, by total weight of the mixture, by weight of binder or by total volume, among others). Therefore, this work serves as a reference to future experimental studies because of the results that were obtained, relating the relative reductions of thermal conductivity with the fibre volume fraction used in the cement-based composite formulations used.

1.2. METHODOLOGY

Usually, the methodology adopted for literature reviews consists of making an analysis of the results and conclusions of published research, identifying gaps in the existing knowledge and providing recommendations for further works. However, in this paper, the strategy followed involved data mining through several publications, which were selected based on their relevance to this paper's theme. Each publication was then analysed, and their data organized in spreadsheets.

After all the data was gathered, it was analysed and the obtained results were calculated, for each publication, in a relative form (equation (1)), in order to find if the addition of fibre's increased or decreased the reference composite's performance. Therefore, the obtained results can provide a good representation of literature's findings. When the fibre's quantity was in mass, the conversion to total volume respected the mixture ratios indicated (Cement : Sand : Water) and the fibre's bulk density.

$$relative\ \lambda = \frac{test\ composite\ \lambda}{reference\ composite\ \lambda} \quad (1)$$

It is important to refer that were analysed values ranging from 0% (vol) to 100% (vol) of natural organic fibre's content, by total volume, and fibre lengths from 0.5 to 50 mm.

2. NATURAL ORGANIC FIBRES

There are many fibres currently in the market, but here the focus is towards natural organic fibres. These fibres are classified as a result of their origin and can be either from animals (polypeptide) or plants (cellulose) (Lilholt and Lawther, 2000; Müssig, 2010).

In the last couple of years, natural organic fibres have been increasingly studied and used as reinforcements to produce low cost and lightweight composites (Lilholt and Lawther, 2000). These fibres exhibit many advantageous properties when compared with others: they have low weight, low density, low thermal conductivity, are easy to obtain, are available from renewable resources and are easy to recycle at the end of their life cycle (Müssig, 2010). However, they also have limitations: high moisture absorption, and the irregular performance they present depending on their place of origin (Lilholt and Lawther, 2000).

Due to their low thermal conductivity, as it can be seen in Table 1, their use as an addition in cement-based composites has the potential to lower their thermal conductivity. Table 1 presents some fibres' characteristics, namely the fibre's name, bulk density and thermal conductivity (Xu *et al.*, 2004; Pfundstein *et al.*, 2008; Korjenic *et al.*, 2011; Panyakaew and Fotios, 2011). It can be seen that the average λ is around 0.040 $W.m^{-1}.K^{-1}$ and the bulk density is also very low, lower than 0.350 $kg.m^{-3}$ in natural organic fibres' boards.

Table 1. Bulk density and thermal conductivity of some natural organic fibres

Fibre	Bulk density ($g.cm^{-3}$)	Thermal conductivity ($W.m^{-1}.K^{-1}$)	Reference
Cellulose	0.050	0.043	Pfundstein et al., 2008
Coconut husk	0.250 – 0.350	0.046 – 0.068	Panyakaew et al.,
Flax	0.032	0.043	Korjenic et al., 2011
Hemp	0.082	0.039	
Jute	0.026	0.046	
Kenaf board	0.150 – 0.200	0.051 – 0.058	Xu et al., 2004

3. INFLUENCE OF NATURAL ORGANIC FIBRE'S INCORPORATION IN THE THERMAL PERFORMANCE OF CEMENT-BASED COMPOSITES

Derived from the results of 124 different cement-based composite mixes, incorporating natural organic fibres of different type and origins, that were sourced from 21 publications (Awwad *et al.*, 2012; Andiç-Çakir *et al.*, 2014; Stirmer, Milovanovic and Sokol, 2014; Zagarella *et al.*, 2014; Belhadj *et al.*, 2014, 2016; Lertwattanaruk and Suntijitto, 2015; Hospodarova *et al.*, 2018; Miron *et al.*, 2017; Boukhattem *et al.*, 2017; Boumhaout *et al.*, 2017; Cardinale *et al.*, 2017; Hospodarova *et al.*, 2017; Belkadi *et al.*, 2018; Petrella *et al.*, 2019; Shon *et al.*, 2019; Fatma *et al.*, 2019), the influence of natural organic fibre's incorporation in the thermal conductivity of cement-based composites was assessed.

In order to analyse the influence from 0 to 100% (vol) of organic fibre's content on the results, it was considered a reference mortar, as the one presented in several of the previously mentioned works, with a ratio of 1:3:0.5, and with a mean value of 1.800 $W.m^{-1}.K^{-1}$ for thermal conductivity and 2,000 $kg.m^{-3}$ for density. Based on those values, and on the thermal conductivity and bulk density values presented in Table 1, the relative reduction that a 100% (vol) of organic fibres would represent was calculated.

It was possible to obtain an exponential regression with a coefficient of determination near 90 % (this value indicates the percentage of total variation of the relative thermal conductivity explained by the regression model consisting of fibre total volume fraction). From a statistical point of view, according to Hair *et al.* (Hair Jr. *et al.*, 2014) a coefficient of correlation (R) between 0.70 and 0.90 presents a

strong correlation between the obtained regression curve and the results of the previous studies. Therefore, the regression equation presented in Figure 1 can aid in the future prediction of the impact that a given fibre volume will have in lowering the thermal conductivity of a cement-based composite.

It is relevant to note that due to the influence of even small fibre incorporation volumes (below 1%), to lower the composite's thermal conductivity, the presented regression doesn't start at 1.00. This is also related to the fact that the coefficient of determination doesn't explain the total variation of the relative thermal conductivity. Therefore, this model has some limitations when considering fibre volumes below 1%.

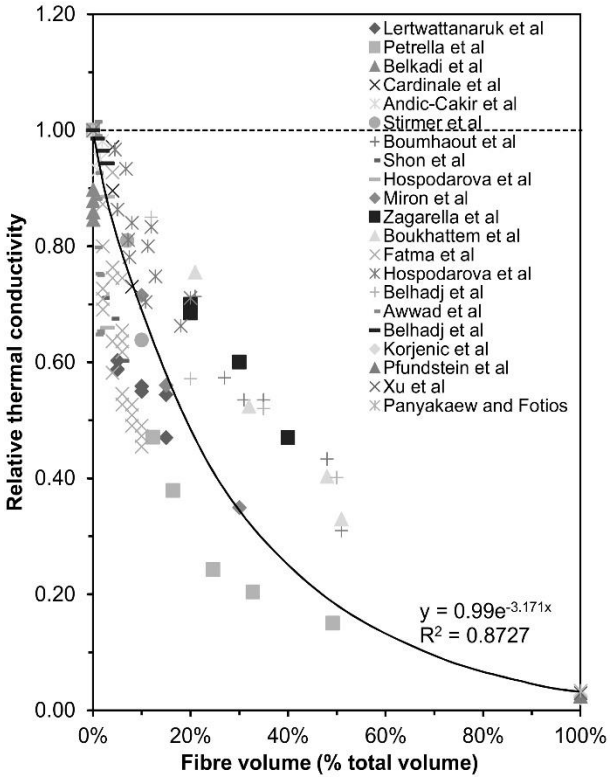

Figure 1. Relationship between the relative thermal conductivity of mixes with varying total fibre volume.

The results obtained show that the introduction of fibres lead to a decrease of the relative thermal conductivity, as expected and reported in other works (Onuaguluchi and Banthia, 2016; Abu-Jdayil *et al.*, 2019), being the only exception one mixture from Awwad *et al.* (Awwad *et al.*, 2012) with a 1% increase. This fact can be associated with equipment accuracy, and due to its low difference to other values, it was considered non-relevant.

From Figure 1 it can also be seen that the addition of 5% (vol) of fibres can lead to an average decrease of 20% of the thermal conductivity of the reference cement-based mix and, when it is considered the maximum amount of fibre (100% (vol)), the attained reduction of the thermal conductivity, from a reference mix, can reach a value of approximately less 100%, corresponding to an average thermal conductivity value of 0.040 $W.m^{-1}.K^{-1}$, which can be seen as the lowest possible value to attain using only natural organic fibres.

4. CONCLUSIONS

The main aim of this investigation was to examine the influence of the total fibre volume of natural organic fibres on the thermal conductivity of cement-based composites, through a statistical analysis of data available in the literature.

It was observed that, as the fibre volume content increases, the relative thermal conductivity, of the cement-based composites, decreases. This is a consensus throughout the literature, regardless of the numerous variables involved. With this study it was possible to predict, from a statistical point of view, and with a strong correlation of factors, the potential decrease of the thermal conductivity of natural organic fibre's cement-based composites based on the fibre volume content, being this the main contribution of this study to the current state-of-the-art.

ACKNOWLEDGEMENTS

The authors gratefully acknowledge the support of CERIS – IST, Universidade de Lisboa and FCT – Fundação para a Ciência e Tecnologia. Marco Pedroso acknowledges FCT for PhD grant FCT SFRH/BD/132239/2017.

REFERENCES

Abu-Jdayil, B. *et al.* (2019) 'Traditional, state-of-the-art and renewable thermal building insulation materials: An overview', *Construction and Building Materials*, 214, pp. 709–735. doi: 10.1016/j.conbuildmat.2019.04.102.

Andiç-Çakir, Ö. *et al.* (2014) 'Physical and mechanical properties of randomly oriented coir fiber–cementitious composites', *Composites Part B: Engineering*, 61, pp. 49–54. doi: 10.1016/j.compositesb.2014.01.029.

Awwad, E. *et al.* (2012) 'Studies on fiber-reinforced concrete using industrial hemp fibers', *Construction and Building Materials*. Elsevier Ltd, 35(2012), pp. 710–717. doi: 10.1016/j.conbuildmat.2012.04.119.

Belhadj, B. *et al.* (2014) 'Effect of substitution of wood shavings by barley straws on the physico-mechanical properties of lightweight sand concrete', *Construction and Building Materials*. Elsevier Ltd, 66, pp. 247–258. doi: 10.1016/j.conbuildmat.2014.05.090.

Belhadj, B. *et al.* (2016) 'Contribution to the development of a sand concrete lightened by the addition of barley straws', *Construction and Building Materials*. Elsevier Ltd, 113, pp. 513–522. doi: 10.1016/j.conbuildmat.2016.03.067.

Belkadi, A. A. *et al.* (2018) 'Effect of vegetable and

synthetic fibers on mechanical performance and durability of Metakaolin-based mortars', *Journal of Adhesion Science and Technology*. Taylor & Francis, 32(15), pp. 1670–1686. doi: 10.1080/01694243.2018.1442647.

Boukhattem, L. *et al.* (2017) 'Moisture content influence on the thermal conductivity of insulating building materials made from date palm fibers mesh', *Construction and Building Materials*. Elsevier Ltd, 148, pp. 811–823. doi: 10.1016/j.conbuildmat.2017.05.020.

Boumhaout, M. *et al.* (2017) 'Thermomechanical characterization of a bio-composite building material: Mortar reinforced with date palm fibers mesh', *Construction and Building Materials*. Elsevier Ltd, 135, pp. 241–250. doi: 10.1016/j.conbuildmat.2016.12.217.

Cardinale, T. *et al.* (2017) 'Investigations on thermal and mechanical properties of cement mortar with reed and straw fibers', *International Journal of Heat and Technology*, 35(Special Issue1), pp. S375–S382. doi: 10.18280/ijht.35Sp0151.

Fatma, N. *et al.* (2019) 'The effect of doum palm fibers on the mechanical and thermal properties of gypsum mortar', *Journal of Composite Materials*, p. 002199831983831. doi: 10.1177/0021998319838319.

Hair Jr., J. *et al.* (2014) *Multivariate data analysis*. 7th edn. Harlow - England: Pearson Education Limited.

Hospodarova, V. *et al.* (2017) 'Influence of Cellulosic Fibres on the Physical Properties of Fibre Cement Composites', *IOP Conference Series: Materials Science and Engineering*, 251(1), p. 012015. doi: 10.1088/1757-899X/251/1/012015.

Hospodarova, V. *et al.* (2018) 'Investigation of Waste Paper Cellulosic Fibers Utilization into Cement Based Building Materials', *Buildings*, 8(3), p. 43. doi: 10.3390/buildings8030043.

Khatib, J. M. (ed.) (2009) *Sustainability of construction materials*. 1st edn. Cambridge - United Kingdom: CRC press.

Korjenic, A. *et al.* (2011) 'Development and performance evaluation of natural thermal-insulation materials composed of renewable resources', *Energy and Buildings*, 43(9), pp. 2518–2523. doi: 10.1016/j.enbuild.2011.06.012.

Lertwattanaruk, P. and Suntijitto, A. (2015) 'Properties of natural fiber cement materials containing coconut coir and oil palm fibers for residential building applications', *Construction and Building Materials*. Elsevier Ltd, 94, pp. 664–669. doi: 10.1016/j.conbuildmat.2015.07.154.

Lilholt, H. and Lawther, J. M. (2000) 'Natural Organic Fibers', in *Comprehensive Composite Materials*. Elsevier, pp. 303–325. doi: 10.1016/B0-08-042993-9/00048-6.

Medina, L. A. and Dzalto, J. (2017) '1.11 Natural Fibers', *Comprehensive Composite Materials II*, 1, pp. 269–294. doi: 10.1016/b978-0-12-803581-8.09877-5.

Miron, I. O. *et al.* (2017) 'Organic Thermal Insulation Based on Wheat Straw', *Procedia Engineering*, 181, pp. 674–681. doi: 10.1016/j.proeng.2017.02.449.

Müssig, J. (ed.) (2010) *Industrial Applications of Natural Fibres*. 1st edn. Chichester, UK: John Wiley & Sons, Ltd. doi: 10.1002/9780470660324.

Onuaguluchi, O. and Banthia, N. (2016) 'Plant-based natural fibre reinforced cement composites: A review', *Cement and Concrete Composites*. Elsevier Ltd, 68, pp. 96–108. doi: 10.1016/j.cemconcomp.2016.02.014.

Panyakaew, S. and Fotios, S. (2011) 'New thermal insulation boards made from coconut husk and bagasse', *Energy and Buildings*. Elsevier B.V., 43(7), pp. 1732–1739. doi: 10.1016/j.enbuild.2011.03.015.

Petrella, A. *et al.* (2019) 'Use of cellulose fibers from wheat straw for sustainable cement mortars', *Journal of Sustainable Cement-Based Materials*. Taylor & Francis, 8(3), pp. 161–179. doi: 10.1080/21650373.2018.1534148.

Pfundstein, M. *et al.* (2008) *Insulating materials: Principles, materials and applications*. 1st edn. Edition Detail.

du Plessis, C. (2016) *CIB Research Roadmap: Sustainable construction*.

Shon, C.-S. *et al.* (2019) 'Can Common Reed Fiber Become an Effective Construction Material? Physical, Mechanical, and Thermal Properties of Mortar Mixture Containing Common Reed Fiber', *Sustainability*, 11(3), p. 903. doi: 10.3390/su11030903.

Stirmer, N., Milovanovic, B. and Sokol, J. M. (2014) 'Cement Composites Reinforced With Sheep's Wool', *Proceedings of the International Symposium on Eco-Crete*, (1), pp. 271–278.

Xu, J. *et al.* (2004) 'Manufacture and properties of low-density binderless particleboard from kenaf core', *Journal of Wood Science*, 50(1), pp. 62–67. doi: 10.1007/s10086-003-0522-1.

Zagarella, F. *et al.* (2014) 'Layered dry envelope components in the Mediterranean areas. A field evaluation of a sheep wool-lime mix', in *SDEWES2014*, pp. 1–12. doi: 10.13140/RG.2.1.2365.8724.

39th Cement and Concrete Science Conference
9-10th September 2019
University of Bath

Sequential Effects of Radiation and Carbonation on the Properties of Cement

A Potts* and L. Leay
Dalton Cumbrian Facility, University of Manchester

E. Butcher and G. Cann
National Nuclear Laboratory

ABSTRACT

Concrete is used in the construction of facilities in the U.K. throughout the nuclear industry. Due to the long operational timescales, understanding how cement and concrete changes over its life as well as how the conditions it is exposed to affect it, is paramount. In this study, hardened cement samples are exposed to a 5% CO_2 atmosphere after being exposed to 1.5 MGy of gamma radiation to assess aging at an accelerated rate. Since the equipment used for irradiation causes heating to 50°C, the effect of heating alone was also assessed. Carbonation depth was found to significantly increase in both heated and irradiated samples when compared to carbonated control samples. Exposing cement to gamma irradiation and/or heat resulted in the formation of a different carbonate mineral phase compared to when the sample was solely exposed to carbonation. This is a similar result to that found in the literature for a simultaneous study, meaning the methodology used in this study could be a viable way to accelerate studies.

1. INTRODUCTION

Cement and concrete are materials used in the nuclear industry for a variety of purposes ranging from waste encapsulation to shielding and structural materials. A key element of concrete for structural use is the time-span in which it operates, typically decades at a time. Furthermore, these structures are not easily replaced, maintained or repaired. Because of this, it is of utmost importance that there is an understanding of how these structures age over time and the different elements that can affect this. In this scenario, gamma radiation is a variable which may affect potential degradation mechanisms. As a lot of uses of concrete will result in it being open to atmosphere, carbonation is one long-timescale degradation mechanism to be considered. This study utilizes sequential gamma radiation and carbonation to understand this long term aging process.

It has long been reported that radiation will damage cement and concrete structures (Hilsdorf, Kropp, and Koch 1959). In the case of gamma radiation, it has been found that dose rate influences the decrease in compressive strength (Soo and Milian 2001). Whilst gamma radiation typically causes the compressive strength to decrease, carbonation normally results in an increase (Ashraf 2016).

The degree of carbonation in a hardened cement paste increases when simultaneously exposed to

gamma radiation (František Vodák et al. 2011; Bar-Nes et al. 2008). Vodak et al. showed the dehydration of the sample via mass measurements, indicating the radiolytic breakdown of the pore water. Bouniol and Bjergbakke (2008) found that unstable calcium peroxide can be formed via the radiolytic breakdown of pore water, however, in the case of very low dose rates there needs to be a minimum amount of peroxide present for this to occur. Higher dose rates were shown to increase the maximum amount of the peroxide formed. It has been suggested that this unstable calcium peroxide can lead to increased carbonation in a radiation field (F. Vodák et al. 2005; Maruyama et al. 2018). Maruyama et al. (2018) reported that samples simultaneously exposed to gamma radiation and carbonation formed vaterite and aragonite predominantly, whereas calcite was dominant under solely carbonating atmospheres.

The studies utilising simultaneous irradiation and natural carbonation generally occur over months of irradiation (František Vodák et al. 2011; Bar-Nes et al. 2008; Maruyama et al. 2018). This paper seeks to examine whether using accelerated conditions sequentially is a viable option for these studies in the future.

2. EXPERIMENTAL SET-UP

Samples were mixed, using a 3:2 ordinary Portland cement (OPC): fly ash (FA) blend, with a w/s ratio of 0.45, using a Kenwood stand mixer. Sellafield spec OPC (BS EN 197-1 CEM I 42,5N) was provided by Hanson Cement and the fly-ash was provided by Power-Mineral ltd, at a specification of BS EN 450-1 NB . The cement was mixed until fully incorporated and then poured into 40 mm cubic

stainless steel moulds. Samples were covered and left overnight, before being removed from their moulds and placed into a water bath. The water bath was set at 20 °C, and contained a lime saturated solution. Samples were cured for 42 days After curing, samples were weighed and 5 faces were covered with aluminium tape, restricting carbonation to 1 direction.

Samples were split into 3 sub groups, and exposed to different 'treatments' before carbonation. One group (IC) was placed into a FOSS therapy services self-shielded gamma irradiator at approximately 22.8 kGy/hr for 65.5 hours, achieving 1.5 MGy total dose. As the gamma irradiator is lead lined the temperature is above atmospheric. To account for this, a second group (HC) was placed into an oven for the same amount of time at 60 °C. A third group (C) was left in atmospheric conditions during this time. The exposure conditions are summarised in Table 12. It should be noted that both the IC and HC samples were exposed to atmosphere during the treatment stage. Following the different 'treatments', all of the samples were placed into a bespoke benchtop carbonation chamber and carbonated at 5% CO_2 for 2 weeks.

Table 12 Breakdown of the different sample groups and what they have been exposed to

Sample	Irradiation	Heat	Carbonation
IC	x	x	x
HC		x	x
C			x

After the carbonation was completed the samples were prepared as shown in Figure 20. One of the mapping slices was sprayed with phenolphthalein indicator, and processed using ImageJ software. Callipers were included in the images as a reference distance. The other slice was used for mapping XRD, where a series of scans were taken from the carbonated edge in-wards using 0.45 mm increments. A Bruker D8 Discover was used, with a scan range 16.5°-55° 2θ, with a 0.02° step size and a total scan time of 3 hours per scan. Due to the long total scan time per sample (90 hours), a custom 3D printed cell holder was used that allowed for N_2 to be flowed over the surface to minimise carbonation effects.

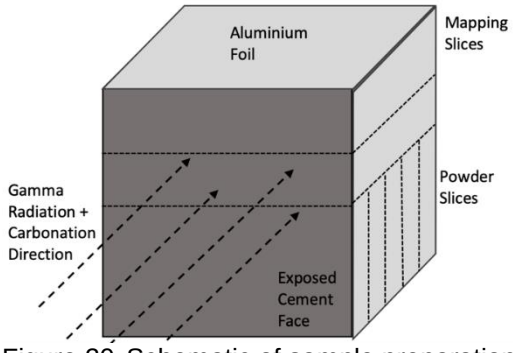

Figure 20 Schematic of sample preparation

3. RESULTS & DISCUSSION

Figure 21 shows significant mass loss in both the irradiated and heat treated samples after the treatment phase, as an average over 3 samples. This is thought to be due to loss of the loosely bound pore water, rather than processes such as ettringite degradation given the short timescale of the treatment. The mass increase following the carbonation period, is thought to be due to carbonation phase formation, however, some may be due to water re-absorption from the relative humidity of the carbonation chamber (73%, controlled using sodium nitrite solution).

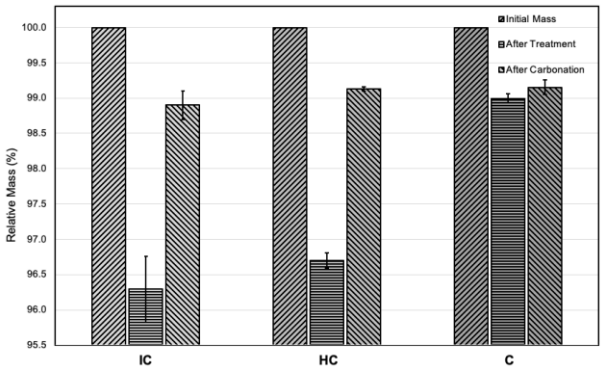

Figure 21 Relative mass changes of the 3 sub groups after treatment and after carbonation

The images of the phenolphthalein indicator spray showed an increase in carbonation depth for the IC and HC samples compared to the C samples, as shown in Figure 22. This is in agreement with the mass loss data, which infers that the greater carbonation depth is due to greater pore access, achieved via driving off loosely bound pore water. The difference in histogram shape implies there may be some more subtle mechanisms occurring.

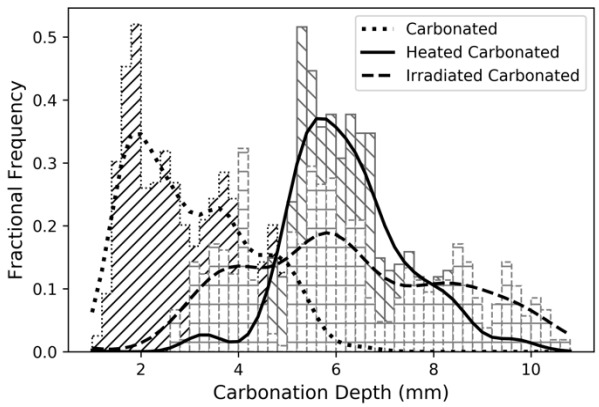

Figure 22, Histogram of the carbonation depths, fitted with a Kernel density function. Normally displayed as 3 images

Mapping XRD investigated how the phases changed from the carbonation edge into the centre of the sample. For both the IC and HC sample, 30 scans were conducted over 12 mm, whereas for the

C sample only 23 scans were taken, due to the reduced carbonation depth. The data was processed in python, with the background fitting using an asymmetric least squares smoothing (Eilers and Boelens 2005). The data for each sample was concatenated and normalised over the entire range of scans before being converted to a heatmap.

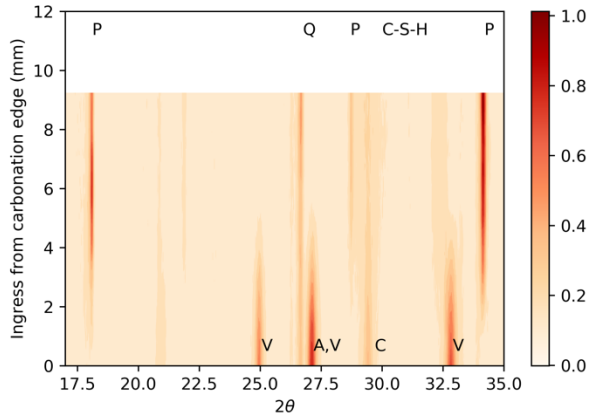

Figure 4a Solely carbonated sample

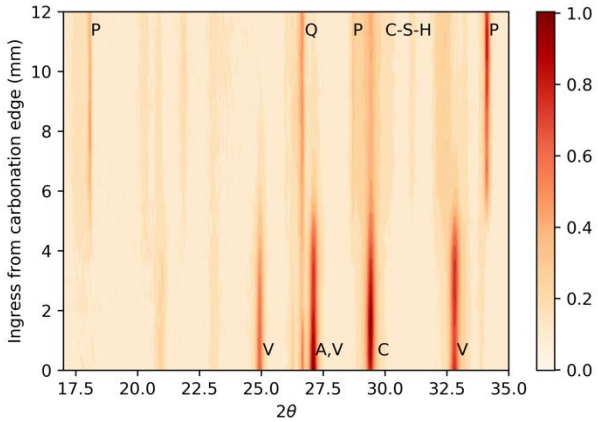

Figure 4b Heat treated and carbonated sample

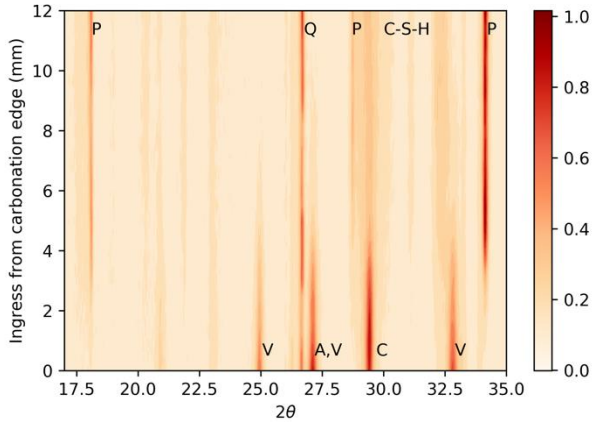

Figure 23c Irradiated and carbonated sample. Peaks labelled with P are portlandite, Q is quartz, V is vaterite, C is calcite, C-S-H is calcium-silicate-hydrate and A is aragonite.

Previous papers have hypothesised that different carbonation phases have different pre-cursors (Auroy et al. 2018). They found that portlandite precipitated calcite, ettringite formed aragonite and C-S-H formed vaterite. Figure 23a shows that vaterite was the main carbonation phase formed in our control sample. This does fit with Auroy et al.'s hypothesis as the fly-ash presence reacts pozzolanically decreasing the portlandite content in the cement . As expected, Figure 23 shows that as the carbonation phase decreases with its ingress into the sample, the precursor phases become more dominant, in particular C-S-H and portlandite. A similar trend is seen in the HC sample, however, calcite and vaterite are formed to approximately equal intensities. In the case of the IC sample, the calcite appears to be more intense than the vaterite formation, with the vaterite intensity being less than in the HC sample.

This is partially in agreement with the findings of Maruyama et al., (2018) where they also found that the carbonation phase reversed upon irradiation. However, in their system it was calcite formed in the control, with irradiated sample forming vaterite and aragonite. The difference in the carbonation phase formed between the 2 studies is believed to be due to the fly-ash, however, the accelerated conditions are also being considered. In their paper, Auroy et al. showed that 3% CO_2 gave similar results to atmospheric carbonation. 5% has been used elsewhere in literature, so it is not believed to be this.

XRD was used to rule out the idea that irradiation or heat treating a sample would change the precursor phases. As mentioned previously, a calcium peroxide mechanism has been put forward in the literature as a potential factor in increased carbonation depth. There is potential that this mechanism could contribute to the carbonation phase switch. This is something Maruyama et al. (2018) mention in their paper, however, the main reason hypothesised there was advanced dehydration of the cement matrix.

4. CONCLUSIONS

This study has shown that enhanced carbonation was predominantly due to the loss of pore water, as demonstrated by the increase in carbonation depth of both the HC and IC. It has also been shown that the calcium carbonate phase formed is different when the cement has been exposed to gamma radiation and/or heat before carbonation. Therefore, this mechanism must not be dependant on a simultaneous scenario, and is likely to be as a result of a change in chemistry caused by heat/ irradiation to the cement matrix. Maruyama et al. (2018) hypothesised that the altered phase formation was due to the enhanced dehydration, however, they also acknowledged the potential for radiation chemistry to have an effect. Our results support both of these conclusions, with the heat treated sample forming both vaterite and calcite whilst the irradiated sample formed calcite dominantly with some vaterite.

There is potential for this sequential accelerated regime to be a viable alternative to the long timescales of simultaneous studies. Some details are still to be investigated, such as a more defined mechanism behind the carbonation phase change. Future studies are planned to investigate whether limestone aggregate (present in industry samples) has an effect on the irradiation and carbonation of cement. Hydration age before exposure to gamma radiation is also to be investigated. These authors would like to carry out a simultaneous accelerated study to compare to this study.

5. ACKNOWLEDGEMENTS

This study is funded by the EPSRC, via an iCase sponsored by Sellafield ltd. We acknowledge the support of The University of Manchester's Dalton Cumbrian Facility (DCF), a partner in the National Nuclear User Facility, the EPSRC UK National Ion Beam Centre and the Henry Royce Institute.

The authors would like to thank Dr. Helmut Glünder for providing the base code for the phenolphthalein measurements .

The author(s) acknowledges the use of the School of Materials X-ray Diffraction Suite at the University of Manchester and for the technical support, advice and assistance provided by Gary Harrison and Dr. John E. Warren. Special thanks to Dr. John E. Warren for building the custom XRD cell holder allowing for the mapping experiments.

5. REFERENCES

Ashraf, Warda. 2016. "Carbonation of Cement-Based Materials: Challenges and Opportunities." *Construction and Building Materials* 120 (September 2016): 558–70. https://doi.org/10.1016/j.conbuildmat.2016.05.080.

Auroy, Martin, Stéphane Poyet, Patrick Le Bescop, Jean Michel Torrenti, Thibault Charpentier, Mélanie Moskura, and Xavier Bourbon. 2018. "Comparison between Natural and Accelerated Carbonation (3% CO2): Impact on Mineralogy, Microstructure, Water Retention and Cracking." *Cement and Concrete Research* 109 (April): 64–80. https://doi.org/10.1016/j.cemconres.2018.04.012.

Bar-Nes, Gabriela, Amnon Katz, Yael Peled, and Yehuda Zeiri. 2008. "The Combined Effect of Radiation and Carbonation on the Immobilization of Sr and Cs Ions in Cementitious Pastes." *Materials and Structures* 41 (9): 1563–70. https://doi.org/10.1617/s11527-007-9348-4.

Bouniol, P., and E. Bjergbakke. 2008. "A Comprehensive Model to Describe Radiolytic Processes in Cement Medium." *Journal of Nuclear Materials* 372 (1): 1–15. https://doi.org/10.1016/j.jnucmat.2006.10.004.

Eilers, Paul H C, and Hans F M Boelens. 2005. "Baseline Correction with Asymmetric Least Squares Smoothing."

Hilsdorf, H, J Kropp, and H Koch. 1959. "The Effects of Nuclear Radiation on Materials†." Vol. 6. https://doi.org/10.1080/00207215908937159.

Maruyama, Ippei, Shunsuke Ishikawa, Junichi Yasukouchi, Shohei Sawada, and Ryo Kurihara. 2018. "Cement and Concrete Research Impact of Gamma-Ray Irradiation on Hardened White Portland Cement Pastes Exposed to Atmosphere." *Cement and Concrete Research* 108 (June 2017): 59–71. https://doi.org/10.1016/j.cemconres.2018.03.005.

Soo, P, and Lm Milian. 2001. "The Effect of Gamma Radiation on the Strength of Portland Cement Mortars." *Journal of Materials Science Letters* 20: 1345–48. http://www.springerlink.com/index/J1636H5141220804.pdf.

Vodák, F., K. Trtík, V. Sopko, O. Kapičková, and P. Demo. 2005. "Effect of γ-Irradiation on Strength of Concrete for Nuclear-Safety Structures." *Cement and Concrete Research* 35 (7): 1447–51. https://doi.org/10.1016/j.cemconres.2004.10.016.

Vodák, František, Vítězslav Vydra, Karel Trtík, and Olga Kapičková. 2011. "Effect of Gamma Irradiation on Properties of Hardened Cement Paste." *Materials and Structures* 44 (1): 101–7. https://doi.org/10.1617/s11527-010-9612-x.

39th Cement and Concrete Science Conference
9-10th September 2019
University of Bath
Paper Number 041

Evaluation of an Optimal Concrete with Recycled Concrete Aggregate and High Density Polyethylene Flakes

J. Smith and K. Arjoon
Department of Civil and Environmental Engineering, University of The West Indies, St. Augustine, Trinidad

ABSTRACT

The purpose of this research was to evaluate the strength parameters namely, compressive, tensile splitting and flexural strength of concrete when the natural coarse aggregate is replaced with Recycled Concrete Aggregate (RCA) and High Density Polyethylene (HDPE) flakes. Mechanical strength tests were performed on specimens with up to 100 percent RCA replacement and up to 25 percent HDPE replacement. The optimum percentage of RCA and HDPE was determined based on the compressive strength, tensile splitting strength, and flexural strength test results, and these optimum percentages were used to create design mixes integrating both recycled aggregates. The flexural, compressive and tensile splitting strength tests were conducted on these design mixes with a combination of various percentages of natural coarse aggregate, RCA and HDPE flakes to determine the most suitable design mix which can be used in the concrete industry. Additionally, sieve analysis, water absorption, aggregate impact value, specific gravity and aggregate angularity were determined for each coarse aggregate. Based on the evaluation of the strength parameters of this study, the optimum design mixes using RCA and HDPE individually which presented the most feasible results essential for the use in the concrete industry utilized 75 percent RCA as a replacement to NCA and 5 percent HDPE flakes as a substitute to NCA.

1. INTRODUCTION

Concrete is a major material used in the construction industry due to its favourable features such as its durability, satisfactory compressive strength, cost effectiveness, availability and fire resistance (Yang, Du and Bao 2011). Conventional concrete is manufactured from natural aggregates, cement and water. The natural aggregates are usually obtained from first quarrying, then crushing and finally, separating into required size fractions to satisfy grading requirements.

The Republic of Trinidad and Tobago is the southernmost nation of the West Indies in the Caribbean with a population of just under 1.4 million. According to the Ministry of Energy and Energy Affairs (2017) of Trinidad and Tobago, there are ninety legal active mining operations in Trinidad and Tobago, where forty-five of these are sand and gravel quarries. In 2013, the aggregate production was estimated to be just above six million cubic yards. Trinidad and Tobago Solid Waste Management Company Limited (SWMCOL) collected 510 kg of mixed plastic beverage containers for the purpose of recycling in 2015.

This study evaluated the use of a native recycled concrete with recycled concrete aggregate (RCA) and high density polyethylene plastic (HDPE) as a substitute to natural concrete aggregate (NCA) by conducting compressive strength (CS) tests, tensile splitting strength (TSS) tests and flexural strength (FS) tests on concrete samples with varying percentages of NCA, RCA and HDPE. Experiments were conducted to determine the possibility of the new mortar utilizing the trapped free water between the old HDPE plates during consolidation before the water is absorbed by the porous RCA.

2. LITERATURE REVIEW

In this study, RCA is considered crushed concrete and and therefore contains a coating of residual mortar around each RCA particle, which significantly increases the porosity and water absorbability. The greater porosity of the RCA reduces the density and lowers the specific gravity compared to NCA (Yong Ho et al. 2013, McNeil and Kang 2013).

Yang, Du and Bao (2011), conducted slump tests with 100% NCA and 100% RCA. The RCA was pre-wetted prior to mixing and the water to cement ratio used for both mixes was 0.47. There was a decrease in slump of approximately 27% when RCA fully replaced the NCA.

The CS of RCA concrete mixes are influenced by the water to cement ratio, the percentage of RCA used to replace the NCA, the quantity of adhered mortar on the RCA particles and the variability in the quality of the RCA obtained from different sources (McNeil and Kang 2013, Ajdukiewicz and Kliszczewicz 2002, Meyer 2009). Batayneh et al. (2007) replaced 20% of the NCA with RCA and obtained a 13% CS reduction. Kang et al. (2014) replaced 50% of NCA with RCA and acquired

strength reductions of 25%, 19% and 17% in CS, TSS and FS. Yang, Du and Bao (2011) replaced 100% NCA with RCA and obtained a decrease in CS, FS, and TSS of 5.7%, 13.8% and 9.3%. Padmini et al. (2009) found that concrete with RCA required lower water to cement ratio and higher cement content to obtain a design CS. Also, medium and high strength RCA was a better choice than the use of RCA derived from lower strength concrete (Tabsh and Abdelfatah 2009, Mwasha 2009).

Failure of RCA concrete samples occurred by fracturing through the recycled aggregate as well as through the ITZ between the recycled aggregate and the mortar. The recycled coarse aggregate fell off easily and there was larger ITZ cracks in the recycled aggregate concrete relative to natural aggregate concrete (Lee and Choi 2013). McNeil and Kang concluded that the concrete modulus of rupture of RCA was lower because of the weakened ITZ due to the residual mortar on the RCA (McNeil and Kang 2013).

Studies by (Ramesan, Babu and Lal 2015) demonstrated that the physical properties of plastic aggregates influenced the workability of the fresh concrete. Some shapes and sizes resulted in increased concrete slump, while others resulted in a decrease in slump or a need for additional superplasticizer. A smooth surface texture and spherical nature of the pellets increased the slump unlike coarse texture and sharp edges of the flakes which reduced the slump. In addition, the inability of the plastic aggregate to absorb water resulted in more free water and greater slump of the concrete (Saikia and Brito 2012, Saikia and Brito 2014, Al-Manaseer and Dalal 1997). The HDPE flakes and the RCA are small elongated, flat plates and angular rough aggregate respectively (Neville 2011). Water pressed together by two plastic plates creates adhesion between the plates and the water (Massey and Ward-Smith 2006). The pressure inside the liquid is less than the surrounding atmosphere by an amount depending on the tension in the free surface, and to separate the plates an additional force is required (Smits 2017). Alternatively, an increased surface tension between the HDPE flakes and the water can give rise to a loss of moisture within the fresh concrete mix and a lowered workability of the sample.

Concrete containing 100% plastic aggregate illustrated a significant reduction in both CS and TSS attributed to the weak bond between the cement paste and the plastic aggregate. However, plastic in concrete increased the ability of the concrete to significantly deform prior to failure, a feature utilized in expansion and contraction of the material (Kumar and Kumar 2016). Additionally, concrete containing plastic can be useful in the repair and overlay of damaged concrete surfaces such as pavements, floors, bridges and dams (Siddique et al. 2008).

3. METHODOLOGY

This study investigated the replacement of NCA with 25%, 50%, 75% and 100% of RCA in concrete to determine the volume percentages required to achieve optimum CS and TSS. Furthermore, HDPE was used to replace NCA in the form of flakes at percentages of 5%, 10%, 15%, 20% and 25%. The percentage of HDPE incorporated did not exceed 25% as the integration of HDPE more than 22% adversely affected the workability and strength parameters of concrete (Matthew et al. 2013). The mix design ratios adopted contained fine aggregate to cement of 2, coarse aggregate to cement of 3, and water to cement (w/c) of 0.5. The superplasticizer, Fosroc Conplast SP430, was consistently utilized in all mixes at a volume of 1.9 ml per kg of concrete to aid the workability of the mix with higher percentage of RCA and HDPE. The RCA was utilized from old crushed concrete laboratory samples, and the HDPE flakes were obtained from a waste disposal site in Trinidad.

Identification of aggregate shape and surface texture was conducted according to (Neville 2011) as well as sieve analysis performed. The size of the coarse aggregates all ranged between 5 mm and 20 mm. Water absorption, specific gravity, and aggregate impact value tests were also used to characterize the NCA and RCA specimens.

A trial mix conducted on NCA without superplasticizers produced a slump value of 30 mm. In an effort to ensure sufficient slump was obtained for the mix with greatest RCA percentage, superplasticizers were used on 100% RCA test specimen. The greater percentage of RCA in the concrete mix results in a greater water absorption rate and a lower slump value. The target CS at 28 days was 35 MPa.

The design mix ratio for optimum RCA and HDPE was performed in two separate stages: an initial mix combining with NCA and RCA or NCA and HDPE flaxes separately (see Table 13) and a second mix incorporating the optimum designs from stage I (see Table 14). The mix designs were selected based on the results of slump tests, CS tests conducted on 101.6 mm cube specimens, and TSS tests conducted on 101.6mm dia. x 203.2 mm depth cylinders at 28 days curing. Six specimens were tested for CS and TSS tests. The sieve analysis, slump tests, CS and TSS tests were again repeated for the second stage mix designs in addition to modulus of rupture tests on 100 mm x 100 mm x 400 mm beams at 28 days curing.

Table 13. Design Mix Percentages of NCA, RCA and HDPE Flakes for Stage I

Design Mix	NCA (%)	RCA (%)	HDPE (%)	Slump (mm)
A	100	0	0	170
B25	75	25	0	170
B50	50	50	0	170
B75	25	75	0	70
B100	0	100	0	45
C5	95	0	5	185
C10	90	0	10	
C15	85	0	15	145
C20	80	0	20	140
C25	75	0	25	140

Table 14. Design Mix Percentages of NCA, RCA and HDPE Flakes for Stage II

Design Mix	Optimum RCA Mix(%)	Optimum HDPE Mix(%)	Slump (mm)
D1	75	25	110
D2	50	50	130
D3	25	75	140

4. RESULTS AND ANALYSIS

The shape and surface texture of the NCA was irregular and smooth, compared with the RCA of angular and rough with honeycombs, and the HDPE flakes were elongated and flaky with a smooth plastic surface. Both the NCA and RCA fell within the upper and lower limits of the sieve analysis, but the flaky elongated shape resulted in a lower percent of the HDPE retained on all sieves.

The results of the CS and TSS tests for the stage I mix of recycled aggregates and natural aggregates are provided in Table 15. The optimum design mixes for RCA and HDPE were B75 and C5 respectively. The increase in CS can be attributed to the fact that the w/c ratio was kept constant at 0.5 for all the mixes, and the CS of material used to create the RCA was 20% greater than the target strength. A lower w/c ratio can enhance the interfacial transition zone and improve CS. These mixes were utilized in the stage II D1, D2, and D3 mixes, and the strength test results are provided in Table 16.

Table 15. CS and TSS Results for Stage I Mix

Mix	CS (MPa)			TSS (MPa)		
	Min	Max	Ave	Min	Max	Ave
A	**38**	**46**	**43**	**2.2**	**2.9**	**2.7**
B25	28	41	35	3.1	3.4	3.2
B50	35	41	37	3.4	4.0	3.6
B75	**35**	**44**	**41**	**3.0**	**3.8**	**3.4**
B100	33	41	35	2.1	2.9	2.6
C5	**40**	**43**	**41**	**3.0**	**3.2**	**3.0**
C10	26	29	27	2.1	2.6	2.3
C15	20	24	22	1.2	1.4	1.3
C20	10	16	13	1.1	1.2	1.1
C25	8	10	9	0.8	0.9	0.9

Table 16. CS, TSS, and FR Results for Stage II Mix Design

Mix	CS (MPa)			TSS (MPa)			FS (MPa)		
	Min	Max	Ave	Min	Max	Ave	Min	Max	Ave
A	38	46	43	2.2	3.0	2.7	4.5	5.3	4.9
D1	39	43	41	2.3	2.8	2.4	4.9	5.4	5.2
D2	36	41	39	2.0	2.8	2.2	4.2	5.0	4.6
D3	32	39	36	1.5	2.4	2.0	4.2	5.1	4.6

The mixes D1, D2 and D3 all attained a CS above the target of 35 MPa, but decreased in CS from the original mix A by 4.7%, 9.3% and 16.3% respectively.

The HDPE selected resulted in a lower slump for RCA replacement of 15 % or more. This could be a result of the flat, flaky, elongated shape of the HDPE resulting and a surplus of water being trapped between the flakes due to high surface tension (Massey and Ward-Smith 2006), and the weak packing as demonstrated with the poor sieve analysis results. The mixing process did not utilize the trapped free water to create a more workable mix. Additionally, the low density of the HDPE resulted in high segregation of flakes during the mixing and vibrating process and the creation of non-uniformed composition. The replacement of HDPE flakes up to 15% resulted in Type 1 failure mode with uniformed cones, but at 20% and 25% HDPE replacement, the failure modes of the specimens were Type 3 or columnar vertical cracking through both ends. The extensive HDPE segregation present in C20 and C25 created weak regions across the specimens resulting in vertical cracking. Poor bonding was also observed due to the surface texture of the HDPE in addition to an increase in voids with the use of the HDPE. The TSS followed similar trends to the CS results.

Based on all the findings of the study, B75, C5 and D1 attained the highest compressive cube strength at 28 days of 41 MPa illustrating a 5%, 4% and 4% reduction in strength relative to the control mix. These design mixes achieved the desired CS, therefore 75% RCA or 5% HDPE flakes or a combination of 1.25% HDPE flakes and 56.25% RCA as a replacement to NCA in concrete are all feasible design mixtures.

All beam A specimens exhibited small voids on all surfaces, and failed within the middle region. The fractured face displayed aggregate failure and some NCA bond failure. Segregation of HDPE flakes were also observed on the top surfaces of the D1, D2, and D3 mixes. The defects observed on the fractured faces were aggregate failure of RCA and NCA, with minor bond failure for all aggregates. Additionally, the HDPE flakes in the D3 specimen held some of the samples together after failure.

5. CONCLUSION

The integration of RCA at all increments resulted in a decrease in CS relative to the control mix due to greater porosity, lower density, and the double ITZ. A 17% increase in CS with inclusion of 25% to 75% RCA was observed, but a decline in CS was obtained for 100% RCA. The increase in HDPE flakes drastically affected the strength of the concrete due to its inability to produce a uniformed mix and its poor bonding capability. However, the combination of a small quantity of HDPE flakes, up to 5%, presented a concrete with a feasible CS, TSS and FS and with good workability. The use of the HDPE flakes in the mix design did not aid the workability, and generally reduced the strength. Although the plastic can be utilized in small quantities, it is a weaker alternative to sustainability benefits of plain RCA. Further investigation can be done on altering the size, shape and surface texture of the HDPE in the mix.

REFERENCES

Ajdukiewicz, Andrzej, and Alina Kliszczewicz. 2002. Influence of recycled Aggregates on Mechanical Properties of HS/HPC. Cement & Concrete Composites 24 (2): 269-279.

Al-Manaseer, A.A. and, T.R. Dalal. 1997. Concrete Containing Plastic Aggregates. Concrete International 19 (8): 47–52.

Batayneh, Malek, Iqbal Marie and Ibrahim Asi. 2007. Use of Selected Waste Materials in Concrete Mixes. Waste Management 27 (12): 1870-1876.

Kang, Thomas, Woosuk Kim, Yoon-Keum Kwak and Sung-Gul Hong. 2014. Flexural Testing of Reinforced Concrete Beams with Recycled Concrete Aggregates. ACI Structural Journal 111 (3): 607-616.

Kumar, Parvesh, and Gaurav Kumar. 2016. Effect of Recycled Plastic Aggregates on Concrete. International Journal of Science and Research (IJSR) 5 (6): 912-915.

Lee, G.C., and H.B. Choi. 2013. Study on Interfacial Transition Zone Properties of Recycled Aggregate by Micro-hardness Test. Construction and Building Materials 40:455-460.

Massey, Bernard, and John Ward-Smith. 2006. Mechanics of Fluids. London and New York: Taylor & Francis.

Mathew, Praveen, Shibi Varghese, Thomas Paul, and Eldho Varghese. 2013. Recycled Plastics as Coarse Aggregate for Structural Concrete. International Journal of Innovative Research in Science, Engineering and Technology 2 (3): 687-690.

Mwasha, Abraham. 2009. Natural and Recycled Guanapo Quarzite Aggregates for Ready Mix Concrete. The Journal of the Association of Professional Engineers of Trinidad and Tobago 38(1): 50-56.

McNeil, Katrina, and Thomas H.-K. Kang. 2013. Recycled Concrete Aggregates: A Review. International Journal of Concrete Structures and Materials 7 (1): 61-69.

Meyer, C. 2009. The Greening of the Concrete Industry. Cement & Concrete Composites 31:601-605.

Neville, A.M. 2011. Properties of Concrete. London, England: Pearson Education Limited.

Padmini, A.K., K. Ramamurthy and M.S. Mathews. 2009. Influence of Parent Concrete on the Properties of Recycled Aggregate Concrete. Construction and Building Materials 23 (2): 829-836.

Ramesan, Anju, Shemy S. Babu, and Aswathy Lal. 2015. Performance of Light-Weight Concrete with Plastic Aggregate. International Journal of Engineering Research and Applications 5 (8): 105-110.

Saikia, Nabajyoti, and Jorge de Brito. 2012. Use of Plastic Waste as Aggregate in Cement Mortar and Concrete Preparation: A review. Construction and Building Materials 34:385-401.

Saikia, Nabajyoti, and Jorge de Brito. 2014. Mechanical Properties and Abrasion Behavior of Concrete Containing Shredded PET Bottle Waste as a Partial Substitution of Natural Aggregate. Construction and Building Materials 52 (15): 236-244.

Siddique, Rafat, Jamal Khatib and Inderpreet Kaur. 2008. Use of Recycled Plastic in Concrete: A Review. Water Management 28 (10):1835-1852.

Smits, Alexander J. 2017. A Physical Introduction to Fluid Mechanics. Accessed May 11, 2017. http://www.efluids.com/efluids/books/Smits_text_part1.pdf.

Tabsh, Sami W., and Akmal S. Abdelfatah. 2009. Influence of Recycled Concrete Aggregates on Strength Properties of Concrete. Construction and Building Materials 23 (2): 1163-1167.

Trinidad and Tobago. Ministry of Energy and Energy Affairs. 2017. Quarrying. Accessed February 07, 2017. http://www.energy.gov.tt/our-business/aggregates/quarrying/.

Yang, Jian, Qiang Du, and Yiwang Bao. 2011. Concrete with Recycled Concrete Aggregate and Crushed Clay Bricks. Construction and Building Materials 25 (4): 1935-1945.

Yong Ho, Nyok, Yang Pin Kelvin Lee, Wee Fong Lim, Tarek Zayed, M. ASCE, Keat Chuan Chew, Giau Leong Low, and Seng Kiong Ting. 2013. Efficient Utilization of Recycled Concrete Aggregate in Structural Concrete. Journal of Materials in Civil Engineering 25 (3): 318-327.

39th Cement and Concrete Science Conference
9-10th September 2019
University of Bath
Paper Number 044

Proposed Alternative Formwork System for Concrete Shells

L.C. Meneghetti
Department of Geotechnical and Structural Engineering, University of São Paulo

B. Sharma
Department of Architecture and Civil Engineering, University of Bath

ABSTRACT

Concrete is the world's second most consumed man-made material, and is responsible for up to 7% of total greenhouse gas emissions. Shell structures are well-known as structurally efficient elements, with pleasing architectural and aesthetic appeal in view of their curved shapes. In contrast to this structural efficiency, the traditional timber and plywood formwork system is highly complex in such cases (in order to reach the shape of the elements), highly labour-intensive and therefore, very costly. This complexity of construction and the empiricism in form finding processes prevalent in the 1960s and 1970s, the heyday of shell-like structures, has finally side-lined them in favour of the traditional slab-beam-columns system. However, current advances in modelling techniques and the advent of computers with ever more powerful data processing capabilities, together with marked progress in material technology (concrete), have again opened up the possibility of employing shells as innovative structural elements. If, on the one hand, modelling techniques allow definition of structurally highly efficient shapes, construction systems must accompany this trend in order to contribute with a more ecologically-oriented, less energy-consuming system. Flexible formwork systems using natural fibre reinforced composites could be a viable alternative for shell construction systems. The presented work will review and assess the potential of sisal fibre composites to form the first hardening layer in building pneumatic formwork shells. The proposed work will develop an innovative and optimized construction system in terms of project (topology), with a low carbon – low ecological footprint.

1. INTRODUCTION

The discovery of Portland cement, a basic element in the production of concrete, has revolutionized the world's architectural landscape. The plastic feature of concrete gives the material the ability to be cast into free shapes, surprisingly explored by Frank Lloyd Wright, Oscar Niemeyer, Le Corbusier, Felix Candela, Eduardo Torroja, Frei Otto, Heinz Isler, and many other renowned architects and engineers. This characteristic of fresh plasticity and consequent flexibility in the moulding of forms is facilitated by use of cement, a hydraulic binder with an annually increasing global production since World War II. In 2016, global production was 4.65 billion tonnes (see https://cembureau.eu/cement-101/key-facts-figures/).

Cement production is the third largest source of CO_2 emissions, due to calcination of the limestone and the high energy required to heat the raw materials at temperatures above 1400°C in rotary kilns. It is estimated that the contribution of Portland cement production is approximately 5 to 7% of the total anthropogenic emissions (Huntzinger & Eatmon, 2009 and Meyer, 2009). Therefore, reducing the use of cement is a key issue to promote sustainability in concrete construction. One of the ways to decrease cement consumption is using free-form casting to design structurally efficient shapes, such as funicular shells, whose stress state is essentially compressive. Single or double curved shells have reduced bending moment and shear stresses. With their membrane-like behaviour (plane stresses only), the shells need to be a few centimetres-thick to manage large spans (Mutoni et al., 2013). During the mid-20th century, thin-shell concrete structures were widely used to cover large spans, but applications began to decline due to the intense work and cost of the formwork system, and the complexity of sizing, often related to empiricism in the form finding methods.

Preferably, in the vast majority of works, the concrete is cast into rigid moulds, resulting in prismatic cross sections which are not the most desirable and efficient, both aesthetically and structurally (Hawkins et al., 2016). The orthogonality of the cross sections leads to the predominance of structural systems composed of orthogonal beams and cross-section pillars, which often leads to an increase in dead loads.

However, advances in numerical modelling techniques that allow the search for structural shape and analysis of free-form elements coupled with concrete technology - mixtures that can be applied in very thin layers fast-hardening layers and with strict surface control, opens again a range of opportunity for the use of concrete shells.

From a structural perspective, concrete shells could be designed in a much more efficient manner so as

to adequately utilise the material properties. In order to guarantee efficiency, the research object now is the development of an alternative easy handled formwork system that is eco-friendly. The proposed study will explore development of pneumatic formwork using natural fibre composites.

2. PNEUMATIC FORMWORK SYSTEM

Shell structures are composed by a free-form or double curve in most of their applications. This complex geometry results in surfaces that are not constructible. For example, it is impossible to flatten the shape of a sphere without major distortion or flaring. Thus, complex formwork systems are necessary to construct these non-orthogonal surfaces.

A potential answer to this design challenge is the application of pneumatic formwork. Pneumatic formwork was first patented in 1926 for the production of culverts and concrete pipes; this involved the inflation of a cylindrical membrane coupled with the setting of workable concrete moulded around it, eventually culminating in the rupture and removal of the membrane (Kromoser and Huber, 2016).

Advantages of this method included high level of prefabrication, quick erection and dismantling, almost unlimited spatial curvatures, large spans and multiple uses (Sobek, 1991). Actually, pneumatic formwork systems have appeared in limited spatial shapes because erection was done by balloon. Since the invention, a number of different systems and erection-procedures have been developed in order to reduce the deformation in the formwork. The control of formwork deformations is of great importance because the shape can change remarkably under the load of fresh concrete (e.g. Bini, 1967; Schlaich and Sobek, 1986; South, 1990; Pronk et al., 2007, Hove, 2008, Kromoser and Kolleger, 2016).

3. SISAL FIBRE

Brazil is the world´s largest producer and exporter of thread and manufactured sisal (*Agave Sisalana*) (CONAB, 2016). In 2017, Brazilian total production recorded 133,000 tons in a planted area equivalent to 206,327 ha (IBGE, 2017), located in the states of Bahia and Paraíba, semi-arid region where total rainfall is scarce and irregular. Sisal is used in the manufacture of ropes, rugs, brooms, bags, handcrafted items and also as an automobile component. In construction applications, research carried out by Lima et al. (2019) and by Savastano Jr et al. (2006) reported the potential of using sisal fibres in cementitious composites, although protection studies against early fibre degradation are required. Frollini et al. (2004) studied sisal as reinforced fibre in phenolic composites.

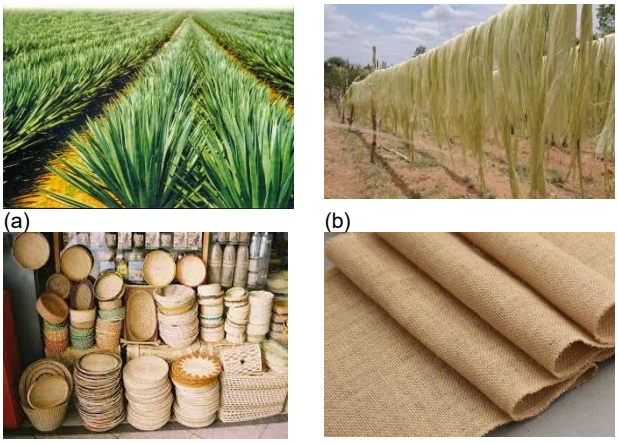

Figure 1. (a) sisal plantation; (b) sisal fibre drying processes; (c) handicrafts and (d) sisal fabric

Figure 1 shows the sisal plant (*Agave sisalana*) besides handicrafts and the fabric itself. In this study, the use of sisal fabric as flexible formwork will be explored.

Flexible formwork composed by sisal fibres can be a viable alternative due to its low cost. When compared to carbon and glass fibre, sisal fibres costs represent 11% of glass fibre and 0.07% of carbon fibre. Furthermore, sisal fibres show good mechanical properties when compared with other natural fibres (Table 1).

Physical and mechanical performance and specific gravity of natural and artificial fibres are presented in Table 1.

Table 1. Physical and mechanical properties of natural and artificial fibres (Bledzki and Gassan, 1999)

Fibre	Specific gravity (g/cm^3)	Ultimate strain (%)	Tension Strength (MPa)	Young modulus (GPa)
Sisal	1.5	2.0-2.5	511-635	9.4-22
Cotton	1.5-1.6	7.0-8.0	287-597	5.5-12.6
Hassey	1.3	1.5-1.8	393-773	26.5
Flax	1.5	2.7-3.2	345-1035	27.6
Glass	2.5	2.5	2000-3500	70
Aramid	1.4	3.3-3.7	3000-3150	63-67
Carbon	1.4	1.4-1.8	4000	230-240

Tests on small-scale models can be used to evaluate the feasibility of alternative composites as a stiffening layer in the construction system of thin shells. The characteristic double curvature is ensured by pressurizing a special natural membrane composite to obtain the desired shape. On the composite, a layer of concrete is applied to support the structural element. The scheme of constructive technique under study is shown in Figure 2.

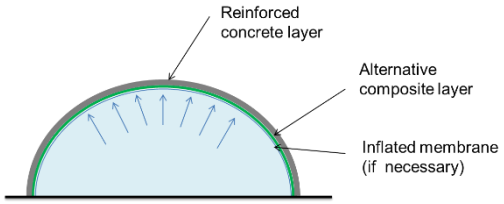

Figure 2. Alternative construction system proposed

3. SUMMARY

The presented work is a proposal for development of an innovative and optimized construction system in terms of design (topology) and low carbon - low ecological footprint. The method includes additional social impact through the diversification of sisal and to the development of rural communities in the Brazilian Northeast, which are dependent on subsistence from sisal.

REFERENCES

Bledzki, L.M., Gassan, J., 1991. Composites reinforced with cellulose based fibres. Progress in Polymer Science 24: 221-274.

CONAB – Companhia Nacional de Abastecimento (2016). Conjuntura especial. Sisal: Exportações em queda. Available in: https://www.conab.gov.br/OlalaCMS/uploads/arquivos/16_07_28_17_

Frollini, E. et al., 2004. Plastics and composites from lignophenols. Natural fibres, plastics and composites. 193-225.

Hawkins, W. et al., 2016. Flexible formwork technologies – a state of the art review. Structural Concrete 17(6): 911-935.

Huntzinger, D.N., Eatmon, T.D., 2009. A life-cycle assessment of Portland cement manufacturing: comparing the traditional process with alternative technologies. Journal of Cleaner Production, 17 (7): 668-675.

IBGE – Instituto Brasileiro de Geografia e Estatística (2017). Levantamento sistemático da produção agrícola. 108 pages. Available in: ftp://ftp.ibge.gov.br/Producao_Agricola/Levantamento_Sistematico_da_Producao_Agricola_%5Bmensal%5D/Fasciculo/2017/lspa_201712.pdf

Kromoser, B., Huber, P., 2016. Pneumatic formwork systems in structural engineering. Advances in Material Science and Engineering. 2016, Article ID 4724036, 13 pages.

Kromoser, B., Kollegger, J., 2016. Building concrete shells without formwork and falsework. In: Proceedings of fib Symposium, Volume: Performance-based approaches for concrete structures. Capetown.

Lima, P.R.L. et al. ,2019. Effect of accelerated agind on the properties of microconcrete reinforced with sisal fibres. Ambiente Construído,19(1): 7-20.

Meyer, C., 2009. The greening of the concrete industry. Cement and Concrete Composites 31: 601-605.

Mutoni, A., Lurati, F., Ruiz, M.F., 2013. Concrete shells – towards efficient structures: construction of an ellipsoidal concrete shell in Switzerland. Structural Concrete 14 (1): 43-49.

Savastano, H. Jr et al., 2006. Mechanical behavior of cement-based materials reinforced with sisal fibre. Journal of Materials Science 41: 6938-6948.

Sobek, W., 1991. On design and construction of concrete shells. Cement 11: 23-27.

39th Cement and Concrete Science Conference
9-10th September 2019
University of Bath
Paper Number 045

Corrosion resistance of steel fibre reinforced concrete (SFRC) subjected to stray alternating current (AC) interference

Dr Kangkang Tang
College of Engineering, Design and Physical Sciences, Brunel University London

ABSTRACT

This paper discusses suitable approaches for the simulation of railway stray alternating current (AC) conditions, upon which the corrosion susceptibility of steel fibres can be assessed. Instrumental methods in electrochemistry including Tafel polarization and Electrochemical Impedance Spectroscopy (EIS) were conducted to assess the corrosion resistance of steel fibres which has great potential to replace conventional steel reinforcement in railway tunnel construction. The analytical model developed based on electric circuit modelling indicates that concrete containing discrete steel fibres has an inherent corrosion resistance to stray AC interference under a chloride-free condition due to the electrical double layer developed on the surface. The presence of chloride at a low concentration (< 0.3 mol/L) in the concrete pore solution does not have significant effect on the corrosion resistance of steel fibres.

1. INTRODUCTION

Railway electrification represents an important carbon strategy in the UK. It is estimated that an electric train consumes at least 20% less power (per passenger per mile) compared to a diesel-powered train (Kemp, 2007). In the UK, only 39% of the national rail network is electrified and the government is committed to promote railway electrification and thus provide more sustainable and comfortable services for the public. Major work has been carried out for the Crossrail project and the High Speed 2 (HS2). For a modern electric train traction system, the transmission of power is normally provided by an overhead wire or a conductor rail; the return circuit is usually through the running tracks to nearby substations. Stray current refers to the current which disperses directly to the ground through the return path. Stray current can accelerate the corrosion of railway tunnel segmental lining concrete and surrounding service cables, water mains and gas pipes. Approximately £550 million is required per annum for the rehabilitation and repair of the stray-current induced corrosion damage to the UK infrastructure (National Physical Laboratory (UK), 2015). ACI 544 (2010), report on the physical properties and durability of fibre-reinforced concrete, states that "*since the fibres are short, discontinuous and rarely touch each other, there is no continuous conductive path for stray or induced currents or currents from electromotive potential between different areas of the concrete*". Based on this information, SFRC appears to be an ideal substitute for conventional steel reinforcement in electric railway systems, with less concern about stray current induced corrosion. On the other hand, the investigation of stray current, especially stray alternating current (AC)-induced corrosion, is still very limited based on a review of the literature. This is despite that AC traction power systems account for 64% of the UK electrified railway network (Keen and Phillpotts, 2010). For a stray DC interference alone issue, Bertolini *et al.* (2007) reported that a DC current density up to 1 mA/cm^2 was enough to initiate serious pitting corrosion in reinforced concrete; AC current density of 4 mA/cm^2 (50 Hz) however did not initiate any corrosion in reinforced concrete containing up to 0.2% chloride (by mass of cement), indicating enhanced corrosion resistance to a stray AC interference. Tang (2019) proposed a mathematical model (Eq. (1)) for the prediction of Faradaic current picked up and transferred by discontinuous steel reinforcement subjected to an AC perturbation, $I_0 \sin(\omega t)$. It shows that the magnitude of AC current (I_0) and angular velocity (ω) are key parameters governing the corrosion of steel reinforcement subjected to an AC perturbation. Increased ω can lead to reduced Faradaic current flowing through discontinuous steel reinforcement and thus the reduced corrosion rate (*CR*). This finding agrees well with the published experimental data (Bosch and Bogaerts, 1998). In addition to ω, R_{ct} (charge transfer resistance) and C_{dl} (double-layer capacitance) represent important parameters governing the kinetic properties of the steel-concrete interface.

$$I(t) = \frac{I_0}{\sqrt{1+\omega^2 \cdot C_{dl}^2 \cdot R_{ct}^2}} \sin(\omega t - \theta) + \frac{\omega \cdot C_{dl} \cdot R_{ct} \cdot I_0}{\omega^2 \cdot C_{dl}^2 \cdot R_{ct}^2 + 1} \cdot e^{-\frac{t}{C_{dl} \cdot R_{ct}}} \quad (1)$$

Chloride represents a common corrosive substance which can lead to the breakdown of steel passive layer. The presence of chloride in concrete can be a result of contaminated aggregate and mixing water. The ingress of chloride from the external

environment, e.g. de-icing agents, can also reach steel reinforcement through the concrete cover. Tang (2017) reported that 0.6 mol/L may be taken as the chloride threshold level for corrosion of steel fibres in the concrete pore solution. This is significantly higher than that of conventional steel reinforcement, i.e. 0.17-0.34mol/L (Angst, Elsener et al., 2009), which indicates the steel fibre has a higher resistance to chloride attack.

2. Experimental and analytical procedures

The primary objective of this project is to simulate the stray AC interferences using laboratory equipment, upon which the corrosion susceptibility of SFRC to a simulated stray AC interference can be assessed. In this work, a galvanostatic polarization technique (control of current) was developed for the simulation of the stray AC environment. The electrochemical cell is shown in Fig. 24. It allows AC voltage to be applied to the steel fibre under a controlled anodic current of 30 mA (50 Hz). This was achieved using the Gamry Interface 1000E potentiostat with the Gamry's Virtual Front Panel (VFP600) software package which applied sine wave current perturbation of 30 mA to the WE at a constant frequency of 50 Hz, when the external potential (*E*) was measured. The AC frequency, i.e. 50 Hz, is the same as the UK National Grid AC frequency. After the 10-min stray AC interference test and Tafel polarization tests were conducted in sequence. Three parallel samples were prepared and tested for each aqueous electrolyte composition simulating the concrete pore solution. Freshly prepared electrodes and electrolytes were taken at start of each test. Tafel polarization was conducted by applying a DC potential perturbation, ±250 mV (vs OCP), was applied to the WE and the current flow between the WE and a 40×50×3mm graphite counter electrode (CE) at a potential scanning rate of 1 mV/sec. Tafel slope analysis was then conducted to determine the corrosion current density (i_{corr}) and corrosion potential (E_{corr}) through a nonlinear regression an. The effect of chloride on the corrosion of steel fibres was investigated by adding NaCl into the electrolyte at different concentrations, i.e. 0, 0.3, 0.6 and 0.8 mol/L. Three parallel samples were prepared and tested in each group. Freshly prepared electrodes and electrolytes were used in each test.

Cyclic Potentiodynamic (CP) polarization was conducted to obtain additional information about the passivation behaviour of steel fibres after the stray AC interference test. The experimental procedure of CP polarization was similar to that of Tafel polarization, despite the potential sweep being mainly along the anodic direction, e.g. -0.5 to 1.5 V from the open circuit potential (OCP). A faster scanning rate of 5 mV/sec was adopted in CP polarization and a reverse scan was conducted when either the maximum potential (i.e. 1.5 V vs OCP) or a maximum current density of 100 mA/cm^2 was achieved. Two parallel samples were prepared and tested in each group.

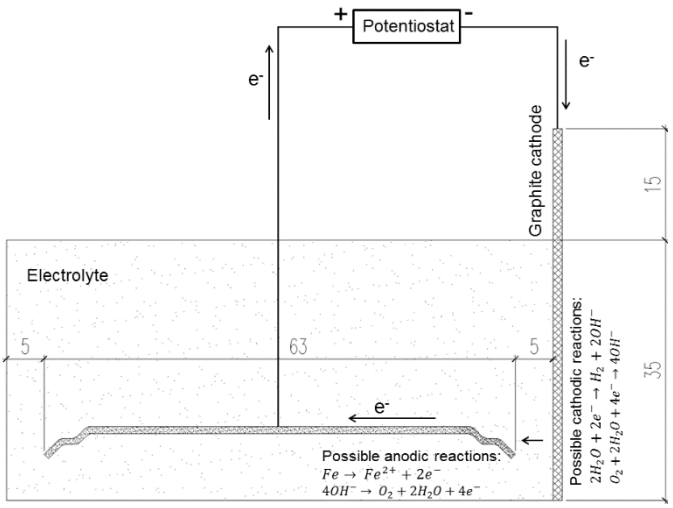

Fig. 1. DC galvanostatic polarization test (all units in mm) (Tang, 2019)

3. Results and discussion

Before the stray AC interference test, Tafel polarization was conducted and the polarization curves are in Fig. 25. The presence of chloride pushed the corrosion potential E_{corr} to more negative values, alongside increased corrosion current densities, i_{corr}, indicating enhanced corrosion reactions. After the stray AC interference test, Tafel polarization was conducted and results of E_{corr} and i_{corr} are presented in Fig. 26. It shows that the pre-exposure of steel fibres to a simulated AC stray current interference shifted the corrosion potential E_{corr} towards more negative values. This agrees with results reported in the literature (Chin and Sachdev, 1983; Goidanich, Lazzari et al., 2010). The presence of AC interference however did not significantly increase i_{corr} when comparing the case where the Tafel polarization procedure was carried out on the as-received steel fibre with the case where it was performed after the exposure of the steel fibre to the simulated AC stray current interference.

CP polarization results obtained before and after the AC interference test (Fig. 27, Fig. 28) show that similar CP voltammograms were obtained with up to 0.3 mol/L NaCl in the electrolyte. Visual observation was conducted to assess the steel fibre surface after exposure to the simulated AC stray current interference: no rust was observed on the steel fibre surface with even 0.8 mol/L NaCl in the electrolyte. In comparison to an aqueous electrolyte, a solid electrolyte such as concrete has different chemical compositions, electrical resistance and electronic structures which can affect the corrosion behaviour

of steel. This has been discussed in a separate paper (Tang, 2019).

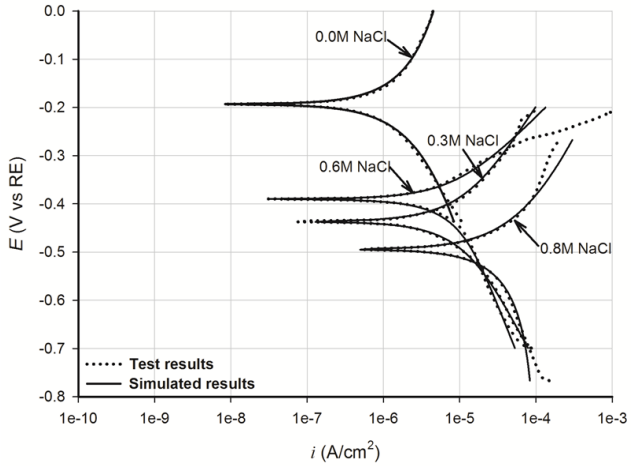

Fig. 2**.** Tafel polarization results (before AC interference) (Tang, 2019)

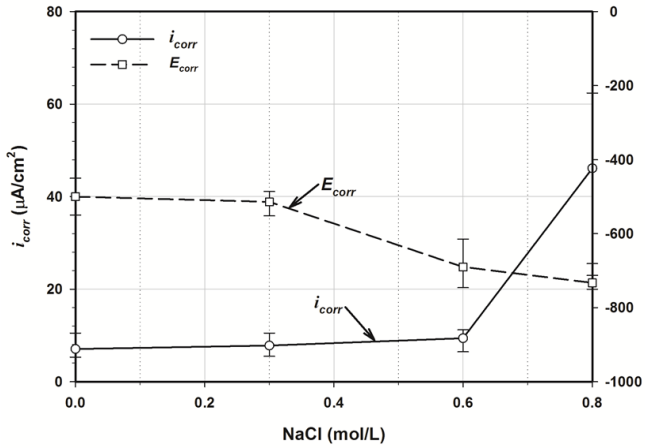

Fig. 3**.** Tafel polarization results (after 10-min stray AC interference) (Tang, 2019)

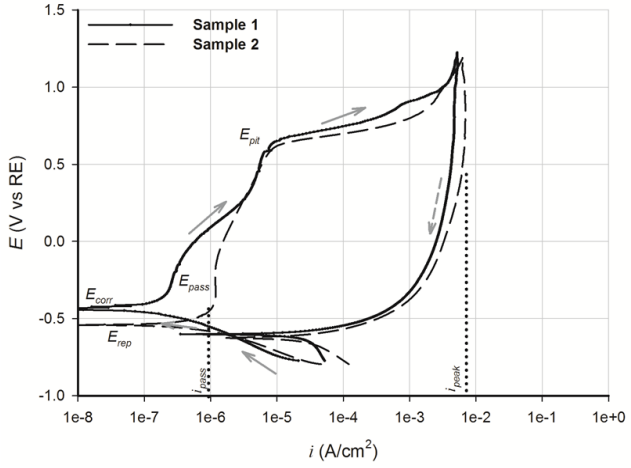

(a) 0.0 mol/L NaCl in the electrolyte

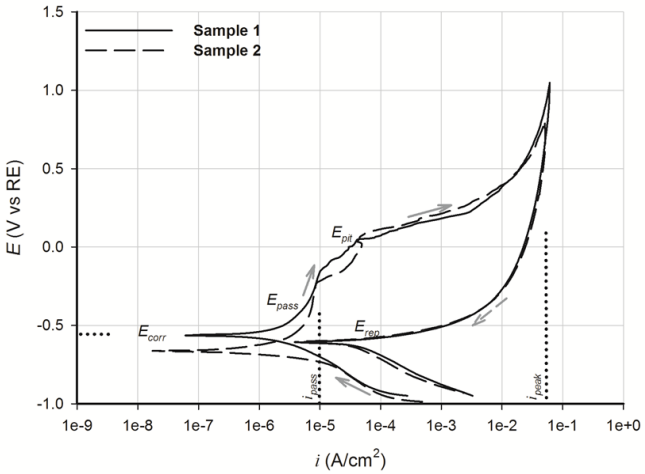

(b) 0.3 mol/L NaCl in the electrolyte

Fig. 3**.** CP polarization test results (before AC interference) (Tang, 2019)

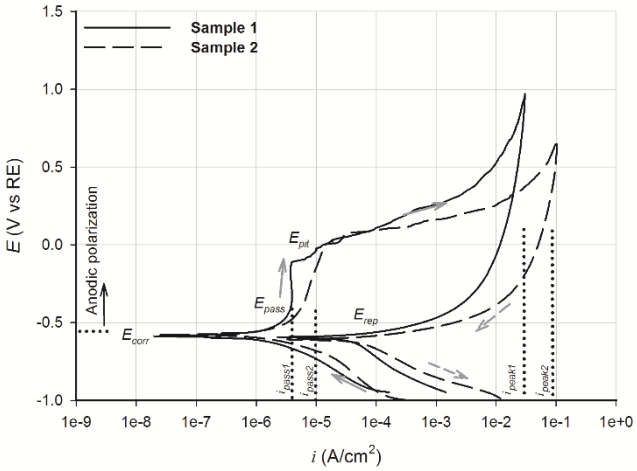

Fig. 4. CP polarization test results (0.3 mol/L NaCl) (after 10-min stray AC interference) (Tang, 2019)

4. Conclusion

The stray current induced corrosive damage to railway infrastructure will become more prominent in the UK as the government is committed to developing more electrified rail networks. The effect of stray the AC interference on the corrosion of steel fibres can be investigated by instrumental methods for electrochemistry. Tafel and cyclic potentiodynamic (CP) polarization provides useful information about electrochemical kinetics relating to the corrosion rate where the values of polarization are low. CP polarization results, especially those obtained at a high-value anodic overpotential, provides useful information which can be used to quantitatively assess the corrosion behaviour of steel fibres subjected to a simulated stray AC interference.

The experimental results indicate that steel fibres demonstrate high inherent corrosion resistance to AC interference (30 mA, 50 Hz). The presence of NaCl up to 0.3 mol/L in the simulated concrete pore solution did not significantly enhance steel fibre corrosion. This can be attributed to the electrical double layer developed on the steel surface which allows a part of the stray AC currents to flow through it without causing corrosive damages to the embedded steel fibre.

REFERENCES

ACI Committee 544 (2010). Report on the physical properties and durability of fiber-reinforced concrete. Farmington Hills, U.S.A., American Concrete Institute.

Angst, U., B. Elsener, et al. (2009). "Critical chloride content in reinforced concrete - a review." Cement and Concrete Research **39**(12): 1122-1138.

Bertolini, L., M. Carsana, et al. (2007). "Corrosion behaviour of steel in concrete in the presence of stray current." Corrosion Science **49**(3): 1056-1068.

Bosch, R. W. and W. F. Bogaerts (1998). "A theoretical study of AC-induced corrosion considering diffusion phenomena." Corrosion Science **40**(2): 323-336.

Chin, D.-T. and P. Sachdev (1983). "Corrosion by alternating current: polarization of mild steel in neutral electrolytes." Electrochemical science and technology **130**: 1714-1718.

Goidanich, S., L. Lazzari, et al. (2010). "AC corrosion – Part 1: Effects on overpotentials of anodic and cathodic processes." Corrosion Science **52**(2): 491-497.

Keen, P. and R. Phillpotts (2010). Low cost electrification for branch lines. Derby, DeltaRail.

Kemp, R. (2007). Traction energy metrics. Lancaster University, UK, Rail Safety and Standards Board.

National Physical Laboratory (UK). (2015). "Estimate of annual costs attributable to corrosion of reinforced concrete structures in the United Kingdom." Retrieved 18/11/2016, from www.npl.co.uk.

Tang, K. (2017). "Stray current induced corrosion to steel fibre reinforced concrete." Cement and Concrete Research **100**: 445-456.

Tang, K. (2019). "Stray alternating current (AC) induced corrosion of steel fibre reinforced concrete." Corrosion Science **152**(15): 153-171.

39th Cement and Concrete Science Conference
9-10th September 2019
University of Bath
Paper Number 046

Scale-up effects involving superplasticised cement grout based on ground granulated blastfurnace slag (GGBS) for nuclear waste immobilisation

John Rasburn, Gavin Cann, Hugh Godfrey, Ed Butcher, Martin Hayes
Immobilisation Science and Technology Team, National Nuclear Laboratory, Havelock Road, Workington, Cumbria CA14 3YQ

Steve Farris, Helen Farris
Sellafield Limited, Sellafield, Cumbria CA20 1PG

ABSTRACT

Many encapsulation operations for the treatment of Intermediate Level Waste (ILW) at the Sellafield nuclear site use a grout based on ordinary Portland cement (OPC) with a high proportion of blastfurnace slag (BFS). The current nuclear industry specification OPC and BFS powders differ in several respects from standard, construction specification materials. For example, as well as being coarser, Sellafield BFS has a more tightly-controlled physical and chemical specification. These factors ensure reproducible performance in terms of processing properties such as high fluidity, absence of bleed, low water-to-solids ratios and hence ultimate longevity of the encapsulated package. However, the ability to use standard construction industry GGBS and CEM I of a wider compositional and physical property range would be desirable to enable increased security of supply, as Sellafield moves into the process of decommissioning, thus requiring materials over an extended timescale. Superplasticisers could offer nuclear encapsulation processes a potential means of accommodating the different rheological characteristics of standard construction industry powders.

In this study, funded by Sellafield Ltd, trials were undertaken to develop an operating envelope for the encapsulation process by assessing the water to cement solids ratio, the proportions of GGBS to CEM I and the addition level of a polycarboxylate ether (PCE) superplasticiser. The fluidity of the grouts was characterised by a flow channel test.

1. INTRODUCTION

Cement encapsulation is used in the UK to package intermediate level waste (ILW) from the reprocessing of nuclear fuel (Fairhall and Palmer, 1992). ILW may be in the form of solids or slurries (Wilson, 1997). Examples include Magnox or stainless steel swarf from the decladding of fuel elements, or miscellaneous scrap metalwork.

The nuclear industry uses bespoke cement powders which present a future supply risk because the volumes required are relatively small. The three main powders of interest are ordinary Portland cement (OPC), blast furnace slag (BFS) and pulverised fuel ash (PFA). These cement powders are manufactured to a tight specification in order to guarantee reproducible performance and product quality in nuclear encapsulation operations. They differ from standard powders used in the construction industry, such as CEM I (BSI 2011) and ground granulated blastfurnace slag (GGBS; BSI 2006). Nuclear industry powders are coarser in order to produce grouts of high fluidity at low water/solids (w/s) ratios of 0.3 – 0.4. High fluidity is required in order to infiltrate the spaces between fragments of solid ILW and hence minimise voids. The low w/s leads to high ultimate strength and low permeability, both of which confer longevity (Kropp and Hilsdorf, 1995), as well as preventing the occurrence of bleed.

BFS is used at a high substitution level for OPC, typically 75% by weight of cementitious powder. (Fairhall and Palmer, 1992). This, in combination with the larger average particle size, enables the reactivity to be tailored to provide both long working times prior to pouring and development of sufficient early strength afterwards. The finished wasteform is monolithic and of high quality.

During a typical production operation in an encapsulation plant for treating solid waste, solid ILW is placed in a 500 L steel drum. Grout is prepared according to the established formulation for the ILW and plant in question. Owing to production requirements, up to 2.5 hours may elapse between the preparation and the pouring of

the grout into the drum, and hence it is important that sufficient fluidity is retained during this hold-up period. Vibrogrouting is applied during grout filling to aid infiltration of the waste. The grouted wasteform is then allowed to cure for up to 24 hours. In some plants, a capping grout is then applied to seal the wasteform and minimise headspace in the waste package.

Superplasticisers greatly enhance the fluidity of cement grouts for a given water content (Marchon *et al*, 2019; Dalas *et al*, 2015). Recently, their suitability for ILW nuclear encapsulation purposes has started to be re-assessed (NDA, 2017). As reprocessing facilities such as Sellafield enter their decommissioning phases, the nature of the ILW is likely to change and greater flexibility of encapsulation operations may be required over a prolonged timescale. Importantly there is also a driver to re-purpose the plants used to encapsulate reprocessing wastes to allow them to treat decommissioning wastes. This situation would benefit from the use of standard construction industry powders if it could be accomplished with only minor modification of existing encapsulation processes. Superplasticisers may facilitate this by imparting high fluidity at low to moderate water contents, thus affording durable and homogeneous products. Additionally, this may help to reduce issues of security of supply by providing a wider range of potential powder sources and by simplifying operational complexity. For example, vibrogrouting could be omitted.

The aim of this work has therefore been to establish a suitable operating envelope for encapsulation operations using grouts based on CEM I, GGBS and a PCE superplasticiser.

2. MATERIALS AND METHODS

The powders used in this work were CEM I 52,5N and GGBS supplied by Hanson Cement UK. XRF compositional data, Rietveld XRD analysis and particle densities obtained by helium pycnometry were supplied by Hanson Cement UK. Loss on ignition, residual moisture contents, and particle size distributions (Malvern Mastersizer 3000) were determined at NNL Workington. For the full-scale trials described below, powder fineness measured by Rigden's air flow method was 430 m^2kg^{-1} for CEM I and 440 m^2kg^{-1} for GGBS.

The superplasticiser was a commercial PCE superplasticiser supplied by Grace Construction Products and marketed as ADVACast 571. This product is a liquid dispersion of solids content 35% and density 1.10 g cm^{-3}. It was added to the mix water prior to powder addition. The volume (in L) of added superplasticiser is expressed as a percentage of the total mass (in kg) of cementitious powder, i.e. both CEM I and GGBS.

Small-scale mixes were carried out on a Hobart planetary mixer to produce mixes of volume 3 litres. Large-scale mixes were carried out on a Colcrete SD10 colloidal grout mixer. This has a maximum capacity of 283 litres and is connected to a 500-litre holding tank for continued agitation of the grout following high-shear mixing, as shown in Figure 1. The mixing procedure involved powder addition at *ca*. 35 kg/min for 9 minutes during high shear mixing followed by an additional 3 minutes of high shear mixing. The grout was then transferred to the holding tank where it was stirred at low shear. Colflow values (as described below) and grout temperatures were measured every 30 minutes. The temperature of the mix water was in the range 7 – 8 °C for both small-scale and large-scale mixes.

Grout fluidity was measured by the Colcrete flow channel test, or 'Colflow', which is an adaption of the flow channel test described in (BSI, 2002). The sample volume for these tests was 200 mL.

Ancillary measurements included isothermal conduction calorimetry using a TAMAir calorimeter operating at 35°C, and bleed measurements at 24 hours of grout samples in sealed 100 mL measuring cylinders. After 90 days, solid specimens from the bleed measurements were used for assessing segregation by cutting the specimens in half and determining the densities of the upper and lower halves by Archimedean weighing.

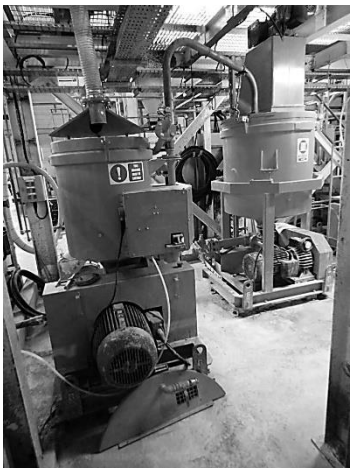

Figure 1. The SD10 mixer and holding tank.

3. RESULTS

This work has followed three stages to date.

In stage one, 29 mixing experiments at the 3-litre scale were carried out in order to explore the effect of superplasticiser dosage on grout performance, particularly in respect to fluidity. These results indicated that grouts of suitable fluidity could be obtained with a superplasticiser dosage of 0.3 v/w% on the mass of cementitious powder. This result suggests that minimal modification of the current plant configuration would be necessary if CEM I, GGBS and superplasticiser were to be adopted. For

example, a formulation of 75 wt% BFS and w/s = 0.35 could be retained with the only necessary modifications being the incorporation of the superplasticiser and substitution of CEM I and GGBS for OPC and BFS powders respectively.

Stage two focused on using this formulation to investigate the effect of scale-up. The results highlighted the importance of the scale of mixing. Mixing experiments were undertaken at both small scale (3 litre) and full scale (250 litre). In addition, a preliminary assessment of the infilling performance was conducted using columns of Magnox swarf or slate fragments (of size <20 mm) as models of tortuous, solid waste assemblies through which thorough grout infiltration was sought.

The results of this stage are summarised in Figure 2, in which normalised Colflow data are plotted against hold-up time for two 3-litre and two 250-litre trials. It should be pointed out that different batches of GGBS, CEM I and the PCE superplasticiser were used in these trials, and hence the intrinsic fluidities will have been affected by variations in both fineness and chemical composition. To compensate for this, the data have been normalised to the initial Colflow at t = 0 minutes.

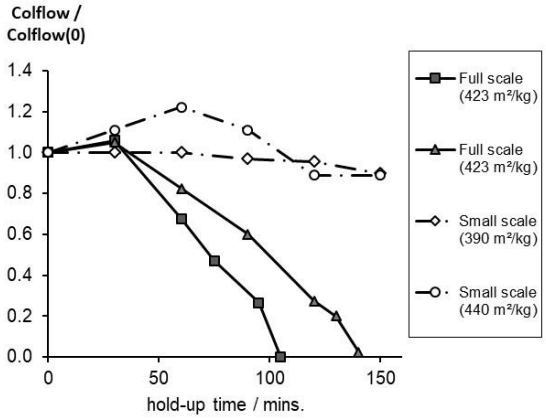

Figure 2. Normalised Colflow data for small-scale mixes (dashed lines and open symbols) and large-scale mixes (continuous lines and filled symbols). The grout formulation was 75% GGBS, 25% CEM I, w/s 0.35 and superplasticiser dosage 0.3% (v/w).

Two significant findings are evident, namely (a) the fluidity is sensitive to the fineness of the GGBS, and (b), at full scale, the fluidity of grout declined more quickly with hold-up time than was the case at small scale. The consequence of (b) was that several of the infilling trials were not successful.

Regarding (b), the contrast in hold-up behaviour between small-scale and full-scale situations, this effect could be attributed to the higher shear characteristics associated with the SD10 mixer and the associated pipework. This can have an adverse effect on the fluidity of grouts or mortars, (Han and Ferron, 2016). particularly self-compacting concretes which feature low w/s ratios in combination with superplasticizer addition (Feys *et al*, 2009). Additionally, the larger volume caused a greater increase in the grout temperature.

In stage three, a series of full-scale trials were conducted with varied formulations to compensate for the reduced fluidity observed with hold-up time at full scale. The formulations were based on an experimental design which produced an array defined by the three independent variables, namely the percentage of GGBS in the cementitious powder blend,
the ratio of water to cementitious solids (w/s) and
the addition level of superplasticiser (S/P).
The array of formulations is shown in Table 1.

Table 1. Trial array and observed maximum Colflow values.

Trial (run) number	%GGBS	w/s	S/P (%v/w)	Max. Colflow / mm
1	55	0.40	0.7	740
2	75	0.50	0.7	860
3	65	0.45	0.5	800
4	65	0.45	0.5	800
5	55	0.50	0.3	390
6	75	0.50	0.3	470
7	75	0.40	0.3	170
8	75	0.40	0.7	780
9	55	0.40	0.3	170
10	65	0.45	0.5	790
11	55	0.50	0.7	820

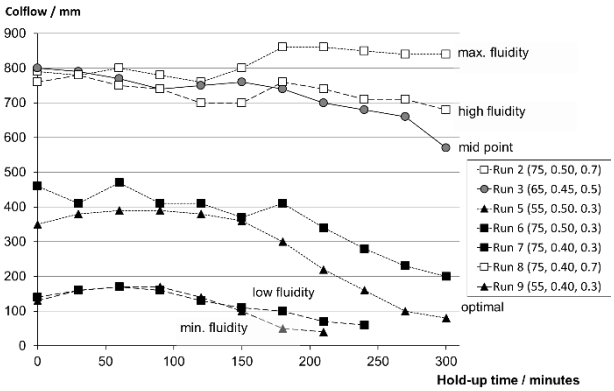

Figure 3. Colflow values as a function of hold-up time for Trials 2, 3, 5, 6, 7, 8 and 9. Legend format: Trial number followed by formulation details as follows (wt% GGBS, w/s, v/w% SP).

Selected data for hold-up performance are presented in Figure 3. It can be seen that the mid-point of the array gave grouts of high fluidity, close to those grouts with maximum fluidity. This indicates that the positioning of the array somewhat over-compensated for the adverse effects encountered in stage two, such as the higher shear at full scale. In most cases, a moderate decrease in fluidity occurred with longer hold-up times. However, for

those formulations with very high initial fluidity, Colflow values increased with hold-up time.

The two optimal formulations indicated in Figure 3 produced grouts which were free of bleed and segregation effects. Interestingly, these formulations were at the extremes of GGBS content, 75% and 55%, while both had w/s 0.5 and superplasticiser at 0.3%.

Bleed did not occur for grouts with 55% CEM I, i.e. lower GGBS, even with high w/s (0.5) and superplasticiser dosage (0.7%). Hence, higher proportions of CEM I can offer a useful means of controlling bleed while retaining acceptable fluidity.

Significant bleed was only observed for the two cases with highest fluidity (Trials 2 and 11). These grouts featured the higher values of GGBS (75%) and superplasticiser dosage (0.7%). With increasing hold-up time, the grouts absorbed more water. Bleed was eliminated at a hold-up time of 270 minutes.

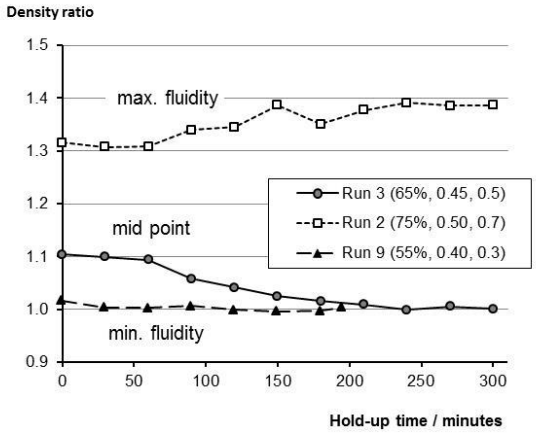

Figure 4. Ratio of density of lower half of specimen to upper half for specimens from 100 mL bleed tests.

Figure 4 illustrates the segregation effect. For most cases, segregation is also reduced by increasing hold-up times, apparent as a reduction in the ratio of the lower and upper densities of the bleed specimens. This is evident for the formulation at the mid-point in the trial array. However, in the case of the maximum fluidity grout (Trial 2), segregation increased with hold-up time, attributable to increased absorption of water and consistent with the observed increase in fluidity.

4. CONCLUSIONS

A short series of full-scale mixing trials have demonstrated that suitable high-fluidity grout formulations can be produced for demanding nuclear encapsulation applications. The formulations used standard construction industry powders and incorporated a superplasticiser.

The trial array covered a wide range of behaviour, including insufficient fluidity at one extreme to formation of bleed and segregation at the other. The positioning of the array in 3-parameter space (%GGBS, w/s, %SP) compensated for adverse effects encountered previously, such as the fineness of the GGBS powder and the decrease in fluidity caused by the higher shear fields at full scale. The associated formulations afford scope for retaining fluidity with GGBS and CEM I powders with different characteristics from other sources.

REFERENCES

BSI, 2006. Ground, granulated blast furnace slag for use in concrete, mortar and grout, Part 1. BS EN 15167-1.

BSI, 2011. Cement, Part 1: Composition, specifications and conformity criteria for common cements, BS EN 197-1.

BSI, 2002, Products and systems for the protection and repair of concrete structures – Test methods – Determination of workability – Part 2: Test for flow of grout or mortar; BS EN 13395-2

Dalas, F., Pourchet, S., Nonat, A., Rinaldi, D., Sabio, S., Mosquet, M., 2015, Fluidizing efficiency of comb-like superplasticizers: The effect of the anionic function, the side chain length and the grafting degree, Cement and Concrete Research, 71, 115 – 123

Fairhall, G.A., Palmer, J.D., 1992. The Encapsulation of Magnox swarf in cement in the United Kingdom. Cement and Concrete Research, 22, 293 – 298.

Feys, D., Verhoeven, R., De Schutter, G., 2009, Why is fresh self-compacting concrete shear thickening? Cement and Concrete Research, 39, 510 – 523.

Han, D., Ferron, R.D., 2016, Influence of high mixing intensity on rheology, hydration and microstructure of fresh state cement paste. Cement and Concrete Research, 84, 95 – 106.

Kropp, J., Hilsdorf, H.K., 1995, Performance Criteria for Concrete Durability, RILEM Report 12, E&FN Spon, Chapman & Hall, London.

Marchon, D., Boscaro, F., Flatt, R.J., 2019, First steps to the molecular structure optimization of polycarboxylate ether superplasticizers: Mastering fluidity and retardation. Cement and Concrete Research, 115, 116 – 123.

NDA, 2017. Geological Disposal: Guidance on the use of polycarboxylate ether superplasticisers for the packaging of low heat generating wastes. WPS/926/01

Wilson, P.D. (1997) The Nuclear Fuel Cycle: From Ore to Waste, Oxford Science Publications

39th Cement and Concrete Science Conference
9-10th September 2019
University of Bath
Paper Number 048

Interaction of strontium chloride solution with calcium aluminate phosphate (CAP) system

M. Simoni., H. E. Ball, C. Burgos, I. Garcia-Lodeiro, T. Hanein, H. Kinoshita

Department of Materials Science and Engineering, The University of Sheffield,
Sir Robert Hadfield Building, Mappin Street, Sheffield, S1 3JD, United Kingdom

ABSTRACT

Processing of contaminated water in Fukushima Daiichi Power Plant results in various aqueous secondary wastes. A significant strontium (^{90}Sr) contamination represents one of the key challenges for their management, and we have been developing a new cementing matrix based on calcium aluminate phosphate (CAP) system with reduced water content for such aqueous secondary wastes. In the present study, the interaction of CAP with $SrCl_2$ was investigated to gain insight into the capability of CAP system in Sr immobilisation. It was found that the immobilisation is possible, and the incorporation of Sr appears to be associated with the formation of insoluble phosphate salts. The obtained results also suggest that 1 kg of CAP powders can incorporate 200 g of Sr under tested condition.

1. INTRODUCTION

One of the most challenging decommissioning activities regarding the Tokyo Electric Power Company (TEPCO) Fukushima Daiichi Nuclear Power Plant is the continuous generation of contaminated water. Currently, a partially closed water circuit provides the necessary cooling to the system (Williams et al., 2015), and water is processed through the Advanced Liquid Processing System (ALPS) (Grambow et al., 2014). As a result, large amounts of contaminated aqueous secondary wastes are currently being stored on-site: 6,000 m^3 of slurries in 2,254 units in 2017 (Journeau et al., 2018).

Among the contaminants, the high concentration of strontium (^{90}Sr) resulted in a radioactivity value of 10^{17} Bq (Journeau et al., 2018), which represents a serious issue in the management of these secondary wastes. Incorporation of these wastes is challenging, in particular with conventional cement matrices based on Portland cement (PC) because of the potential hydrogen gas generation and associated risks of fire and explosions (Saji, 2014), due to the radiolysis of the water contents intrinsically present in the conventional cement matrices as pore solution and hydration products.

In order to condition these secondary wastes, we have been developing a new cement matrix based on calcium aluminate phosphate (CAP) system (Garcia-Lodeiro et al., 2018). Differing from the conventional cements, solidification of CAP system is based on acid-base reaction (Sugama et al., 1992). Since the water content is not crucial once the system is mixed, it is possible to reduce its water content by curing the system at 60-90°C without compromising the integrity of the solid products (Garcia-Lodeiro et al., 2018).

To gain further insight into the capability of CAP system as a cementing matrix for the aqueous secondary wastes contaminated with strontium, the present study investigated the interaction of a CAP system with dissolved strontium. A CAP simulant was mixed with a significant amount of water in presence of strontium ions, and the change in the concentration of key elements are examined in comparison with the system without presence of strontium ions.

2. EXPERIMENTAL

MATERIALS

Materials used in the present study are based on the previous work (Garcia-Lodeiro et al., 2018). The CAC (Secar 51, Kerneos) was used as the primary precursor of CAP, together with a reagent grade of linear metaphosphate ($(NaPO_3)_n$ 97%, Acros Organics) as a source of polyphosphate (PP). An orthophosphate ($NaH_2PO_4.2H_2O$ 99%, Acros Organics) was also added as a source of monophosphate (MP) which are usually used in CAP systems to avoid the rapid setting of CAP (Chavda et al., 2014). For the aqueous solutions of strontium ions, strontium chloride hexahydrate ($SrCl_2 \cdot 6H_2O$, Alfa Aesar, 99+%) was used together with distilled water.

METHODS

Aqueous solutions used for the reactions were prepared by dissolving $SrCl_2 \cdot 6H_2O$ in distilled water at 0.1M. The CAP powders were prepared in dry state by hand-mixing Secar 51 (69 wt%), PP (27.6 wt%) and MP (3.4 wt%), based on the previous study (Garcia-Lodeiro et al., 2018).

0.3 g of premixed CAP powder was added to the 30 mL of aqueous solution placed in a plastic container while stirring at 400 rpm using a magnetic stirrer,

and the system was left for reaction at room temperature for a designated period of time: 60 seconds, 1h, 2h, 4h, 8h or 24h. A separate batch was prepared for each designated period. For comparison, the exact same procedure was repeated but using only distilled water without adding $SrCl_2 \cdot 6H_2O$.

At the end of designated reaction period, the liquid phase (>20 mL) was sampled using a syringe and membrane filter (< 0.22 µm). The pH of the liquid sample was determined using a Mettler pH/Cond bench meter SE S470-K equipped with an expert proISM probe (error = ±0.01). The probe was calibrated before each measurement using three buffer solutions at pH 4.01, 7.0 and 9.21. The liquid samples were stored in sealed plastic containers at 20°C until analysed using Inductively coupled plasma - optical emission spectrometry (ICP-OES), performed with a Spectro-Ciros Vision Optical Emission Spectrometer. The concentration of Sr, Cl, P, Na, Al and Ca were determined simultaneously.

3. RESULTS AND DISCUSSION

EVOLUTION OF pH

The pH data for both the systems studied (with and without $SrCl_2 \cdot 6H_2O$) are presented in Figure 1.

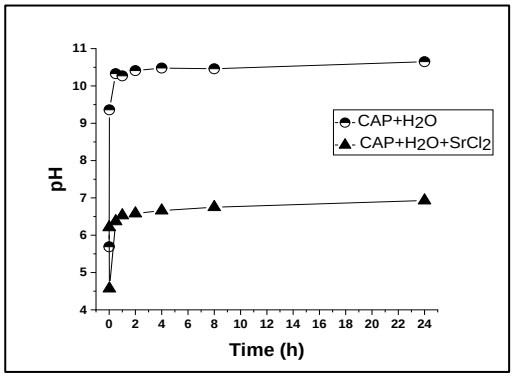

Figure 1. pH of both systems with and without $SrCl_2 \cdot 6H_2O$.

After 24 hours of reaction, pH increased in both the systems, reaching 10.65 without $SrCl_2 \cdot 6H_2O$ and 6.93 with $SrCl_2 \cdot 6H_2O$. This increase must be related to the partial dissolution of the CAC powder. The expected pH of Secar 51 in aqueous solution (10 %) is 10.5-11 (Kerneos Inc., 2016). The data obtained clearly indicates that the pH of the system is lower when $SrCl_2 \cdot 6H_2O$ was present throughout all the studied reaction times.

BEHAVIOUR OF CAP

As shown in Figure 2, the concentration of calcium and aluminium continue increasing when $SrCl_2 \cdot 6H_2O$ is not present throughout the reaction times studied, achieving final concentrations of 630 mg L^{-1} and 551 mgL^{-1}, respectively. The higher concentration of these ions suggests more dissolution of CAC clinker phases and/or relatively less precipitation of their solid reaction products. On the other hand, after 24h of mixing in presence of $SrCl_2 \cdot 6H_2O$, Ca concentration reaches only up to 75.4 mg*L^{-1} and that of Al was below detection limit (<0.001 mg*L^{-1}), suggesting limited dissolution of CAC clinker phases and/or increased formation of their solid reaction products.

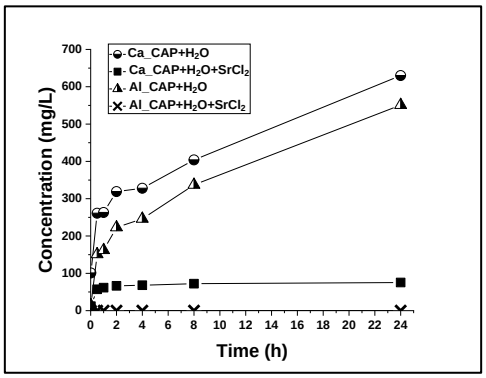

Figure 2. Concentration of Ca and Al in the systems with and without $SrCl_2 \cdot 6H_2O$.

It has been reported that the main binding phases of CAP are amorphous phosphates (Sugama and Carciello 1995, Swift et al. 2013, Chavda et al 2014, Garcia-Lodeiro et al. 2018), and this is likely the case also for the systems studied in the present investigation. As shown in Figure 3, the trend observed in the concentration of phosphorus coincides with those for calcium and aluminium: the concentration of phosphorus becomes much lower in the system with $SrCl_2 \cdot 6H_2O$. Therefore, the difference between these systems (with or without $SrCl_2 \cdot 6H_2O$) in calcium and aluminium ion concentration must be caused mainly by the formation of reaction products, rather than the suppressed or enhanced dissolution of CAC clinkers in these systems.

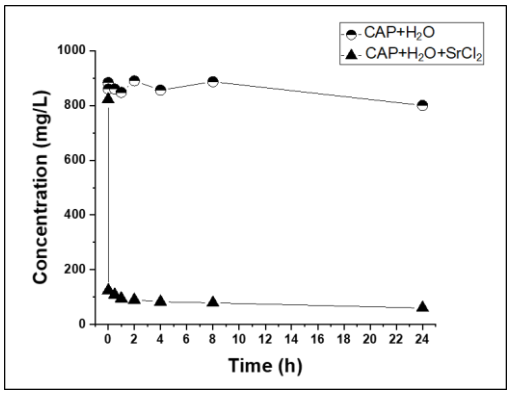

Figure 3. Concentration phosphorous in the systems with and without $SrCl_2 \cdot 6H_2O$.

Orthophosphate changes its form depending on the pH of the aqueous environment (Asadi-Eydivand et al., 2014): a significant portion can form $H_2PO_4^-$ at pH<7 whereas majority becomes HPO_4^{2-} at pH>8. Therefore, the amorphous phosphate products formed in the presence of $SrCl_2 \cdot 6H_2O$ could be

different from those formed without the presence of $SrCl_2 \cdot 6H_2O$, and this may also be contributing to the different trends of the calcium and aluminium ion concentration between these two systems. Further investigation is required to elucidate this aspect.

IMMOBILISATION OF STRONTIUM

The trend observed for strontium ions was similar to that for phosphorus as shown in Figure 4, suggesting the precipitation of Sr phosphate salts.

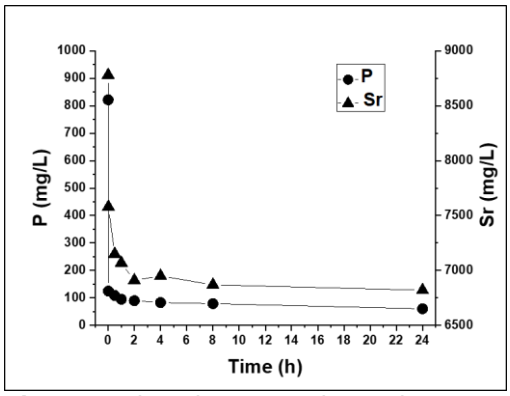

Figure 4. Phosphorous and strontium concentration in the system with $SrCl_2 \cdot 6H_2O$.

Based on the initial (C_0) and final (C) concentrations of strontium after 24 hours of reaction, the efficiency of strontium immobilisation (η %) was estimated using Equation 1.

$$\eta = \left[1 - \frac{C}{C_0}\right] \times 100 \qquad (1)$$

After 24 hours of mixing, the concentration of strontium changed from 8780 mg/L to 6820 mg/L, which corresponds to η = ~22 % immobilisation. This also indicates that 1 kg of CAP powders immobilized 200 g of strontium.

CONCLUSIONS

The presence of $SrCl_2 \cdot 6H_2O$ indicated a significant impact to the system. The pH of the solution was much lower throughout the reaction times studied when $SrCl_2 \cdot 6H_2O$ was present. The reduced concentrations of calcium, aluminium and phosphorus suggest an enhanced precipitation of the respective reaction products.

The tested amount of CAP was capable of immobilising 22 % of strontium present in the system, which corresponds to 1 kg of CAP powders immobilising 200 g of strontium.

REFERENCES

Asadi-Eydivand M. et al., Artificial neural network approach to estimate the composition of chemically synthesized biphasic calcium phosphate powders, Ceramics International, 40(8), 2014, pp. 12439-12448.

Chavda M.A. et al., Phosphate modification of calcium aluminate cement to enhance stability for immobilisation of metallic wastes, Advances in Applied ceramics, 113(8), 2014, pp. 453-459.

G. Williams et al. The Fukushima Daiichi accident. Technical Volume 5/5: Post accident recovery, IAEA, 2015.

Garcia-Lodeiro I. et al. Reduction of water content in calcium aluminate cement with/out phosphate modification for alternative cementation technique, Cement and concrete research, 109, 2018, pp. 243-253.

Grambow B. and M. Mostafavi, State of Fukushima nuclear fuel debris tracked by Cs137 in cooling water, Environmental Science: Processes & Impacts, 16(11) 2014, pp. 2472-2476.

Journeau C. et al., Fukushima Daiichi fuel debris simulant materials for the development of cutting and collection technologies, Journal of Nuclear Science and Technology,55(9), 2018, pp. 985-995.

Fiche de donnees de securite, Secar 51(R), Kerneos Inc, 2016.

Saji G., Review on water radiolysis in the Fukushima Daiichi Accident: Potential cause of Hydrogen generation and explosion [Report]. - [22nd International conference of Nuclear engineering], American Society of Mechanical Engineers, 2014.

Swift P. et al., Phosphate modified calcium aluminate cement for radioactive waste encapsulation Advances in Applied ceramics, 112(1), 2013, pp. 1-8.

Taylor P.C., et al., Development of performance properties of ternary mixtures and concrete pavement mixture design and analysis (MDA): Effect of paste quality on fresh and hardened properties of ternary mixtures, [Iowa State University], 2012.

Influence of Power Ultrasound on the Portland cement pore solution compositions

Ahmad Ehsani [1] , Eshmaiel Ganjian[1], Mark Tyrer[1], Timothy J. Mason[1] and Mark Bateman[2]

[1] Coventry University, Faculty of Engineering, Environment and Computing, Built & Natural Environment Research Centre, Coventry, UK
[2] Coventry University, Faculty of Engineering and Computing, School of Energy, Construction and Environment, Coventry, UK

Abstract
The composition of the cement pore solution reflects the kinetics of hydration process and determine essential insight into the rate at which cement phases hydrated. This characterization can therefore provide information about the stable and unstable solid phases which may precipitate and dissolve, respectively. Power ultrasound (PUS) is currently under consideration to improve the hydration of cementitious materials and to promote the effectiveness of replacing supplementary cementitious materials; SCMs, in terms of mechanical, microstructural and transport properties. This could enhance the properties of cementitious composites, reduce the quantity of waste materials, as well as decreasing the CO_2 footprint of cementitious materials. This study investigates the effect of direct PUS on the Portland cement pore solution compositions at early hydration using inductively coupled plasma-optical emission spectroscopy (ICP-OES) technique. The sonication influence is also inspected by microstructure study of the cement paste using scanning electron microscopy (SEM). The results shows PUS increases high and low concentration ions in the cement pore solution due to the physical and chemical effect of acoustic cavitation, speeding up the hydration process and enhancing the Portland cement performance. The SEM micrographs indicates the more volume of compacted solid phases of hydration products.

Keywords: Pore solution, Power Ultrasound, Portland cement paste, ICP-OES, Hydration, Sonocrystallization

39th Cement and Concrete Science Conference **Paper Number 50**
9-10th September 2019
University of Bath

Metal Mobility in Cement Paste from Co-Processing of Energy-From-Waste Air Pollution Control Residue

Utku SOLPUKER, Julia A. STEGEMANN, Judith Q. ZHOU, Anna BOGUSH
Centre for Resource Efficiency & the Environment, Department of Civil, Environmental and Geomatic Engineering (CREE), University College London, Chadwick Building, Gower Street, WC1E 6BT, London, UK

Wensheng ZHANG
Key Laboratory of Cement-based Materials Science in the Building Materials Industry and
State Key Laboratory of Green Building Material, China Building Materials Academy, Beijing, China

Jiangxiong WEI
School of Materials Science and Engineering, South China University of Technology, China

ABSTRACT

Co-processing of industrial wastes can be an effective use of raw materials in cement production and wise waste management practice that contributes to a more sustainable cement industry, but may enrich metal concentrations in cement products. In this study, air pollution control residues from municipal waste combustion (APCR), were used to make co-processed and blended cements. Cement clinkers were prepared using untreated APCR, and APCR that was washed to remove soluble salts, as alternative raw materials in a laboratory cement kiln. Diffusion-controlled leaching behaviour of metals from monolithic cube specimens (15.625 cm^3) over a 64d period, as well as batch leaching tests with distilled water, were conducted for hydrated cement pastes prepared using the co-processed and blended cement powders after 6 months curing. pH and conductivity of the leachates were measured and aliquots of the leachate were analysed for major anions and cations, and trace elements using IC, ICP-AES and ICP-MS, respectively. Leaching, expressed as an emission in mg/m^2, was metal-dependent; in some cases co-processed pastes showed lower leaching than blended pastes, but the reverse was also observed in other cases
.

1. INTRODUCTION

Three mass % of combusted municipal solid waste (MSW) is captured as air pollution control residue (APCR), which is considered as hazardous waste in many jurisdictions. In the cement industry, APCR has been considered as an alternative raw material in clinker production (co-processing). This practice, however, can increase the concentration of toxic and environmentally harmful trace elements in cement products, and, therefore, the risk of pollution of the soils and groundwater via leaching.

Leachability of metals from hydrated cement can be affected by the speciation of the elements of concern, e.g., incorporation into cement clinker phases, and/or cement hydrates or formation of hydroxides and other species, and also by diffusion control of leaching [1]. Diffusion is reported to be the dominant process controlling the leaching of trace elements from high quality monolithic concrete under normal exposure conditions [2].

In this study, cement clinkers were prepared using untreated APCR from MSW combustion, and the same residues after washing to remove soluble salts (w-APCR), as alternative raw materials in a laboratory cement kiln. Leachability of cement pastes made with these co-processed clinkers was compared with that of cement pastes made by blending these wastes with Portland cement.

2. EXPERIMENTAL PROCEDURE

Preparation and of cement clinkers with 5 and 35% by mass of APCR and 5 and 34% w-APCR in a laboratory kiln at 1450^{o}C, and mineralogical investigation of these clinkers, is described elsewhere [3]. Cement powders were prepared by intergrinding the clinkers with gypsum, and used to make cement pastes with a water-to-cement ratio of 0.35. Blended cement pastes incorporating the same proportions of APCR and w-APCR were made for comparison. Both types of pastes were cast in 25 x 25 x 25 mm cubes, and cured for 6 months under humid conditions at 22^{o}C before assessment of their leachability.

Leaching of inorganic components from the monolithic paste specimens under diffusion control was examined using the “Tank Test”, which is described in [4] and summarised in Figure 1. 100 mL size polypropylene jars were used as the tank

where the paste specimens were hung from the jar lids such that they were covered by approximately equal amounts of leachant in all directions. The total volume of leachant (*V*) was 75 ml and 18.2 MΩ purity water was used as the leachant. After specimens were left submerged in the tank for the designated number of days to complete each leaching period, they were transferred to a new tank with an equal volume of leachant, with analysis of the leachate from the previous period.

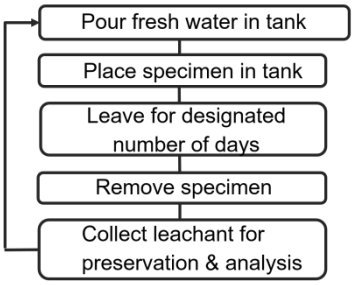

Figure 1. Tank leaching test procedure [1].

48h batch leaching tests of the cement pastes, ground to <150 um, with distilled water at a liquid-to-solid ratio of 10 mL/g dried mass were also conducted, as part of the acid neutralisation capacity test [5], to determine the steady-state concentrations of elements, near equilibrium in water.

The pHs and conductivities of the leachates were measured immediately, and the leachates were then filtered using a 0.45 µm filter membrane. Aliquots of the filtrate were analysed for major anions by ion chromatography, major cations by inductively coupled plasma atomic emission spectroscopy, and trace elements by inductively coupled plasma mass spectroscopy.

3. RESULTS

Figures 2 and 3 compare the pH and conductivity results for the batch leaching tests and the different periods of the tank leaching test for the blended and clinker cement pastes containing APCR and w-APCR. The pH measurements for the "Tank Test" leachates were 0.3-1.0 units lower, and the conductivities were 3 to 11.5-fold lower, than those of the batch test leachates, indicating that the "Tank Test" leachates are not at equilibrium. We can therefore be satisfied that a high driving force for leaching under diffusion control is being maintained.

The pH values of the "Tank Test" leachates of the blended cement pastes from the first three periods range from 9.8-11.3 (Figure 2a), possibly indicating that the sample surfaces have been carbonated; however, lower solution conductivities in these periods (Figure 1b) may indicate kinetic limitations on dissolution of the paste minerals. The "Tank Test" leachates for the blended cement pastes become more alkaline (pH 10.8-11.7) after the first three periods and the pH continues to increase slightly to 64d, as the leaching periods become longer, whereas the leachate conductivities (523-4350 uS/cm) remain approximately constant after the first three periods. The marked decrease in the pH and the conductivity of the leachate of the control sample after 64d is most likely due to carbonation.

Although the concentration of the APCR and w-APCR in the blended cement pastes does not seem to have a systematic impact on the pH of the leachates, the leachate conductivities do depend on the waste content (Figure 2b). This is consistent with high concentrations of soluble salts in the APCR [6], which is diluted in the pastes depending on the proportion of waste in the formulation. The variation in the conductivity is less for the pastes prepared with w-APCR, which contains much lower concentrations of soluble salts (Figure 2b). The leachate of the control sample has the lowest conductivity among all the leachates.

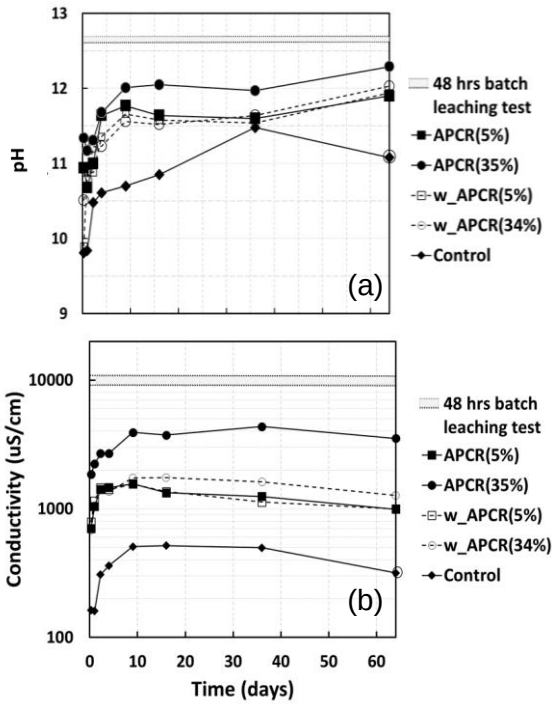

Figure 2. (a) pH and (b) conductivity of the leachates from over the 64d period of the tank leaching test of the blended cement pastes. Shaded regions show the range of pH and conductivity measurements from batch leaching tests of the blended cement pastes. Missing value for control sample at 64d replaced with the value measured at 100d.

The pH values (pH 11.9-12.3) and the leachate conductivities (1700-5600 µS/cm) of the "Tank Test" leachates of the clinker cement pastes are generally higher than leachates of the blended cement pastes (Figure 3a, b). There is less variation in the pH values of the clinker cement pastes than the blended cement pastes and except the control sample, there is a small decrease in the pH values

at 64 d (Figure 3a). The leachate conductivities again depend on the waste content, but less strongly than for the blended pastes, as much of the chloride in the APCR is removed from the clinker by volatilisation at the high kiln temperature [3] and the leachate conductivity of the clinker cement paste control sample is much higher than that of the commercial cement used as a control for the blended cement pastes. (Figure 3b).

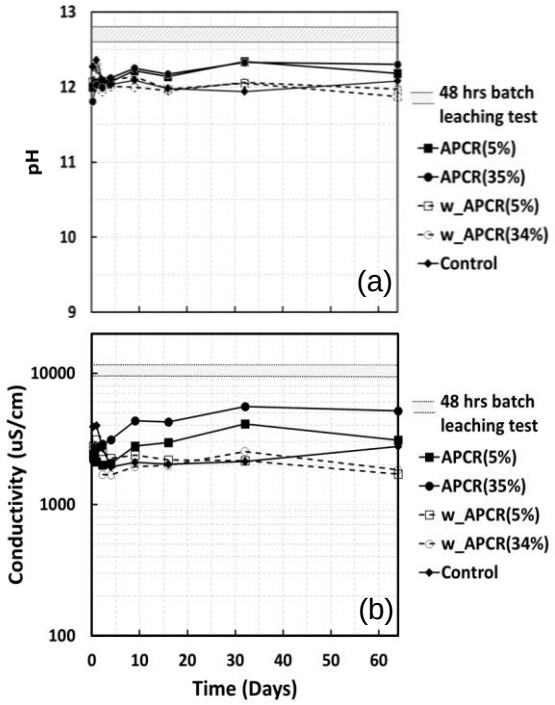

Figure 3. (a) pH and (b) conductivity of the leachates from over the 64d period of the tank leaching test of the clinker cement pastes. Shaded regions show the range of pH and conductivity measurements from batch leaching tests of clinker cement pastes.

The derived cumulative leaching of Cr, Cu, Sb and Pb from the blended and clinker cement pastes (i.e., corrected to avoid accumulation of measurement errors from one period to the next) over time is shown in Figure 4, together with their total amounts in the specimens, expressed as mg/m^2 of specimen surface area; calculated cumulative leaching of these elements under diffusion control after 64d is summarised in Table 1. It may be observed that Cr leachability was similar for the lower APCR and w-APCR additions to both the blended cements (Figure 4a) and clinker cements (Figure 4e), but higher from the clinker cement than the blended cement at the higher APCR and w-APCR additions; Sb leachability was higher from the clinker (Figure 4g) than the blended (Figure 4b) cement pastes at both waste concentrations. By contrast, Cu is better retained in the clinker pastes (Figure 4b) than in the blended pastes (Figure 4f). Both blended and clinker cement pastes show similar Pb leachability (Figures 4b and 4h). Pb leaching from the 5% APCR and w-APCR pastes is similar to that of the control sample.

Rather than the straight line with a slope of 0.5 expected for diffusion-controlled leaching with consistent boundary conditions, most of the cumulative release cases presented in Figure 4 have slopes different than 0.5 for at least part of the 64d. This indicates the other presence of other mechanisms, such as depletion of a component, delayed leaching, etc. [4].

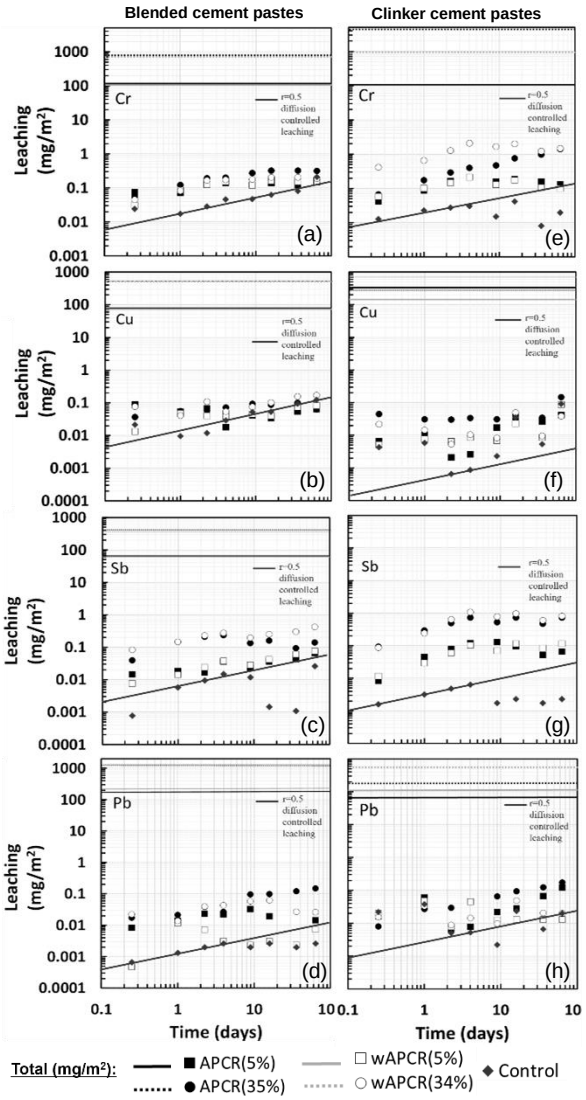

Figure 4. Cumulative release of Cr, Cu, Sb and Pb in blended and clinker cement pastes with varying proportions of APCR and washed APCR (w-APCR). Horizontal lines show the total amounts of Cr, Cu, Sb and Pb in the specimens.

Table 1. Calculated cumulative leaching at 64d (ε_{64} (mg/m^2)).

Paste Type	APCR (5 wt.%)	APCR (35 wt.%)	w-APCR (5 wt.%)	w-APCR (34 wt.%)
		Cr		
Blended	0.30*****	0.60*****	0.3*****	0.4*****
Clinker	0.40*****	1.40	0.4*****	3.5*****
		Cu		
Blended	0.08	0.20*****	0.09	0.20
Clinker	0.03	0.08	0.03	0.03
		Sb		
Blended	0.06	0.39*****	0.09*	0.45
Clinker	0.19*****	1.29*****	0.18*	1.60*
		Pb		
Blended	0.05*****	0.17	0.01	0.10*****
Clinker	0.12*****	0.18	0.07*****	0.07*****

*= Measured cumulative leaching at 64d.

3. CONCLUSIONS

The "Tank Test" shows that the co-processed cement pastes containing APCR from municipal waste combustion are more alkaline and have higher conductivity readings than the blended cement pastes. Although plotting of the test results suggests that diffusion controlled leaching is complicated by other mechanisms, the test shows that emission of Cr and Sb from pastes made with clinker from co-processing of APCR or w-APCR may be higher than from pastes made by blending APCR or w-APCR with blended cement; the opposite effect was observed for Cu, whereas there was little difference in the Pb emission from the two types of cement pastes.

REFERENCES

[1] Takahashi S, Sakai E and Sugiyama T, 2007. Study on leaching of hexavalent chromium from hardened concretes using tank leaching test, J. of Advanced Concrete Technology, 5(2): 201-207.

[2] Yang Y, Huang Q, Yang Y, Huang Z and Wang Q, 2011. Formulation of criteria for pollution control on cement products produced from solid wastes in China, J. Environmental Management, 92: 1931-1937.

[3] Bogush AA, Stegemann, JA, Zhou Q, Wang Z and Zhang W, 2017. Co-processing of Energy-from-Waste Air Pollution Control Residue in the Cement Kiln as a Potential Recycling Option, Paper, 119, 37th Cement and Concrete Science Conference, 11-12 September, University College London.

[4] EA NEN 7375:2004. Leaching Characteristics of Moulded or Monolithic Building and Waste Materials: Determination of Leaching of Inorganic Components with the Diffusion Test. Netherlands Normalisation Institute, translated by the Environment Agency.

[5] Environment Canada, 1990. Compendium of waste leaching tests. Report EPS 3/HA/7, Wastewater Technology Centre, Burlington, Ontario.

[6] Bogush AA, Stegemann JA, Wood I, Roy A, 2015. Element composition and mineralogical characterisation of air pollution control residue from UK energy-from-waste facilities. Waste Management, 36: 119-129.

39th Cement and Concrete Science Conference
9-10th September 2019
University of Bath
Paper Number 051

New ecosustainable cement from industrial waste joining

Perugini V. [a] [b]
[a] School of Science and Technology, Geology Division, University of Camerino, Italy
[b] SGM Experimentations Srl; Via Yuri Gagarin, 69, 06073, San Mariano di Corciano, Perugia, Italy
e-mail: vincenzoperugini.phd@gmail.com

ABSTRACT

Environmental sustainability in construction and infrastructures industry requires to maximize waste reusing, leading reduction quarrying, landfill dumping and greenhouse gas emission. Different industrial waste, as e.g. fly ash, blast furnace slag, silica fume and others, are currently used as supplementary cementitious material for partial clinker or cement replacement, promoting both circular economy and higher concrete durability. Nevertheless, considering composition of several industrial waste, both today used and not, as e.g. electric arc furnace slag, biomass ashes, ceramic waste, argillaceous or pyroclastic muck, higher clinker Portland saving, o cement replacement, could be promoted. This study is pointed to detect the possibility to produce cement matching physical and chemical parameters of the current EN standard for common cement, using new combination of industrial waste and low clinker Portland content. Although high saving and good sustainability, new cements assure pozzolanicity and high strength, especially at 28 days of maturation, in the same way to the common blended cements, blast furnace cements and composite cements containing slag and pozzolan.

1. INTRODUCTION

Environmental sustainability needs to increase circular economy, through a larger waste reusing. This could take place improving refinement of the waste and transforming them in byproduct, which allows their reusing in new products. In many cases new combinations of materials allows to compensate specific defects, making the mixing suitable to be used. Although transport, due to the environment impact and economic costs, should be limited, in many cases could be convenient to transport them farer from the original source allowing new combinations and uses. Suitability for a larger range of industrial processes can be achieved by eliminating small contaminations, through easy treatments that allow to reuse them in new industrial processes, or by mixing different types of waste in order to prepare a right material for new applications. Being clinker Portland and cement production responsible for about 7 % of CO_2 emission, replacement of 50% of the amount of clinker in cement production, or cement in concrete through SCM use, would reduce strongly greenhouse gas emissions, as well as a relevant part of quarrying and landfill dumping. This work is pointed to promote reusing of waste from different sources in binders and concrete industry, for a larger cement replacement, thanks to their pozzolanicity, or latent hydraulicity, and thanks to the improvement of performances allowed by means some combinations.
In accordance to EN 197-1, combinations of different supplementary cementitious materials (SCM), as blast furnace slag and fly ash, or other pozzolanic materials, can be used in the production of Composite cement type V. In the same way, other materials can be added in lower quantity, up to 5%, as filler or secondary component. Joining of different type of waste, as granulated blast furnace slag (GBS), electric arc furnace slag (EAF), thermally treated clay, ceramic waste, fly ash from burning coal, biomass ashes, tunneling waste and calcined clay, would allow to perform larger clinker Portland saving in cement, or higher Portland cement replacement in concrete production. In accordance to the international standards, e.g. EN and ASTM, blast furnace slag, is commonly used in percentage up to 50%, and higher, while electric arc furnace slag is not commonly used, because of the possible deleterious presence of expansive forms of lime (CaO) and Periclase (MgO).

Prevalent focus of this research work is to demonstrate the possibility to use electric arc furnace slag (EAF), after its composition assessment and expansion evaluation, especially in combination with other supplementary cementitious materials (SCM), as e.g. joining it to granulated blast furnace slag (GBS), or pozzolanic materials, as fly ash, natural pozzolan, calcined clay, ceramic waste or biomass ash.

2. MATERIALS AND METHODS

This experimentation involves materials from five different origins: calcined clay and ceramic waste (3 samples); burning coal fly ashes from electrical power plant (3 samples); ash from biomass power plant (3 samples); slag from iron industry (2 granulated blast furnace slag GBS and 1 electric arc

furnace slag EAF); natural pozzolans from volcanic origins (3 samples). As shown in table 1, all materials were assessed regarding chemical composition, including biomass ash, to use as secondary component in lower percentage. As shown in figure 1, mineralogical composition of EAF sample was investigated, in order to detect mineral phases suitable to increase cement hardening, as well as free lime (CaO) and periclase (MgO) contents, which could be able to determine dangerous expansion of the cement. All pozzolanic materials have been tested regarding strength activity index, in accordance to EN 450-1, and capability to assure pozzolanicity to the cement, in accordance to EN 196-5, if added in percentage of 25% to the Portland cement, as shown in Figure 2.

Finally, as shown in table 2 and 3, 13 experimental blended cements having 50% and 70% of clinker Portland replacement were produced in laboratory, in order to evaluate mechanical strength in standard mortar, stability and pozzolanicity of the cements containing electric arc furnace slag (EAF) in comparison to the commercialized cements type III/A and III/B containing respectively 50% and 70% of blast furnace slag (GBS), as well as those of the composite cements type V/A (S-P) and V/B (S-V) containing a mix of blast furnace slag and natural pozzolan, or blast furnace slag and fly ash. Being produced in Europe from over 25 years, in accordance to EN 197-1, these four blended cement are used as reference cement for comparison, in addition to the reference Portland cement. All tested cements have been produced in laboratory, using the same sample of reference cement (OPC) type I class 52,5 R, including for the mentioned cements type III/A, III/B, V/A (S-P) and V/B (S-V), which would be also available in commercial way, in order to assure the same mineralogical properties and grinding finesses, for a right performance comparison. Slag, both GBS and EAF type, are grinded at specific surface of 350 m^2/Kg, while all pozzolanic materials are grinded at 500 m^2/Kg. For each type of material, only the samples marked in bold in table 1 have been used to produce the experimental cements. Samples used are: sample named GBS 1 as Blast furnace slag; sample named EAF, which is the only one indicated as arc furnace slag; used calcined clay is that named C.Clay, obtained from calcination of argillaceous waste at 750°C; fly ash is that named Fly A. 1; natural pozzolan is that named N.Pozz. 2; used biomass ash, as shown in table 2, is that named Bio A. 2, which is added to the composite cement n. 14 containing EAF slag and calcined clay.

3. TEST AND OUTCOMES

Chemical elemental assessment by means X-ray fluorescence, in accordance to EN 15309:2007, as shown in table 1, regarding EAF slag, indicates iron content (Fe_2O_3) of 36,3 %, while total lime (CaO) is 30,9%, silica (SiO_2) is 14,1%, alumina (Al_2O_3) is 6,6% and magnesium (MgO) is 3,8%. Mineral phases assessment of the same EAF slag through XRD analysis, carried out using TESCAN VEGA 3 analyser, equipped with detector Bruker QUANTAX Compact EDS. As shown in figures 1 regarding the range 2Theta between 31° and 51°, evaluation indicates a very low CaO and MgO content. Considering the glass percentage of about 35% and the signal intensity of CaO and MgO phases in XRD spectra, in comparison to that of Larnite ($Ca_2 SiO_4$), Wustite (FeO), Browunmillerite ($Ca_2 [Al, Fe^{+3}]_2 O_5$) and Magnetite (Fe^{+2}, $Fe_2^{+3} O_4$), content of free lime and periclase, potentially dangerous, are lower than 2,5 %, while Larnite content is about 30%. MgO content available in periclase form into the EAF slag, is usually lower than total detected MgO, due to its presence in different mineral phases contained in little traces.

Table 1. Materials involved in the experimentation

Sample	***Blast furnace slag - North Italy***	Blast furnace slag - South Italy	***Electric arc furn slag - North Italy***	***Calcined Clay waste - Noth Italy***	C&D Waste - North Italy BO	Ceramic waste - North Italy RE	***Fly ash - Cerano, Italy***	Fly ash - Cerano, Italy (2)	Fly ash - Civitavecchia, Italy	Natural Pozzolan - Pavia, Italy	***Natural Pozzolan - Borghetto, Italy***	Natural Pozzolan - Campi Flegrei, Italy	Biomass ash - Central Italy RI	***Biomass ash - Central Italy FR***	Biomass ash - South Italy KR
Sector	*Slag*			*C. Clay*			*Fly Ash*			*Nat. Pozzolan*			*Biomass Ash*		
	GBS 1	*GBS 2*	***EAF***	***C.Clay***	*C&D W.*	***C.W.***	***Fly A. 1***	*Fly A. 2*	*Fly A. 3*	*N.Poz. 1*	***N.Poz. 2***	*N.Poz. 3*	*Bio. A. 1*	***Bio. A. 2***	*Bio. A. 3*
L.O.I.	***0,4***	0,9	***1,7***	***0,7***	6,3	1,6	***6,9***	6,9	2,3	16,4	***9,0***	4,8	8,7	***5,7***	9,4
SiO_2	***40,2***	35,0	***14,1***	***56,6***	58,0	68,7	***50,1***	47,1	51,6	45,2	***53,0***	57,7	34,1	***51,7***	26,0
Fe_2O_3	***0,6***	0,4	***36,3***	***8,2***	4,7	1,2	***4,4***	5,9	6,9	4,8	***5,4***	5,0	4,6	***3,6***	2,7
Mn_3O_4	***0,2***	0,3	***3,1***	***0,2***	0,1	0,0	***0,04***	0,05	0,06	0,1	***0,1***	0,1	0,1	***0,1***	0,2
TiO_2	***0,5***	0,5	***0,5***	***0,4***	0,6	0,6	***1,5***	1,5	1,2	0,5	***0,6***	0,4	0,5	***0,5***	0,3
P_2O_5	***0,0***	0,0	***0,5***	***0,0***	0,1	0,1	***1,4***	1,5	1,0	0,1	***0,1***	0,2	1,8	***2,0***	1,9
Al_2O_3	***11,2***	11,1	***6,6***	***23,4***	12,9	17,7	***27,5***	27,8	25,4	9,9	***18,2***	17,2	10,1	***8,3***	6,0
CaO	***35,5***	42,9	***30,9***	***0,3***	11,2	2,8	***5,0***	5,9	7,0	16,0	***4,7***	3,3	22,5	***15,2***	35,0
MgO	***10,2***	7,8	***3,8***	***2,7***	2,3	0,8	***1,1***	1,5	2,0	3,2	***1,5***	0,8	3,6	***2,3***	4,7
SO_3	***0,3***	0,3	***0,4***	***0,5***	0,3	0,1	***0,4***	0,4	0,6	1,1	***0,2***	0,2	5,0	***1,9***	7,8
Na_2O	***0,3***	0,3	***0,8***	***2,3***	1,3	4,0	***0,3***	0,4	0,6	0,9	***1,6***	2,7	1,5	***1,1***	0,9
K_2O	***0,5***	0,3	***0,1***	***4,7***	2,1	2,0	***1,2***	0,9	1,1	1,9	***5,3***	7,4	5,6	***6,6***	5,0
				Pozzolanicity assessment											
$SiO_2+Al_2O_3+Fe_2O_3$				**88,2**	75,6	87,7	**81,9**	80,7	83,9	59,8	**76,7**	79,9			
Reactive SiO_2				***27,6***	25,4	39,5	***38,1***	38,0	37,3	26.1	***37***	42,1			
SAI 7 days				***0,76***	0,77	0,81	***0,77***	0,78	0,77	0,75	***0,76***	0,78			
SAI 28 days				***0,77***	0,80	0,98	***0,78***	0,79	0,79	0,76	***0,79***	0.82			
SAI 90 days				***0,90***	0,91	1,06	***0,89***	0,90	0,89	0,86	***0,90***	0,92			

Moreover, regarding the evaluation of stability of the EAF slag, in accordance to the EN 196-3 and 197-1 for materials potentially expansive, Le Chatelier pincers test indicates a perfect matching to the limit of 10 mm of expansion for a mixture of 70% of Portland cement type I and 30% of it. Similarly, as shown in table 3, al experimental cements, containing EAF or without it, match the limit of 10 mm.

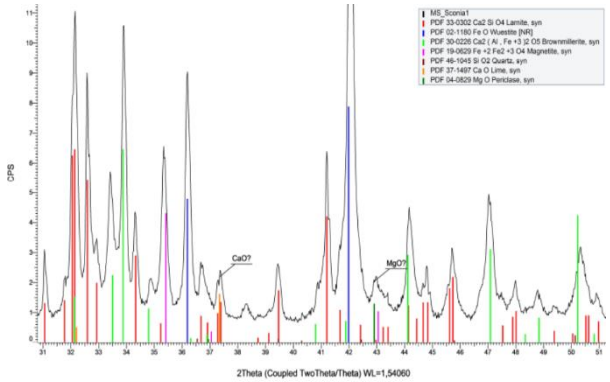

Figure 1. XRD diffractogram of EAF slag and mineralogical assessment, for range 2Theta between 31° and 51°.

As shown in the second part of table 1, all pozzolanic materials match the limits of ASTM C618 and EN 459-1 for silica, alumina and iron oxide content, except sample 1 of natural pozzolan having 59,8 %, which is not used for experimental cements production. In any cases, reactive silica content is higher than 25%, while strength activity index, is higher than 0,75 at 7 and 28 days and higher than 0,85 at 90 days, in accordance to EN 450-1. Figure 2 shows the matching of pozzolanicity parameters, as capability to reduce calcium ion concentration, for all pozzolanic materials, if added at percentage of 25%, after 15 days. Experimental cements containing EAF slag, as partial replacement of GBS in the cement III/A and III/B, or total replacement in the types V/A and V/B, show the substantial matching of mechanical strength at 2, 7 and 28 days, in comparison to same cements without it, as well as for volume stability. Regarding the pozzolanicity assessment in accordance to EN 196-5 of the composite experimental cements containing pozzolanic materials in addition to the EAF slag, although the meaning of Fratini test for ternary cement is questionable, the comparison between cement type V containing EAF and fly ash with Pozzolanic cement containing 25% of flay ash, used by us as reference products and available on the market as CEM IV/A (V), indicates a very low content of calcium ion concentration since 8 day of maturation. Results are shown in figure 3. As displayed in table 3, figure 4 and figure 5, the addition of EAF slag to the ternary cements produced in laboratory, both at dosage of 25% in case of cement replacement of 50% and 35% in case of total cement replacement of 70%, shows a relevant contribute to the hardening, being strength of cement containing it similar or higher to those containing GBS.

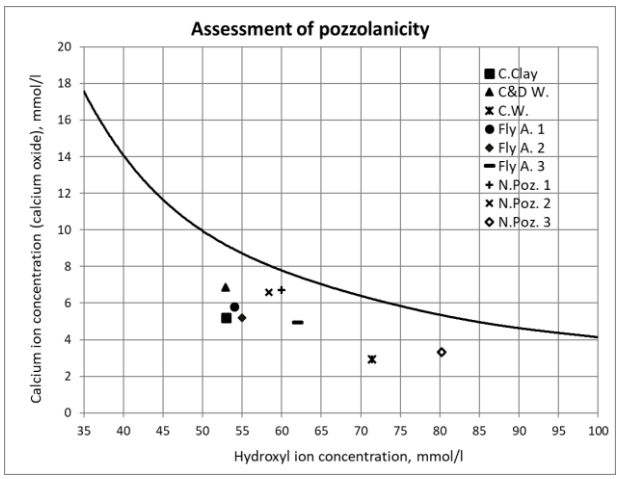

Figure 2. Pozzolanicity assessment of pozzolanic materials added to the cement at 25%, after 15 days.

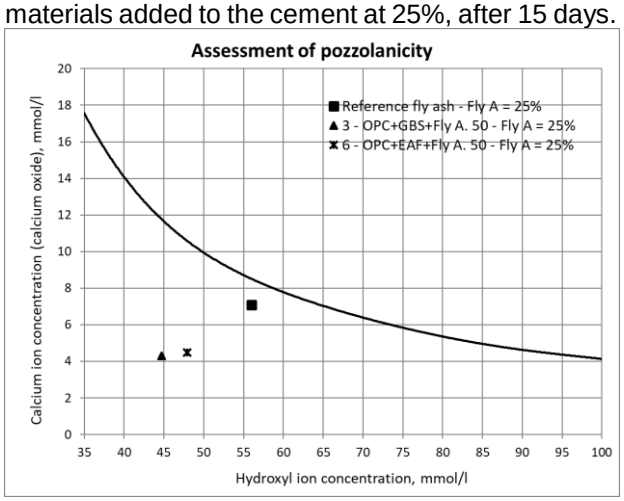

Figure 3. Pozzolanicity assessment of cements made using EAF and fly ash, in comparison to the pozzolanic cement containing 25% of fly ash.

Table 2. Experimental blended cements composition

Mix	Composition	*OPC*	*EAF*	*GBS*	*Fly A.*	*N.Poz.*	*C.Clay*	*Bio A.*
		%	%	%	%	%	%	%
1	OPC	*100*						
2	OPC + GBS 50	*50*		*50*				
3	OPC+GBS+Fly A. 50	*50*		*25*	*35*			
4	OPC+GBS+N.Poz. 50	*50*		*25*		25		
5	OPC + GBS + EAF 50	*50*	*25*	*25*				
6	OPC+EAF+Fly A. 50	*50*	*25*		25			
7	OPC+EAF+C.Clay 50	*50*	*25*				25	
8	OPC + GBS 70	*30*		*70*				
9	OPC+GBS+Fly A. 70	*30*		*35*	*35*			
10	OPC+GBS+N.Poz. 70	*30*		*35*		35		
11	OPC + GBS + EAF 70	*30*	*35*	*35*				
12	OPC+EAF+Fly A. 70	*30*	*35*		35			
13	OPC+EAF+C.Clay 70	*30*	*35*				35	
14	OPC+EAF+C.Clay+Bio A. 70	*30*	*35*				30	5

Experimental cement n. 14, containing 5% of biomass ash, as partial substitution of the calcined clay, and similar composition to the cement n. 13 which contains calcined clay and EAF slag, shows comparable or higher mechanical performance than blended cements having the same total percentage of clinker Portland replacement, 70% in the specific case. Moreover, both cements n. 13 and n. 14

containing calcined clay in addition to the EAF, show higher performance in comparison to the other pozzolanic materials.

Table 3. Experimental blended cements performance

Mix	Composition	Compressive Strength			Expansion	pozzolanicity
	maturation age (days)	2	7	28	mm	days
1	OPC	36	47,6	56,7	2	n.d.
2	OPC + GBS 50	15,2	37,9	52,5	3	n.d.
3	OPC+GBS+Fly A. 50	12,6	24,3	38,4	2	8
4	OPC+GBS+N.Poz. 50	11,3	25	38,2	2	8
5	OPC + GBS + EAF 50	17,9	37,2	50,9	4	n.d.
6	OPC+EAF+Fly A. 50	14,9	27,2	42,7	2	8
7	OPC+EAF+C.Clay 50	15,9	28,1	44,6	2	8
8	OPC + GBS 70	14	33,8	51,2	1	n.d.
9	OPC+GBS+Fly A. 70	8,2	21,3	36,1	2	8
10	OPC+GBS+N.Poz. 70	6,2	19,7	35,1	2	8
11	OPC + GBS + EAF 70	17,5	35,4	50,7	3	n.d.
12	OPC+EAF+Fly A. 70	11,2	23,4	38,1	2	8
13	OPC+EAF+C.Clay 70	13	23,8	39,5	3	8
14	OPC+EAF+C.Clay+Bio A. 70	13,1	24,7	41,4	2	8

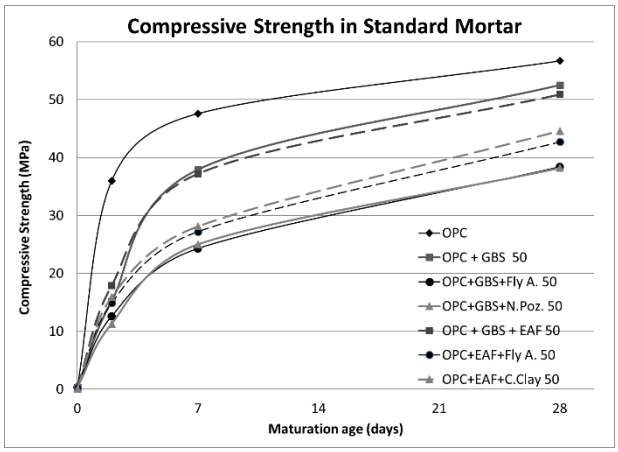

Figure 4. Mechanical strength in standard mortar, at 7, 14 and 28 days of maturation, of the experimental blended cements having 50% clinker Portland replacement.

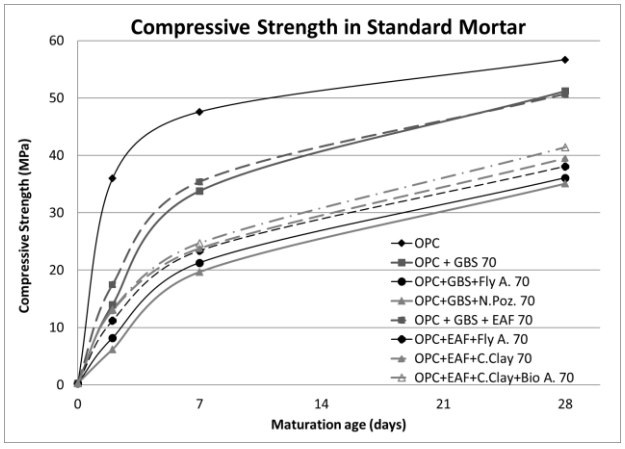

Figure 5. Mechanical strength in standard mortar, at 7, 14 and 28 days of maturation, of the experimental blended cements having 70% clinker Portland replacement.

As shown in figures 4 and figures 5 by the dotted and dash lines, at both percentages of cement replacement of 50% and 70%, EAF slag assures higher mechanical performance in comparison to the GBS, if used in combination with pozzolanic materials, as fly ash and calcined clay.

3. CONCLUSION

In conclusion, this research demonstrates the possibility to increase circular economy by means use of electric arc furnace slag (EAF), in cement and concrete industry, after its chemical and physical properties assessment, in percentages up to 35%, especially in combination with others additional supplementary cementitious material having pozzolanic properties. Results indicate increasing of mechanical performance for a large part of combinations if used as partial replacement of blast furnace slag (GBS), in the blast furnace cement type III, today produced in accordance to EN 197-1, as well as for total substitution in the composite cement type V. Moreover, addition of biomass ash, in low percentage, as secondary components, if well ruled considering the amount of dangerous elements, as e.g. chlorine, alkali and phosphorus, which could be introduced by them in the concrete, as well as final concrete exposition and required durability, could contribute to the mechanical strength of the concrete, allowing in the same time higher sustainability, thanks to the reduction of environmental impact due to the waste disposal in to the landfills.

REFERENCES

Perugini V., 2018. Nobilitation of clay waste from tunnelling; 38th Cement and Concrete Science Conference, Coventry, UK. 10th & 11th September 2018.

Perugini V., Schwotzer M., 2017. Properties of new cement from ceramic waste; 1st International Conference on Construction Materials for Sustainable Future, 19-21 April 2017, Zadar, Croatia.

Amin M. N., Khan K., Saleem M. U., Khurram N., Niazi M. U. K., 2017. Influence of Mechanically Activated Electric Arc Furnace Slag on Compressive Strength of Mortars Incorporating Curing Moisture and Temperature Effects. Sustainability - MDPI, Basel, Switzerland

Hendriks C.A., Worrell E., Price L., Martin N., Ozawa Meida L., De Jager D., Riemer P., 1998. Emission reduction of greenhouse gases from the cement industry. Proceedings of the 4th International Conference on Greenhouse Gas Control Technologies, Interlaken, Switzerland.

Chakchouk A., Trifi L., Samet B. and Bouaziz S.,2009. Formulation of blended cement: Effect of process variables on clay pozzolanic activity. Construction and Building Materials. 23, 1365–1373.

Cook D.J., 1986. Calcined clay, shale and other soils. In: Cement Replacement Materials. Swamy RN (ed), Surrey University Press, London. 40-72

Stabilization/Solidification of Zn-contaminated Sludge by Geopolymers

L. Wang[1,2], D.A. Geddes[1], J.L. Provis[1] and D.C. Tsang[2]

[1] Immobilisation Science Laboratory, Department of Materials Science and Engineering, The University of Sheffield.
[2] Department of Civil and Environmental Engineering, The Hong Kong Polytechnic University.

ABSTRACT
Stabilization/solidification (S/S) is a low-cost and high-efficiency remediation method for hazardous materials, however, conventional cement-based S/S method has environmental constraints and sustainability concerns. This study proposes a geopolymer-based approach for the S/S of Zn-contaminated sludge, and accordingly elucidates the chemical interactions between geopolymer binders and toxic elements. Thermal and calorimetry analyses showed that Zn incorporation significantly delayed the hydration reaction of geopolymers. As results, the final setting time of geopolymers postponed from approximately 6 h to 30 h. Quantitative X-ray diffraction and ^{29}Si nuclear magnetic resonance analyses further indicated that the addition of Zn resulted in the low content as well as poor polymerization of hydrates. Compared to sodium silicate-based activator, potassium silicate-based activator had relatively high compatibility with Zn element. During the S/S process, Zn engaged in the formation of N/K-A/Z-S-(H) gel, accounting for the low leachability of Zn. For practical application, the strong pH buffering capacity of sludge hindered the pH increase. Therefore, sufficient dosage of activator was required for ensuring satisfactory solidification and contaminant immobilization of the geopolymer-based S/S products. The leachability of Zn in geopolymer-treated samples confirmed with the criterion. This study demonstrated that geopolymer can serve as an environmentally compatible material for S/S of contaminated sludge.

Keywords: alkali-activated materials; microstructure analysis; precipitate chemistry; green remediation; stabilization/solidification.

39th Cement and Concrete Science Conference
9-10th September 2019
University of Bath
Paper Number 053

Effects of Sodium Silicate Proportion on Strength Development of Calcined Clay Geopolymer Mortar

A. S. Bature[a], M. Khorami[a], E. Ganjian[a] and M. Tyrer[a]
[a] Centre for Research in the Built and Natural Environment, Coventry University, CV1 5FB, UK

ABSTRACT
Geopolymers are derived from the synthesis of reactive alumino silicate source with alkali metal source to produce a binder that has lower carbon footprint compared to the traditional Portland cement. The long-term supply of precursors for geopolymers in the UK will be difficult to secure based on the dominant used materials – PFA, GGBS and white Metakaolin. Iron rich lateritic clay may offer a good alternative due to its low embodied energy and abundance. In this study, seven mixes were designed and tested. The first five mixes were based on varying the molar oxide ratios of the mortar mixes by activating the flash calcined lithomarge clay with different proportions of 54.5% Na_2SiO_3 solution. The last two mixes were grouts based on different water to geopolymer solid ratios. The important characteristics of the fresh and hardened mortars that were investigated based on the relevant standards are: strength development, setting times, UPV and rheological properties. The mix that achieved the peak strength of 30 MPa at 28 days cured under sealed condition has molar oxide ratios - SiO_2/Al_2O_3, Na_2O/Al_2O_3, Na_2O/SiO_2 and H_2O/Na_2O of 4.12, 1, 0.24 and 14.1 respectively. The results also showed that a more controllable and consistent rheology was achieved by increasing the water to geopolymer solid ratio of the grout.
Keywords: Calcined lithomarge clay, Na_2SiO_3, geopolymer, mortar, compressive strength

1. INTRODUCTION

The concrete industry is exploring and implementing broad range of measures that continue to improve its sustainability index. Development of alternative low-carbon binders based on geopolymers is one of the option widely recognized in the industry (Flatt, Roussel et al. 2012). Geopolymers are derived from the synthesis of reactive alumino silicate source with alkali metal source to produce a binder that has similar / superior properties than traditional Portland cement. The commonly used precursors are PFA, GGBS and white Metakaolin, but their long-term supply may be difficult to secure at cost-effective price (Geddes, Hayes et al. 2018).

Calcined clay is presently receiving attention as an aluminosilicate source that has the potential of extending the application of geopolymers because of its global abundance and low embodied energy, but its strength performance depends substantially on the calcination process, mineralogy of the clay, type and proportion of chemical activator *etc*. (Scrivener, John et al. 2016). Until recently, iron rich lateritic clay was considered as unsuitable precursor for geopolymers due to the reported harmful action of some ferrous compounds Fe++ that block the development of the geopolymeric reaction, the dubious role of iron oxide goethite, FeO(OH) reported in the literature, and the limitation of some analytical techniques such as Nuclear Magnetic Resonance Spectroscopy (NMR) in analysing the geopolymeric molecular structures due to the large iron content of the lateritic clay (Davidovits 2012).

The binding phase of calcined clay is almost exclusively aluminosilicate that forms a highly coordinated 3-Dimensional Si-O-Al polymeric network through polycondensation reaction typical of geopolymer binder (Provis, Fernández-Jiménez et al. 2014). According to (Davidovits 2008), the binding phase for iron rich calcined clay geopolymers is poly ferro sialate (Fe – Si – O – Al). Moreover, geopolymer synthesis is reported to be very sensitive to the molar oxide ratios of the mixture (Flatt, Roussel et al. 2012). Different authors have specified molar oxide ratios ranges for various application of geopolymers. However, within the specified ranges, diverse properties are achieved depending largely on the nature and proportion of activator and precursor used in the mixture, among other things. One of the main draw backs to widespread adoption of geopolymers in the construction industry is utilization of caustic alkali metal source such as NaOH solution due to health and safety concerns, as well as necessity for elevated temperature curing.

It is against this backdrop that this paper focuses on studying the viability of activating flash calcined lithomarge clay with user friendly sodium silicate solution, to produce sealed cured geopolymer mortar, by determining the appropriate mass and molar oxide ratios that produce peak strength mortars. The relationship between the water to geopolymer solid ratio and the rheological properties of the Calcined clay based geopolymer mortar was also studied and reported.

2. Experimental methods

The Calcined clay used in this study was supplied by Banah UK ltd which was processed by flash

calcining low purity kaolin clay obtained from the altered basalt – lithomarge in Northern Ireland and grounded in a ball mill (Mcintosh, Lawther et al. 2015). The calcined clay marketed as banahmeta has 31% reactive silica, specific surface (BET) of 75 m^2g, specific gravity of 2.89 and particle sizes which are 50% (d50) and 90% (d90) finer than 5-8 µm and 16-24 µm respectively. The oxides composition of the calcined clay obtained from the XRF is presented in table 2.1.

Table 2. 1: Major oxide compositions (wt. %) of the calcined clay

Oxide (% by weight)	SiO_2	Fe_2O_3	Al_2O_3	TiO_2	MgO	CaO	LOI
Calcined clay	35.18	25.4	29.6	2.9	1.3	0.9	< 2 %

The alkali metal source used in this study was the commercially available sodium silicate solution produced by Inoxia Ltd, UK that has 54.5% solid component. The water glass solution has the modulus (SiO_2/Na_2O molar ratio) of 2.05. The sharp sand which is finer than 4.5 mm sieve size and larger than 75 µm was used as the fine aggregate component of the mortar obtained from a local supplier in Coventry.

The mixing of the various mortar mixes was carried out using a 5 Litre Hobart mixer based on the procedure specified by BS EN 196 – 1 (EN 2005). The mixes were then placed in the 50 mm x 50 mm steel cubes moulds and compacted uniformly using the vibration table. The samples were then demoulded after 24 hrs and cured in a sealed condition by wrapping the samples with the cling film and stored in a conditioned room (20 ± 2 °C and over 50% relative humidity). The sealed curing control atmospheric carbonation on the samples, as well as avoid lost or gain of moisture.

Five mortar mixes were designed based on absolute volume method. The proportion of the sodium silicate solution in the mortar mixes was varied, while the two grout mixes have varied water to geopolymer solid ratios. The details of the mixes are presented in table 2.1.

Table 2.1: Mortar and grout mixes (kg / m^3)

[1]Mss:Mcc	**Sand (kg/m^3)**	**Calcined clay (kg/m^3)**	**54.5% Na_2SiO_3 (kg/m^3)**	**Water (kg/m^3)**
0.8	1221	330	264	84
0.9	1221	313	281	84
1	1221	297	297	84
1.1	1221	283	311	84
1.3	1221	264	330	84
W/S				
0.36	-	293.2	293.2	29
0.48	-	293.2	293.2	86

[1]Mss:Mcc is the mass ratio of sodium silicate solution to calcined clay.

3. Results and discussion

3.1 Effect of sodium silicate solution proportions on the density and strength of the calcined clay geopolymer mortar

Figure 3.1 shows the measured density at 7 and 28 days for the various calcined clay geopolymer mortar mixes. The density measured for the peak strength sealed cured mortar slightly increased with increase in curing age due to the hardening and drying of the samples that was characterized by the reduction of voids. At 7 and 28 days, the density computed was 2122 kg/m^3 and 2191 kg/m^3 respectively which can be described as normal weight mortar.

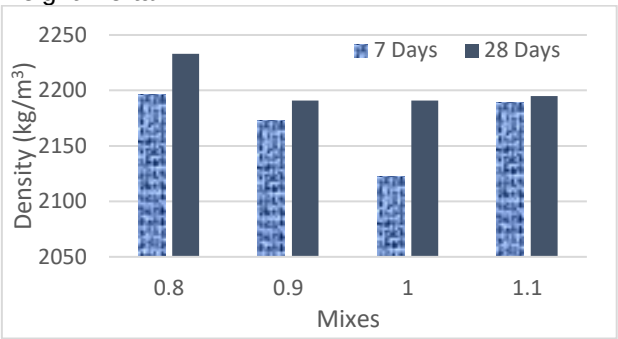

Figure 3.1: Density of calcined clay geopolymer mortar mixes

The result presented in figure 3.2 shows a rapid strength increase between 2 and 7 days, and that peak strength at all ages was achieved by the mass ratio of 1, which is thought to have sufficient alkali modulus and dosage that is required for the reaction. Increasing the mass ratio above 1 may have precipitated more than the required free Si which disrupt the reaction and resulted in the decrease strength. This concur with (Liew, YM, Kamarudin et al. 2012) that concluded that, a deterioration in strength is expected with increasing Na_2SiO_3 solution beyond the optimum because of the hindering of the geopolymerization reaction through the Al–Si phase precipitation that prevent contact between the reacting materials and the activating solution. On the other hand, the low mass ratio below 1 may have yielded insufficient free Si that is required to complete the geopolymerization, which resulted in the low strength mortar.

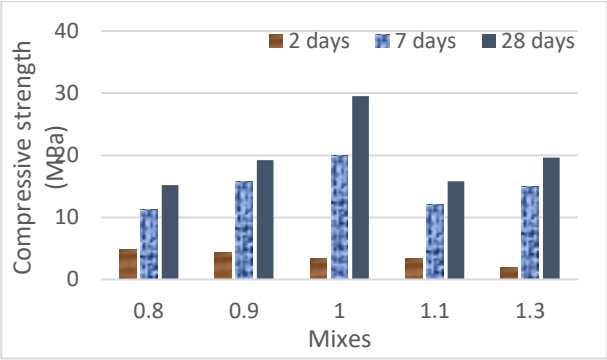

Figure 3.2: Compressive strength development of the calcined clay geopolymer mortar mixes

Moreover, from the molar oxide ratios calculated for the mortar mixes presented in table 3.1, it can be seen that the mix that achieved the peak strength has SiO_2/Al_2O_3 and Na_2O/Al_2O_3 molar ratios of 4.12 and 1.0 respectively, which correspond to the ideal ratios prescribed by (Davidovits 2008). Also, the Na_2O/SiO_2 of 0.24 and H_2O/Na_2O of 14.10 for the highest strength mix are similar to the optimum strength composition values obtained by many authors, as reported by (Liew, Yun-Ming, Heah et al. 2016). In summary, the strength achieved by the mixes presented in figure 3.2, maximized at an optimum and then decreased gradually due to the sensitivity of the geopolymer synthesis to variation in the molar oxide composition. Consequently, even though the molar oxide ratios of all the mixes fall within the range specified by (Davidovits 2008), a significant difference in strength is observed, which stress the need for mix optimization in geopolymers.

Table 3.1: Molar oxide ratios for the mortar mixes

Mss : Mcc	Na_2O/Al_2O_3	SiO_2/Al_2O_3	Na_2O/SiO_2	H_2O/Na_2
0.8	0.8	3.7	0.22	14.75
0.9	0.9	3.9	0.23	14.4
1	1	4.12	0.24	14.10
1.1	1.1	4.32	0.25	13.87
1.3	1.25	4.64	0.27	13.58

3.2 Effect of water to geopolymer solid ratio on setting times and rheology of the grout

The rheological properties for the calcined clay geopolymer grouts based on mass ratio of 1 and water to geopolymer solid ratio of 0.36 and 0.48 were obtained. A more consistent and controlled rheology was achieved by the calcined clay geopolymer grout which has water to geopolymer solid ratio of 0.48 compared to the 0.36 mix. At the shear rate of 40 S^{-1}, the grout shear stress measured was 4.20 Pa and a viscosity of 241 PaS. At the shear rate of 20 S^{-1}, the grout shear stress was 4.01 Pa and the viscosity was 133.4 PaS. The measured shear stress of the grout was influenced by both the high H_2O/Na_2O ratio of 14.1 and water to geopolymer solid ratio of 0.48. Almost similar rheological properties were obtained by (Geddes, Hayes et al. 2018) for a flash calcined clay activated with potassium silicate solution. The high plastic viscosity measured was due to the viscous nature of the sodium silicate solution used as the alkali metal source for the grout.

The setting time indicates the early strength development of the geopolymer paste for the two mixes that were based on calcined clay to sodium silicate solution mass ratio of 1. The measured setting times were very high for the calcined clay based geopolymer pastes compared to what is obtainable from traditional Portland cement paste. The initial setting time was 7.5 hrs, while the final setting time was 8.25 hrs for the mix that has water to geopolymer solid ratio of 0.36. Also, increasing the water to solid ratio of the geopolymer paste to 0.48, the initial and final setting times increased to 10.25 hrs and 11 hrs respectively. This concur with (Blackstock, Neill et al. 2017) that reported that, the setting process of geopolymers derived from calcined lithomarge takes several hours. However, a relatively short setting times was achieved by (Kwasny, Soutsos et al. 2018) by blending calcined clay with GGBS which supply calcium into the system, thereby lowering the setting times through quick precipitation of C(N)-A-S-H gel. On the other hand, the paste hardened and gained sufficient strength that, it can be demoulded within 20 hrs when cured at room temperature. This hardening behaviour is desired for the moulds daily turn-around especially in precast industries, while the delayed setting times may be useful in the transportation and handling of the calcined clay based geopolymer concrete, especially in applications where extended workability is required.

3.3 Effect of mix proportion on internal mechanisms of the calcined clay geopolymer mortar

The UPV values indicate the quality of the internal structure of the mortar sample (Khatib 2008). At 7 and 28 days, the computed UPV values for the peak strength mortar were 2.3 Km/s and 2.4 km/s respectively. The increase in the computed pulse velocities with increase in curing age of the peak strength mortar is caused by decrease in the pores of the sample due to advancement of the geopolymerization reaction. The UPV results presented in table 3.2 also showed that at 28 days, the values obtained for all the mixes fall within the UPV range of 2.2 to 4.5 km/s which is classified as good by the UPV test standard.

Table 3.2: UPV results of the mortar mixes

Mixes	0.8	0.9	1	1.1	Reference range
UPV (km/s) at 28 days	2.6	2.8	2.3	2.5	2.2 – 4.5

The microstructure for the mortar prepared with 54.5% Na_2SiO_3 solution to calcined clay mass ratio of 0.8 cured under sealed condition for 28 days is presented in figure 3.3. The structure reveals a densified and packed structure (a), as well as loose and discrete geopolymer matrix (b) which may have

caused the decreased strength achieved by the mix. In other words, the morphology shows precipitation of a sponge-like matrix indicated by globular units on the surface resulting from the geopolymerization.

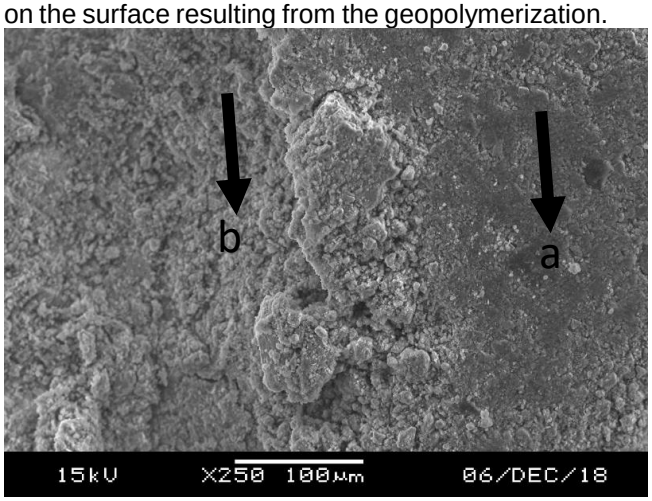

Figure 3.3: SEM micrograph for the (Mss:Mcc=0.8) mix mortar

The microstructure of the mortar samples prepared with 54.5% Na_2SiO_3 solution to calcined clay mass ratio of 1 cured for 28 days under sealed condition is presented in figure 3.4. The morphology reveals a compact rock mass bulk geopolymer structure (a) which may be the cause of the high strength achieved by the mix. Also, fine-grained matrix is seen on the surface (b) which indicate that the geopolymerization reaction of the calcined clay takes place on the surface.

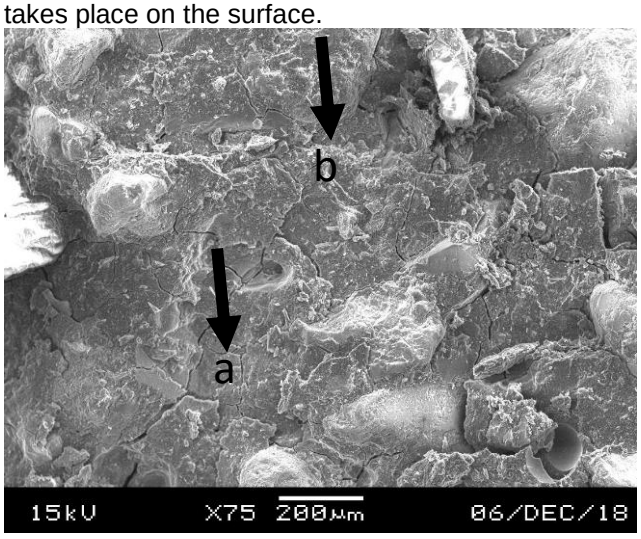

Figure 3.4: SEM image for the (Mss:Mcc =1) mix mortar

4. Conclusion

Some of the draw backs limiting wide-spread adoption of geopolymers in many parts of the world are: utilization of aluminosilicate sources that are competitively utilized as SCMs, the use of corrosive alkali metal sources and elevated temperature curing. This study therefore utilized iron rich flash calcined clay that has the potential of becoming a cost-effective alternative precursor, user friendly alkali metal source and sealed curing condition. The result shows that geopolymer synthesis of the calcined clay mortar is very sensitive to the variation in molar oxide ratios. Whereas, all the mixes prepared with the 54.5% sodium silicate solution have molar ratios which fall within the range specified by different authors in the literature, the strength obtained maximized at an optimum and then decreased subsequently with the variation in the molar oxide composition.

The calcined clay geopolymer grout shows high sensitivity to water to geopolymer solid ratio in terms of setting times and rheological performance. The high setting time achieved by the two grout mixes may be useful for applications that require extended workability or long-distance haulage of ready-mix concrete. On the other hand, the high plastic viscosity of the samples due to the viscous nature of the sodium silicate solution used in the mixes may affect the workability of the calcined clay based geopolymers, despite the low shear stress values.

REFERENCES

BLACKSTOCK, J.M., NEILL, J. and MCINTOSH, J.A., 2017. ***Geopolymeric concrete and methods of forming it from a basaltic precursor***.

DAVIDOVITS, J., 2012-last update, Red Geopolymer ement could become the standard. Available: https://www.geopolymer.org/news/red-geopolymer-cement-could-become-the-standard/2019].

DAVIDOVITS, J., 2008. *Geopolymer chemistry and applications.* Geopolymer Institute.

EN, B., 2005. 196-1.(2005). *Methods of testing cement-Part,* **1**.

FLATT, R.J., ROUSSEL, N. and CHEESEMAN, C.R., 2012. *Concrete: An eco material that needs to be improved.*

GEDDES, A.D., HAYES, M., BERNAL, A.S. and PROVIS, L.J., 2018. Understanding early age properties of metakaolin geopolymers, 2018.

KHATIB, J., 2008. Performance of self-compacting concrete containing fly ash. *Construction and Building Materials,* **22**(9), pp. 1963-1971.

KWASNY, J., SOUTSOS, M.N., MCINTOSH, J.A. and CLELAND, D.J., 2018. Comparison of the effect of mix proportion parameters on behaviour of geopolymer and Portland cement mortars. *Construction and Building Materials,* **187**, pp. 635-651.

LIEW, Y., KAMARUDIN, H., AL BAKRI, A.M., BNHUSSAIN, M., LUQMAN, M., NIZAR, I.K., RUZAIDI, C. and HEAH, C., 2012. Optimization of solids-to-liquid and alkali activator ratios of calcined kaolin geopolymeric powder. *Construction and Building Materials,* **37**, pp. 440-451.

LIEW, Y., HEAH, C. and KAMARUDIN, H., 2016. Structure and properties of clay-based geopolymer cements: A review. *Progress in Materials Science,* **83**, pp. 595-629.

MCINTOSH, A., LAWTHER, S., KWASNY, J., SOUTSOS, M., CLELAND, D. and NANUKUTTAN, S., 2015. Selection and characterisation of geological materials for use as geopolymer precursors. *Advances in Applied Ceramics,* **114**(7), pp. 378-385.

PROVIS, J.L., FERNÁNDEZ-JIMÉNEZ, A., KAMSEU, E., LEONELLI, C. and PALOMO, A., 2014. Binder Chemistry–Low-Calcium Alkali-Activated Materials. *Alkali Activated Materials.* Springer, pp. 93-123.

SCRIVENER, K., JOHN, V. and GARTNER, E., 2016. Eco-efficient cements: Potential, economically viable solutions for a low CO2, cement based materials industry. *United Nations Environment Program, Paris,* .

39th Cement and Concrete Science Conference
9-10th September 2019
University of Bath

Paper Number 054

Short and Long Term Performance of Hybrid Fibre Reinforced Concrete

Moayad Baabdullah[a,b], John Forth[b] and Leon Black[b]
Civil Engineering Department, King Abdulaziz University, KSA
School of Civil Engineering, University of Leeds, UK

ABSTRACT

This paper investigates the effects of the addition of steel and polypropylene fibres on both the mechanical properties and the time-dependent flexural performance of Hybrid Fibre Reinforced Concrete (HFRC) beams under sustained loading with a focus on the long-term deformations (shrinkage, tensile creep and compressive creep). The only variable of this study is the fibre volume fraction; the steel fibre content is 1% and the polypropylene fibre contents are 0.1%, 0.15% and 0.2%. A total of four beams were tested over an effective span of four meters. Three beams were strengthened internally with hybrid fibres; the remaining beam was used as a control specimen without fibre. The experimental results showed that HFRC exhibits better mechanical properties compared to the control mix. For long term deformations, HFRC showed lower shrinkage and tensile creep than normal reinforced concrete. Measured surface strains were noticeably lower in both the tension and the compression zones of the HFRC beams, which ultimately resulted in a lower long-term deflection.

1. INTRODUCTION

The increasing demands of shallower and longer concrete spans has led to a reduction of flexural member stiffness, as a consequence, increased deflection. Fortunately, the randomly dispersed fibres in concrete (Fibre Reinforced Concrete) are useful in accounting for issues such as brittle behaviour and crack formation (Banyhussan et al., 2016); as a result, lower deflection is expected.

Hybrid Fibre Reinforced Concrete (HFRC) represents a situation where more than one type of fibre is added to concrete in appropriate proportions to achieve optimal performance (Banyhussan et al., 2016).

The most common combinations of fibres that provide a positive interaction include (Banthia & Gupta, 2004):

Dimension of Hybrid Fibres: the first category of fibre is shorter and thinner, enabling it to bridge the micro-cracks and, thus, controls the growth of the cracks. The other type of fibre is meant to arrest the propagation of macro-cracks because of its longer length, as shown in Figure 1.
Function of Hybrid Fibres: the first type of fibre is flexible to improve the early stage and fresh properties of the concrete, for instance, plastic shrinkage. The second fibre is stiffer and stronger to improve the mechanical properties of the composite.

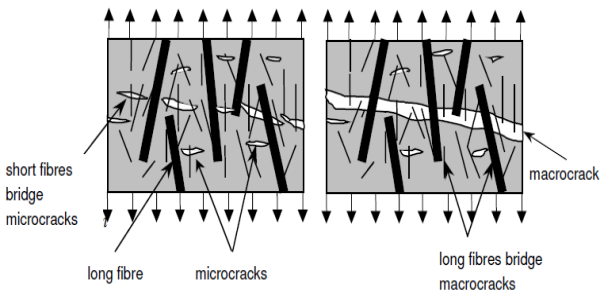

Figure 1. Fibre bridging (Ivan, 2006)

Hybrids made up of polypropylene fibre, which is used to reduce plastic shrinkage cracks together with steel fibre which is added to reduce cracking width and to improve mechanical properties, had shown high levels of positive interaction (Banthia and Gupta, 2004).

The time-dependent flexural performance of the reinforced concrete members is mostly affected by the long term deformations (Scott and Beeby, 2005). Due to the clear effects of the addition of steel and polypropylene fibres on the long term deformations (Chen and Liu, 2005; Sun et al., 2001), the shrinkage and creep behaviours of the HFRC were studied separately.

The main goal of this paper is to investigate the effects of the addition of steel and polypropylene fibres on both the mechanical properties and the time-dependent deformations of Hybrid Fibre Reinforced Concrete (HFRC) beams under sustained loading.

2. EXPERIMENTAL PROGRAMME

The experimental tests were conducted at the George Earle Laboratory in the School of Civil Engineering at the University of Leeds, England.

2.1 MATERIALS PROPERTIES

The cement is high strength 52.5N cement. The coarse aggregate is a 20 mm maximum size quartzite aggregate. The fine aggregate is a 5 mm maximum size natural river sand. Due to the decreased fibre concrete workability, superplasticiser was added to all HFRC mixtures. Hooked steel fibre (ST) and fibrillated polypropylene fibre (PP) were used, as shown in Figure 2. The physical and mechanical properties of the fibres are presented in Table 1. The used reinforcement rebars have a 500 MPa yielding strength.

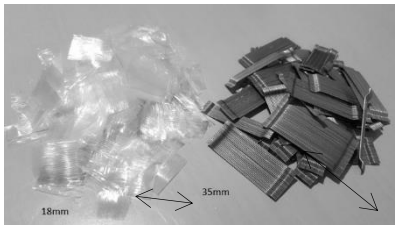

Figure 2. Steel fibre (right) and polypropylene fibre (left)

Table 1. Physical and mechanical properties of fibres

Fibre property	Steel fibre	Polypropylene fibre
Length, mm	35	18
Diameter, mm	0.55	0.05
Tensile strength, Mpa	1345	165

2.2 EXPERIMENTAL PLAN

A total of four mixes of concrete were examined. The control mixture proportions were designed to be grade C40/50. The same mix design was used for the concrete matrix in all the HFRC mixes. Therefore, fibre volume fractions are considered to be the only variables. The corresponding fibre volume fractions are given in Table 2.

All tests were performed according to British Standards. Specimens were casted for every mixture to evaluate the short-term 28 days mechanical properties and the long-term deformations for three months, as given in Table 3.

Table 2. Volume fraction of fibres used in various mixes

Mix	ST %	PP %	Name
1	0	0	Control
2	1	0.1	ST1-PP0.1
3	1	0.15	ST1-PP0.15
4	1	0.2	ST1-PP0.2

Table 3. Test standards and specimen sizes

Test	Form type	#	Size(mm)
Flexural bending	beam	1	150*300*4200
Flexural strength	prism	3	100*100*500
Compressive strength	cube	3	100*100*100
Splitting tensile strength	cylinder	3	150*300
Compressive creep	prism	2	75*75*200
Tensile creep	bobbin	2	75*365
Shrinkage	prism	2	75*75*200

To monitor the long-term deflection, a large-scale beam (150 mm depth x 300 mm width x 4200 mm length) of each mix was tested under a four-point bending test at 28 days and the load sustained for three months, as shown in Figures 3.

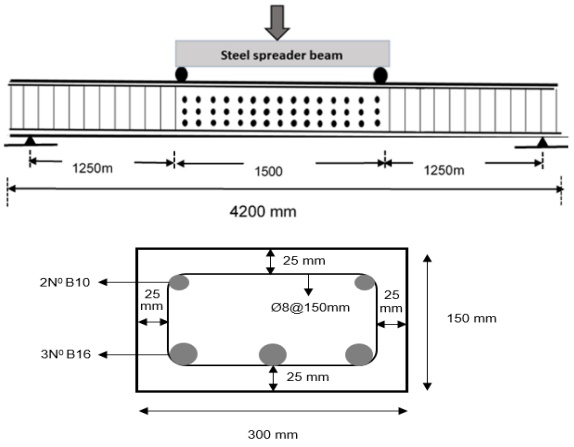

Figure 3. Beam dimensions and reinforcement details

To monitor the long-term curvature and the neutral axis depth, a group of DEMEC gauges (150 mm) were placed on the sides of the beam to measure the surface strain on the pure moment zone using a hand-held mechanical strain gauge. To monitor the long-term mid-span deflection, a Linear Variable Differential Transformer (LVDT) was placed under the middle of the beams, as shown in Figure 4.

Figure 4. Flexural bending test

Specimen	Compressive strength (MPa)	Splitting tensile strength (MPa)	Flexural strength (MPa)
Control	51.9	3.9	5.9
ST1-PP0.1	56.3 (8.48%)	5 (28.21%)	8.3 (40.68%)
ST1-PP0.15	56.5 (8.86%)	5.3 (35.9%)	9.8 (66.1%)
ST1-PP0.2	56.7 (9.25%)	5.7 (46.15%)	10.5 (77.97%)

To reach the stabilised crack pattern which is the stage when all cracks are formed and any further loading does not cause more cracks but widens the existing ones, all beams were examined under sustained loading of 23 kN to produce 200 Mpa stress in the tensile reinforcements, which is enough to reach the stabilised crack pattern (Soltani et al., 2013).

3. EXPERIMENTAL RESULTS AND DECUSSATIONS

The experimental results for the effects of polypropylene and steel fibres on the compressive strength, splitting tensile strength and flexural strength, are summarised in Table 4.

Table 4. Experimental results for HFRC mechanical properties

The results of the compressive strength test indicated that the addition of steel fibre slightly enhanced the compressive strength. However, the addition of polypropylene fibres revealed a negligible effect. The experimental results also demonstrated a clear improvement in splitting tensile and flexural strengths by 28-46% and 40%-77% respectively; the strengths tend to increase as the fibre content increases.

On the other hand, Figures 5, 6, 7 and 8 show the effects of polypropylene and steel fibres on shrinkage, compressive creep, tensile creep, and long-term deflection.

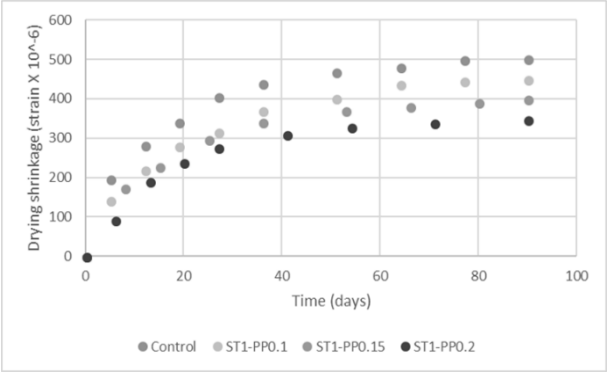

Figure 5. Drying shrinkage of HFRC

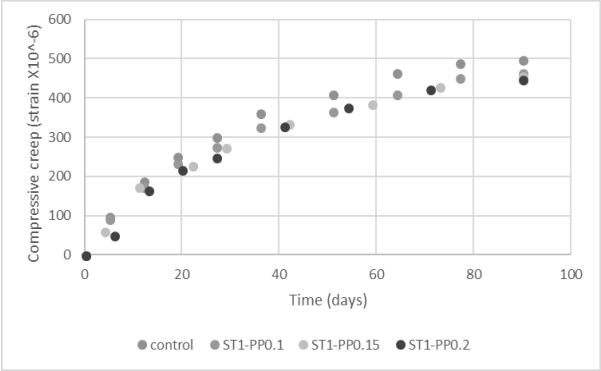

Figure 6. Compressive creep of HFRC

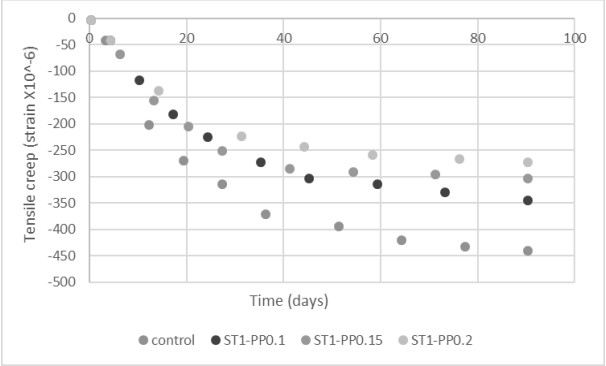

Figure 7. Tensile creep of HFRC

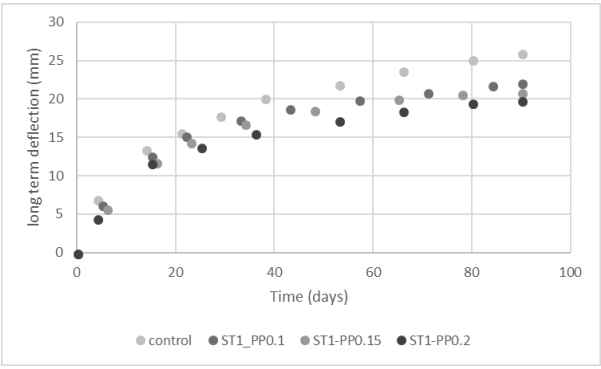

Figure 8. Long term deflection of HFRC

The results of the compressive creep tests have shown that the addition of steel fibre resulted in a minor decrease in the compressive creep. However,

the addition of polypropylene fibres displayed no significant effect. The experimental results also proved a clear reduction in shrinkage and tensile creep; the long term deformations tend to decrease as the fibre content increases. A lower long-term deflection was also observed as the fibre content increased.

This improvement in both strength performance and long term deformations could be a result of controlling crack progression, which is highly improved by the addition of fibres. The discontinuous polypropylene fibres are added to eliminate plastic shrinkage cracks by bridging across micro-cracks and, therefore, slowing the development of macro-cracks. On the other hand, the randomly distributed steel fibres are added to arrest the propagation of macro-cracks because of its longer length and higher strength and, therefore, preventing the widening of the cracks.

4. CONCLUSIONS

Four different concrete mixtures were tested to evaluate the effects of the addition of steel and polypropylene fibres on both the mechanical properties and the long term deformations of Hybrid Fibre Reinforced Concrete.

The experimental results presented that:

There was a significant enhancement of the splitting tensile strength and the flexural strength. The strengths tend to increase as the fibre content increases.
The addition of steel fibre slightly improved compressive strength. However, an insignificant effect was observed after the addition of polypropylene fibres.
There was a considerable decrease in shrinkage and tensile creep which tend to decrease as the fibre content increases.
The addition of steel fibre presented a slight reduction in compressive creep. However, the addition of polypropylene fibres displayed no significant effect.
HFRC beams displayed lower long-term deflection than normal reinforced concrete. This could mainly be because of the improved tensile creep and shrinkage and, thus, lower cracking progression within the tensile stresses zone.

Improving the quality of concrete is beneficial for structural safety, integrity and durability. The addition of steel and polypropylene fibres demonstrated a considerable improvement in HFRC performance in its both mechanical properties and time dependent deformations. Therefore**,** it might increase the possibility of using HFRC as a key construction material in future structural applications.

However, the enhancement of the deformation behaviour of HFRC is not included in EC2, which means predicting the long-term deflection of HFRC beams using EC2 will be overestimated. Therefore, modifications to the EC2 method needs to be proposed in future studies.

ACKNOWLEDGEMENT

Authors would like to thank the technical team at the University of Leeds for providing technical lab support, as well as King Abdulaziz University for financially supporting this research.

REFERENCES

Banthia, N., & Gupta, R., 2004. Hybrid fiber reinforced concrete (HyFRC): fiber synergy in high strength matrices. *Materials and Structures*, *37*(January), 707–716.
Banyhussan, Q. S., Yıldırım, G., Bayraktar, E., Demirhan, S., & Şahmaran, M., 2016. Deflection-hardening hybrid fiber reinforced concrete: The effect of aggregate content. *Construction and Building Materials*, *125*, 41–52.
Chen, B., & Liu, J., 2005. Contribution of hybrid fibers on the properties of the high-strength lightweight concrete having good workability. *Cement and Concrete Research*, *35*(5), 913–917.
Ivan, M. (2006). *High-Performance Hybrid-Fibre Concrete*.
Scott, R. H., & Beeby, A. W., 2005. Long-Term Tension-Stiffening Effects in Concrete. *ACI Structural Journal*, 102, 31-39.
Soltani, A., Harries, K. A., & Shahrooz, B. M. (2013). Crack Opening Behavior of Concrete Reinforced with High Strength Reinforcing Steel. *International Journal of Concrete Structures and Materials*, *7*(4), 253–264.
Sun, W., Chen, H., Luo, X., & Qian, H., 2001. The effect of hybrid fibers and expansive agent on the shrinkage and permeability of high-performance concrete. *Cement and Concrete Research*, 31(4), 595–601.

39th Cement and Concrete Science Conference **Paper Number 056**
9-10th September 2019
University of Bath

Magentic resonance imaging of water transport and drying-wetting cycles in cement pastes

Magdalena Janota, Peter J McDonald, David A Faux
Department of Physics
University of Surrey

Abstract
The durability of cementitious materials is closely related to the transport properties of water within the materials. Traditional techniques such as gravimetry or permeability testing to measure sorption offer at best limited information on the distribution of water within a sample. On the other hand, magnetic resonance imaging (MRI) is a very powerful method not only to visualise where water is within a sample, but also, through spin relaxation time contrast to provide information on the locally filled pore size distribution. In this study, we use 1D and 3D SPRITE MRI methods sensitive to short relaxation time to separate and resolve with circa 0.5 mm resolution water in gel (nanometre) and capillary (micron) sized pores during repeated wetting and drying cycles of 60 mm size samples. The study aims to explore the extent to which time-dependent microstructural changes occurring in response to water content changes cause anomalous sorption behaviour. A series of water distribution maps will be shown along with preliminary analysis using a new transport model under development.

Sorption measurements in cement paste using garfield imaging

Örs Istok, Peter McDonald, David Faux
Department of Physics
University of Surrey

Abstract

Moisture transport in cementitious materials is often found to be anomalous deviating from a square root of time dependency. Many explanations have been proposed for this anomaly including delayed hydration, physical interaction between calcium silicate hydrates (C-S-H) and water and pore blocking amongst others [1, 2]. It is now known that cement gel porosity is dynamic that is, it changes both reversibly and irreversibly and does so over an extended period, in response to rapidly changing water content [3, 4].

In this work, water sorption experiments through thin cement paste samples are performed using Gradient At the Right angle to the Field (GARField) magnetic resonance profiling. The objective is to disentangle transport phenomena from changing pore size distribution phenomena in order to better understand anomalous water transport. GARField is an effective spatially resolved method that uses a high, static magnetic field gradient to measure short NMR T_2 relaxation time components that characterize water in different pore sizes (nanometer) in cement gel with high spatial resolution (micron) [5]. The sorption of water in 1-D is measured at different depths from the wet surface. The results obtained on a time scale of 7 days show moisture transport into and through gel pores and inter-layer spaces. The most significant changes in pore filling and pore size distribution occur during the first few hours of rewetting but continue over a few days. The obtained data is explored with a new model which considers that the apparent diffusion coefficient is a function of concentration and the changing pore size distribution.

References:

[1]. M. Saeidpour, L. Wadso, Evidence for anomalous water vapour sorption kinetics in cement based materials, Journal of Cement and Concrete Research, Vol. 70, pp. 60-66, 2015.
[2]. H.M. Jennings, A. Kumar, G. Sant, Quantitative discrimination of the nano-pore-structure of cement paste during drying: New insights from water sorption isotherms, Journal of Cement and Concrete Research, Vol.76, pp. 27-36, 2015.
[3]. A.M. Gajewicz, E. Gartner, K. Kang, P.J. McDonald, V. Yermakou, A 1H NMR relaxometry investigation of gel-pore drying shrinkage in cement pastes, Journal of Cement and Concrete Research, Vol. 86, pp. 12-19, 2016.
[4]. C. Zhou, F. Ren, Z. Wang, W. Chen, W. Wang, Why permeability to water is anomalously lower than that to many other fluids for cement based materials, Journal of Cement and Concrete Research, Vol. 100, pp. 373-384, 2017.
[5]. N. Fischer, R. Haerdtl, P.J. McDonald, Observation of the redistribution of nanoscale water filled porosity in cement based materials during wetting, Journal of Cement and Concrete Research, Vol. 68, pp. 148-155, 2015.

Molecular dynamic study of paramagnetic impurities and water in hydrates

Arifah Abdu Rahaman, Dr David Faux and Prof Peter McDonald
Physics Department
University of Surrey
Abstract

Time-domain nuclear magnetic resonance (NMR) is a valuable laboratory-based experimental method for probing the behaviour of water in cementitious material. The method measures the ^{1}H water nuclear spin relaxation rates T_1 and T_2 that are exquisitely sensitive to micro- and nano-structure. Fast-field-cycling NMR (FFC-NMR) yields the T_1^{-1} relaxation rate as a function of frequency providing yet further detail.

In cement, the relaxation rate response is dominated by the interactions of water with paramagnetic ions such as Fe^{3+} which may be located in the solid or aqueous phases. In order to interpret the experimental results, it is necessary to have a model for the water dynamics in the vicinity of the paramagnetic ions. Although several models provide good fits to $T_1^{-1}(f)$ for solid-bound paramagnetic ions (Faux and McDonald (2018); Faux, McDonald, and Howlett (2017)), a model describing $T_1^{-1}(f)$ for aqueous paramagnetic ions is lacking. We seek to overcome this limitation.

Results of molecular dynamics simulations of aqueous ions are presented. Results are shown to inform a simplified theoretical model that adequately describes the nano-scale dynamics of water surrounding paramagnetic ions. The model is then used to provide fits to literature experimental data for a range of aqueous paramagnetic ions using a small number of parameters. Numerical values of the parameters provide insight into the dynamics of the water close to the surrounding ions. The model will contribute to the interpretation of FFC-NMR results from cement-like material such as cement paste, plasters and mortar.

References

Faux, D. A., & McDonald, P. J. (2018). A model for the interpretation of nuclear magnetic resonance spin-lattice dispersion measurements on mortar, plaster paste, synthetic clay and oil-bearing shale. *Microporous and Mesoporous Materials, 269*, 39-42. doi:https://doi.org/10.1016/j.micromeso.2017.09.002

Faux, D. A., McDonald, P. J., & Howlett, N. C. (2017). Nuclear-magnetic-resonance relaxation due to the translational diffusion of fluid confined to quasi-two-dimensional pores. *Physical Review E, 95*(3), 033116. doi:10.1103/PhysRevE.95.033116

Lattice Boltzmann Modelling of Water in Models of C-S-H with Dynamic Porosity

Miryea N. Borg, Peter J. McDonald, David Faux
Department of Physics
University of Surrey

Abstract

The microstructure of cement hydrates have a nanoscopically semi-crystalline, microscopically amorphous structure that has recently been shown to undergo reversible and irreversible changes over a prolonged period following “instantaneous” water sorption and desorption [1].

Lattice Boltzmann methods have previously been used to investigate cement permeability [2]. We seek to develop new Lattice Boltzmann methodologies that allow us to investigate water dynamics within the Etzold model of hydrate microstructures. The Etzold model is a computer-based three dimensional version of the well known Feldman and Sereda quasi continuous sheet model.

The Lattice Boltzmann method is implemented, including a Shan-Chen multi-phase and partial bounce back multiscale approach, to understand the effect of capillary forces moving hydrate “particles” or “sheets” within the hydrate structure. The effect of moving boundaries between hydrate sheets experiencing transient pressures is analysed.

The new Lattice Boltzmann methods allow us to investigate structural changes arising from capillary / disjoining-pressure forces. Results to illustrate the basic ideas will be presented.

[1] A. M. Gajewicz, E. Gartner, K. Kang, P. J. McDonald, V. Yermakou, A ^{1}H NMR relaxometry investigation of gel-pore drying shrinkage in cement pastes, Cem. Concr. Res. 86 (2016) 12-19.

[2] M. Zalzale, P. J. McDonald, K. L. Scrivener, A 3D Lattice Boltzmann effective media study: understanding the role of C-S-H and water saturation on the permeability of cement paste, Model. Simul. Mater. Sci. Eng. 21 (2013) 085016.

39th Cement and Concrete Science Conference **Paper Number 060**
9-10th September 2019
University of Bath

The Effect of Carbonation on the Performance of Concrete Under Extreme Loading

T. Lord, L. Black
School of Civil & Structural Engineering, University of Leeds

J. Wang, Y. Wang, Q. Li
School of Mechanical, Aerospace & Civil Engineering, University of Manchester

ABSTRACT

This paper introduces the initial work of PLEXUS project RC3, part of the UKCRIC pump priming project, into the effect of carbonation on the performance of concrete under extreme loading. A 20MPa micro-concrete was cast, cured under ideal conditions for 4 days, before being moved to ambient conditions for 24 days. The strength and flexure was measured at 28 days, before the concrete underwent accelerated carbonation for 28 days, at 57% RH and 4% CO_2 at 20°C. Following carbonation, there was found to be a 16% increase in unconfined compressive strength, 31% increase in confined compressive strength, and an increase in stiffness.

Samples of the same concrete, both carbonated and non-carbonated, will be tested under extreme dynamic loading, in order to determine the effect of carbonation on the performance under extreme loading, with differences under quasi-static loading having been found. CEM I 40 and CEM II 20 concretes will also be investigated under quasi-static and extreme loading in order to investigate the effects of mix design.

Keywords: Split-Hopkinson pressure bar; dynamic loading; concrete; carbonation; extreme loading

INTRODUCTION

A large proportion of the UK's infrastructure budget is spent of repair and maintenance of existing infrastructure, with over 30% of the total UK infrastructure expenditure being repair and maintenance (Martin, 2018). Understanding how material ageing affects structural performance is therefore vital in updating and maintaining safety cases and extending infrastructure service life. Carbonation is known to lead to changes in phase assemblage and porosity, effecting the durability and performance of concrete (Šavija and Luković, 2016). While the effect of carbonation on concrete under quasi-static loading is understood, the effect of carbonation, and other deterioration/ageing processes, on the performance of concrete under extreme loading is poorly researched and understood, whether the loading be dynamic or thermal, or a combination of both.

Carbonation has long been known to increase the compressive strength of concrete (Blakely, 1956). As carbon dioxide diffuses into the cement matrix, it forms carbonic acid in the pore water, which reacts with cement phases. The new calcium carbonate phases formed are more voluminous than those of original reaction products, and so capillary porosity is reduced and compressive strength increases. The reduction in capillary porosity also reduces the rate of further CO_2 diffusion into the concrete, with a route time law governing the carbonation rate into ordinary Portland cement (OPC) concretes.

When OPC is blended with Supplementary Cementitious Materials (SCM's), the hydrate phases differ, altering the carbonation process and so changing the rate of carbonation, dependent on the mix design and exposure (Šavija and Luković, 2016). When pulverised fly ash (PFA) is used to replace the OPC in a cement mix, the pozzolanic reaction of the PFA consumes calcium hydroxide, or portlandite (CH), reducing the amount available for carbonation reactions.

The Split-Hopkinson Pressure Bar test (SPHB), applies a high dynamic load (strain rate 10^2-10^4 s^{-1}, while typical static, or older style dynamic testing would apply strain rates of 0.1 s^{-1})(Davies and Hunter, 1963) to a sample through the use of a pressurized air hammer on an incident bar, which then applies that force to a sample, with the force then applied through the sample to a transmission bar, and some reflected back to the incident bar. The transmission bar is used as the measurement of forces and strains within the sample at such high strain rates is difficult, whereas measuring the resultant compressive waves on the transmission and incident bars provides good data for the high strain rate response of the sample (Sudheera, Rammohan and Pradeep, 2018). This type of testing is used to determine the response of

materials to extreme loading events, such as collision or explosion.

Where uniaxial unconfined compression measures the static strength of a material, when loads are applied suddenly, the forces will not dissipate instantly, and surrounding material will act to confine the element, enabling significantly higher strain to occur, and where failure is associated with ductile behaviour, and material damage, pore collapse, and de-bonding of the interfacial transition zone (Karinski *et al.*, 2017). As such, uniaxial testing can be carried out with a confinement sleeve around the sample, in order to mimic the confinement conditions a concrete element would be under during dynamic loading. While this doesn't fully show the effects of dynamic loading, due to the low loading rate, it can provide a more accurate representation of the material response under high dynamic loading.

2. MATERIALS AND METHODS

2.1 Materials

A CEM I 20 MPa concrete was cast into 52mm diameter, 100mm length cylindrical moulds, and cured for 7 days under ideal conditions of 99 ± 1% relative humidity and 20 ± 1˚C, before being moved to ambient laboratory conditions and cured for a further 21 days. Due to the requirement for ~50mm diameter samples for testing, a 'micro-concrete' graded aggregate was used, from 40µm to 5mm. 5mm was the maximum aggregate size allowable in order to maintain a 10:1 sample to aggregate size ratio.

Following curing, 'fresh' samples, at 28 days, were tested for confined and unconfined compression, and tension. Under compression, gauges were used to monitor the strain on the sample during testing. Accelerated carbonation was also carried out on samples for 28 days, with 4 ± 0.5% CO_2 content, and 57 ± 5% RH, in line with the highest concentration and humidity that will maintain natural carbonation reactions (Leemann and Moro, 2017). Following carbonation, the same tests were carried out on the samples. Control samples were stored under laboratory ambient conditions while accelerated carbonation was being carried out, in order to distinguish between the effects of further ageing compared to accelerated carbonation on the samples, relative to those tested fresh after 28 days curing.

A low strength concrete was used in order to maximise the depth of carbonation within the sample, during the timeframe allowable within this project. A higher strength concrete would have required a longer accelerated carbonation period to reach the same carbonation depth. The concrete mix design is given in table 1.

Table 1 - CEM I 20 concrete mix design

Material	**Mix Quantity (kg/m^3)**
Water	225
Cement	343
Aggregate	1716

2.2 Methods

Uniaxial compressive strength testing was carried out using an RDP Howden Stiff Tester, at a ramp rate of 3mm per minute. Where used, confinement of samples under compression was carried out at 5MPa using a Hoak pressure cell confinement sleeve, and a compressive ramp rate of 3mm per minute. Samples were tested to failure, with the sample strain measured throughout. Where strain measurements were carried out, during compressive and tensile testing, 20mm strain gauges were used and attached to the side of the cylinders about their mid-point.

For tensile testing, the cylinders were cut such that the length was approximately 25mm, and Brazilian tensile testing carried out using the same RDP Howden Stiff Tester, and a ramp rate of 3mm per minute.

3.0 RESULTS AND DISCUSSION

3.1 Compressive Strength

Figure 1 shows the unconfined, uniaxial stress versus strain curves for the 'fresh and carbonated samples, tested in triplicate until failure. Within the initial loading phase, up to strains of 500 x 10^{-6}, the carbonated samples showed increased stiffness compared to the fresh samples. All carbonated samples had a higher failure stress than that of the fresh samples, with the carbonated samples having a mean failure stress of 26.0 MPa, a 16% increase compared to the 22.5 MPa mean failure stress of the fresh samples.

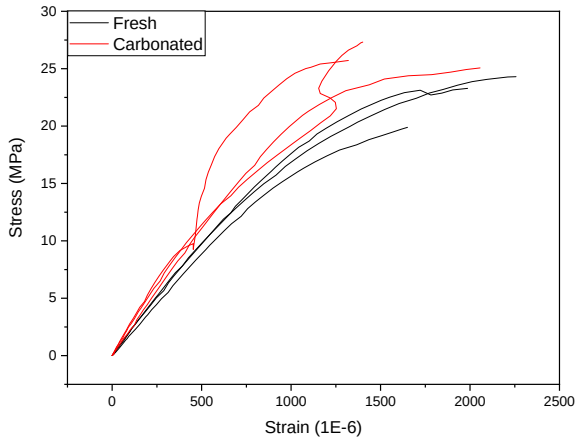

Figure 1 - Stress vs strain uniaxial compression plot for thee carbonated samples (red) and three fresh samples (black)

As well as an increase in failure stress, the failure mechanism in some of the carbonated samples, for unconfined compression, differed from that of the fresh samples, showing an increased stiffness and more brittle failure, shown in the stress v strain curves in figure 1. While all un-reinforced concrete in general undergoes brittle failure, characterised by sudden failure and a complete loss of strength, there is an element of plastic behaviour close to the failure point, seen in the reduction of the slope in all fresh samples up to failure. Two of the carbonated samples however, show a more stiff and brittle failure, reaching higher failure stress with significantly less overall strain.

In figure 2, the crack direction of a failed carbonated cylinder is compared to that of a fresh cylinder, where the crack direction is in line with the direction of loading, and normal to the face of the cylinder on which the stress was applied. In the fresh samples, the cracking was in a shear direction, suggesting a different and less brittle failure mechanism. The difference in stiffness and failure mode is expected to be significant when tested under extreme dynamic loading, with the force propagation likely to be different in materials of different stiffness.

Figure 2. Crack propagation in failed carbonated sample (left) and failed 'fresh' sample (right)

3.2 Confined Compression

Figure 3 shows the confined and unconfined uniaxial compression plots for the 'fresh' samples. The large difference in strain was clearly visible, with an order of magnitude difference between the confined and unconfined samples. Of the three unconfined tests, the maximum strain was 2.21 x10^{-3}, while in the confined compression tests, the maximum strain was 2.48 x10^{-2}, showing the ability of concrete to undergo much higher strain when confined. The confinement pressure for these tests was 5MPa.

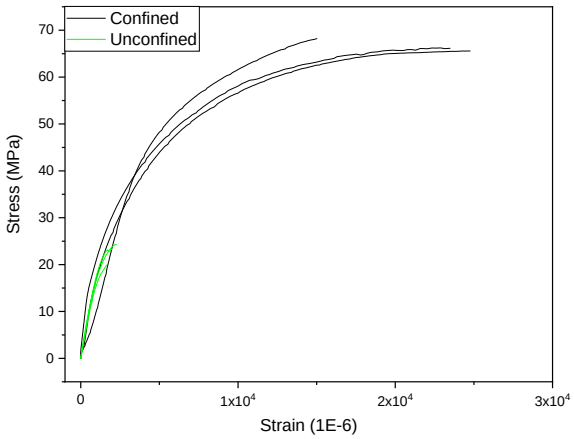

Figure 3 – Stress versus strain plot, for uniaxial compression of confined and unconfined CEM I 20MPa cylinders

Carbonated samples were also tested in confinement, with figure 4 showing the comparison between fresh and carbonated samples. As with unconfined compression, the carbonated samples once again showed an increase in failure stress, having a mean of 87.8 MPa, a 31% increase compared to the mean of 67.1 MPa for the fresh samples.

Initially, the carbonated samples again showed increased stiffness compared to the fresh samples, before then undergoing a significant increase in deformation before failure, compared to the fresh samples. The difference in failure stress and maximum strain, as with unconfined testing, means that under extreme strain rate loading, the stress propagation and failure mechanism between the carbonated and non-carbonated samples will be different.

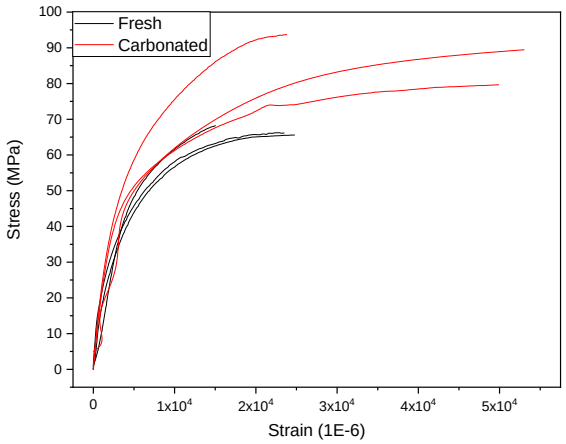

Figure 4 – Stress versus strain plot, for confined uniaxial compression, of carbonated versus 'fresh' samples.

4.0 CONCLUSION

Confined and unconfined compression testing was carried out on a CEM I 20 MPa concrete, on both

fresh and carbonated samples. The carbonated samples, in both tests, were found to have increased stiffness. In unconfined compression, there was a 16% increase in mean failure stress in the carbonated samples compared to the fresh samples. In confined compression, the increase in mean failure stress was 31%.

As well as an increase in failure stress, in unconfined compression, the carbonated samples reached lower strain before failure, while in confined compression, they reached significantly higher strain before failure compared to the fresh samples, suggesting different failure mechanisms.

5.0 FURTHER WORK

The work presented in this paper is the initial investigation of a larger project, investigating the effect of carbonation on the performance of concrete under extreme loading. For quasi-static testing, further work will be carried out to investigate the effect of carbonation of different concrete mixes, with a CEM I 40 MPa and a CEM II 20 MPa also to be investigated.

Carbonated and fresh samples will be taken to China for Split-Hopkinson Pressure Bar testing, in order to examine the performance of the concrete under extreme dynamic loading.

Longer term work will investigate the effect of different types of concrete deterioration, as well as a combination of extreme thermal and dynamic loading, using UKCRIC facilities at the Universities of Leeds and Manchester.

ACKNOWLEDGEMENT

The authors would like to thank EPSRC, through the PLEXUS (EP/R013535/1) project, as part of the UKCRIC programme, for funding this research.

REFERENCES

Blakely, I. L. and F. A. (1956) 'Some Effects of Carbon Dioxide on Mortars and Concrete', *Journal of the American Concrete Institute*, 53(9), pp. 295–308. doi: 10.14359/11515.

Davies, E. D. H. and Hunter, S. C. (1963) 'The Dynamic Compression Testing of Solids by the Method of the Split Hopkinson Pressure Bar', *Journal of Mechanical and Physical Solids*, 11, pp. 155–179.

Karinski, Y. S. *et al.* (2017) 'Uniaxial confined compression tests of cementitious materials', *Construction and Building Materials*. Elsevier Ltd, 153, pp. 247–260. doi: 10.1016/j.conbuildmat.2017.07.010.

Leemann, A. and Moro, F. (2017) 'Carbonation of concrete: the role of CO2 concentration, relative humidity and CO2 buffer capacity', *Materials and Structures*. Springer Netherlands, 50(1), p. 30. doi: 10.1617/s11527-016-0917-2.

Martin, J. (2018) 'Developing new statistics of infrastructure : August 2018', *Office for national statistics*, (August), pp. 1–19.

Šavija, B. and Luković, M. (2016) 'Carbonation of cement paste: Understanding, challenges, and opportunities', *Construction and Building Materials*, 117, pp. 285–301. doi: 10.1016/j.conbuildmat.2016.04.138.

Sudheera, Rammohan, Y. S. and Pradeep, M. S. (2018) 'Split Hopkinson Pressure Bar Apparatus for Compression Testing: A Review', *Materials Today: Proceedings*. Elsevier Ltd, 5(1), pp. 2824–2829. doi: 10.1016/j.matpr.2018.01.071.

39th Cement and Concrete Science Conference **Paper Number 061**
9-10th September 2019
University of Bath

Properties of Magnesia Binder Systems and their use in Salt Mines

Hans-Joachim Engelhardt
BGE TECHNOLOGY GmbH, Department of Repository Safety
Eschenstraße 55, 31224 Peine, Germany

ABSTRACT

In salt mining, there are numerous applications for building materials, in particular in the implementation of backfilling measures and the construction of shaft, drift, and borehole seals. In conjunction with these projects or as separate measures, injections are carried out. The materials used must be manufacturable and applicable under the circumstances of the mining industry, must not damage the highly soluble rock formations and have to guarantee the required properties in the long term. Magnesia binders basically meet these requirements. They are made of magnesium oxide or hydroxide and magnesium chloride solution, which react to magnesium oxychlorides.

Extensive efforts have been made to develop methods for the systematic optimization of their properties. Nowadays, the materials can be tailored to the particular needs by changing the properties of the binder, the composition of the mixing solution and by adding fillers, aggregates, and additives. In addition, the plant technology was developed in order to be able to produce large quantities of magnesia binders in a suitable quality and to transport the mixtures over long distances. Constitutive models describe the development of solid material properties and the heat evolution and can be used to demonstrate safety. This way, magnesia binders were also qualified for the application in the field of radioactive waste disposal. Examples are their use in the Asse II salt mine and the Morsleben radioactive waste repository.

BASICS OF THE MATERIAL SYSTEM

The material system of magnesia binders is based on the reaction of caustic magnesium oxide powder and/or magnesium hydroxide. These binders are mixed with concentrated magnesium chloride solutions. In this case, the hardening of the mixtures results from the crystallization of magnesium oxychlorides (MOC). These chemical compounds consist of magnesium hydroxide, magnesium chloride, and crystal water. Magnesium oxychlorides (magnesium chloride hydroxides) are named after the molar ratio of their constituents. At ambient temperature, the so-called 3-1-8 phase or the 5-1-8 phase are formed. Equations (1) and (2) illustrate the reactions of magnesium oxide:

$$3\ MgO_{(s)} + MgCl_{2(aq)} + 11\ H_2O_{aq} \rightarrow 3\ Mg(OH)_2 \cdot MgCl_2 \cdot 8\ H_2O \text{ (3-1-8 MOC phase)} \quad (1)$$

$$5\ MgO_{(s)} + MgCl_{2(aq)} + 13\ H_2O_{aq} \rightarrow 5\ Mg(OH)_2 \cdot MgCl_2 \cdot 8\ H_2O \text{ (5-1-8 MOC phase)} \quad (2)$$

The metastable 5-1-8 phase is transformed into the thermodynamically stable 3-1-8 phase in contact with magnesium chloride solutions that occur in most salt formations, especially if they contain potash salts such as kieseritic hartsalt or carnallitite. In addition, high-temperature phases, which contain lower amounts of crystal water, are eventually converted into the 3-1-8 phase.

The amount of MOC phases depends on the amount of binder, the amount and concentration of the mixing solution, and the temperature (cf. e.g. Hengjing & Guan 2018, Karimi & Monshi 2012, Liu 2017). These dependencies are used to control the properties of the hardened materials. In addition, it is possible to optimize the material properties for the respective applications by adding reactive and inert fillers, aggregates, and additives such as hardening accelerators or superplasticizers. Accordingly, with regard to the grain size of the mixtures, concrete (Sorel concrete), mortar, grouts or fine-grained suspensions can be distinguished. Aggregate is usually used to lower the binder content and to limit the increase in temperature during curing, while ensuring flowability due to its low water demand. However, the possibility of adding aggregate decreases if smaller cavities are to be filled due to the requirement of a minimum ratio of the pore size or the crack width to the grain size. Accordingly, injection materials (grouts) are characterized by fine-grained particles and relatively high contents of mixing solution in order to guarantee a sufficient flowability.
Characteristic of the materials is the high viscosity of the mixing solution and, consequently, of the carrier liquid of the suspensions, a relatively high reaction heat of the binder system, and the solubility of the MOC phases in solutions with low magnesium

chloride content. This solubility is unproblematic when the materials are used in salt and in particular in potash mines, where highly saline solutions with magnesium chloride contents corresponding to the saturation with bischofite, carnallite, kainite, or polyhalite can occur. In this environment, the use of magnesia binder is advantageous, because the magnesium chloride solutions limit or avoid rock damages caused by dissolution or recrystallization processes. In a mineralogical and chemical sense, Magnesia binders are compatible with the host rock.

Additional advantages are the volume expansion during hardening or the development of a swelling pressure when the materials cannot expand. These processes improve the bonding to the salt rocks which is basically excellent. Magnesia binders can attain a high strength and stiffness. The development of the material properties can be mathematically described in dependence of the hardening time (equivalent age) and the heat development on the basis of constitutive models, as they are also used to predict the behavior of materials containing cement according to EN 197. Magnesia binders react with carbonate species. This carbonation opens up additional applications for this interesting type of building material. More information on magnesia binder can be found in literature. An overview of the material behavior and possible fields of application are given for example in Walling & Provis (2016).

FIELDS OF APPLICATION AND MATERIAL OPTIMIZATION

Originally, magnesia binders were used in the salt mining industry primarily as a component of drift and borehole seals. For the backfilling of large mine cavities salt, such as residues of the potash salt processing, was used. The reasons for this approach were the quality variations in the raw materials, which made the production of larger quantities difficult, and, in addition to cost aspects, the relatively short workability time (pot life) of the magnesia binder. In salt mines, the ambient temperatures are often unusually high. For this reason, the significant decrease in workability time with increasing temperature limited the applications of magnesia binders. In the meantime, however, extensive improvements in material quality and homogeneity have been achieved in coordination with the producers. In addition, the optimization of the formulations and the quality assurance measures as well as the considerable increase in the knowledge about the material behavior led to a considerable extension of the application spectrum of magnesia binder. So today, the manufacturability with standard equipment of the building material technology is guaranteed and extremely large pumping lengths are feasible.

Backfilling of cavities

Contrary to salt backfill that compacts over long time periods, magnesia binders can achieve high stabilization effects in the short term. This is of particular importance when high degrees of excavation have led to damage of the host rock. Such situations are present in some areas of the Asse II mine as a result of intensive rock salt and potash extraction. Consequently, according to the current state, more than 350,000 m³ of cavities have been backfilled with Sorel concrete. The basic formulation used is described in Table 1. According to the ratio of the magnesium content of the binder to the Mg content of the mixing solution, the concrete is a 3-1-8 formulation.

Table 1. Composition of Sorel concrete A1. $Mg_S/Mg_{aq.}$ ratio = 3.0 – 3.5.

Components	**[wt.-%]**	**[kg/m³]**
Magnesium oxide	11.3	218
Crushed salt (dry)	63.7	1,237
$MgCl_2$ solution	25.0	485

According to the composition of the 3-1-8 phase, 1 kg of MgO can bind around 2.4 kg solution (cf. Eq. (1)). In comparison, 1 kg of Portland cement clinker has only a binding capacity of 0.25 kg of water. These values illustrate that the amount of solution decreases sharply during hardening, and most magnesia binders are characterized by a low pore space saturation. The pores are mainly filled with gas, and the hardened materials can compact when compressive loads occur. Due to this fact, a requirement to limit the volume compaction of the backfill material has been defined. However, recipe varieties that have higher porosities and thus a higher compaction capacity can be used in individual areas of the salt mine as a so-called residual cavity filling.

As a result of the compaction of the salt backfill, which occurs mainly due to its own weight, cavities occurred at the roof of the Asse II mine chambers. In order to limit the convergence of the host rock, these roof clefts have also been backfilled with Sorel concrete.

Drift seal construction including rock grouting

Another essential element of the backfilling and sealing concept of the Asse II salt mine are drift seals (“flow barriers”). Their basic construction concept consists of a core seal fixed by abutments and supporting backfill on both sides. The higher-permeable excavation damaged zones (EDZs), which form in all types of rock as a consequence of the excavation of cavities, are removed as far as possible with boom-mounted cutting heads. To impede fluid flow, the construction material has to have a low permeability and a good bonding to the host rock. In order to achieve short-term pressure

build-up at the drift contours, the concrete has to have sufficient mechanical strength and stiffness. Similar to the backfilling material, it has to be at least constant in volume. So far, 32 flow barriers have been installed. According to the current plan, 21 flow barriers still need to be constructed.

Current planning deals with the construction of a drift seal made of magnesia binder in the Morsleben repository for radioactive waste. Due to the extensive and positive experience gained during the construction of flow barriers in the Asse II mine, it was decided to realize a similar design in the Morsleben repository. Nevertheless, adjustments are required, because the structure in Morsleben is to be built in anhydrite rock, which converges in much slower than rock salt.

Due to the fact that crack systems in the host rock may reduce the flow resistance of seals, injections are an integral part of many closure concepts. To achieve a high degree of filling and thus sealing, injection materials with decreasing particle sizes should be used with decreasing crack width. Moreover, finer materials should have a lower viscosity as a result of the frictional forces during the flow process. This results in an increase in the amount of mixing solution and/or the use of superplasticizers. In accordance with these principles, a series of injection materials has been developed. Table 2 shows the composition of an ultrafine mixture. The solids are supplied as a premix.

Table 2. Composition of sealing material MFBBa-17/3/30.

Components	**[wt.%]**	**[kg/m³]**
Magnesium oxide	17.0	334
Magnesium hydroxide	3.0	59
Barite	30.0	589
$MgCl_2$ solution	50.0	981

With regard to the implementation of injections, a great advantage of magnesia binders is that these materials can be used in connection with water glasses (sodium silicate solutions) and with the newly developed material group of the water glass-magnesium oxide mixtures.

Borehole seals

Because of their long lengths, boreholes could connect cracks or dilatant rock zones in the host rock and could act as flow paths that are bypassing seals. As a result, their sealing is of particular importance. To meet the requirements, numerous recipes have been developed and tested. A proven recipe is described in Table 3. Figure 1 shows the mixture and Figure 2 shows the related quality assurance measures.

Table 3. Composition of the sealing material IM-Asse-1. $Mg_S/Mg_{aq.}$ ratio = 3.2 – 3.5. IM is the abbreviation for the German word “Injektionsmörtel” (injection grout).

Components	**[wt.%]**	**[kg/m³]**
Magnesium oxide	17.4	322
Crushed salt	44.6	826
$MgCl_2$ solution	38.0	704

Figure 1. Sealing material IM-Asse-1 in a storage tank with agitator.

Figure 2. Quality assurance measures of borehole sealing materials.

However, due to the type of magnesium oxide used, large volume boreholes cannot be sealed with this recipe. Consequently, a new recipe was developed based on established injection material (Table 4, Figure 3). The pot life was increased significantly by changing the type of the magnesium oxide binder and by optimizing its calcination process in consultation with the producer. The second part of the work focused on the adaptation of the material properties by adjusting the proportions of the components. Table 3 shows the composition of the resulting recipe. After a sealing measure, which was successfully carried out in the Gorleben salt mine, it was decided to use this mixture for sealing

boreholes in the Asse II salt mine. For a first sealing measure at this site, the material was mixed above ground and transported in tanks to the job site on the 700-m-level. This procedure was a first for high-quality magnesia binders.

Table 4. Composition of the sealing material ETO-I.

Components	**[wt.%]**	**[kg/m³]**
Magnesium oxide	23.0	488
Crushed salt	15.0	318
Barite	25.0	531
$MgCl_2$ solution	37.0	786

Figure 3. Sealing material ETO-I flowing into the tank of the filling pump.

The workability time of magnesia binder is significantly reduced with increasing temperature. This situation may require special measures, such as modifications of the recipe, of the mixing technique or a cooling of the raw materials and/or the material mixture. However, cooling of magnesia binders has not been state-of-the-art. For this reason, different approaches were examined and evaluated. It was decided to cool the raw materials down to a temperature below zero degrees Celsius due to the fact that no solid salt precipitate at this temperature in highly concentrated magnesium chloride solutions. The decrease in fluidity is limited and is caused by the increase in viscosity of the mixing solution, but not by an increase in the solids content.

Additional applications

Organic substances can degrade. Products of this process are carbon dioxide, HCO_3^-, and CO_3^{2-}. In a repository, these phases could increase the concentration of dissolved radionuclides, for example, as a result of an increase in the pH value. It has long been known of magnesia binders that their binder and their reaction products carbonate relatively quickly. This property is used to fix the carbonate phases and consequently to reduce the mobility of radionuclides. This way, magnesia binder can be used to ensure a favorable chemical environment in repositories.

ACKNOWLEDGEMENTS

The development of the magnesia binders up to operational readiness was supported by colleagues from BGE TECHNOLOGY GmbH and BGE (Bundesgesellschaft für Endlagerung mbH). BGE is the operator of the Gorleben salt mine and the German radioactive waste repositories. Furthermore, many employees were involved in the implementation of the construction measures at the locations of the BGE.

REFERENCES

Polster, M.; Engelhardt, H.-J. & Heydorn, M. (2006) Development of a constitutive law for modeling the hydration of magnesia binder 16th Int. Conf. On Building Materials, 20th-23th September 2006, Bauhaus-University Weimar, p. 0925–0932.

Engelhardt, H.-J.; Meyer, Th.; Schmidt, H.; Heydorn, M. & Weber, J. (2018) Injection Processes for Rock Salt and Salt Backfill – Tried and Tested Materials and New Developments. Mining Report Glückauf, 154 (4): 298-305.

Liu, Z.; Balonis, M.; Huang, J.; Sha, A. & Sant G. (2017) The influence of composition and temperature on hydrated phase assemblages in magnesium oxychloride cements. J. Am. Ceram. Soc.: 1-16.

Karimi, Y. & Monshi, A. (2012) Investigations on the mechanical and hydration properties of sorel cement by changing the concentration of magnesium chloride. J. Ceram. Process. Res., 13 (6): 725-729.

Köster, R.; Kretschmer, I.; Engelhardt, H.-J.; Hayart, M. & Snihotta, M. (2019) Experience and work steps in filling exploratory drillings in the former exploratory mine Gorleben and in the Asse II mine. 21. Drilling and Blasting Technology Colloquium, Technical University Clausthal, 30.-31. January 2019.

Hengjing, B.A. & Guan, H. (2018) Influence of $MgO/MgCl_2$ Molar Ratio on Phase Stability of Magnesium Oxychloride Cement. Journal of Wuhan University of Technology-Mater Sci. Ed., 24 (3): 476-481.

Walling, S.A. & Provis, J.L. (2016) Magnesia-Based Cements: A Journey of 150 Years, and Cements for the Future? Chem. Rev, 116 (7): 4170-4204.

39th Cement and Concrete Science Conference
9-10th September 2019
University of Bath
Paper Number 062

Statistical Data Classification for the Optimised Synthesis of MonoHydroCalcite (MHC)

M. Ara Carballo-Meilan, L. McDonald, M.S. Imbabi
School of Engineering, University of Aberdeen, King's College, Aberdeen AB24 3UE

F.P. Glasser
Founding Director, Chairman and CSO, Carbon Capture Machine (UK)

ABSTRACT

A novel carbon capture and conversion process is under investigation by the authors. In this process, flue gas CO_2 is dissolved into slightly alkaline water that, faced against brines from connate formation waters, produced waters, and waters from a range of industrial processes, selectively precipitates Ca and other ions into high purity carbonate minerals that have useful properties and commercial value. The effect of experimental parameters such as additives like magnesium ions, concentration, pH, temperature, CO_3^{2-}/Ca^{2+} molar ratio, configuration of the feed, mixing mode and contact time on the crystal size, polymorphism and morphology of $CaCO_3$ is well-known. The authors chart new ground in their investigation of the impact that the aforementioned variables have on polymorphism. A literature search was to identify studies related to the synthesis of different polymorphs of $CaCO_3$ was combined with network analysis to rank the publications using network centrality measures, to create a dataset for further statistical analysis. Betweenness centrality was the metric adopted to prioritize the inclusion of information in the dataset. The raw dataset comprised of 37 attributes and a total of 591 experiments. The scope of the study has been limited to the spontaneous precipitation method and the synthesis of single form amorphous calcium carbonate (ACC), calcite, monohydrocalcite (MHC) and its mixtures. This was experimentally investigated, and the results from synthesis of MHC reported herein provide first confirmation of viability of the approach

1. INTRODUCTION

The crystallization of calcium carbonate ($CaCO_3$) polymorphs from the reaction between calcium and carbonate ions has been much studied. Despite the apparent simplicity of this reaction, the simultaneous and rapid occurrence of nucleation, crystal growth and other processes such as agglomeration during precipitation remains a challenge for control of the final properties of the solid, including polymorphism, in an industrial process still remains difficult. Interest in $CaCO_3$ research traverses many disciplines; $CaCO_3$ has many interesting characteristics that make it suitable for a broad range of applications. The effect of experimental parameters such as impurity ions like magnesium ion, or concentration, pH, temperature, CO_3^{2-}/Ca^{2+} molar ratio, configuration of the feed, mixing mode and contact time on the crystal size, polymorphism and morphology of $CaCO_3$ is wellknown but has not been quantified. Typically, a researcher would select subsets of experimental conditions from the variables that are known to affect more the outcome and then carry out further experimentation in the laboratory to verify some hypothesis. This decision is mainly based on literature searchers conducted by the researcher and his or her previous professional experience.

A decision tree (DT) is a supervised learning algorithm used in data mining to classify cases into categories. DTs are able to solve a wide array of classification problems in many different fields such as pharmaceutical manufacturing process (Gams et al. 2014), modelling building energy demand (Yu et al. 2010), weather forecast (Sá et al. 2016), diagnosis of diseases (Karegowda, Manjunath, and Jayaram 2010), detection of forest fires (Stojanova et al. 2006), agriculture (Cunningham and Holmes 1991), finance (Olson, Delen, and Meng 2012), computer vision and many more (Ali et al. 2012). A network analysis uses graph theory concepts to unravel relationships (links) between researchers or papers (nodes) within a field (network). In this context, the role of a paper within the network is determined using centrality measurements such as betweenness centrality, closeness centrality and degree centrality; and its importance acquires a multidimensional view, having different meanings based on the chosen metric.

In the present work, an alternative approach for the determination of an optimal set of experimental conditions during precipitation analysis was developed. Initially, relevant research papers in the field of the precipitation of calcium carbonate were compiled using network analysis. Betweenness centrality was the metric adopted to prioritize the inclusion of information in the dataset. After selecting publications, their experimental conditions

were compiled and analysed using decisionmodelling techniques. The idea was to describe under which experimental conditions a researcher is more likely to find a particular polymorph after the reactive crystallization process. Furthermore, the DT was as well used to indicate which of those parameters are more relevant for the classification, and therefore able to play a greater role during precipitation. Then, the If-Then decision rules obtained from several DT algorithms were applied to assist precipitation in the laboratory.

2. METHODOLOGY

The methodology consisted of three distinctive stages. Initially, a set of experiments were compiled from Scopus scientific database to form a raw dataset. This literature dataset was then statistically processed to extract an optimum array of experimental conditions for further study. The identification of rules from the data was done using a decision tree learner. The 4 major stages in the modelling process of a decision tree were data collection, data preparation, model construction and evaluation. Finally, scoping experiments were performed using an optimal set of experimental conditions highlighted by the statistical models. Literature search and data collection was conducted in February, 2019 and focused on empirical studies where several polymorphs of $CaCO_3$ were synthesized. This information was processed using bibliographic data analysis techniques to create a document co-citation matrix that in the case of MHC consisted of 11,961 papers. Sci2 Tool and Gephi were the software chosen for the bibliographic mapping study. Then, network centrality measures were calculated to rank those papers in importance. The initial experimental conditions and main results from papers with the highest betweenness centrality were stored in the dataset. Some examples of papers with high betweenness centrality included (Kimura and Koga 2011; Loste et al. 2003; Nishiyama, Munemoto, and Fukushi 2013). In this way, the total collected number of experiments was 591. Time constrains did not allow for the inclusion of a bigger dataset. These experiments were limited to the synthesis of ACC, calcite, MHC and its mixtures. The dataset contained 37 different attributes. The variables represented general characteristics of the final precipitate such as the identity of the polymorph, its molecular water content, its polymorphic abundance (%), the $CaCO_3$ precipitated yield (%), the amount of Mg (molar %) contained in the first phase and the mean particle size (nm). Additionally, the occurrence and non-occurrence of calcite, ACC, MHC and the presence and absence of mixtures were recorded as categorical variables. System attributes included the type of reactants, their initial molar concentrations, solution volumes and molar ratios, the type of synthetic route, reaction temperature, initial and final pH, sampling location, contact time (min), stirring speed (rpm), reactant order of addition, the mixing mode and the reactant rate of addition (ml/min).

Dataset preprocessing steps such as cleaning, data transformation, attribute selection and data exploration were used to analyse the initial dataset and prepare it for the subsequent modelling. The available dataset were split randomly in two groups named training/validation set and test set. Data exploration was performed over the training set. The training set was also used by the learning scheme to build the classifier, the validation set was used for parameter optimization and to compare and select the best classifier. However, the final true model performance was assessed using only the test set, which was set aside from the beginner of the modelling process. The training set was balanced (same proportion of each class) and the test set also had each class well represented. In the model construction the following algorithms were applied and compared: *J48 pruned*, *AdaBoost*, bagging, *Random Forest*, *OneR* and *ZeroR*. Pruning optimization, ensemble learning, cost sensitive evaluation of a binary classifier and attribute selection meta-learners were some of the strategies used in this work to improve the decision tree classification performance. Waikato analysis for knowledge environment (Weka version 3.8.1) was used as data mining software to assist the model construction and evaluation process (Hall et al. 2009). The performance of the studied classifiers was calculated using both *Acc* (accuracy or percent of correctly classified instances) and *AUC* (Area under the ROC curve) as a combined measure of the overall quality (Canada and Nadeau 2001; Kuncheva, del Rio Vilas, and Rodríguez 2007). Differences in *AUC* and *Acc* among classifiers were determined using stratified 10x10-fold cross validation in the Weka Experimenter and the corrected paired t-test statistic with 95% confidence level (two tailed). This corresponded to a total of 100 experimental runs per dataset and classifier. Finally, a decision list was extracted from the decision trees and interpreted in the context of a precipitation experiment. The synthesis of ACC took place in took place in a 2 L borosilicate glass reactor at a fixed temperature of 19 °C. The carbonate solution (1 M, 0.8 L, pH = 9.1) was prepared using a sodium carbonate/bicarbonate mixture with a molar ratio CO_3^{2-}:HCO_3^- of 1:4 (20 % CO_3^{2-}). The salt solution (0.582 M, 0.8 L, pH = 8.2) was prepared using a $MgCl_2 \cdot 6H_2O$ (0.4 M) and $CaCl_2$ (0.182 M) mixture. The pH of the salt solution was raised using NaOH (1M) up to 9.1. Both, carbonate and salt solutions were simultaneously added to the reactor at a constant rate. Vigorous stirring was provided during the duration of the run. After a contact time of 10 min, the solids from the reactive suspension were quenched by vacuum filtration and washed with acetone several times. Then, they were immediately dried overnight in an oven at 25 °C. The product was stored in an air-tight container and kept in the desiccator until further analysis.

Characterization involved pH measurements with a Hanna Checker pH meter, polymorph identification using an X-ray diffractometer (XRD) and analysis the chemical composition of the precipitate with a PerkinElmer FT-IR spectrometer Spectrum Two™.

3. RESULTS & DISCUSSION

In the synthesis of ACC, the composition of the reactant solutions corresponded to the following molar ratios: CO_3/Ca = 5.5, CO_3/Mg = 2.5, Mg/Ca = 2.2, Mg content = 68.75%. The initial pH of both reactants was 9.1. At the end of the run, the pH of the suspension was 7.5. The filtered and dried solid appeared thick and gelatinous, suggesting amorphous phase (Sarkar and Mahapatra 2010). Under the given conditions and based on the decision tree model (not shown), the precipitation of ACC was expected and the occurrence of mixtures should not occur. Band assignment of ACC is described in Table 1. The strong absorption band around 30004000 cm^{-1} in Figure 1 corresponds to OH stretching

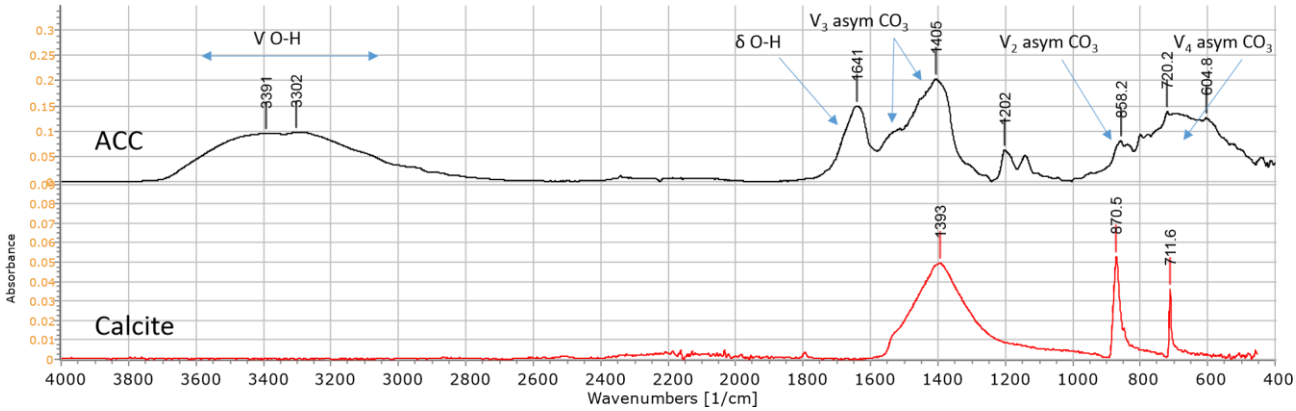

Figure 1 IR spectrum of ACC precipitate and calcite

vibration of hydrated water and it is characteristic in ACC, as opposite to the anhydrous forms that do not show this broad band (Brecevic and Nielsen 1989; Koga and Yamane 2008). The sharper band at 1650 cm^{-1} (O-H bending) corresponds as well to the structural water within ACC (Rodriguez-blanco, Shaw, and Benning 2011). Figure 1 also shows two carbonate absorption bands around 1450 cm^{-1}. This is a sign of asymmetry around the carbonates and is exclusive of ACC, MHC and vaterite (Addadi, Raz, and Weiner 2003). The peak at 712 cm^{-1} is broad, indicating no presence of calcite or aragonite. However, the symmetric stretch absorption around 1080 cm^{-1} is not present and instead there is a split peak at 1202 and 1141 cm^{-1} that remains unassigned. Some authors (Shen et al. 2006) observed a blue shift of the typical ν_1 absorption band of ACC (Table 1) and attributed to the dissolution of ACC particles. It was also reported that a peak at 1236 cm^{-1} in the IR spectra of ACC is likely due to the stretching vibrations of CO_3^{2-} in vaterite (Koga and Yamane 2008). The ACC peaks in the carbonate region are sharper than the corresponding peaks in more stable ACC (Addadi, Raz, and Weiner 2003), which could suggest less amorphousness and a transient stage rather than a stable ACC. The four characteristic peaks in the IR spectra of calcite are 711.6, 870.5, 1393 and 1796 cm^{-1}. The peaks are very sharp characteristic of crystalline polymorphs and the spectrum is included for comparison purposes.

Table 1 IR absorption characteristic peaks of carbonate ions in ACC

Characteristic Peaks	Description	Ref.
Broad peak at 1080, 1088 cm^{-1}	Symmetric stretch in non-centrosymmetric structures (ν_1)	(Addadi, Raz, and Weiner 2003)
1420 and 1474 cm^{-1} 1384 and 1472 cm-1	Split peak of the asymmetric stretch of CO_3^- (ν_3)	(Addadi, Raz, and Weiner 2003) (Shen et al. 2006)
Broad absorption at 866, 863, 860 cm-1	CO_3^- out-of-plane bending (ν_2)	(Addadi, Raz, and Weiner 2003; Shen et al. 2006) (Konrad et al. 2018)
Very broad absorption at 713 cm-1	CO_3^- in-plane bending (ν_4)	(Addadi, Raz, and Weiner 2003)

The sample appears to be non-crystalline by X-ray powder diffraction (**Figure 2**). No distinguished reflections characteristics of a crystalline $CaCO_3$ are observed. This is the typical XRD pattern of ACC described elsewhere (Blue et al. 2017; Koga and Yamane 2008; Shen et al. 2006). Results seems to suggest that amorphous calcium carbonate was synthesized with small vaterite impurities, indicating a non-stable state of the ACC product. The product was then transformed into MHC following a multistage synthesis route.

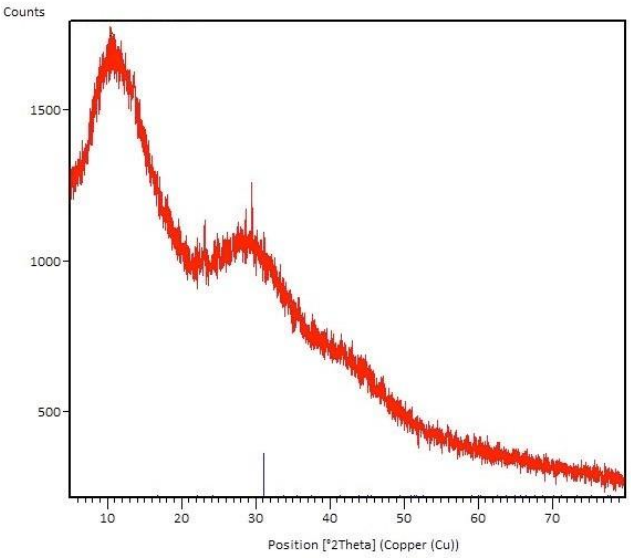

Figure 2 XRD spectrum of synthetic ACC.

4. CONCLUSIONS

A successful classification model was created using data from scientific publications. A number of if-then decision rules were created covering the occurrence and non-occurrence of several $CaCO_3$ forms (MHC, ACC, Calcite and mixtures). The decision rules were used to evaluate a scoping experiment aimed at the synthesis of amorphous $CaCO_3$ and MHC. Initial trials were successful in terms of product yield and purity. Wellperforming algorithms were used in this study, however the inclusion of more data in the training set is expected to lead to even better results.

ACKNOWLEDGEMENT

Funding for this research has been graciously provided by OMYA AG and Carbon Capture Machine (UK) Ltd.

REFERENCES

Addadi, Lia, Sefi Raz, and Steve Weiner. 2003. “Taking Advantage of Disorder: Amorphous Calcium Carbonate and Its Roles in Biomineralization.” *Advanced Materials* 15(12): 959–70.

Ali, J, R Khan, N Ahmad, and I Maqsood. 2012. “Random Forests and Decision Trees.” *IJCSI*

International Journal of Computer Science Issues 9(5): 272–78.
Blue, C. R. et al. 2017. “Chemical and Physical Controls on the Transformation of Amorphous Calcium Carbonate into Crystalline CaCO3 Polymorphs.” *Geochimica et Cosmochimica Acta* 196: 179–96.
Brecevic, Ljerka, and Arne Erik Nielsen. 1989. “Solubility of Amorphous Calcium Carbonate.” *Journal of Crystal Growth 98* 98: 504–10.
Canada, Health, and Claude Nadeau. 2001. “Inference for the Generalization Error.” *Health (San Francisco)* (514): 1–49.
Cunningham, Sally Jo, and Geoffrey Holmes. 1991. “Developing Innovative Applications in Agriculture Using Data Mining.” *The proceedings of the*: 12.
Gams, Matjaž et al. 2014. “Integrating Artificial and Human Intelligence into Tablet Production Process.” *AAPS PharmSciTech* 15(6): 1447– 53.
Hall, Mike et al. 2009. “The WEKA Data Mining Software: An Update.” *SIGKDD Explorations* 11(1).
Karegowda, Asha Gowda, A S Manjunath, and M A Jayaram. 2010. “Comparative Study of Attribute Selection Using Gain Ratio and Correlation Based Feature Selection.” *International Journal of Information Technology and Knowledge Management* 2(2): 271–77.
Kimura, Tomoyasu, and Nobuyoshi Koga. 2011. “Monohydrocalcite in Comparison with Hydrated Amorphous Calcium Carbonate: Precipitation Condition and Thermal Behavior.” *Crystal Growth and Design* 11(9): 3877–84.
Koga, N, and Y Yamane. 2008. “Thermal Behaviors of Amorphous Calcium Carbonates Prepared in Aqueous and Ethanol Media.” *Journal of Thermal Analysis and Calorimetry* 94(2): 379–87.
Konrad, Florian et al. 2018. “Influence of Aqueous Mg Concentration on the Transformation of Amorphous Calcium Carbonate.” *Journal of Crystal Growth* 498(April): 381–90.
Kuncheva, Ludmila I., Victor J. del Rio Vilas, and Juan J. Rodríguez. 2007. “Diagnosing Scrapie in Sheep: A Classification Experiment.” *Computers in Biology and Medicine* 37(8): 1194–1202.
Loste, Eva, Rory M Wilson, Ram Seshadri, and Fiona C Meldrum. 2003. “The Role of Magnesium in Stabilising Amorphous Calcium Carbonate and Controlling Calcite Morphologies.” *Journal of Crystal Growth* 254(1–2): 206–18.
Nishiyama, Risa, Takashi Munemoto, and Keisuke Fukushi. 2013. “Formation Condition of Monohydrocalcite from CaCl2 – MgCl2 – Na2CO3 Solutions.” 100: 217–31.
Olson, David L., Dursun Delen, and Yanyan Meng. 2012. “Comparative Analysis of Data Mining Methods for Bankruptcy Prediction.” *Decision Support Systems* 52(2): 464–73.
Rodriguez-blanco, Juan Diego, Samuel Shaw, and Liane G Benning. 2011. “The Kinetics and Mechanisms of Amorphous Calcium Carbonate (ACC) Crystallization to Calcite, via Vaterite.” *Nanoscale* 3: 265–71.
Sá, J a S et al. 2016. “Lightning Forecast Using Data Mining Techniques On Hourly Evolution Of The Convective Available Potential Energy.” In , 1–5.
Sarkar, Arpita, and Samiran Mahapatra. 2010. “Synthesis of All Crystalline Phases of Anhydrous Calcium Carbonate.” *Crystal Growth and Design* 10(5): 2129–35.
Shen, Qiang et al. 2006. “Properties of Amorphous Calcium Carbonate and the Template Action of Vaterite Spheres.” *Journal of Physical Chemistry B* 110(7): 2994–3000.
Stojanova, Daniela et al. 2006. “Learning to Predict Forest Fires.” *Knowledge Creation Diffusion Utilization* 9(14): 255–58.
Yu, Zhun, Fariborz Haghighat, Benjamin C M Fung, and Hiroshi Yoshino. 2010. “A Decision Tree Method for Building Energy Demand Modeling.” *Energy and Buildings* 42(10): 1637–46.

39th Cement and Concrete Science Conference
9-10th September 2019
University of Bath

Paper Number 063

A Preliminary Investigation of the Rheology of Precipitated Calcium Carbonate Admixture (PCC-A) Portland Cement Blends

L. McDonald, M. Ara Carballo-Meilan, M. S. Imbabi
School of Engineering, University of Aberdeen, King's College, Aberdeen AB24 3UE

F. P. Glasser
Founding Director, Chairman and CSO, Carbon Capture Machine (UK)

ABSTRACT
A new precipitated calcium carbonate Portland cement additive (PCC-A), has shown interesting results in preliminary rheology tests, namely its changing resistance to shear stress of the cement paste as PCC-A grain size is varied. When very fine particles (<1 µm) are blended with Portland cement, the workability - the resistance of the cement paste to shear stress - displays an inverse trend to that of Portland-limestone cements whereas the workability of particles in the range between 1-10 µm is comparable in workability to Portland-limestone cement at high water-cement ratios (w/c) and becomes less workable than PLC at lower w/c. This study aims to determine the rheological behaviour of PCC-A blended Portland cements with two PCC-A grain sizes & varied water/cement ratios and to determine the reasons for the observed difference in rheological behaviour of PCC-A & limestone blended Portland cements. Rheological properties are tested using a rotational rheometer with a concentric cone spindle to induce shear in hydrated cement paste samples containing varying amounts of PCC-A, grain sizes and water-cement ratios. The results show that the optimum PCC-A content to achieve the greatest level of workability is 5% for nano-PCC and 15% formicro-PCC.

1. INTRODUCTION

The rheological properties of fresh cement pastes are important define the flow behavior of cementbased materials as well as insight into their chemical properties (Papo *et al*., 2010). As cement-based materials are often used in applications where fluidity of the mix is important, for example in casting concrete slabs and where pumping is required, e.g. in oil wells and multistorey buildings, understanding the rheology of the cement-based material is essential.

Limestone has been used as an SCM due to its low environmental cost, production cost, filler effects and can improve workability (Detwiler and Tennis, 1996). The increase in workability of PLC makes it suitable for producing self-leveling concretes and mortars. Limestone used in cement is composed of at least 70% calcium carbonate (BS EN 197-1, 2011). By substituting limestone additives with a precipitated calcium carbonate additive (PCC-A), the environmental cost can be further reduced and the effects on workability vary with quantity of PCC-A while providing a cement with higher compressive strength (McDonald *et al.,* 2019).

The inclusion of PCC-A to Portland cement leads to a significant of the carbon emissions of cement due to it being manufactured from CO_2. The reduction can be calculated from the mass fractions of the PCC-A and OPC in the blend multiplied by their respective CO_2 emissions in producing 1 tonne, which is between -150 to -300 $kgCO_2$/tonne for PCC-A and 950 $kgCO_2$/tonne for OPC (Boesch and Hellweg, 2010). The optimum PCC-A content, and hence CO_2 reduction, to achieve maximum compressive strength for two PCC-A grain sizes is shown in Figure 1, observed after 28 days of curing in a water bath at ambient temperature. Nano sized PCC-A (median grain size 500 nm) provides the greatest benefit to strength at 11.8% PCC-A, an increase of 14%. Micro-scale PCC-A (median grain size 7 µm) provides the greatest increase in strength at lower PCC-A content than nano-PCC blends at 6.8%.

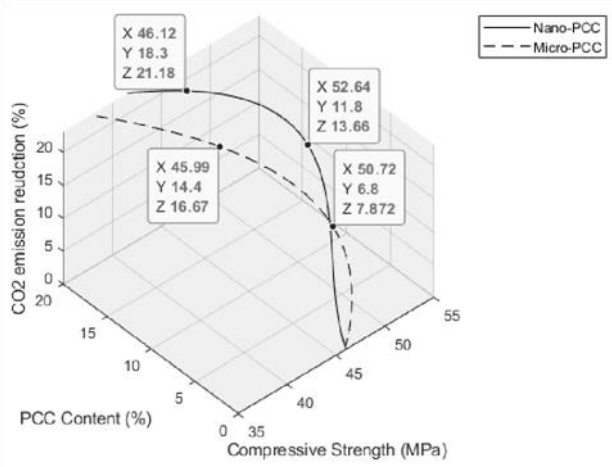

Figure 1. Optimum PCC-A content to acheive the highest strength and the corresponding CO_2 emission reduction, strength tested at 28 days with 0.5 w/c.

The reduction in CO_2 emissions of a nano-PCC and micro-PCC with a strength similar to that of OPC (46 MPa) are 21.18% and 7.87% respectively. The consequence of the increased strength is that the workability of the pastes decreases in blends with nano-PCC.

This paper aims to provide a preliminary understanding of the rheology of PCC-A Portland Cements and how they compare with OPC and PLC.

2. METHODS AND MATERIALS

In this investigation, two PCC-As with different grain sizes were used, one very fine nano-scale PCC (<1 µm, median size 500 nm) and the other a fine-grained micro-scale PCC (1-10 µm, median size 7 µm). Both PCC-As were rhombohedral calcite with trace amounts of halite (<0.2% by weight) from the production process.

The primary cement used was a CEM I ordinary Portland cement (OPC), kindly provided by Hanson Cement. The OPC was blended with 1 to 20% PCC by weight before hydration. A CEM II Portland-limestone cement (PLC) containing 18% calcite has also been used for comparison with PCC-blended cements.

A range of w/c were used in the test ranging from 0.3 to 0.5. Cement blends were mixed with the water and hand mixed for 90 seconds before being transferred to a 40mm diameter sample pot. The sample pot was connected to a rheometer which was fitted with a 25mm diameter coaxial cylinder spindle. The cement blend was subject to a preshear at a strain rate of 120 s^{-1} for 60 seconds to ensure that each test began from the same state of destructuration (Nehdi and Rahman, 2004). After pre-shearing, the shear rate was continuously increased from 0 to 100 s^{-1} over 120 seconds after which the shear rate was maintained for 15 seconds before being reduced to 0 s^{-1} over 120 seconds (Figure 2. Progression of shear rate with time throughout duration of test procedure. As viscosity of a fluid is temperature dependent, the temperature throughout the test was monitored with a digital thermometer integrated within the rheometer and kept constant at 24°C.

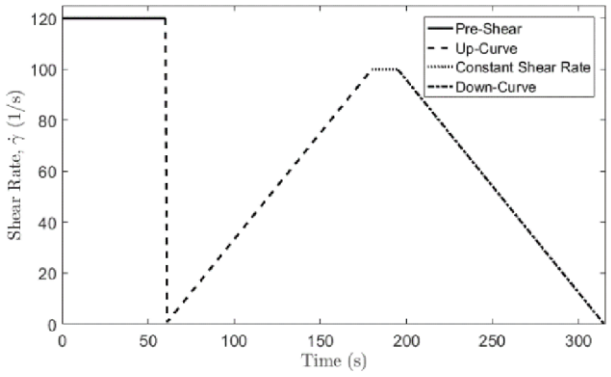

Figure 2. Progression of shear rate with time throughout duration of test procedure.

3. RESULTS AND DISCUSSION

The data collected during the test allowed for the shear stress to be calculated from the recorded torque of the rheometer and a parameter devised from the geometry of the spindle & sample pot, $k_!$= 10.796·10^3 m^{-3} such that $\tau = k_\tau \cdot T$, where τ is shear stress in Pa and T is torque in m·Nm. Plotting the measured shear stress against the shear rate provides a hysteresis curve indicative of thixotropic behaviour as the up-curve has a higher stress than the down-curve, as shown in Figure 3.

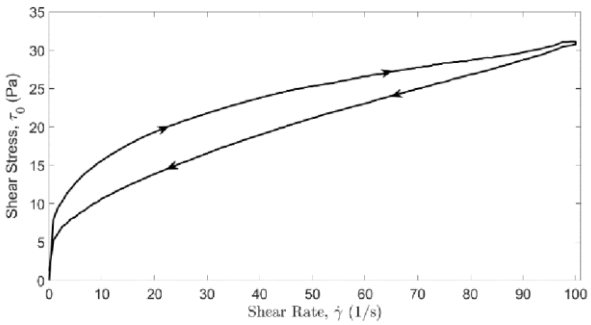

Figure 3. Hysteresis curve obtained for 10% nano-PCC blend at 0.5 w/c. Arrows indicate progression of test with time.

The yield stress, $\tau_!$, and the plastic viscosity, $\mu_!$, for each cement blend are determined from the down-curve as it tends to have a smoother profile than the up-curve. The Casson Rheological Model:

$$\sqrt{\tau} = \sqrt{\tau_!} + \mu_! \sqrt{\gamma}$$

was used to determine the yield stress and plastic viscosity of the blends as it provided a better fit for the shear rate range used during these tests than other models. An example of using the model to determine the parameters is shown in Figure 4. By plotting the square root of shear stress against the square root of shear rate, $\tau_!$, and $\mu_!$, can be calculated by taking the square of the gradient and intercept of the line of best fit, respectively.

By using the Casson Model, $\tau_!$ and $\mu_!$ have been determined for all tested blends. Due to the increasing stiffness of nano-PCC blends at 0.3 w/c, data could not be obtained beyond 5% nano-PCC.

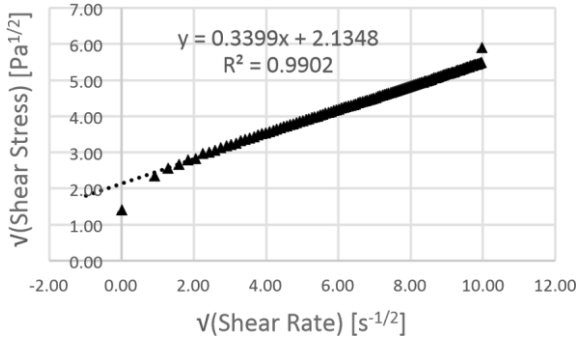

Figure 4. Using the Casson Model to determine the yield stress and plastic viscosity of 5% PCC blend, 0.4 w/c.

The yield stress for all blends tested are presented in Figure 5. It was found that at 0.5 w/c micro-PCC provides an increase in workability over OPC but not as much as PLC does, this trend occurs at 0.3 w/c with the workability of 15% micro-PCC being very similar to that of PLC. However, at 0.4 w/c the addition of micro-PCC provides a more workable mix than that of both OPC and PLC.

Nano-PCC blends exhibit a yield stress similar to that of OPC at 0.5 w/c for all grain sizes however, as the w/c is reduced higher quantities of nanoPCC greatly reduce the workability of the blend to the point where at 0.3 w/c the rheometer was unable to induce shear in the cement paste and no data could be obtained. The increased water demand of nano-PCC blends is likely due to the increased surface area of the PCC-A particles which are thought to provide nucleation points for CH precipitation as determined in simulations by Mohamed *et al*. (2015).

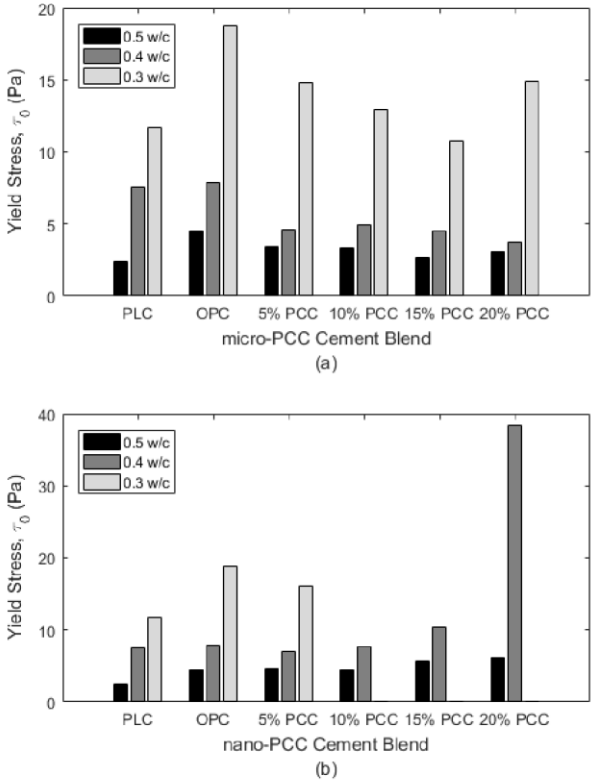

Figure 5. Yield stress calculated using the Casson Model for micro-PCC (a) and nano-PCC (b).

The plastic viscosity of the cement blends (Figure 6) was more consistent than the yield stress. With increasing PCC-A content, plastic viscosity increases and in almost all cases the plastic viscosity of PCC-A blends is higher than the comparative PLC and OPC pastes.

At 5% micro-PCC the plastic viscosity is lower than that of OPC and comparable to that of PLC. This indicates that the micro-PCC required to obtain the same workability as the PLC is significantly lower than the calcite content of the PLC. It should be noted that the compressive strength of PCC-A blended cements is greater than that of OPC between 5 and 20% PCC-A and significantly greater than that of PLC (McDonald *et al*., 2019).

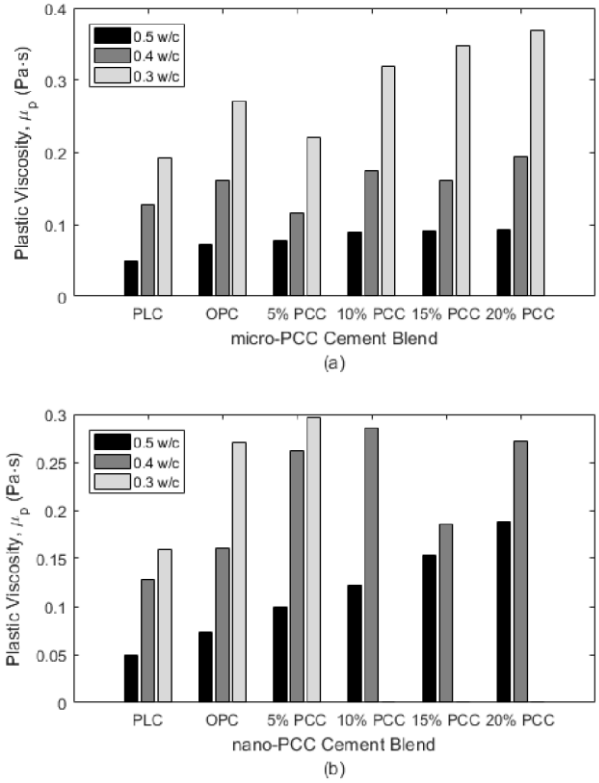

Figure 6. Plastic viscosity of micro-PCC (a) and nano-PCC (b) blends determined using the Casson Model.

4. CONCLUSIONS

- The inclusion of micro-PCC to Portland cement reduces the yield stress of the fresh cement paste. At low water-cement ratios the optimum quantity of micro-PCC for a workable mix is 15%.
- Nano-PCC blends however have an optimum content of 5% at low water-cement ratios. At higher nano-PCC content the workability of the mix greatly decreases and becomes entirely unworkable.
- The plastic viscosity of both nano- and microPCC blends increases with increasing PCC content.
- The decrease in workability of at high PCC-A contents is likely due to the small grain-size by increasing the surface area for which water is dispersed in the paste and provides a greater number of nucleation points for the formation of CH leading to rapider setting of the cement paste.

ACKNOWLEDGEMENT
Funding for this research has been graciously provided by Carbon Capture Machine (UK) Ltd.

REFERENCES

Detwiler, R.J., Tennis, P.D., 1996. The use of limestone in Portland cement: A state-of-the-art review. Portland Cement Association

Papo, A., Piani, L., Ceccon, L., Novelli, V., 2010. Flow behaviour of fresh very high strength Portland cement pastes. Particulate Science and Technology, 28:74-85

Nehdi, M., Rahman, M.-A., 2004. Estimating the rheological properties of cement pastes using various rheological models for different test geometry, gap and surface friction. Cement and Concrete Research, 34:1993-2007

BS EN 197-1, 2011. Cement. Composition, specifications and conformity criteria for common cements. British Standards Institution McDonald, L., Glasser, F.P., Imbabi, M.S., 2019.

A New, Carbon-Negative Precipitated Calcium Carbonate Admixture (PCC-A) for Low Carbon Portland Cements. Materials, 12(4):554

Mohamed, A.R., Elsalamawy, M., Ragab, M., 2015. Modelling the influence of limestone addition on cement hydration. Alexandria Engineering Journal, 54:1-5

Boesch, M.E., Hellweg, S., 2010. Identifying improvement potentials in cement production with life cycle analysis. Environmental Science Technology, 44:9143-9149.

39th Cement and Concrete Science Conference
9-10th September 2019
University of Bath
Paper Number 65

Modelling the Hydration of Cement-Glass Mixtures

M.V.A. Florea, G. Liu., H.J.H. Brouwers
Department of the Built Environment
Eindhoven University of Technology

ABSTRACT

Fine recycled glass powder has been previously investigated as a secondary cementitious material in cement mixtures. Up to 70% fine recycled waste glass was employed in mixtures with 0.3 water/binder ratio. A low Ca/Si C-S-H gel was observed in high volume recycled glass containing samples. Based on experimental observations from TGA, SEM and EDX, a hydration reaction model initially developed for OPC and slag-blended cements is modified for the incorporation of waste glass. The challenges of such an approach, particularly the hydration degree of fine glass and the role portlandite plays in the pozzolanic reaction, are discussed and evaluated.

1. INTRODUCTION

In recent years, the recycling ratio of waste glass has increased in many countries due to the concerns towards the protection of natural resources; for instance an increasing amount of the waste glass are collected from urban wastes and reused to produce containers like bottles and jars. However, some recycled glass fractions cannot be used in the manufacturing of new glass products, either because they are contaminated, or because some recycled glass pieces are too small to meet the manufacturing specifications. Such recovered glass is then used for producing non-container glass products. One ideal application for these glass fractions is to be used as concrete ingredients such as aggregates and supplementary cementitious material, because the amorphous glass has the potential to exhibit pozzolanic reactivity (Shayan and Xu, 2006) (Du and Tan, 2014).

Therefore, many studies investigated using fine waste glass powder to partly replace cement as supplementary cementitious materials. Glass fractions can exhibit higher pozzolanic activity than fly ash when the particles are fine enough (Liang and Poon, 2011) (Schwarz and N. Neithalath, 2008) (Bignozzi et al. 2015) (Zheng 2016).

Recent studies about influences of contamination in waste glass usually focused on heavy metal contaminated waste glass, such as glass from cathode ray tubes (CRT), where cement could be used to immobilize the heavy metal in CRT glass (Hui, Poon and Ling 2013) (Ling and Poon 2011). However, the waste glass fractions contaminated by organics (sugar, fibre) received less attention. This kind of waste glass usually combines with very fine particles and is mixed with organic matters, making it difficult to clean and recycle for re-producing new glass products. For the sustainable use of this kind of organic containing glass fractions, it is desirable to use such filter glass as building material. However, the organic contamination will influence the application of the waste glass fractions in concrete. The waste glass in this study is a filter glass powder, which is filtered out of the furnace while drying the glass fraction during the manufacturing of glass products. It has a very fine particle size and contains considerable amounts of organic matters such as fibres and saccharides from labels and glue. Saccharides could be absorbed on the surfaces of cement particles and hydration products, which inhibits the hydration process and hydration products growth (Juenger and Jennings 2002). The present study aims to perform a comprehensive evaluation and to have a better understanding of the influencing of filter glass as supplementary cementitious material on cement hydration, products and microstructure, providing some theoretical basis for its application.

2. MATERIALS AND METHODS

The cement applied in this study is CEM I 42.5N supplied by ENCI, Netherlands. The used glass powder is a filter glass which was filtered out in a glass drying furnace, provided by a glass recycling plant.

The filter glass powder after washing was used as references, they were washed by distilled water with the L/S 2 and 250 rpm for 24 hours. Then these two glass powders were milled, sieved and utilized as supplementary cementitious materials in present study. The specific surface area of milled filter glass powder is 0.65 m^2/g.

Different pastes were prepared with the water / binder ratio of 0.3, where cement was replaced by with 0%, 30%, 50% and 70% by mass by the filter glass (termed C0, C3, C5 and C7 respectively) or washed filter glass (termed CW3, CW5 and CW7). All details regarding methodology can be found in (Liu, Florea and Brouwers, 2018).

Table 1. Chemical composition of raw materials

Chemical composition	Filter glass (%)	Washed filter glass (%)	CEM I 42.5N (%)
Na_2O	11.4	11.5	/
MgO	1.42	1.39	1.55
Al_2O_3	2.74	2.577	3.44
SiO_2	66.9	68.3	14.4
SO_3	0.25	0.13	4.42
K_2O	0.84	0.79	0.45
CaO	14.2	13.6	69.2
TiO_2	0.19	0.14	0.38
Cr_2O_3	0.15	0.14	0.01
MnO	0.03	0.03	0.09
Fe_2O_3	0.95	0.78	3.85
ZnO	0.06	0.04	0.11
BaO	0.07	0.06	0.01
Cl	0.20	0.06	0.07

3. EXPERIMENTAL RESULTS

The thermogravimetric results of different mixtures are shown in Fig. 1. The TG and DTG curves of samples containing 70% filter glass and washed filter glass powder are presented in Fig. 1 (a). It can be seen that all samples present a significant mass loss from 40 °C to 105 °C. This mass loss is assigned to the physical bound water in mixtures. As the temperature increases, the mass loss is obviously increasing before 200 °C. After the evaporation of physically bound water, the C-S-H and AFm begin to lose the chemically bound water gradually at higher temperatures [53]. The following two significant mass losses are attributed to the decomposition of calcium hydroxide (400 °C-460 °C) and calcium carbonate (600 °C-700 °C). During the testing temperature range of 40 °C to 1000 °C, samples with waste glass powder show less total mass loss than the reference sample (C0). Additionally, the highest content of filter glass powder sample (C7) shows the least mass loss, which is also observed in washed filter glass containing samples. It is noticeable that washed filter glass samples show less total mass loss than the filter glass samples with the same replacing level after 28 days curing.

The calcium hydroxide content normalized by mass of cement are shown in Fig. 1 (b). The content of calcium hydroxide is calculated from the TG results by adding the amount of portlandite (recalculated from water loss between 400 and 460º C) and the amount recalculates from the CO_2 loss of calcite for each sample. Fig. 1 (b) shows the calcium hydroxide content (normalized by cement) after 28 days and 90 days curing in different samples. The addition of both filter glass and washed filter glass promotes the formation of calcium hydroxide. Filter glass powder containing samples, especially for high volume filter glass incorporation sample, present a slightly lower calcium hydroxide content after 28 days curing but higher after 90 days than samples containing washed filter glass. For the sample containing washed filter glass, calcium hydroxide consumption can be observed in all samples. Apparently, more calcium hydroxide is consumed in washed filter glass containing samples with the increasing of the replacement ratio compared with the sample containing filter glass powder. The lower calcium hydroxide consumption after 28 days and the delay of calcium hydroxide formation in samples with filter glass addition may indicate that the pozzolanic reaction of glass powder is partially influenced by the retardation effect of saccharides.

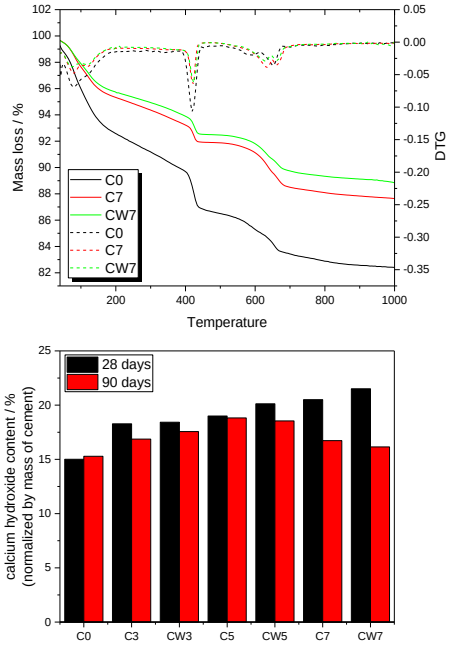

Figure 1. (a) TG/DTG data of C0 and C7 and CW7; (b) CH content of all samples from TG results

The SEM- EDX are used together to determine the micro-structure and chemical composition of hydration products of pastes containing filter glass powder and washed filter glass powder. The results are shown in Fig. 2. It can be observed that the plain cement paste (C0) shows a relatively dense microstructure. The hydration products ideally fill the space between the unreacted cement particles and show a homogeneous structure. The result of EDX obtained around the unreacted cement particle shows a Ca/Si ratio of 2.02.The filter glass and washed filter glass incorporation leads to a more porous structure at micro scale. As can be seen in Fig. 2 (b) and (c) that 30% filter glass (C3) and washed filter glass (CW3) samples shows more porosity than the plain sample, and EDX and SEM images with 8000 × exhibit that the glass particles around 10 μm are covered by the C-S-H gel with a low Ca/Si ratio. For example, Ca/Si with 1.09 and 1.67 are observed in C3 and CW3, respectively. At the same time, most of the glass particles around 10 μm in C7 show clean and smooth surface with a

Ca/Si with 0.14, which is due to the largely unreacted glass particles.

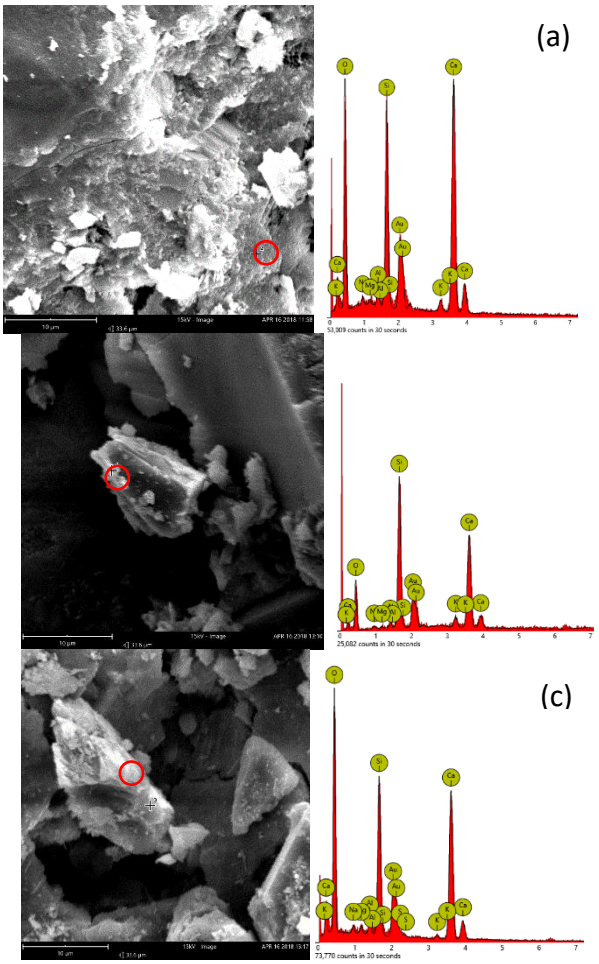

Figure 2. SEM images and EDX results: (a) plain sample C0 (b) 70% filter glass sample C7 (c) 70% washed filter glass sample CW7.

These may indicate that a limited pozzolanic reaction occurred on the surface of these glass particles, and the products from cement hydration fill the pores between glass particles with weak binding forces. The EDX result of the glass particles surface in sample C7 also presents high Si and O content, which can be referred to the raw glass phase, while the morphological image of sample containing 70% washed filter glass powder exhibits a rough surface of glass particle. The glass particles in CW7 are covered by the reaction products. The EDX result of the gel on the surface of glass particle shows a low Ca/Si of 0.93, which can be considered as the products from the pozzolanic reaction of glass powder.

Compared with the glass particles in high volume filter glass and washed filter glass containing samples, it is obviously that the washed filter glass particles show a clear sign of pozzolanic reaction. The glass particle could be dissolved in the alkaline environment and the silicate released from glass phase reacts with the calcium hydroxide from cement hydration. The filter glass powder contains organic matter and saccharides contamination, which poisons the surface of cement particle and the growth of calcium hydroxide. Consequently, the dissolution of glass particles is inhibited, which limits the pozzolanic reaction on the surface of glass particles.

4. HYDRATION MODELLING

In order to model the hydration of the cement-glass powder pastes, a hydration reaction model for ground granulated blast furnace slag (GGBS)-Portland cement blended pastes was adapted (Florea and Brouwers 2014) (Chen and Brouwers 2007). Similar to the GGBS, the glass is considered to be able to partly take place to the hydration reactions, with its own reaction degree. In a first stage, the glass is considered to contribute silica ions, which contribute to the formation of C-S-H with C/S ratios which lower with the increase of glass percentage, as detailed in the SEM/EDX discussion above. However, when comparing the estimated CH amounts with the ones measured by TG (Fig. 1), it was found that the model significantly underestimates the formed CH after 28 days. A degree of hydration of the cement was set at 0.65, according to the TG measurements for C0 (plain OPC paste). It can be observed in Fig. 1 (b) that the CH content of the pastes increases with the increase of glass substitution, which cannot be accounted for if OPC is considered to be the only calcium source. While for the 30% glass containing sample the increase in CH generation could be attributed to an increase in degree of hydration of OPC, for higher replacement ratios the change would still not be sufficient. Therefore, a second assumption is proposed: besides its contribution of silica to the formation of lower C/S C-S-H phases, alkalis and Ca ions are also considered to be made available from the glass dissolution.

For this scenario, a hydration degree of glass is needed (while in the first assumption, enough silica was assumed to be generated by the dissolution of glass for the measured C/S ratios). The degree of hydration of glass can be calculated from its silica contribution, at each replacement ratio.

The calculated degree of reaction varied with the replacement ratio as follows: 0.15 for 30% glass, 0.25 for 50% glass and 0.38 for 70% glass. A number of effects can be taken into account for this such a trend. In the case of lower glass contents, the OPC hydration products can coat the glass particles, making their dissolution slower or effectively stopping it in many cases. For a higher glass percentage, the continuous uptake of dissolved silica into the cement hydration products can promote the further dissolution of the glass. However, these assumptions need further experimental validation. It is worth mentioning that, when considering a glass degree of hydration of 0.30-0.35, intermediate between he calculated values for 50% and 70% glass replacement, the model accurately predicts the CH values obtained from TG, when the extra Ca ions available are

considered to form portlandite. However, Ca ions can also participate in the formation of other OPC hydration products, while Na ions can form Na-S-H phases. All these possibilities need further experimental tests. The final model needs to be validated with other glass compositions, as well as available data from literature.

5. CONCLUSIONS

This study aims to study and model the effects of the addition of waste glass to OPC pastes. Two types of waste glass (washed and unwashed) and 3 replacement ratios (30%, 50% and 70% by mass) were considered. It was found that the unwashed glass, due to its high content of saccharides, will significantly delay cement hydration and it will also not participate itself to the hydration reactions. In the case of washed glass powder, this effect is no longer observed. Therefore, the washed glass-containing samples were further used for modelling the hydration reactions of the blended pastes.

The modelling part suggested a reaction degree of the glass of around 0.3, and underlined the importance of taking into account not only the contribution of silica ions to the hydration reactions, but also of the additional released Ca ions. This study will continue in order to elucidate the following open questions:

The reactivity of the washed glass will be evaluated

The kinetics of reaction of the OPC in the presence of various amounts of waste glass will be studied

A more detailed evaluation of the hydration phases formed in each substituted paste will be performed

The role of the Na ions in the hydration reactions will be evaluated and modelled

The consumption of CH between 28 and 91 days of hydration will be incorporated into the model through a pozzolanic reaction of the glass particles

Various compositions of OPC and glass will be used to further refine the model

Literature data will be collected and employed for the validation of the model.

ACKNOLEDGEMENTS

This research was carried out under the funding of China Scholarship Council and Eindhoven University of Technology. Furthermore, the authors wish to express their gratitude to the sponsors of the Building Materials research group at TU Eindhoven.

REFERENCES

Shayan, A., Xu, A., 2006. Performance of glass powder as a pozzolanic material in concrete: A field trial on concrete slabs. Cem. Concr. Res., 36(3):457–468.

Du, H., Tan, K. H., 2014. Waste Glass Powder as Cement Replacement in Concrete. J. Adv. Concr. Technol., 12(11):468–477.

Ling, T.C., Poon, C.S., 2011. Properties of architectural mortar prepared with recycled glass with different particle sizes. Mater. Des., 32(5):2675–2684.

Schwarz, N., Neithalath, N., 2008. Influence of a fine glass powder on cement hydration: Comparison to fly ash and modeling the degree of hydration, Cem. Concr. Res. 38(4):429–436..

Bignozzi, M.C., Saccani, A., Barbieri,L., Lancellotti, I. 2015. Glass waste as supplementary cementing materials: The effects of glass chemical composition, Cem. Concr. Compos., 55: 45–52.

Zheng, K., 2016. Pozzolanic reaction of glass powder and its role in controlling alkali-silica reaction. Cem. Concr. Compos., 67:30–38.

Hui, Z., Poon, C. S., Ling, T. C., 2013. Properties of mortar prepared with recycled cathode ray tube funnel glass sand at different mineral admixture. Constr. Build. Mater. 40:951–960.

Ling T. C., Poon, C. S., 2011. Utilization of recycled glass derived from cathode ray tube glass as fine aggregate in cement mortar. J. Hazard. Mater., 192 (2):451–456.

Juenger M.C.G., Jennings, H.M. 2002. New insights into the effects of sugar on the hydration and microstructure of cement pastes. Cem. Concr. Res., 32(3):393–399.

Liu, G., Florea, M.V.A., Brouwers, H.J.H., 2018. The hydration and microstructure characteristics of cement pastes with high volume organic-contaminated waste glass powder. Construction and Building Materials. 187:1177-1189.

Florea, M.V.A. & Brouwers, H.J.H., 2014. Modelling of chloride binding related to hydration products in slag-blended cements. Construction and Building Materials. 64:421-430.

Chen, W., Brouwers, H.J.H., 2007. The hydration of slag, part 2: reaction models for blended cement, Journal of Materials Science 42:444-464.

39th Cement and Concrete Science Conference
9-10th September 2019
University of Bath
Paper Number 066

How Anatase (TiO_2) affects the hydration of white Portland cement (wPC) and its effect on C-S-H nanostructure

Xiaohong Zhu, Ian G. Richardson, Phil Purnell
School of Civil Engineering, University of Leeds, Leeds, LS2 9JT

ABSTRACT

This study investigated the effect of the inert TiO_2 on the hydration and C-S-H nanostructure of wPC. Two TiO_2 replacement levels (30% and 60%) were selected and two types of active fillers (PFA and GGBS) were used for comparison in this study. The effects of these fillers on the hydration of wPC up to 91 days were evaluated through isothermal conduction calorimetry (ICC), TG-DSC and NMR. The C-S-H nanostructure changes due to the presence of TiO_2 were analysed using Richardson and Groves' model. The main findings are: the hydration of wPC was initially retarded for the first day due to the presence of TiO_2, whilst increased after 1 day. The hydration of belite significantly increased at later age as evidenced by NMR. Thus, the hydration degree of wPC increased due to the incorporation of TiO_2, which further slightly increased the MCL and slightly decreased Ca/Si ratio of C-S-H.

1. INTRODUCTION

TiO_2 is a "filler" that can be used in the cement system, which is proven to have certain effects on the hydration of cement (Chen, Kou et al. 2012, Lee 2012). Meanwhile, TiO_2 is also a photocatalytic material (Ohno, Sarukawa et al. 2002), which has a smog-abating property, can be used for the removal of NOx and as the self-cleaning/disinfection tiles (TOTO) or glass (Nippon Sheet Glass). The cement/TiO_2 composites (also named as photocatalytic cement) can be widely used as infrastructure applications for air pollution treatment. Due to these applications, there is an interest in study of how TiO_2 affects the hydration of its substrate. In this study, the hydration of wPC incorporated with TiO_2 was studied up to 91 d by using ICC, TG-DSC, and NMR. Two traditional supplementary cementitious materials (SCMs), PFA and GGBS, were used as a purpose of comparison.

2. EXPERIMENTAL DETAILS

The commercial white Portland cement (Hanson Castle, UK), anatase-type TiO_2 (Sigma-Aldrich, UK), PFA (Drax, UK) and GGBS (Francis flower, UK) were used in this study. The XRF analysis of their bulk oxide compositions is given in Table 1. The iron was hand-removed from PFA by using a magnet until limited particle could be attracted, which aimed to reduce the paramagnetic effect in NMR experiments.

A water/binder (w/b) ratio of 0.50 was used for all cement slurries. Two replacement levels (30% and 60%) for wPC by TiO_2 were selected. 30% PFA and 60% GGBS were used to replace wPC for comparison. The blended powders were pre-stirred for 5 min. All five cement pastes were hand-mixed for 2 min and cast into an 8 mL plastic tubes. After which, these tubes were sealed with Parafilm and put into a rotor for continuous rotation for 24 h at a speed of 9 r/min to avoid bleeding. The specimens were then cured in a water bath at 25 °C for specific testing ages (except the 5 h ones). The samples at certain ages were then crushed and hydration-stopping with Isopropanol (IPA), followed by drying in a vacuum desiccator. The treated samples were ground into fine powder for further TG-DSC and NMR experiments.

The ICC experiments were performed with a TAM-Air (8 channels) with an external mixing method. The pastes with 0.50 w/b ratio were put into a 20 mL plastic tube and shaken on an orbital shaker for 2 min before putting into the equipment. An analog quartz paste was used as a reference.TG-DSC experiments were recorded by a Stanton Redcroft Simultaneous Thermal Analyser STA 780 under N_2 atmosphere. The testing temperature ranged from room temperature to 1000 °C with a speed of 20 °C/min. The calcium hydroxide (CH) content (by residual mass) was determined by the tangent method (Richardson, Girão et al. 2016). NMR experiments were performed with a Bruker Avance III with a 9.4T WB magnet. The operating frequency was 74.49 MHz for ^{29}Si with a magic angle of 54.7°. The spectra were acquired with between 2048-4096 scans for wPC samples with an acquisition time of 0.04 ms. Other operation parameters include a spin rate of 6kHz, a pulse recycle delay of 40s, and a pulse duration of 5.5 µs The spectra were de-convoluted with Igor 5.0 with Voigt line shape (Richardson, Girão et al. 2016).

Table 1. Bulk oxide compositions of GGBS, PFA, and wPC (by mass %).

Composition	SiO_2	Al_2O_3	Fe_2O_3	MgO	CaO	Na_2O	K_2O	SO_3	$LOI_{900°C}$
GGBS	35.07	12.43	0.41	8.41	40.67	0.38	0.58	0.78	-0.15
Fe-Removed PFA	51.26	25.27	6.80	1.78	2.47	1.98	3.57	0.48	4.03
Residual PFA	49.02	24.38	10.92	1.59	2.43	1.42	3.46	0.47	4.07
wPC	24.49	2.09	0.30	0.59	68.08	0.25	0.09	1.95	0.95

3. RESULTS AND DISSCUSSIONS

3.1 Hydration and CH evaluations

Figures 1and 2 show the normalized heat release results of wPC containing TiO_2, PFA, and GGBS up to 80 h. The dashed line was calculated based on the heat release of neat wPC multiply by the wPC proportion in blended systems (i.e. 0.7 and 0.4), which was used for further comparison mentioned later. It is obvious to see that the heat release of slag-containing samples always has a higher value than any other system, which is due to the self-hydraulic property of GGBS (Richardson and Cabrera 2000). Nevertheless, the heat release of PFA or TiO_2 groups were initially lower than the reference group and then surpassed the neat wPC at around 20 h for PFA and 30 h for TiO_2 in both 30% and 60% replacement levels.

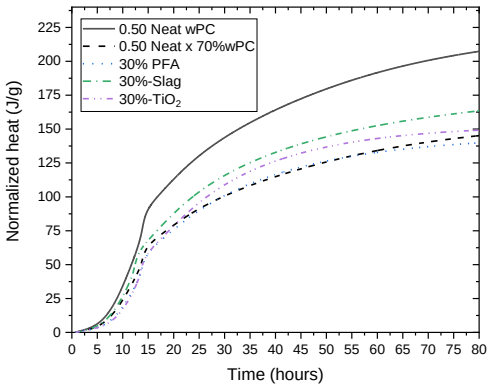

Figure 1. Hydration heat release of 30%TiO_2/PFA-70%wPC and neat wPC systems.

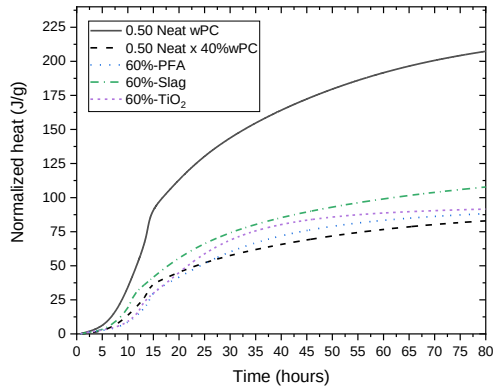

Figure 2. Hydration heat release of 60%TiO_2/Slag-40%wPC and wPC systems.

Figure 3 gives the CH content development of both 30% and 60% replacement level systems determined by TG-DSC analysis. There is no doubt that the CH content increased over hydration time. Similarly, the same ratios (i.e. 0.7 and 0.4) were also used to multiply by the CH in neat wPC for a purpose of comparison, which was denoted as CH^{exp} (Taylor, Richardson et al. 2010, Richardson, Girão et al. 2016). The CH contents in the blended system were denoted as CH^{act}. The ratios of CH^{act} to CH^{exp} were calculated for each blended system and plotted in Figure 4.

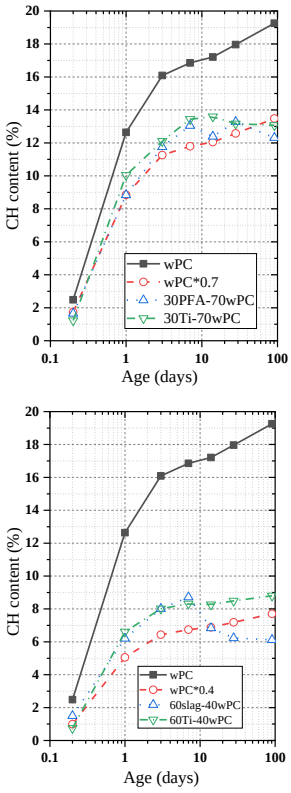

Figure 3. CH content evaluation of 30%TiO_2/PFA-70%wPC (left), 60%TiO_2/GGBS-40%wPC (right) and neat wPC systems.

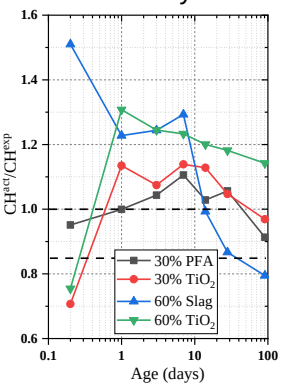

Figure 4. CH^{act}/CH^{exp} of different samples from TG-DSC results.

The ratios shown in Figure 4 clearly exhibit that the PFA or TiO_2 samples had a lower CH content when compared to neat wPC, which can be explained as initial retardation occurred in such systems. Whereas, the slag increases the CH content initially. These results are consistent with ICC results as shown in Figures 1 and 2. The initial retarder effect of PFA was also found and discussed by Richardson et. al (Richardson, Girão et al. 2016). However, the CH^{act}/CH^{exp} ratio rose at intermediate ages for TiO_2/PFA containing samples, which indicates that an acceleration happened during this period. As expected, the PFA and GGBS will consume the CH and CH^{act}/CH^{exp} ratios in these two systems gradually decreased to lower than 1. The changing ages for 30% PFA and 60% GGBS samples are around 40 d and 14 d, respectively. For TiO_2 samples, these values are higher than 1 (except one point), which reflected that TiO_2 is inert and will not consume CH in the cement system. In general, the hydration of wPC was initially retarded by TiO_2 but accelerated after around 1 day.

3.2 ^{29}Si NMR results of blended wPC

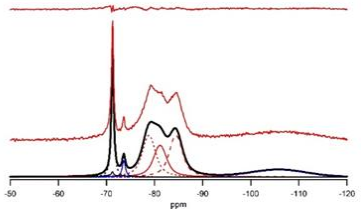

wPC-91d

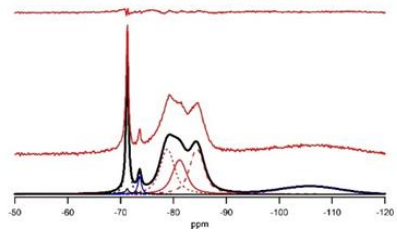

30PFA-70wPC-91d

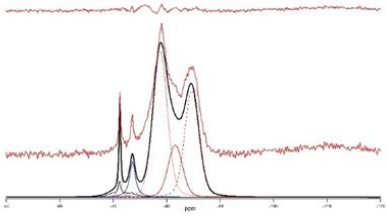

30Ti-70wPC-91d

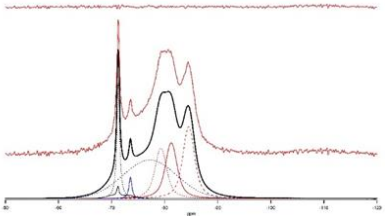

60Slag-40wPC-91d

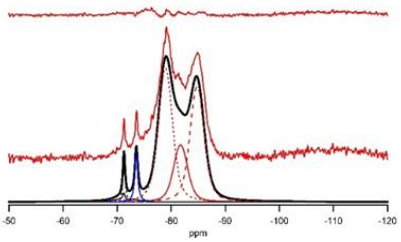

60Ti-40wPC-91d

Figure 5. NMR deconvolution examples for blended cement hydrated for 91 d.

The 91 d ^{29}Si NMR results shown in Figure 5 demonstrate the silicate groups' distribution in hydrated blended wPC. At the same replacement ratio as TiO_2, both PFA and GGBS containing samples showed a higher belite peak, which confirmed that the hydration degree of wPC at later age was increased by adding TiO_2. Meanwhile, the comparison of the same replacement ratio with PFA and GGBS samples also indicates that the acceleration effect of TiO_2 is not only limited to the relatively increased water to cement ratio.

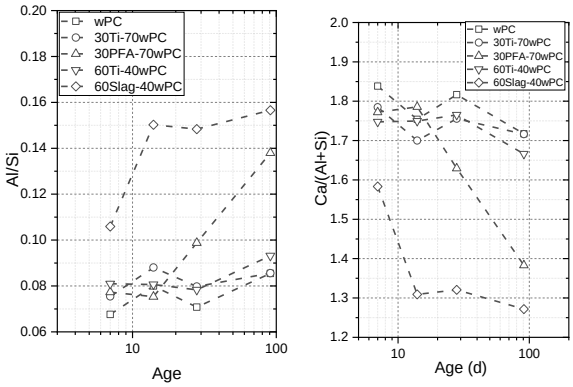

Figure 6. Al/Si ratio (from NMR deconvolution) and Ca/(Al+Si) (calculated from a universal relationship: Si/Ca=0.428+2.366(Al/Ca) (Richardson, Girão et al. 2016).)

Figure 6 gives the Al/Si ratio calculated from quantitative NMR (the details of the calculation method can be found in (Richardson 2004)). Furthermore, the Ca/(Al+Si) ratio was calculated based on a universal relationship between Si/Ca and Al/Ca ratios in such systems, which was obtained by using the regression method (Richardson, Girão et al. 2016). Other than PFA and GGBS, TiO_2 showed a similar development trend of Ca/(Al+Si) as neat wPC, but with lower values. By combining the facts that individual belite was significantly reduced by adding TiO_2, the lower values may be caused by the consumption of belite. It is summarised that a higher hydration degree of wPC is related to a longer mean chain length (MCL) of C-S-H (Richardson, Girão et al. 2016), which is an indicator for a lower Ca/(Al+Si) ratio.

3.3 Nanostructure development of C-S-H in blended wPC

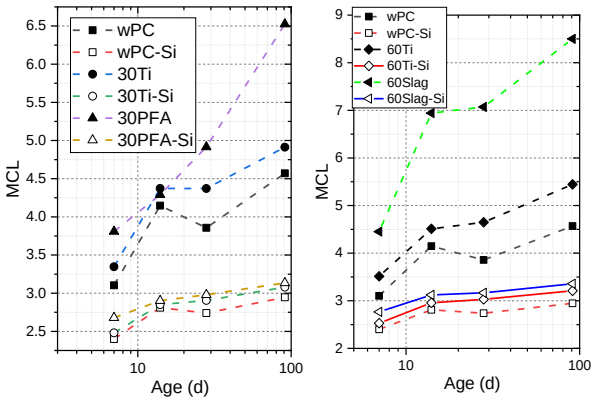

Figure 7. MCL (total and MCL_{Si}) of C(A)SH in 30% (left) and 60% (right) replacement levels samples.

The MCL of the blended samples is calculated based on NMR results in Section 3.2. The addition of SCMs can significantly increase the MCL at a later age due to the supplementary Al incorporated. However, the addition of TiO_2 only increased the MCL slightly at all the ages and replacement levels. This phenomenon must be associated with the increased hydration degree (mainly belite) of TiO_2 containing samples at a later age, which will give a higher MCL (Richardson, Girão et al. 2016).

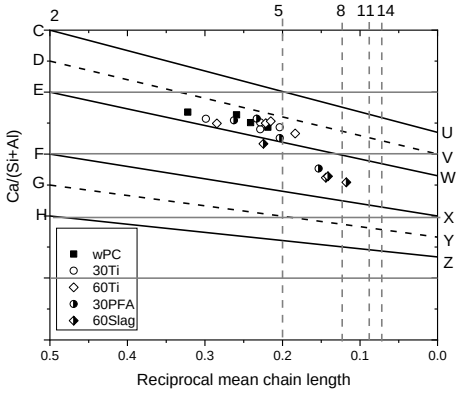

Figure 8. Relationship between reciprocal MCL and Ca/(Si+Al) ratio in wPC-TiO_2/PFA/GGBS samples. The explanations of the symbols in this figure can be found in Ref. (Richardson 2004).

Figure 8 provides the relationship between the reciprocal MCL and Ca/(Si+Al) ratio. It is clear that all the points from neat wPC, TiO_2-blended wPC and early-age SCMs-blended wPC fall into the regions of D-V-E-W. With the lower Ca/(Al+Si) ratios achieved by SCMs at later ages, the points moved towards F-X (tobermorite with minimum protonation) line. Within this region, the nature of C-S-H in such systems can be explained by both T/J and T/CH models proposed by Richardson (Richardson 2004).

An example of chemical composition formulations of a 91 d wPC and 30%TiO_2 blended wPC are given in both T/J and T/CH points of view based on minimum protonation assumption.

The T/J formulation of 91d wPC is:
$[Ca_{3.71}(Si_{0.907}Al_{0.093})_{4.57}O_{14.71}]\cdot(OH)_{5.90}\cdot Ca_{4.80}\cdot mH_2O$

The T/CH formulation of 91d wPC is:
$[Ca_{5.57}(Si_{0.907}Al_{0.093})_{4.57}O_{14.71}]\cdot 2.95Ca(OH)_2\cdot mH_2O$

The T/J formulation of 91d 30%TiO_2 blended wPC is:
$[Ca_{3.94}(Si_{0.906}Al_{0.094})_{4.91}O_{15.74}]\cdot(OH)_{6.48}\cdot Ca_{5.21}\cdot mH_2O$
The T/CH formulation of 91d 30%TiO_2 blended wPC is:
$[Ca_{5.91}(Si_{0.907}Al_{0.093})_{4.91}O_{15.74}]\cdot 3.24Ca(OH)_2\cdot mH_2O$

4. SUMMARY

The effects of TiO_2 on the hydration of wPC were evaluated through ICC, TG-DSC, and NMR analysis. The C-S-H changes in these systems were calculated by using NMR results. The main findings can be summarized as follows: The addition of TiO_2 will retard the first day of wPC hydration as evidenced by ICC and CH content development. However, an acceleration effect was identified for later age through ICC, CH content, and NMR results. The addition of TiO_2 will not change the basic structure of C-S-H in such system but will slightly lower the Ca/(Si+Al) ratio and increase the MCL of C-S-H. The reason for this is due to the increased hydration degree of belite with added TiO_2.

ACKNOWLEDGEMENTS

X.Zhu gratefully acknowledges the CSC-Leeds Joint Scholarship (Grant No. CSC201706050152) for the funding of his PhD project.

REFERENCES

Chen, J., S.. Kou and C. Poon (2012). "Hydration and properties of nano-TiO_2 blended cement composites." Cement and Concrete Composites **34**(5): 642-649.

Lee, B. Y. (2012). Effect of Tianium Dioxide nanoparticles on early age and long term properties of cementitious materials. Ph.D, Georgia Institute of Technology

Ohno, T., K. Sarukawa and M. Matsumura (2002). "Crystal faces of rutile and anatase TiO_2 particles and their roles in photocatalytic reactions." New Journal of Chemistry **26**(9): 1167-1170.

Richardson, I. G. (2004). "Tobermorite/jennite- and tobermorite/calcium hydroxide-based models for the structure of C-S-H: applicability to hardened pastes of tricalcium silicate, β-dicalcium silicate, Portland cement, and blends of Portland cement with blast-furnace slag, metakaolin, or silica fume." Cement and Concrete Research **34**(9): 1733-1777.

Richardson, I. G. and J. G. Cabrera (2000). "The nature of C-S-H in model slag-cements." Cement and Concrete Composites **22**: 259-266.

Richardson, I. G., A. V. Girão, R. Taylor and S. Jia (2016). "Hydration of water- and alkali-activated white Portland cement pastes and blends with low-calcium pulverized fuel ash." Cement and Concrete Research **83**: 1-18.

Taylor, R., Richardson I. G. and Brydson R. M. D. (2010). "Composition and microstructure of 20-year-old ordinary Portland cement–ground granulated blast-furnace slag blends containing 0 to 100% slag." Cement and Concrete Research **40**(7): 971-983.

39th Cement and Concrete Science Conference **Paper Number 068**
9-10th September 2019
University of Bath

How does a Geopolymer structure develop? – A FTIR and XRD Study

Dewayani Sharma, Daniel A. Geddes, John L. Provis
Department of Materials Science and Engineering, University of Sheffield, UK

Susan A. Bernal
School of Civil and Structural Engineering, University of Leeds, UK

Martin Hayes
National Nuclear Laboratory, UK

ABSTRACT

Geopolymer cements have the potential to be used as an alternative to Portland cement by the nuclear industry, to immobilise potentially dangerous radioactive materials that currently cannot be disposed of by conventional cementation methods. Geopolymers develop as main binding phase a three-dimensional gel type network. The process of formation of this binder occurs through the dissolution of the precursor used (e.g. calcined clays), precipitation of reaction products whose chemistry and mineralogy is controlled by the type of activator and curing conditions used, and have the potential of immobilising/encapsulating problematic radioactive wastes. However, in order to understand structural evolution and the mechanism by which the geopolymer gel forms, in-situ techniques need to be used. In-situ ATR-FTIR, Raman spectroscopy and X-ray diffraction can help to develop this understanding, with the potential to control the properties of the final product through different initial curing procedures and reaction conditions. In-situ characterisation of the early hours of reaction of geopolymer binders provides new insight about the fresh to hardened state development. In this study metakaolin-based geopolymers activated with potassium silicate, which have been proposed as potential nuclear waste disposal methods, have been assessed. These results can be used to predict the gel structure development of these systems and also allow for a development of geopolymers as a potential nuclear waste disposal technology.

39th Cement and Concrete Science Conference
9-10th September 2019
University of Bath
Paper Number 069

Effect of Aluminum on C-S-H Structure, Stability and Solubility

Sonya Barzgar [a,b], Barbara Lothenbach [a], Mohamed Tarik [c], Christian Ludwig [b,c]
[a]Empa, Laboratory of Concrete/Construction Chemistry, 8610 Dubendorf, Switzerland
[b]École Polytechnique Fédéral de Lausanne (EPFL), ENAC IIE GR-LUD, 1015 Lausanne, Switzerland
[c]Paul Scherrer Institute (PSI), ENE LBK CPM, 5232 Villigen PSI, Switzerland

ABSTRACT

Cement production accounts for approximately 5% of man-made CO_2 emissions. Lowering these CO_2 emissions is currently one of the most important research topics within the cement community. To reduce these emissions, the Portland cement (PC) is partially replaced by supplementary cementitious materials (SCM). Reaction of these SCM with PC during hydration leads to the formation of additional calcium silicate hydrates (C-S-H), which is the single most important phase in cements based on silica-rich SCM. The high Al_2O_3 and SiO_2 content of the SCM results in C-S-H compositions with more silicon and aluminum than in Portland cement which affects stability and durability of such cements. Therefore, it is crucial to determine the role of aluminum on C-S-H properties to predict the formed hydrate phase assemblages and their effects on durability.

The aluminum sorption isotherms including very low Al concentrations have been determined for C-S-H with Ca/Si ratios from 0.6 to 1.4. The solubility and composition of calcium-silicate hydrates incorporating aluminum "C-(A)-S-H" as a function of different parameters such as Ca/Si ratio, pH, aluminum and alkali contents were investigated. The aluminum sorption isotherms at different Ca/Si ratios revealed a strong correlation between the Al concentration in solution and Al uptake in C-S-H. Moreover, the experimental data showed a dependency of Al uptake in C-S-H on the alkali hydroxide content. Higher dissolved concentrations of Al were observed at higher pH values and a reduced uptake of Al in C-S-H.

1. INTRODUCTION

Concrete is one of the world's most affordable, reliable, durable and readily available construction materials. Due to the high amount of concrete used, cement production accounts for approximately 5% of CO_2 emissions. Reducing these CO_2 emissions is one of the most important and urgent research topics within the cement community (Gartner, 2004). To reduce the CO_2 emission, Portland cement can partially be replaced with limestone or supplementary cementitious materials (SCM) such as blast furnace slags, by-products from steel production, fly ash from coal combustion, or calcined clays. The reaction of Portland cement with different SCM changes the composition of the hydrates (Lothenbach et al., 2011). Calcium silicate hydrate (C-S-H) is the most important hydrate formed during the reaction of Portland cement. In the presence of SCM, C-S-H can have different composition compared to the C-S-H in Portland cements. The Ca/Si ratio of the C-S-H present in Portland cement is in the range of 1.5 - 1.9, however, in SCM blends it is in the range of 0.6 – 1.9 (Antoni et al., 2012). The high silica concentration in SCM such as fly ash or silica fume lowers the Ca/Si ratio of C-S-H, which changes the structure of C-S-H phases. These low Ca/Si C-S-H phases are able to take up more aluminum and alkalis, but less chloride and sulfates. Because of that, the performance of concrete can be affected in terms of mechanical properties and durability.

In the presence of aluminum in the solution, C-S-H is able to incorporate aluminum to produce what is generally called C-A-S-H (Haas and Nonat, 2015). C-(A)-S-H structure consists of calcium oxide polyhedra sheets flanked with "dreierketten" – tetrahedral (alumino) silicate chains – on both sides and counter-ions (e.g., Ca and OH^-) and water in an interlayer between two sheets. Incorporation of aluminum into the silica tetrahedral chains has been observed (Ortaboy et al., 2017).

The structure and aluminum uptake of C-S-H with low Ca/Si ratio and their impact on hydration is still not completely understood. The comparison of the few available datasets (Pardal et al., 2012; L'Hopital et al., 2015; L'Hopital et al., 2016a, b), however, revealed the dependency of aluminum uptake on the reaction time and/or synthesis method used. Most of these data have been measured by ion chromatography with a limit of detection of 0.004 mM Al, which is only little below the aluminum concentration (0.01 to 0.05 mM), where stratlingite and aluminum hydroxide start to precipitate. Thus, very little information is available on the effect of aluminum concentrations on the different binding sites in the C-S-H structure, and on how the different aluminum binding sites influence each other, (L'Hopital et al., 2016). This information proved to

be crucial for the thermodynamic models development. The main aim of this study is to investigate the Al uptake in C-S-H at different hydroxide concentrations by using ICP-MS to be able to determine the effect of pH on Al uptake in C-S-H. The experiments were performed by synthesizing C-S-H samples containing different Al/Si ratios, Ca/Si ratios and alkali hydroxide contents and filtration of solid-solution samples after 3 months equilibration.

2. EXPERIMENTAL DETAIL

In this study, the sorption isotherms including measurements of very low aluminum concentrations are investigated at different sodium hydroxide (NaOH) concentrations. During synthesis, calcium oxide (CaO), silica fume (SiO_2) and calcium aluminate (CA: $CaO{\cdot}Al_2O_3$) were added into Milli-Q water or NaOH solutions. To obtain C-A-S-H with different compositions, the proportions of CaO, SiO_2 and CA were varied as shown in Table 1. The synthesis of these samples was made inside a nitrogen-filled glovebox to minimize carbonation. The samples were stored in 100 mL PE-HD containers placed on a horizontal shaker moving at 100 rpm and equilibrated at 20°C. After equilibration for 3 months, the solid and liquid phases were separated by the filtration of samples inside the glove box. Afterwards, the elemental concentrations of calcium, silica and aluminum in the filtrates were determined with inductively coupled plasma mass spectrometry (ICP-MS) (with detection limit for Al of ~1 ppb (ng/mL)). Also, pH measurements were made at room temperature with a Knick pH meter (pH-Meter 766) equipped with a Knick SE100 electrode.

Furthermore, the zeta potential of samples was measured with an acoustophoresis electroacoustic method using a Zeta Probe from Colloid dynamics. The calibration was made with potassium tungstosilicates, KSiW. First measurement of zeta potential was made on unfiltered C-A-S-H samples prior to filtration inside the glovebox. Then, a second measurement was carried out on the filtrated solution to determine any interferences due to ions present in the solution which is considered as background and thus deducted from the initial measurement.

Moreover, the Al/Si ratios in C-S-H were calculated by performing mass balance with considering also the fraction of Al in the solution. The secondary phases which are present in the solid samples were quantified from the weight loss in TGA measured by using a TGA/SDTA851e Mettler Toledo device and approximately 30 mg of sample. The molar Al/Si ratios in C-S-H was calculated from mass balance taking into account the initial quantities, the amount of Al in secondary phases and the fraction of Al in solution.

Table 1. Total Ca/Si, Al/Si molar ratios and alkali concentrations used to prepare CASH samples.

Molar Ca/Si	Molar Al/Si	NaOH (mol/L)
0.8	0	0
	0.001	0.1
	0.003	0.5
	0.01	1
	0.03	
	0.1	
	0.2	

3. RESULTS

Figure 1 shows the influence of increasing pH on the Al uptake in C-S-H as well as on the dissolved Al concentration at Ca/Si ratio of 0.8. At given pH values, the Al uptake in C-S-H increases strongly with the Al concentrations in solution. For the sample at pH 10.5, where no NaOH had been added, the presence of a low amount of katoite (C_3AH_6) and aluminum hydroxide (AH_3) is observed at the highest Al/Si ratios. Thus, at higher Al/Si ratios, the Al/Si ratio on C-S-H is less than the total Al/Si ratio in solid (Al/Si = 0.1 and 0.2 have decreases to 0.07 and 0.16, respectively) which is due to the presence of katoite and AH_3. However, at lower Al/Si ratios, no other phases are observed such that Al/Si ratio in C-S-H is the same as the initial ratio in solid.

The sorption isotherms in Figure 1 show that the presence of alkali hydroxide leads to much higher dissolved Al concentration but to less aluminum in the solid phases at the same Al concentrations. The addition of alkali hydroxide increases the pH values and thus prevents stratlingite and aluminum hydroxide formation.

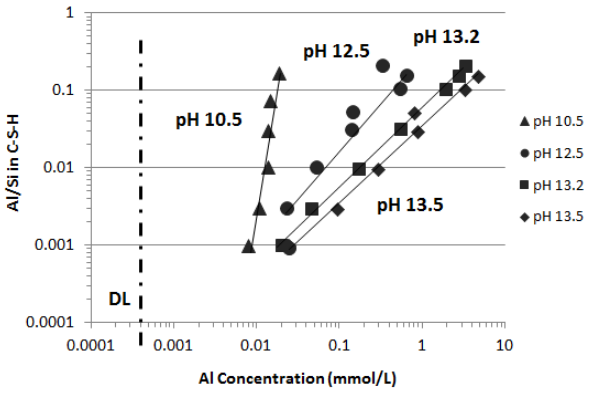

Figure 1. The effect of pH on the Al uptake in C-S-H at Ca/Si ratio of 0.8 after 3 months equilibration (pH 10.5: no NaOH; pH 12.5: 0.1 M NaOH; pH 13.2: 0.5 M NaOH and pH 13.5: 1 M NaOH). The Al/Si ratios in C-S-H were obtained from mass balance.

The zeta potential measures the charge of a particle not directly at the surface but in some distance; such that cations near the surface and even some in the

diffuse layer, contribute to the measured charge (James et al., 1992 and Giese et al., 1996). The zeta potential measurements (Figure 2) show a negative charge for C-S-H. Increasing the pH by adding 0.1 M NaOH increases the negative charge on C-S-H surface, in agreement with the observation reported by L'Hopital et al., 2015. At very high alkali hydroxide concentrations, however, the zeta potential measurements are affected by the increase in ionic strength which moves the distance where the zeta potential is measured such that the measured values appear higher.

The zeta potential measurements illustrate that at higher pH values, the C-S-H surface gets more negatively charged due to the ongoing deprotonation of the silanol sites (Churakov et al., 2014). This negative surface charge suppresses Al uptake, as the main hydroxide complex of aluminum above pH of 7, $Al(OH)_4^-$ is also negatively charged. In addition, higher pH values lead to a stronger predominance of the $Al(OH)_4^-$ complex and thus to a higher tendency of Al to remain in solution.

This increase in negative charge on C-S-H together with increasing predominance of negatively charged $Al(OH)_4^-$ at high pH values is assumed to be responsible for the lower Al uptake at high pH values as shown in Figure 1.

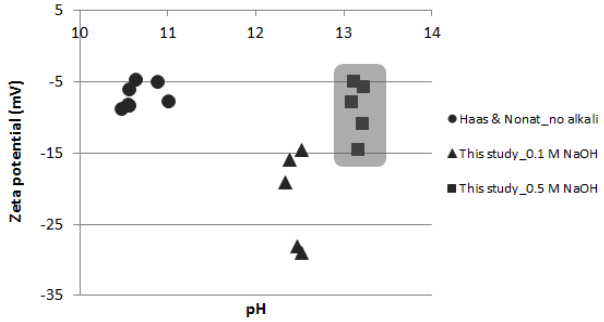

Figure 2. The Zeta potential data for C-S-H samples (Ca/SI = 0.8) in the absence and presence of NaOH. Note that the values at 0.5 M NaOH (shaded area) are affected by the increase in ionic strength.

4. CONCLUSIONS

In this study, the effect of aluminum uptake in C-S-H is investigated using ICP-MS and zeta potential measurements. The determination of sorption isotherms including also very low dissolved aluminum concentrations revealed that Al uptake in C-S-H is increased at higher Al concentrations and that high pH values decrease the Al uptake in C-S-H at the same Al concentrations in solution. However, high pH values prevent the formation of other Al-containing phases such as katoite or aluminum hydroxide, which increases the dissolved concentration of aluminum in solution and thus directly the amount of aluminum in C-S-H. The zeta potential measurements have shown that high pH increases the negative charge on C-S-H surface which suppresses together with the predominance of $Al(OH)_4^-$ at high pH values, the Al uptake in C-S-H.

5. ACKNOWLEDGEMENTS

The financial support of Swiss National Science Foundation (SNF) (project No. 200021_169014 / 1) is gratefully acknowledged.

REFERENCES

Antoni, M., Rossen, J., Martirena, F., and Scrivener, K., 2012. Cement substitution by a combination of metakaolin and limestone. Cement and Concrete Research, 42(12):1579-1589.

Churakov, S.V., Labbez, C., Pegado, L., and Sulpizi, M., 2014. Intrinsic acidity of surface sites in calcium silicate hydrates and its implication to their electrokinetic properties. The Journal of Physical Chemistry, 118(22):11752-11762.

Gartner, E., 2004. Industrially interesting approaches to "low-CO_2" cements. Cement and Concrete Research, 34(9):1489-1498.

Giese, J.R.F., Wu, W., and Van Oss, C.J., 1996. Surface and electrokinetic properties of clays and other mineral particles, untreated and treated with organic or inorganic cations. Journal of Dispersion Science and Technology, 17(5):527-547.

Haas, J., and Nonat, A., 2015. From C–S–H to C–A–S–H: Experimental study and thermodynamic modelling. Cement and Concrete Research, 68:124-138.

James, M., Hunter, R.J., and O'Brien, R.W., 1992. Effect of particle size distribution and aggregation on electroacoustic measurements of .zeta. potential. Langmuir, 8(2):420-423.

L'Hôpital, E., Lothenbach, B., Le Saout, G., Kulik, D., and Scrivener, K., 2015. Incorporation of aluminium in calcium-silicate-hydrates. Cement and Concrete Research, 75:91-103.

L'Hôpital, E., Lothenbach, B., Kulik, D., and Scrivener, K., 2016. Influence of the Ca/Si ratio on the aluminium uptake in C-SH. Cement and Concrete Research, 85:111-121.

L'Hôpital, E., Lothenbach, B., Scrivener, K., and Kulik, D., 2016. Alkali uptake in calcium alumina silicate hydrate (C-A-S-H). Cement and Concrete Research, 85:122-136.

Lothenbach, B., Scrivener, K., and Hooton, R.D., 2011. Supplementary cementitious materials. Cement and Concrete Research, 41(12):1244-1256.

Ortaboy, S., Li, J., Geng, G., Myers, R.J., Monteiro, P.J., Maboudian, R., and Carraro, C., 2017. Effects of CO_2 and temperature on the structure and chemistry of C–(A–)S–H investigated by Raman spectroscopy. RSC Advances, 7(77):48925–48933.

Pardal, X., Brunet, F., Charpentier, T., Pochard, I., and Nonat, A., 2012. ^{27}Al and ^{29}Si solid-state NMR characterization of calcium-aluminosilicate-hydrate. Inorganic Chemistry, 51(3):1827-1836.

39th Cement and Concrete Science Conference
9-10th September 2019
University of Bath
Paper Number 070

Evaluation of Impact of Fly Ash on the Improvement on Type II Concrete Strength

Sayedali Mostofizadeh and Kong Fah Tee
School of Engineering, University of Greenwich

ABSTRACT

Geopolymer concrete (GPC) is a novel material in the construction industry with a qualified performance and efficiency which is environmentally and eco-friendly compatible with the use of natural pozzolans as sustainable material to confront with CO_2 emission due to Portland cement (PC) product. The mechanical properties and durability of this concrete type have been investigated in terms of the factors influencing these two concrete properties. In this study, an attempt has been made on the compressive strength of the concrete mixtures composed of fly ash (FA) as partial or entire replacement of Type 2 Portland Cement (T2PC) with dosages of 0, 10, 20, 30, 50, 70 and 100%. The experimental tests were conducted for compressive strength at 7, 28, 90 days. Also, the effectiveness of curing period, chemical activator were concentrated by utilizing various molarity of alkaline solutions from 4.16M to 12.96M in this research given that the sodium silicate (SS) to sodium hydroxide (SH) by the weight ratio of 2.5 was constantly kept throughout the laboratory program in this study. The results indicated the compressive strength was enhanced while increasing the value of FA as T2PC alternative up to 20% and exceed this amount, the significant reduction of concrete strength was notified which was associated with the relatively low balance of the ion amounts incorporating in the chemical and hydration reactions of concrete product.

Keywords: Geopolymer Concrete, Fly Ash, Compressive Strength, Alkaline Solutions, Portland Cement

1. INTRODUCTION

The inclusion of fly ash as a supplementary in concrete mixtures has been one of the main interests for the recent few decades due to its capability to develop the strength and durability of concrete as well as decrement of CO_2 emission. Hence, a large number of investigations have been carried out in favour of this point to evaluate the efficiency of fly ash in the chemical reactions corresponding to cement hydration and pozzolanic mechanism. Indeed, fly ash does not participate in the reaction with water at initial hydration stage. Nevertheless, it is able to precipitate the rate of cement hydration because of filler effect (Moon et al., 2016). The filler effect improves cement hydration via seeding effects providing further nucleation sites in case of hydration products on filler surfaces leading to the increase of the effective water to cement ratio (W/C) ensuring adequate space for hydration product development (Bentz, 2006).

The cementitious compounds such as calcium silicate hydrate (C-S-H), calcium aluminate hydrates are formed approximately 7 days after mixing by the chemical reaction of calcium hydrate produced by Portland cement hydration along with the silicate in fly ash (Hewlett, 2003). Furthermore, the materials composed of rich sources of alumina (Al) and silica (Si) such as Kaolin, fly ash can be used as raw materials in presence of alkaline solutions (Hadi et al., 2019), for instance silicates and hydroxides of alkalis in order to undergo polymerization reactions (Mehta and Siddigue, 2016). In fact, the mechanism includes the chemical reaction of Al and Si with alkaline activator resulting in the formation of Si-O-Al-O as polymeric chains of 3D ring structure (Duxsun et al., 2007).

As for environment beneficial aspects, usage of fly ash in high dosage can help to decrease the value of Portland pastes needed for concrete projects resulting in the reduction of greenhouse gas emissions and fly ash is effectively recycled as an industrial by product. In a study by Sengul et al. (2005), the effect of fly ash as cement alternative (0-70%) for improvement of compressive strength was studied. The results showed that the concrete mixtures with the utilization of fly ash had higher strength especially over longer time period (56 and 128 days ages) in comparison with that without fly ash (Sengul et al., 2005).

In regard to the differences between various types of Portland paste, it is urgent to point out that types ll and V are mainly designed in order to resistant against sulphate attack (Ghafoori et al., 2015). Sulphate attack is typically a significant phenomenon which causes severe damage to concrete structures due to chemical reaction

between hydration products of C_3A and sulphate ions entering the concrete from outside environment. Consequently, the products generated from this reaction can create stresses leading to expand and then crack. Therefore, keeping the low content of C_3A in Portland type ll is actually margin difference between type l and ll cement as it can commonly be seen that the Portland pastes meeting both designations will be labelled as Type l/ll (ASTM C150, 2015; ASTM D304-09, 2009; Kosmatka et al., 2002; Shi et al., 2006).

This study is confined to the use of low calcium fly ash based geopolymer concrete in which it was partially and totally utilized as the replacement of Portland type ll at 0, 10, 20, 30, 50, 100% in the curing condition to evaluate its effect on compressive strength at ages of 7, 28 and 90 days.

2. Materials and Methods

2.1. Materials

In this study, low-calcium FA known as 450-N, (fineness category N, loss on ignition category B) based on BS EN 450-1 was used as aluminosilicate sources. The FA was supplied by CEMEX manufacture in which the details of chemical combination are shown in Table 1. SH and SS solutions prepared from VWR company with the density of 2.13 gr/cm^3 (20ºC) were blended together as alkaline activator. The concentration of sodium hydroxide solution was variable from 4.16M to 12.96M in the case of the mixes involving FA higher than 20% of Portland paste by weight, whereas the ratios of SS/SH and alkaline solution/FA (AS/FA) were kept constant for all concrete mixtures (Table 2). The CEMll/A-L 32.5 R in accordance with BS EN 197-1 was conducted as T2PC for this study.

2.2. Concrete Mix proportions

One hundred-eight specimens consisted of T2PC and FA were prepared to clarify the effects of main factors subjected to FA and alkaline solution on the compressive strength of this concrete type. These factors are FA content (0%, 10%, 20%, 30%, 50%, 70%, 100%), and alkaline solution molarity (4.16M, 7.13M, 10M, 12.96M). A labelling system was considered to clearly present the concrete mixes. Each mix was assigned four characters. The first two letters represent the inclusion of Portland and FA in concrete compound. Subsequently, the following two numbers represents the percentage of each cementitious material incorporating in concrete mixtures. For example, PF9010 means the binder comprised of 90% T2PC and 10% FA respectively.

There were three series of experimental tests categorized based on curing conditions and values of alkaline solutions. In the first series, the effect of FA content on the strength of T2PC was assessed without using alkaline solution for all dosage of 0-100% of FA inclusion in concrete specimens. In the second series, two different curing conditions including ambient temperature (21±2ºC) and oven heat (110ºC) with/without alkaline solutions were investigate in the case of the mix containing 30% FA to accurately achieve the optimal mix design for conducting the following tests involving higher than 30% FA content. In the third series of laboratory tests, the effects of alkaline solutions were evaluated in terms of the mixtures utilizing FA dosages in the ranges of 30%, 50%, and 70% in order to compare with those in the first series. Gelenium 51 prepared from BASF company with dosage of 2.5% by cement weight (30ml) was used as superplasticizer in all concrete mixes, except for PF10000 and PF9010A. Further details of mix designs are exhibited in Table 3.

Table 1. Chemical and physical characteristics for fly ashes to be used in concrete applications (SFS-EN 450-1 and ASTM C 618)

CHARACTERISTIC	LIMIT VALUE (%)	
	SFS EN 450-1	ASTM C618
Loss on ignition at 950°C	A<5, B<7, C<9	<6
SiO_2, Al_2O_3, Fe_2O_3	>70	F>70, C>50
Chloride	<0.1	--------
Sulfate as SO_3	<3	<5
Free CaO	<1.5	--------
Tot. alkalis (Na_2O+K_2O)	<5	--------
MgO	<4	--------
P_2O_5	<5	--------
Fineness (45 µm)	S<12, N<40	<34
Activity index 28 days	>75	--------

Table.2. Mix proportion of alkaline solutions

Mix	SH (gr)	SS (gr)	Water (ml)	SS/SH	SH (M)	AS/FA
PF7030A	250	625	1500	2.5	4.16	0.25
PF7030B	250	625	1500	2.5	4.16	0.25
PF5050B	428	1070	1500	2.5	7.13	0.25
PF3070B	600	1500	1500	2.5	10	0.25
PF00100	830	1600	1500	2.5	12.96	0.25

2.3. Testing Methods

The test was conducted using an Avery Denison testing machine type 7226CB calibrated in accordance with BS EN ISO 7500-1:2004 standard and is traceable to UKAS. This standard includes determination of compressive strength of cube concrete specimens which is used to apply a

compressive axial load to molded concrete cubes at the rate of 5.7 kN/S until failure occurs. The compressive strength in all concrete mixtures is obtained by dividing the maximum load attained over the test, by the cross-section area of the concrete samples. The concrete cubes of 150 mm width and 150 mm length, cured in the curing conditions mentioned above, were examined after aging for 7, 28 and 90 days.

Table.3. Mixture proportion of experimental concrete

Mix	CAg 20 Kg	CAg 10 Kg	FAg kg	FA Kg	T2PC Kg	W (L)
PF10000	32.84	16.4	26.52	0	12	7.2
PF9010A	32.84	16.4	26.52	1.2	10.8	7.2
PF9010B	32.84	16.4	26.52	1.2	10.8	6.6
PF8020	32.84	16.4	26.52	2.4	9.6	6
PF7030A	32.84	16.4	26.52	3.6	8.4	6
PF7030B	32.84	16.4	26.52	3.6	8.4	6
PF7030C	32.84	16.4	26.52	3.6	8.4	6.6
PF5050A	32.84	16.4	26.52	6	6	6
PF5050B	32.84	16.4	26.52	6	6	5.5
PF3070A	32.84	16.4	26.52	8.4	3.6	5.7
PF3070B	32.84	16.4	26.52	8.4	3.6	4
2PF00100	32.84	16.4	26.52	12	0	3

CAg20: Coarse Aggregate 20 mm, **FAg**: Fine Aggregate
CAg10: Coarse Aggregate 10mm, **W**: water

3. Results and Discussions

The experimental results associated with compressive strength were presented as the average of three cube specimens tested for each mixture at the ages of 7, 28, 90 days in Figure 1. The values of concrete strength were seen to be enhanced at all ages with the increment of fly ash up to 20% FA as the replacement of T2PC cement and beyond that, it steeply declined. The optimum value of 54.11 MPa was observed for the cubic specimens with 20% FA and 80% T2PC at 90 days. The increase in this peak point with the inclusion of 20% FA is probably due to the additional chemical reaction of FA with the present C-H molecules acquired from the hydration process of PC and H_2O leading to the formation of calcium silicates in which the behavioural performance of C-S-H was simply explained in Part 1. It is worth to note that this compressive strength development can be observed as long as sufficient particles are present in the concrete content. Obviously, the deficiency of each chemical molecules such as calcium (Ca), silicate (SiO_3), hydrate (H_2O) can have a preventive role for the formation of polymeric chain of C-S-H resulting in disturbance of balance between the particles forming the chain, in which this factor can be justifiable in the reduction of compressive strength of concrete mixtures including fly ash higher than 20% without using alkaline solution.

Also, the assessment of concrete strength results between the concrete mixtures with/without alkaline liquid showed that the higher values of compressive strength belonged to the concrete binders which had no alkaline solutions in their content up to 50% fly ash whereas the concrete mix involving 70% FA and SH with SS/SH ratio of 2.5 had higher compressive strength than that of concrete mix with 70% FA and without alkaline solution. However, the obtained results for the range of 30-70% fly ash for the concrete mixes with/without alkaline solutions reflect a steeply reduction of compressive strength.

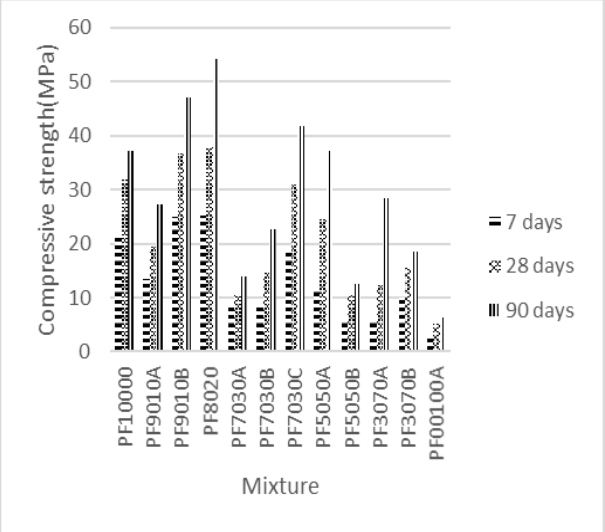

Figure 1. Compressive strength of T2PC with FA inclusion as PC replacement at 7, 28, 90 days.

4. Conclusions

Over one-hundred concrete specimens were examined to evaluate the effects of FA and alkaline solutions on the development of T2PC compressive strength. The laboratory observations can be summarized as follows:

The compressive strength of low calcium FA based geopolymer concrete is enhanced with the inclusion of FA as T2PC replacement up to 20% at all ages. The improvement in concrete strength was observed due to additional calcium available in the

chemical products formed by hydration mechanism which coexisted with the polymeric products alumina-silicate (Mehta et al., 2016).

The concurrent usage of FA with the dosage exceed 20% along with alkaline solutions significantly decreased the concrete strength due to the relatively lower balance in the formation of geopolymeric chains needed for high compressive strength as the amounts of calcium ion are not sufficient for this goal compared to the mixes containing FA in the range of 10-20% as T2PC alternative.

Concrete specimens including 30% fly ash and alkaline solutions kept under the heat of oven 110°C for initial 24 hours as curing condition were found to have relatively low compressive strength among all concrete mixtures at all ages. Thus, the typical curing condition based on BS 1881 is strongly recommended in terms of the concrete binders consisting of T2PC and low-calcium FA up to 30% as cement replacement and beyond that, further considerations such as appropriate ratio of alkaline solution and using superplasticizer in which their chemical combinations compatible with polymeric products are suggested for this purpose.

REFERENCES

ASTM C150/C150M-15, 2015, Standard specification for Portland cement, American Standard for Testing and Materials, West Conshohocken, PA.

ASTM D3042-09, 2009, Standard test method for insoluble residue in carbonate aggregates, American Standard for Testing and Materials, West Conshohocken, PA.

Bentz, D.B., 2006, Influence of water-to-cement ratio on hydration kinetics: simple models based on spatial considerations, Cement and Concrete Research. 36:238-244.

Duxson, P., Provis, J.L., Lukey, G.C., Van, J.S., Deventer, 2007, The role of inorganic polymer technology in the development of 'green concrete', Cement and Concrete Research, 37(12):1590-1597.

Ghafoori, M., Diawara, H., Islam, M., 2015, Effects of class F fly ash on sulfate resistance of Type V Portland cement concretes under continuous and interrupted sulfate exposures. Construction and Building Materials, 78:85-91.

Hadi, M., Zhang, H., Parkinson, S., 2019. Optimum mix design of geopolymer pastes and concretes cured in ambient condition based on compressive strength, setting time and workability, Journal of Building Engineering, 23:301-313.

Hewlett, P.C., 2003, Lea's Chemistry of Cement and Concrete, 4th Edition, Butterworth Heinemann, London.

Kosmatka, S.H., Kerkhoff, B., Panarese, W.C., 2002, Design and Control of Concrete Mixtures, Portland Cement Association, 14th Edition.

Mehta, A., Siddigue, R., 2016, Properties of low-calcium fly ash based geopolymer concrete incorporating OPC as partial replacement of fly ash, Construction and Building Materials, 150:792-807.

Moon, G.D., Oh, S., Choi, Y., 2016, Effects of the physicochemical properties of fly ash on the compressive strength of high-volume fly ash mortar, Construction and Building Materials, 124:1072-1080.

Ohenoja, K., Wigren, V., Österbacka, J. et al., 2019, Waste and Biomass Valorization, https://doi.org/10.1007/s12649-019-00615-y

Sengul, .O, Tasdemir, .C. Tasdemir, M.A., 2005, Mechanical properties and rapid chloride permeability of concretes with Ground fly ash, ACI Mater. J. 102:474-482.

Shi, Caijun, Roy, Della, and Krivenko, Pavel, 2006, Alkali-Activated Cements and Concretes, CRC Press.

39th Cement and Concrete Science Conference
9-10th September 2019
University of Bath
Paper Number 71

Novel Nanostructured Aluminosilicates to develop Carbon Neutral Cement

Pooja Anil Kumar Nair[a], Kevin Paine[a], Asel Sartbaeva*,
Lisa Price*, Juliana Calabria-Holley[a],
[a] BRE Centre for Innovative Construction Materials, Department of Architecture and Civil Engineering, University of Bath, Bath BA2 7AY, UK
* Department of Chemistry, University of Bath, Bath BA2 7AY, UK
University of Bath

ABSTRACT

Cement is responsible for approximately 5% of all anthropogenic CO_2 emissions in the world. It is possible to capture CO_2 within cement via carbonation. The captured CO_2 reacts with hydration products to form calcite minerals. Cement pastes naturally carbonates over time however this process is slow and is generally limited to the exposed surfaces. The aim of this research was to accelerate the carbonation in the initial stage of hydration to develop a high strength and less permeable material. Aluminosilicates were synthesised using sol-gel technology by varying sol-gel parameters. Faujasite was used as a bench mark material due to its well defined aluminosilicate structure and known capacity to capture CO_2. This paper investigates the compatibility of the tailored aluminosilicates with the cement and subsequent changes in the cement paste morphology modified with 15% aluminosilicate used as a replacement for Portland cement. The studies have shown that the synthesized aluminosilicate (Na-T-10) have developed a denser morphology even at the initial stages (3 and 7 day) indicating highly reactive nucleation sites that act as seeding agents for the production of porous C-S-H. Development of such highly reactive porous aluminosilicates has shown good potential for CO_2 capture. High compatibility with cement paste is evident with the microstructural characterisation as though 15% of cement was replaced with the nano structured aluminosilicate. The materials have shown the development of C-S-H and portlandite which further suggests that these aluminosilicates are highly reactive in cement pastes.

1. INTRODUCTION

Cement is responsible for approximately 5% of all anthropogenic CO_2 emissions in the world. Statista Global in 2018 predicted that the consumption of cement is going to be 4.4 billion metric ton by 2020 which will further increase to 4.8 billion metric ton by 2030. Hence, the primary focus of sustainable material researchers is to reduce the carbon footprint and develop a sustainable cementious material.The major contributor of carbon dioxide emission in Portland cement is C_2S and C_3S. One of the major challenges faced by material scientists is to reduce the cement content at the same time maintain the strength of the cementitious paste. Calcium silicate hydrate (C-S-H) is the main hydration product of the clinker phase. The C-S-H is a nano porous gel which is the main constituent that impart strength to the harden cement. Over the years, several approaches have been taken so as to limit the clinker content by using supplementary cementitious material (SCM), chemical admixtures, graphene, fibre reinforced polymer (FRPs), zeolites and optimisation of amount and size of aggregates[1][2][3][4][5]. A recent approach to use CO_2 within the cement mixes has shown to improve properties of cementitious material. For instance, use of CO_2 in the curing stage has proven to reduce the setting time and increase the compressive strength[6] however there is a very small increase in compressive strength. Direct carbonation of cementitious materials to produce low carbon cementitious material has shown successful results in the development of carbon neutral cement[7][8][9][10]. However there are several drawbacks in terms of sophisticated mechanisms and also lack of comprehensive compatibility evidence. The use of CO_2 is a new approach in the development of carbon neutral cement and opens endless possibilities in the field of concrete and cement technology. There are several debates on cement hydration, nano structure of the hydration products and drawbacks due to carbonation in cement. The idea of this research is to develop tailored aluminosilicates that can replace cement up to 15% and to study the respective change in the microstructure using advanced technology. The studies show that nano structurally controlled aluminosilicate has the potential to alter the microstructure of cement pastes and at the same time act as a carbon sink. These aluminosilicates after carbon capture could provide additional nucleation sites which can therefore act as a seeding agent for the production of calcite within the cement matrix creating a denser paste. The paper

also tries to identify how the alteration of the aluminosilicate nano structure change the microstructural properties of cement by benchmarking the difference with a known CO_2 adsorbent zeolite faujasite. The CO_2 capture capacity is not discussed however the material capacity to adsorb CO_2 was tested using a Hidden Intelligent Gravimetric Analyser (IGA-001) and the nanostructured aluminosilicate shows potential capacity in adsorbing CO_2.

2. EXPERIMENTAL

SYNTHESIS OF ALUMINOSILICATES

The aluminosilicates were synthesised using sol-gel technology. Tetraethoxysilane (TEOS) reagent grade 98% supplied by Sigma-Aldrich, 99%, supplied by Fisher Scientific were used as the silica precursors and aluminium nitrate nonahydrate (ANN) with 99.99% purity supplied by Fisher Scientific was used as the alumina precursor. Sodium hydroxide was used as a base catalyst. The molar ratios of the materials are presented in Table 1. In the nomenclature, the number 10 stands for 10% Al_2O_3 and the prefix T is when TEOS is used as the silica precursor. The synthesis was carried out for 72 hours followed by controlled heating at 100℃ for 12 hours. The samples were filtered with water and further dried at 100℃ for 24 hours.

The zeolite synthesised was faujasite (FAU Linde Type Y) following the well-established synthesis procedure of David Ginter[11]. Faujasite mixes were designated as FAU-Y. The synthesised aluminosilicates and FAU-Y were characterised using transmission electron microscopy (TEM), field emission scanning electron microscopy (FE-SEM), powdered X-ray diffraction (XRD), nitrogen adsorption (NAD) and thermal gravimetric analysis (TGA)

Table 1: Formulation and parameters for sol-gel synthesis

Designation	TEOS (mols)	APTES (mols)	ANN (mols)	H_2O (mols)	NaOH (mols)
T-10	1	-	0.2	16.5	-
Na-T-10	1	-	0.2	4.5	0.5

CEMENT PASTE MIXES WITH ALUMINOSILICATES

CEM1 (BS EN 197-1:2011) was used for studying the compatibility of the additives and changes in the microstructure. 15% of cement was replaced by the synthesised aluminosilicate and FAU-Y. The water to cement ratio (w/c) was 0.5. The cement pastes were cast in prismatic moulds of size 160mm x 20mm x 10mm. They were demoulded after 24 hours and were cured in water tanks at 20℃. The samples were cured for 3, 7 and 28 days and crushed at respective ages followed by passing through 125µm sieves. The samples were characterised microstructurally using SEM, TGA and XRD. All cement paste samples (Table2) follow the same designation as presented in Table 1 with an added prefix ‘C’ where ‘C’ stands for cement.

Table 2: Mix design for cement pastes.

Designation	Cement	Aluminosilicate	w/c	Dosage(% by mass of dry cement)
Control	CEM1	-	0.5	15
FAU-Y-C	CEM1	FAU-Y	0.5	15
T-10-C	CEM1	T-10	0.5	15
Na-T-10-C	CEM1	Na-T-10	0.5	15

MICROSTRUCTURAL CHARACTERISATION AND TESTING OF THE CEMENT PASTE

The phase composition of portlandite, ettringite and C-S-H of the materials were analysed using XRD and TGA. The compositional analysis was carried in the powder form (< 125 µm). Morphological changes were investigated using FE-SEM. The sample preparation followed the same protocols as elsewhere[12].

3. RESULTS AND DISCUSSION

MATERIAL CHARACTERISATION

The structure of aluminosilicates were tailored by varying the sol-gel parameters, such as the base catalyst, in order to evaluate how the overall structure and composition of the aluminosilicate improved the microstructure of cement and subsequent CO_2 capture. FAU-Y is a well known form of crystalline zeolite. Na-T-10 has developed a semi-crystalline structure with nitratine framework and aggregated clusters of amorphous aluminosilicate, unlike T-10 which is completely amorphous. The XRD image in Figure 1 shows sharp peaks of Nitratine ($NaNO_3$) peaks in Na-T-10.

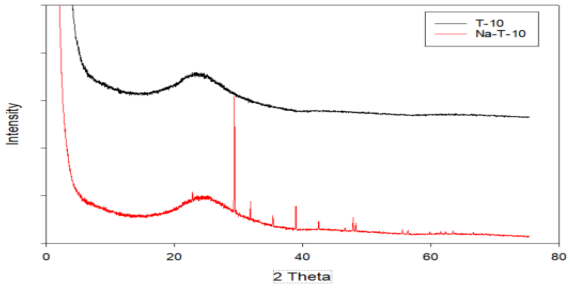

Figure 1: XRD of Na-T-10 and T-10 highlighting the crystalline peaks of NaNO3 formed in Na-T-10

The TEM of Na-T-10 in Figure 2, confirmed the crystalline framework of nitratine around the amorphous aluminosilicate particles of Na-T-10. This crystalline framework might have activated the formation of additional nucleation sites in the cement which led to formation of nano porous C-S-H pastes discussed further ahead.

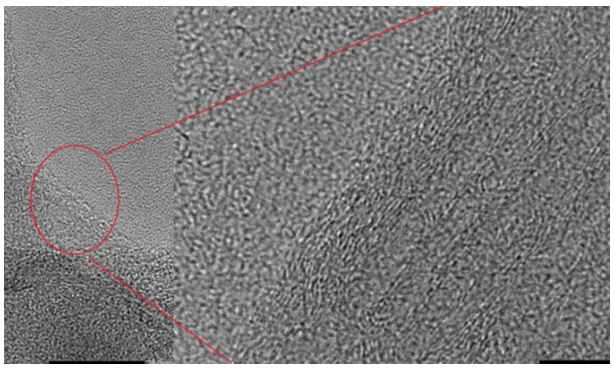

Figure 2: TEM of Na-T-10 highlighting the outer crystalline framework of $NaNO_3$.

The surface area analysis (Table3) using NAD showed high surface area and porosity for the synthesised sol-gel aluminosilicate which enhanced the CO_2 capacity of the material.

Table 3: Surface area of sol-gel based aluminosilicates.

Material	Surface Area (m^2/g)
T-10	454.15
Na-T-10	276.17

MICROSTRUCTURAL ANALYSIS OF CEMENT REPLACED BY ALUMINOSILICATE

The DTG test (Figure 3) shows the loss of bound water content from over a wide range between 40℃ to 200℃. The decomposition of portlandite in the range of 400℃ to 600℃. The difference between the 3 and 7 days are not significant and therefore only 7 days aged samples are presented. In this paper initial changes in the microstructure is analysed.

From the DTG curves a sharp dip is seen at around 130℃ which indicates the probability of well-structured Na-T-10 acting like a seeding agent and by creating reactive nucleation sites that has formed a nano porous C-S-H.

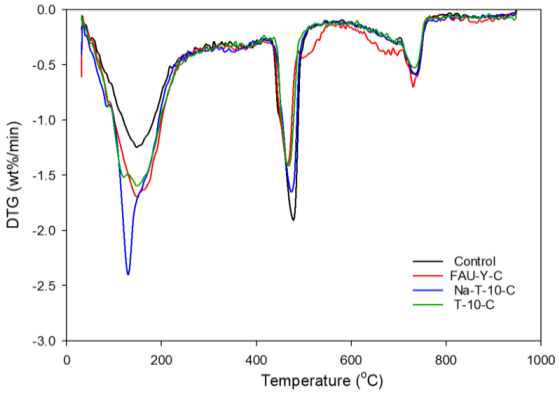

Figure 3: DTG of 7 day specimens

Though the XRD (Figure 4) and SEM images (Figure 5) picks up unreacted zeolite crystals along with the unreacted clinker content, the structured aluminosilicates has created reactive sites and formed comparable amount of hydration products which is validated with the SEM images.

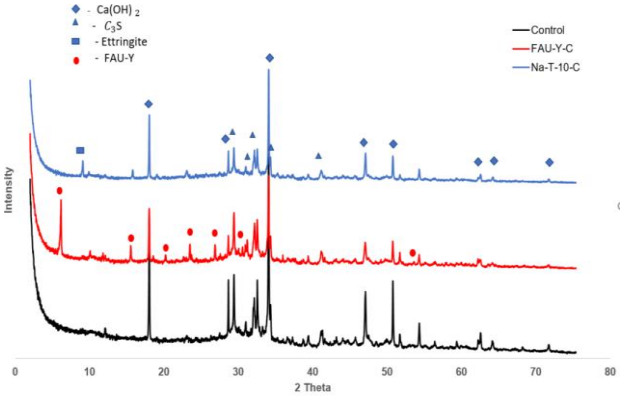

Figure 4: XRD of 7 day aged specimen.

From Figure 5 it is evident that addition of aluminosilicates has changed the morphology of the hydration products. The refinement of structure of aluminosilicate increases the potential of creating additional nucleation sites. In Figure 5-C, the clusters C-S-H has aggregated over the portlandite. It is interesting to see that the portlandite is hidden in the clusters of C-S-H structure in the paste and this is a repeating phenomenon throughout the 7 day aged pastes (Figure 6). For the control sample (Figure 5-A) shows less clusters of C-S-H and the correspondent DTG curve (Figure3) shows a higher content of portlandite T-10-C and zeolite based cement pastes in the initial ages have shown much less of the hydration by-product (portlandite). However the morphology of the specimen T-10-C is showing significant changes in the structure of the hydration products indicating the possibility of T-10 particles being highly reactive due to its high surface area (Table 3).

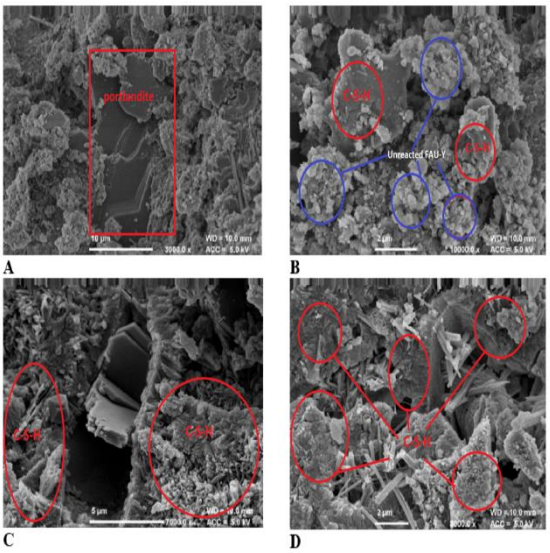

Figure 5: SEM of 7day aged specimens. A.Control, B. FAU-Y-C, C. Na-T-10-C, D. T-10-C.

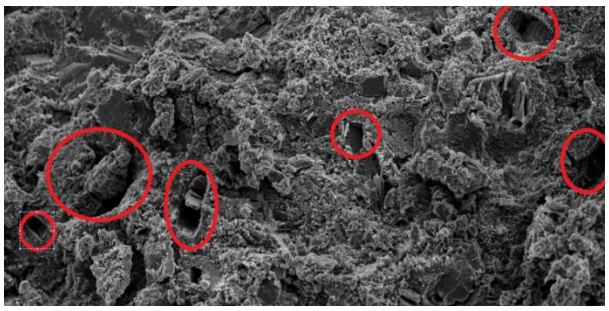

Figure 6: Portlandite covered inside C-S-H shell of Na-T-10-C.

CONCLUSIONS

The microstructural analysis shows that different synthesis routes yield different aluminosilicate structures which in turn impart different microstructure properties. Though 15% of cement was replaced by mass, by both zeolite and the two sol-gel aluminosilicates, comparable dense morphology was formed. This indicates that the aluminosilicates create reactive nucleation sites for formation of the nano porous C-S-H gel, which has the potential to act as sites of CO_2 storage or calcite deposit, however further studies are needed to confirm this. The synthesised porous aluminosilicates have also shown reasonable CO_2 capture capacity which is not explained in the paper due to restriction in content. From the analysis, it is evident that nano porous C-S-H network was more developed than the control proving the compatibility of the synthesised material. Furthermore, the structurally controlled Na-T-10 aluminosilicate has shown the potential to develop more reactive sites therefore it can act as a seeding agent to form C-S-H networks. The findings so far suggest that the synthesised aluminosilicates are compatible with cement and act as suitable candidates for CO_2 capture due to its porous nature. However, more research is under way to study the compatibility of the CO_2 capturing by these sol-gel synthesised porous aluminosilicate and the interactions between the adsorbents and cement paste at physical and chemical scales. This area of research is highly innovative and requires further analysis as the $CaCO_3$ formation is activated through development of highly nano porous C-S-H network.

REFERENCES

[1] K. L. Scrivener and A. Nonat, “Hydration of cementitious materials, present and future,” *Cem. Concr. Res.*, vol. 41, no. 7, pp. 651–665, 2011.

[2] R. D. Hooton and J. A. Bickley, “Design for durability: The key to improving concrete sustainability,” *Constr. Build. Mater.*, vol. 67, no. PART C, pp. 422–430, 2014.

[3] P. Frontera, S. Marchese, F. Crea, R. Aiello, and J. B. Nagy, “The strength effects of synthetic zeolites on properties of high performance concrete,” *WIT Trans. Built Environ.*, vol. 85, pp. 449–458, 2006.

[4] M. Şahmaran, N. Özkan, S. B. Keskin, B. Uzal, I. Ö. Yaman, and T. K. Erdem, “Evaluation of natural zeolite as a viscosity-modifying agent for cement-based grouts,” *Cem. Concr. Res.*, vol. 38, no. 7, pp. 930–937, 2008.

[5] J. Carlos, D. Cruz, J. María, and D. Colorado, “A Much Better Concrete with Zeolite Additions- State of the Art Review,” 2014.

[6] M. Sciences, L. Thesis, and R. Kools, “CO 2 sequestration and utilization in cement-based materials,” 2018.

[7] D. Heinz and L. Urbonas, “Modification of cementitious building materials by treatment with CO2,” *Chem. Technol.*, vol. 67, no. 1, 2016.

[8] K. Vance, G. Falzone, I. Pignatelli, M. Bauchy, M. Balonis, and G. Sant, “Direct carbonation of $Ca(OH)_2$ using liquid and supercritical CO_2: Implications for Carbon-Neutral Cementation,” *Ind. Eng. Chem. Res.*, vol. 54, no. 36, pp. 8908–8918, 2015.

[9] D. Hirabayashi, K. Sawada, and Y. Enokida, “Carbonation Behavior of Pure Cement Hydrates under Supercritical Carbon Dioxide Conditions,” *Waste Manag. 2012 Conf. Improv. Futur. waste Manag.*, no. January, pp. 1–10, 2012.

[10] T. R. Naik, R. Kumar, and R. N. Kraus, “Carbon dioxide sequestration cementitious products,” no. January, 2009.

[11] H. Robson, K. P. Lillerud, and X. Patterns, *Published on behalf of the Synthesis Commission of the International Zeolite Association*. .

[12] Muzzamil Shakil, J. C. Holley, K. A. Paine, and M. P. Ansell, “The effects of sol-Gel silicates on hydration kinetics and microstructure of Portland cement.”

39th Cement and Concrete Science Conference
9-10th September 2019
University of Bath
Paper Number 072

Sodium sulfate activated slag-limestone composite cements

Katharine Button, Alastair Marsh, Samuel Adu-Amankwah, Susan A. Bernal
School of Civil Engineering, University of Leeds, UK

ABSTRACT

Composite cements based on ternary systems of blast furnace slag, limestone and Portland cement have been studied extensively. These materials offer significant environmental savings compared with slag cement systems. Limestone plays a key role in stabilizing monocarboaluminates and consequently ettringite by reacting with additionally dissolved aluminates and increasing the overall degree of reaction of slag. In order to maximise the environmental potential of these cements, the present study centres on producing composite cements without Portland cement, using instead a near-neutral salt activator, sodium sulfate. There is a good consensus that sodium sulfate activated slag cements can develop good mechanical properties. These systems also reach alkalinities comparable to those of Portland cement based cements, which make them an attractive alkali-activated alternative, as their use does not pose additional health and safety hazards, as it is the case when using conventional alkali-activators such as hydroxides and silicates.

In this study two slags were activated with sodium sulfate using different amounts (0, 5 and 10 wt.%) of limestone powder as replacement for slag. Kinetics of reaction were determined in fresh pastes using isothermal calorimetry. Characterisation of hardened pastes was conducted using X-ray diffraction, and solid state ^{27}Al MAS nuclear magnetic resonance spectroscopy. Results reveal that after 7 days of curing, limestone is acting as filler as reaction of this material was not identified. However, as reaction progresses slight changes in the phase assemblages were detected, which could be an indication of limestone dissolution.

INTRODUCTION

Alkali activated materials have been increasingly investigated over the past decades, gaining interest as low carbon cements for producing concretes. Produced from aluminosilicate precursors, alkali-activated cements are now commercialised in several countries and are being produced on an industrial scale (Provis et al. 2014). Activating solutions such as hydroxides, alkali silicates or a combination of both are used for the activation of slags. However, the high pH of these substances make them corrosive, viscous and thus difficult to handle. Alongside this, these activators can be costly and energy intensive to manufacture and cannot be naturally sourced (McLellan *et al.,* 2011). Other activating solutions can be used for producing these cements, one of the most promising being sodium sulfate (Na_2SO_4). This is an environmentally friendly activator, which is naturally found as thenardite – an anhydrous Na_2SO_4 – and mirabilite ($Na_2SO_4.10H_2O$) (Provis et al. 2014). Sodium sulfate is known as a near-neutral salt with a pH of 7. The utilisation of this salt has many technical advantages, including production of cements with alkalinities comparable to those of conventional Portland cements, reducing the risks associated with handling of alkaline activators. Near-neutral salt activated slag cements also present an increased workability of the fresh state paste compared to alkali silicates (Bernal 2016), hence reduced water contents are required to achieve desirable workability.

Limited research has been done on activated slags using Na_2SO_4 due to the concern of slow early age strength development (Bernal et al. 2014). However, these systems can reach a 28-day mechanical strength comparable to NaOH activated slags (Shi et al. 2006). In addition, compared to Portland cement, Na_2SO_4 activated slags are able to resist degradation caused by exposure to elevated temperatures (up to 600°C) (Rashad et al. 2012). Also, these cements have great potential to be used for specialised applications including immobilisation of sulfate bearing nuclear wastes (Mobasher et al. 2013).

The majority of blast furnace slag that is currently produced is already used by the construction industry. Consequently, there is a need to develop mix designs inspired by Portland cement, slag and/or calcined clays with limestone composites. These systems develop desirable properties and are attracting significant attention as the one of the most sustainable and long-term solutions for reducing the environmental footprint associated with the construction industry (Juenger et al. 2019). In this study composite cements were produced using blast furnace slag and limestone, blended with sodium sulfate instead of Portland cements. Kinetics of reaction were determined by isothermal calorimetry, and phase assemblage evolution was determined using X-ray diffraction, and solid state ^{27}Al MAS nuclear magnetic resonance (NMR) spectroscopy.

EXPERIMENTAL METHODOLOGY

Materials and sample preparation

Two commercial slags and limestone were used for producing the cements evaluated. Table 1 shows the chemical composition of these materials. Particle size distribution of the anhydrous slags were comparable with an average d_{50} of 11.7 μm slag 1 (S1) and 12.5 μm slag 2 (S2) respectively. The limestone used in this study was slightly coarser than the slags, with a d_{50} of 15.3 μm.

Table 1. Oxides composition of blast furnace slag and limestone determined by X-ray fluorescence. LOI correspond to loss on ignition at 900 °C

Oxides	Slag 1 (wt.%)	Slag 2 (wt.%)	Limestone (wt.%)
CaO	43.64	44.44	53.91
Al_2O_3	11.25	9.77	0.93
SiO_2	33.59	35.73	2.19
MgO	5.4	6.27	0.74
SO_3	3.3	1.63	0.18
Others	2.56	2.09	0.63
L.O.I.	-	0.07	41.42

The activating solution was produced by dissolving anhydrous sodium sulfate (Alfa Aesar, 99%) in deionized water at 40°C, being dispensed with an accuracy of +/- 1mL until complete dissolution was reached. This solution was then used after it reached room temperature. Anhydrous slag and limestone were homogenized using the Roller Ball Mill Capco Ball Mill Jar 2VS for 3 hours, and then mixed with the activating solution. Mix design of the cements produced is shown in Table 2.

Table 2. Mix design of sodium sulfate activated composite cements

Sample ID	Slag 1 (g)	Slag 2 (g)	Limestone (g)	Na_2SO_4 (g)
100%-S1	100	-	0	8
95%-S1	95	-	5	8
90%-S1	90	-	10	8
100%-S2	-	100	0	8
95%-S2	-	95	5	8
90%-S2	-	90	10	8

All pastes were produced with a binder (slag + limestone + anhydrous sodium sulfate)/ water ratio of 0.40, and an activator dose of 8g Na_2SO_4 per 100 g of slag. These activation conditions were selected based on previous studies by the authors for similar systems (Bernal 2016). Paste samples were poured and cured in sealed 5mL centrifuge tubes in a water bath at 21°C until testing (up to 28 days).

Test conducted

Fresh pastes were produced by mixing the slag/limestone blend with the activating solution. Once a homogeneous mix was reached 9.0g of paste were poured in plastic ampoules and immediately placed inside a TAM Air Calorimeter at 20 ± 0.02°C for 16 days.

After 7 and 28 days of curing hardened samples were ground and immediately characterised without any solvent exchange treatment to arrest hydration, minimise disturbance of hydrated phases. X-ray diffractograms were collected using a PANalytical MPD Pro on freshly ground samples backfilled into sample holders. A CuK α anode was used operating at 40kV and 40mA equipped with an X'Celerator detector over a range of 5-80°2θ with a step size of 0.0334°. A 10mm incident beam mask was used with automatic incident divergence and fixed anti-scatter slits. All data was acquired in the continuous scan mode. Corundum was used as a reference standard. Data analysis was performed using TOPAS Academic software v4.2. ^{27}Al MAS NMR spectra were collected using a Bruker Avance III HD spectrometer with a 400 mHz wide bore magnet (magnetic field 9.4T), with an operating frequency of 104.3mHz, using a zirconia rotor and spun at 20000Hz in a 2.5mm solid-state MAS probe.

RESULTS AND DISCUSSION

Kinetics of reaction

Significant differences in the heat flow released are identified (Figure 1) as a function of slag chemistry. For S1 cements, an acceleration/ deceleration period is identified within 48 hours after mixing. A comparable degree of reaction was observed for these cements independently of the amount of limestone in the mix. Conversely, cements produced with S2 show an induction period of up to 4 days after mixing, and reduced degrees of reaction compared with cements produced with S1. The substitution of 5% of slag by limestone does not induce noticeable changes in the kinetics of reaction. Replacements of 10% slag by limestone accelerate the kinetics of reaction of S2 cements, although the overall degree of reaction after 15 days is comparable to that observed in cements with reduced limestone contents.

The differences in reaction kinetics are mainly attributed to differences in slags chemistry, as their particle size distribution and crystallinity are comparable. S1 has a higher content of Al_2O_3 than S2, which might be leading to the faster formation of Al-bearing phases in these systems. This is consistent with findings reported for silicate activated slags where higher contents of Al_2O_3 lead to faster reaction kinetics (Ben Haha et al. 2012).

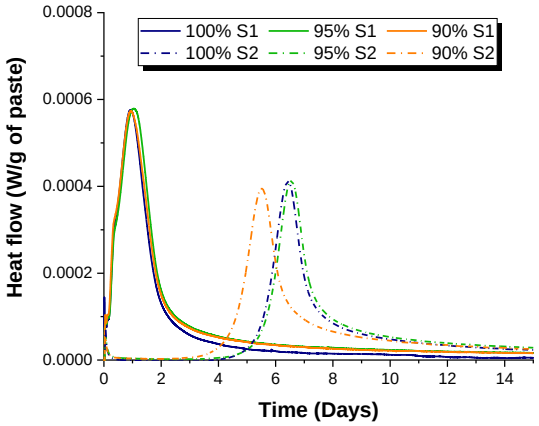

Figure 1. Isothermal calorimetry curves of sodium sulfate activated composite cements

S1 also presents a much higher content of SO_3 than S2. The role of sulfates/ sulfides within the slag in the kinetics of reaction of alkali-activated systems needs investigation, as it is unknown how this might affect how the reaction proceeds. In the case of S2 cements, the faster reaction identified in mixes containing 10% limestone is likely a consequence of the increased concentration of activator per gram of slag activated.

Mineralogical characterization

All mix designs show (Figure 2) similar diffraction patterns, with a broad reflection centred around 30° 2θ, consistent with the diffusive scattering characteristic of the anhydrous slag, as well as formation of a poorly crystalline calcium silicate hydrate (C-S-H) typically identified in sodium sulfate activated slag cements (Mobasher et al. 2016). The main crystalline phase identified in all mixes was ettringite ($3CaO{\cdot}Al_2O_3{\cdot}3CaSO_4{\cdot}32H_2O$; powder diffraction patterns (PDF) # 041-1451) whose intensity does not seem affected by the amount of limestone in the system. As expected, an increased limestone replacement induces higher intensity peaks assigned to calcite. The main difference between diffraction patterns of specimens with 7 and 28 days of curing is the intensity of ettringite peaks, which is higher at later curing ages. This is consistent with the progressive activation reaction at extended curing times.

Formation of AFm phases such as monocarbo- or hemicarboaluminates was not identified in these cements, conversely to those typically observed in composite cements containing limestone (Adu-Amankwah et al. 2017). This indicates that dissolution of limestone is not occurring in the composite cements produced with sodium sulfate, at least during the first 28 days of curing.

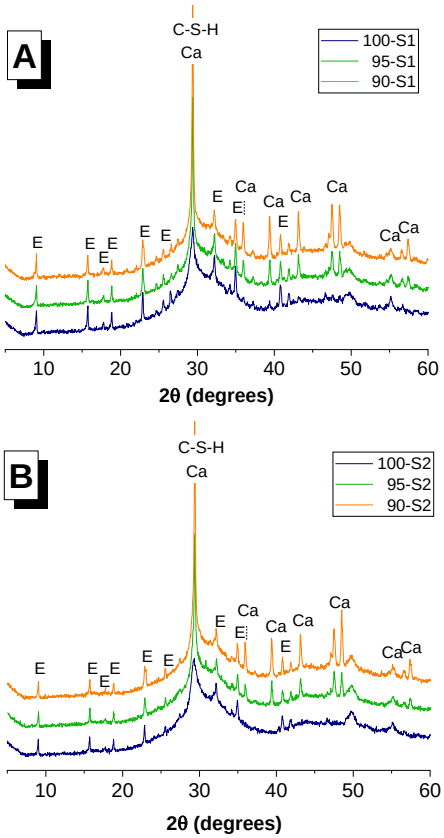

Figure 2. X-ray diffractograms of 28 day cured Na_2SO_4 activated composites cements produced with (A) S1 and (B) S2 slags. E - ettringite; Ca – calcium carbonate and C-S-H – calcium silicate hydrate

In Na_2SO_4 alkali activated slags traces of hydrotalcite are often observed (Mobasher et al. 2016) (Rashad et al. 2013). However, the formation of crystalline hydrotalcite type phases is not identified in any of the composite cements evaluated here. It is likely that the limited amount of Al_2O_3 within these systems is exhausted rapidly through the formation of ettringite, limiting formation of AFm type phases and/or poorly crystalline layered double hydroxides.

^{27}Al MAS NMR spectra of 28 days cured composite cements show (Figure 3) that upon Na_2SO_4 activation, the Al^{VI} region exhibits a resonance at 14.75 ppm assigned to ettringite (AFt), consistent with that observed by X-ray diffraction (Figure 2). The intensity of this band changes as a function of slag chemistry being more intense in cements produced with S1 slag. Two additional resonances at 11.15 ppm and 5.35 ppm are assigned to AFm/ LDH type phase (often hydrotalcite) and a third aluminate hydrate phase (T) (Mobasher et al. 2016) respectively. Despite these phases not being observed by X-ray diffraction, NMR spectroscopy reveals that traces of these phases are present in the assessed cements, most likely with a poorly crystalline structure. Composite cements produced with S2 show an enhanced peak at 11.15 ppm indicating a higher percentage of AFm/LDH phases,

which can be attributed to the increased MgO content in S2.

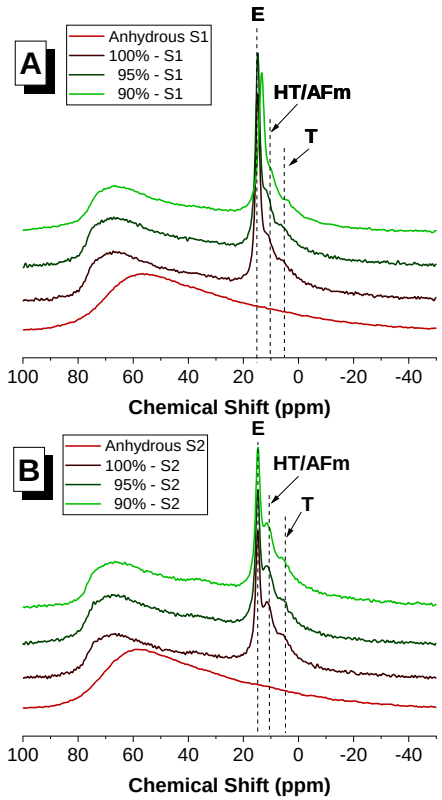

Figure 3. 27Al MAS NMR spectra of 28 days cured composite cements produced with (A) S1 and (B) S2 slags. E - ettringite, HT- hydrotalcite, T- third aluminate hydrate

The tetrahedral Al environments in the Al^{IV} region cannot be assigned to a single phase and partly correspond to the remainder of unreacted slag in the cements, and to the Al substituted in C-S-H type gels forming upon alkali-activation.

CONCLUSIONS

The slag chemistry influences the kinetics of reaction of composite cements activated with sodium sulfate. Cements produced with a slag with higher Al_2O_3 reacts faster. In the slag with less Al_2O_3, 10 wt.% limestone replacement accelerates the reaction kinetics, associated with an increased concentration of activator per gram of slag activated.

In all systems the main crystalline reaction product identified was ettringite. Negligible limestone dissolution was observed up to 28 days of curing, indicating that limestone is mainly acting as a filler. ^{27}Al MAS NMR results indicate that formation of poorly crystalline AFm/HT type phases is occurring particularly in cements produced with S2, hence, further investigation of these cements will be conducted at extended curing times to elucidate if dissolution of limestone might be favoured once the sulfates in pore solution are depleted.

ACKNOWLEDGEMENTS

This research was funded by EPSRC through the EC Fellowship EP/R001642/1.

REFERENCES

Adu-Amankwah, S., Zajac, M., Stabler, C., Lothenbach, B. and Black, L., 2017. Influence of limestone on the hydration of ternary slag cements. Cement and Concrete Research, 100: 96-109.

Ben Haha, M., Lothenbach, B., Le Saout, G. and Winnefeld, F., 2012. Influence of slag chemistry on the hydration of alkali-activated blast-furnace slag—Part II: Effect of Al_2O_3. Cement and Concrete Research, 42(1): 74-83.

Bernal, S.A., Provis, J.L., Fernández-Jiménez, A., Krivenko, P.V., Kavalerova, E., Palacios, M. and Shi, C., 2014. Binder chemistry–high-calcium alkali-activated materials. In Alkali activated materials: 59-91. Springer, Dordrecht.

Bernal, S.A., 2016. Advances in near-neutral salts activation of blast furnace slags. RILEM Technical Letters, 1: 39-44.

Juenger, M.C., Snellings, R. and Bernal, S.A., 2019. Supplementary cementitious materials: New sources, characterization, and performance insights. Cement and Concrete Research, 122: 257-273.

McLellan, B.C., Williams, R.P., Lay, J., Van Riessen, A. and Corder, G.D., 2011. Costs and carbon emissions for geopolymer pastes in comparison to ordinary Portland cement. Journal of cleaner production, 19(9-10): 1080-1090.

Mobasher, N., Bernal, S.A., Hussain, O.H., Apperley, D.C., Kinoshita, H. and Provis, J.L., 2014. Characterisation of $Ba(OH)_2$–Na_2SO_4–blast furnace slag cement-like composites for the immobilisation of sulfate bearing nuclear wastes. Cement and Concrete Research, 66: 64-74.

Mobasher, N., Bernal, S.A. and Provis, J.L., 2016. Structural evolution of an alkali sulfate activated slag cement. Journal of Nuclear Materials, 468: 97-104.

Provis, J.L. and Bernal, S.A., 2014. Geopolymers and related alkali-activated materials. Annual Review of Materials Research, 44: 299-327.

Rashad, A.M., Bai, Y., Basheer, P.A.M., Collier, N.C. and Milestone, N.B., 2012. Chemical and mechanical stability of sodium sulfate activated slag after exposure to elevated temperature. Cement and Concrete Research, 42(2): 333-343.

Rashad, A.M., Bai, Y., Basheer, P.A.M., Milestone, N.B. and Collier, N.C., 2013. Hydration and properties of sodium sulfate activated slag. Cement and concrete composites, 37: 20-29.

Shi, C., Roy, D. and Krivenko, P., 2003. Alkali-activated cements and concretes. CRC press.

39th Cement and Concrete Science Conference
9-10th September 2019
University of Bath
Paper Number 073

Structural changes in sodium carbonate activated slag binders induced by CO_2 exposure

Maria Criado[1,2], Xinyuan Ke[1,3], John L. Provis[1], Susan A. Bernal[1,4*]

[1]Department of Materials Science & Engineering, University of Sheffield, UK
[2]Eduardo Torroja Institute-CSIC, Spain
[3]Department of Architecture & Civil Engineering, University of Bath, UK
[4]School of Civil Engineering, University of Leeds, UK

ABSTRACT

The physical and chemical interaction between CO_2 and cementitious materials is referred to as carbonation, and is considered one of the main threats to our built environment. In alkali-activated materials, carbonation reactions can lead to significant changes in phase assemblages, an increase in porosity, and a loss in mechanical strength; however, the kinetics of carbonation are strongly dependent on factors controlling phase assemblage evolution in these systems, such as the type of precursor used in their production, the nature and amount of the activator utilised, and the curing conditions adopted. In this study the structural changes of sodium carbonate activated slag cements induced by accelerated carbonation under controlled exposure conditions (1% CO_2, 65% relative humidity and 23°C) are evaluated. The results are compared with those obtained for specimens exposed to natural carbonation conditions, to identify any changes in the type of carbonation products forming, as a function of CO_2 concentration. Conversely to what has been reported for silicate activated slag systems, when using sodium carbonate as activator, negligible carbonation of the specimens is identified upon natural or accelerated carbonation. The outcomes of this study demonstrate that the development of highly durable and carbonation resistant alkali-activated cements is feasible when using sodium carbonate as the alkali source.

1. INTRODUCTION

Carbon dioxide concentrations are the highest recorded in human history at present. This poses a significant threat to our cement-based built environment, as CO_2 once enters a concrete, it dissolves in pore water leading to an acid-base reaction known as carbonation (Fernandez-Bertos et al. 2004). In Portland cement systems, the formation of $Ca(OH)_2$ buffers the carbonation reaction. As the Portland cement fraction in concretes is reduced by addition of supplementary cementitious materials (SCMs), the content of $Ca(OH)_2$ is depleted by the pozzolanic reaction. This increases the carbonation susceptibility of SCMs containing concretes (Papadakis 2000). These is of great concern as most modern concretes contain high volumes of SCMs. Carbonation of concretes with SCMs reduced their mechanical strength, increases their porosity, in addition to reducing the internal pH of the concrete (Bucher et al. 2017). This reduces the ability of the concrete cover to protect the steel from corroding, and can reduce the service life of reinforced concretes.

Alkali activated cements are Portland clinker-free systems, produced by the chemical reaction of an alkali-activator and an aluminosilicate source (Provis 2014). For these alternative cements, carbonation is one of the main durability concerns for their use in structural application. However, the carbonation rates reported for these systems vary significantly under small modifications of the precursors used for their production, the type of activator added, and the carbonation exposure conditions adopted (Bernal et al. 2014). The large number of variables that influence performance poses a great challenge to elucidate the role of different factors in carbonation performance of alkali-activated cements.

Recent studies demonstrated that it is possible to produce carbonation resistance alkali-activated cements using sodium carbonate as activators (Ke X., et al. 2018). This as consequence of the phase assemblage of these cements, which favours CO_2 uptake without modifying the mechanical performance of the specimens. In this study, the phase assemblages of solid paste cylinders upon exposure to natural carbonation for 6 months, in a laboratory environment, are reported. Results are compared to those of accelerated carbonation specimens exposed to 1 $\%CO_{2(eq)}$, at a relative humidity of 65% and room temperature (21°C).

2. EXPERIMENTAL PROGRAMME

2.1. Materials and sample preparation

A commercial ground granulated blast furnace slag was used, containing CaO (41.3 wt.%), SiO_2 (36.0 wt.%), Al_2O_3 (11.3 wt.%), and MgO (6.5 wt.%). This

slag had a Blaine fineness of 5056 ± 22 cm^2/g (average value of four measurements), and an average particle size d_{50} of 11.2 ± 0.1 µm determined using laser diffraction. The activating solution was prepared by pre-dissolving commercial sodium carbonate powder (Sigma Aldrich, Na_2CO_3 ≥ 99.5%) into distilled water. Sodium carbonate-activated slag pastes were produced with an activator dose of 8 g Na_2CO_3 per 100 g slag, and a water/(slag+Na_2CO_3) mass ratio of 0.40. Pastes were mixed using an overhead mixer with a high-shear blade, cast in centrifuge tubes, then sealed and stored at room temperature (20 ± 3 °C) until testing.

2.2. Response to CO_2 exposure

Cylinder samples cured for 28 and 180 days were exposed to ~0.04% CO_2, described as *naturally carbonated*, and elevated carbonation conditions (1.0 ± 0.2% CO_2), described as *accelerated carbonated*. Under both carbonation conditions, temperature and relative humidity were controlled at 20 ± 2 ºC and 65 ± 5%. The carbonation depth was determined by spraying a 1 wt.% phenolphthalein solution onto a freshly split surface. Fuchsia colour indicates a pH > 10, while no colour is associated with a reduced pH (< 8).

Paste specimens from the non-carbonated core and the carbonated edge of the sample were analysed, with the aim to account for the structural evolution taking place in these cements as they continued to mature during the period of CO_2 exposure. Specimens were analysed through: (i) X-ray diffraction (XRD), using a Bruker D2 Phaser instrument with Cu-Kα radiation and a nickel filter, a step size of 0.02° and a counting time of 1 s/step, from 5° to 55° 2θ; and (ii) thermogravimetry-mass spectroscopy (TG-MS), in a Perkin Elmer TGA 4000 instrument coupled with a Hiden mass spectrometer: 30 mg of sample was tested from 30°C to 1000°C at a heating rate of 10°C/min, under nitrogen flowing at 40 mL/min.

3. RESULTS AND DISCUSSION

3.1. Carbonation profile

A sharp carbonation front was not identified, either in naturally or accelerated carbonated specimens. Instead, changes in colour along with severe cracking were observed (see Table 1). These results are consistent with other studies (Nedeljković et al. 2018) identifying a correlation between light grey regions, and the colourless regions observed after spraying of the phenolphthalein indicator. Changes in colour from dark green to light grey of slag-based specimens are associated with the oxidation of sulfides present in the slag as oxygen enters the material (Chaouche et al. 2017).

Table 1. Photographs of specimens exposed to 1% $CO_{2(eq)}$ for 14 days. All samples have a 15.5 mm diameter

Curing age	No indicator	With indicator
28 days		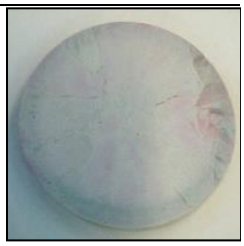
180 days	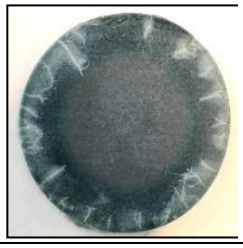	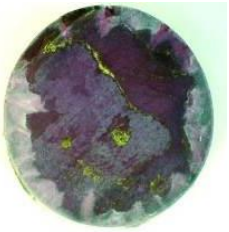

After 6 months of natural carbonation all samples, independent of the curing time, presented a few millimeters of light grey areas. Conversely, when exposing cylinder specimens to accelerated carbonation, significant differences were observed, when samples were cured for 28 or 180 days prior to CO_2 exposure. 28-day cured samples were completely carbonated after 14 days of 1% CO_2 exposure, exhibiting significant cracking, while those cured for 180 days presented just a few millimeters of colouration/alkalinity change (Table 1). These results highlight that extended curing times improves the resistance to carbonation of sodium carbonate activated slag cements. This is likely due to densification of the material as reaction progresses, as well as formation of an increased fraction of reaction products with the ability to chemically bind CO_2 at extended curing times (Ke et al. 2018).

3.2. X-ray diffraction

X-ray diffraction patterns of 28-day cured specimens after 7 days of natural and accelerated carbonation are shown in Fig. 2. Similar phase assemblages are observed at the edge and centre of the tested cylinders according to the carbonation exposure conditions. In the case of accelerated carbonated specimens, this is consistent with the total carbonation of the samples (Fig 1); however, as naturally carbonated specimens presented clear ‘carbonated’ and ‘non-carbonated’ regions it was expected that there would be more significant differences in the phase assemblage evolution between the edge and centre of the specimens. This indicates that even under natural carbonation conditions, some degree of carbonation will occur in the core of highly dense samples.

Prior to carbonation, the main crystalline phases identified are an aluminum substituted calcium silicate hydrate (powder diffraction file (PDF) # 00-019-0052), along with a layered double hydroxide with a hydrotalcite type structure (PDF# 00-014-0525). Traces of the calcium carbonate polymorphs vaterite (PDF# 00-033-0268) and calcite (PDF# 00-005-0586) were identified in non-carbonated samples, most likely as a consequence of weathering of the samples during testing, as these phases were not observed in the anhydrous slag (Ke et al. 2018) prior to mixing.

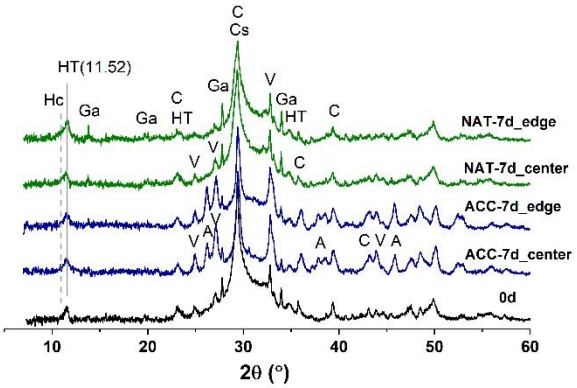

Fig 2. X-ray diffractograms of 28 d cured sodium carbonate activated slag cements carbonated under natural and accelerated conditions, where the following phases are present: Hc- hemicarboaluminate, HT – hydrotalcite, Ga – gaylussite, C – calcite, V- vaterite, Cs – calcium silicate hydrate

Upon carbonation all samples exhibit formation of hemicarboaluminate (PDF # 00-036-0129), along with increasing intensity of reflections corresponding to vaterite and calcite, consistent with the decalcification of C-A-S-H type gels, observed in previous studies in carbonated alkali-activated slag cements (Ke et al. 2018). In the case of accelerated carbonated pastes, it is clear that there is a sharpening of the C-A-S-H reflection, along with a reduction in intensity of the diffusive scattering. Formation of the calcium carbonate polymorphs aragonite (PDF # 00-041-1475) was solely observed under accelerated carbonation conditions. Aragonite was not identified as a carbonation product in cements with comparable chemistry tested using powdered samples (Ke et al. 2018). This indicates that the carbonation reaction products change depending on testing solid or powdered samples, due to differences in internal relative humidity and CO_2 concentrations in the tested specimens.

In naturally carbonated specimens gaylussite (PDF # 00-021-0343) is observed. Higher intensity reflections of hydrotalcite and gaylussite were identified at the edge of the sample. Gaylussite has been identified as a reaction product forming at early age (<7 d) in sodium carbonate activated slag cements (Bernal et al. 2015). The fact that this phase is present in aged samples, after natural carbonation, might indicate that this phase is not fully dissolved at longer curing times. Instead, what might be changing over the time of curing is its crystallinity.

3.3. Thermogravimetry analysis

The derivative of the mass loss, along with mass spectrometry results, for samples after 7 days of natural and accelerated carbonation are shown in Fig 3. The mass loss below 200°C is mainly attributed to removal of water loosely bound to the hydrated products forming in these cements, including a C-A-S-H type gel. The distinct shoulder observed at 133 °C is attributed to dehydration of LDH type phases, mainly hemi- and monocarboaluminates (Lothenbach et al. 2008), as observed by XRD (Fig. 2). In accelerated carbonated specimens, significant mass losses between 200 and 650 °C are identified, consistent with the decarbonisation of the different calcium carbonate polymorphs present in these specimens.

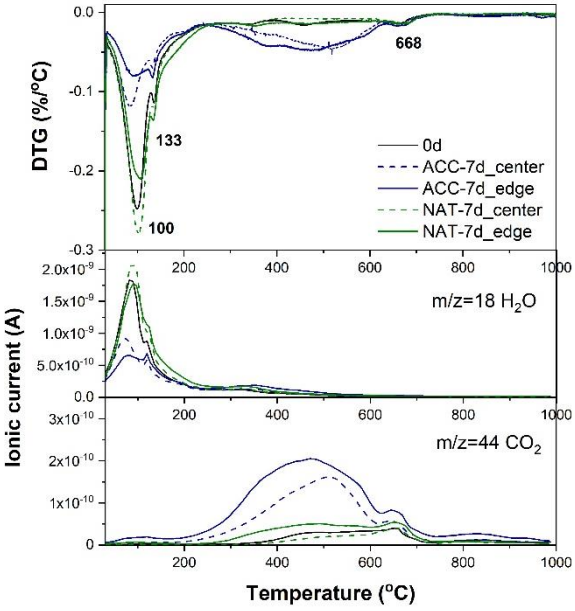

Fig 3. Derivative of the mass loss and mass spectrometry results for sodium carbonate activated slag pastes exposed to natural and accelerated carbonation

Slight differences in mass loss were identified between 200 and 400 °C in accelerated carbonated samples collected from the edge and from the centre of the solid tested specimens. This is consistent with the observed differences in the XRD reflections corresponding to aragonite and vaterite (Fig 2). This indicates that at the surface of the samples formation of aragonite prevails over other calcium carbonate polymorphs, despite the fact that it is expected that the CO_2 concentration at the edge of the sample is higher than in the centre of the specimens.

Although some carbonation products were identified by XRD (Fig 2) in naturally carbonated pastes, in both the edge and centre of the specimens, the thermogravimetry results indicate that these phases are presented in negligible amounts. This indicates that the evaluated specimens did not experience significant carbonation after 7 days of CO_2 exposure under natural conditions, consistent with the observed by Ke et al. (2018). In that study it was concluded that sodium carbonate activated cements have the ability to withstand exposure to CO_2.

4. CONCLUSIONS

Significant differences in carbonation progress are identified in alkali-activated slag specimens with different curing durations prior accelerated carbonation testing. This is likely consistent with the densification of the specimens as reaction progresses, and formation of larger fraction of CO_2-binding phases (e.g layered double hydroxides) takes place. These results highlight that resistance to carbonation of sodium carbonate activated slag cements significantly improves as the material ages.

Different carbonation reaction products were identified in specimens exposed to natural or accelerated carbonation conditions. Vaterite and calcite are the main carbonation reaction products observed under natural carbonation conditions, along with gaylussite, which seems to be a carbonation product of the pore solution. At high CO_2 concentrations, the three calcium carbonate polymorphs were observed, where aragonite seem to be the main carbonate forming at the surface of the specimens.

These results elucidate for sodium carbonate activated slag cement that the type and amount of carbonation products forming under natural and accelerated carbonation conditions are different. The evaluation of paste monoliths instead of powdered samples also reveals the strong effect of CO_2 gradients within the sample, and/or changes in internal humidity from the surface of the centre of the specimens, leading to formation of different types and amounts of carbonation products. It is thus recommended for microstructural studies to involve the evaluation of solid samples so that phase assemblage changes likely to occur during service can be more accurately identified.

ACKNOWLEDGEMENTS

This research was funded by the European Research Council under the European Union's Seventh Framework Programme (FP7/2007-2013) / ERC Grant Agreement #335928 (GeopolyConc). XK is grateful to U. Bath for her Prize Fellowship. The participation of SAB in this research was partially funded by EPSRC through ECF EP/R001642/1.

REFERENCES

Bernal, S.A. and Provis, J.L., 2014. Durability of alkali-activated materials: progress and perspectives. Journal of the American Ceramic Society, 97(4): 997-1008

Bernal, S.A., Provis, J.L., Myers, R.J., San Nicolas, R. and van Deventer, J.S.J., 2015. Role of carbonates in the chemical evolution of sodium carbonate-activated slag binders. Materials and Structures, 48(3), 517-529.

Bucher, R., Diederich, P., Escadeillas, G. and Cyr, M., 2017. Service life of metakaolin-based concrete exposed to carbonation: Comparison with blended cement containing fly ash, blast furnace slag and limestone filler. Cement and Concrete Research, 99,18-29.

Chaouche, M., Gao, X.X., Cyr, M., Cotte, M. and Frouin, L., 2017. On the origin of the blue/green color of blast-furnace slag-based materials: Sulfur K-edge XANES investigation. Journal of the American Ceramic Society, 100(4):1707-1716.

Fernandez-Bertos F., Simons, S.J.R., Hills, C.D. and Carey, P.J., 2004. A review of accelerated carbonation technology in the treatment of cement-based materials and sequestration of CO_2. Journal of Hazardous Materials, 112(3):193-205.

Ke, X., Criado, M., Provis, J.L. and Bernal, S.A., 2018. Slag-based cements that resist damage induced by carbon dioxide. ACS Sustainable Chemistry & Engineering, 6(4): 5067-5075.

Lothenbach, B., Le Saout, G., Gallucci, E. and Scrivener, K., 2008. Influence of limestone on the hydration of Portland cements. Cement and Concrete Research, 38(6), pp.848-860.

Nedeljković, M., Zuo, Y.B., Arbi, K. and Ye, G., 2018. New test method for assessing the carbonation front in alkali-activated fly ash/slag pastes. Key Engineering Materials, 761, pp.148-151.

Papadakis, V.G., 2000. Effect of supplementary cementing materials on concrete resistance against carbonation and chloride ingress. Cement and Concrete Research, 30(2): 291-299

Provis, J.L., 2014. Geopolymers and other alkali activated materials: why, how, and what?. Materials and Structures, 47(1-2): 11-25

39th Cement and Concrete Science Conference
9-10th September 2019
University of Bath
Paper Number 075

Frost durable concrete – the role of aggregates

Onome Onedo, Leon Black, Susan A. Bernal, Sam Adu-Amankwah
School of Civil Engineering, University of Leeds, LS2 9JT, Leeds, UK

ABSTRACT

Exposed to cyclic freezing and thawing, saturated concrete may deteriorate due to the expansive action of ice, reflecting as internal micro-cracks and/or scaling of surface matter. Air entraining agents (AEAs) have been used conventionally to protect susceptible concrete. AEAs retain an array of air bubbles in the concrete matrix, providing pressure-relieving mechanism to mitigate ice-induced tensile stresses. Previous studies identified the critical spacing factor i.e. minimum spacing between entrained air voids as the most important parameter in frost resistant concrete. However, factors including progressive cement hydration, nature of hydration products and handling of fresh concrete can destabilize the entrained air network. This study investigated the prospect of using porous lightweight aggregates to mitigate freeze-thaw degradation in concrete.
Concrete specimens were formulated with quartzite or manufactured lightweight aggregates. Two cement types, CEM I and slag-limestone ternary cement were evaluated. Fresh state properties including air content, density and flow table diameter were evaluated, while compressive strengths were determined on the hardened concrete. Permeability of the samples were assessed in terms of the apparent sorptivity co-efficient. Subsequently, test specimens were subjected to freeze-thaw conditions in deionized water using a modified capillary suction, internal damage and freeze-thaw (CIF) test method. Relative dynamic modulus, water uptake and the mass of scaled matter were measured regularly to ascertain the extent of freeze-thaw damage. The results indicate significantly improved internal damage resistance in the lightweight concrete. In contrast to the normal weight quartzite mixes, the cement type played a secondary role with respect to internal damage and surface scaling. This demonstrates the viability of lightweight aggregates as reliable alternative to AEAs.

1. INTRODUCTION

Degradation of concrete due to cyclic freezing and thawing presents a major durability challenge in cold climates. When in contact with water, capillary pores in concrete may become saturated and at freezing temperatures, the expansive ice induces tensile stresses on the pore walls. Above critical saturation, of ~ 91 % [1-3], freezing of the pore water causes deterioration since the increased volume due to ice formation can no longer be accommodated. Such deterioration may manifest as internal structural damage or surface scaling. The underlining mechanisms for these are often treated independently [1, 4]. Recent studies [5, 6] show that, deicing salt is not a precursor for surface scaling contrary to suggestions elsewhere [7, 8]. Microstructural effects involving phase assemblage and pore structure modifications have been espoused.
Nevertheless, incorporation of air entraining agents (AEA) significantly improves resistance to both surface scaling and internal damage [4, 9, 10]. In AEA concrete purposely incorporated air bubbles, stabilized in the hardened concrete matrix, provide a pressure relieving mechanism upon freezing [2]. Unlike entrapped air, the distribution of voids in AEA concrete is more homogenous with consistent size ranges. To effectively relieve pressures caused by ice formation in confined pores, a range of air void spacing factors for different water to cement (w/c) ratios have been reported [1, 3]. A spacing factor below 200 µm factor was recommended. However, the AEA dosage does not necessarily correlate with the spacing factors [11]. Meanwhile, instability of AEA bubbles as a function of composition and handling is also recognized.
Limited data on freeze-thaw resistance of lightweight aggregate concrete is reported. Mao and Ayuta [12] found improved resistance but these low-density aggregates were less effective. Kucharczyková *et al.* [13] reported similar findings. However, efficiency of the aggregates diminished once they were saturated.
This study focuses on assessing the freeze-thaw resistance of structural Lytag concrete. The aggregates comprise evenly dispersed discrete cenospheres trapped in an interconnected honeycomb matrix. Pores range from nano- to micrometer sizes, with a water permeable membrane [14]. It is hypothesized that lightweight aggregates present a pore network capable of relieving stresses from ice-growth in the cement matrix. The efficiency of Lytag concretes is compared to concrete mixes formulated with normal weight, quartzite aggregate.

2. MATERIALS AND METHODS

Table 1 shows the investigated concrete mixes.

Table 1. Concrete mix design (kg per m^3 of concrete) and fresh concrete properties

Mix ID	CEM I	GGBS	Limestone	Effective water	Aggregates		Plasticiser	Density (kg/m^3)	Flow dia. (mm)	Air content, %
					Fine	Coarse				
C - NW	320.3			160.2	648.1	1181.5	6.4	2370	460	1.1
C - LW	320.3			160.2	116.7	340.3	6.4	1680	580	5.6
T - NW	163.9	121.8	27.4	160.2	644.5	1175.2	6.4	2360	440	1.3
T - LW	163.9	121.8	27.4	160.2	116.7	340.3	6.4	1650	540	6.0
Density (NW / LW), kg/m^3	3120	2930	2720	1000	2610 / 470	2570 / 740	1060			

Note: The SO_3 content in the T- mixes was raised to 3 %. Water absorption for NW and LW aggregates were 2 and 15 % respectively.

These were prepared from CEM I 52.5 R and slag-limestone ternary blend, herein designated C and T. Normal weight (NW) and lightweight (LW) aggregate concrete were examined. In the lightweight concrete, both the fine and coarse aggregates were replaced.

The fine aggregate was expanded clay (by Leca® UK) and the coarse aggregate, 10 mm Lytag (by Aggregate UK). The concrete mix design was based on the yield method, taking into account relative densities of all constituent materials. The w/c ratio was maintained at 0.5 and the fine to coarse aggregate ratio was 0.54. Moisture absorption by the aggregates was accounted in the mix design. Additionally, a high range water reducing admixture was added for comparable workability.

Concrete sample preparation was based on BS EN 12390:2. Assessed fresh state properties were density, air content (using an 8-litre test container according to BS EN 12350-7:2009) and flow table test. In measuring the density and air contents, full compaction of the concrete was achieved on a vibrating table. Reasonable care was taken to avoid over-vibration. For calculating the fresh air content, the aggregate correction factor was not determined and hence assumed nil. Specimens were kept in the mould for 24 hours before de-moulding and samples immediately stored in water for 7 days. Conditioning was based on PD CEN/TR 15177:2006.

Capillary suction was performed after conditioning at 65 % relative humidity and 20 ◦C for 21 days. Prior to this, the 150 mm cubes were cut into halves. Three samples per mix were tested for capillary water absorption using the surface cast against PTFE sheet as test surface. The lateral sides were sealed in epoxy resin. The test surfaces were placed on 5 mm high stainless spacers in a test container. The container was filled with deionized water with the test surface 5 mm under water. The mass change due to suction was recorded regularly for the first 64 minutes using an electronic balance with 0.1g reading accuracy. Apparent sorptivity was taken as the slope of the mass of absorbed water versus square-root of time plot.

The CIF method according to PD CEN/TR 15177: 2006 was used for freeze-thaw resistance testing in deionized water after saturating the samples by capillarity for 7 days. Internal structural damage, sample mass change and the scaled matter were measured at regular intervals up to 56 freeze-thaw cycles. The temperature versus time profile used in the present study, however, differed from the prescribed profile for CIF in terms of the freezing and thawing rate. A complete freezing and thawing cycle took 24 hours cycles as opposed to the 12 hour cycle in PD CEN/TR 15177: 2006.

The scaled mass was collected at regular intervals, then dried at 40 °C to constant mass. The deviation from the prescribed 110±10°C drying temperature was to preserve all phase assemblages in the specimen, particularly ettringite and the carboaluminate phases. Internal structural damage was determined based on regular measurement of the transit time using a Proceq Pundit Lab+ ultrasonic pulse velocity kit as prescribed.

3. RESULTS AND DISCUSSION

Fresh state properties of the mixes are shown in Table 1. Lightweight aggregate mixes were more workable, irrespective of binder type. This is due to the additional water added to account for absorption by the lightweight aggregates. Approximately 70% of the pores in such aggregates may be saturated instantaneously [14]. Thus, excess free water was available to lubricate the particles. One would expect increased workability in the blended cement. However, partial replacement of CEM I with more finely ground slag counteracted this. The lightweight mixes conformed to density class D1.8 (EN 206:2013); representing 30% reduction in density compared to the normal weight mixes.

Air content of the fresh concrete is an important parameter for freeze-thaw resistance [1, 2, 7]. The lightweight concrete mixes showed higher total air content being comparable to the reported ranges in

AEA concrete [9, 11]. The porous aggregates, rather than the additional water for absorption by the aggregates seems the most plausible explanation. The interfacial transition zone (ITZ) formed with the Lytag can be heterogeneous [14] but remain permeable. This implies exchange of matter (i.e. ice, water or vapour) with the paste phase can be sustained at longer saturation times.

Figure 1 shows 28d compressive strength of the samples, revealing an approximately 30 % reduction in strength for the lightweight mixes. The extent of strength reduction was independent of the cement type, highlighting the significance of density on strength. The trends are also consistent with the air content measured in the fresh concrete (Table 1). Observation of the specimens at the end of the strength test revealed cracks through the lightweight aggregates governed the failure mode as opposed to through the paste matrix, as noted in the normal weight concrete. The potential for internal curing in lightweight concrete would be expected to promote further hydration. However, such benefits may be long term since excess free-water is already present at 0.5 w/c ratio.

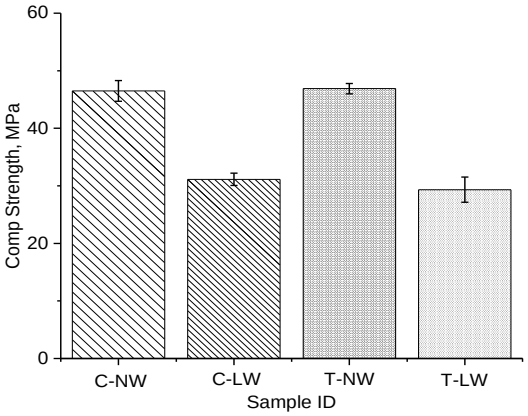

Figure 1. Effect of aggregate type compressive strength of concrete at 28d

Figure 2 shows the capillary water absorption results during the first hour of saturation. The absorbed water volume is typical of air entrained concrete [10]. The lightweight mixes showed greater water sorption compared to the normal weight blends, indicative of greater porosity. This is consistent with the trend observed in the air content presented in Table 1. Consequently, it can be ascribed that water-filled pores herein were dominated by the lightweight aggregates. The apparent sorptivity co-efficient, taken as slope of the absorption versus square root of time plot, confirms greater water permeability amongst the lightweight concrete samples. The effect of the cement type was also apparent. For a given aggregate, the ternary cement concrete showed reduced sorptivity compared to the CEM I mix, indicative of lower permeability. This may seem inconsistent with the compressive strength data in Figure 1, where the effect of cement type was negligible. However, one must recognize that, the aggregate type, rather than the paste, governed failure under compression. In relation to freeze-thaw resistance, greater sorptivity has two implications: above critical saturation, damage may be accelerated in a similar fashion to entrained air voids [10]. Meanwhile, once under-saturated, they serve as pressure relieving centres, leading to improved resistance.

Freezing of capillary water is not congruent. The range of pores within which freezing take place depends on saturation degree, pore size, pore fluid composition and temperature [1, 15]. The pore size is important because it determines whether water is adsorbed to pore wall and hence unfreezable or vice versa. The water absorbed during freeze-thaw exposure provides a basis on which to quantify the degree of saturation.

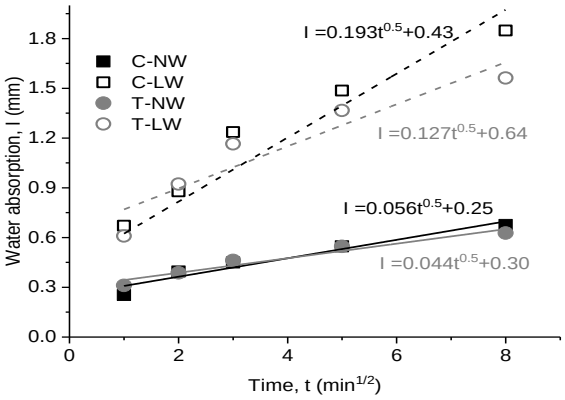

Figure 2. Effect of aggregate type on water absorption of concrete samples in the first hour of capillary suction, showing apparent sorptivity coefficient.

The mass loss due to drying after the 21d conditioning was used as indicative capillary pore volume, which may be re-saturated by capillary suction and during freeze-thaw. The degree of saturation, S, was thus determined as the ratio of absorbed water to this pore volume. Figure 3 shows the results as a function of the cement and aggregate types. Up to 30% saturation occurred within the first hour of capillary suction and 50% after 7 days. This suggests the equilibration resulted in drying of pores with smaller hydraulic radius (either in the aggregate or paste). These saturate at a slower rate compared to the bulk meso to macro-sized capillary pores [15]. The time to reach critical saturation (i.e. 91%) is shown in Figure 3. Although a higher water absorption rate was observed in the LW aggregate concrete (Figure 2), they were clearly under-saturated even after 56 cycles. At the end of the test, the degree of saturation was approximately 70% and 80% in the CEM I and ternary concrete respectively. This indicates that, the initial saturation (see Figure 2) affected the test surface rather than the bulk concrete. Meanwhile, the normal weight concrete mixes were over-saturated confirming greater susceptibility in the ternary mix [5]. An accelerated moisture uptake accompanied the

critical saturation (see Figure 3), suggesting uptake through additionally formed micro-cracks.
Internal damage and surface scaling results are presented in Figure 4. The normal weight aggregate samples already exceeded the 80% failure limit before 56 FT cycles, occurring sooner in the ternary samples.

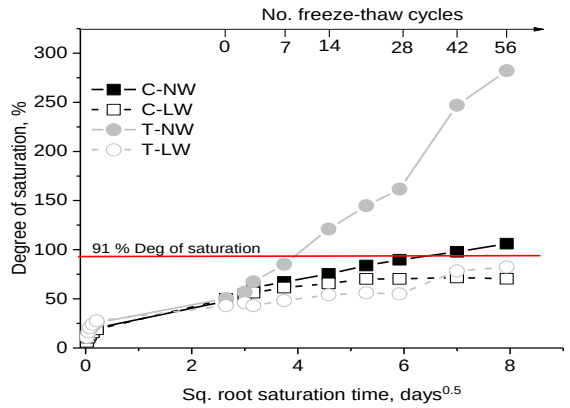

Figure 3. Degree of saturation of concrete as a function of the type of cement and aggregate

No internal damage was observed in the LW mixes, consistent with other studies on lightweight concrete [12, 13].

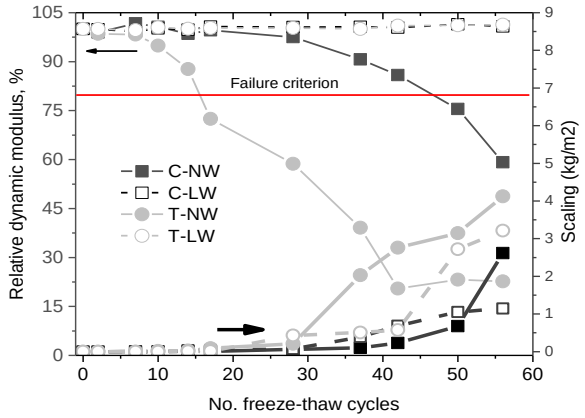

Figure 4. Effect of aggregate type on internal damage (RDME) and surface scaling of concrete

Onset of internal damage coincided with critical saturation (Figure 3). Consequently, saturation seems to be the most important factor controlling internal damage. The results clearly demonstrate lightweight aggregates are effective in this regard. As pointed out already, these contain various sized pores which may be under-saturated even after prolonged exposures [14], preserving the matrix during freezing. The extent of under-saturation however, reduced with increasing cycles (Figure 3). This is explained by localized saturation and hence, cracking can be envisaged a longer FT cycles.
Nevertheless, surface scaling evolved in all mixes (Figure 4). The effect of aggregate type was negligible. Consistently, the ternary mix showed greater susceptibility to scaling. This underscores importance of the microstructure on surface scaling. With the scaled matter essentially cement paste (on the surface); their condition at the time of commencing perhaps dictated resistance. In all mixes however, scaling was delayed until about 30 cycles, again deviating from internal damage. Consequently, the progress of internal damage may equally influence the surface scaling.

4. CONCLUSIONS

The effects of lightweight and normal weight aggregates on freeze-thaw resistance of concrete have been investigated. For the same mix design, the lightweight aggregate concrete showed greater apparent sorptivity and lower compressive strength. However, they remained under-saturated throughout the 56 freeze-thaw cycles. This prevented internal damage. Despite this, scaling still occurred with comparable magnitudes as normal weight concrete. These findings represent an important step in understanding the relationship between microstructure and freeze-thaw resistance of concrete.

ACKNOWLEDGEMENTS

This research was carried out, in part, at the UKCRIC National Centre of Infrastructure Materials at University of Leeds, sponsored by EPSRC grant EP/P017169/1.

REFERENCES

[1] Fagerlund G. Internal frost attack - State of the art. In: Setzer MJ, Auberg R, editors. Frost Resistance of Concrete Proceedings of the International RILEM Workshop. Essen1997. p. 321 - 38.
[2] Powers TC. A Working Hypothesis for Further Studies of Frost Resistance of Concrete. ACI Journal Proceedings. 1945;41(1):245-72.
[3] Powers TC, Helmuth RA. Theory of volume changes in hardened Portland cement paste during freezing. Highway Research Board. 1953;32.
[4] Valenza JJ, Scherer GW. Mechanism for Salt Scaling. Journal of the American Ceramic Society. 2006;89(4):1161-79.
[5] Adu-Amankwah S, Zajac M, Skocek J, Haha MB, Black L. Relationship between cement composition and the freeze–thaw resistance of concretes. Advances in Cement Research. 2018;30(8):387-97.
[6] Penttala V. Surface and internal deterioration of concrete due to saline and non-saline freeze–thaw loads. Cement and Concrete Research. 2006;36(5):921-8.
[7] Foy C, Pigeon M, Banthia N. Freeze-thaw durability and deicer salt scaling resistance of a 0,25 water-cement ratio concrete. Cement and Concrete Research. 1988;18(4):604-14.
[8] Marchand J, Pigeon M, Bager D, Talbot C. Influence of Chloride Solution Concentration on Deicer Salt Scaling Deterioration of Concrete. Materials Journal. 1999;96(4):429-35.
[9] Liu Z, Hansen W. Freezing characteristics of air-entrained concrete in the presence of deicing salt. Cement and Concrete Research. 2015;74:10-8.
[10] Li W, Pour-Ghaz M, Castro J, Weiss J. Water Absorption and Critical Degree of Saturation

Relating to Freeze-Thaw Damage in Concrete Pavement Joints. Journal of Materials in Civil Engineering. 2012;24(3):299-307.
[11] Michel Pigeon PP. Air Void Stability, Part I: Influence of Silica Fume and Other Parameters. Materials Journal. 1989;86(5):482-90.
[12] Mao J, Ayuta K. Freeze–Thaw Resistance of Lightweight Concrete and Aggregate at Different Freezing Rates. Journal of Materials in Civil Engineering. 2008;20(1):78-84.
[13] Kucharczyková B, Keršner Z, Pospíchal O, Misák P, Daněk P, Schmid P. The porous aggregate pre-soaking in relation to the freeze–thaw resistance of lightweight aggregate concrete. Construction and Building Materials. 2012;30:761-6.
[14] Swamy RN, Lambert GH. The microstructure of Lytag aggregate. International Journal of Cement Composites and Lightweight Concrete. 1981;3(4):273-82.
[15] Setzer MJ. Basis of testing the freeze-thaw resistance: surface and internal deterioration. In: Setzer MJ, Auberg R, editors. RILEM Proceedings Frost Resistance of Concrete: E&FN Spon; 1997. p. 157-73.

39th Cement and Concrete Science Conference **Paper Number 077**
9-10th September 2019
University of Bath

Characterization of sorption cycles in the cement hydrates

Monisha Rastogi, Mohsen Ben Haha
HeidelbergCement Technology Center, Leimen, Germany

Karen Scrivener
EPFL, Lausanne, Switzerland

ABSTRACT

Sorption induced deformations, attributed to changes in moisture content, in cementitious materials potentially contribute towards degradation and failure. Majority of the moisture movement is governed by calcium-silicate-hydrate (C-S-H), which is the binding matrix in cement-based materials. Hence, investigation of sorption response of C-S-H and the associated microstructural changes is imperative for durability assessments. In this regard, representative C-S-H samples were synthesized at 20 and 55 °C using white cement and silica fume with high water to cement ratio of 0.7. Characterization techniques such as SEM, MIP, XRD, and TGA were employed to evaluate various attributes including microstructure, pore size distribution, quantification of the phases, and content of portlandite, respectively. Hardened cement pastes were subjected to short-term water sorption cycles using dynamic vapor sorption technique. Thereafter, the samples were compared for their pore size distribution, overall moisture content and specific surface area.

1. INTRODUCTION

The cyclic changes in the water content of cementitious materials induce moisture movement, which is generally attributed to capillary suction, condensation, and gradient density of water vapor among others. Owing to strong capillary pressure on pore walls shrinkage (during drying) or swelling (during wetting) occurs, which damages the microstructure of cementitious materials.

Calcium silicate hydrate (C-S-H) is the main binding phase of hardened cement paste (hcp) which governs most of the moisture movement. The pore space of hcp is composed of capillary pores (~5-50 nm), gel pores (~2-5 nm), and interlayer water (<0.5 nm). Recently, ^{1}H NMR spectroscopy was employed to successfully classify the RH range in which a particular type of porosity is affected, by probing the desorption isotherm(Gajewicz, Gartner, et al. 2016). It was observed that capillary pores are affected in the RH range of 99-85 %, whereas gel pores and interlayer pores need 85-25 % and below 25 % RH, respectively.

Investigating moisture response (drying/wetting) of C-S-H is often challenging owing to its colloidal nature. ^{1}H NMR, small angle X-ray scattering and capturing nitrogen and water vapor sorption isotherms (WVSI) are few techniques that facilitate comprehension of the microstructural changes during sorption (Juenger and Jennings 2001, Adolphs 2005, Baroghel-Bouny 2007, Muller, Scrivener, et al. 2013, J).

In this experimental investigation, WVSI technique was used to investigate the moisture response in the representative sample with a dominant C-S-H phase. WVSI establishes the relationship between the equilibrium water content of the cementitious material and relative humidity, at a given temperature. The individual sorption isotherm can be divided into adsorption and desorption branches. As the process is not perfectly reversible, the branches do not follow the same path and hysteresis is observed. Ink bottle, the difference between the liquid-vapor interface curvature, and varying solid-liquid contact angle are some of the reasons that have been attributed to the origin of hysteresis. Additionally, the shape of the hysteresis is governed by the type of pores present in the sample.

WVSI has several advantages such as (i) the smaller diameter (0.28 nm) of water molecule, which allows it to enter the smaller pores as compared to nitrogen or argon (conventional gas sorption techniques); (ii) moisture sorption cycles are recorded at room temperature; and (iii) owing to the polar nature of the water molecule, it can interact with the adsorbate. Sorption of water is governed by several competing factors which include dipole polarization effects arising from surface charges, surface-water interaction mechanisms, hydrogen bonding between water and oxygen or hydroxyl ions, Van der Waals forces, and hydration of ions residing at or near surfaces. Using a combination of models/approaches could help to elucidate the moisture sorption isotherms, especially with respect

to the internal pore surface. Other parameters obtained from such models can provide crucial inputs toward solving the diffusion equation for drying and wetting of concrete and methane release among others.

The aim of this study is to capture the short-term WVSI of the samples cured at different temperatures. Characterization of these WVSIs facilitated a comparison of the morphology of the two samples for differences arising due to different curing temperature and the first drying cycle.

2. Experimental method

2.1 Materials

White clinker was obtained from Aalborg Portland, Denmark. The composition of the anhydrous powder is C_3S (65.3%), C_2S (28.8%), C_3A (1.9%), CH (2.51%) with the rest of the phases contributing less than 1% (by weight). The clinker was subjected to grinding until d_{50} and d_{90} values of 5 µm and 18 µm, respectively, were obtained. Condensed silica fume (SF; 10 wt.%) was obtained from ELKEM and used for its high pozzolanic activity. Table 1 corresponds to the XRF analysis of the clinker and SF used in this study. Hemihydrate (HH) was used to prevent flash setting.

Table 1: Chemical composition of white cement and silica fume as determined by X-ray fluorescence elemental analysis

Chemical content	SiO_2	Al_2O_3	MnO	Fe_2O_3	CaO	MgO	K_2O	Na_2O	SO_3	Total
weight % clinker	25,25	2,07	0,01	0,13	69,91	0,64	0,15	0,22	0,19	99,48
weight % SF	96,19	0.19	0.01	0	0.23	0.45	0.8	0.16	0	99.1

Finely ground white clinker, 5.5% HH, and 10% SF were mixed with water to attain a w/b of 0.7. Thereafter, this slurry was intensively mixed by using Ultra-turrax® at 24000 rpm for 90s and at lower speeds (8000-12000 rpm) for 30 s to achieve homogenization.
Finally, this homogenized mixture was transferred to different vials (4 cm X 7 cm) corresponding to the two temperatures of 20 and 55 ℃ and were cured in water. After a few hours, the samples were inspected for any signs of bleeding that could occur owing to higher w/b ratio. No bleeding was observed in the samples, which could be attributed to the high surface area of SF.

2.2 Methods

For X-ray diffraction analysis and Rietveld refinement, fresh discs of 3 mm thickness were cut from the sealed cylinders after 90 days.
Bruker D8 Advance (θ-2θ configuration) with monochromatic CuKα radiation (λ = 1.54059 Å) and a step-size of approximately 0.02° was used to acquire data in the range of 5° to 70° (2θ). To calculate the degree of hydration of clinker phases Rietveld refinement was performed with Topas software using quartz as the external standard.

Solvent exchange with isopropanol was performed on the samples after 90 days. Thin discs of thickness~ 2 mm were cut from the hardened cement cylinders and stored in isopropanol, which was replaced after 1 hour and 1 day. After 3 days of isopropanol immersion, the samples were stored in desiccators with silica gel beads under vacuum conditions to facilitate evaporation of isopropanol.
The disc was crushed and the resulting powdered samples (weighing 30 ± 2 mg) were subjected to thermogravimetric analysis (TGA) using a Netzsch STA 449 F3‘‘Jupiter” device. Nitrogen purging with the heating rate of 20K/min was used during the heating and cooling cycle.

Scanning electron microscope (SEM) images were acquired using FEI Quanta 200 coupled with a Bruker XFlash 4030 EDS detector. 2 mm thick disc (solvent exchanged) was impregnated with epoxy resin under vacuum condition in a mold. The samples were de-molded the next day and subsequently polished down to 1 µm using diamond spray and petrol-based lubricant.

Mercury intrusion porosimetry (MIP) was used to investigate the pore size distribution for these samples. Crushed samples (after solvent exchange) were investigated up to a maximal pressure of 400 MPa using a Pascal 140/440 Porosimeter (Thermo Scientific). Washburn equation was used to calculate the cumulative pore volume, by taking the contact angle and the surface tension of mercury to be 140° and 0.48 N/m, respectively.

Moisture sorption isotherms were recorded using dynamic vapor sorption (DVS) technique by employing DVS Adventure from Surface Measurement Systems: Fresh samples were used for DVS measurements (no solvent exchange). Sample weighing~30 mg were crushed and subjected to 98 % RH, followed by step-wise data acquisition from 98 % to 3 % with a step size of 5%. This process was used to acquire the first desorption cycle and the adsorption isotherm was obtained by reversing the RH steps. Mass equilibrium was identified as the point at which the percent mass change per unit time (dm/dt) was less than 0.0025mg/10min, or if the time at a given RH step exceeded 360 min.

3. Results and Discussion

Pozzolanic SF facilitated in converting the portlandite into C-S-H. TGA and XRD were used to calculate the amount of portlandite and degree of hydration of clinker phases, respectively, in the samples cured at different temperature for 90 days. Amount of portlandite in the sample cured at 20℃ was found to be 9-12g/100g, whereas for the

sample cured at 55℃ a low value of 4-6g/100g cement was observed. Degree of hydration for the samples was estimated by Rietveld refinement and found to be roughly 87% and 93% for samples cured at 20℃ and 55℃ after 90 days, respectively.

Figure 1 corresponds to the SEM image of the microstructure of hcp cured at 55 ℃ for 90 days. The image reveals satisfactory homogenization of the raw materials (as SF tends to agglomerate) along with the presence of Headly grains.

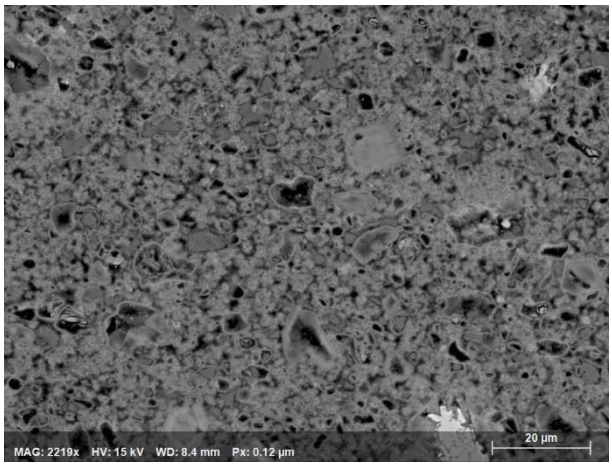

Figure 1. SEM image of the sample cured for 90 days at 55 ℃ with 10% SF.

MIP technique was employed to compare the intruded volume and the pore size distribution of the samples cured at 20 and 55 ℃. It was observed that the total intruded volume was more for the sample cured at 55 ℃, whereas the characteristic diameter for mercury penetration was almost same (60-70 nm) for both the samples.

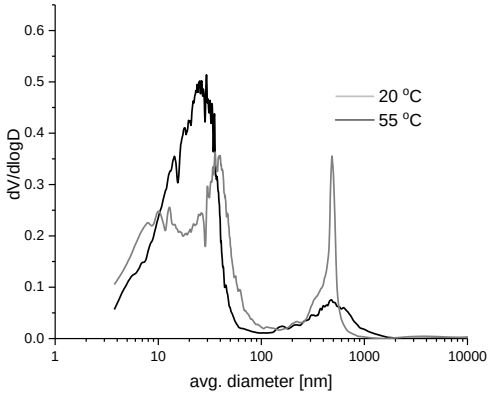

Figure 2. Pore size distribution for the samples from MIP analysis cured at 20 and 55 ℃.

Furthermore, the volume of the accessible mercury in the range of fine pores (4 to 10 nm) was higher in the samples cured at 20℃ suggesting higher gel porosity. However, capillary porosity was higher for the samples cured at a higher temperature. Nevertheless, we concede that MIP is not sufficient to provide insights into the absolute total pore volume or pore size distribution (especially in the range of gel pores). However, satisfactory capillary pore size distribution can be obtained using this technique.

Short-term sorption isotherms were recorded using DVS for the samples cured at two different temperatures after 90 days of curing. Figure 3 shows the first two sorption cycle for the samples cured at 55℃**.** The overall moisture content of the samples cured at 20℃ (not shown here) was higher than that of the samples cured at 55 ℃. The sorption isotherms were investigated using the BJH model to obtain the pore size distribution.

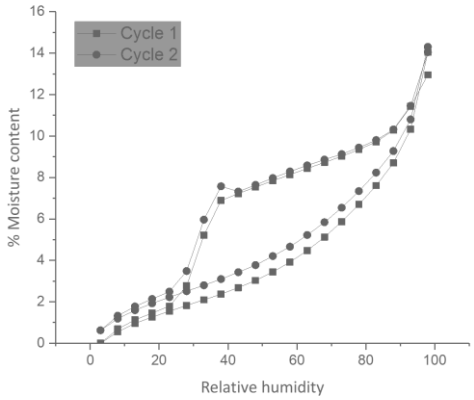

Figure 3. First two desorption cycle corresponding to samples cured at 55 ℃

The model was applied to both desorption and adsorption branches of the first cycle. The distribution obtained from desorption isotherm elucidates pore necks diameters whereas that from adsorption corresponds to pore diameters. The BJH model is based on the following assumptions: (1) pores are cylindrical, and (2) amount of adsorbate in equilibrium is retained by the adsorbent with two mechanisms

a) Physical adsorption on walls

b) Capillary condensation in the inner capillary volume to evaluate the pore size distribution and thickness of the adsorbed layer as a function of relative humidity.

Figure 4 shows the pore size distribution obtained from BJH analysis using both branches for the samples cured at 20 and 55 ℃ for 90 days. It was observed that the gel water content decreases as the curing temperature of the samples increases. Notably, using the BJH model for desorption isotherm may produce a peak at pore width~3.4 nm which is attributed to the tensile strength effect. It arises as a macroscopic meniscus cannot exist beyond mechanical stability and this causes spontaneous evaporation of the pore liquid resulting in this artificial step. Additionally, the first and

second cycles were observed to be almost comparable except in capillary pore domain of RH, which suggests that the first drying cycle did not cause any irreversible changes

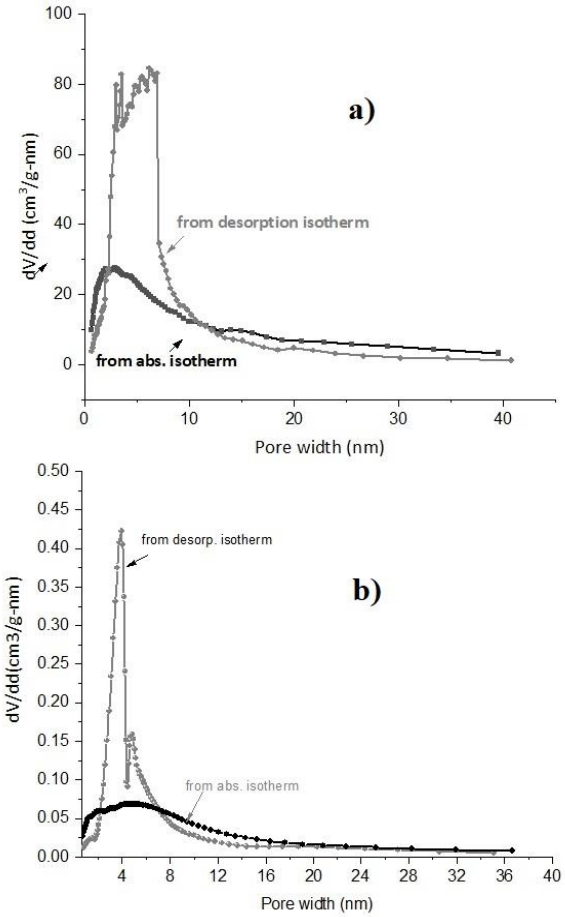

Figure 4. Pore size distribution from BJH adsorption and desorption branch for the sample cured at (a) 20 and (b) 55 ℃ for 90 days.

From the shape of the hysteresis, it could be concluded that the samples cured at 55 ℃ comprise mostly of slit pores whereas cylindrical and spherical pores are prominent in samples cured at 20 ℃. H3 type of hysteresis, according to the classification provided by IUPAC was found in both the samples.

BET surface area was estimated using the adsorption branch in the RH range of 5 % to 35 %. The BET surface area of samples cured at 20 ℃ was calculated to be 156 m^2/g whereas for the sample cured at 55 ℃ a value of 110 m^2/g was obtained.

4. Conclusion

Samples cured at 20 and 55 ℃ with C-S-H as the dominant phase were investigated using WVSI. Several characterization techniques were employed to consider the samples as a satisfactory starting point, which includes sufficient homogenization, degree of hydration, and lower portlandite content, among others. Short term BJH analysis facilitated in revealing the pore size distribution of the samples cured at different temperatures. It could be concluded that gel porosity decreases as the temperature increases. The first drying cycle did not induce irreversible changes. The BET surface area of the samples cured at 20 ℃ is higher than for the samples cured at 55 ℃. Finally, it could be concluded that capturing WVSI is a useful technique to analyze the influence of curing temperature, drying cycle and moisture response of the samples.

4. Acknowledgment

The research leading to these results has received funding from H2020-MSCA-ITN ERICA project with grant agreement ID 764691.

5. References

Adolphs, J. (2005). Surface energies of hardened cement paste depending on relative humidity. Materials and structures 38(4): 443-448.

Baroghel-Bouny, V. (2007). Water vapour sorption experiments on hardened cementitious materials: Part I: Essential tool for analysis of hygral behaviour and its relation to pore structure. Cement and Concrete Research 37(3): 414-437.

Gajewicz, A., E. Gartner, K. Kang, P. McDonald and V. Yermakou (2016). A 1H NMR relaxometry investigation of gel-pore drying shrinkage in cement pastes.Cement and Concrete Research 86: 12-19.

Juenger, M. C. G. and H. M. Jennings (2001). The use of nitrogen adsorption to assess the microstructure of cement paste. Cement and Concrete Research 31(6): 883-892.

Muller, A., K. Scrivener, A. Gajewicz and P. McDonald (2013). Use of bench-top NMR to measure the density, composition and desorption isotherm of C–S–H in cement paste. Microporous and Mesoporous Materials 178: 99-103.

39th Cement and Concrete Science Conference
University of Bath
9-10th of September 2019

Paper Number 078

Calcium-silicate-hydrates from reactive dicalcium silicate binder

Adrian Alexandru Pirvan, Mohsen Ben Haha
Global Research&Development, HeidelbergCement Technology Center, Germany

Emmanuelle Boehm-Courjault, Karen L. Scrivener
Laboratory of Construction Materials, École Polytechnique Fédérale de Lausanne, Switzerland

ABSTRACT

Knowledge of the microstructure of hydrated cement paste is essential for forecasting its performance. The main phase responsible for transport properties in a hydrated cement is the C-S-H. Thus, in order to study the C-S-H it is necessary to isolate this phase. Reactive belite recently developed by Link et al. has several advantages in comparison to traditional OPC, making it easier to study C-S-H in a real microstructure. For the same degree of hydration, the reactive belite will form more C-S-H and less $Ca(OH)_2$ compared to OPC. This results in a microstructure composed almost entirely of C-S-H. Additionally, the reactive belite is far more reactive than the traditional OPC-belite, achieving full hydration of its reactive constituents after the first 7 days of reaction. First research activities focused on successfully synthesizing the alternative belite binder with high hydraulic activity. Subsequent hydration studies were performed on pastes with different water-to-binder ratios as well as with different contents of reactive silica. The changes in the chemical composition of the C-S-H together with the variations in the portlandite content were observed and quantified. Additionally, porosity measurements were performed for all systems. The hydration processes were systematically followed by isothermal calorimetry, X-ray diffraction and scanning electron microscopy (SEM). The tendency of these alternative belite-binders to form a rich C-S-H matrix allowed us to study the effect of C-S-H chemical composition on its morphology, its ionic ad- and ab-sorption capacities and on its resulting pores distribution (gel and capillary pores) necessary to understand the transport properties.

1. INTRODUCTION

Nowadays, cement industry delivers the most used man-made material on the planet (John, Matschei, and Stephan 2018). Ordinary Portland cement (OPC) is an artificial material worldwide produced from locally available resources including limestone, clay, gypsum and other materials. In spite of its high usage, there are still open questions regarding its performance at different ages. Cement is a multicomponent system that evolves from the moment it is mixed with water. The main hydrated product in a cement paste is a gel-like phase termed calcium-silicate-hydrate (C-S-H). There is a general agreement that the C-S-H is the only percolating phase in hydrated cementitious systems. This means that the properties of C-S-H dictate some of the most important macroscopic properties in a hydrated cement matrix such as mechanical properties, transport properties and implicitly durability related issues (corrosion resistance).

C-S-H is a poorly ordered phase. As a result, characterization techniques such as XRD cannot reveal much information about its crystallinity. The structure of C-S-H has been associated with that of the natural mineral tobermorite, having layers of calcium and oxygen with silicate tetrahedra attached and interrupted by water and further calcium ions (Jennings 2000). Due to the importance of C–S–H as the binding phase of Portland cement, it has been extensively studied over many decades. For investigation purposes, C-S-H can be obtained either by precipitation from chemical reactants in solution or by hydrating Portland clinker, Portland cement or alite. Generally, the resulted hydrated systems were studied all together and the C-S-H characteristics were separated from those of the other hydrates.

An effective way to study C-S-H without influences from other hydrate phases can be to consider the hydration of the reactive belite binder developed by Link et al. (Link 2017). □-C_2SH was obtained by hydrothermal method and it was further thermally activated to obtain a binder containing an X-ray amorphous calcium silicate phase with a Ca/Si ratio of 2, *x*-C_2S, □-C_2S, □-C_2S and dellaite, in various proportions depending on the processing parameters. Upon mixing with water, the X-ray amorphous phase is the first to react with water. The hydration of *x*-C_2S follows afterwards and then that of □-C_2S. □-C_2S is a very slow reactive phase. Hydration of blends of reactive belite binder and reactive silica results in changes in the C-S-H microstructure. Link observed that the morphology of the C-S-H was changed from a predominantly needle-like structure to a predominantly foil-like structure (Link 2017). This is in agreement with other studies that focused on establishing a relationship between the Ca/Si ratio of the C-S-H

and the developed microstructure. Richardson reported that in a cement paste, two types of hydrates can be identified: an 'inner product' (Ip) C-S-H of homogeneous globular morphology and an outer product with two distinct morphologies a fibrillar-like structure and a foil-like structure that appear to correlate with the C/S ratio (Richardson 2004).

Processes such as chloride ingress, sulfate attack, carbonation or calcium leaching can cause irreversible changes in the hydrated matrix and thus affect the overall performance of concrete (Angst et al. 2009). Chloride induced corrosion, as the major cause for degradation of reinforced concrete has been the subject of extensive research over the past decades. Reinforcing steel corrosion is mainly induced by the ingress of chlorides upon exposure to seawater or deicing salts. Zhnag reported that blended cements where the Ca/Si ratio is lower than that of OPC have a better behavior when it comes to chloride penetration (Zhang et al. 2017). Studies made by Moffatt (Moffatt and Thomas 2018) showed that the addition of SCMs such as fly ash and silica fume can greatly decrease the penetration of chloride in concrete in comparison to OPC.

So far, no chemical interaction has been reported between chloride ions and C-S-H in cement. However, since C-S-H is the major phase in a hydrated cement matrix, a better understanding of the chloride binding in C-S-H is highly desirable. This can lead to improved retention of chloride and thus lowering the chloride ingress.

2. EXPERIMENTAL

The starting material used in this study is an industrially synthesized □-C_2SH, with a purity of 92 % as determined by QXRD. □-C_2SH was synthesized via the hydrothermal route. A mixture of calcium hydroxide, reactive silica and 5% α-C_2SH seeds was used to prepare a paste with a water-to-solid ratio of 2. The molar ratio of CaO/SiO_2 was 2.0. The mixture was autoclaved at 190 °C for 16 hours. The resulted material was then dried at 105 °C for 24 hours. The chemical composition of the synthesized □-C_2SH was determined by XRF and is given in Table 1.

After drying, the □-C_2SH was mechanically activated by grinding for 3 minutes using a disk-mill and then thermally activated at 460 °C for either 1 or 2 hours. The annealed binder was rapidly cooled down in air and soft ground for 1 minute. Pastes were prepared using water-to-binder ratios of 0.35, 0.4, 0.5 and 0.8, mixed at high speeds and at a high shearing rate. Hydrate characteristics were observed at different ages (1, 3, 7, 14 and 28 days) by stopping the hydration reaction using the solvent exchange technique. One part of the sample was sliced in pellets of 3 mm and kept in isopropanol for 48 hours followed by 30 min in petroleum ether, for complete removal of the isopropanol. Subsequently, the samples were stored in desiccator for at least 48 h. Another part of the hydrated sample was crushed by hand in a mortar and kept in isopropanol for 20 min, then vacuum filtered. After that, the crushed sample was flushed twice with petroleum ether to remove the isopropanol and also kept in desiccator for at least 48 h prior to any analysis.

Table 1. Chemical composition of □-C_2SH determined by XRF analysis

Oxide	CaO	SiO_2	MgO	K_2O	Al_2O_3	LOI (1050° C)
Amount, %	56.83	30.78	0.53	0.14	0.03	11.48

Thermogravimetric analysis (TGA) was carried out on hydrated powder specimens. The weight loss was monitored while heating up a 30-31 mg sample from 30 to 1050 °C at 20°C/min. XRD patterns were recorded on powder samples with particle size below 60 □m and Rietveld refinement was used to determine the mineralogical composition. Hydration kinetics were followed by means of isothermal calorimetry on pastes prepared with water-to-binder ratio of 0.8. Heat flow was measured for 7 days under isothermal conditions at 20°C.

Scanning electron microscopy (SEM) images were acquired in secondary electrons mode and used to observe the morphology of the hydrates. In order to determine the Ca/Si ratio of the C-S-H and the homogeneity of the elements in the hydrates, SEM images were acquired in back-scattered electron (BSE) mode too. Both freshly fractured surfaces as well as thin pellets from the hydrated samples embedded in epoxy resin were used for SEM data acquisition. All TGA, QXRD and SEM measurements were carried out on hydrated specimens after 1, 3, 7, 14 and 28 days of hydration. Additionally, MIP measurements were carried out on fractions between 0.1 mm and 0.2 mm from hydrated specimens cast with w/b ratios of 0.35, 0.4, 0.5 and 0.8 at 14 or 28 days of hydration. BET specific surface was determined by nitrogen absorption for the binder powder after annealing at 460 °C for 1 hour.

3. RESULTS AND DISCUSSION

Quantitative XRD (QXRD) was used to determine the purity for the □-C_2SH (Figure. 1 a). Apart from 91.95% □-C_2SH, small amounts of calcite, scawtite and portlandite were also detected.

An optimum annealing step is essential for obtaining a highly reactive dicalcium silicate binder. In order to achieve this, all water should be entirely removed from the structure and a full conversion of □-C_2SH into amorphous and *x*-C_2S phase has to take place during the annealing step.

QXRD results carried out after the annealing step show a maximum content of these aforementioned phases of 81 % (Figure 1 b), with the main phase being the amorphous one with over 60%. An unhydrated binder with such a high amorphous

content, makes the quantification of hydration degree difficult. The only phase whose consumption over time can be determined is *x*-C_2S. However, an approximate degree of hydration can be determined considering that *x*-C_2S starts to react once the amorphous is depleted.

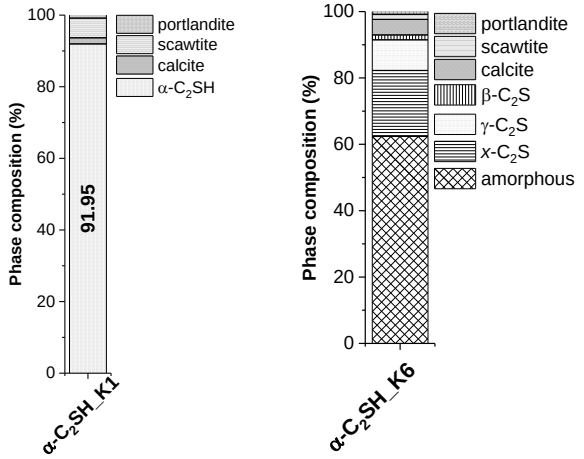

a **b**

Figure 1. Chemical composition of □-C_2SH (a) and of dicalcium silicate binder (b), determined by quantitative XRD (QXRD).

Up to 7 days, the heat flow curve, measured by isothermal calorimetry shows the main peak of hydration occurring in the first 12 hours following mixing with water. No second hydration reaction is observed up to 7 days.

The morphology of the □-C_2SH and of the binder and the particles sizes were evaluated by means of SEM images. The □-C_2SH particles were found to be small in size (< 10 □m) with plate-like aspect, different shapes and different dimension ratios (due to grinding). The materials before and after annealing have similar morphology, proving that removing the water from the structure did not change the microstructure. BSE images collected from powder samples hydrated for 1 day at water-to-binder ratio 0.5 indicate a hydrate network formed from elongated particles with needle-like aspect of different lengths and mostly intergrown (Figure 2).

The microstructure of the hydrated binder was observed under SEM in BSE mode. The light areas represent inert impurities particles. Given that the material is ground to a d_{50} < 10 □m, we observed a high tendency to form denser agglomerates of hydrates surrounded by a more porous matrix of outer C-S-H. The lack of inner C-S-H is explained by the high reactivity of the binder and its rapid hydration, combined with the small particle size. Having a matrix formed exclusively by outer C-S-H (Figure 3) is an advantage over the heterogeneous microstructure of OPC, which contains both inner and outer C-S-H product, as well as other hydrates and unreacted clinker grains. So far, SEM investigations indicate that these binders are made of small-seized particles. Additionally, BET measurements evidenced a surface area of approximatively 10 m^2/g. These aspects are known to lead in practice to high water demands in order to achieve proper workability. Indeed, a water-to-binder ratio of 0.8 was required. However, this resulted in a high matrix porosity as observed by SEM and MIP.

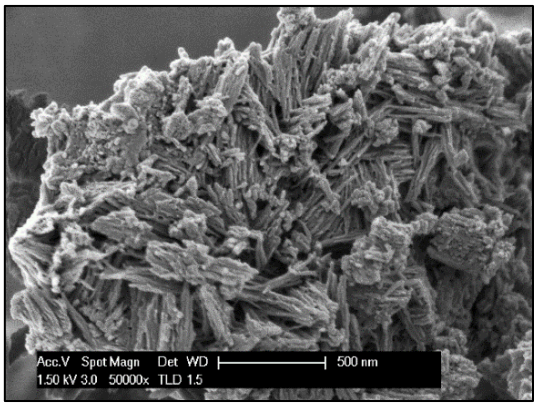

Figure 2. SEM image of hydrated binder prepared with a w/b ratio of 0.5 after 1 day hydration (Image taken by Emmanuelle Boehm-Courjault at LMC, EPFL, CH)

With the aid of a superplasticizer (BASF ACE 30) pastes of lower water-to-binder ratios such as 0.5, 0.4 and 0.35 could be prepared as well. Full hydration can be still achieved in these samples considering that the stoichiometric amount of water necessary for full hydration corresponds to a water-to-binder ratio of 0.45 and that the amount of reactive phases in the dicalcium silicate binders is approximatively 80 %.

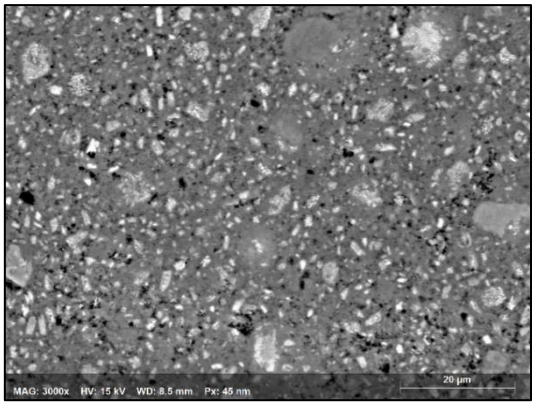

Figure 3. BSE images on polished surface of 14 days hydrated binder with w/b=0.4

Two effects were noticed when compared the pastes cast with different w/b ratios for the same hydration age. First, the total porosity quantified by MIP decreased to almost half for the paste cast with w/b ratio 0.5 compared to the paste cast with w/b 0.8 (Figure 4). This resulted in a reduction of the amount of air voids and capillary pores. The effect of w/b ratio on the reduction of gel pores can be quantified only by ^1H NMR spectroscopy.

Secondly, TGA clearly indicates differences between samples prepared with high and low w/b ratios. When comparing systems hydrated with w/b

ratios of 0.8, 0.5, 0.4 and 0.35, the following aspects could be noticed:
a) Despite a lower initial water content, when decreasing w/b ratio, the total weight loss increases.
b) The amount of portlandite content in the hydrated specimens decreased with lowering w/b ratio and for the paste with the lowest w/b ratio (0.35) no portlandite effect could be observed on the DTG curve. The possibility of portlandite carbonation was excluded, as calcite effect is insignificant on the DTG curve (Figure 5).
c) The amount of C-S-H increases with lowering w/b ratio. Most likely this can be explained by the fact that the more Ca^{2+} ions are incorporated in the C-S-H, the more water molecules they can attract and retain in hydrated microstructure. The possibility of very fine portlandite precipitated in the C-S-H outer product is not excluded. The best way to confirm or reject the hypothesis of the presence of portlandite would be to analyze the systems by means of ^{1}H NMR and reveal the different water populations found in the microstructure.

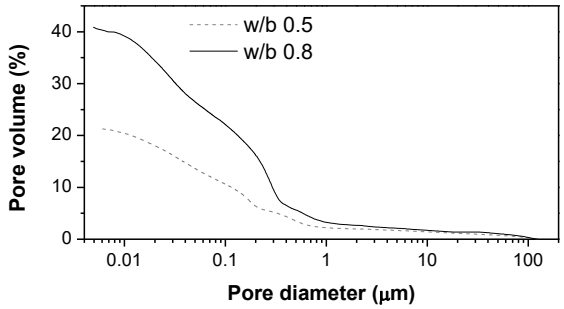

Figure 4. MIP curves for hydrated pastes prepared with different water-to-binder ratios

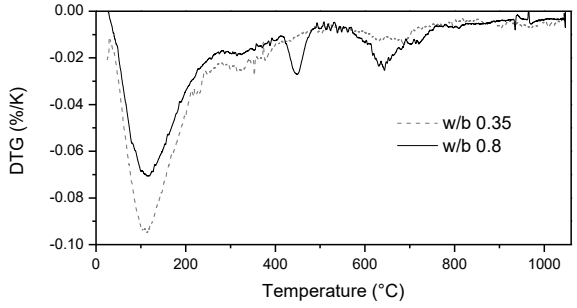

Figure 5. DTG curves for hydrated pastes prepared with different water-to-binder ratios

By observing the microstructure of the two systems hydrated with the lower w/b ratios, no significant portlandite clusters could be observed. As expected, the microstructure for the samples prepared with the lower w/b ratios is denser compared to the systems hydrated with w/b ratio of 0.8 and 0.5. Also, when comparing the chemical composition of C-S-H for the four systems, an increase of the Ca/Si ratio was observed, from 1.67 (in the system with w/b ratio 0.8) to almost 2.0 (in the systems with w/b ratio 0.35 and 0.4).

4. CONCLUSIONS AND PERSPECTIVES

The dicalcium silicate binder hydrates rapidly and forms a hydrated system composed mainly of C-S-H, without significant amounts of unreacted phases nor other hydrates such as portlandite. Thus, this material can be considered an excellent candidate for obtaining a C-S-H rich microstructure suitable for studying the transport properties, the influences of additional elements and the changes in the C-S-H chemical composition.
In what follows, to gain more knowledge on the transport of chloride ions through the C-S-H matrix, two types of tests will be performed. First, the chloride binding test in C-S-H will be carried out on the neat belite binder considered as reference system, to assess the content of bound chloride that can be retained in C-S-H structure. Secondly, hydrated samples saturated in water will be subjected to rapid chloride diffusivity tests (migration) to evaluate how free chloride is transported through the porous network.
Thirdly, studying the transport properties as a function of the chemistry of the system will be carried out by hydrating different mixtures of the reactive binder blended with other materials. For example, silica will be used to lower the Ca/Si ratio in the C-S-H while aluminium and alkali will be considered as foreign elements. The properties and performances of the modified systems will be evaluated by comparison against the neat hydrated belite system.

AKNOLEDGEMENTS

The research leading to these results has received funding from H2020-MSCA-ITN ERICA project with Grant Agreement 764691.

REFERENCES

Angst, Ueli, Bernhard Elsener, Claus K. Larsen, and Øystein Vennesland. 2009. “Critical Chloride Content in Reinforced Concrete - A Review.” *Cement and Concrete Research* 39(12): 1122–38.

Jennings, Hamlin M. 2000. “A Model for the Microstructure of Calcium Silicate Hydrate in Cement Paste.” *Cement and Concrete Research* 30(6): 101–16.

John, Elisabeth, Thomas Matschei, and Dietmar Stephan. 2018. “Nucleation Seeding with Calcium Silicate Hydrate – A Review.” *Cement and Concrete Research* 113(May): 74–85. https://doi.org/10.1016/j.cemconres.2018.07.003.

Link, Tim. 2017. “Entwicklung Und Untersuchung von Alternativen Dicalciumsilicat-Bindern Auf Der Basis von α -C 2 SH.” Bauhaus-Universität Weimar.

Moffatt, E. G., and M. D.A. Thomas. 2018. “Performance of 25-Year-Old Silica Fume and Fly Ash Lightweight Concrete Blocks in a

Harsh Marine Environment." *Cement and Concrete Research* 113(March): 65–73.
Richardson, I. G. 2004. "Tobermorite/Jennite- and Tobermorite/Calcium Hydroxide-Based Models for the Structure of C-S-H: Applicability to Hardened Pastes of Tricalcium Silicate, β-Dicalcium Silicate, Portland Cement, and Blends of Portland Cement with Blast-Furnace Slag, Metakaol." *Cement and Concrete Research* 34(9): 1733–77.
Zhang, Lina et al. 2017. "Novel Understanding of Calcium Silicate Hydrate from Dilute Hydration." *Cement and Concrete Research* 99(July 2015): 95–105. http://dx.doi.org/10.1016/j.cemconres.2017.04.016.

39th Cement and Concrete Science Conference
9-10th September 2019
University of Bath
Paper Number 079

Study of the use of Agricultural Waste as a Supplementary Cementitious Material

T. I. M. Abdel-Magid, S. Allen, K. Paine and P. Walker
Department of Architecture and Civil Engineering, University of Bath

ABSTRACT

The use of supplementary cementitious materials has attracted attention in recent years both for their potential applications and beneficial cost in the construction industry. Supplementary cementitious materials can be of mineral or plant origin. Agricultural waste (agro-waste) is under focus especially in low and middle income countries as a source for fuel and also as a construction material. Such use comes either as a stand-alone material or as a cement replacement in concrete materials. The wider use of such materials in construction is considered as potential sustainable alternatives to Portland cements. This paper discusses the prospective use of certain agro-wastes as a partial replacement for cement in concrete mixes and stabilised earth bricks. The materials considered in this study have included: corncob, sorghum husk, sorghum stalk, peanut husk and sesame stalk ashes. Selected agro-wastes have been incinerated under controlled temperature conditions at 500°C and 700°C. The resultant ashes have been characterised using Thermal Gravimetric Analysis (TGA), Energy Dispersive X-Ray Analyser (EDX) and X-Ray Diffraction Analysis (XRD) methods. Silica, used as a pozzolanic indicator, was found to be present in varying quantities. More tests to verify suitability and determine the feasibility of these agro-wastes are currently underway. The paper presents the preliminary results and outcomes, and describes proposed methodology for future tests.

1. INTRODUCTION

Producing sustainable materials has been a concern ever since the construction industry has recognised itself to be one of the largest contributors of greenhouse gas (GHG) emissions. The construction sector is also one of the largest consumers of non-renewable raw materials, and a top contributor to energy consumption, GHG emissions, and waste flow worldwide (IEA, 2019). In developing countries, such as Sudan, the challenge to produce sustainable construction materials is exacerbated by the cost of materials. In the search for cheaper alternatives agricultural wastes, such as rice husk and bagasse, have been researched to assess their suitability as a cement component in concrete (Habeeb and Mahmud, 2010; Chao-Lung, Anh-Tuan and Chun-Tsun, 2011; Ahsan and Hossain, 2018; Xu *et al.*, 2018) or brick production (Sutas, Mana and Pitak, 2012; Shakir *et al.*, 2013). These studies proved the potential use of agricultural waste as a cementitious material due to their pozzolanic nature. For a material to be categorized as pozzolanic it should react with hydrated lime in the presence of water to produce cement hydrates. this reaction is mainly caused by amorphous silica, which does not react with other compounds until its network is broken by the alkaline environment of the cement paste (Papatzani, Badogiannis and Paine, 2018). Typically pozzolanic materials should have a combined content of amorphous silica (SiO_2), iron oxide and aluminium oxide greater than 70% of total mass (Aprianti *et al.*, 2015).

Agricultural materials are mainly constructed of cellulose, hemicellulose and lignin in different percentages, with the cellulose and hemicellulose occupying up to 80% of the composite (Mlonka-Mędrala *et al.*, 2019). Burning the wastes of agricultural crops results in decomposition of these three components, and the elimination of carbon. This has potential to , produce a waste product rich in amorphous silica.

Research has shown that different burning and cooling temperatures affect the quality and composition of the ash. For example, the amount and phase of silica, as well as fineness, particle size and surface area are affected (Zain *et al.*, 2011). These properties in turn affect the reactivity of the resultant ash, and hence how quickly a concrete mix will gain strength, as well as affecting the other green concrete properties (Givi *et al.*, 2010; Cordeiro and Kurtis, 2017).

For the purpose of this study, the waste of the four most commonly cultivated plants in Sudan (sorghum, corn, peanut and sesame) were selected to study their pozzolanic behaviour and potential to use them as supplements to cement.

2. Materials

Materials used in this study were sesame husk, sorghum husk and stalk, peanut husk and corncob husk ashes. Corncobs were bought from the local markets in Bath, UK; all of the other materials were imported from Sudan from relevant production sites in Algadarif, Portsudan, and Khartoum.

2.1 Material Treatment

Initially agro-waste materials were washed thoroughly to remove any residual contaminants from harvest or storage. They were then dried in an oven at 105°C and weighed regularly until constant mass was reached, which indicated all water had evaporated. The materials were then ground to fine powder using a domestic coffee grinder, and finally screened through a 100mm sieve.

3. Results and Discussions

3.1 X-ray Diffraction (XRD)

XRD test was carried out on the specimens, the results are as depicted in Figure 1, the samples under study were found to be amorphous. The peaks are not well defined, with the X-rays diffracted in different directions and at different intensities. This is a typical pattern expected for an amorphous material with no distinct pattern of atoms (Cullity, 1978). This result is encouraging to believe that silica existing in the material is amorphous among other components.

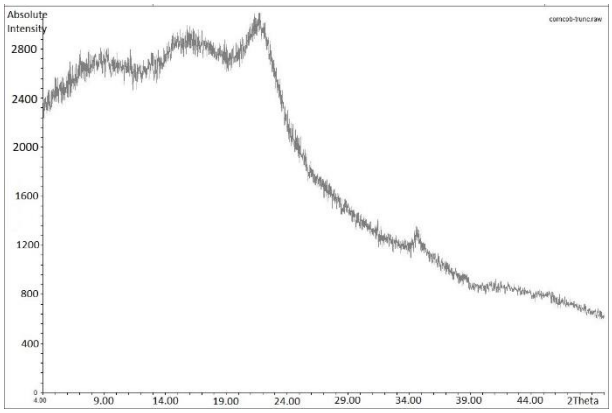

Figure 1: X-Ray Diffraction pattern of a corncob sample

3.2 Thermogravimetric Analysis (TGA)

The TGA test was conducted for the five specimens. For each material, the test was carried out twice on a 25-35mg sample. For the first round, the materials were burnt until 500°C, while burning for the second round continued up to 700°C. Test was carried out to determine the expected mass loss, chemical composition and the thermal decomposition of the waste. Specimens were burnt in air at a heating rate of 10°/min. To preserve the initial amorphous state of the samples, the cooling rate was gradual.

From the TGA, and the derivative thermogravimetric (DTG) curves, shown in Figure 2a, it can be seen that the results were consistent with the literature. The bound water evaporation slightly affected the mass loss curve at the start until a temperature of 160°C. The pyrolysis of the samples was expected to go through four stages, starting with the water evaporation then continuing to decomposition in the order of hemicellulose, cellulose and lignin (Yang *et al.*, 2007). Decomposition of the hemicellulose is concurrent with the major loss in mass (~0.80wt.%/°C) at 240°-320°C. The next small convex in the TGA curves between 310°C and 450°C is coinciding with the decomposition of cellulose (Yang *et al.*, 2007).

The mass loss can be seen from the TGA curves presented in Figure 2, with the highest loss to reach 97-98% of mass in peanut husk and corncob. Sorghum stalk and sesame stalk showed the median loss of 93-96% of mass. The sorghum husk showed the least mass loss (89-90% of mass). From the curves it is obvious that the difference in mass is negligible between 500°C and 700°C, also no significant change on the curve occurs, which means no significant decomposition is taking place in samples after 500°C.

Differential Scanning Calorimetry (DSC) works on the principle of measuring the difference in temperature between a reference crucible and the sample (Lawrence, 2006). As can be observed from Figure 2 (b, d, f, h and J) the decomposition of two of the material components (hemicellulose and lignin) coincided with the DTG curves at 240-320^{o}C, and it can be described as an exothermic reaction. While the decomposition of the cellulose, resulted in a small convex in the DSC curve at 310-450^{o}C, and is supposed to be an endothermic reaction (Yang *et al.*, 2007) it shows as exothermic. This could be attributed to the fact that the material has all three components and the results are overlapping, the endothermic (negative) curve of hemicellulose might be the reason the next exothermic (positive) convex is considerably small.

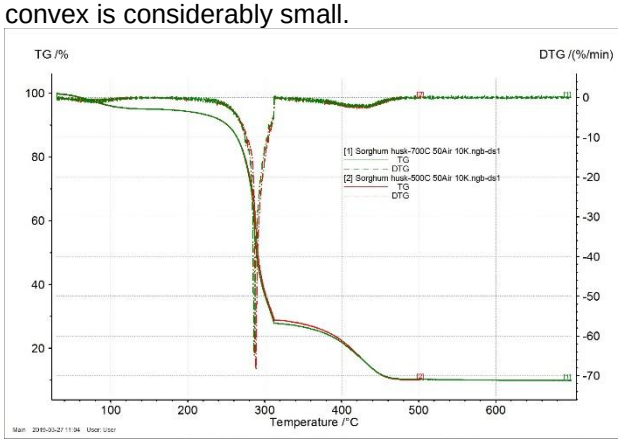

a)

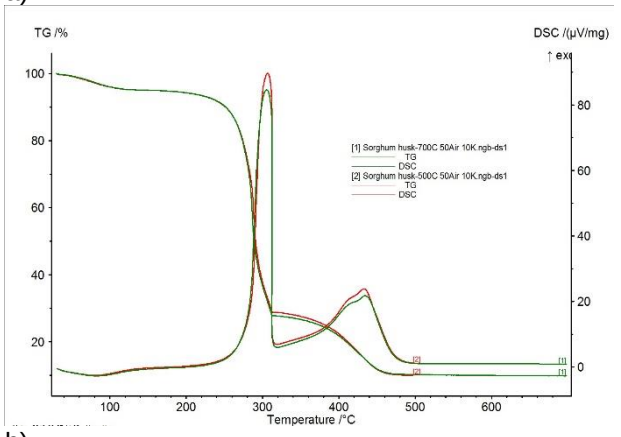

b)

Figure 2: TGA-DTG-DSC results: a) Sorghum husk TGA-DTG b) Sorghum husk TGA-DSC

3.3 Energy Dispersive X-Ray Spectroscopy (EDX)

Samples were prepared on a carbon tape and tested using Scanning Electron Microscope. The equipment used was a Jeol 6480LV SEM, with an Oxford instrument X-ACT 10mm^2 Si drift detector. Both raw and burnt materials were tested; results are as presented in Figures 3a and b respectively. Specimens were compared with rice husk which literature showed as having good potential for partially replacing cement. Other elements like Na, Mg, Al, P, S and Cl were present on the specimens, but they have been omitted from presentation due to their very low concentration.

From Figure 3 it can be seen that burning decreased the amount of carbon present. Even so, a large amount was present (around 40%); this could be attributed to the fact that the specimens were tested on a carbon tape. The burnt materials possessed relatively high amounts of Si, K and Ca. The highest amount of silicon (~20%) was present in the sorghum husk, followed by the sorghum husk and corn cob in 500ºC (~7%). Peanut husk showed very small amounts of silicon, whilst sesame hardly presented any silicon at all. It is noted that EDX shows materials not compounds. As such, this present silicon does not confirm conclusively the existence of silicon dioxide.

The process of peeling sorghum husk from the stalk could be inconvenient for field application. Hence, future tests are to be conducted on the sorghum stalk and husk as a one entity.

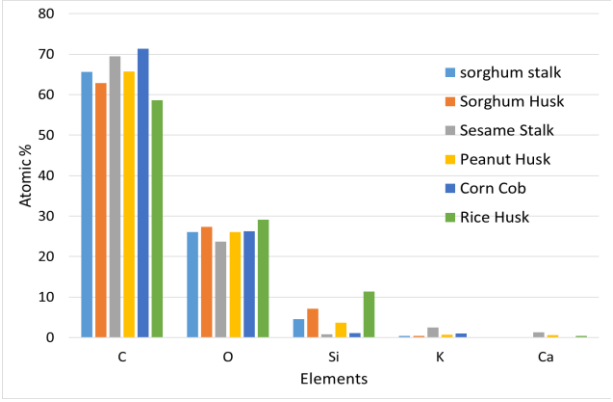

a)

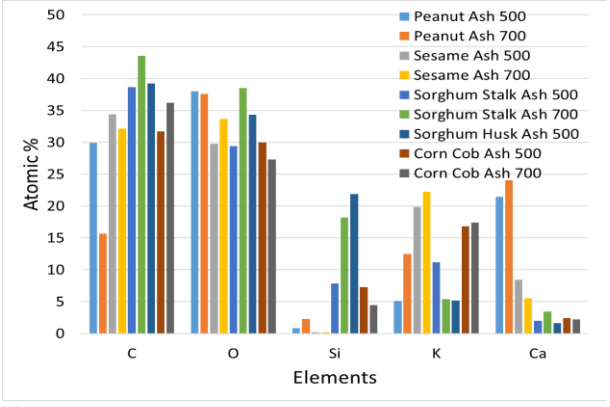

b)

Figure 3. EDX results a) raw materials b) burnt materials in 500°C and 700°C.

4. Future Work

The tests discussed in this concept paper were conducted to test he potential viability of sorghum husk, sesame stalk, peanut husk, and corncob ashes as a partial supplement of cement. From the preliminary tests the upcoming research is going to focus on sorghum husk and stalks, and corncob ashes as a cement replacement in concrete. Peanut husk and sesame stalk are going to be tested as an unburnt material in brick production or insulating materials.

From the tests it was found that there was no need to burn materials beyond 500ºC; this will be the target temperature in future work. With the help and support of the BRE Chair of Fire Safety Engineering located within the University of Edinburgh, the materials are to be prepared and burnt. Future tests are to be conducted in collaboration with the University of Edinburgh, School of Engineering.

Particle size, surface area and fineness are to be tested. X-ray fluorescence tests are going to be applied to evaluate the presence of silicon dioxide and other compounds in the materials.

Samples are going to be prepared in order to test the pozzolanicity. Targeted tests include: calorimetry, Portlandite consumption and bound water. Afterwards samples with lime and cement are to be prepared and tested for physical including compressive and tensile strengths.

Development of a computer model, using GEM-Selektor v3.4, a thermodynamic modelling software, is planned. After preparing a model, and verifying it with the tested samples, other properties of the cement paste and concrete are going to be studied, such as heat of hydration and reactivity. Sensitivity analysis is going to be applied using the model regarding the change in the materials percentages in the paste.

Future work also includes a Life Cycle Assessment (LCA), where the environmental impact of using these wastes in concrete production is going to be assessed with the aid of OpenLCA software. For this step, product category rules are going to be collected and studied for the involved products, and data quality assessment should be conducted as the LCA goes on. Sensitivity analysis is going to be performed to see how the change in material percentage will affect the mid-point and end-point results of the assessment. Cost benefit is also planned as the final step of this research.

REFERENCES

Ahsan, M. B. and Hossain, Z. (2018) 'Supplemental use of rice husk ash (RHA) as a cementitious material in concrete industry', *Construction and*

Building Materials. doi: 10.1016/j.conbuildmat.2018.05.101.
Aprianti, E. *et al.* (2015) 'Supplementary cementitious materials origin from agricultural wastes – A review', *Construction and Building Materials*. Elsevier, 74, pp. 176–187. doi: 10.1016/J.CONBUILDMAT.2014.10.010.
Chao-Lung, H., Anh-Tuan, B. Le and Chun-Tsun, C. (2011) 'Effect of rice husk ash on the strength and durability characteristics of concrete', *Construction and Building Materials*. Elsevier Ltd, 25(9), pp. 3768–3772. doi: 10.1016/j.conbuildmat.2011.04.009.
Cordeiro, G. C. and Kurtis, K. E. (2017) 'Effect of mechanical processing on sugar cane bagasse ash pozzolanicity', *Cement and Concrete Research*. Elsevier Ltd, 97, pp. 41–49. doi: 10.1016/j.cemconres.2017.03.008.
Cullity, B. D. (1978) *Elements of X-Ray Diffraction*. Edited by M. Cohen. Addison-Wesley Publishing Company Inc.
Givi, A. N. *et al.* (2010) 'Assessment of the effects of rice husk ash particle size on strength, water permeability and workability of binary blended concrete', *Construction and Building Materials*. Elsevier Ltd, 24(11), pp. 2145–2150. doi: 10.1016/j.conbuildmat.2010.04.045.
Habeeb, G. A. and Mahmud, H. Bin (2010) 'Study on properties of rice husk ash and its use as cement replacement material', *Materials Research*, 13(2), pp. 185–190. doi: 10.1590/S1516-14392010000200011.
IEA: International Energy Agency (2019), Sustainable Buildings, Available from: http://www.iea.org/etp/buildings/ (Accessed 25 June 2019)
Lawrence, R. M. H. (2006) 'A study of carbonation in non-hydraulic lime mortars', *PhD Thesis*, p. 344.
Mlonka-Mędrala, A. *et al.* (2019) 'Laboratory studies on the influence of biomass particle size on pyrolysis and combustion using TG GC/MS', *Fuel*. doi: 10.1016/j.fuel.2019.04.091.
Papatzani, S., Badogiannis, E. G. and Paine, K. (2018) 'The pozzolanic properties of inorganic and organomodified nano-montmorillonite dispersions', *Construction and Building Materials*, 167, pp. 299–316. doi: 10.1016/j.conbuildmat.2018.01.123.
Shakir, A. a *et al.* (2013) 'Development Of Bricks From Waste Material: A Review Paper', *Australian Journal of Basic and Applied Sciences*, 7(8), pp. 812–818.
Sutas, J., Mana, A. and Pitak, L. (2012) 'Effect of rice husk and rice husk ash to properties of bricks', *Procedia Engineering*. Elsevier B.V., 32, pp. 1061–1067. doi: 10.1016/j.proeng.2012.02.055.
Xu, Q. *et al.* (2018) 'Characteristics and Applications of Sugar Cane Bagasse Ash Waste in Cementitious Materials', *Materials*, 12(1), p. 39. doi: 10.3390/ma12010039.
Yang, H. *et al.* (2007) 'Characteristics of hemicellulose, cellulose and lignin pyrolysis', *Fuel*. doi: 10.1016/j.fuel.2006.12.013.
Zain, M. F. M. *et al.* (2011) 'Production of rice husk ash for use in concrete as a supplementary cementitious material', *Construction and Building Materials*. Elsevier Ltd, 25(2), pp. 798–805. doi: 10.1016/j.conbuildmat.2010.07.003.